CONFERENCE PROCEEDINGS 7

Fourth International Bridge Engineering Conference

Volume 2

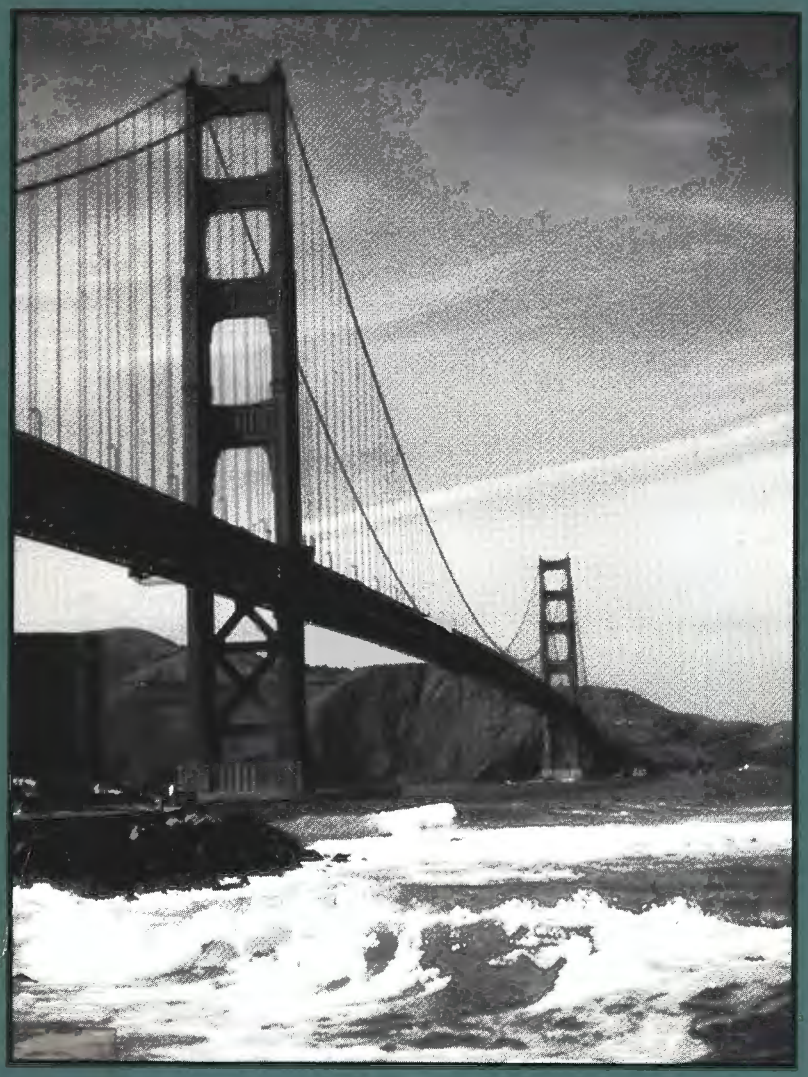

TRANSPORTATION RESEARCH BOARD

NATIONAL RESEARCH COUNCIL

CONFERENCE PROCEEDINGS 7

Fourth International Bridge Engineering Conference

Volume 2

San Francisco, California
August 28–30, 1995

Sponsored by

Transportation Research Board
Federal Highway Administration
Federal Railroad Administration
American Association of State Highway and Transportation Officials
California Department of Transportation

TRANSPORTATION RESEARCH BOARD

NATIONAL RESEARCH COUNCIL

NATIONAL ACADEMY PRESS
WASHINGTON, D.C. 1995

Conference Proceedings 7
ISSN 1073-1652
ISBN 0-309-06109-1

Subscriber Category
IIC bridges, other structures, and hydraulics and hydrology

Printed in the United States of America

NOTICE: The conference that is the subject of this report was approved by the Governing Board of the National Research Council, whose members are drawn from the councils of the National Academy of Sciences, the National Academy of Engineering, and the Institute of Medicine. The members of the committee responsible for the report were chosen for their special competence and with regard for appropriate balance.

The papers in this report have been reviewed by a group other than the authors according to procedures approved by the Governing Board of the National Research Council. The views expressed are those of the authors and do not necessarily reflect the views of the Transportation Research Board, the National Research Council, or the sponsors of the conference.

The conference was sponsored by the Federal Highway Administration and the Federal Railroad Administration of the U.S. Department of Transportation, the American Association of State Highway and Transportation Officials, and the California Department of Transportation.

Contents

BRIDGE PERFORMANCE

BRIDGE CONSTRUCTION

BRIDGE MANAGEMENT SYSTEMS, PART 2

VOLUME 2

BRIDGE REHABILITATION

SEISMIC RESPONSE OF BRIDGES

Introduction

Transportation systems of the world represent a huge investment on the part of governments and taxpayers. There is widespread concern over the status of the infrastructure, and despite indications of increased investment, it is clear that the funds available are not likely to meet all the needs of this sector in the long run. More than ever, wise investment decisions concerning roads and bridges will be crucial to the future of transportation.

This conference is the fourth in a series of International Bridge Engineering Conferences. Previous conferences were held in St. Louis, Missouri, in 1978; Minneapolis, Minnesota, in 1984; and Denver, Colorado, in 1991. Those conferences were well attended, and valuable information was presented and published. Much has transpired since the 1991 conference that should be brought to the attention of the user community.

Objective

The objective of the conference is to provide an international forum for the exchange of bridge research results and technical information on planning, design, construction, repair, rehabilitation, replacement, and maintenance of bridges. The focus is on problems and solutions of interest to bridge engineers and administrators of highway, railroad, and transit agencies. Research results emanating from the AASHTO-sponsored NCHRP bridge studies as well as those of federal, state, and international research agencies' programs are being highlighted.

Format

The conference, conducted over 2½ days, includes an opening session (not included in the Conference Proceedings) followed by concurrent paper sessions on various topics. All papers presented in those sessions are included in these Proceedings.

Conference sessions cover the following topics:

- Bridge Management Systems
- Bridge Aesthetics
- Bridge Performance
- Bridge Construction
- Long-Span Bridges
- Bridge Loads and Dynamics
- FRP Composites and Other Materials
- Bridge Rehabilitation
- Seismic Response of Bridges
- Bridge Bearings, Joints, and Details
- Prestressed Concrete Bridges
- Bridge Structural Systems
- Bridge Substructures: Scour and Ship Impact
- Bridge Fatigue and Redundancy
- Wood Bridges

Conference Proceedings

The proceedings of the Fourth International Bridge Engineering Conference is being published in two volumes. The two-volume set will be distributed to all conference attendees and is available for purchase through the Transportation Research Board. All papers contained in these proceedings underwent full TRB peer review.

BRIDGE REHABILITATION

Cracking, Fracture Assessment, and Repairs of Green River Bridge, I-26

John W. Fisher and Eric J. Kaufmann, *Lehigh University*
Michael J. Koob, *Wiss, Janney, Elstner Associates, Inc.*
Gerald White, *North Carolina Department of Transportation*

The Green River Bridge, I-26 near Asheville, North Carolina, was opened to traffic in 1969. In October 1992, during an inspection, two long transverse cracks were discovered in the bottom flange plate of a main girder; these cracks resulted in closure of the eastbound bridge. Numerous shorter cracks were observed at the web to flange plate connecting fillet welds throughout the girders. The Green River Bridge is a five-span, twin structure having a total length of 320 m (1,050 ft). Each bridge is a two-girder system, and ASTM A441 modified Corten B weathering steel was used to fabricate the bridge. The investigation into the cause of the cracking included metallographic and fractographic examination of core samples containing cracks, chemical composition and toughness testing of material, and instrumentation and field testing to determine live load stress levels. Test results of the flange plate material containing the large cracks showed it to have high carbon content, large grain structure, very low toughness, and high hardness. A field hardness survey was carried out on all bottom flange plates to determine locations of plates in the structure with similar properties. The fatigue and fracture assessment found that the cracks discovered in the Green River Bridge occurred at the time of fabrication. All cracks appeared to result from hydrogen-related cold cracking. Orientation of the large cracks was influenced by welding residual stresses that caused the crack tip to turn to a nearly horizontal orientation (parallel to the stress field). Because of this favorable crack tip orientation, the large cracks could tolerate dead and live load stresses and fatigue crack growth and brittle fracture were prevented. The main retrofit recommendation was to bolt cover plates on all bottom flange plates subjected to tensile stresses using high-strength bolts. This retrofit will provide internal redundancy in all spans and reduce live load stress range levels in the two-girder system by about 50 percent. Repairs were completed in October 1994.

The Green River Bridge, located about 50 km (30 mi) southeast of Asheville, North Carolina, carries Interstate 26 across the Green River. This twin structure consists of five spans having a total length of 320 m (1,050 ft): a continuous unit of spans 80, 100, and 80 m (260, 330, and 260 ft) long over the river and simple spans of 30.5 m (100 ft) at each end. A view looking west between the twin bridge structures is shown in Figure 1. Each bridge carries two lanes of traffic.

The steel superstructure consists of a two-girder system using welded girders 4.3 m (14 ft) deep spaced 7.3 m (24 ft) apart. Transverse floor beams frame into these girders on approximately 73-m (24-ft) centers and support two longitudinal deck stringers. A typical cross sec-

FIGURE 1 View looking west between twin bridge structures.

tion through the bridge is shown in Figure 2. The bridge is 25 years old, and ASTM A441 modified U.S. Steel Corten B weathering steel was used to fabricate the superstructure.

In October 1992, during a North Carolina Department of Transportation (NCDOT) inspection by an engineering consultant, two long transverse cracks were found in the bottom flange plate of a main girder 7.3 m (14 ft) deep. These cracks measured 100 and 70 mm (4 and 2¾ in.), respectively, and extended through the web-to-flange plate fillet weld with extension into the bottom flange plate (Figure 3). Further inspection found many shorter cracks, of lengths up to 19 mm (¾ in.) at the web-to-flange plate connecting fillet welds throughout the girders. Two typical cracks with lengths of approximately 19 mm (¾ in.) are shown in Figure 4.

After it discovered the two long cracks, NCDOT closed the eastbound bridge. The cracks were evaluated to determine their causes and to develop retrofit recommendations to repair the bridge structures. The evaluation included metallographic and fractographic studies on core samples removed from the eastbound bridge that contained cracks, instrumentation and field testing of the westbound bridge to measure live load stress levels, testing of flange plate hardness, removal of additional cores for material testing, and recommendations for retrofitting.

The information collected from the various tasks—particularly the testing, examination of core samples, and main retrofit recommendation—is reviewed. Using the repair recommendations for the steel superstructure from this study, NCDOT developed contract plans for repairing the bridge. In September 1994, the repairs were completed to both east- and westbound structures, and they were reopened to traffic.

Primary Girder Geometry

In general, the 4.3-m-deep welded plate girders are fabricated using flange plate 610 mm (24 in.) wide with varying thickness and a web plate 16 mm (⅝ in.) thick. The 30.5-m (100-ft) end spans use three bottom flange plates 610 mm (24 in.) wide by 25 mm (1 in.) thick. A total of 25 plates make up the bottom flange of each three-span continuous girder. These plates vary in thickness from 32 to 95 mm (1¼ to 3¾ in.) thick and 610 to 760 mm (24 to 30 in.). Bolted or welded splices are used between adjacent plates. Figure 5 shows a partial evaluation of the bridge girder with flange plate dimensions and splices indicated. In total, there are 124 bottom flange plates in the four primary girders of the two bridge structures.

Cracks and Sample Removal

Cracks in the web-to-bottom flange connecting weld were observed in both eastbound and westbound structures. However, cracks of significant size that extended into the girder flanges were found only in the eastbound structure. The greatest incidence of cracking was in Girder 301G1-3, where four cracks extended into the flange plate. Figure 5 shows the location of the large cracks found in Girder 301G1-3. To determine the causes of these cracks, cores were extracted that included the largest web-flange weld cracks in Girder 301G1-3, so that fractographic studies could be carried out, and these large cracks could be removed from the eastbound structure. Three cores 75 mm (3 in.) in diameter were removed with a hole saw and contained cracks originating from the web-flange fillet weld connection. A 25-mm (1-in.) hole was also removed with a hole saw at the parapet crack tip. These cores were designated as 17, 17-1, 23, and 25, as shown schematically in a plan view of the bottom flange in Figure 6. Core 17 contained the largest crack, which consisted of two transverse weld metal cracks on opposite sides of the web that extended into the flange plate. Core 17-1 was removed at the termination of the large crack about 100 mm (4 in.) from the web plate; it contains the crack tip. Figure 7 is a view of Core 17 showing the crack. Figure 8 shows a polished and etched cross section cut longitudinally through one fillet weld in Core 17. It also shows the transverse weld metal crack and crack extension into the flange plate. The curved orientation of the crack, becoming nearly parallel to the plate surface, is shown clearly and indicates that the cracks developed without significant load on the girder allowing the crack to follow the principal stresses from fabrication.

Core 23 and 25 also contained weld metal cracks in the web-flange plate fillet weld. The two cracks ob-

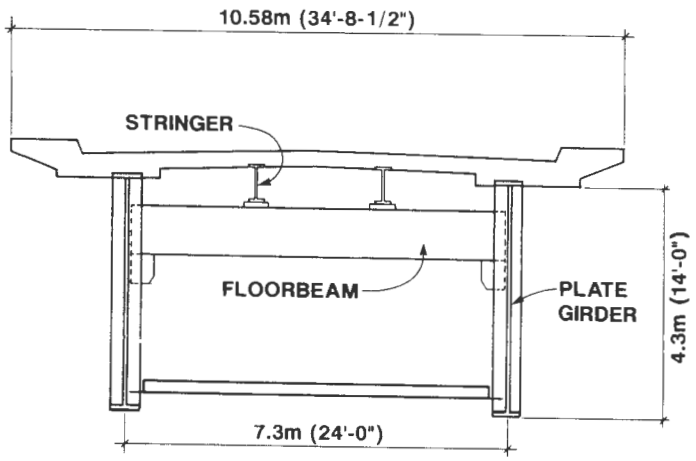

FIGURE 2 Typical cross section.

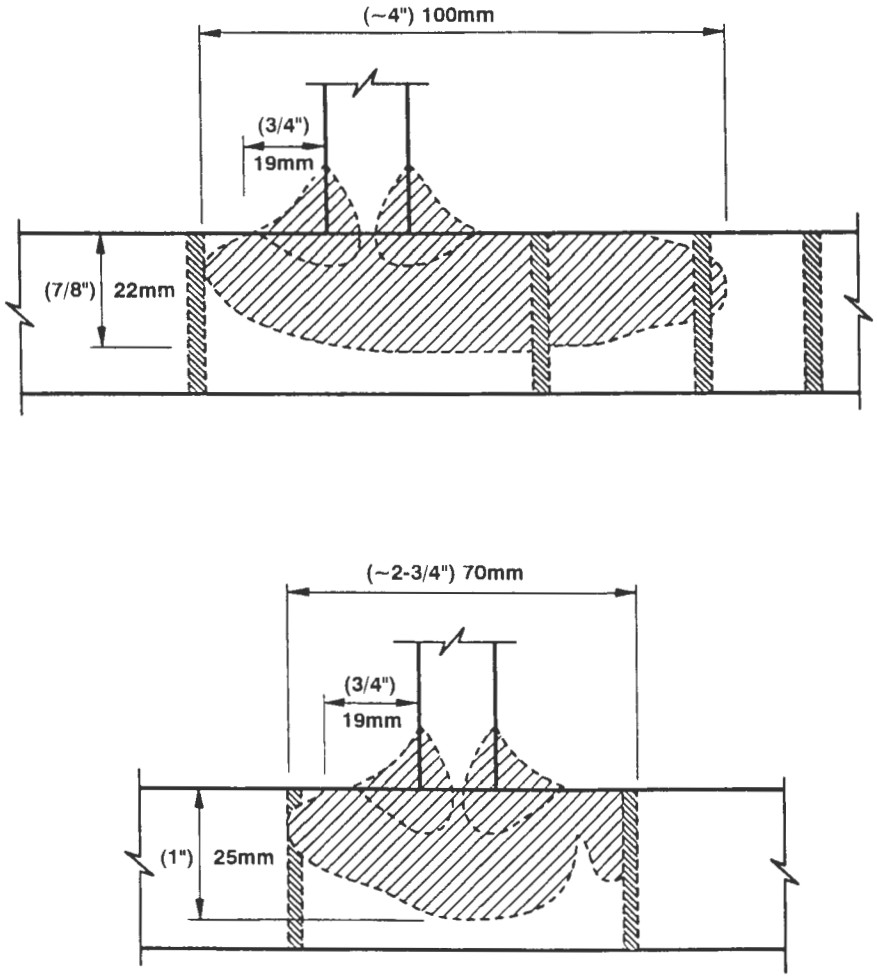

FIGURE 3 Projected crack geometry on plane perpendicular to girder flange: *top*, schematic of crack in flange at Core 17; *bottom*, schematic of crack in flange at Core 25.

FIGURE 4 Typical cracking found in web-to-flange plate fillet weld. Magnetic particles highlight two cracks.

served in Core 25 extended into the flange plate. The single weld crack detected in Core 23 terminated near the weld toe and did not extend into the flange plate.

Fractographic Examination

Cores 17 and 25, which contained the largest cracks, were opened to expose the crack surface. Figure 9 shows the crack surfaces from Core 17, where the transverse weld metal cracks and crack propagation into the flange are outlined clearly. The crack tip on one side was included; however, on the other side it can be seen to extend to the edge of the core. The crack surfaces show heavy accumulation of corrosion product, indicating exposure to the environment for several years. The crack surface is also very coarse in appearance, unlike most fatigue crack surfaces. The crack geometry shows that it propagated to within 10 mm (3/8 in.) of the underside surface of the bottom flange. No indication of crack propagation beyond the weld metal and into the web plate is indicated.

The crack surfaces from Core 25 were similar in appearance, as seen in Figure 10. The crack tip was inadvertently removed while obtaining a slice of the core for material testing. The crack tip extended into the flange about 3 mm (1/8 in.) farther than shown and to within 6 mm (1/4 in.) of the underside surface of the bottom flange plate. Heavy oxidation of the crack surface is also exhibited. Figure 10 shows two views of the fractured core; the crack in Core 25 extended into the girder flange similarly to the curved path exhibited in Core 17.

Because of heavy oxidation over most of the crack surface in both cores, fractographic examination was concentrated near the core edges and crack tips where corrosion was less severe. After as much of the corrosion product as possible was removed ultrasonically, the crack surfaces were examined with the scanning electron microscope (SEM). Figure 11 is a micrograph of the crack surface of Core 17 at the location marked "A" in Figure 9. Even though some corrosion product remains on the fracture surface, cleavage fracture is seen clearly in the micrographs. Evidence of cleavage fracture was noted at all other locations within the original crack. No evidence of stable crack extension (fatigue growth) was observed. Examination of the transverse weld metal crack surface did not yield information on the mechanism of fracture at this location because of excessive corrosion.

In an attempt to determine if any crack extension beyond the area of brittle fracture occurred under cyclic

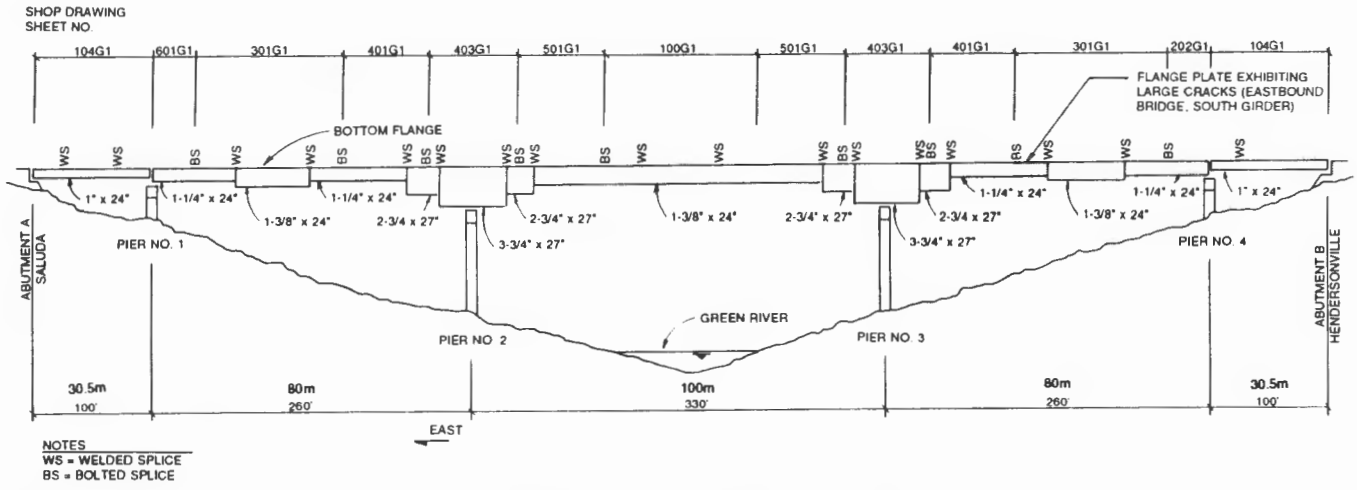

FIGURE 5 Partial evaluation of bridge showing bottom flange plate splices and dimensions.

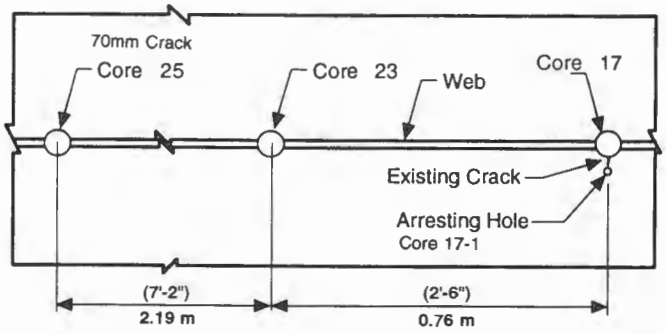

FIGURE 6 Partial schematic plan of Girder 301G1-3 at location where Cores 17, 17-1, 23, and 25 were removed.

FIGURE 9 Exposed crack surface of Core 17 showing heavy oxidation.

FIGURE 7 Core 17 showing transverse weld metal crack extending into flange; Cores 23 and 25 are similar. Arrow on web indicates west direction.

FIGURE 10 Exposed crack surface of Core 25 showing path of crack into flange plate.

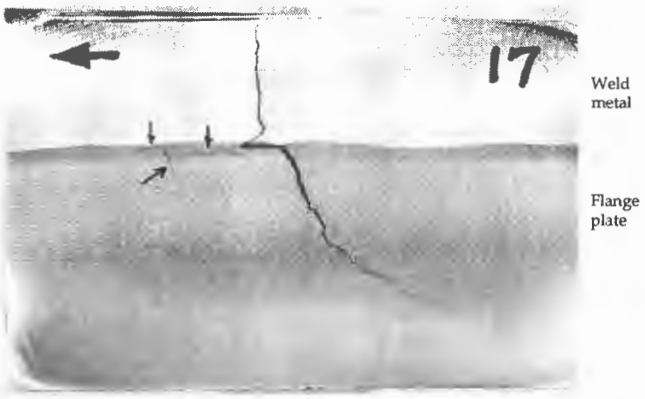

FIGURE 8 Longitudinal section through Core 17 showing transverse weld metal crack and propagation of crack into flange. Arrows show HAZ crack that propagated into base metal adjacent to primary crack.

loading, the boundary region of the original cracks was also examined. The crack surface within the small core (Core 17-1) removed at the crack tip of the large crack associated with Core 17 was examined. The micrograph of the crack surface again indicated cleavage fracture. The micrograph of the boundary between the crack surface and low-temperature fracture generated in separating the core crack surfaces did not indicate stable crack extension. Examination along the crack boundary of other core samples also did not reveal any clear evidence of fatigue crack extension. However, examination of Core 25 indicated possible evidence of fatigue crack growth at the boundary between the original crack and low-temperature fracture region. The heavy corrosion of the crack surface made it impossible to verify this elsewhere on the crack surface.

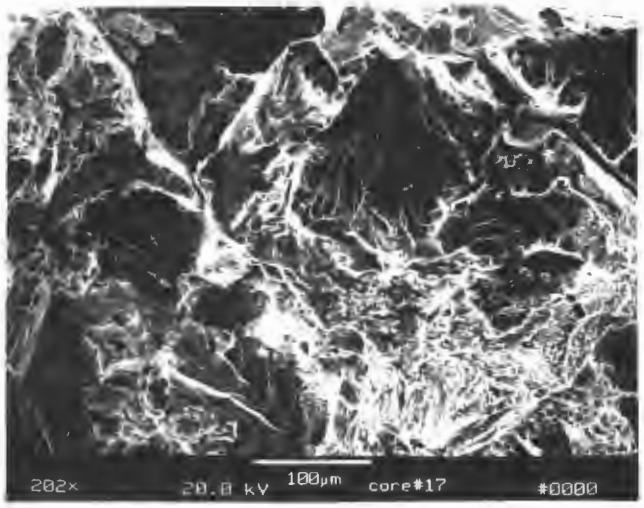

FIGURE 11 SEM micrograph of Area A (see Figure 9) of Core 17 showing cleavage fracture and corrosion product on crack surface (150×).

Material Testing

Charpy V-Notch Tests

Since the flange cracks in Cores 17 and 25 were close to through-thickness, Charpy V-notch (CVN) specimens could be machined only from Core 23 material. Six L-T orientation CVN specimens were made. Three specimens could be machined from the web plate of the girder. Specimens were tested at 4.5°C (40°F) (AASHTO Zone 2 test temperature). The average absorbed energy at 4.5°C for the flange plate specimens was 4 J (3 ft-lb), and the specimens exhibited a very coarse fracture surface appearance. At 54°C (130°F) the average absorbed energy was 10 J (8 ft-lb). Specimens machined from the 16-mm (5/8-in.) web plate indicated high toughness with an average of 67 J (50 ft-lb) at 4.5°C. The web plate material is well above the AASHTO Zone 2 requirement of 33 J (25 ft-lb) at 4.5°C for fracture-critical members.

Microstructure and Chemical Composition

The microstructure of the 32-mm (1¼-in.) flange plate obtained from Core 17 at mid-thickness is shown in Figure 12. The microstructure is predominantly pearlite with a small amount of ferrite outlining large prior austenite grain boundaries. The microstructure is typical of an annealed medium carbon steel (0.40 to 0.80 weight percent carbon) and explains the very low CVN test results obtained.

An analysis of the chemical composition of the flange material was also performed in addition to the web plate and flange to web weld metal from Core 17. The results of the analysis are given in Table 1.

The composition of the flange plate does not satisfy the requirements of ASTM A441 modified Corten B specified for the girders or any other structural-quality steel. However, the web plate meets the compositional requirements of this specification. The weld metal analysis shows a fairly high carbon content, most likely the result of pickup from the high-carbon flange material. The high carbon content of the flange plate and subsequent high carbon content of the weld metal is largely responsible for the transverse weld metal and heat-affected zone (HAZ) cracks observed in the core samples, as their susceptibility to hydrogen-induced cracking increases markedly with higher carbon content.

Hardness Testing

Rockwell hardness measurements were conducted on the flange plate for each core sample. An average hardness of Rockwell B, R_B 91 was measured. This hardness value is high and corresponds to a tensile strength of approximately 635 MPa (92 ksi).

Additional Core Samples

Five additional core samples were removed from the bottom flange of several girder sections in the eastbound bridge for material characterization to determine whether the improper flange material used in Girder

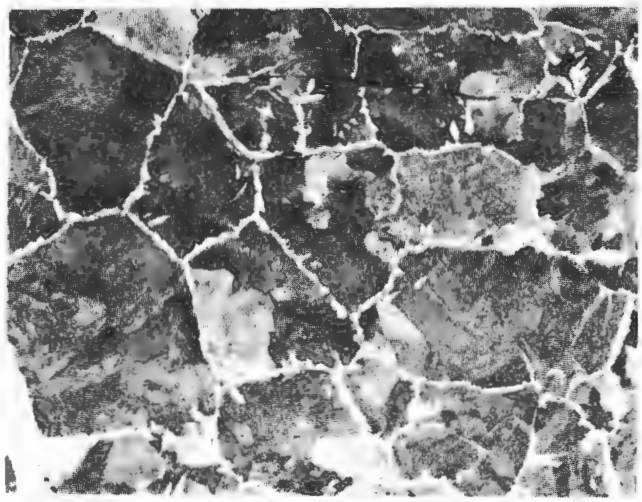

FIGURE 12 Flange plate microstructure of Core 17 (77×).

TABLE 1 Results of Analysis of Chemical Composition of Flange Material

Element	Flange Plate	Web Plate	Weld Metal	ASTM A441 Mod.
Carbon	0.47	0.20	0.19	0.10-0.19
Manganese	0.69	1.23	1.20	0.90-1.25
Phosphorus	0.012	0.016	0.013	0.04 max
Sulfur	0.023	0.047	0.026	0.05 max
Silicon	0.22	0.22	0.30	0.15-0.30
Nickel	0.03	0.04	0.79	--
Chromium	0.06	0.59	0.33	0.40-0.65
Molybdenum	0.01	0.03	0.17	--
Copper	0.04	0.30	0.26	0.25-0.40
Vanadium	<0.01	0.04	0.02	0.02-0.10
Aluminum	0.01	0.03	0.01	--
Niobium	0.005	0.008	0.009	--

301G1-3 was isolated to that girder or used in other girders in the bridge. Chemical composition, microstructure, hardness, and CVN tests were performed on the core samples.

Charpy V-Notch Tests

All five core samples showed an adequate level of toughness at 4.5°C (40°F). None of the additional cores tested provided results like those obtained from Core 23. The lowest toughness value was 20 J (15 ft-lb) at 4.5°C, which is well above the 4 J (3 ft-lb) at 4.5°C measured in Core 23.

Microstructure and Chemical Composition

Metallographic specimens were prepared for each additional core sample. The microstructures all consist of ferrite and pearlite in nearly the same proportions, with varying ferrite grain size in each plate thickness. This grain structure is the expected microstructure for the ASTM A441 Modified Corten B material specified.

An analysis of the chemical composition of the additional flange plate cores showed that the composition of the flange material is similar and within the A441 specification. The chemical compositions recorded should not have harmed the weldability if proper welding procedures were followed.

Hardness Measurements

The hardness measurements performed on these samples were less in all cases and more typical of A588-type material. Hardness values ranged from R_B 84.5 to 89.2 with an average value of 86.6 for these samples. The higher hardness of the 32-mm (1¼-in.) flange plate material provided a nondestructive means of detecting this type of material at other locations in the bridge using portable hardness-testing equipment. Field hardness measurements were performed on all 124 bottom flange plates. High hardness readings were measured, similar to those recorded in Core 17, in five plates. Field testing measurements of the flange plates where the cores were removed showed good correlation between the laboratory and field measurements.

Instrumentation and Field Testing

A testing program was carried out in December 1992 to measure live load stress ranges at selected bridge cross sections on the westbound structure. Strain measurements were recorded under dynamic loadings using heavily loaded control trucks and normal traffic. Layout of the strain gauges and numbering system is shown in Figure 13. Most instrumentation was placed on the north girder under the right, or truck, lane. In total, 16 strain gauges with 6-mm (¼-in.) gauge lengths were installed.

Two six-wheel dump trucks, similar to H-20 vehicles, were used as the control trucks. Each truck was loaded, providing a gross vehicle weight of approximately 227 KN (51 kips). Maximum responses using the control vehicles were obtained for a passage of the two trucks side by side. Gauge responses for the side-by-side control load are shown for instrumented Sections A and B in Figures 14 and 15, respectively.

Strain was recorded under normal traffic for a continuous period of 24 hr. Gauge measurements for a typical passage of heavy vehicle during this period are provided in Figures 14 and 15. In addition, the 24-hr data were scanned for the largest strain event during the test period. Four maximum responses were noted in this pe-

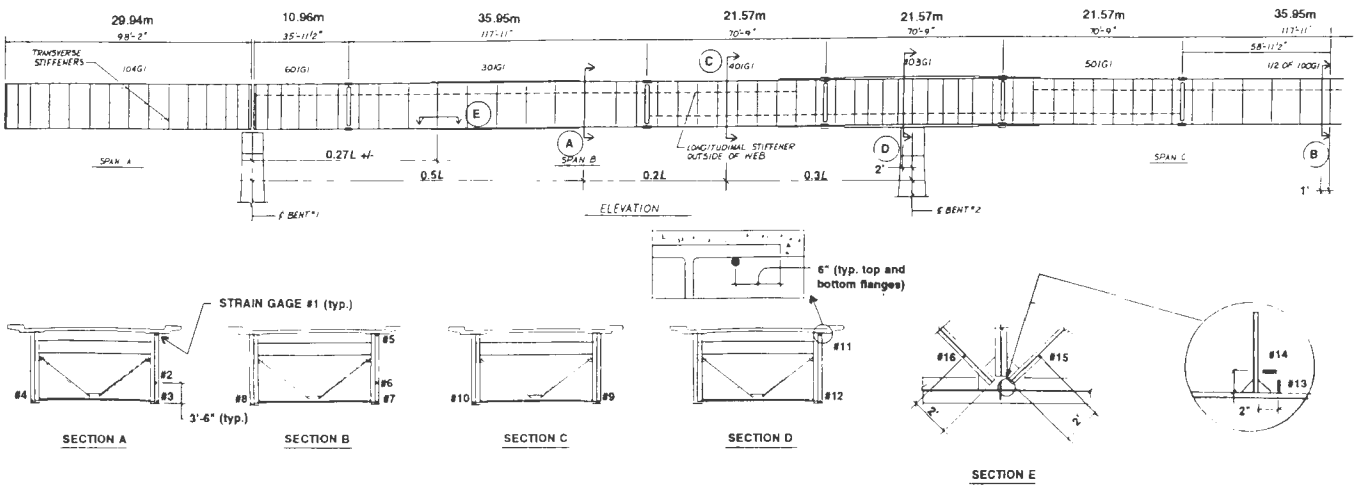

FIGURE 13 Strain gauge layout.

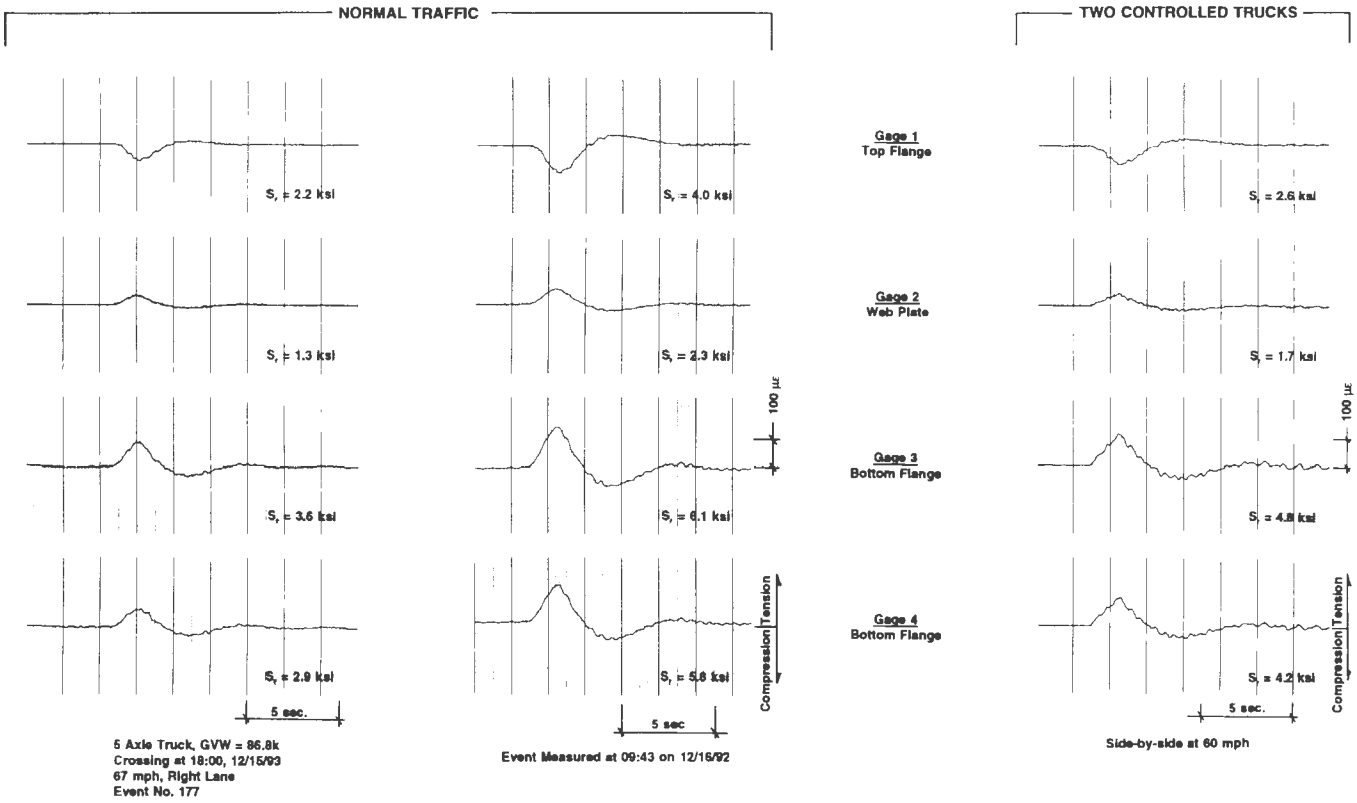

FIGURE 14 Dynamic strain gauge data measured at Section A (1 ksi = 6.9 MPa).

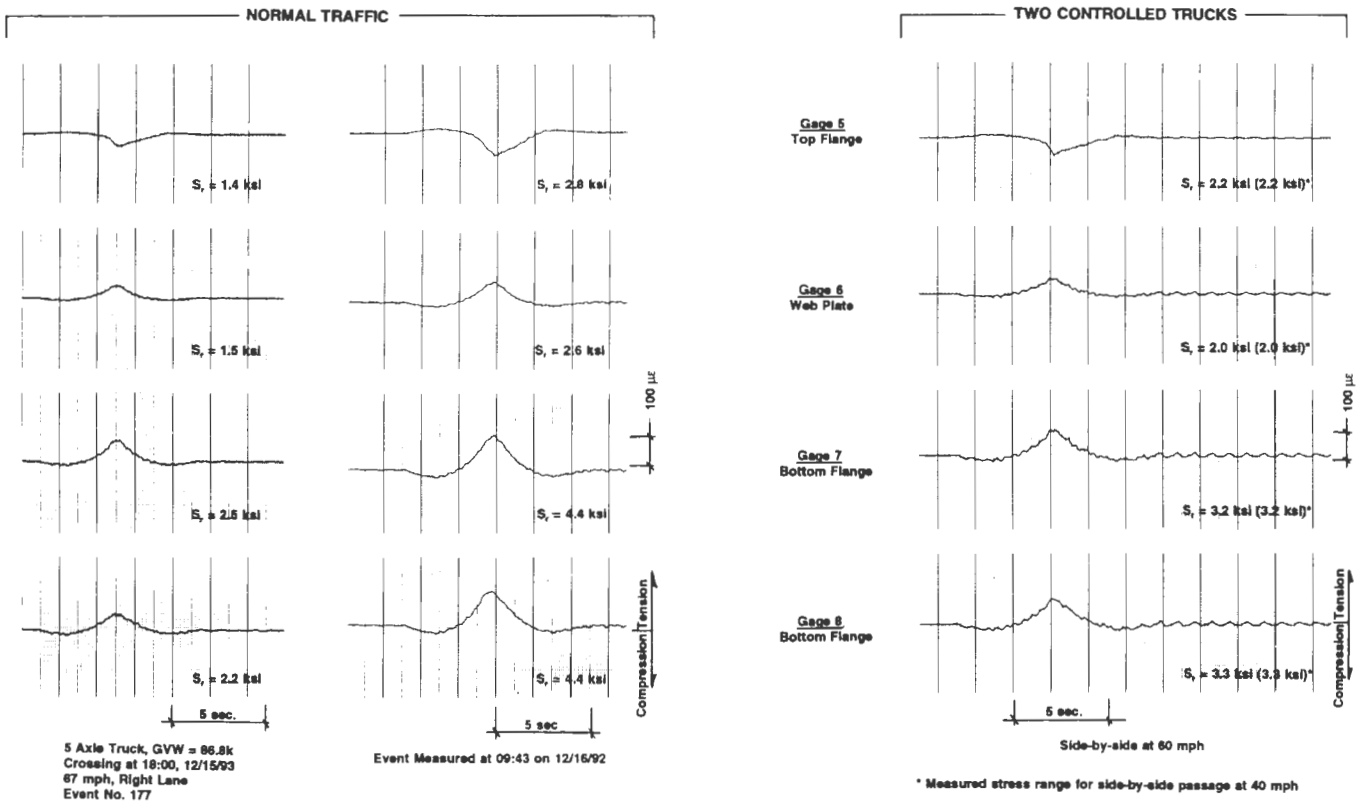

FIGURE 15 Dynamic strain gauge data measured at Section B (1 ksi = 6.9 MPa).

riod, and one record is shown in Figures 14 and 15 for the instrumented Sections A and B. These maximum responses most likely resulted from the passage of two heavy trucks crossing the bridge approximately side by side.

On the basis of the testing program carried out on the westbound bridge of the Green River structure, a summary of stress ranges for the 16 gauged locations is provided in Table 2. Gauge 3 at Section A located at midspan of the 80-m (260-ft) side span of the continuous unit measured the highest tensile stress ranges for all loadings:

- 18.7 MPa (2.7 ksi) under a control single truck loading,
- 33.1 MPa (4.8 ksi) under a control side-by-side loading,
- 25.5 MPa (3.7 ksi) for a single heavy truck from normal traffic, and
- 42.1 MPa (6.1 ksi) for a maximum event from normal traffic.

Maximum stress ranges for the 100-m (330-ft) main span measured for all loadings were recorded at Gauge 7 at Section B:

- 13.1 MPa (1.9 ksi) under a control single truck loading,
- 22.1 MPa (3.2 ksi) under a control side-by-side loading,
- 17.9 MPa (2.7 ksi) for a single heavy truck from normal traffic, and
- 30.4 MPa (4.4 ksi) for a maximum event from normal traffic.

Even though the structure was not designed composite, the structure shows some composite action between the girder and bridge deck. The continuous span unit indicates that the neutral axis occurs about 1.5 m (5 ft) below the top flange of the 4.3-m-deep girder.

Fracture Analysis

The large cracks observed in Girder 301G1-3 at Cores 17 and 25 were evaluated for fatigue and fracture susceptibility. Figure 3 shows a schematic of the cracks projected on a plane perpendicular to the bending stresses in the girder flange. As discussed previously, the crack tip nearest the bottom surface of the flange exhibits a nearly horizontal orientation and hence is not

TABLE 2 Summary of Measured Stress Ranges Under Controlled and Normal Heavy Truck Traffic Loadings

Measured Stress Range MPa (ksi)[1]								
	Controlled Loads				Normal Traffic Heavy Load[2]		Maximum Normal	
Strain Gage	Truck 1 R.L		Side-by-side		Single Vehicle		Traffic Loads[3]	
1	-8.3	(-1.2)	-17.9	(-2.6)	-13.8	(-2.0)	-27.6	(-4.0)
2	6.9	(1.0)	11.7	(1.7)	8.3	(1.2)	15.9	(2.3)
3	18.7	(2.7)	33.1	(4.8)	25.5	(3.7)	42.1	(6.1)
4	11.7	(1.7)	29.0	(4.2)	20.0	(2.9)	40.0	(5.8)
5	-6.2	(-0.9)	-15.2	(-2.2)	-10.4	(-1.5)	-19.3	(-2.8)
6	8.3	(1.2)	13.8	(2.0)	10.4	(1.5)	17.9	(2.6)
7	13.1	(1.9)	22.1	(3.2)	17.9	(2.6)	30.4	(4.4)
8	9.0	(1.3)	22.8	(3.3)	15.2	(2.2)	30.4	(4.4)
9	13.8	(2.0)	24.8	(3.6)	20.0	(2.9)	31.7	(4.6)
10	11.0	(1.6)	24.8	(3.6)	17.9	(2.6)	33.1	(4.8)
11	3.5	(0.5)	6.9	(1.0)	4.8	(0.7)	9.7	(1.4)
12	-4.1	(-0.6)	-10.4	(-1.5)	-6.9	(-1.0)	-13.1	(-1.9)
13	-2.8	(-0.4)	-5.5	(-0.8)	-3.5	(-0.5)	-6.2	(-0.9)
14	9.7	(1.4)	19.3	(2.8)	13.8	(2.0)	24.1	(3.5)
15	11.7	(1.7)	9.7	(1.4)	11.7	(1.7)	11.0	(1.6)
16	-9.7	(-1.4)	9.7	(1.4)	-11.0	(-1.6)	9.0	(1.3)

[1] Positive value denotes tension, negative value denotes compression
[2] Event No. taken from the NCDOT weigh-in-motion data.
[3] Maximum events scanned from the 24 hr data. These responses apparently resulted from the passage of two normal traffic trucks crossing the bridge approximately side-by-side.

particularly sensitive to crack extension as the stress intensity factor is much reduced.

Material fracture toughness in the flange plate is very low, 4 J (3 ft-lb) at 4.5°C (40°F). This brittle behavior is due to the coarse grain structure and chemical composition of the 32-mm (1¼-in.) flange plate of Girder 301G1-3. The toughness characteristics of this material appear very similar to the jumbo sections of A572 steel, as reported by Fisher and Pense (*1*).

From the dynamic and static fracture toughness estimates obtained for the jumbo sections, the CVN test results from Girder 301G1-3 are directly comparable to the test results from the jumbo sections. Since K_c test results are available from the jumbo sections, it is concluded that the static fracture toughness of the flange plate is about 44 MPa $\sqrt{m}$ (40 ksi $\sqrt{in.}$) (*1*).

The most severe crack appears to be in Core 25 (Figure 14), where a circumscribed elliptical-shaped crack is exhibited. At that location the crack tip is nearly perpendicular to the bending stresses in the girder flange and hence most likely to be susceptible to crack extension.

For an elliptical-shaped crack, the stress intensity factor is given by

$$K = F_e \sigma \sqrt{\pi a} \tag{1}$$

where a equals the minor semidiameter

$$F_e = \frac{[\sin^2 \theta + (a/c)^2 \cos^2 \theta]^{1/4}}{E(k)} \tag{2}$$

$$E(k) = \int_0^{\frac{\pi}{2}} (1 - k^2 \sin^2 \theta)\, d\theta, \; k^2 = \frac{c^2 - a^2}{c^2}$$

$$\cong \frac{3\pi}{8} + \frac{\pi}{8}\left(\frac{a}{c}\right)^2, \; c < 2a \tag{3}$$

This crack model is reasonable and verified by experimental studies on welded details since the web is restraining the crack opening.

For Core 25, a = 25.4 mm (1 in.) and c = 35.6 mm (1.4 in.). At Point A, where some evidence of crack extension may exist, Equation 2 results in F_e = 0.71.

Therefore, Equation 1 yields

$$K = 0.71\,\sigma\sqrt{\pi a} = 0.282\,\sigma = \text{MPa}\ (1.257\,\sigma = \text{ksi}) \quad (4)$$

On the basis of the dead load stress at these cracked locations in Girder 301G1-3 of about 93 MPa (13.5 ksi) and the maximum stress range measured at Section A, ignoring reversal, the maximum stress at Core 25 is about 128 MPa (18.5 ksi). Therefore, the maximum stress intensity is

$$K_{max} \sim 26.4\ \text{MPa}\ \sqrt{\text{m}}\ (24\ \text{ksi}\ \sqrt{\text{in.}}) < K_c \sim 44\ \text{MPa}\ \sqrt{\text{m}}\ (40\ \text{ksi}\ \sqrt{\text{in.}}) \quad (5)$$

The large crack in Core 17 with a smaller minor diameter and a larger major diameter provides a smaller estimate of stress intensity. Therefore, the fact that these cracks had been in the structure since it was constructed and did not result in a brittle fracture is reasonable.

No evidence of fatigue crack extension was observed in Cores 17 and 17-1 with the more favorable crack geometry. At Core 25, the stress intensity range is provided by

$$\Delta K = 0.282\ S_r = \text{MPa}\ (1.257\ S_r = \text{ksi}) \quad (6)$$

This provides a stress intensity range of 6.6 MPa $\sqrt{\text{m}}$ (6 ksi $\sqrt{\text{in.}}$) for the maximum stress range of 33 MPa (4.8 ksi) determined by the field testing. This does exceed the crack growth threshold ΔK_{th} = 3.3 MPa $\sqrt{\text{m}}$ (3 ksi $\sqrt{\text{in.}}$). Hence, it is very possible that some crack extension developed at the crack tip in Core 25 where the crack tip was perpendicular to the bending stress [under infrequent heavy loads analogous to the two control trucks side by side or the four maximum events 42 MPa (6.1 ksi) measured during the 24-hr period]. Fortunately, these events apparently do not occur often enough to result in major crack extension. No crack extension was detected where the crack tip was nearly horizontal. Brittle fracture was avoided because of the near horizontal orientation of the cracks adjacent to the bottom surface of the tension flange where ΔK would be much smaller.

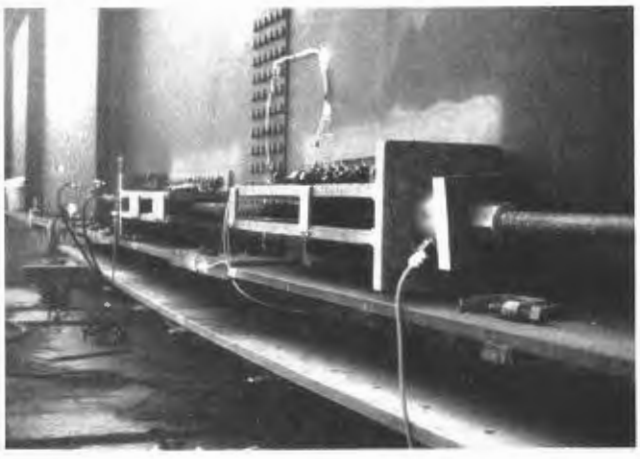

FIGURE 16 Post-tensioning assembly installed at girder bolted splice connection used to install coverplate retrofit.

Summary of Findings

The test results from the examination of core samples containing cracks and additional cores to evaluate material properties as well as the field testing measurements of stress range, the hardness survey, and nondestructive evaluation have demonstrated that the cracks discovered in the I-26 Green River Bridge occurred at the time of fabrication. Specific findings are as follows:

- Fractographic examination indicates that the two large cracks removed from Girder 301G1-3 developed at the time of fabrication. These large cracks resulted from the use of a steel plate material containing very high carbon levels, large grain structure, and very low toughness. This material did not meet ASTM A441 modified Corten B steel requirements, and it was not a weldable steel.
- All of the evaluated cracks appear to have resulted from hydrogen-related cold cracking. The many transverse cracks in longitudinal fillet welds of all the bridge girders appear to be cold cracks.
- The large cracks in Girder 301G1-3 were tolerant of dead and live load stresses, mainly because the crack tip had a favorable orientation to applied forces. This orientation prevented fatigue crack growth and brittle fracture.
- All tested web plate material revealed good toughness that exceeded the CVN requirements for Zone 2. The web toughness was beneficial and prevented more serious crack extension in the girders.
- The additional core samples removed randomly from other flange plates with thicknesses between 32 and 95 mm (1¼ and 3¾ in.) all exhibited acceptable levels of notch toughness.

Recommendations for Retrofitting

The fatigue life of the Green River Bridge can be extended greatly by retrofitting the fracture-critical primary girders. A two-girder nonredundant system containing numerous small cracks requires retrofit measures that will provide redundancy in all spans and will reduce the stress ranges, further reducing the pos-

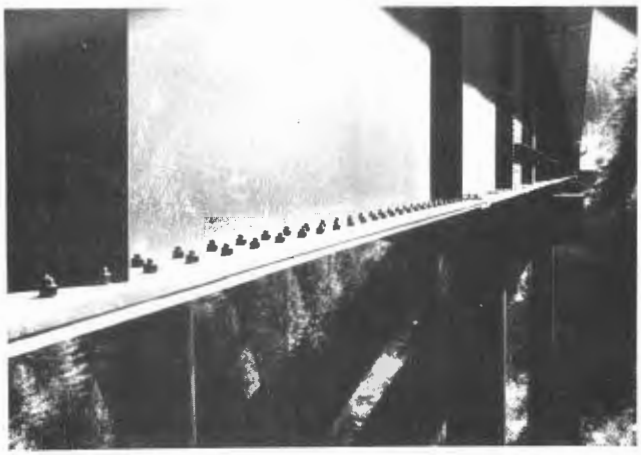

FIGURE 17 Completed bottom flange coverplate installation.

sibility of fatigue crack extension from the flange–to–web plate fillet weld cracks.

The numerous flange–to–web plate fillet weld cracks cannot be removed by coring or drilling. Therefore, all bottom flanges subjected to tensile stresses should be coverplated using full-flange-width coverplates connected with high-strength bolts. The top tension flanges of the girders over the piers do not require any modification, as no cracks were detected in any of these flanges. This retrofit measure provides an alternative load path in all tension regions of the main girder.

The recommended retrofitting was included in the construction work to rehabilitate the bridge. The project consisted primarily of cover plating the main girders and concrete bridge deck repairs. The cover plates match the typical flange width of 610 mm (24 in.) and range in thickness from 25 to 38 mm (1 to 1½ in.). Four rows of bolts are used to attach the plates. These rows are positioned 100 and 200 mm (4 and 8 in.) from each flange edge using a typical bolt spacing of 300 mm (12 in.) on center along each row. Alternate bolt rows are staggered by 150 mm (6 in.) longitudinally. The total weight of coverplates for both bridges (four girder lines) is 1605 KN (360,500 lb) of structural steel, and the attachment used 16,200 ASTM A325 bolts of 22-mm (⅞-in.) diameter.

All coverplate material was specified to meet ASTM A588 and CVN requirements of 33 J (25 ft-lb) at 4.5°C (40°F). In addition, all coverplate material and fabrication was required to meet AASHTO requirements (2).

NCDOT developed the coverplate retrofit details and installation procedure. The coverplate retrofit was designed to run continuous through girder bolted splice connection regions with the new coverplate positioned tight against the bottom flange. This was accomplished by post-tensioning the splice area, removing the bottom flange connection plate, clamping the coverplate into position, and match drilling the existing connection bolt pattern, and reinstalling the existing bottom flange connection plates. Figure 16 shows the post-tensioning bracket assembly installed at a bolted splice connection just prior to a bottom flange connection plate removal. Note that the new coverplate is positioned about 8 in. below the girder bottom flange, ready for final positioning.

All coverplate drilling was performed dry without coolant or lubricant for the hole cutters. A completed girder bottom flange retrofit is shown in Figure 17. The construction cost to fabricate the material and install the coverplates was $600,000. All superstructure retrofitting and bridge deck rehabilitation work was completed in October 1994 and paid for by NCDOT.

ACKNOWLEDGMENTS

NCDOT was responsible for designing the retrofit scheme. Lehigh University carried out the materials tests and metallographic and fractographic assessments. Wiss, Janney, Elstner Associates (WJE) carried out the instrumentation and field testing, removed the cores, and made the field hardness surveys.

The authors wish to recognize and extend their appreciation to all of the people who assisted with and contributed to this evaluation. Personnel of NCDOT, including Gary Rudisill, Neb Bullock, Mark Robbins, and Rodger Rochelle, were very helpful. WJE staff that contributed substantially to the project were Richard Walther, Roger Pelletier, and Robert Gessel. B. T. Yen assisted with the Lehigh University work.

REFERENCES

1. Fisher, J. W., and A. W. Pense. Experience with the Use of Heavy W Shapes in Tension. *Engineering Journal*, American Institute of Steel Construction, Vol. 24, No. 2, 1987.
2. *Guide Specifications for Fracture Critical Nonredundant Steel Bridge Members.* AASHTO, Washington, D.C., 1986.

Crack Evaluation and Repair of Cantilever Bracket Tie Plates of Edison Bridge

John W. Fisher, Ben T. Yen, Eric J. Kaufmann, and Zuo-Zhang Ma,
Lehigh University
Thomas A. Fisher, *HNTB Corporation*

The Edison Bridge on Route 9 over the Raritan River in New Jersey is a riveted two-girder floor beam structure that was built in 1944. Cracks were discovered in several tie plates connecting the cantilever brackets to the main girder and floor beam in the continuous span, the 25.8-m (84-ft, 6-in.) spans, and the 40.4-m (132-ft, 6-in.) spans. Several cracked tie plates were removed so that the cause of cracking could be evaluated. The investigation included metallographic and fractographic examinations of crack surface areas that were not damaged extensively by corrosion. Striation spacing measurements showed that the cyclic stress driving the crack was independent of crack length, characteristic of displacement-induced fatigue. Field testing to determine the live load stress levels confirmed that in-plane bending of tie plates was the principal cause of the fatigue cracking and that the cantilever bending stresses were negligible. The measurements also suggested that a loss of frictional composite action occurred as the slab deteriorated. This led to high cyclic stresses in tie plates, with the maximum stress range varying between 69 and 138 MPa (10 and 20 ksi). Fatigue cracking initiated at flame-cut plate edges subjected to the maximum in-plane bending stress from distortion. Cracking was also aggravated by corrosion loss of section. Future inspection procedures were developed to enhance crack detection, which is highly variable because of the uncertainty of composite action. Retrofit recommendations for failed tie plate replacement were developed as well as means to eliminate the problem when the structure is rehabilitated.

The Edison Bridge on Route 9 over the Raritan River in New Jersey is a riveted two-girder floor beam structure having a total length of 1321 m (4,332 ft). It consists of two three-span continuous structures of 183 m (600 ft), one three-span continuous structure of 198 m (650 ft), eight simple-span structures of 40.4 m (132 ft 6 in.), six simple spans of 46.5 m (152 ft 6 in.), and six spans of 25.8 m (84 ft 6 in.). The noncomposite concrete slab is directly supported by haunches on the main girders, transverse floor beams, and the cantilever brackets. The main girders are spaced 12 m (39 ft) apart, and the cantilever brackets extend 2.9 m (9 ft 6 in.) beyond the girders. The structure was built in 1944.

Figure 1 shows a portion of one of the continuous-span structures and a typical cross section applicable to all spans. Figure 2 is a view showing the longitudinal girder, a floor beam bracket, and stringer.

Cracks were discovered in several tie plates connecting the cantilever brackets to the main girders and floor beams in simple and continuous spans.

This paper provides an evaluation of the cracking that developed in the tie plates, suggestions for retro-

fitting the structure for the short term (10 to 15 years), and recommendations for long-term repair and rehabilitation.

Examination of Cracked Tie Plates

Three cracked tie plates were removed from the structure for examination. A tie plate removed from the eighth 40.4-m (132-ft, 6-in.) span southbound had a crack that extended nearly across the width of the plate. Figure 3 shows one of the plate sections and the diagonal crack that extended about two-thirds across the tie plate. The balance was flame cut during removal. A section of tie plate containing a crack removed from the 183-m (600-ft) continuous span 15.2 m (50 ft) south of Pier 2 was also delivered for examination. A view of the cracked plate is given in Figure 4, with the balance of the plate cut away.

The cracks in all tie plates initiated along the tapered edge of the plate several inches from the start of the taper on the bracket side, as is apparent in Figures 3 and 4. This edge was probably a flame-cut edge given the overall shape of the tie plate, although corrosion has since eroded the original plate edge surface and all evidence of the cutting method. The plates also showed substantial general corrosion damage over the surface as well. The extent of corrosion on all three tie plates indicates that they were debonded from the overlying haunched slab for a substantial period of time. The crack in Tie Plate 3 initiated from the plate edge and propagated to a rivet hole (Figure 4). The crack reinitiated at the rivet hole and continued to propagate across the tie plate.

The length of the crack in Figure 3 was 432 mm (17 in.). The crack shown in Figure 4 for Tie Plate 3 was 279 mm (11 in.) long. No other cracks were detected elsewhere in the tie plate.

Fractographic Examination

The crack surfaces from each of the tie plates were examined visually and with the scanning electron microscope (SEM) to verify the crack extension mechanism. Measurements of fatigue striations were also obtained where possible along the length of the crack since the striation spacing can be used to indirectly estimate the stress range in the tie plate. This technique has been applied with some success to fatigue cracking in bolts and plate elements in a variety of structures.

The crack surfaces from all tie plates showed varying amounts of damage by corrosion. The damage was most severe at the crack origin and diminished toward the crack tip, where the small crack opening tended to protect the surface from the environment. Before being examined with the SEM, the crack surfaces were cleaned ultrasonically to remove as much of the corrosion product as possible and permit observation of the underlying crack features.

A view of the crack surface from Tie Plate 3 is shown in Figure 5. The smooth and flat surface is typical of fatigue cracking. The crack surface from Tie Plate 3 was also found to be free of corrosion product near the crack tip region. The crack origin region was covered with a heavy layer of corrosion product that could not be lifted from the surface. Beachmarks are clearly seen on the crack surface near the crack tip. A low-magnification (7×) SEM micrograph of this area also shows finer beachmark detail than can be seen with the unaided eye. The surface in this area was also examined at higher magnification for fatigue striations. Figure 6 shows an SEM micrograph at 2,040× magnification that shows the fatigue striations on the crack surface, which is located 241 mm (9.5 in.) from the origin.

Fatigue crack growth was also detected in Tie Plate 1, seen in Figure 3. The crack origin was covered completely with corrosion product, which obscured any detail of crack initiation. Efforts to remove the corrosion product at the crack origin and over most of the crack surface were not successful since the corrosion process had completely consumed the underlying fracture features. Closer to the crack tip, some areas were free of corrosion and some evidence of fatigue beachmarks could be seen (Figure 7). The crack surface in this area was examined further with the SEM. Figure 8 shows a high-magnification micrograph (2,040×) showing well-defined fatigue striations.

The crack surface from Tie Plate 2 was consumed entirely by corrosion except near the crack origin. Corrosion damage was severe since this tie plate was located near an expansion joint, which provided frequent wetting from the weather. Evidence of grout was seen on the crack surface, suggesting that the crack existed at the time the bridge was last resurfaced, in 1985. Despite efforts to remove the corrosion product, no fracture features could be discerned on the crack surface.

Material Properties

Although none of the tie plate crack surfaces examined showed evidence of crack instability, limited material property tests were conducted on Tie Plate 1 to characterize the strength and notch toughness properties of the plate. Considering the date of erection, the material was most likely supplied under the ASTM A7 specification. Tensile test results confirmed this, providing a yield strength of 300 MPa (43.4 ksi), ultimate strength of 456 MPa (66.2 ksi), and elongation of 27 percent.

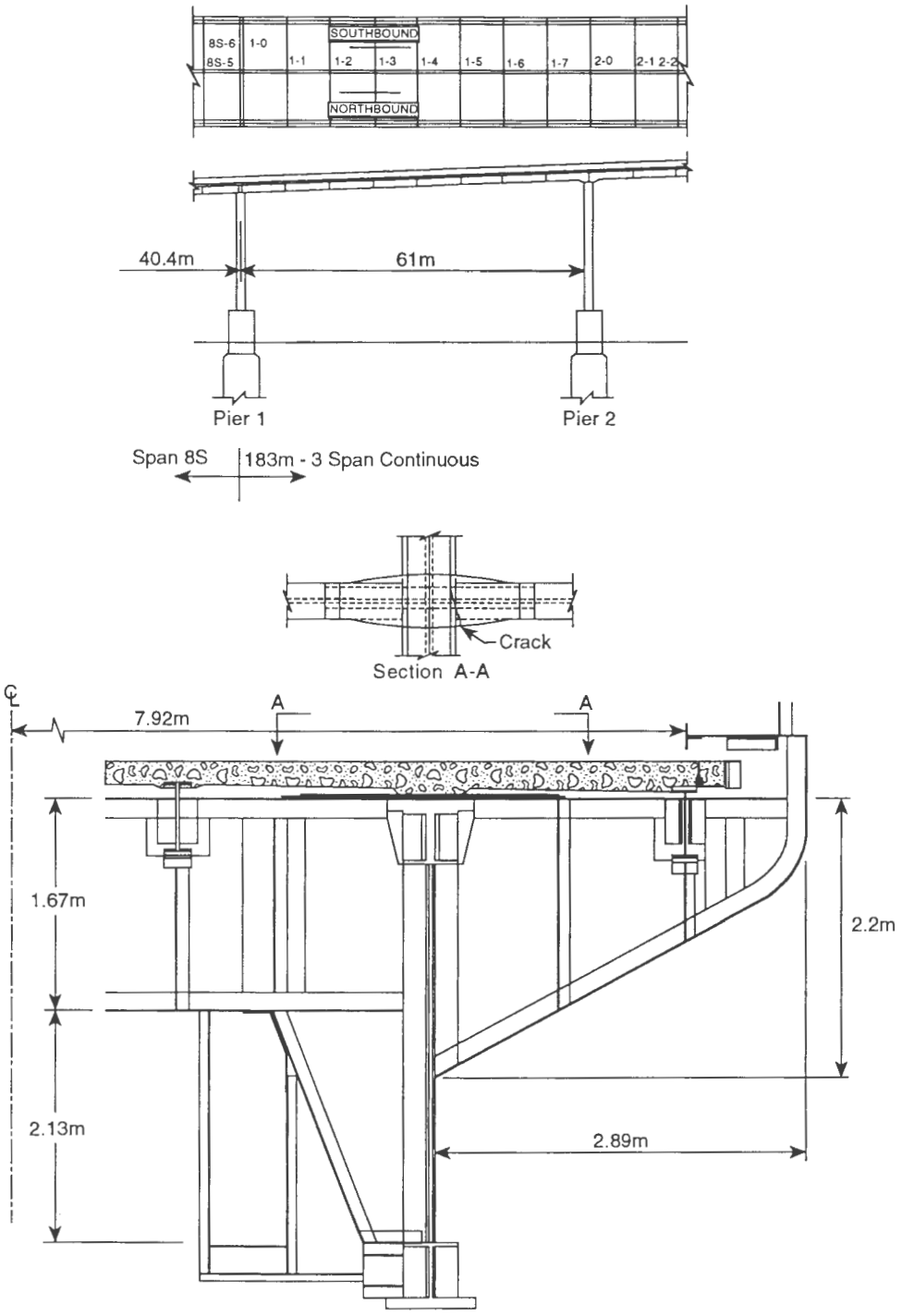

FIGURE 1 Typical span and elevation of Edison Bridge.

The relatively high yield strength (for ASTM A7) is not uncommon in the thin plate of this material.

Subsize Charpy V-notch (CVN) specimens were also fabricated from the tie plate. These tests provided about 135 J (100 ft-lb) at 4°C (40°F). Approximate standard CVN test specimen results, corrected for specimen thickness, averaged 182 J (135 ft-lb). The results show that crack instability would not be expected in the tie plate at minimum service temperatures as low as −34°C (−30°F) under the low strain rates that these elements are subjected to and because of the high toughness of the material.

FIGURE 2 View of girder-cantilever bracket.

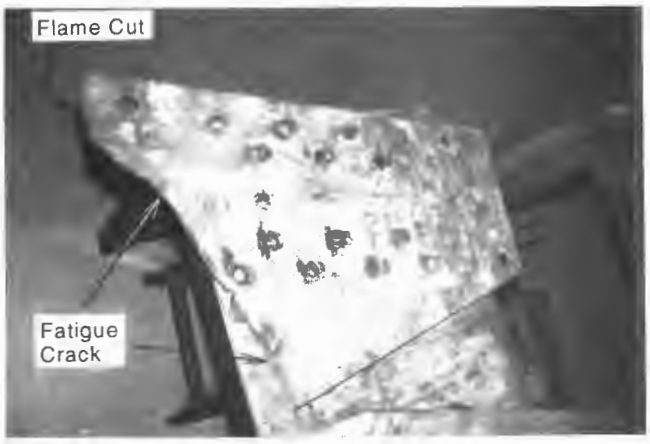

FIGURE 3 View of cracked tie plate 1 from 30.4-m span.

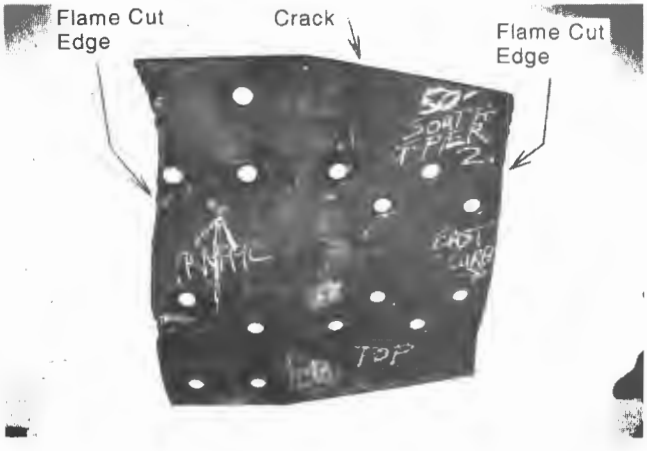

FIGURE 4 Crack in Tie Plate 3 from 183-m continuous span.

Results of Striation Measurements

Each of the micrographs showing striations was measured to determine the average striation spacing. Since the spacing varies under variable loading, measurements were taken by counting striations on the micrograph and computing an average spacing. This count was performed over several areas. The location on the crack surface relative to the crack origin of each of the micrographs shown was also recorded. The corresponding stress intensity range, ΔK, was calculated using the crack growth relationship

$$\frac{da}{dN} = C\Delta K^3 \tag{1}$$

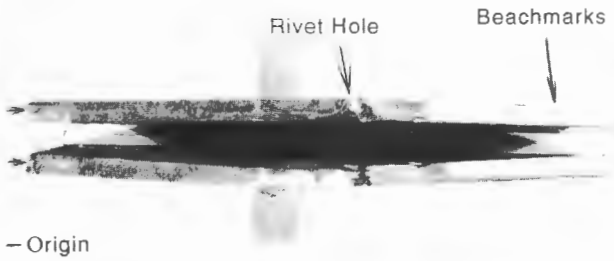

FIGURE 5 Crack surface of Tie Plate 3 showing beachmarks, rivet hole, and crack origin.

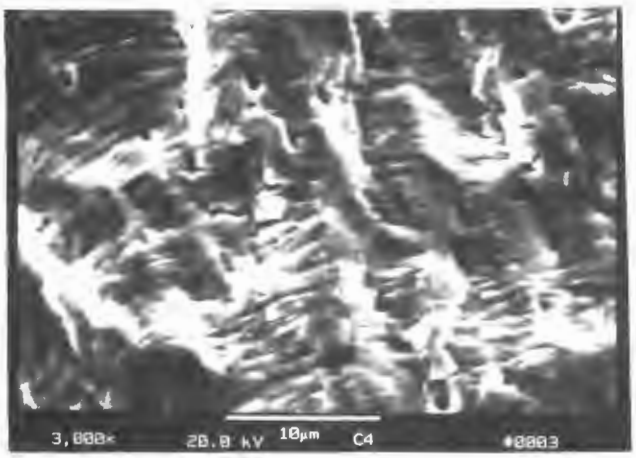

FIGURE 6 SEM micrograph showing fatigue striations in Tie Plate 3 beachmark area (2,040×).

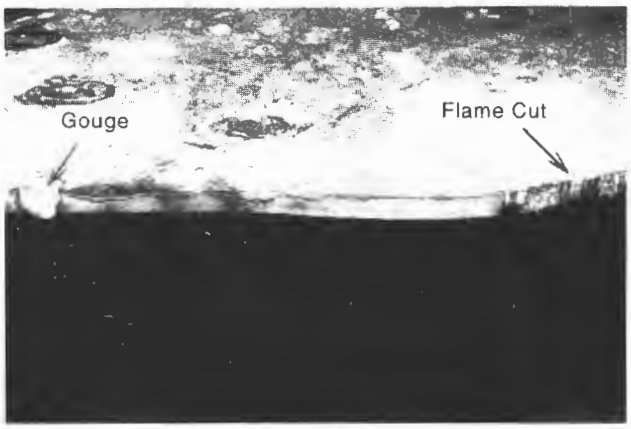

FIGURE 7 Crack surface in Tie Plate 1 near flame-cut end.

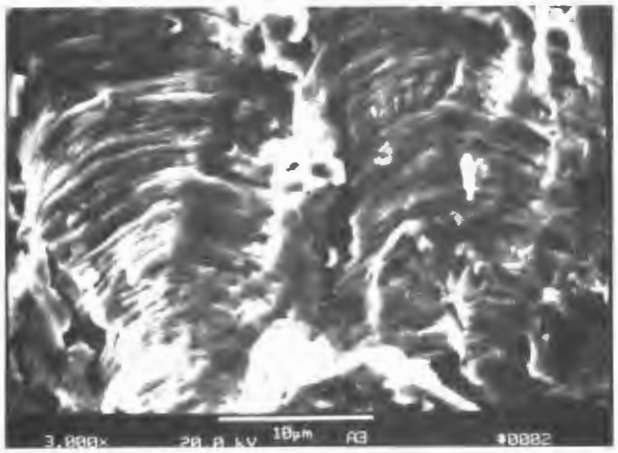

FIGURE 8 SEM micrograph showing fatigue striations in Tie Plate 1 near crack tip (2,040×).

$C = 2.18 \times 10^{-13}$ where a and ΔK are in units of millimeters and MPa $\sqrt{m}$, respectively. Because of corrosion over most of the crack surfaces, measurements could be obtained over only a limited range of crack lengths in each plate that varied from 203 to 318 mm (8 to 12.5 in.). The calculated stress intensity range of 37 MPa $\sqrt{m}$ (34 ksi $\sqrt{in.}$) is nearly the same in both tie plates and was independent of crack size. The estimated stress ranges in the tie plates calculated using an edge crack model in pure bending are as follows:

$$\Delta K = \frac{\left[0.923 + 0.199\left(1 - \sin\frac{\pi a}{2b}\right)^4\right]}{\cos\frac{\pi a}{2b}} \Delta\sigma\sqrt{\pi a} \qquad (2)$$

where b is the width of the tie plate along the plane of the crack (Figure 9). The effect of shear is to cause the crack to follow the principal stress that is apparent in the crack paths seen in Figures 3 and 4. This measured 610 mm (24 in.) for Tie Plate 1 and 559 mm (22 in.) for Tie Plate 3. Stress ranges of 29 to 51 MPa (4.17 to 7.4 ksi) were calculated from the striation measurements. These most likely represent the most frequently occurring stress cycles. Finer striations not discernible using the SEM are undoubtedly present on the crack surfaces as well as infrequent larger stress cycles not detected over the small area of fracture surface observed.

Field Measurements

To assess the causes of crack initiation and growth, field measurements of the live load strain response were obtained on several tie plates of the spans shown in Figure 1. Gauges were also placed on the web copes of the floor beam cantilever brackets and on one cross section of the east girder. Figure 10 shows the strain gauges on the bracket web cope and the edge of the tie plate near the location at which the fatigue cracks were observed to develop before repair. The gauges were installed on each edge of the tie plate as well as on the floor beam side.

The strain gauges were connected to a 21-channel recorder through cables and signal conditioners. The recording equipment was placed on Pier 1 or Pier 2, under the bridge deck, so as to clear the roadway for full traffic. Altogether, about 3 hr 20 min of strain response was obtained on each gauge on August 24 and 25, 1993.

Results of Strain Measurement

The recorded strain variation at each strain gauge was examined through an oscilloscope. Figure 11 shows strain-time records for several gauges in the area of Pier 2 during passage of a northbound truck. The upward excursion of a trace indicates live load compression; downward is tension. The stress range was defined by

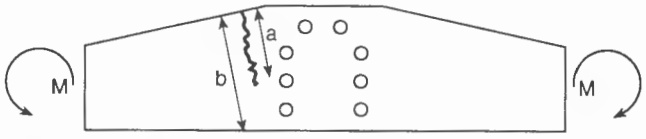

FIGURE 9 Schematic of crack in tie plate model.

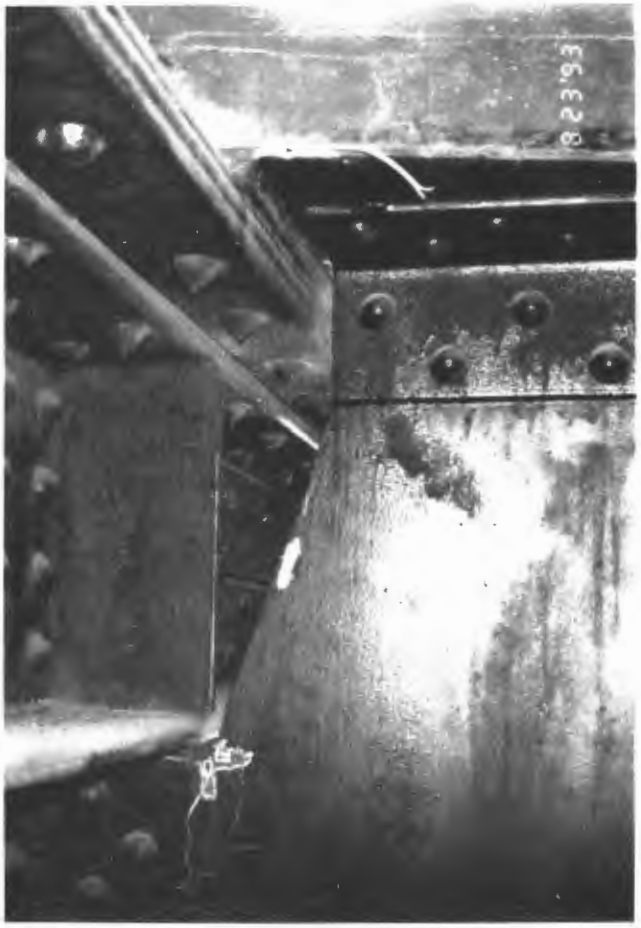

FIGURE 10 View of gauges on tie plate edge and at bracket cope.

the peak-to-peak excursion while the vehicle crossed the structure.

From examination of these traces, and from results of other bridges with similar conditions of tie plate stresses, a number of observations can be made:

- The variations of live load strains in the tie plates are analogous to those in the girder flanges. This indicates that the stresses in the tie plates are generated by the relative longitudinal displacement between the girder top flange and the bridge deck (*1,2*).
- The tie plates are bending horizontally when trucks travel on the bridge. This is depicted by the opposite excursion of strain traces for Gauges 1 and 2, 3 and 4, and 7 and 8, in Figure 12, as well as for other strain gauge pairs in the north-south direction on all tie plates. From the response of gauges at Pier 2 and at floor beam 1-6E, 15.2 m (50 ft) south of Pier 2, it is apparent that the vehicles are traveling about 15.2 m/sec (50 ft/sec). The peak excursion at Pier 2 in one direction occurs as the vehicle moves from the end span at Pier 1 to Pier 2. The stress cycle reverses as the vehicle continues for about 45.7 m (150 ft) in 3 sec and then returns gradually to its starting point after about 4 more seconds (~61 m or 200 ft). Figure 12 (*top*) shows the simultaneous stresses in Gauges 1 through 4 at the moments of peak stresses due to a northbound truck, corresponding to the strain traces at times t_3 and t_4, which are identified by the vertical lines in Figure 11. These stress gradients show the full reversal of the stress cycle at Pier 2-0E. A similar plot of the instantaneous gradients at Tie Plate 1-6E is shown in Figure 12 (*bottom*). The maximum stress range due to this truck was 93 MPa (13.5 ksi) at Gauge 4. The same truck induced the maximum live load stresses in Tie Plate 1-6E with the maximum stress range equal to 116 MPa (16.8 ksi) at Gauge 8.
- Northbound trucks generated higher stress ranges in tie plates over the east (northbound) girder. Southbound trucks induced higher stress ranges in the west girder tie plates. The measurements suggest that the tie plates near Pier 2 act as though a significant amount of composite behavior has been lost with time. The loss of composite action increases the in-plane bending that the tie plate experiences. The low levels of stress range measured at Pier 1 indicate that there is little loss of composite action in either span at Pier 1. It is also apparent that the axial stress in the tie plates produced by the cantilever load on the bracket is small compared with the in-plane bending.

The HS-20 design axial stress range in the tie plate is estimated to be about 30 MPa (4.3 ksi). The measured axial stress in the tie plate was less than 50 percent of the design estimate. The in-plane bending of the tie plate that results from the relative longitudinal movement is dominant but highly variable because of differences in composite behavior.

- The magnitudes of stress range due to the same truck differ from tie plate to tie plate. Experience at other bridges has shown that tie plates over end bearings and piers would be subject to more horizontal bending, thus higher stress ranges (*1,2*). This condition did not seem to hold true for this bridge system. The tie plates at Pier 1 (end bearings) had very low stress ranges, whereas the tie plates at FB1-6 near the contraflexure point had the highest.

The stress range spectra for Gauges 4 and 8 on the east side near Pier 2 are shown in Figures 13 and 14. These plots show the skewed distribution characteristics of the truck gross vehicle weight distribution. Between 526 and 689 stress cycles greater than 10 MPa (1.5 ksi) were observed at these gauges during the 3 hr 20 min of record at Pier 2. None of the stress cycles at Pier 1 was high enough to warrant developing a stress range spectra, as the maximum stress range was 23 MPa (3.4 ksi).

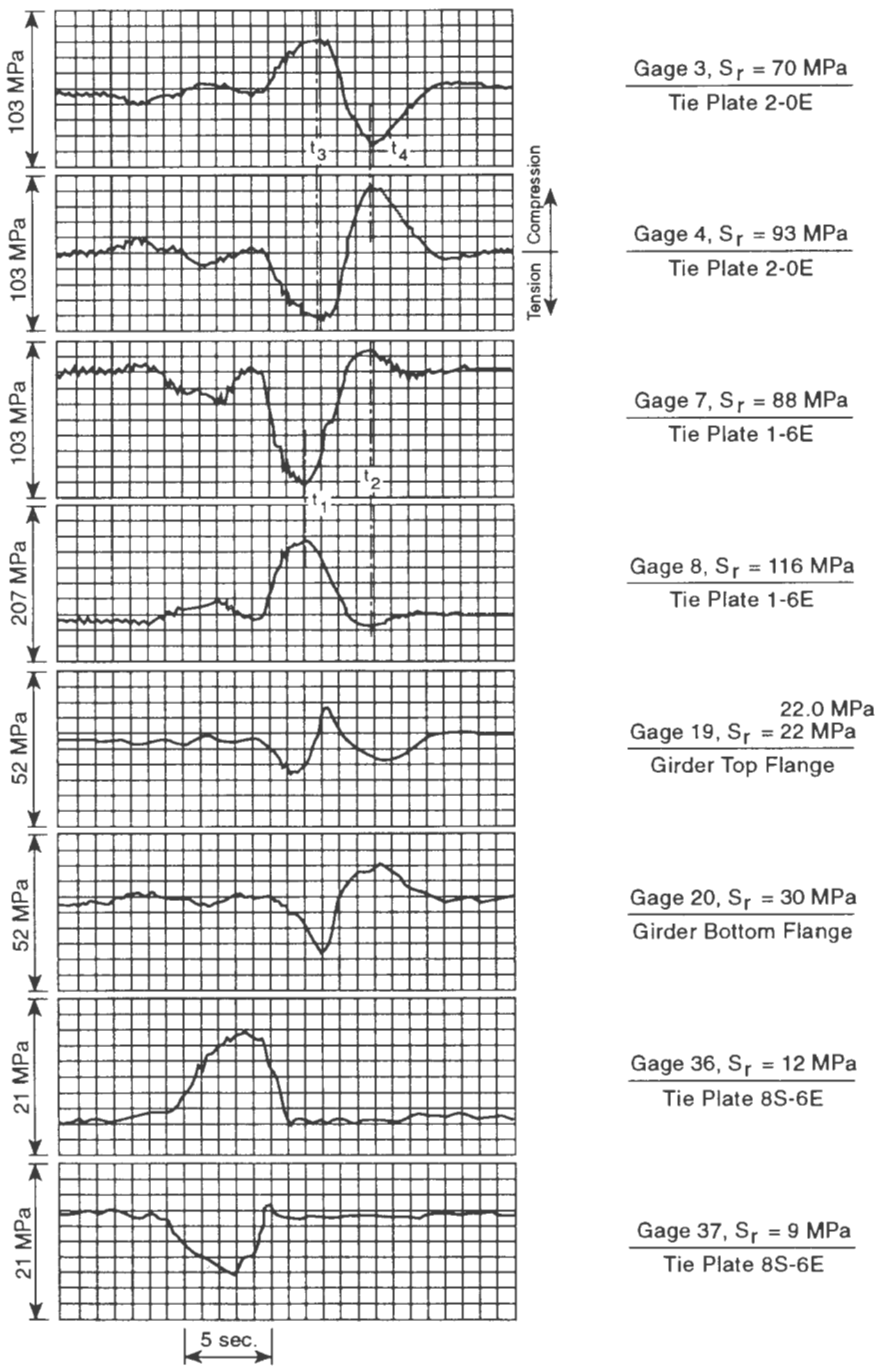

FIGURE 11 Typical strain-time response of tie plates and main girder in 61-m span (see Figure 1).

- The stress ranges in the flanges of the east girder are comparable to those recorded at similar girders. The maximum stress range was 30 MPa (4.4 ksi) at the Bottom Flange Gauge 20, and 22 MPa (3.2 ksi) at the Top Flange Gauge 19 (see Figure 11).
- The stress ranges at the strain gauges at the cope of cantilever were not high. The maximum was 16 MPa (2.3 ksi) at a horizontal gauge.

Discussion of Results

From the experimental results and field examination of the bridge, it was apparent that the concrete deck of the bridge was in contact with the top flange of the girders and the top flange of the floor beams. However, the width of the concrete "pedestal" along the girder top flange is different in different spans. For the three-span

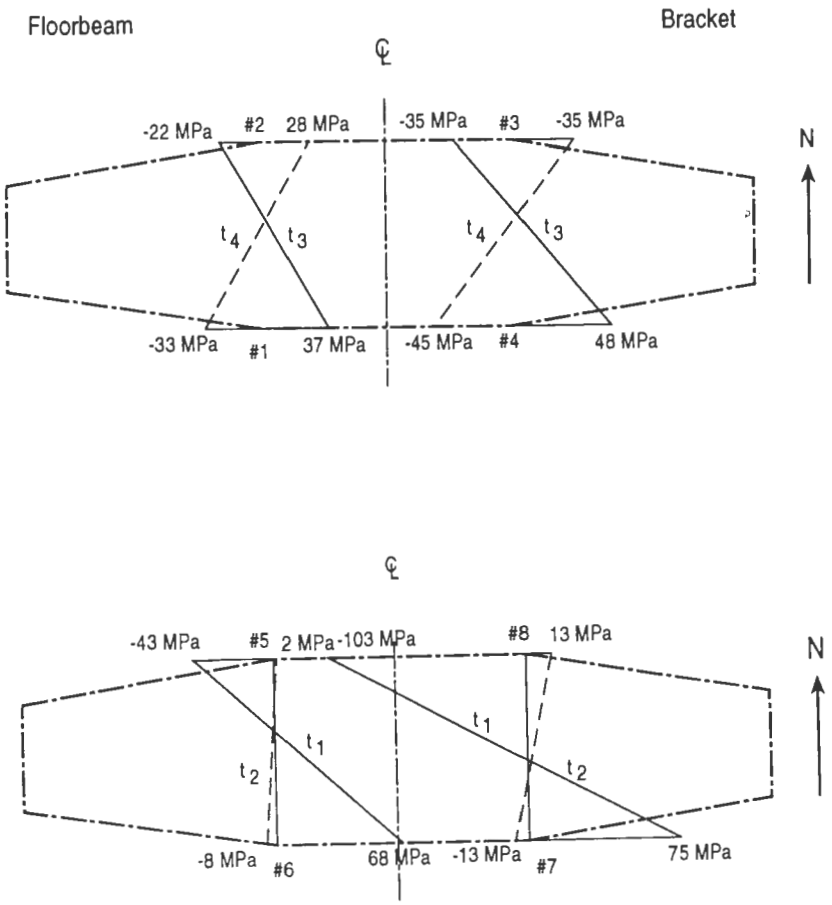

FIGURE 12 Stress gradients in tie plates of 61-m Span 1 during passage of northbound truck: *top*, Tie Plate 2-0E; *bottom*, Tie Plate 1-6E.

183-m (600-ft) continuous structure between Piers 1 and 4, the bottom width of this "pedestal" is narrower than the width of the girder top flange. There were signs of separation and relative vertical and horizontal movement between the deck and the girder near Pier 2. At some floor beams, a visible gap existed between the two components. On the other hand, the pedestals of the deck above the girders of the simple 40.4-m (132-ft, 6-in.) spans were the same width as the girder top flange. There was no visible separation between the deck and the top flange at Pier 1 for either span at that location. This separation contributes to the loss of composite behavior and enhances the longitudinal movement between the girder and the deck of the 183-m structure and thus the horizontal bending of the tie plates near Pier 2.

The highest magnitude of stress range in a tie plate was measured at Tie Plate 1-6E, which was a replacement plate installed in August 1993. The new tie plate is not in contact with the concrete deck. At Tie Plate 8S-6W, the deck appears to be in direct contact with the girder flange, and the measured stress range was less than 21 MPa (3 ksi). This reinforces the assumption that tight contact between the deck and the girder top flange generates interaction between these components and decreases the horizontal bending of the tie plates because of the composite action. The experimental results also demonstrate that the axial stress in the tie plates from wheel loading on the cantilever bracket is small compared with the in-plane bending. In the continuous span near Pier 2 where loss of composite behavior was most apparent, the in-plane bending stresses were typically four to six times as great as the axial stresses in the tie plates.

The relative horizontal movement between the deck and the girder at Tie Plate 1-0E was 0.94 mm (0.037 in.). This is smaller than the magnitudes observed on other bridges where the deck is not in contact with the girder flange. The existence of relative movement indicates that the tie plate is being bent horizontally, which was confirmed by the strain measurements.

The stress range data summarized in Figures 13 and

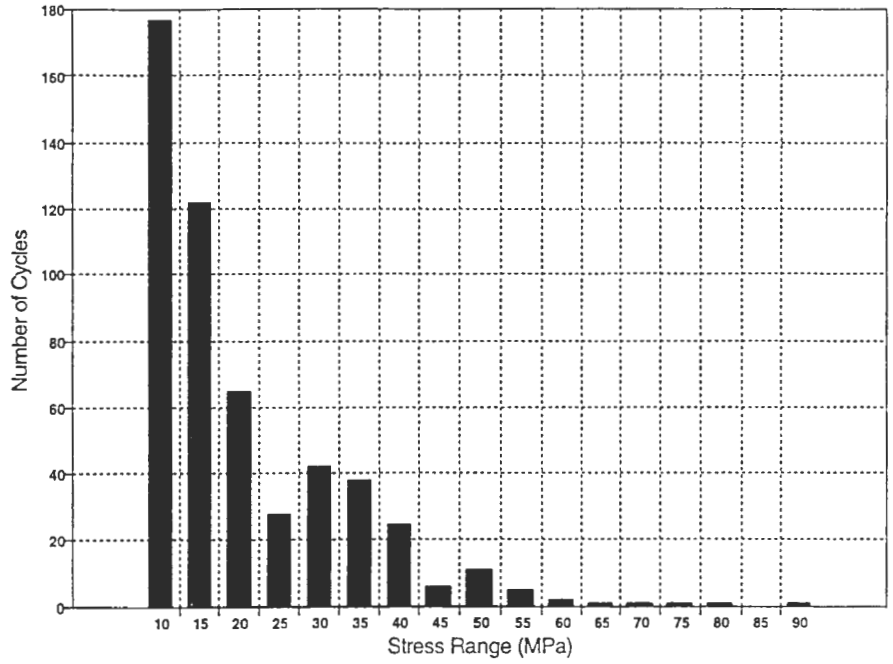

FIGURE 13 Stress range histogram for Gauge 4 on Tie Plate FB2-0E.

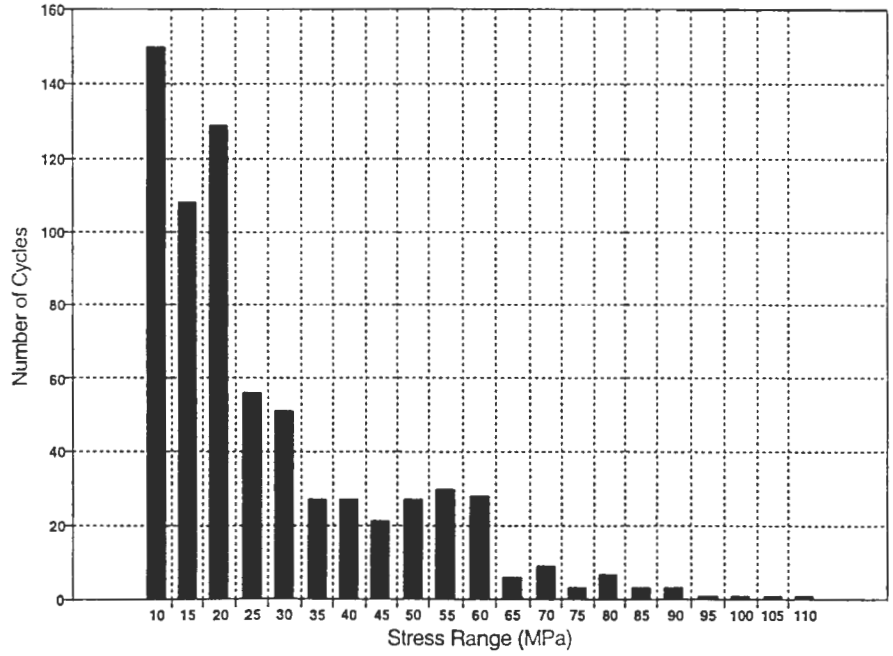

FIGURE 14 Stress range histogram for Gauge 8 on Tie Plate FB1-6E.

14 show the stress cycles greater than 10 MPa (1.5 ksi). The effective stress range can be calculated as

$$S_{re} = \left[\sum \alpha_i S_{ri}^3\right]^{1/3} \quad (3)$$

where α_i is the frequency of occurrence of stress range S_{ri}.

For Gauge 4 with a maximum stress range of 93 MPa (13.5 ksi), the effective stress range for the spectrum shown in Figure 13 was 25 MPa (3.6 ksi). For Gauge 8 shown in Figure 14, the maximum stress range was 116 MPa (16.8 ksi) and the effective stress range was 36 MPa (5.2 ksi).

Fatigue cracks are initiated only from the flame-cut edge or corrosion-notched region of the tie plate by stress cycles higher than 69 to 110 MPa (10 to 16 ksi). These are the fatigue limit resistance levels applicable to Categories C and B, which apply to these conditions. Cracking of the tie plate at FB1-6E is consistent with the stress range levels shown in Figure 14. The other tie plates in the vicinity of Pier 2 have smaller and fewer stress cycles, and this has prevented additional cracks up to now. However, the infrequent stress cycles of high magnitude will continue to accumulate so that other tie plates can be expected to develop cracks in the future where there is clear evidence of loss of composite behavior.

The composite behavior in the Edison Bridge appears to be highly variable, based on the measurements at Piers 1 and 2. The response at Pier 1 demonstrated that the continuous 61-m (200-ft) span as well as the 40.4-m (132-ft, 6-in.) simple span behaved more like a composite system, with few stress cycles exceeding 14 MPa (2 ksi). No cracks will develop at those stress range levels. Furthermore, neither of these locations exhibited the degree of movement that was observed at Pier 2.

Because of the uncertainty of the degree of composite behavior as a function of time, it is difficult to analytically characterize the structural behavior and predict damage accumulation in the tie plates for the short term (10 to 15 years). It is necessary to make a more qualitative assessment that relies on visual observations of the movement between the slab and the girder that may be apparent from the separation or generation of powder. This can be related to the experimental measurements made at Piers 1 and 2. Where there is little evidence of movement, cracking will not develop and inspection of the tie plates need not be carried out. Where movement is apparent, cracks will be more likely to develop and the tie plates should be inspected at reasonable intervals.

At FB1-6E with reduced composite behavior, the stress range spectrum plotted in Figure 14 suggests that stress cycles large enough to initiate a fatigue crack are occurring more than 20 times each hour. This corresponds to about 175,000 damaging stress cycles a year. At flame-cut tie plate edges and corrosion-notched locations, fatigue cracks are likely to develop after 2 to 4×10^6 cycles. This would correspond to 11 to 15 years of service after such stress cycles start to occur. It is not possible to establish when this loss of composite action occurred in the past.

It should also be noted that the measured effective stress range is consistent with the magnitude of stress range associated with fatigue crack extension in the tie plates.

Summary

1. Examination of the crack surfaces in two of the tie plates confirmed that all the cracks were propagated in fatigue. No evidence of rapid crack extension was detected. Severe corrosion of the third crack surface destroyed all evidence of crack extension.
2. The fatigue crack growth characteristics of the tie plates were consistent with the stress range measurements.
3. The fatigue cracks in all three plates initiated from the flame-cut tapered edge. Corrosion had eroded the original edge and destroyed the heat-affected zone.
4. All locations with evidence of movement (i.e., powder visible and separation apparent) that have original tie plates are likely to have stress cycles that exceed their fatigue limit. Hence, cracks will eventually develop at these locations. Nine tie plates had cracked as of 1993, and additional cracks will form in the future. Because it is uncertain when composite action was lost, locations with movement should be inspected annually for cracks.
5. The studies of the cracked tie plates suggest that crack growth after a crack initiates will not cause the tie plate to crack in two during a year of service. The remaining net section can contribute to the resistance of the cantilever bracket web connection should such cracks form.
6. Tie plate locations of the structures with no significant evidence of movement will not experience fatigue cracking for at least 10 years. These tie plate locations need not be given annual inspections.
7. New tie plates with the same width and flame-cut edges installed to replace cracked plates will provide 10 to 15 years of service before cracks initiate.
8. New tie plates that are installed in the future as a short-term fix (i.e., 10 to 15 years) will provide longer lives if the flame-cut edges are ground to provide a smooth edge without the flame-cut serration. They should not crack in less than 15 years.

9. When the structure is rehabilitated and the deck replaced for a long-term fix, a positive shear connection should be provided between the longitudinal girders, transverse floor beams and bracket, and the concrete slab. This will reduce the out-of-plane bending well below the fatigue limit and prevent these cracks from forming.

ACKNOWLEDGMENTS

This study and investigation was carried out for the New Jersey Department of Transportation. The authors wish to recognize and extend their appreciation to all who assisted with this evaluation. Personnel from New Jersey Department of Transportation were very helpful with the field studies, and their assistance was appreciated.

REFERENCES

1. Tada, H., P. Paris, and G. Irwin. *The Stress Analysis of Cracks Handbook*. Paris Productions, Inc., St. Louis, Mo., 1985.
2. Fisher, J. W. *Fatigue and Fracture in Steel Bridges, Case Studies*. John Wiley & Sons, New York, 1984.
3. Fisher, J. W., and C. E. Demers. *Fatigue Cracking of Steel Bridge Structures*, Vol. 1. Report FHWA-RD-89-166. FHWA, U.S. Department of Transportation, March 1990.

Determination of Heat-Straightening Parameters for Repair of Steel Pedestrian Bridge

Henryk Zobel, *Warsaw University of Technology, Poland*

Repair of damaged steel bridges by oversized vehicles is one of the most common problems for maintenance personnel. The application of the thermomechanical method of repair to a pedestrian bridge in Warsaw, Poland, over one of the busiest expressways is presented. The comparison of three kinds of straightening is shown. The thermomechanical procedure was the most effective, but it needs still more theoretical and experimental research.

The deformation of bridges results from the impact of oversized vehicles, fire, and earthquake. Deformations are removed using methods that can be grouped into three categories: thermal, mechanical, and thermomechanical. Experienced personnel in the steel fabrication industry, construction companies, and maintenance operations know which straightening method is appropriate for a given type of deformation. This knowledge is obtained from experience and as such is not often shared. Therefore, it is useful to publish successful procedures for removing the most common deformations. The repair of a damaged pedestrian bridge is described. This type of structure is popular in many cities in Poland, and damage from the impact of an oversized vehicle occurs often.

Choosing the most economical and effective method of repair was, as always, a basic problem. It was also required that traffic continue on the road under the bridge while the heat-straightening repairs were made.

A computer simulation of various kinds of heating with or without the aid of external forces was done. Computer programs based on the method of finite differences (FDM) and of finite elements (FEM) were used for this purpose (*1,2*).

FDM was used to calculate the time-dependent temperature distribution in the I-beam heated by line, rectangular, and V-patterns. FEM was used for thermoplastic analysis of the steel structure.

Specific Problem

The pedestrian bridge crosses one of the busiest expressways in Warsaw (Figure 1). The structure consists of two statically determinate frames joined by a simply supported beam. The frames are connected by cross beams. A noncomposite concrete slab is placed on the steel structure, which is of steel type St3M (A-36).

In one of the frames, the web of the spandrel beam was damaged by the impact of the oversized vehicle. Only the web was deformed. The bottom flange remained perpendicular to the web (Figure 1). The area of permanent deformation covered two-thirds of the length of the beam. The maximum deformation was

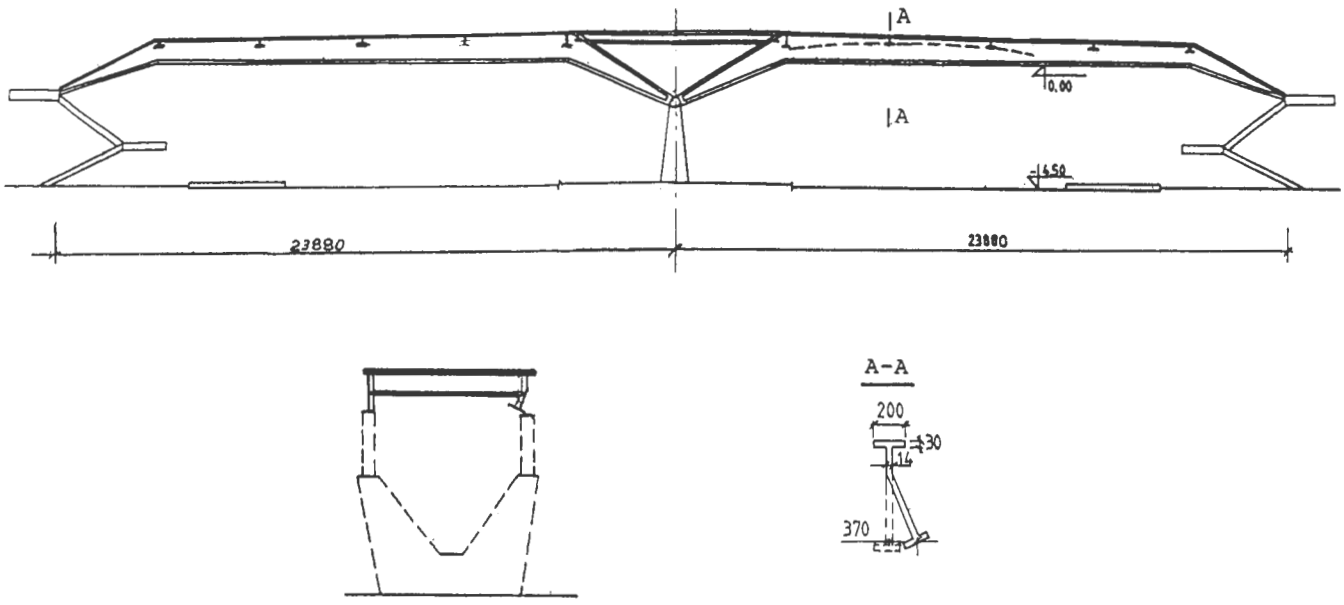

FIGURE 1 General view of pedestrian bridge.

370 mm. There were no sharp indentations, cracks, dents, or nicks.

Because of traffic congestion on the expressway, it was necessary to use a repair technique that would not disturb the activities of the city too much. Under these circumstances, it was decided to repair the damaged girder using the thermal or the thermomechanical method. It was assumed that the whole repair process would be completed over three weekend nights.

Because of a lack of experience in such repair procedures in Poland and little information from publications related to similarly damaged girders (*3–16*), it was necessary to perform more detailed theoretical and experimental analysis.

Computer Analysis

A series of time-independent temperature distributions generated from the heat flow analysis and, in one case, mechanical external forces were used as load steps for a nonlinear finite element analysis that produced strains, displacements, and stresses (*17,18*).

For this case, it was very difficult to assume an initial temperature distribution. Therefore, a transient analysis was used to produce a direct step-by-step solution. A 15-sec time step size was selected initially to ensure a stable solution (*18*). To simulate the heating and subsequent cooling process, a number of temperature profiles were selected so that incremental temperature change would not be too large (less than 100°C).

Nonlinearity was simulated through yielding of steel to obtain its temperature-dependent properties such as elastic modulus, yield stress, and coefficient of thermal expansion. The strains are assumed to develop instantaneously, that is, independent of time. The elastoplastic response of the steel was determined from the flow rule, yield criterion, and hardening rule.

Since the analysis is limited to a study of the plastic behavior of I-beams subjected to bending stresses, the assumption that the stresses through the cross section are nearly uniaxial is acceptable. Figure 2 illustrates the stress-strain curve for mild steel accounting for strain hardening. The Prandtl-Reuss flow rule combined with isotropic strain hardening can be used. Yielding of steel is based on the von Mises yield criterion. The flow and hardening rules are well-documented and have been applied to similar problems (*1,9,12,18*).

At first only the thermal method was considered. Three combinations of pure heating were tested. Case 1 checked the effectiveness of line heating along the deformation limit line combined with a system of V-patterns applied to the bottom flange of the beam (Figure 3). It was assumed that the line heating is made during heating of one pair of V-patterns. Two operators perform the line heating, moving from the center of the deformation limit line to the end, and the V-patterns are also made by two operators in the sequence shown in Figure 3. For analysis, the bottom flange and a portion of the I-beam were treated like a T-beam.

Five pairs of V-patterns were applied simultaneously with different spacings (average 700 mm), as shown in Figure 3. It was assumed that the temperature in the V-pattern exactly underneath the torch would be 650°C. The depth and width of the V-pattern were equal to 100

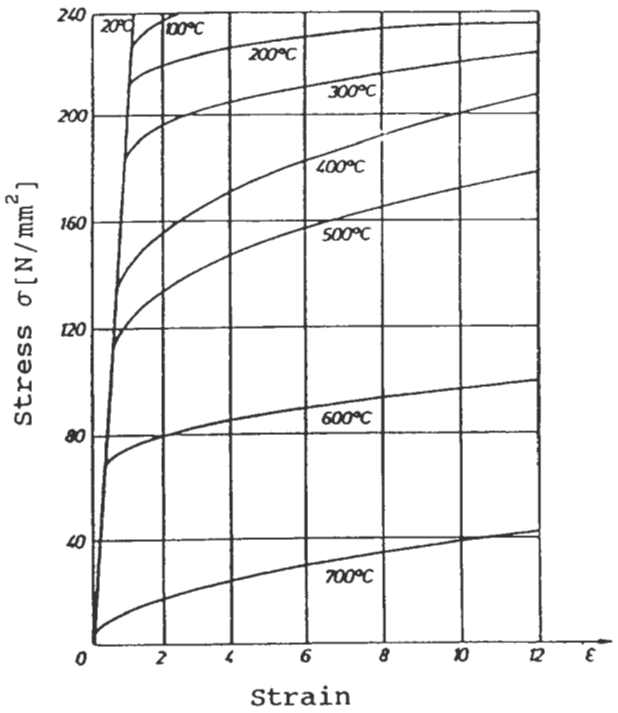

FIGURE 2 Stress-strain relation as function of temperature.

mm. For Case 1 the computed values of deformations were smaller than those required. Since the actual total deformation was about 5 mm, the maximum value of permanent deformation after heating was 1 mm.

Case 2 checked heating of the web of the I-beam by a system of V-patterns that were followed immediately by rectangular patterns on the bottom flange located directly underneath them (Figure 4). Several trials were made using groups of three, four, five, and six V-patterns with different spacings (150 and 120 cm). It was assumed that the maximum temperature under the torch was 650°C.

The depth of V-pattern was equal to the distance from the deformation limit line of the web to the bottom flange (from 400 to 600 mm). Two widths of V-pattern were assumed to be equal to its depth or three-fourths of its depth. The length of the rectangle on the bottom flange was equal to the width of the V-pattern heat. The width of the rectangle was equal to the width of the bottom flange.

The results were better than those for Case 1. The maximum total actual deformation was 6 to 7 mm, and the permanent heat-induced deformation was only 1.5 to 2 mm after one heating. Heat action would not be sufficient to restore the girder to its original shape.

Therefore, it was decided to consider Case 3 to accelerate the process. The beam was heated similarly to Case 2. V-patterns were done on the web and followed immediately by heating rectangular portions of the bottom flange directly under V-patterns.

Simultaneous to the heating, three pairs of external forces (producing a bending moment) were introduced. Force values of 3, 5, and 10 kN with a moment arm of 4000 mm were used. The points of application of the forces were located between two V-patterns (Figure 5).

The results of the analysis of Case 3 determined the preliminary parameters required in the heat-mechanical staightening procedure. They were as follows:

- Width of single V-pattern: 400 mm;
- Depth of single V-pattern: 450 to 600 mm;

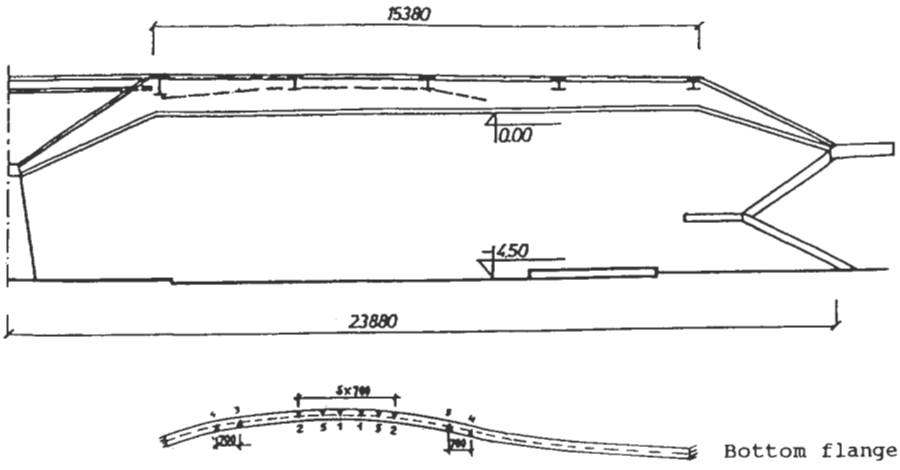

FIGURE 3 Case 1: removal of deformations.

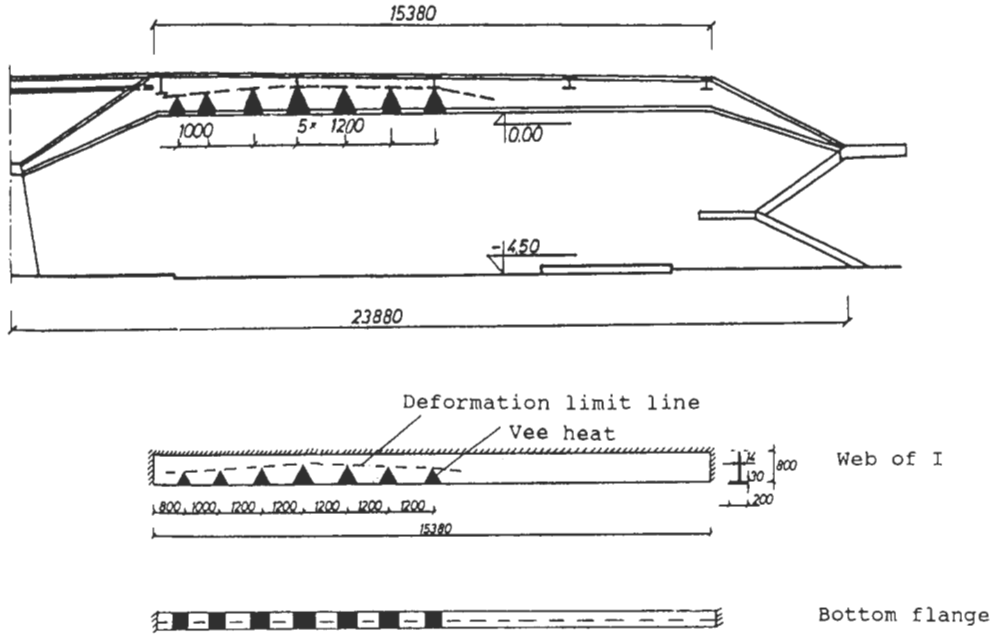

FIGURE 4 Case 2: removal of deformations.

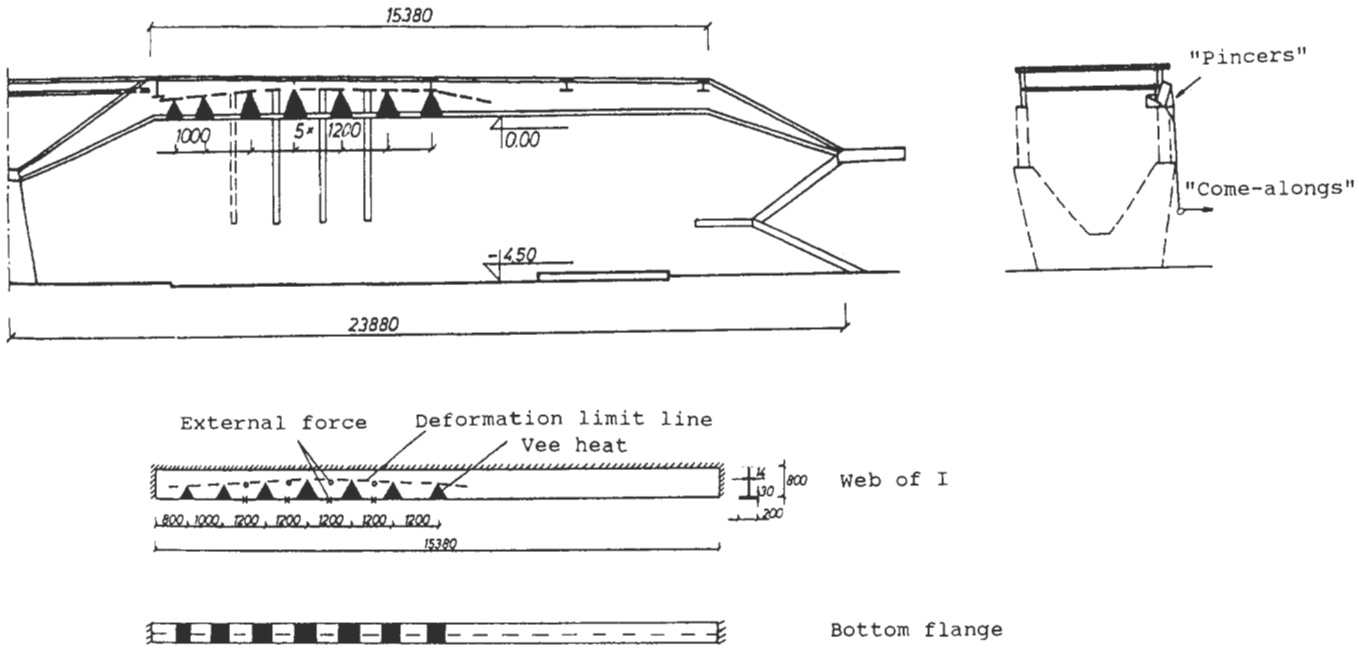

FIGURE 5 Case 3: removal of deformations.

- Spacing of V-pattern: three of their widths, or 1200 mm; and
- Value of one external force: 3 kN.

It was expected that deformations of 90 to 100 mm would be removed during one cycle. Considering the magnitude and values of the deformation, it was decided to apply three or four cycles of combined heating and mechanical action.

For all loading cases it was assumed that the temperature of the steel would not exceed 723°C. This temperature limit will prevent burn-through of the steel and change in the microcrystalline structure.

Field Repair Operations

Field repair operations were organized with the cooperation of the team from the Road and Bridge Research Institute, Warsaw, Poland, led by M. Lagoda (*19*).

The temperature on the surface of the web was measured continuously using thermal detectors. Values of external forces and deformations of the whole structure were also measured. Computer simulation determined the application of simultaneously applied V- and rectangular heats and external forces. The external forces were applied using specially designed pincers (Figure 5), which were pulled by "come-alongs" attached to a heavy truck.

Pure heating using combined V- and rectangular patterns (Case 2) gave a maximum total deformation of 6 mm but only a permanent deformation of 1.5 mm after cooling. This initial trial was not enough to complete the repair, but it compared well with the results of the theoretical analysis.

Next, the thermomechanical method (Case 3) was applied. The number of V's on the web and rectangles on the bottom flange were changed from two groups of three to one group of six done simultaneously. The spacing of the heat patterns was reduced to about 100 cm. The number of pincers was increased from three to five. Theoretically predicted values of external forces were too small, failing some pincers, which were replaced the next day with ones that could accommodate forces in the range of 4.5 to 5 kN.

The main straightening operation was performed during the second night. Three cycles of simultaneous heating and mechanical bending of the web were completed. Each lasted about 40 min, and there was a 1-hr break between cycles. Six operators were required to heat simultaneously the six V-patterns on the web and immediately heat the rectangular parts of bottom flange located directly under the V's. Three more operators pulled come-alongs at the same time, and another three operators distended both flanges of the girder by using three hydraulic jacks. The jacks were placed opposite the heated side of the web. All six V-patterns were peened immediately after each heating-bending cycle was finished. One V-heat and one pincer were transferred from the right to the left side of the web during the third cycle.

Heat was applied as follows: the V-patterns were placed on the external side of the web, to cause shrinking. The heat path in each pattern was kept as close as possible. The speed of the torch was to be 15 cm/min, which was dependent on the operator's skill. The distance between the steel plates and torch head was to be about 8 mm, but it was practically impossible to control that parameter. Continuous control of steel temperature was good. The temperature of 723°C was exceeded only twice for periods not longer than 15 sec. The value of external forces in the come-alongs was checked using ordinary dynamometers.

The deformations in secondary components of the bridge were cleaned up and removed during the third night. Finally, the whole structure was cleaned and painted.

Results of the repair given in Table 1 confirm that the thermomechanical method of straightening is effective from the technical as well as the economical point of view. The deformations are sufficiently large and were straightened in a relatively short time. The permanent deformation of the web in Section A-A (Figure 1) was 366.5 mm, and it was straightened almost completely.

Unfortunately, some local deformations remained in the girder. They are located mainly along the deformation limit line in the web. One local buckle still exists in the bottom flange, where it was hit by the truck. These deformations do not exceed 20 mm and can be removed later by the pure heating method.

It is possible to control most of the technological parameters of the process with sufficient accuracy by carefully monitoring the steel temperatures at the locations where the heat is applied as well as stresses at selected points in the structure.

Conclusions

The following conclusions can be drawn from the thermomechanical heat-straightening procedures described:

1. Pure heating works only when deformations are small. The limits can be determined from computer simulations and in practice.
2. For large deformations it is necessary to combine both heating and mechanical force to straighten members.
3. It is easier to remove large deformations than smaller ones. Smaller deformations require more precise

TABLE 1 Deformation After Heat Straightening

Number of cycle	Total deformation (mm)	Permanent deformation (mm)
I night (heating only)	6	1.5
II night (heating and "pincers")		
1 cycle	120	45.0
2 cycle	250	140.0
3 cycle	330	180.0
		Σ = 366.5

effort and more time and should be done only by skilled and experienced technicians.

4. Torch operators never work in the same manner. Therefore, it is necessary that they be taught how to apply heat patterns to the structure, which is a different skill than welding. The most important rule is to keep the torch at a constant distance from the heated surface and to move it with a constant velocity.

5. Field modification of theoretically designed thermomechanical repairs is always needed. Determination of temperature distribution, real values of modulus of elasticity, yield stress, and coefficient of thermal expansion at elevated temperature are still unknown parameters.

6. It is essential to determine a force and temperature distribution in the structure and to know which part will be plastified and what the corresponding temperature will be. For future life of the structure, it is important to predict which part remains plastified and whether this is dangerous. As assumed in Cases 2 and 3, the statical scheme of the structure under consideration was not appropriate because of difficulties in determining the real restrain from the concrete slab.

7. There is a need to correct calculation techniques and selection of heating parameters in regard to dimensions and spacing of the V-patterns. Those given in the literature conflict and relate mostly to small elements tested only in the laboratory. The techniques given by Baldwin and Guell and by Brockenbrough (*5–8*) are for heat curving, but they proved to be realistic.

8. The observations made during this operation suggest that the depth of the V-heat should be about two-thirds to three-fourths of the steel plate (web or flange) width (depth) or that it must cover the depth of the web deformations. The width of the V-pattern should be about three-fourths of its depth. The estimated spacing of V-patterns needs more research and field verification: according to these observations, it could be two to three widths of the V-heat.

9. The behavior of steel structures in elevated temperatures—that is, in the plastic state—is not always predictable, and the results of theoretical calculations differ greatly from practice.

10. It is more economical to repair structures than to replace them, as shown by the repair techniques described.

REFERENCES

1. Zobel, H. *Thermal Behaviour of Steel Beam Bridges* (in Polish). Civil Engineering Research Paper 116, University of Technology, Warsaw, Poland, 1993.
2. *ANSYS—Engineering Analysis System—Theoretical Manual and User's Manual.* Swanson Analysis Systems Inc. Houston, Pa., 1989.
3. Avent, R. R., and G. M. Fadous. Heat-Straightening Prototype Damaged Bridge Girders. *Journal of Structural Engineering*, ASCE, Vol. 115, No. 7, July 1989, pp. 1631–1649.
4. Avent, R. R. Heat-Straightening of Steel: Fact and Fable. *Journal of Structural Engineering*, ASCE, Vol. 115, No. 11, Nov. 1989, pp. 2773–2793.
5. Baldwin, J. W., and D. L. Guell. *Permanent Deflections and Loss of Camber in Steel Bridge Beams.* Final Report,

Projects 12-1 and 12-6, HRB, National Research Council, Washington, D.C., Nov. 1971.
6. Brockenbrough, R. L. Criteria for Heat Curving Steel Beams and Girders. *Journal of Structural Division*, ASCE, Vol. 96, Oct. 1970, pp. 2209–2226.
7. Brockenbrough, R. L. *Fabrication Aids for Continuously Heat-Curved Girders*. Applied Research Laboratory of U.S. Steel Co., Monroeville, Pa., April 1972.
8. Brockenbrough, R. L. *Fabrication Aids for Girders Curved with V-Heats*. Applied Research Laboratory of U.S. Steel Co., Monroeville, Pa., Jan. 1973.
9. Czudek, H., and H. Zobel. Application of Heating Techniques To Remove Some Kinds of Deformations in Steel Bridges. *Proc., 3rd International Workshop on Bridge Rehabilitation*, Darmstadt, Germany, June 1992, pp. 223–234.
10. Holt, R. E. Primary Concepts for Flame Bending. *Welding Journal*, June 1971, pp. 416–424.
11. Nicholls, J. I., and D. E. Weerth. Investigation of Triangular Heats Applied to Mild Steel Plates. *Engineering Journal*, American Institute of Steel Construction, Oct. 1972, pp. 137–141.
12. Passek, W. W., W. G. Orłow, and W. M. Dusznickij. Heat Straightening of Deformated Steel Structures (in Russian). In *Improvement of Fabrication Technologies of Steel Bridge Structures*, Vol. 103, Moscow, 1977, pp. 94–104.
13. Roeder, C. W. Experimental Study of Heat-Induced Deformation. *Journal of Structural Engineering*, ASCE, Vol. 112, No. ST10, Oct. 1986, pp. 2247–2262.
14. Shanafelt, G. O., and W. B. Horn. *NCHRP Report 271: Guidelines for Evaluation and Repair of Damaged Steel Bridge Members*. TRB, National Research Council, Washington, D.C., 1984.
15. Stewart, J. P. Flame Straightening Technology. La Salle, Quebec, Canada, 1988.
16. Zobel, H. Repair of Steel Bridges by Heat Straightening (in Polish). Report to General Directorate of Public Roads, Warsaw, Poland, Jan. 1992.
17. Passek, W. W. Computer Analysis of Temperature Distribution During Removal of Deformations in Steel Structures (in Russian). In *Improvement of Fabrications Technologies of Steel Bridge Structures*, Vol. 103, Moscow, 1977, pp. 122–129.
18. Schneider, S. P., and C. W. Roeder. Analytical Predictions of Plastic Deformations of Heated Steel. *Journal of Structural Engineering*, ASCE, Vol. 114, No. 6, June 1988, pp. 1285–1302.
19. Lagoda, M., and H. Zobel. Heat-Mechanical Straightening of Plate Girder Bridge. *Proc., 4th International Conference on Safety of Bridge Structures*, Wrocław, Poland, Sept. 1992, pp. 345–350.

Strengthening of Continuous-Span Composite Steel-Stringer Bridges

T. J. Wipf, F. W. Klaiber, F. S. Fanous, and H. El-Arabaty, *Iowa State University*

On the basis of current bridge rating standards, many continuous-span composite steel-stringer concrete deck bridges in the United States are classified as deficient and in need of rehabilitation and strengthening, or replacement. Through several Iowa Department of Transportation research projects, methods of strengthening such bridges have been developed. Ways in which two of these strengthening procedures—post-tensioning and superimposed trusses—have been applied to actual bridges are described, and a design methodology is explained briefly. The strengthening systems were implemented and tested on two existing three-span bridges; both bridges were 45.72 m (150 ft) long and had roadway widths of 7.37 m (24 ft). From two analyses, it was determined that both bridges, when subjected to legal live loads, were overstressed in both the positive and negative moment regions. The bridges, instrumented for strain and deflection measurements, were loaded with trucks before and after strengthening to determine the effectiveness of the strengthening systems. To alleviate the flexural overstress in Bridge 1, a post-tensioning scheme was designed in which the positive moment regions of all beams were post-tensioned. This strengthening scheme reduced the overstresses in both the positive and negative moment regions. In Bridge 2, superimposed trusses were employed over the piers on the exterior stringers in addition to the post-tensioning of the positive moment regions of all beams. In both bridges, considerable end restraint was measured; it was also determined that the guardrails were making a structural contribution. The transverse and longitudinal distribution of post-tensioning forces is summarized, behavior changes are noted, and the effectiveness of both strengthening systems is discussed. A design methodology developed for practicing engineers for use in designing a strengthening system for a given continuous-span bridge will also be described briefly. Both strengthening schemes were determined to be cost-effective and practical techniques.

Of the large percentage of bridges in the United States classified as deficient and in need of rehabilitation or replacement, many are deficient because their load-carrying capacity is inadequate for today's traffic. Strengthening often can be a cost-effective alternative to replacing the bridges or posting them for restricted loads.

The concept of strengthening single-span composite steel-beam concrete deck bridges by post-tensioning has been developed through several Iowa Department of Transportation (Iowa DOT) research projects (*1–6*). Since the completion of the initial design manual (*5*) Iowa DOT has used the allowable stress design methodology for the post-tension strengthening of many single-span bridges.

As a result of the previous success with post-tension strengthening of single-span composite bridges, a re-

search program for strengthening continuous-span composite bridges—similar to the program for single-span bridges—was undertaken. In Phase 1 (*7*) it was verified that continuous-span bridges can be strengthened by post-tensioning. In most continuous-span bridges, the desired stress reduction in the positive moment regions as well as in the negative moment regions can be obtained by post-tensioning only the positive moment regions. This finding was determined theoretically by using a finite element analysis and experimentally by testing various post-tensioning schemes on a 1/3-scale three-span continuous bridge model.

This paper presents the results of Phase 2 (*8,9*), in which two three-span continuous bridges were strengthened by post-tensioning and then tested. The primary goals of this phase of the study were to design and install the strengthening systems on continuous-span steel-beam concrete deck bridges, instrument the bridges for measuring deflections and strains, and document the bridges' behavior for a period after installation of the strengthening systems.

The final phase of the investigation, Phase 3 (*10*), has also been completed. The design methodology developed provides a procedure for determining the magnitude of forces required to strengthen a given continuous-span bridge. Finite element analysis and the experimental results from the two bridge tests described in this paper were used to formulate and calibrate the methodology. As a result of the complexity of the design procedure, a spreadsheet was developed to help engineers determine the strengthening forces required for a given bridge.

Description of Bridges

An advisory committee assisted in locating the two three-span continuous bridges selected for strengthening. For clarification, the bridges henceforth will be referred to as Bridge 1 (located in northwest Iowa) and Bridge 2 (located in central Iowa). The framing plan for the two bridges and the bridges' cross sections are shown in Figure 1. As illustrated, the bridges have a total length of 45.72 m (150 ft), and spans of 13.94 m (45 ft 9 in.), and center spans of 17.83 m (58 ft 6 in.). The four beams in these bridges are coverplated top and bottom near each of the two piers and are spliced at the center-span nominal dead-load inflection points. Except for a small difference in the size of diaphragms at the piers (Bridge 1 pier diaphragms are shown in Figure 1), the two bridges are identical.

Analysis of the bridges indicated that they required strengthening to reduce flexural overstresses as well as additional shear connectors to improve composite action. The strengthening system designed for Bridge 1 involved post-tensioning the positive moment regions of all beams (12 regions). In the end spans, post-tensioning tendons were positioned above the bottom beam flange; in the center span, as a result of large clearances, it was possible to position the tendons below the bottom beam flange. Tendon forces were applied to theoretically reduce all steel beam stresses to levels below operating load levels, thus removing the need for load posting; in all but a few isolated locations, steel beam stresses are actually below inventory stress levels. In total, 6427 kN (1,444 kips) of post-tensioning force was required to strengthen Bridge 1.

The post-tensioning system designed for Bridge 2 was similar to that used on Bridge 1 in that the positive moment regions of all beams (12 regions) were post-tensioned. In addition to the post-tensioning, however, Bridge 2 had superimposed trusses installed on the exterior stringers at the piers (Figure 2). At each of these locations, there are trusses on both sides of the beam web—eight superimposed trusses on the bridge. By post-tensioning the tendons in the trusses, upward forces are produced at the upper truss joints. The combination of trusses and post-tensioning of the positive moment regions makes it possible to reduce stresses the desired amount at all locations in the bridge. Clearance restrictions in Bridge 2 dictated that post-tensioning tendons be positioned above the bottom beam flange at all locations. The total theoretically required tendon forces, increased to account for potential losses, were 6311 kN (1,418 kips). The post-tensioning forces in the positive moment region were significantly smaller than those required to strengthen Bridge 1 [6427 kN (1,444 kips) for Bridge 1 versus 3338 kN (750 kips) for Bridge 2] because of the contribution of the superimposed trusses. In addition to the post-tensioning forces, Bridge 2 had 2973 kN (668 kips) of force applied to the trusses.

As noted previously, both bridges required additional shear connectors for composite action. Because the number of load cycles that had been applied to each bridge was unknown, the number of additional shear connectors required was based on ultimate strength. Double-nutted high-strength bolts 25.4 mm (1 in.) in diameter—essentially the same as those tested and employed in single-span bridges—were used as shear connectors. Added to each interior and exterior beam of the two bridges were 58 and 52 high-strength bolt shear connectors, respectively (220 per bridge).

Field Testing Program

Bridge 1 was strengthened and tested one summer and retested approximately 1 year later. Except for removing and reapplying the post-tensioning forces the second year, the testing program used each year was essentially

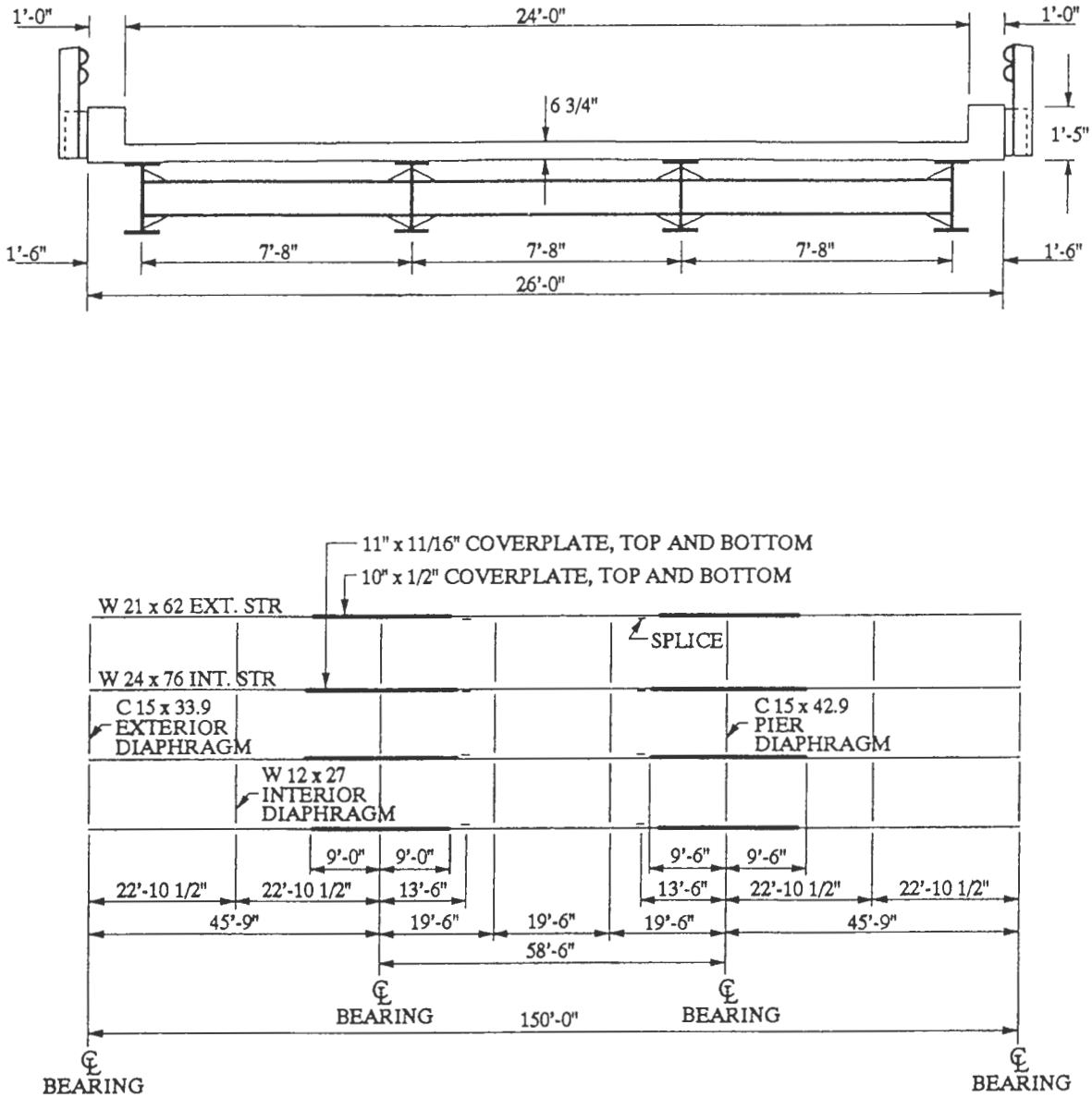

FIGURE 1 Cross section (*top*) and framing plan (*bottom*) of Bridges 1 and 2 (1 ft = 0.305 m).

the same. Bridge 2 was strengthened and tested a few years after Bridge 1. Both bridges were subjected to the following four loading conditions to determine their behavior, strains, and longitudinal and vertical displacements:

1. A heavily loaded truck at various predetermined locations on the bridge;
2. Various stages of the strengthening sequence—because all 12 beams of Bridges 1 and 2 and the trusses of Bridge 2 required post-tensioning, it was necessary to apply the strengthening forces in stages;
3. The same heavily loaded truck at the same locations, after strengthening of the bridges was completed, to determine the effectiveness of the strengthening systems; and
4. Two heavily loaded trucks at various predetermined locations on the bridge, to maximize the moments at various locations.

Although there were some small variations in the instrumentation used on the two bridges, the instrumentation on Bridges 1 and 2 was essentially the same. Instrumentation for the field tests consisted of electrical-resistance strain gauges (strain gauges), direct-current displacement transducers (DCDTs), dial gauges, and crack monitors. Strain gauges (two gauges per location) were mounted on the lower flanges of all beams near

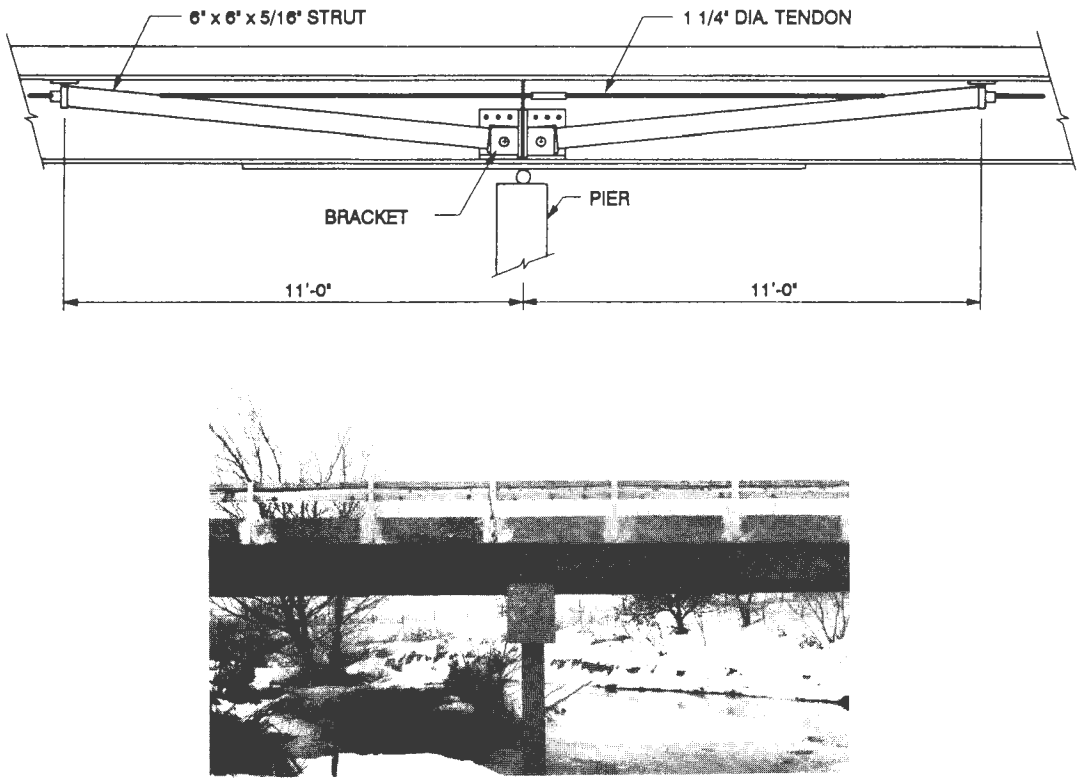

FIGURE 2 Superimposed truss system (1 ft = 0.305 m).

the centerline of each span and near the supports [0.38 m (15 in.) from the centerlines of the piers and end abutments]; thus, there were 14 strain gauges per beam. Strain gauges were also mounted on the tendons so that applied post-tensioning forces and changes in post-tensioning forces due to live load could be measured accurately. A few strain gauges were also mounted on the guardrails of both bridges.

Eight stages of post-tensioning were applied to Bridge 2. Post-tensioned forces were first applied to the trusses (Stages 1 and 2) and then to the beams (Stages 3–8) so that the applied strengthening forces were always applied symmetrically with respect to the centerline of the bridge. Because Bridge 1 only had post-tensioning of the beams, it was strengthened in six stages, which were similar to Stages 3–8 used on Bridge 2. Vertical deflections of the bridges (midspan of all beams) were determined using DCDTs. Longitudinal movements of the bridges relative to the supports were determined using dial gauges and crack monitors. The data from the strain gauges and DCDTs were recorded by a computer-controlled data acquisition system.

As noted, Bridge 1 was retested approximately 1 year after it was strengthened to determine any changes in its behavior and any loss in prestressing forces. Photographs of Bridges 1 and 2 are shown in Figure 3. Bridge 1, which had only post-tensioning of the positive moment regions, is shown in the top of the figure; the bottom illustrates Bridge 2, which was strengthened with post-tensioning in the positive moment regions and with superimposed trusses in the negative moment regions.

Test Results

Only a very limited portion of the results of this investigation is presented in this paper. Additional results on the strengthening and testing of Bridges 1 and 2 may be found in work by Klaiber et al. (*8,9*).

As previously noted, it was necessary to apply the strengthening forces to the two bridges in stages: six stages for Bridge 1, and eight stages for Bridge 2. Except for one location, forces slightly larger than theoretically required were applied to Bridge 1. In Bridge 2, the applied truss post-tensioning forces and a few of the applied beam post-tensioning forces were slightly less than the theoretical values. The effect of one post-tensioning stage on the post-tensioning forces in beams that had been post-tensioned previously was apparent in both bridges. This effect is more significant on beams in the same span and on beams in adjacent spans that are in line with those being post-tensioned. The greatest loss

FIGURE 3 Photographs of strengthened bridges: *top*, Bridge 1; *bottom*, Bridge 2.

observed was 5.9 percent, and the greatest gain was 2.9 percent.

When the post-tensioning forces were removed from Bridge 1 during its retesting 1 year later, it was determined that the largest loss in post-tensioning force on one beam was 10.3 percent and that the largest gain on one beam was 3.8 percent. The average change was a 2.1 percent loss, which is slightly less than the 3.7 percent loss initially assumed in the design of the strengthening system.

Shown in Figures 4 and 5 are the bottom flange strains in an exterior beam (*top*) and an interior beam (*bottom*) resulting from the strengthening of Bridges 1 and 2, respectively. Also shown in these figures are the theoretical bottom flange beam strain variations (obtained from finite element analyses), assuming no restraint at the abutment supports. Except for a few locations, there is excellent agreement between the experimental and theoretical strains in both bridges. Apparent in both bridges is the presence of end restraint at the abutments. Although only the positive moment regions of Bridge 1 were post-tensioned, strain reduction in the negative moment regions is readily apparent. The magnitude of the post-tensioning forces applied to Bridge 1 was based on the desired strain reduction in the negative moment region. In other words, the positive moment regions in Bridge 1 are "overstrengthened." Since Bridge 2 had the superimposed trusses in the negative moment regions, it was possible to apply significantly smaller post-tensioning forces in the positive moment regions. The effect of the trusses is apparent when one compares the theoretical strain curves of the exterior beams in Bridges 1 and 2 [Figures 4 and 5 (*top*)].

In both bridges, a few strain gauges were installed on the guardrails. In some instances, guardrail strains of more than 50 microstrains/inch were recorded, which was a significant percentage of the beam strains that occurred when the load was near the guardrail strain gauges. In other words, the guardrails are carrying a portion of the applied truck loading.

Analysis

The analysis of continuous-span bridges due to the effect of vertical loads is addressed in the AASHTO *Standard Specifications for Highway Bridges*. Wheel load fractions are provided to aid the designer in determining the percentage of the vertical loads distributed to each of the bridge stringers.

Analysis of continuous-span bridges strengthened using post-tensioning and superimposed trusses presents a much more involved problem. The forces acting on the bridge in this case include axial forces and concentrated moments induced by the tendons at the various bracket locations, as well as vertical forces induced at the bearing points of the superimposed trusses. The lateral stiffness of the deck and the diaphragms results in the transfer of a significant portion of the strengthening forces from the strengthened stringer to other stringers. Forces and moments are transferred from one span to the others by the longitudinal continuity of the stringers and the deck. To the authors' knowledge, no practical procedures are available for computing the distribution of the previously described strengthening forces and moments throughout a given continuous-span bridge.

A finite element model was developed to analyze various bridges for different force conditions. Details of the model are provided by Klaiber et al. (*9*). The model was validated using the experimental data presented in this paper.

Development of Strengthening Design Methodology

The use of a finite element model for analyzing bridges under the effect of the forces from a strengthening sys-

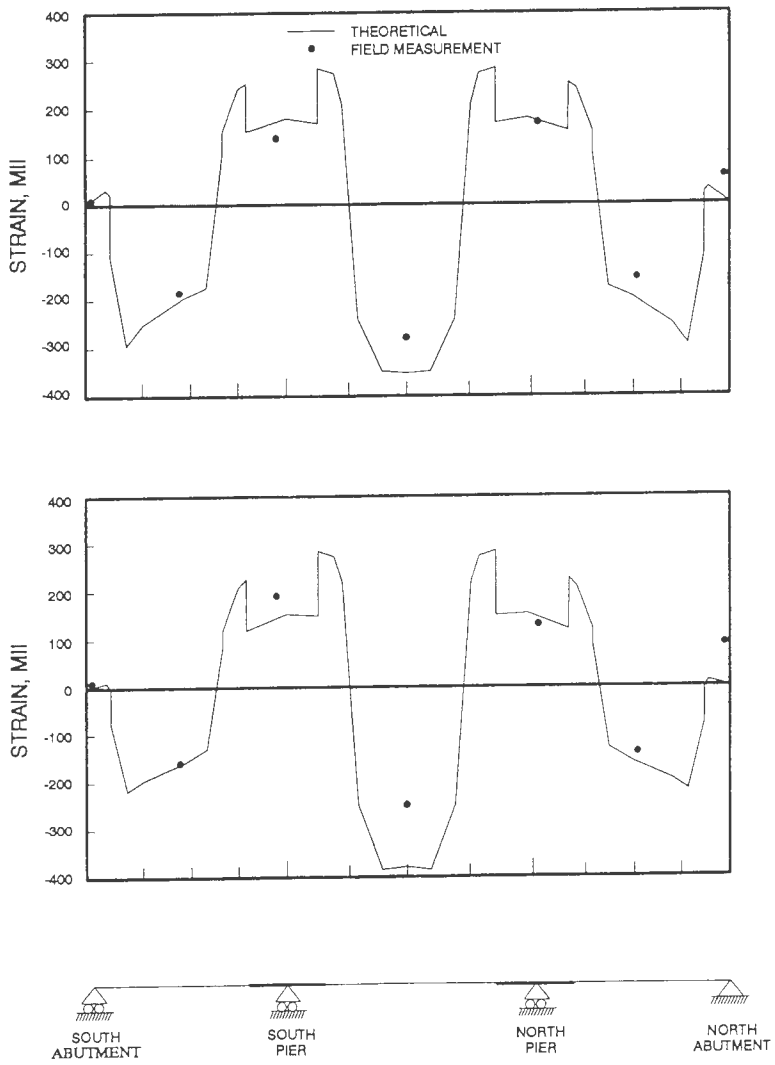

FIGURE 4 Bridge 1 bottom flange beam strains resulting from strengthening (all six stages applied): *top*, exterior stringer; *bottom*, interior stringer.

tem requires access to a large computer, a finite element solution package, and pre- and postprocessing programs. To simplify the design process for a typical continuous-span composite bridge, the authors developed a simplified design methodology for use by the practicing engineer. The development of the design methodology is explained briefly in the following paragraphs.

The design methodology is based on dividing the strengthening system into a number of separate schemes. In each scheme, the post-tensioning forces (or superimposed trusses) were applied so that symmetry was maintained. When designing a strengthening system, the designer can add a number of these schemes together to obtain the desired stress reduction at the various locations on the bridge. The possible strengthening schemes A through E are shown in Figure 6.

A representative example of the axial force and moment diagrams on the bridge stringers, as well as on the full bridge, due to strengthening Scheme A (post-tensioning of the exterior stringers of the end spans) is shown in Figure 7. These results were obtained from the finite element model developed; no vertical scale has been provided in Figure 7, as the comparison is independent of the magnitude of the strengthening forces. Note that the critical sections that have been identified (four for force distribution and six for moment distribution). The number and location of critical sections vary for the five schemes. For Scheme B, there are also four force and six moment critical sections. For Schemes C and D, there are three force and four moment critical sections. Because Scheme E applies only moment, there are only five critical moment sections.

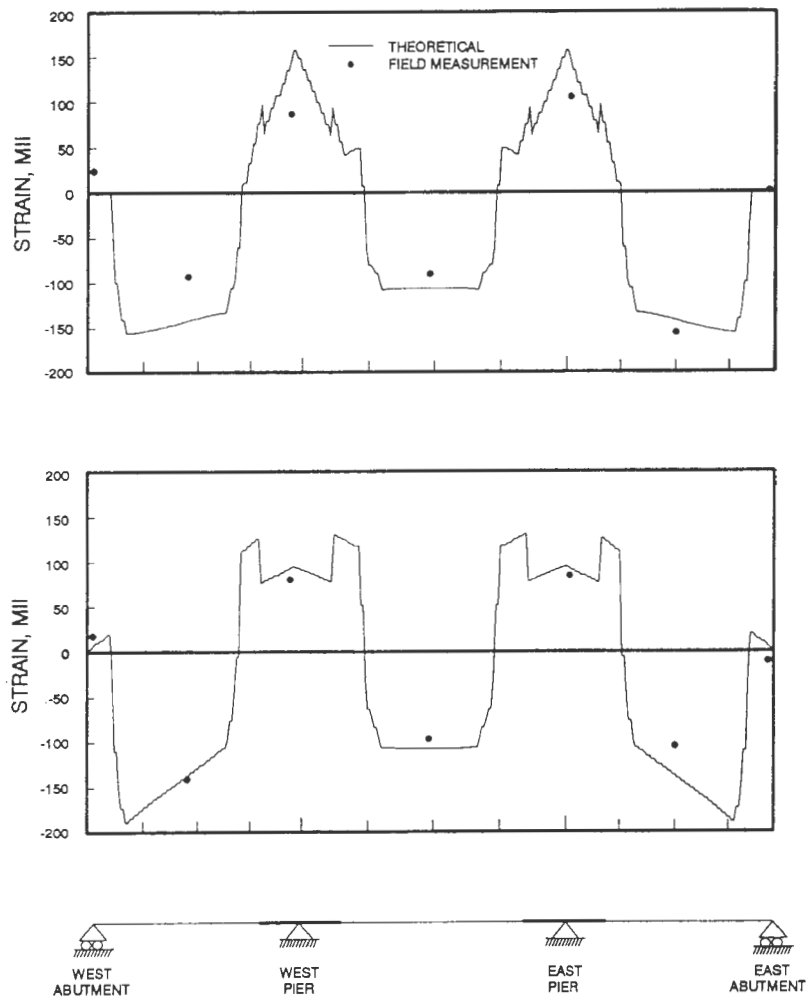

FIGURE 5 Bridge 2 bottom flange beam strains resulting from strengthening (all eight stages applied): *top*, exterior stringer; *bottom*, interior stringer.

For the development of the stringer force and moment diagrams on the stringers without using finite element analysis, several approximations were made to various force and moment diagrams that resulted from the finite element analysis. The first approximation is that the moment on the total bridge section at any section can be determined by analyzing the bridge as a continuous two-dimensional beam. The strengthening forces on the idealized beam are taken equal to the total strengthening forces on all bridge stringers, and the beam moment of inertia at any location is taken equal to the total moment of inertia of the bridge section at this location.

To verify this assumption, several actual bridges were analyzed using the finite element analysis and the idealized beam model; the results from the two analyses were then compared. An example of this comparison (for Scheme C) is shown in Figure 8. As illustrated, the total moments along the bridge obtained by both methods are very close. In analyzing a number of bridges strengthened with the different schemes, it was determined that the difference between the moments computed using the two methods did not exceed 7 percent at critical locations.

Another approximation (made for each of the strengthening schemes) was that the force and moment diagrams for the individual stringers were idealized by straight line segments between the critical sections. The locations of the critical sections were selected to describe accurately the actual diagrams. This straight-line idealization allows the designer to reconstruct the axial force and moment diagrams along the stringers once the magnitudes of force and moment are known at these critical sections.

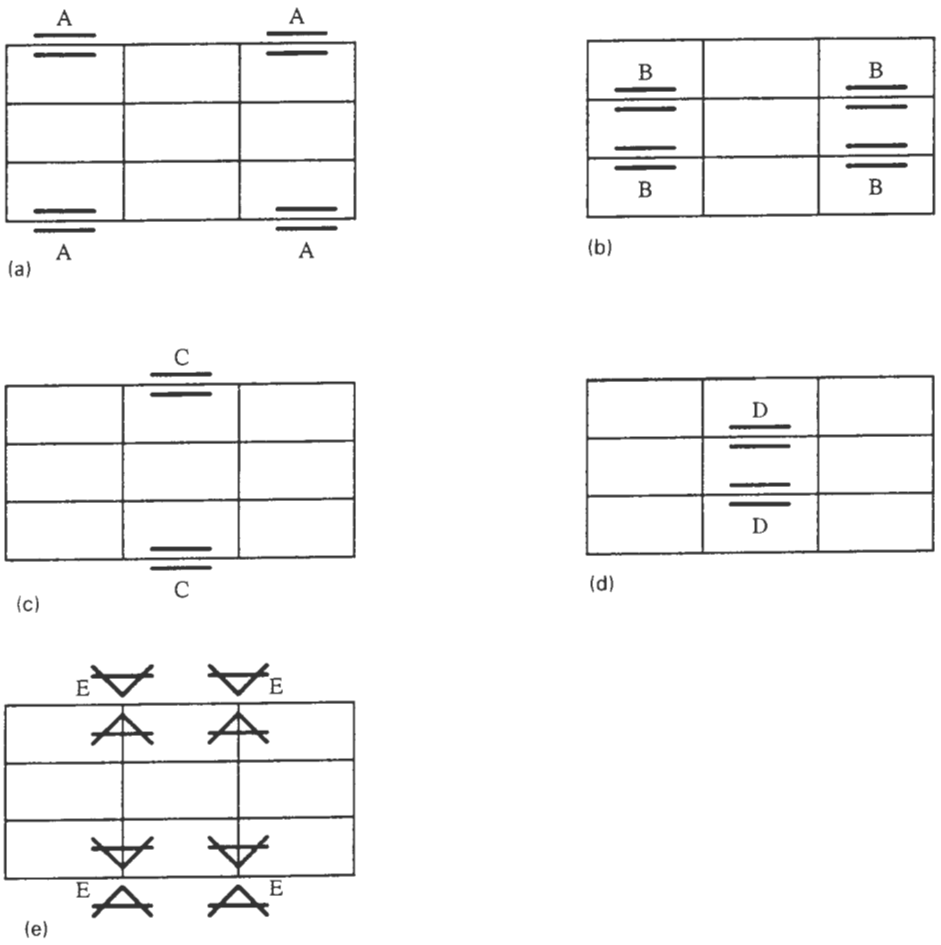

FIGURE 6 Various locations of post-tensioning and superimposed trusses: (*a*) Scheme A: post-tensioning end spans of exterior stringers; (*b*) Scheme B: post-tensioning end spans of interior stringers; (*c*) Scheme C: post-tensioning centerspans of exterior stringers; (*d*) Scheme D: post-tensioning centerspans of interior stringers; (*e*) Scheme E: superimposed trusses at piers of exterior stringers.

Definition of Force and Moment Distribution Fractions

In recognition of the complexity of finite element analysis, a simplified approach was developed that uses force and moment fractions to distribute the strengthening forces to the various stringers. The force (or moment) distribution fractions at the critical sections are defined as follows:

$$\text{Force (or moment) fraction at } (i) = \frac{\text{axial force (or moment) in strengthened stringer at } (i)}{\text{total axial force (or moment) on bridge at } (i)}$$

where (i) indicates the critical section.

So that regression formulas for the force and moment fractions could be developed, several bridges were modeled and analyzed using the finite element model mentioned previously. The 2,400 bridges analyzed included standard Iowa DOT bridges and nonstandard bridges.

All bridges were analyzed with the tendons positioned at an elevation of 88.9 mm (3½ in.) above the top surface of the bottom flange. The effect of changing the elevation of the tendons within a range of 76.2 to 127.0 mm (3 to 5 in.) was investigated and found to have a minimal effect on the distribution fractions. Thus, the force and moment fractions determined in this investigation are valid for any elevation above the bottom flange in this range.

In each of the 2,400 analyses, force and moment fractions were determined at the critical sections using the finite element results. These values were used in developing the design distribution fractions at these sections.

A sensitivity study was conducted to determine the parameters that significantly affected the force and

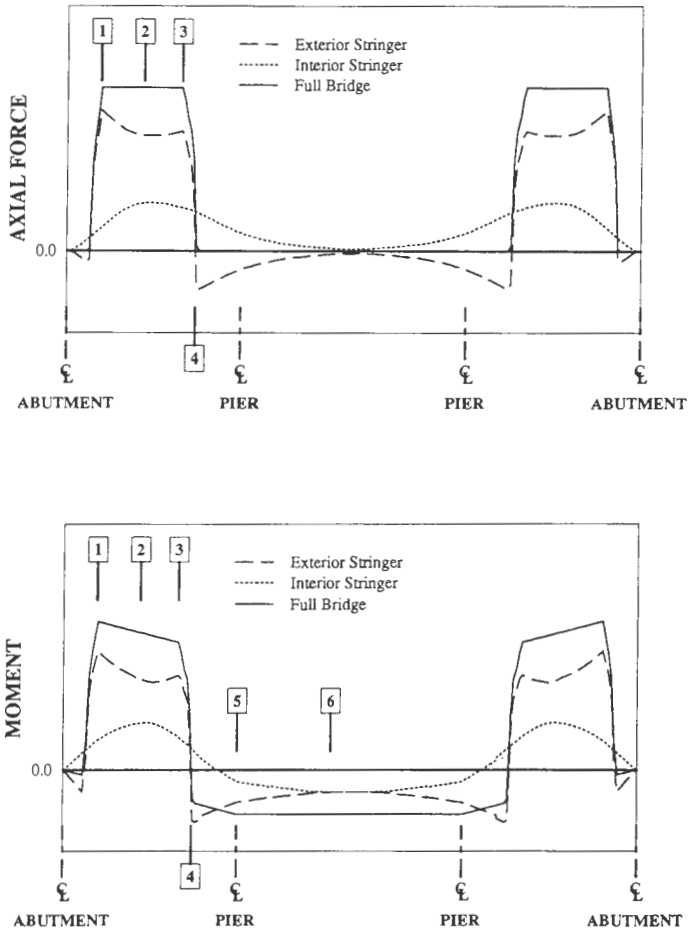

FIGURE 7 Locations of distribution fractions, Scheme A: *top*, axial force diagram; *bottom*, bending moment diagram.

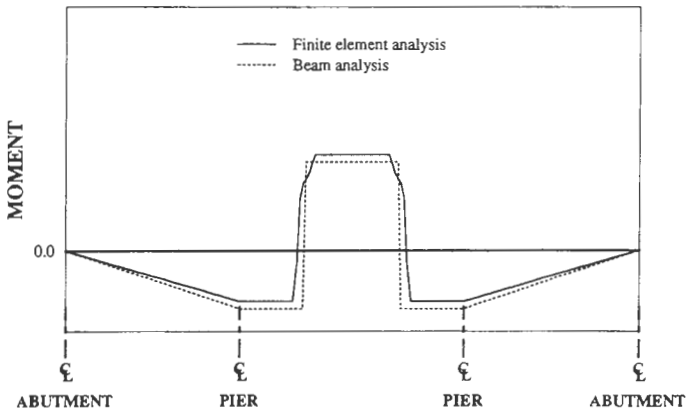

FIGURE 8 Total moments on bridge section, Scheme C.

moment fractions. These parameters included bridge length, angle of skew, ratio of end span to centerspan length, deck thickness, stringer spacing, stringer moments of inertia (composite and noncomposite), and the ratio of the post-tensioned portion of the span to the span length for the various strengthening schemes. To simplify the force and moment formulas, the bridge variables were included as dimensionless parameters.

Limits have been provided for the variables and for the force and moment fractions computed using the regression formulas. Variables and the computed force and moment fractions of the Iowa standard V12 and V14 series bridges are well within the established limits. For bridges with measurements that vary significantly from those of the standard bridges, the formulas do not give accurate force and moment fractions. In these cases it is strongly recommended that a finite element analysis be performed to determine the axial forces and moments in the bridge stringers.

As described, several approximations have been made to provide a simplified procedure for determining the response of the bridge to the strengthening system

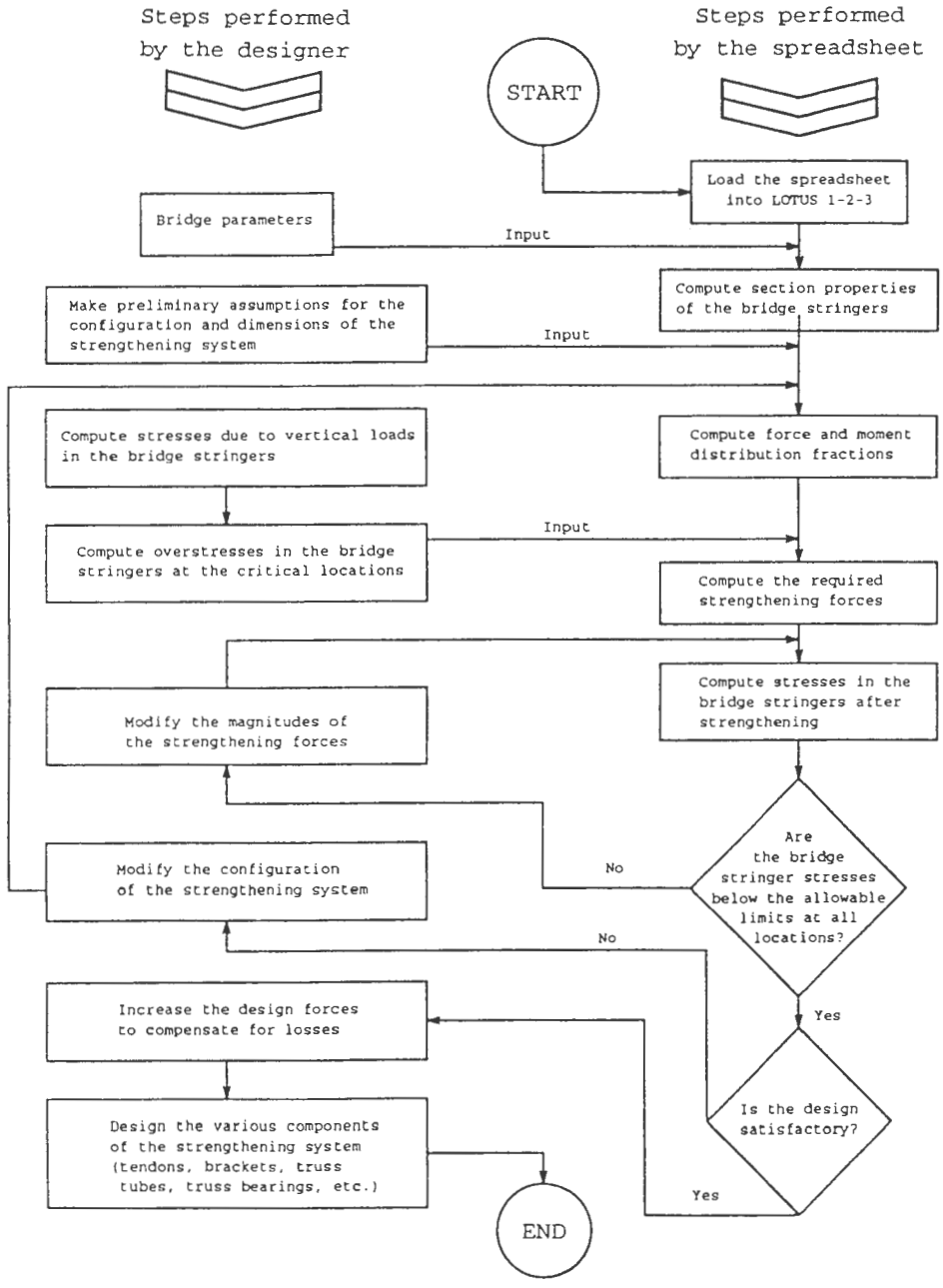

FIGURE 9 Design procedure for strengthening system.

and for designing the required strengthening system. Although the errors resulting from these approximations are small, their collective effect might be significant in some cases. There are several potential sources of error in the design methodology developed: analysis of a given bridge as continuous beams with variable moments of inertia, idealization of force and moment fractions, force and moment fractions, and post-tensioning losses.

Because of the complexity of the design procedure and the large number of formulas, it is difficult to account for the errors in the regression formulas using the error limits corresponding to each formula. Thus, it is recommended to increase all strengthening forces by a conservative 8 percent. The designer, however, needs to check that the stringer stresses based on the original strengthening forces and on the increased strengthening forces are both within the allowable limits.

Recommended Design Procedure

The various steps required in the design of a strengthening system for a typical continuous-span composite bridge are described briefly. For a detailed explanation of the design process, the reader is referred to Klaiber et al. (*10*).

A Lotus 1-2-3 spreadsheet was developed to assist the engineer with designing the required strengthening system. With each section of the spreadsheet, a "Help" area has been provided for guidance. The spreadsheet calculates the required strengthening forces and provides the designer with the final stress envelopes of the bridge stringers. Figure 9 illustrates the steps of the design procedure—those steps that are completed by the spreadsheet and those that must be completed by the designer.

Listed in the following is the procedure for determining the configuration of the strengthening system and the tendon forces required to strengthen a given three-span continuous bridge. Steps 1, 3, 4, and 5 must be completed by the designer; all the other steps, which tend to be more complex and time-consuming, are performed by the spreadsheet.

1. Determine section properties of the exterior and interior stringers for the following sections: (a) steel beam, (b) steel beam with coverplates, (c) composite stringer (steel beam and deck), and (d) composite stringer with coverplates (steel beam, coverplates, and deck).
2. Determine all loads and load fractions for exterior and interior stringers for (a) dead load, (b) long-term dead load, and (c) live load and impact.
3. Compute the moments and stresses in the exterior and interior stringers due to (a) dead load, (b) long-term dead load, and (c) live load and impact.
4. Compute the overstresses at the critical section locations to be removed by strengthening.
5. Make an initial assumption on the strengthening schemes required for tendon lengths and bracket locations. These values are used to compute the initial force and moment fractions.
6. Determine the post-tensioning forces and the vertical truss force that produce the desired stress reduction at the critical sections.
7. Check the final stresses in the exterior and interior stringers at various sections along the length of the bridge; one should especially check the stresses at the coverplate cut-off points, bracket locations, and truss bearing points.
8. Increase the strengthening design forces by 8 percent to account for post-tensioning time losses and errors due to approximations in the design methodology.

Summary and Conclusions

Field tests have been performed on two strengthened bridges to determine the effectiveness of the post-tensioning and superimposed truss concepts. The strengthening system that was designed and installed behaved generally as predicted from analytical results. A finite element model simulating the bridge and the strengthening system was validated from the field test results of the two bridges. A design methodology using this model was developed so that practicing engineers can design a strengthening system for similar continuous-span bridges. Both strengthening schemes were determined to be practical, cost-effective strengthening techniques. The design methodology that uses a computer spreadsheet is relatively simple to use and provides the required strengthening forces.

ACKNOWLEDGMENTS

The research presented in this paper was conducted by the Bridge Engineering Center, Engineering Research Institute of Iowa State University, and was funded by the Highway Research Advisory Board and the Highway Division, Iowa DOT, Ames. The authors thank the engineers at Iowa DOT, especially William A. Lundquist, Bridge Engineer, and John P. Harkin, Chief Structural Engineer, for their support, cooperation, and counsel. Special thanks are accorded the many graduate and undergraduate students who assisted with the various phases of the project.

REFERENCES

1. Klaiber, F. W., K. F. Dunker, and W. W. Sanders, Jr. *Feasibility Study of Strengthening Existing Single-Span Steel-*

Beam Concrete Deck Bridges. Final Report, ERI Project 1460, ISU-ERI-Ames 81251. Engineering Research Institute, Iowa State University, Ames, 1981.

2. Klaiber, F. W., K. F. Dunker, and W. W. Sanders, Jr. Strengthening of Single-Span Steel-Beam Bridges. *Journal of the Structural Division*, ASCE, Vol. 108, No. 12, Dec. 1982, pp. 2766–2780.
3. Klaiber, F. W., D. J. Dedic, K. F. Dunker, and W. W. Sanders, Jr. *Strengthening of Existing Single-Span Steel-Beam and Concrete Deck Bridges*. Final Report, Part I, ERI Project 1536, ISU-ERI-Ames 83185. Engineering Research Institute, Iowa State University, Ames, 1983.
4. Dunker, K. F., F. W. Klaiber, B. L. Beck, and W. W. Sanders, Jr. *Strengthening of Existing Single-Span Steel-Beam and Concrete Deck Bridges*. Final Report, Part II, ERI Project 1536, ISU-ERI-Ames 85231. Engineering Research Institute, Iowa State University, Ames, 1985.
5. Dunker, K. F., F. W. Klaiber, and W. W. Sanders, Jr. *Design Manual for Strengthening Single-Span Composite Bridges by Post-Tensioning*. Final Report, Part III, ERI Project 1536, ISU-ERI-Ames 85229. Engineering Research Institute, Iowa State University, Ames, 1985.
6. Dunker, K. F., F. W. Klaiber, and W. W. Sanders, Jr. Post-Tensioning Distribution in Composite Bridges. *Journal of Structural Engineering*, ASCE, Vol. 112, No. 11, Nov. 1986, pp. 2540–2553.
7. Dunker, K. F., F. W. Klaiber, F. K. Daoud, W. E. Wiley, and W. W. Sanders, Jr. *Strengthening of Existing Continuous Composite Bridges*. Final Report, ERI Project 1846, ISU-ERI-Ames 88007. Engineering Research Institute, Iowa State University, Ames, 1987.
8. Klaiber, F. W., K. F. Dunker, S. M. Planck, and W. W. Sanders, Jr. *Strengthening of an Existing Continuous-Span, Steel-Beam, Concrete-Deck Bridge by Post-Tensioning*. Final Report, ERI Project 3030, ISU-ERI-Ames 90210. Engineering Research Institute, Iowa State University, Ames, 1990.
9. Klaiber, F. W., T. J. Wipf, F. S. Fanous, T. E. Bosch, and H. El-Arabaty. *Strengthening of an Existing Continuous-Span Steel-Stringer, Concrete Deck Bridge*. Report 94403. Engineering Research Institute, Iowa State University, Ames, 1993.
10. Klaiber, F. W., F. S. Fanous, T. J. Wipf, and H. El-Arabaty. *Design Manual for Strengthening of Continuous-Span, Composite Bridges*. Report 94404. Engineering Research Institute, Iowa State University, Ames, 1993.

The opinions, findings, and conclusions expressed herein are those of the authors and not necessarily those of Iowa DOT or the Highway Research Advisory Board.

Controlling Lead-Based Paint Emissions During Rehabilitation of the Williamsburg Bridge: A Partnering Approach

Ralph D. Csogi, *Greenman-Pedersen, Inc.*

The Williamsburg Bridge Main Cable and Suspension System Rehabilitation Project began in 1991 amid public outcry that the communities surrounding the bridge were being contaminated with lead from construction activities. The Occupational Safety and Health Administration was about to lower the construction lead exposure limit to match industry standards. Intense scrutiny existed at the advent of this project: work was about to begin on a structure containing layers of flaking lead-based paint; in addition, the principal protective coating for the main cables would be a 92 percent pure lead paste, all of which would result in a waste stream containing 100 tons of lead. This project was atypical in the sense that containment activities had to address solid wastes (paint chips) and liquid wastes (preservative oil for main cable work) and had to be implemented at the lofty main cable areas over active traffic, transit, and pedestrian ways. The approach taken to make this project an environmental and contracting success was twofold. The first was to incorporate partnering on an informal basis to attain a common environmental standard with which all of the project's parties could concur. The second was to identify each operation that generated a hazardous material and to develop a specific engineering control to address every activity within the operation, from containment to disposal. Each control was tested and evaluated with the appropriate monitoring methods. Each engineering control ultimately was incorporated into the project's Hazardous Waste and Raw Material Management Plan. This "performance-based" approach allowed the development of a readily accepted environmental plan.

By 1890 in New York City, traffic on the Brooklyn Bridge had exceeded everyone's expectations while ferry traffic across the East River continued to flourish. It was clear that a second crossing was necessary, and in fact one had been proposed in 1883, the same year that the Brooklyn Bridge opened. After being delayed for nearly 12 years by ferry interests, legislation was finally passed on May 27, 1895, to build the Williamsburg Bridge.

Leffert Lefferts Buck was commissioned to design this new crossing in 1896. It would have a clear span of 1,600 ft (488 m), making it the longest suspension bridge in the world. It would be 1½ times wider than the Brooklyn Bridge, carry six rail lines, and "yet no feature of the Brooklyn Bridge was to be copied unless it was impossible to substantially improve upon it" (*1*, p. 31). By comparison, the Williamsburg Bridge would dwarf the Brooklyn Bridge in every regard except for its construction cost. The Williamsburg Bridge would be built for $1 million less than the Brooklyn Bridge even though it used twice the tonnage of steel. Table 1 presents a general comparison of the two bridges.

TABLE 1 Comparison of Brooklyn Bridge and Williamsburg Bridge Construction Data

	Brooklyn Bridge	Williamsburg Bridge
Construction Data		
Construction Commenced	January 3, 1870	November 7, 1896
Opened to Traffic	May 24, 1883	December 19, 1903
Total Cost *(a)*	$25,094,577	$24,188,090
Physical Characteristics		
Total Length	6,016 feet (1,835 m)	7,308 feet (2,229 m)
Length of Main Span	1,595½ feet (487 m)	1,600 feet (488 m)
Diameter of Cable	15 3/4 inches (40 cm)	18 5/8 inches (47 cm)
Length of Each Main Cable	3,578 feet (1,091 m)	2,985 feet (910 m)
Total Length of Wire in 4 Cables	14,357 miles (23,115 km)	17,404 miles (28,020 km)
Total Weight of Steel	24,000 tons (21,768 Mg)	47,800 tons (43,355 Mg)
Number of Roadways *(b)*	2/6 lanes	4/8 lanes
Number of Transit Lines *(b)*	none	2
Number of Pedestrian Walkways *(b)*	1	1

(a) includes cost of land
(b) current configuration differs from the original design

Numerous economic factors at the time may have played a role in the cost savings. However, many believe that the decision to use nongalvanized wire in the main cable construction contributed greatly to the material savings. This decision, coupled with the early inadequate cable wrapping systems and preventive maintenance, resulted in the premature decay of the main cable suspension system. The corrosion and decay were believed to be so extensive that by the late 1980s, the main cables were suspected to be at the end of their service life (2). This condition led to many studies, a blue-ribbon technical advisory committee, and an international design competition for replacement alternatives. After years of study and debate, the decision was made to salvage the bridge (2).

Rehabilitation of Williamsburg Bridge

The Williamsburg Bridge will be rehabilitated in essentially four major contracts currently estimated to be valued at $750 million. The first contract, which is the topic of this paper, is nearing 75 percent completion; it addresses the rehabilitation of the main cables and suspension system. The remaining three contracts will reconstruct the superstructure areas in longitudinal "slices"—first the south roadways, then the transit tracks in the center of the bridge, and finally the north roadways. This reconstruction work will be a hybrid in which the approaches to the bridge will be demolished completely and rebuilt from the foundations up, while the main bridge areas will be repaired and redecked with a new orthotropic deck system.

The work under the current contract rehabilitates the four main cables from anchorage to anchorage and replaces all of the main bridge suspenders. The suspender replacements are direct in the sense that no temporary suspenders are required. As one suspender is removed, a new suspender is installed and jacked to the same load as the existing suspender was measured to contain. The only exception is that if an unusually high or low suspender load is found, then 156 kips (695 kN) is used as the new suspender load.

The main cable rehabilitation work has been much more involved, requiring the erection and use of footwalks below each of the main cables to conduct the work. The main cable rehabilitation work generally proceeds in "bays" 20 ft (6 m) long, each bay centered on an existing cable band. The cable bands are steel castings that carry the suspenders on the main span. However, since the end spans are not suspended, these castings merely act as stay bands. Work begins by removing the cable band casting (and suspender) and the outer wire wrapping to expose the main cable wires. The exposed wires within the bay are cleaned of the old lead paste, previously applied preservative oils, and cor-

rosion by-products. The main cable is then opened into "slots" by driving wooden or plastic wedges in a radial pattern into the cable at 18-in. (45-cm) intervals; Figure 1 shows details of this arrangement. Raw linseed oil is poured into these slots and allowed to penetrate into the interior wire areas of the cable. Waste oil is collected using a series of troughs, hoses, and drums.

After the 20-ft (6-m) section of cable has been saturated with oil, the wedges are removed and any broken outer wires are repaired by splicing lengths of new bridge wire in place. Following these repairs, the cable is recompacted using a four-part hydraulic compactor, "squeezing" the main cable at 1-ft (30-cm) intervals, and applying temporary strapping material to maintain the compacted shape. A new cable band casting is installed, and, where applicable, a new suspender is positioned and loaded. These series of operations were repeated along the entire length of each cable, beginning at the low areas of the cable and proceeding to the towers.

After the oiling operation, crews installed the main cable protection systems on the rehabilitated areas. The first level of protection for the main cable is a thick, red lead paste consisting of 92 percent pure lead oxide powder and 8 percent linseed oil. The paste is applied to the outer main cable wires before wire wrapping. Custom-designed wire wrapping machines spirally apply No. 9 (4-mm) wrapping wire onto this red lead paste "bedding" from casting to casting. This operation is illustrated in Figure 2.

The final protective measure for the main cable areas is a neoprene system applied over the wire wrapping. Three coats of liquid neoprene are painted over the wire wrap and sheets of 1/8-in. (3-mm) neoprene 6 in. (15 cm) wide are wrapped spirally in an overlapping fashion from cable band to cable band. The neoprene system is finally coated with three applications of liquid chlorosulfonated polyethylene, or Hypalon.

Clearly, each of the cable operations created a waste stream that included dislodged paint chips, lead-contaminated linseed oil (collected from the oiling work), and red lead-coated rags, and protective suits.

Lead and the Williamsburg Bridge

The Williamsburg Bridge does not differ substantially from most bridges of its era with regard to lead-based coatings. The coatings on the original (nonrehabilitated) members contained 42 percent total lead and 8,500 ppm as determined by the toxicity characteristic leaching procedure (TCLP) (Eder Associates, unpublished data). Lead paint debris is classified as hazardous because of its toxicity. If five mg/L of lead or more is extracted from the debris when tested by TCLP, the debris is considered hazardous. The cable areas, once unwrapped, have a dried layer of old red lead paste mixed with a variety of preservative materials ranging from graphite compounds to fish oil. Samples of these materials have been found to contain 29.2 percent total lead (CONSAD Research Corporation, unpublished data).

Unfortunately, not all of the lead associated with the painted areas of the bridge stayed on the structure. Since the last large-scale painting effort, approximately 15 years ago, the bridge generally exhibits flaking, peeling, and debonded paint coatings that are shaken free of the structure with literally every passage of a subway train. These paint chips have fallen and accumulated in the soils beneath the bridge and on the rooftops and in playgrounds adjoining the bridge. Lead accumulations in these areas are also suspected to be linked to leaded fuel emissions originating from the hundreds of thousands of vehicles using the bridge each year. Studies by the New York City Department of Transportation (NYCDOT) have found the lead content in some soils directly beneath the bridge to be 2,020 ppm and that in rooftop samples to be 63 ppm (GRB Environmental Services, unpublished data). The Environmental Protection Agency's (EPA's) interim guidance for establishing lead clean-up levels at Superfund sites is 500 to 1,000 ppm total lead and is used when the corrected or predicted land use is residential.

But the most problematic emission source, which attracted the greatest media and public attention, was construction activities—in particular abrasive blasting for repair or bridge painting operations. As a result of a poorly contained maintenance painting and abrasive blasting operation (a separate contract) in spring 1992 that affected the community adjoining the bridge in Brooklyn, extremely negative attention was directed to the Williamsburg Bridge just before the start-up of the cable rehabilitation. The media focused on the elevated lead levels in the soils, on roofs, and in the playgrounds, and not only of the Williamsburg Bridge but of numerous bridge facilities throughout the New York metropolitan area. Abrasive blasting and related bridge painting work on public works projects was virtually stopped for 18 months until dramatic changes in containment and monitoring practices were instituted. This was certainly not the climate in which to begin a project that would generate a high volume of lead waste and require the application of nearly pure lead (red lead paste for the wire wrapping work) as a protective coating.

The main question at the time was, How will the contractor perform the work required and ensure that the communities and areas adjoining the bridge were being protected? Ancillary to that question was, How

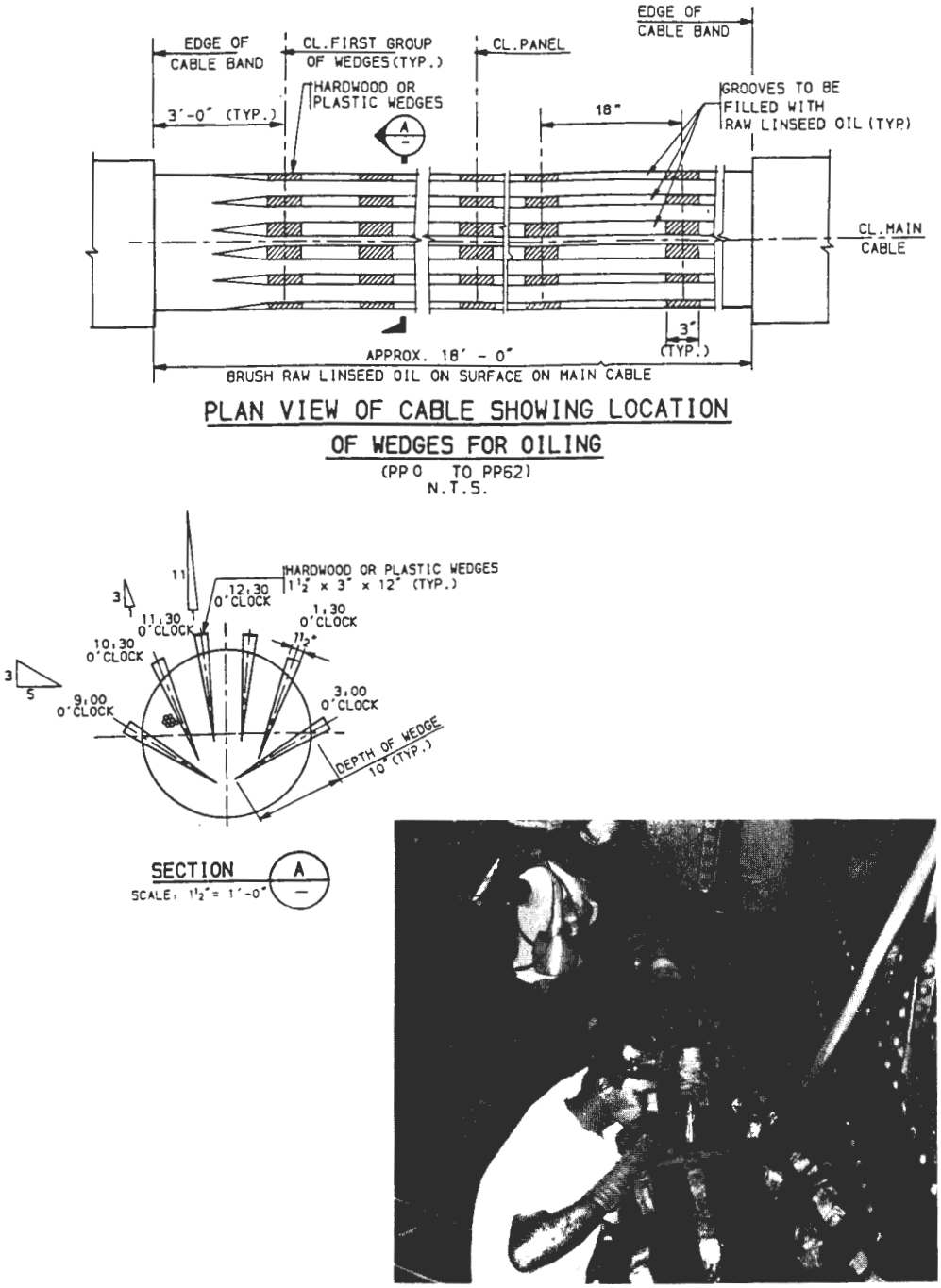

FIGURE 1 Typical main cable wedging arrangement.

will it be done cost-effectively? Contract specifications and language cited guidelines for worker safety and requirements for handling and disposing of lead. However, very little was specified regarding work practices and containment levels other than to assign responsibility to the contractor. Outside the contract specifications, NYCDOT developed its Lead Paint Removal Protocol to address the removal of lead-based paints from its structures in the wake of the 1992 Williamsburg Bridge painting incident. But this document was geared toward removal for bridge painting and localized repair work and did not apply to the type of work involved in the cable rehabilitation. What was needed was a specific work plan that was developed with the contractor to be cost-effective and that addressed the unique nature of the cable rehabilitation work.

FIGURE 2 Wire wrapping main cable areas.

Hazardous Waste and Raw Material Management Plan

The objectives of the Hazardous Waste and Raw Material Management Plan (HWRMMP) were to identify the individual hazardous waste emission sources on an operation-by-operation basis and to develop engineering controls to contain the waste within acceptable levels. In addition, procedures were developed to control the handling of waste products from the point of generation to the storage areas. Each procedure was tested on the bridge using the workers who ultimately would perform the day-to-day rehabilitation work. This test served as an initial training session and afforded an opportunity to perform the appropriate monitoring activity to assess the effectiveness of the control and handling procedures. Once acceptable, the procedure was incorporated into the HWRMMP manual. The various New York City agencies and community groups would have the assurances of a tested work plan for handling and controlling the project's lead-based materials.

A key element of this process was that each engineering control was developed jointly with the contractor, the project's environmental engineering firm, and the construction inspection firm. It was agreed to perform this development work under an informal partnering agreement to expedite the development process and to become as cost-effective as possible to both the owner (NYCDOT) and the contractor. As each engineering control was developed, it was judged whether the additional cost would be borne by the owner or whether the control was inherent to the contract work and therefore accommodated in the contractor's original bid price. Having these discussions during the development of the HWRMMP has mitigated any post-project claims; to date the project is claim-free.

As previously outlined, the main cable areas were unwrapped, the cable was wedged open for the application of oil, and the cable was rewrapped using both a wire wrap and neoprene jacketing system. In addition, all of the cable bands and suspenders were removed and replaced. Plan development began by identifying each work activity along with the hazardous waste that it would generate. The next task was to develop an engineering control or containment structure for each activity. Tables 2 and 3 present summaries of the main cable rehabilitation activities, the generated wastes, and a brief description of the containment method. The final task was to develop a procedure for transporting waste containing flaking paint or dripping oils in areas over active traffic to the storage areas at roadway level.

It was important to identify the tasks requiring containment because of the linear constraints posed by the footwalks. Since almost all of the cable work was performed from these footwalks, which also served as an access way for workers and equipment, containment areas had to be at the "top end" of the rehabilitation cycle. It would be impractical to have workers continually moving through the containment areas to access other operations. After the data presented in Tables 2 and 3 were compiled, it was apparent that in the typical work progression for a span of main cable, the wrapping and cleaning would have to proceed uninterrupted ahead of the oiling operations, followed by the wire wrapping. However, the cleaning for the neoprene system would require stricter containment and consequently, cleaning for neoprene could not begin until the unwrap-oil-wrap cycle was complete. The main cable rehabilitation schedule would be driven essentially by the unwrapping and cleaning operations and the ability to move a containment structure efficiently along the footwalks.

Wire Wrapping Removal and Cleaning Operations

The first construction activity in the cable rehabilitation cycle is to remove the spirally applied wire wrapping and clean the outer main cable wires of corrosion and remnant protective coating products. The wrapping wire was coated with many layers of flaking lead-based paint, and the cable wires contained a variety of dried materials such as lead paste, fish and linseed oils, and, in some areas, more lead-based paint.

To remove the wire wrapping, the wire was initially chisel-cut to loosen an area of it. The wire was loosened in an area approximately 6 in. (15 cm) long and cut with snips along this length. The bundle was opened from the cut line (in the shape of a large C) and removed from the cable. This process was repeated until

TABLE 2 Summary of Cable Rehabilitation Operations, Generated Wastes, and Containment Methods: Main Cable Operations

Rehabilitation Operation	Generated Waste	Containment Methods
Existing Wire Wrapping Removal	Moderately-sized flakes of lead-based paint with some lead contaminated dust released from underlying dried coating.	*1st level* - pouch tarp to catch paint chips. *2nd level* - floor tarp placed on footwalk to catch any errant chips. *3rd level* - tarped sides and roof around cable to act as a secondary containment and wind block.
Cleaning Main Cable Wires	Fine dust containing lead and various preservative materials such as graphite and fish oil.	Same as wire wrapping removal only with pouch lowered for access to underside of cable and door flaps closed for dust containment.
Main Cable Wedging	Some small sized pieces of corrosion product commingled with dried lead paste.	Footwalk floor tarp to catch waste with wind blocks when necessary.
Main Cable Oiling	Lead contaminated oil.	Metal and plastic catch pans with a hose bib connected on downhill side. Hoses were connected to troughs and emptied into containment drums located at roadway level.
Compacting Oiled Cable Section	Lead contaminated oil as cable is squeezed.	Same as main cable oiling. Once compacted, cable is wrapped with plastic shrink wrap and the trough is removed.
Wire Wrapping	Red lead paste contaminated rags, tyvek suits, tarps, empty containers, etc.	Burlap faced tarps (burlene) used as floor tarps to catch any drips. Also, burlap used to prevent "tracking" of any red-lead by continually wiping the worker's boots.
Cleaning Wire Wrap for Neoprene Jacketing System	Lead dust generated by grinding excess (dried) red lead paste from wire wrap.	Floor tarps and tent arrangement similar to that used for wire wrapping removal.

TABLE 3 Summary of Cable Rehabilitation Operations, Generated Wastes, and Containment Methods: Suspender Replacements

Rehabilitation Operation	Generated Waste	Containment Methods
Cable Band Removal	Small amounts of lead-based paint chips.	Floor tarps to catch chips and when applicable, side wind block tarp.
Suspender Removal	Large amounts of paint chips as the suspender flexes and is lowered to the roadway.	Plastic shrink wrap applied to the entire length of each suspender.
New Cable Band Installation (upper attachment for new suspender)	Lead contaminated rags, clothing, etc. as in the wire wrapping operation. The casting is set in a thick bedding of red lead paste.	Same as wire wrapping containment.
Suspender Installation	None	None
Removal and Replacement of the suspender/truss connection (lower attachment for suspender)	Paint chips resulting from cleaning to bare metal for new steel connection. Some minor lead fume from torch cutting. Paint is generally removed prior to cutting, however, there are some inaccessible areas inside the truss framing where the paint cannot be fully removed.	Tarp containment structure to catch paint chips. This containment is built on the underdeck traveling maintenance and inspection platform. HEPA vacuum system to remove lead paint fume.

the area from one cable band to the next was free of wrapping wire. When the outer wires were exposed, they were cleaned by scraping the heavy deposits and then using a power tool (wire wheel).

Hazardous waste was generated in copious amounts and ranged from large flakes of lead-based paint as the wire wrap was bent and removed to a fine dust containing lead particles from the power tool cleaning. The containment structure devised for this work was constructed primarily from tarps and secured to the footwalk and footwalk "high lines." These high lines doubled as hand-ropes and a system to move (slide) the heavy compacting and wire wrapping equipment. Figure 3 illustrates the general arrangement on the footwalk areas.

The tarp containment structure has three basic components and levels of protection. The first containment level consists of a tarp "pouch," which is suspended approximately 1 ft from the main cable. This pouch is used to catch the large chips coming from the wire wrap and to temporarily hold the wire wrapping bundles as they are removed. This collection method is also illustrated in Figure 3. The second level of containment is a floor tarp placed directly on the wooden footwalk planking. This tarp also wraps up the sides of the footwalk side rails. This tarp is used to catch any chips that miss the pouch. The third level of containment addresses the high winds experienced at the cable areas. These windblocks are again tarps, affixed to the footwalk rails and high lines; they serve as a tent over the other containment measures to keep dust and chips from blowing from the work areas. These windblocks also extend across the footwalks to form "flap" doors to provide full containment. This containment system afforded a simple, inexpensive, yet effective method to contain the generated wastes and was readily moved along the footwalks as work progressed. The only precursor to moving this system was that it was vacuumed with a high-efficiency particulate air (HEPA) filtered vacuum to prevent the release of any loosely adhering dust particles.

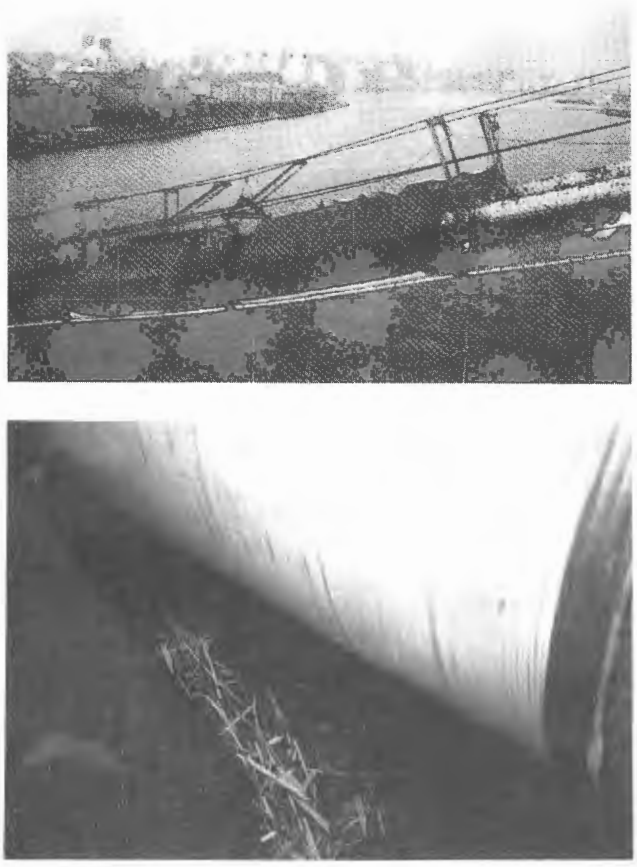

FIGURE 3 Containment system for wire wrapping removal and cleaning operations (*top*); paint chips contained in tarp pouch below main cable (*bottom*).

Worker safety inside these tarped structures was provided with half-face respirators and disposable tyvek suits. Air monitoring was conducted inside the containment areas using MSA Flowlite low flow pumps with 37-mm filter cassettes and calibrated at 2 L/min. Lead concentrations in these areas ranged from 0.71 to 4.63 $\mu g/m^3$ during the power tool cleaning activities (Eder Associates, unpublished data). It should be noted that at the time of this sampling, the Occupational Safety and Health Administration's (OSHA's) regulatory limit was 200 $\mu g/m^3$ (*3*). These results were well below this standard and below OSHA's interim final rule established at 50 $\mu g/m^3$ in June 1993 (*4*). Outside of the containment areas, no particulates were detected above ambient conditions using real-time monitoring equipment.

Waste material handling procedures were developed to convey the paint chips safely from the containment area to disposal drums several hundred feet below, at roadway level. Most of the waste wire wrap and chips were contained in the tarp pouch below the cable. Dislodged paint chips were put into nylon bags at the point of generation, and the bags and wire wrap were placed in a lightweight plastic tub. The tub was lowered by a crane line to a tarped receiving area at roadway level. The contents were emptied into the disposal drum and the drum manifested for disposal. After the pouches were emptied, the interior of the containment structure was vacuumed clean with a HEPA vacuum.

Main Cable Wedging, Oiling, and Compacting Operations

Following the cleaning crews were the wedging, oiling, and recompaction operations. Hardwood or plastic

wedges were driven into 20-ft (6-m) sections of main cable after the cable band casting within the 20-ft (6-m) bay was removed. The wedges were driven manually with hammers in a radial pattern, as shown in Figure 1, so that oil could be introduced into the central areas of the cable. Raw linseed oil was poured into the slots created by the wedges at a rate of 1 gal/linear ft and allowed to penetrate the interior areas. After the cable was oiled, a hydraulically activated compactor was used at 1-ft intervals to compact the main cable wires back to a reduced diameter. The cable was held in this compacted shape with temporary metal strapping. The final operation, performed in a 20-ft bay, was to install a new cable band on a bedding of red lead paste.

These operations created a wide variety of wastes; fortunately, none of them were readily airborne, and the need for full containment was mitigated. The containment system did have to address both solid (corrosion products and red lead-contaminated materials) and liquid (used linseed oil) waste. As the wedges were driven into the cable, the wires moved from their compacted positions and released moderate quantities of corrosion products, old lead paste, and many dried preservative compounds. Containment for this work was accomplished with floor tarps similar to those used in the cleaning containment system. Windblocks were used as necessary to keep the materials within the floor tarp areas.

Linseed oil was poured into the cable from self-capping 5-gal containers. Oil generally dripped from the bottom of the cable section being oiled, but it did travel to lower areas and drip from the new cable bands. To minimize this, bungee cords coated with petrolatum (petroleum-based jelly) were placed radially on the cable at the lower end of the bay being oiled to create a drip point. Metal troughs were used below the cable to catch the oil, which was then piped through hoses to disposal drums at roadway level. In the cases in which oil was observed leaking from the lower castings, half barrels were fitted up to the casting to collect oil. These barrels were drained periodically to the trough system.

The contractor originally had intended to collect and recycle the linseed oil for a paint manufacturer. However, the paint manufacturer elected to perform a series of tests to determine the quality of the oil for recycling purposes and, in doing so, detected small amounts of lead. This lead evidently went into suspension as the oil penetrated and traveled through the cable areas. The lead concentrations were low, 8 to 22 ppm (Eder Associates, unpublished data), but they were above the allowable 5 ppm and the waste oil was characterized as a hazardous waste. All of the applicable regulations pertaining to the storage, transportation, and disposal were incorporated into the waste handling procedures. This included secondary containment barrels, as illustrated in Figure 4, for the waste oil drums stored at roadway level and a fully documented spill response plan.

Suspender Removal and Replacement Operations

The suspenders were replaced one at a time, and five suspenders had to be in place between adjacent removals. The suspenders were unloaded using large impact wrenches to loosen the tension rod nuts, and the suspender was lowered to the roadway using a crane line. With the existing connection clear, structural modifications were performed at the lower attachment point at the truss chord level. Once the cable work at the upper attachment point was completed, a new suspender was hoisted into position and loaded with a hydraulic jacking system.

Full containment for the suspender removal and truss chord connections was required in two very different configurations. The lead-based paint was flaking pro-

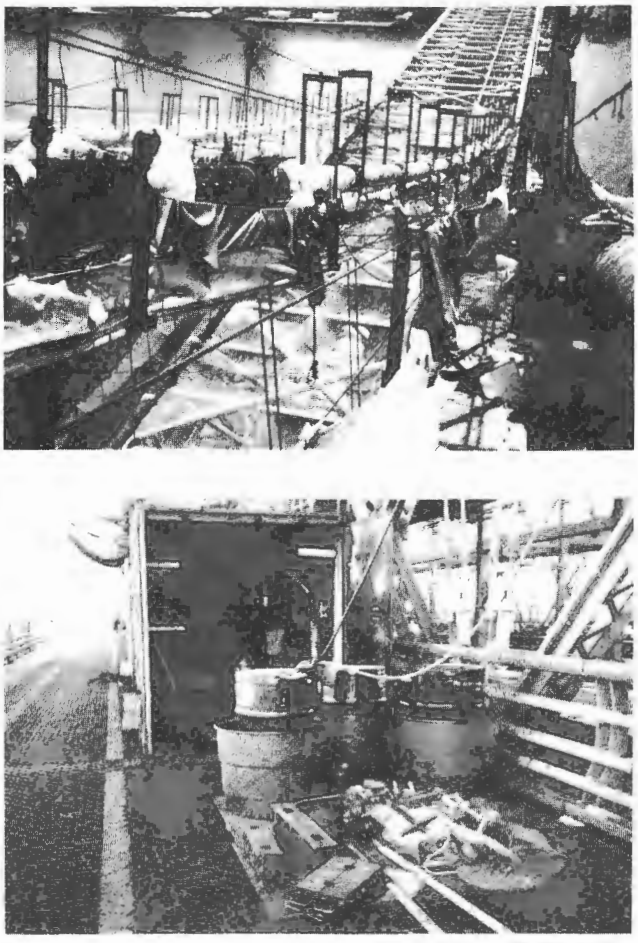

FIGURE 4 Containment system for main cable oiling: *top*, troughs for dripping oil; *bottom*, oil conveyed by hoses to disposal drums.

fusely from the suspender areas as a result of badly deteriorated paint coatings. Several efforts were made to contain the paint chips, beginning with a large footprint of tarps at roadway level to catch chips as the suspender was lowered. As it flexed and curled onto the roadway, the suspender literally rained flakes of paint. This method was abandoned on the first attempt. The next idea considered was a tarp "jacket" loosely fitted to the suspender and hoisted along its length to contain the flaking material and to direct it onto a tarp at roadway level. This approach was abandoned because of its unwieldy nature when applied to the very long suspenders.

The solution was to completely encapsulate the entire length of the suspender ropes with a plastic shrink wrap material. The application of this material is illustrated in Figure 5, along with the lowering operation. As the suspender was lowered, the paint chips were contained in the plastic wrap, and the handling operations were conducted chip-free as long as care was exercised so as not to tear the wrapping. Lowered suspenders were cut into manageable pieces at the point of removal. The cut sections were unwrapped at the designated disposal area, and the dislodged paint chips were collected in disposal drums.

The lower suspender attachment consisted of a pinned structural connection to the existing lower truss chord. The existing connection was removed by removing rivets and torch-cutting several plates from the chord area. The truss chord web areas were cleaned of paint in the faying surface areas, and the new connection was bolted in place. This work was performed in the underdeck areas, and access was afforded from a motorized maintenance platform that ran the length of the main span on traveler rails.

The primary waste from this operation was lead-based paint chips, generated during the removal of the existing suspender connection and from power tool cleaning in the faying areas for the new components. In addition, vaporized lead was released occasionally during the torch-cutting work where lead-based paints

FIGURE 5 Paint chip containment for suspender removal operations: *left*, shrink wrap being applied to suspender from movable scaffolding; *right*, plastic-wrapped suspender being lowered to roadway level.

could not be fully removed before cutting. Not all of the paint was accessible within the tight confines of the truss chord.

Full containment was required for these operations and was extremely difficult to attain because of the need to continually move the containment and the numerous penetrations that were required for the bridge's structural framing. Tarps again were used to facilitate the continual remobilizations and to accommodate the variety of configurations presented by the framing. The traveling platform floor grating and sidewalls were first covered with plywood, and floor tarps were affixed to the plywood. When the traveler was in position under the connection being replaced, side tarps were raised and secured to the framing to create a containment structure. This configuration was used for power cleaning and the required level of worker protection was half-face respirators with protective tyvek suits. When torch cutting was planned, a roof tarp was positioned over the top of the bottom chord and a HEPA vacuum nozzle was fitted into the containment area. As cutting progressed, any lead fume was captured and filtered with the HEPA vacuum system. During the cutting operations, workers were required to use full-face masks with supplied breathing air.

Since the containment structure was below the bridge and directly adjacent to roadways in which traffic was generally slow or stopped, public exposure was an added concern. Air monitoring was conducted both inside the containment and at roadway level to ensure public safety. Real-time monitoring was performed using a miniram particulate dust indicator so that any releases could be detected and corrected immediately. Typical readings adjacent to traffic for the cleaning operations were 0.0 to 0.07 $\mu g/m^3$.

Wire Wrapping and Cleaning for Neoprene Operations

Once the cable rehabilitation work was complete, new protective coatings were applied to the exposed cable areas. The first level of protection was a spirally applied wire wrapping seated in a thick bed of red lead paste. This paste was used as a dense, malleable coating on the outer wires and served to protect against water intrusion in the event of a break or a gap in adjacent wrapping wires. Lead paste was considered to be the optimum material to seal the ungalvanized main cable wires since it is relatively inert and would not promote galvanic action or otherwise present a dissimilar metals condition within the cable. A neoprene jacket was applied to the wire wrapping by coating it with liquid neoprene, spirally wrapping neoprene sheetstock onto this coating, and top coating with Hypalon paint.

The principal waste generated by these operations is red lead. The wire wrapping wastes were in the form of contaminated rags, protective suits, tarps, empty red lead containers, and virtually anything that the lead touched. The secondary waste was generated during the power tool cleaning work and consisted of a fine red lead dust. As the wrapping wire was applied, the red lead squeezed out between the wires and contaminated the outer surface. Most of this paste was wiped clean; however, a fine residue eventually dried on the wire wrap. Before the application of the liquid neoprene, the wrapping was wire-wheel abraded and a fine dust was released. The containment for the cleaning operations after wire wrapping was straightforward in that it was identical to the cable cleaning operations (after removing existing wire wrap). The same waste characteristic was exhibited—a fine dust-containing lead.

The containment for the wire wrapping was similar to that of the wedging and oiling work with the use of burlap-faced tarps rather than plain plastic tarps. These tarps serve a dual function in that they contain any dropped or spattered material in the work area, and with the burlap surface, settled dust is trapped in the fabric and the workers' boots are wiped continually. This dramatically reduces the tracking of lead to other areas on the bridge. Every attempt was made to keep the red lead paste migration to a minimum. Of all of the generated wastes, red lead paste is the most difficult to control. It cannot be swept or vacuumed, and it does not readily wipe off of surfaces. Because of its superior adherence properties and extremely high lead content, the greatest risk to workers is ingestion. Worker training was essential to inform the crews of the need to completely remove any paste from their hands before eating, to dispose of all contaminated clothing, and even to keep their work clothes on site and not at home. Work clothes containing minor amounts of lead paste could contaminate other clothing in the household wash.

Conclusion

The HWRMMP has played a major role in the success of the main cable rehabilitation project. With the main cable work nearing completion, there has been no negative media coverage, work stoppages, or community opposition. To date, 105 tons (95 Mg) of solid hazardous waste and 12,500 gal (47 300 L) of contaminated oil has been collected safely, manifested, and shipped off site.

It has been traditional to specify a certain level of containment for a project and add the contractual language to place the environmental responsibility on the contractor under a lump-sum bid price. This results in

either a high cost for the environmental portion of the contract or, when underbid, an inordinate number of claims for changes in scope.

A key element of the approach taken on the Williamsburg Bridge Main Cable Project was its focus on identifying the emission sources and preparing a performance-based approach to the environmental issues. The project's environmental consultant, the construction manager, the owner, and the contractor must work together in preparing this plan. Sufficient time must be included in the mobilization phase of the project to perform the testing and demonstrations necessary to the plan development. The owner must be willing to allocate the additional funds for the development phase and consider it an investment given the potential for large losses should a public health problem occur. The owner should also consider new payment methods. Instead of a unit bid price or lump-sum bid price arrangement, an estimated amount should be set aside and stated in the bid documents as a fixed-price lump sum. During the plan development stage and the actual work phases, the contractor is paid from this fixed-price account or on a time, material, and equipment basis. Any unanticipated scope changes are readily accommodated.

The next phase of the Williamsburg Bridge will begin in 1995 and will have the challenge of demolishing nearly 1 mi of elevated approach structure. These approaches are coated with lead-based paints and lie directly adjacent to the communities' residences, schools, and playgrounds. Work has already begun on developing a performance-based approach for the demolition effort and for containing and handling all the project's hazardous materials.

ACKNOWLEDGMENT

Eder Associates of Locust Valley, New York, is acknowledged for its conceptualization and a diligent implementation of the HWRMMP for the Williamsburg Bridge Rehabilitation Projects.

REFERENCES

1. Reier, S. *The Bridges of New York*. Quadrant Press, New York, 1977.
2. *Summary Report to the Commissioners of Transportation of the City and State of New York*. Williamsburg Bridge Technical Advisory Committee, 1988.
3. Occupational Safety and Health Administration. *Safety and Health Regulations for Construction*. OSHA 2207, 29 C.F.R., Part 1926, 1991.
4. Occupational Safety and Health Administration. *Lead Exposure in Construction*. Interim Final Rule. Docket H-004L, 29 C.F.R., Part 1926.62, 1993.

SEISMIC RESPONSE OF BRIDGES

Improved Screening Procedure for Seismic Retrofitting of Highway Bridges

Ian G. Buckle and Ian M. Friedland, *National Center for Earthquake Engineering Research*

Recent damaging earthquakes in California and elsewhere have demonstrated once again the seismic vulnerability of highway bridges in the United States. Retrofitting programs for correcting deficiencies in existing bridges have been proposed since the 1970s, but until very recently only California has been active in the field. In 1983 FHWA published a set of retrofitting guidelines for bridges; recently they were revised to reflect advances made in the state of the art during the past decade. The improved screening procedure, which has been recommended in the revised FHWA manual, is presented. Differences between the old and new procedures include a new priority-ranking process, revised seismic performance categories, expanded definitions for bridge importance, and new flow charts to illustrate and clarify the assignment of structure vulnerabilities.

The recent occurrence of damaging earthquakes in California, Costa Rica, and the Philippines has demonstrated, once again, the vulnerability of highway bridges that have not been designed adequately to resist seismic loads. Although seismic design codes have been in place in the United States for a number of years, more than 75 percent of the U.S. bridge inventory was constructed before these codes became effective. There is therefore a pressing need to develop and implement appropriate seismic retrofit programs throughout the United States.

The practice of seismic retrofitting is, however, limited to a few states, primarily California, Illinois, Nevada, and Washington. This situation exists partly because bridge owners are faced with many competing demands on their limited resources. But it is also due to the limited availability of tools and technologies for retrofitting. It is therefore of importance that bridge owners have rational methodologies for screening bridges for their seismic risk and ranking those that are deficient according to their vulnerability, importance, cost, and other societal factors.

One of the first attempts to develop a rational prioritization methodology was undertaken by the Applied Technology Council (ATC) in the early 1980s. The ATC-6-2 project was conducted for FHWA and resulted in the publication of the 1983 FHWA report *Seismic Retrofitting Guidelines for Highway Bridges* (*1*). The guidelines introduced a preliminary screening procedure and a method for evaluating an existing bridge. They also described potential retrofitting measures for the most common seismic deficiencies.

Since 1983 several states have developed their own screening and priority-ranking procedures. Usually these have been based on the ATC-6-2 methodology, augmented by additional parameters and, in some cases, nontechnical considerations. Two papers by Buckle have summarized the preliminary screening and prioritization procedures in use by five states as of 1992 (*2,3*).

Since then, several other states have begun seismic retrofit programs and rapid screening procedures have also been proposed for bridges in Canada (*4*).

In the 10 years since publication of the FHWA guidelines, the state of the art in seismic retrofit has advanced substantially. As a consequence, the FHWA publication has been revised and reissued as a manual for the seismic retrofitting of highway bridges (*5*). The revision reflects experience gained with the use of the 1983 guidelines as well as new knowledge acquired through research and earthquake reconnaissance studies. It also reflects recent changes in seismic design philosophy that have been proposed for the design of new highway bridges under projects sponsored by AASHTO through NCHRP (Project 20-7, Task 45, for the revision of current seismic design criteria and Project 12-33 for limit state design specifications), and by the California Department of Transportation (Caltrans) through the ATC (Project ATC-32, for the review of Caltrans seismic bridge design specifications).

As part of this review, the screening procedures in the 1983 guidelines were examined and modified as appropriate. This paper summarizes these modified procedures, which are based on the previous methodology but refined as necessary to include a new priority-ranking process, revised seismic performance categories, expanded definitions for bridge importance, and new flow charts to illustrate and clarify the assignment of structure vulnerabilities. For completeness of presentation, some of the material in this paper is taken directly from the 1983 guidelines; the pioneering work by the authors of these earlier guidelines is again recognized.

Seismic Retrofitting of Highway Bridges

Not all bridges in a highway system can be retrofitted simultaneously; instead, those bridges with the highest priority should be retrofitted first. The screening and ranking of bridges for retrofitting requires not only consideration of the engineering factors but also an appreciation for the economic, social, administrative, and practical aspects of the problem. But it should always be remembered that seismic retrofitting is only one of several possible courses of action. Others are closing the bridge, replacing the bridge, and taking no action at all and accepting the risk of seismic damage.

Bridge closure (or replacement) usually is not justified by seismic deficiency alone and generally will be considered only when other deficiencies exist. Therefore, for all practical purposes, a choice must be made between retrofitting and accepting the seismic risk. This choice will depend largely on the importance of the bridge and on the cost and effectiveness of the various retrofitting alternatives. If the cost is high and the bridge is critically important, retrofit (or even replacement) may be the best strategy. If the cost is high and importance is not an issue, accepting the risk may be the most attractive option.

Regardless of the outcome, bridges must first be screened and those found to be deficient subjected to a second, more detailed evaluation. If a bridge is still considered vulnerable, retrofit measures are designed and cost data obtained. At this point the decision to proceed with retrofitting must be made considering cost, remaining useful life, importance, and other socioeconomic factors. In general, therefore, the seismic retrofitting process can be divided into the following three major steps:

1. Preliminary screening,
2. Detailed evaluation, and
3. Design of retrofit measures.

This paper describes only the first step: the preliminary screening procedure as recommended in the revised FHWA manual for seismic retrofitting (*5*).

Preliminary Screening Methodologies

The intent of a preliminary screening methodology is to develop a prioritization scheme on which to base a retrofit program. The methodology requires access to, or a compilation of, a seismic inventory of all bridges to be screened, followed by the execution of one of several possible numerical rating (or ranking) schemes. Since not all the issues can be reduced to a numerical factor, a critical review of the results is usually undertaken and other factors, such as redundancy and economic constraints, are taken into account when a prioritized list is finally assembled.

Buckle (*2,3*) notes that many screening and prioritization schemes in use today include three important components:

- Seismicity of the bridge site,
- Vulnerability of the structural system, and
- Importance of the bridge.

These schemes usually address each of these variables separately by requiring that an importance, seismicity, and vulnerability rating be calculated for each bridge. These individual ratings are then combined to arrive at an overall seismic rating.

More recently, Basöz et al. have proposed a methodology to priority rank highway bridges for seismic retrofitting on the basis of risk (*6*). Risk, in this approach, is expressed primarily as a function of the expected dollar loss. The vulnerability and importance of

a bridge are the two main criteria used for the overall ranking purposes. A lifeline network analysis is then used to integrate the vulnerability and importance criteria.

The revised FHWA manual described earlier recommends a modified screening and prioritization scheme in which the quantitative variables (seismic, geotechnical, and structural vulnerabilities) are separated from the qualitative factors (importance and other socioeconomic issues) in a two-step process. To do so, the ranking system requires first the calculation of a bridge rank that is based on engineering factors and then the assignment of a priority index based on this rank and socioeconomic (e.g., importance) and nonseismic issues. Figure 1 illustrates this screening procedure as it might apply to bridges in different seismic performance categories (SPCs).

Bridge Classification

Before seismic retrofitting can be undertaken for a group of bridges, they should first be classified according to their SPC. This classification is determined by a combination of seismic hazard and structure importance.

Seismic hazard may be quantified by the acceleration coefficient (A); when multiplied by the acceleration due to gravity (g), the product, Ag, represents the likely peak horizontal ground acceleration that will occur due to an earthquake sometime within a 475-year period. More rigorously, this acceleration has a 10 percent probability of being exceeded within a 50-year time frame (*7*). Maps showing the distribution of A throughout the United States are given elsewhere (*5,7*).

Bridge importance is not so readily quantified. Two importance classifications are specified in the FHWA manual: essential and standard. *Essential* bridges are those that should continue to function after an earthquake or that cross routes that should continue to operate immediately after an earthquake. All other bridges are classified as *standard*. The determination of the importance classification of a bridge is subjective, and consideration should be given to societal/survival and security/defense requirements.

The societal/survival evaluation addresses a number of socioeconomic needs and includes, for example, the need for access for emergency relief and recovery operations just after an earthquake. Security/defense requirements may be evaluated using the 1973 Federal-Aid Highway Act, which requires that each state develop a plan for defense highways. The defense highway network provides connecting routes to military installations, industries, and resources not covered by the Federal-aid primary routes.

An essential bridge, then, satisfies one or more of the following conditions:

- It is required to provide secondary life safety; for example, it provides access to local emergency services such as hospitals. This category also includes bridges that cross routes that provide secondary life safety and bridges that carry lifelines such as electric power and water supply pipelines.
- Its loss would create a major economic impact; for example, such a bridge serves as a major link in a transportation system.
- It is formally defined by a local emergency plan as critical; say, it enables civil defense, fire departments, and public health agencies to respond immediately to disaster situations. This category also includes bridges that cross routes that are defined as critical in a local emergency response plan and bridges that are located on identified evacuation routes.
- It serves as a critical link in the security/defense roadway network.

From these considerations for seismic hazard and importance, four SPCs are defined as given in Table 1. As in the 1983 FHWA guidelines (*1*), these SPCs are used to set minimum retrofit requirements. For example, a bridge in SPC A need not be retrofitted at all, whereas an SPC B bridge need be evaluated only for connections and seat widths.

Note that these SPCs are assigned differently than those in the AASHTO specifications for new design, where no allowance for structure importance is made in seismic zones with acceleration coefficients of less than 0.29 (*7*). In view of the high cost of retrofitting, it is important to distinguish between essential and standard structures, especially so in low to moderate seismic zones. Such a distinction also enables a more rational allowance for the nature of the seismic hazard in the central and eastern United States, where the maximum credible earthquake is expected to be much larger than the "design" earthquake (475-year event). This implies that if an essential bridge in the East is to survive a large earthquake, it may need to be retrofitted to a standard higher than that required by the previous guidelines, which did not distinguish between essential and standard bridges in low to moderate seismic zones. This observation is reflected in the assignment of SPCs for essential bridges in Table 1.

Seismic Inventory of Bridges

The first step in implementing a seismic rating system is to compile an inventory with the objective of establishing the following basic information: (a) the struc-

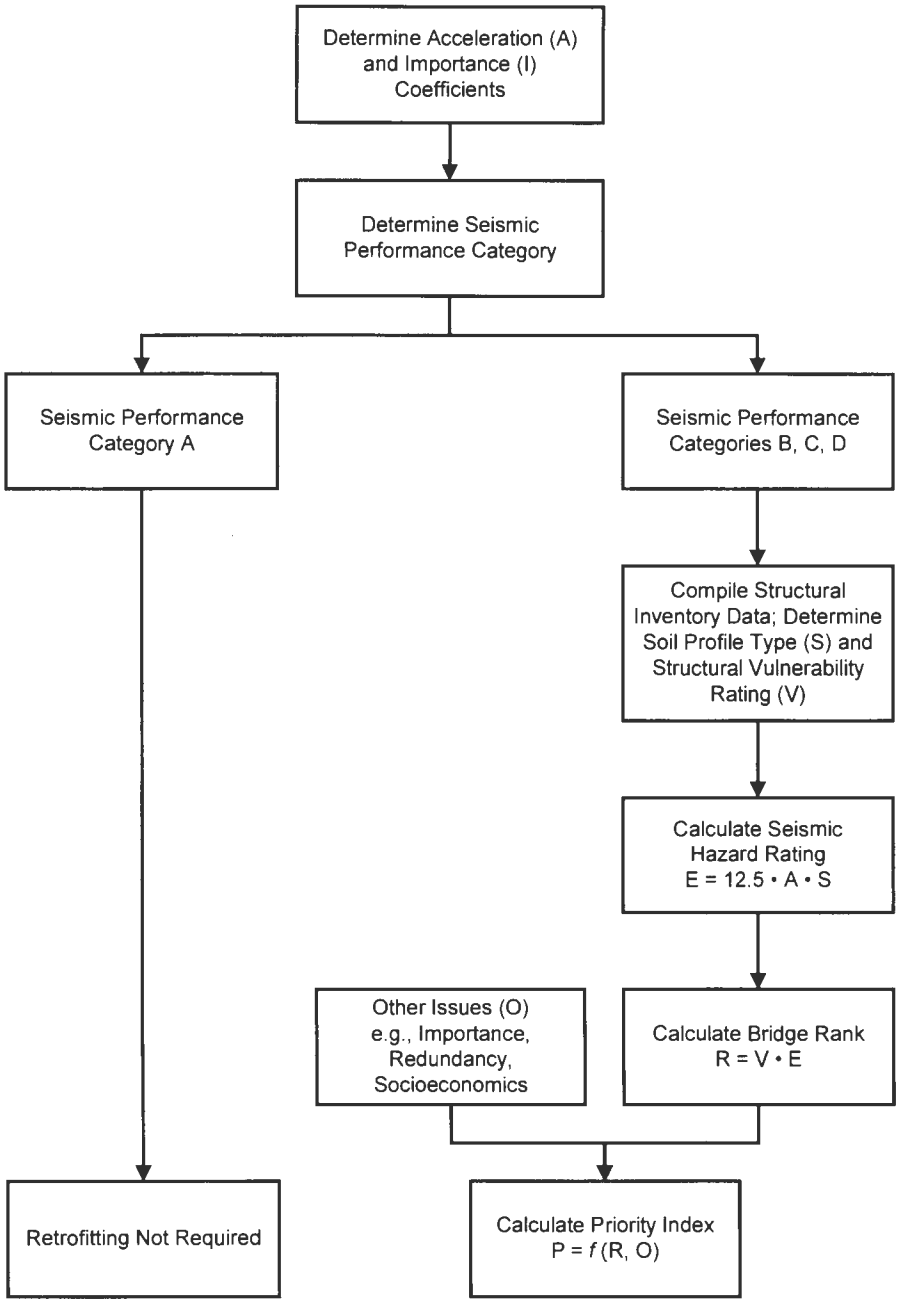

FIGURE 1 Preliminary screening procedure (*5*).

TABLE 1 Seismic Performance Categories

Acceleration Coefficient	Importance Classification	
	Essential	Standard
$A \leq 0.09$	B	A
$0.09 < A \leq 0.19$	C	B
$0.19 < A \leq 0.29$	C	C
$0.29 < A$	D	C

tural characteristics needed to determine the vulnerability rating for each bridge; and (b) the seismic and geotechnical hazard at each bridge site. This information may be obtained from a bridge owner's records, FHWA's National Bridge Inventory, as-built plans, maintenance records, the regional disaster plan, on-site bridge inspection records, and other sources.

Also required at this time is the importance of each bridge so that an SPC may be assigned. An example of a form on which to record this inventory data is shown in Figure 2.

Seismic Rating System

To calculate the seismic rating of a bridge, consideration should be given to structural vulnerability, seismic and geotechnical hazards, and various socioeconomic fac-

BRIDGE SEISMIC INVENTORY DATA FORM

GENERAL:
- Bridge Name_____ BIN Number_____
- Location_____
- ADT_____ Detour Length_____ Essential Bridge: Yes___ No___
- Alignment: Straight___ Skewed___ Curved___ Remarks_____
- Length_____ Feature carried_____
- Width_____ Feature crossed_____
- Year Built_____
- Seismically Retrofitted: Yes___ No___ Description/Date_____
- Geometry: Regular___ Irregular___ Remarks_____

SITE:
- Peak Acceleration_____
- Soil Profile Type: I____ II____ III____ IV____

SEISMIC PERFORMANCE CATEGORY: A___ B___ C___ D___

SUPERSTRUCTURE:
- Material and Type_____
- Number of Spans____
- Continuous: Yes____ No____ Number of Expansion Joints____

BEARINGS:
- Type_____
- Condition: Functioning____ Not Functioning____
- Type of Restraint (Trans)_____
- Type of Restraint (Long)_____
- Actual Support Length_____ Minimum Required Support Length_____
- Remarks_____

COLUMNS AND PIERS:
- Material and Type_____
- Minimum Transverse Cross-Section Dimension_____
- Minimum Longitudinal Cross-Section Dimension_____
- Height Range_____ Fixity: Top_____ Bottom_____
- Percentage of Longitudinal Reinforcement_____
- Splices in Longitudinal Reinforcement at End Zones: Yes____ No____
- Transverse Confinement_____ Conforms to Design Guidelines: Yes___ No___
- Foundation Type_____

ABUTMENTS:
- Type_____
- Height_____
- Foundation Type_____ Location: Cut_____ Fill_____
- Wingwalls: Continuous_____ Discontinuous_____ Length_____
- Approach Slabs: Yes_____ No_____ Length_____

SEISMIC RANK:
- Vulnerability Ratings
- Connections, Bearings and Seatwidths . . . . . (V_1)_____
- Other Components: CVR_____, AVR_____, LVR_____ . . (V_2)_____
- Overall Rating . . . . . (V)_____

- Seismic Hazard Rating: (E)_____
- Seismic Rank: (R = V x E)_____

FIGURE 2 Sample bridge seismic inventory form (*5*).

tors including importance. This is accomplished first by making independent ratings of each bridge in the areas of vulnerability and seismic hazard and second by considering importance and other issues (redundancy, nonseismic structural issues, and various societal and economic issues) to obtain a final, ordered determination of bridge retrofit priorities.

The rating system is therefore composed of two parts: the first is quantitative, the second qualitative. The quantitative part produces a seismic rating (called the bridge rank) based on structural vulnerability and seismic hazard. The qualitative part modifies the rank in a subjective way that accounts for such factors as importance, network redundancy, nonseismic deficiencies, remaining useful life, and other similar issues for inclusion in an overall priority index. Engineering and societal judgments are thus the keys to the qualitative stage of the screening process. This leads to the definition of a priority index as follows:

$$P = f(R, \text{importance, nonseismic factors, societal and economic issues . . .}) \quad (1)$$

where P is the priority index and R is a rank based on structural vulnerability and seismicity.

In summary, bridge rank is based on structural vulnerability and seismic hazard, whereas retrofit priority is based not only on bridge rank, but also on importance, nonseismic deficiencies, economic factors, network redundancy, and the like.

Calculation of Bridge Rank

As noted, the bridge rank, R, is based on a structural vulnerability rating, V, and a seismic hazard rating, E. Each rating lies in the range 0 to 10, and the rank is found by multiplying these two ratings:

$$R = V \times E \quad (2)$$

It follows that R can range from 0 to 100, and the higher the score, the greater the need for the bridge to be retrofitted (ignoring, at this time, all other factors). Recommendations for assigning values for V and E are described in the following sections.

Vulnerability Rating

Although the performance of a bridge is determined by the interaction of all its components, it has been observed in past earthquakes that certain bridge components are more vulnerable to damage than others: the connections, bearings, and seats; columns and foundations; abutments; and soils. Of these, bridge bearings appear to be the most economical to retrofit. For this reason, the vulnerability rating proposed in the calculation of bridge rank is determined by examining the connections, bearings, and seat details separately from the remainder of the structure. A separate rating, V_1, is calculated for these components. The vulnerability rating for the rest of the structure, V_2, is determined from the sum of the ratings for each of the other components that are susceptible to failure. The overall rating for the bridge is then given by the maximum of V_1 and V_2. A flow chart summarizing the process is shown in Figure 3.

The determination of these vulnerability ratings requires considerable engineering judgment. Ratings may assume any value between 0 and 10. A value of 0 means a very low vulnerability to unacceptable seismic damage, a value of 5 indicates a moderate vulnerability to collapse or a high vulnerability to loss of access, and a value of 10 means a high vulnerability to collapse. Intermediate values may, of course, be assigned.

For bridges classified as SPC B, it is usually sufficient to calculate only the vulnerability ratings for bearings, joint restrainers, and support lengths along with a rating for liquefaction effects for bridges on certain sites. Experience has shown that most connection, bearing, and seat deficiencies can be corrected economically.

For bridges classified as SPC C or D, vulnerability ratings are also generated for the columns, abutments, and foundations. Experience with retrofitting these components is much more limited than for bearings. They are generally more difficult to retrofit and doing so may not be as cost-effective.

The vulnerability ratings V_1 and V_2 can then be compared to indicate the type of retrofitting needed. If the rating for the bearings is equal to or less than the rating of other components, simple retrofitting of only the bearings may be of little value. Conversely, if the bearing rating is greater, then benefits may be obtained by retrofitting only the bearings. A comparison of these two ratings during the preliminary screening process may be helpful in planning the type of comprehensive retrofit program needed, but it should not serve as a substitute for a detailed evaluation of individual bridges.

Connections, Bearings, and Seatwidths

Transverse restraint of a bridge superstructure is almost always provided at the bearings. Common types of restraints include shear keys, keeper bars, and anchor bolts. Restraints are usually brittle by nature (i.e., nonductile) and may be subjected to large seismically induced forces resulting from the redistribution of force from ductile components such as the columns. In ad-

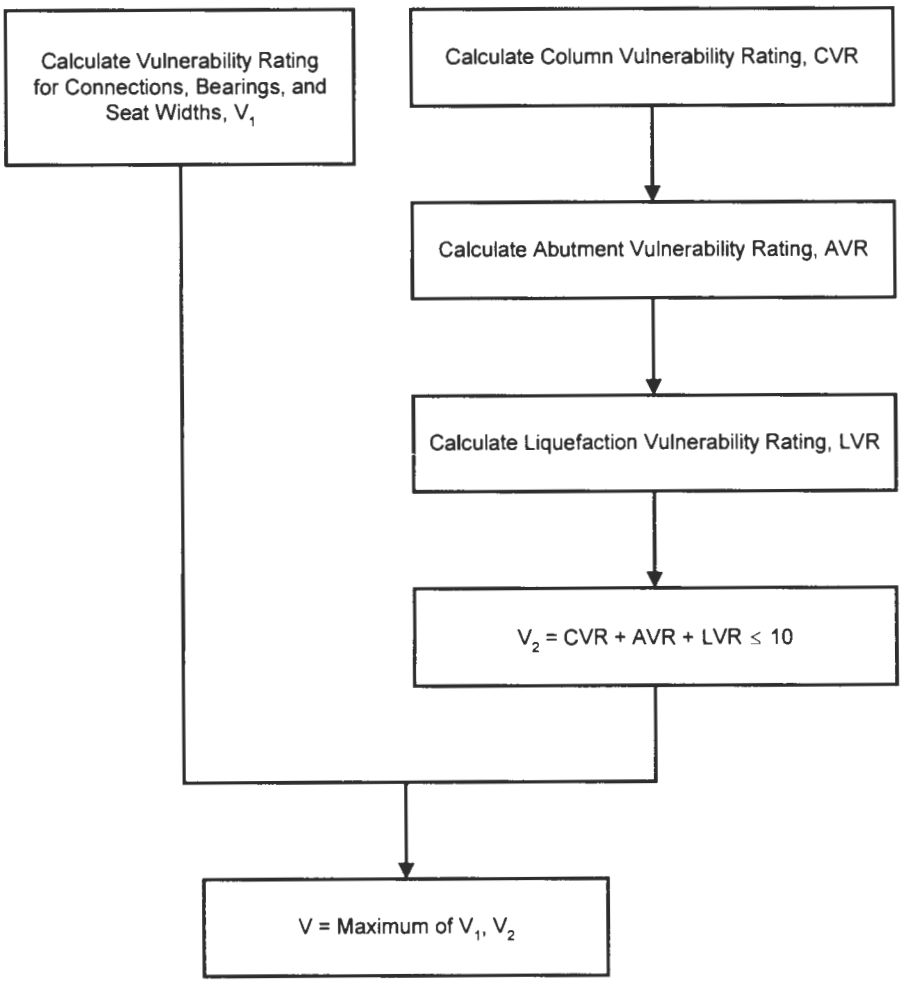

FIGURE 3 Procedure for calculating vulnerability rating, *V* (*5*).

dition, when several individual bearings with keeper bars are present at a support, the keeper bars do not resist load equally because of slight variations in clearances. Therefore, individual restraints may be subjected to very high forces. In some structures, collapse may occur because of loss of support resulting from large relative transverse or longitudinal movements at the bearings. The expected movement at a bearing is dependent on many factors and cannot be easily calculated. The AASHTO specifications require a minimum support length at all bearings in newly constructed bridges (*7*). Since it may be difficult to predict relative movement, the minimum support lengths, as required by the AASHTO specifications, may be used as the basis for checking the adequacy of longitudinal support lengths.

Support skew has a major effect on the performance of bridge bearings. Rocker bearings have been the most vulnerable in past earthquakes, and, at highly skewed-supports, these bearings may overturn during even moderate seismic shaking. In such cases, it is necessary to consider the potential for collapse of the span, which will depend largely on the geometry of the bearing seat. In some cases, settlement and vertical misalignment of a span due to an overturned bearing may be a minor problem, resulting in an only temporary loss of access that may be restored by backfilling with asphalt or other similar material. The potential for total loss of support should be the primary criteria when rating the vulnerability of the bearings.

A suggested step-by-step method for determining the vulnerability rating for connections, bearings, and seat-widths (V_1) is illustrated in Figure 4. Details are described elsewhere (*5*).

Columns, Abutments, and Liquefaction Potential

The vulnerability rating for the other components in the bridge that are susceptible to failure, V_2, is calcu-

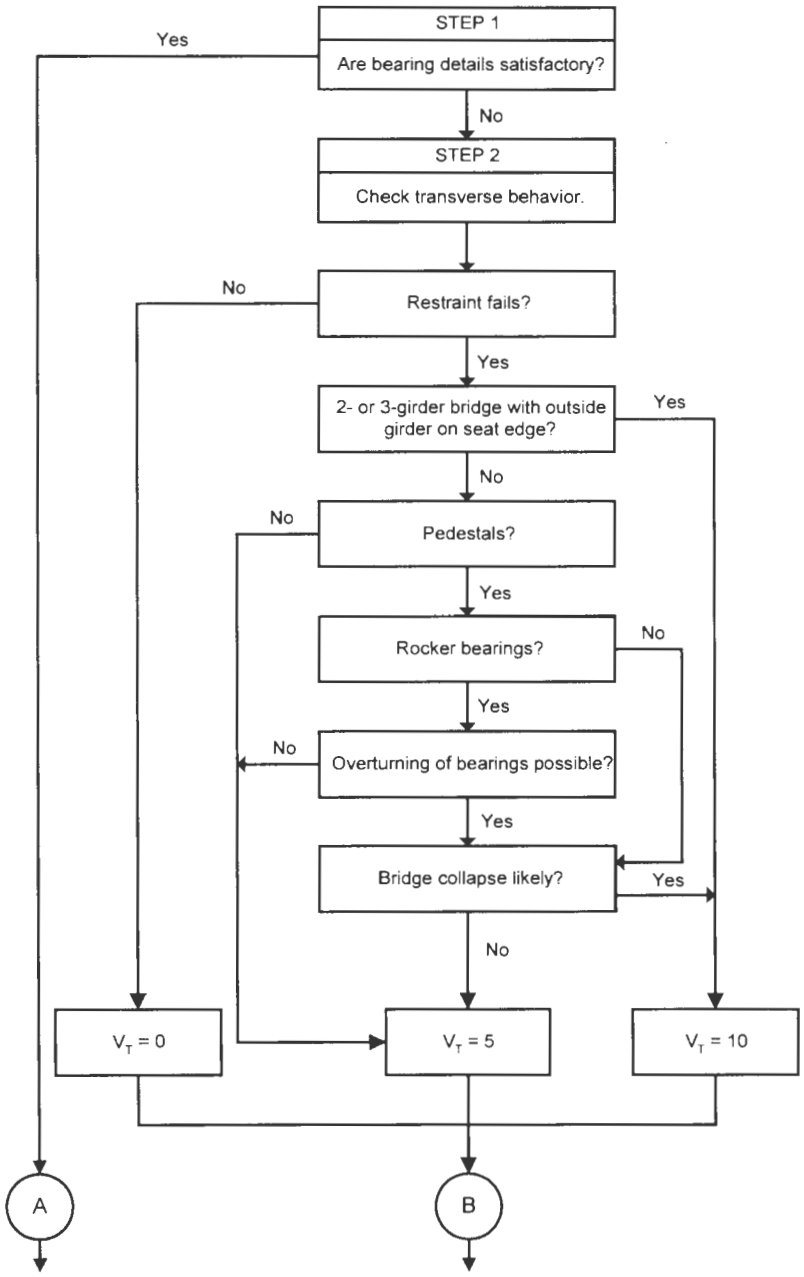

FIGURE 4 Procedure for calculating vulnerability rating for connections, bearings, and seat widths, V_1; L = actual seat width and N = seat width required by AASHTO (*5,7*) (*continued on next page*).

lated from the ratings for the individual components as follows:

$$V_2 = \text{CVR} + \text{AVR} + \text{LVR} \leq 10 \quad (3)$$

where

CVR = column vulnerability rating,
AVR = abutment vulnerability rating, and
LVR = liquefaction vulnerability rating.

Suggested methods for calculating of each of these component ratings are also given elsewhere (*5*). Brief notes on each rating are presented in the following:

- *Column Vulnerability Rating.* Columns have failed in past earthquakes because of lack of adequate transverse reinforcement and poor structural details. Excessive ductility demands have resulted in degradation of column strength in shear and flexure. In several col-

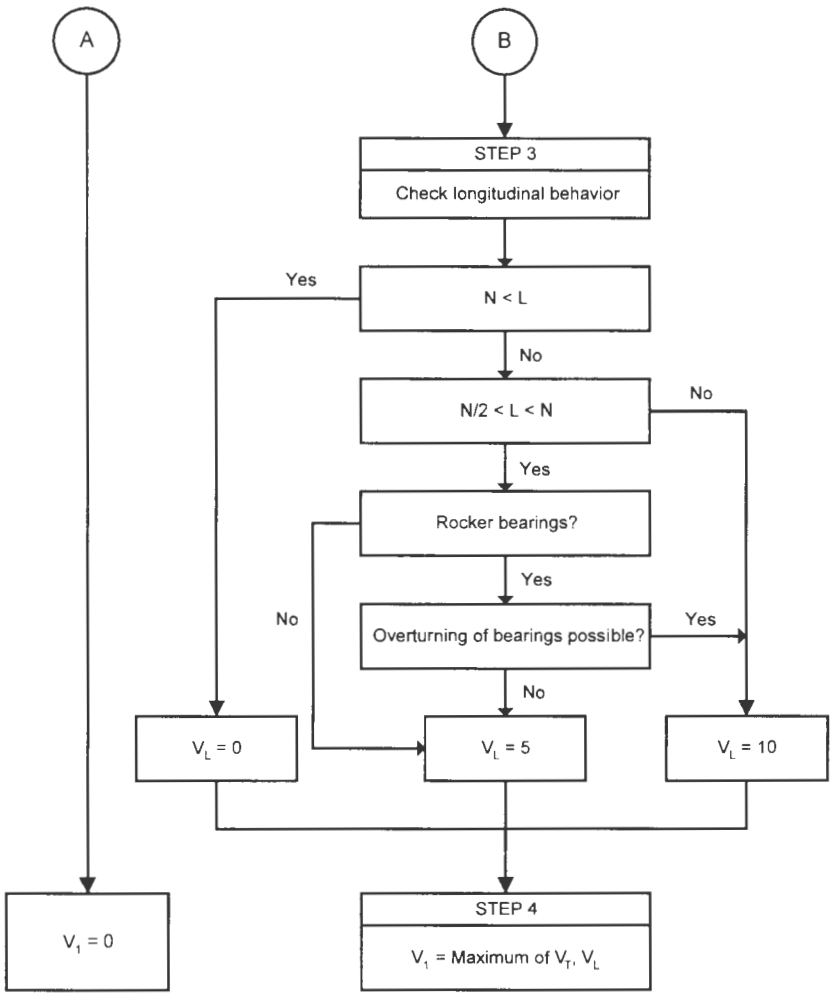

FIGURE 4 (*continued*).

lapses in past earthquakes, columns have failed in shear, resulting in column disintegration and substantial vertical settlement. Column failure may also be due to pull-out of the longitudinal reinforcing steel, mainly at the footings. Fortunately, most bridge column failures occur during earthquakes with high ground accelerations of relatively long duration. Values for CVR range from 0 (negligible vulnerability) to 10 (maximum vulnerability). Details are given elsewhere (*5*).

• *Abutment Vulnerability Rating.* Abutment failures during earthquakes do not usually result in total collapse of the bridge. This is especially true for earthquakes of low to moderate intensity. Therefore, the AVR should be based on damage that may temporarily prevent access to the bridge.

One of the major problems observed in past earthquakes has been the settlement of approach fill at the abutment. Settlements ranging from 3 to 15 percent of the fill height have been observed in past earthquakes. This difference in behavior is assumed to be due to differences in abutment types (wall versus spill-through), construction of fills, and groundwater levels.

Additional fill settlements are possible in the event of structural failures at the abutments due to excessive seismic earth pressures or seismic forces transferred from the superstructure. Certain abutment types such as spill-through abutments and those without wing walls may be more vulnerable to this type of damage than others. Except in unusual cases, the maximum AVR should be 5. Details are given elsewhere (*5*).

• *Liquefaction Vulnerability Rating.* Although several types of ground failure can result in bridge damage during an earthquake, instability resulting from liquefaction is the most significant. The vulnerability rating for foundation soil is therefore based on

–A quantitative assessment of liquefaction susceptibility,

–The magnitude of the acceleration coefficient, and

–An assessment of the susceptibility of the bridge structure itself to damage resulting from liquefaction-induced ground movement.

The vulnerability of different types of bridge structures to liquefaction has been illustrated by failures during past earthquakes such as the 1964 Alaskan earthquake. The observed damage has demonstrated that bridges with continuous superstructures and supports can withstand large translational displacements and usually remain serviceable (with minor repairs). However, bridges with discontinuous superstructures or nonductile supporting members are usually severely damaged by liquefaction. These observations have been taken into account in developing the vulnerability rating procedure described elsewhere (*5*). The maximum value for LVR is 10, which should be assigned, for example, to multispan bridges in moderate to high seismic zones on soils with moderate to high susceptibility to liquefaction.

Seismic Hazard Rating

As a measure of seismic hazard, the peak ground acceleration in rock or competent soil is used, modified by the site coefficient to allow for soil amplification effects. The seismic hazard rating is defined as follows:

$$E = 12.5 \cdot A \cdot S \leq 10 \quad (4)$$

where A is the acceleration coefficient as given in the AASHTO specifications (*7*) and S is the site coefficient as given here: E ranges from 0.625 ($A = 0.05$, $S = 1$) to 10 ($A = 0.4$, $S = 2$).

Soil Profile Type	*Site Coefficient*
I	1.0
II	1.2
III	1.5
IV	2.0

In locations where the soil properties are not known in sufficient detail to determine the soil profile type with confidence, or where the profile does not fit any of the four types, the site coefficient shall be based on engineering judgment. Soil profiles are defined as follows:

- Soil Profile Type I: A soil profile composed of rock of any description, either shale-like or crystalline in nature, or of stiff soils where the soil depth is less than 60 m (200 ft) and the soils overlying rock are stable deposits of sands, gravels, or stiff clays.
- Soil Profile Type II: A soil profile with stiff cohesive or deep cohesionless soil where the soil depth exceeds 60 m (200 ft) and the soils overlying the rock are stable deposits of sands, gravels, or stiff clays.
- Soil Profile Type III: A soil profile with soft to medium-stiff clays and sands, characterized by 9 m (30 ft) or more of soft to medium-stiff clays with or without intervening layers of sand or other cohesionless soils.
- Soil Profile Type IV: A soil profile with soft clays or silts greater than 12 m (40 ft) in depth.

Calculation of Priority Index

Once a rank has been calculated for each bridge using Equation 2, the bridges in the inventory may be listed in numerical order of decreasing rank. This order should be modified to include such factors as bridge importance, network redundancy, nonseismic deficiencies, remaining useful life, and various societal and economic issues.

Some guidance on assigning importance has been given earlier in this paper. Network redundancy is generally beneficial, but if a bridge is part of a highly redundant highway network, the likelihood that alternative routes and structures will also be damaged in the same earthquake must be considered. If, for example, an overpass can be bypassed by using the on- and off-ramps, then a relatively convenient detour may be nearby, provided that these ramps are undamaged and remain open. If, on the other hand, the structure in question is a river crossing, the nearest detour may be several miles away; however, the possibility of its also being damaged may not be so great. As a consequence, it is not clear which bridge should receive the higher priority when considering redundancy alone.

In many cases, a judgment call will be necessary to decide these issues, so experience and common sense play a major role in assigning the priority index to individual bridges.

Comparison of Screening Procedures

Table 2 summarizes the most important differences between the screening procedure contained in the 1983 FHWA guidelines and that presented here. Major differences are apparent in the definition of the seismic performance categories and the calculation of a prioritized list of bridges for retrofitting.

The principal reason for upgrading the minimum requirements for essential bridges is to ensure that seat-widths and bearings will be checked for all bridges in this importance category, regardless of the seismic hazard. This is consistent with the requirements for all new bridges, and it appears reasonable to require similar standards for essential existing bridges. More rigorous requirements are also recommended for essential bridges in the moderate seismic zones, which reflects the expec-

TABLE 2 Comparison of Screening Procedures

	1983 FHWA Guidelines (Ref. 1)		1995 FHWA Manual (Ref. 5)	
Seismic Performance Categories	**Bridge Importance**		**Bridge Importance**	
	Essential	**Standard**	**Essential**	**Standard**
Acceleration Coefficient				
$A \leq 0.09$	A	A	B	A
$0.09 < A \leq 0.19$	B	B	C	B
$0.19 < A \leq 0.29$	C	C	C	C
$0.29 < A$	D	C	D	C
Seismic Rating Procedure				
Structure Vulnerability	$V = \max(V_1, V_2) \leq 10$ where V_1 = vulnerability of bearings and V_2 = vulnerability of other components		$V = \max(V_1, V_2) \leq 10$ where V_1 = vulnerability of bearings and V_2 = vulnerability of other components	
Seismic Hazard	$S = 25.A \leq 10$ where A = acceleration coefficient		$E = 12.5.A.S \leq 10$ where A = acceleration coefficient and S = site coefficient based on 4 soil profiles	
Importance	I = 6–10 essential bridges = 0–5 standard bridges			
Rank (max value = 100) and Priority Index	$R = w_1V + w_2S + w_3I$ where w_1, w_2, w_3 are weighting factors (sum = 10.0)		$R = V \cdot E$ P = priority index = f(R, importance, and socio-economic factors)	

tation that earthquakes will occur in the eastern and central United States that will be much larger than the design earthquake. If essential bridges are to remain operational in these circumstances, more extensive retrofitting may be required than previously recommended.

The two-step process for developing the prioritized list of bridges for retrofitting recognizes the difficulty (if not impossibility) of assigning numerical factors to such issues as importance and redundancy. Research in this area and the application of geographic information systems to highway networks may improve the situation and help quantify some of these subjective issues. In the meantime, the process described herein clearly separates the engineering from the societal factors and should improve the reliability and credibility of the results produced by this particular screening procedure.

Table 2 also indicates that the numerical expression for bridge rank is changed from an additive relationship to a multiplicative one. A disadvantage in this change is that the value for rank is now more sensitive to slight changes in the values assigned to the parameters *V* and *E*. On the other hand, a particular advantage is that in low seismic zones, the rank becomes a small number regardless of the vulnerability. This is a more reasonable result than that obtained under an additive rule. The balance of the argument appears to favor the multiplicative expression; indeed, this recommendation follows the trend already adopted by several state departments of transportation (*3*).

Summary

Seismic retrofitting of highway bridges is a pressing need for many state departments of transportation. Up-to-date guidance concerning screening procedures, evaluation methods, and retrofit options is required and, in response to this need, FHWA recently revised its 1983

retrofitting guidelines. This paper has described a new screening procedure that is one of several improvements contained in the revised FHWA manual. This procedure separates the quantitative from the qualitative assessments in a two-step process. In addition to other modifications concerning importance, SPCs, and editorial changes, the improved screening procedure is expected to give more credible results while enhancing the safety of the U.S. highway bridge inventory—especially for those bridges that are essential to emergency response and recovery immediately after a major earthquake.

ACKNOWLEDGMENTS

This paper is based on the new FHWA *Seismic Retrofitting Manual for Highway Bridges*, which is a revision of the 1983 FHWA guidelines for seismic retrofitting. The earlier work was developed by the ATC, and the authors are indebted to those engineers and researchers who developed this pioneering work in the early 1980s.

In preparing the revised FHWA manual from which the paper is drawn, the authors acknowledge the assistance of John Kulicki of Modjeski and Masters, Roy Imbsen of Imbsen and Associates, Ray Zelinski of Caltrans, Anne Kiremidjian of Stanford University, and Nigel Priestley of the University of California, San Diego. The revised manual was prepared under an FHWA contract; the FHWA technical representatives were John O'Fallon and James Cooper.

REFERENCES

1. *Seismic Retrofitting Guidelines for Highway Bridges*. Report FHWA/RD-83/007. FHWA, U.S. Department of Transportation, 1983.
2. Buckle, I. G. Screening Procedures for the Retrofit of Bridges. *Proc., 3rd U.S. Conference on Lifeline Earthquake Engineering*, ASCE Technical Council Lifeline Earthquake Engineering, Monograph 4, New York, 1991, pp. 156–165.
3. Buckle, I. G. Screening Procedures for the Seismic Retrofit of Bridges. *Proc., 3rd International Workshop on Bridge Rehabilitation*, Technical University of Darmstadt and the University of Michigan, Darmstadt, Germany, 1992, pp. 445–454.
4. Filiatraut, A., S. Tremblay, and R. Tinansi. A Rapid Screening Procedure for Existing Bridges in Canada. *Canadian Journal of Civil Engineering*, Vol. 21, 1994, pp. 626–642.
5. Buckle, I. G., and I. M. Friedland, eds. *Seismic Retrofitting Manual for Highway Bridges*. Report FHWA-RD-94-052. FHWA, U.S. Department of Transportation, 1995.
6. Basöz, N., A. Kiremidjian, and E. Straser. Prioritization of Bridges for Seismic Retrofitting. *Proc., 5th U.S. National Conference on Earthquake Engineering*, Vol. 4, Earthquake Engineering Research Institute, 1994, pp. 881–890.
7. *Standard Specifications for Highway Bridges; Division I-A: Seismic Design*, 15th ed. AASHTO, Washington, D.C., 1992.

Effectiveness of Hinge Restrainers as Seismic Retrofit Measure

M. Saiidi and E. Maragakis, *University of Nevada*

A summary of (a) the performance of hinge restrainers based on a field investigation of several bridges after the 1989 Loma Prieta earthquake and (b) important aspects of restrainer design for bridges with narrow seat widths is presented. The observed characteristics of restrainer behavior are described. The field investigations showed that the entire restrainer system (which consists of the restrainers, connection hardware, diaphragms, and the superstructure) and not merely the restrainers should be considered at the time of design. The weak link in the system for bridges with narrow seats needs to be the superstructure. The sensitivity studies revealed that small changes in the assumptions made in the design can affect the required number of restrainers. It was also found that the most critical case for restrainer design corresponds to the condition when the restrainer gap is zero, whereas the critical abutment forces during the earthquake may occur when the restrainer gap is maximum.

One of the lessons learned from the 1971 San Fernando earthquake in southern California was that highway bridges with narrow seat widths at the hinges may be susceptible to collapse because of movements that are beyond the available seat width (*1*). Following that earthquake the California Department of Transportation (Caltrans) identified 1,250 bridges of its inventory of approximately 13,000 structures as having vulnerable hinges (*2*). To prevent excessive movements at the hinges, these bridges were retrofitted with steel cable or high-strength rod hinge restrainers under Caltrans' Phase I retrofit program. This phase was completed in 1985 at a cost of $55,000,000 (*3*). Following the 1989 Loma Prieta earthquake in northern California (*4*), many states initiated a seismic retrofit program that included the installation of hinge restrainers in many of their existing bridges (*5*). The Loma Prieta earthquake provided an opportunity to study the effects of restrainers on the responses of bridges. The purpose of this paper is to provide an overview of the important characteristics of the restrainer response during the Loma Prieta earthquake and to discuss some of the factors that affect the design of restrainers.

Restrainer Response During Loma Prieta Earthquake

Damage Overview

The Caltrans Maintenance Division identified 23 bridges that were retrofitted with restrainers and that were damaged by the Loma Prieta earthquake. General structural data about these bridges were compiled on the basis of bridge plans. A summary of the main features of each bridge and the damage has been presented elsewhere (*6*). The number of spans in the damaged

bridges ranged from 3 to more than 100 in some of the major viaducts. The number of hinges also varied considerably. The damaged bridges were originally constructed between 1941 and 1971. Some of these bridges underwent reconstruction in a variety of forms at later dates. Because all of the major parameters for the damaged bridges were highly variable, no clear pattern could be identified among these bridges except for the year of construction, which reflects the bridge design provisions of the time.

The most common damage caused by the Loma Prieta earthquake was excessive hinge opening and cracking of columns. Large hinge movements caused cracking of the abutments in some cases. The lack of reported damage in footings is, in part, attributed to the lack of inspections of the column bases. There was no apparent correlation between the number of spans and damage. The lack of pattern in the damage may be attributed to the fact that the intensity of the ground motion varied considerably among the bridges. Judging by the hinge openings and pounding damage in the hinges, it appeared that restrainers were activated in many instances, but they failed only in two cases. Field observations cannot generally determine the extent of stresses in the restrainers if they are not damaged. Therefore, detailed analyses are necessary. The Caltrans damage reports indicated that restrainer connector damage was noted only in a few cases. Furthermore, very few diaphragms were damaged by the earthquake. Pounding at the hinges was observed in many cases, which indicated relatively large movements.

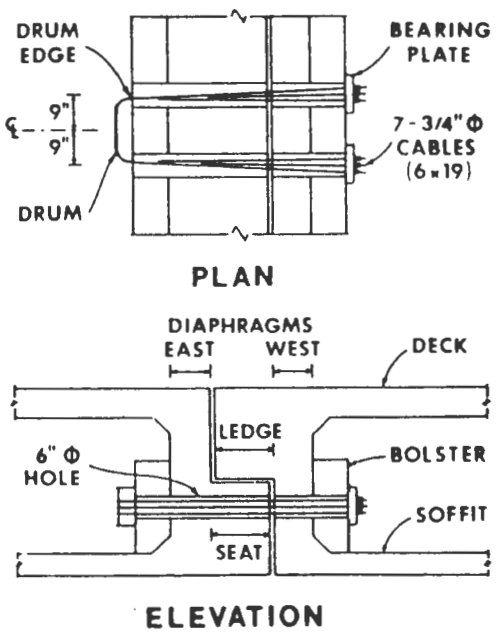

FIGURE 1 Details of a C-7 restrainer (1 ft = 0.305 m; 1 in. = 25.4 mm).

Field Investigation of Hinge Damage

Three of the damaged bridges were investigated in the field by the authors. These structures were the Central Viaduct in San Francisco, the Route 580/24/980 Separation in Oakland, and the northeast connector in the Route 92/101 Separation in San Mateo.

Central Viaduct

The Central Viaduct structure is a long, multispan bridge, a segment of which is of double-deck reinforced concrete construction changing into a single-deck steel girder construction. The reinforced concrete segment is a cast-in-place multicell box girder type constructed in 1957. It was retrofitted in 1972 with hinge restrainers because of its narrow hinges, which have a nominal width of 150 mm (6 in.). Both C-5 and C-7 (7) restrainer types are used in different hinges (Figure 1). The Loma Prieta earthquake caused some visible cracking of the piers and pier cap column joints in the double-deck segment of the bridge. As a result the bridge was closed to traffic at the time of the visit, which took place on June 10, 1991. The hinges were inspected from the top of the upper deck to determine any significant hinge rotation or opening. The hinge gaps at the east and west edges of the superstructure were measured. No significant permanent rotation was noted except for one hinge in which a differential gap of 13 mm (½ in.) was noted between the east and the west edges. This and another hinge were inspected from inside the superstructure cells. The restrainer type in one hinge was C-7, and the one in the other was C-5. None of the restrainers showed any sign of damage. The uppermost cable in the restrainer with seven cables had left some marks on the corners of the C-drum, indicating that the cables experienced significant tension. It appeared that, as a result of tensioning and detensioning, the cables had shifted downward by approximately 13 mm (½ in.). Because the vertical space on the drum is limited, the shift pushed the second cable out from the bottom. The effectiveness of this cable in developing its full yield strength in the future may be questionable because of friction and stress concentration.

580/24/980 Separation

The 580/24/980 Separation structure was retrofitted in 1980 with high-strength rod hinge restrainers of 32 mm (1.25-in.) in diameter. The superstructure type is cast-in-place multicell reinforced concrete box girder. The bridge contains many hinges, incorporating a variety of

configurations and numbers of restrainers. The restrainers are generally distributed around the diaphragms. A reinforced concrete bolster is provided in skewed hinges. Significant spalling of concrete at the bottom of the superstructure was noted at two hinges as a result of the 1989 Loma Prieta earthquake. Figure 2 shows the crack pattern and the spalled areas, which are marked by hatched zones. The damaged hinges were perpendicular to the bridge axis and had no bolsters. The damage in the soffit in the East Connector Viaduct was evident near the west edge of Hinge 20. At that hinge two sets of restrainers were installed, with one consisting of five rods placed in one row at 0.3 m (1 ft) from the top of the lower slab and the other consisting of six rods placed in two rows of three each. The damage occurred in the west cell, in which the rods had been placed in one row. There was a punching-type failure of the diaphragm (Figure 3). No damage was evident in the cell with two rows of rods. The punching shear cracks extended to the bottom slab, thus causing the concrete to spall off the soffit. This was visible from outside the cell. The damage in the soffit of the North Connector Viaduct was similar. The cause of damage is attributed to the inadequate punching shear strength of the diaphragms. The restrainers in the damaged cells were placed in one row. The associated critical punching shear sections are shown in Figure 4. Note the relatively small and narrow area when the rods are placed in one row. Tests on the punching shear strengths of reinforced concrete slabs have shown that the shear strength drops as the aspect ratio of the loaded area increases (*8*). Based on an effective depth of 0.3 m (12 in.) and a concrete strength of 28 MPa (4,000 lb/in.^{2}), the permissible punching shear strengths are estimated to be 1290 and 1420 kN (290 and 320 kips) in Hinges 20 and 33, respectively. Because of the proximity of the rods to the bottom slab and because the bottom slab presented a weak area, the lower part of the critical section shown in Figure 4(*a*) did not actually develop

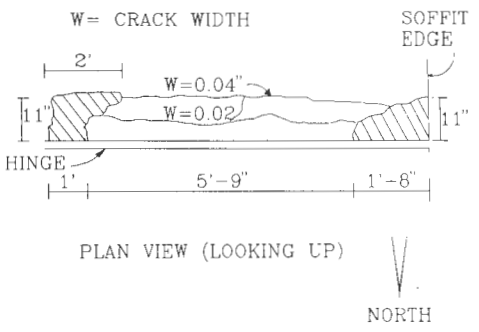

FIGURE 2 Crack pattern in the soffit of 580/24/980 Separation structure (1 ft = 0.305 m; 1 in. = 25.4 mm).

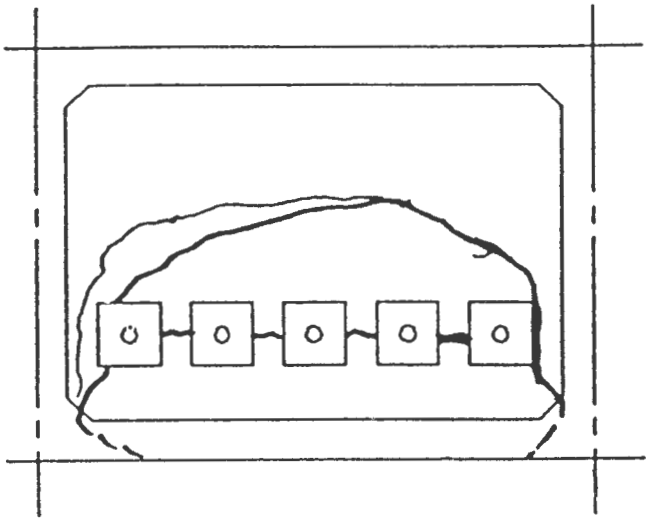

FIGURE 3 Punching shear failure inside the cell.

in the bridge. Rather, the punching shear failure lines extended to the bottom slab (Figure 2). Therefore, the actual permissible strength was even lower than these values. The total yield force is 3340 kN (750 kips) for five high-strength rods and 4000 kN (900 kips) for six high-strength rods. The punching shear strengths of the diaphragms were 1290 to 1420 kN. It can be observed that approximately 40 percent of the restrainer yield force was sufficient to cause the diaphragms to fail.

It should be noted that in excess of 100 sets of restrainers are used in the structure and that damage was observed in only two of the diaphragms. It was recommended to Caltrans that all of the cells that are retrofitted with one row of rods and that are not retrofitted with a bolster be reevaluated and that the diaphragms be strengthened.

92/101 Separation

The northeast connector in the 92/101 Separation structure was investigated because of excessive crack openings in the soffit of the superstructure that were noted after all of the earthquake damage had been repaired. The superstructure is a cast-in-place, four-cell box section supported on single-column piers of various heights. The hinges are equipped with eight sets of five 17-mm (¾-in.) straight cable restrainers placed in all of the cells. The Caltrans Maintenance Division records indicate that the structures at the interchange suffered significant damage during the earthquake. The damage ranged from spalling of superstructure concrete near several joints to excessive hinge movements. Figure 5 shows a sample of the crack patterns. The crack widths are marked in inches. Note that the cracks were nearly

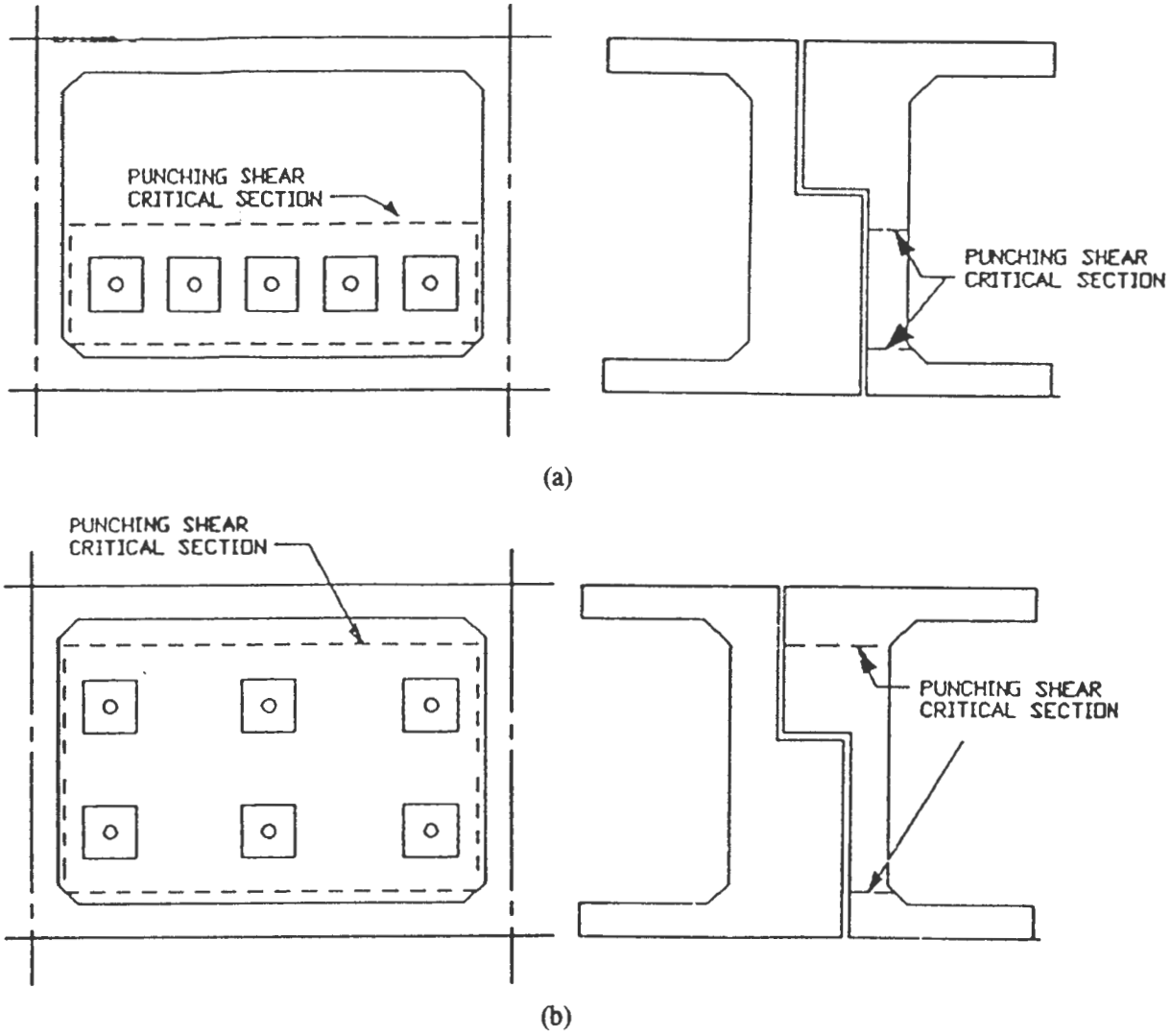

FIGURE 4 Punching shear failure lines for (*a*) one row of restrainers and (*b*) two rows of restrainers.

parallel with slight inclination and that they extended to nearly the full height of the girder. The fact that the cracks were nearly vertical suggested that they were not caused by shear. Because the location of the cracks was close to the hinge, the moments had to be relatively small and the cracks could not have been caused by flexure alone. The damage to one of the columns and the spalling of concrete at the hinge could indicate relatively large movement of the superstructure and the activation of the restrainers. The total yield force for the restrainers was 6960 kN (1,560 kips). The direct tensile cracking strength of the superstructure is 10 200 kN (2,300 kips), based on a concrete compressive strength of 28 MPa (4,000 lb/in.^{2}) and assuming a tensile strength of 0.5 $\sqrt{f'_c}$ (6 $\sqrt{f'_c}$), where f'_c is the concrete compressive strength in terms of megapascals (pounds per square inch). The comparison of these figures suggests that it is unlikely that restrainer forces alone caused the cracks. However, it is possible that the restrainer tensile force in the superstructure reduced the flexural strength and helped open the flexural cracks that were developed by vertical loads.

The sensitivity of the flexural strength and the cracking moment of the superstructure to axial tension was calculated. It was determined that for a restrainer force of one-half of the yield force (a force level expected during a moderate earthquake) the ultimate positive and negative moment capacities would drop by approximately 30 and 13 percent, respectively. When the restrainers approach the yield level, the ultimate positive and negative moment capacities drop by approximately 65 and 25 percent, respectively. Although it was not evident in this bridge, the axial tension could also significantly reduce the shear strength of the section (*8*).

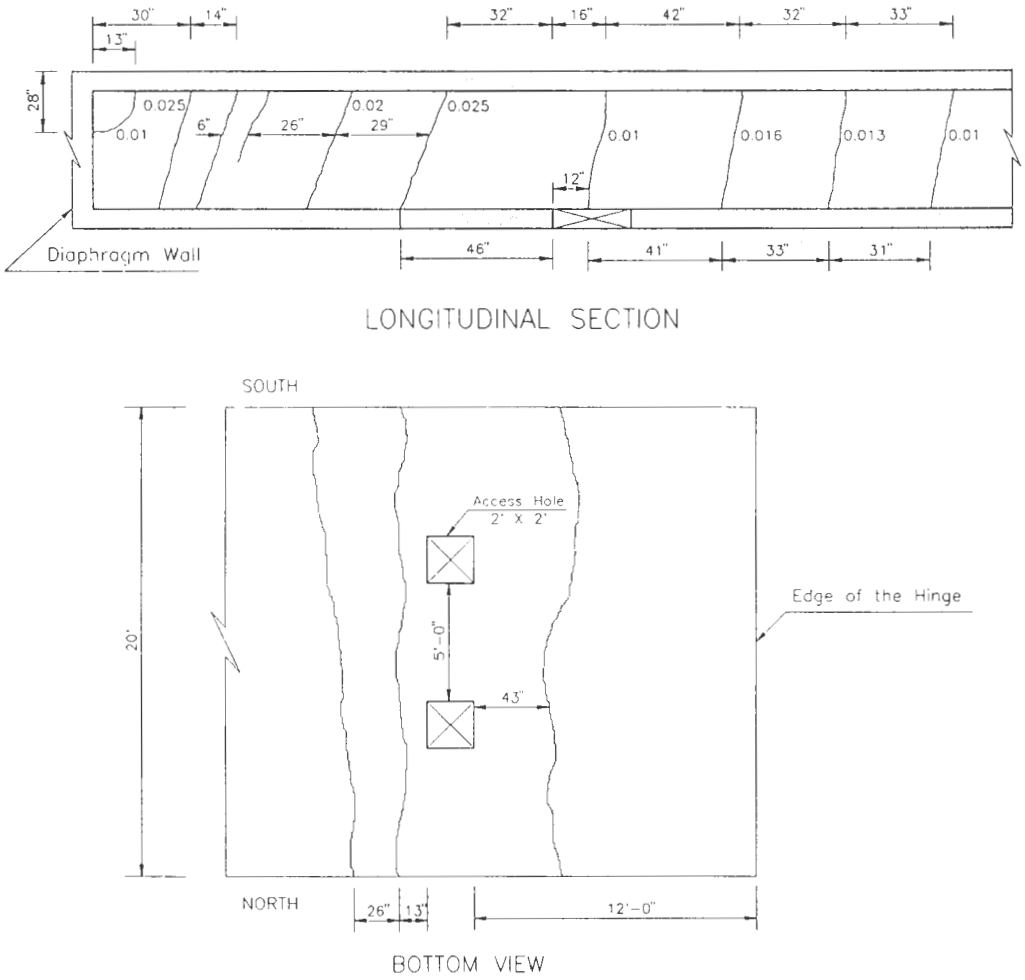

FIGURE 5 Girder and bottom slab cracks in the 92/101 Separation structure (1 ft = 0.305 m; 1 in. = 25.4 mm).

In prestressed concrete members the tension will reduce the effective prestress force. These effects are not usually considered in design, but they can be critical. It can be observed that the placement of too many restrainers can have detrimental effects on the superstructure.

Characteristics of Restrainer Response in the Field

Hinge restrainers need to be treated as systems consisting of three components: (a) the restrainers, (b) the connecting hardware and the diaphragms (if any), and (c) the superstructure adjacent to the hinge. Although restrainer systems performed reasonably well during the Loma Prieta earthquake, in a few instances they pointed out the fact that each component of the system can be vulnerable. Because the design and construction of restrainers have gone through an evolution leading to many variations in restrainer systems, and because the intensity of the ground motion varied for different bridges, it is not generally possible to pinpoint which component presents the weak link.

Restrainer systems can be designed so that the weak link is at a predetermined component. Because the function of hinge restrainers is different in old bridges [those with a nominal seat width of 150 mm (6 in.)] and new bridges [those with a nominal seat width of 0.6 m (2 ft)], the restrainer design philosophy can be different for each group. In older bridges the function of restrainers is to prevent excessive relative movement at hinges. As a result restrainers should be designed to prevent yielding even under the maximum credible earthquake. No yielding should be allowed in the connecting hardware or the diaphragms. Cracking of the superstructure under tension from the restrainers may be tolerable. However, the effect of the tension on the

moment and shear capacity of the superstructure needs to be accounted for in retrofit design.

The purpose of restrainers in new bridges is to provide overall integrity for the superstructure. Yielding of the restrainers can result in large hinge movements, but because the seats are wide, the movement may not necessarily be critical. As long as the restrainers have a reasonable level of strain hardening, restrainer yielding may be tolerable. Furthermore, the relative ease of restrainer replacement after earthquakes makes restrainers a good candidate for being the weak link in the restrainer systems for new bridges.

Design of Restrainers for Existing Bridges

The design of restrainers for new bridges is frequently based on a modal analysis of the bridge. For existing bridges restrainers are used as a retrofit measure, and their design is based on an equivalent static analysis method that incorporates many of the primary factors affecting the seismic responses of bridges (7). Several simplifying assumptions are made on the basis of engineering judgment and observations made during past strong earthquakes. Although the performances of restrainers that have been designed by the current methodology have generally been satisfactory during recent moderate earthquakes, many aspects of the restrainer design method have not been studied in detail. This section presents a study of some of these aspects of the hinge restrainer design method. More details are presented elsewhere (6).

Several simplifying assumptions are made in calculating the effective stiffness and mass. An initial restrainer gap of 19 mm (0.75 in.) is assumed. This corresponds to the extreme high ambient temperature. A "frame" is defined as the part of the bridge that is between two adjacent hinges or that is between a hinge and the adjacent abutment. The assumptions influence the equivalent vibration period of different frames or groups of frames and eventually affect the number of required restrainers. The example bridge presented elsewhere (7) (Figure 6) was used to illustrate the effects. The bridge has three intermediate hinges that are numbered from left to right and a hinge at the left abutment. The peak bedrock acceleration is assumed to be 0.6 *g*. Only 19-mm (¾-in.) cable restrainers were considered in the study.

Influence of Changes in Stiffness and Mass

To determine the relative movements in the unrestrained condition, the bridge structure on each side of the hinge is considered separately. As each frame moves away from the hinge, it closes the gap at an adjacent hinge, thus mobilizing a second frame. If the frame continues to move in the same direction, another hinge may close, which leads to the mobilization of a third frame or an abutment. The current design method accounts for the closure of only one adjacent hinge and permits the mobilization of only one adjacent frame regardless of the displacement. This assumption simplifies the analysis and is intended to be conservative. It is also assumed that the mass for only one frame should be used in computing the effective period of vibration for the segments, even when more than one frame is mobilized.

Column 3 in Table 1 lists the number of restrainer groups (each consisting of 10 cables) required on the basis of the current method. The effect of allowing more than one frame to contribute to the stiffness and mass, when displacements are sufficiently large to close the hinge gaps, can be observed in column 4 in Table 1. Two cable lengths of 1.5 and 2.1 m (5 and 7 ft) are considered in design. Hinge 1 did not need a restrainer when 2.1-m (7-ft) cables were used. It can be observed that by changing the treatment of the mass, the number of cables is reduced drastically. The general explanation for this reduction is the fact that the added masses increased the effective period considerably. The period elongation, in turn, reduced the acceleration response spectrum (ARS) value, and the reduced ARS value led

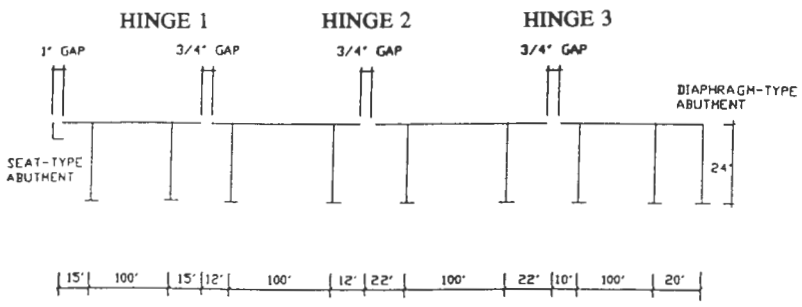

FIGURE 6 Bridge model used in parametric studies (1 ft = 0.305 m; 1 in. = 25.4 mm).

TABLE 1 Number of Required 10-Cable Units for Different Designs

(1) Hinge	(2) Cable Length m (ft.)	(3) Original Design	(4) Modified Eq. Stiff. & Mass	(5) Zero Rest. Gap
1	1.5 (5) 2.1 (7)	10 8	4 -	15 13
2	1.5 (5) 2.1 (7)	12 7	7 2	15 14
3	1.5 (5) 2.1 (7)	13 11	6 2	16 15

to smaller displacements. Because restrainers are designed to control relative movements at hinges, smaller displacements required fewer cables. Note that the current method is conservative in that it requires a larger number of restrainers. However, the level of conservatism is not uniform among different hinges.

Influence of Reducing Restrainer Gap to Zero

During extreme low ambient temperatures the superstructure segments become shorter. As a result the restrainer gap may diminish, whereas the hinge and abutment gaps increase. When the restrainer gaps in the example bridge are reduced to zero, the allowable cable "deflection" and the seat width required to maintain a 75-mm (3-in.) minimum bearing specified in design will be reduced. The effects of these changes on the number of required restrainers are shown in Column 5 in Table 1. As expected, a larger number of restrainers is required to maintain the minimum bearing width. The results suggest that if an earthquake occurs when the ambient temperature is low, retrofit restrainers designed by the current method may not be able to reduce the relative hinge movements below the critical limits. The Northridge earthquake of January 1994 led to the unseating of several hinges (9). Although no detailed analysis of the collapsed bridges has been performed as of this writing, the present study suggests that the cold temperature at the time of failure could have been a contributing factor to the failure of some of the restrainers.

Sensitivity to Calculated Maximum Displacement

The cross-sectional area of the restrainers is designed on the basis of the calculated maximum displacement of the unretrofitted frames. The maximum displacement is determined by using an equivalent linear analysis assuming that one-half of the columns in each frame have yielded. A modal analysis is used and is based on equivalent stiffness and mass (7). Because this analysis is approximate, it can only provide an estimate of the frame movement. Although this approximation may be within engineering accuracy for most applications, it falls short of providing an acceptable design for restrainers. This is because restrainers are designed on the basis of the difference between the estimated maximum displacement and an acceptable seat width. To determine the effect of slight variations in the estimated maximum displacements, the restrainers in the example bridge were redesigned assuming a ± 20 percent displacement error. The results indicated that the number of restrainers can change by as much as ± 70 as a result of this error.

Discussion on Restrainer Design

The results discussed in the previous sections indicate that the assumptions made in the design of restrainers can greatly change the results. An improvement in the methods used to calculate the stiffness and mass leads to a reduction in the number of the restrainers, thus suggesting that the current method is conservative. However, when the restrainer gap is reduced, the number of the restrainers increases considerably, thus suggesting that the current method is unconservative. The field observations during the 1989 Loma Prieta earthquake indicated that the current design method may be safe and conservative. The 1994 Northridge earthquake led to larger hinge movements and unseated several spans.

The high degree of sensitivity of the results to the assumptions is due to the fact that the equivalent static method is extremely approximate for calculating the relative hinge movements. It is not appropriate to modify the current restrainer design method by merely re-

ducing the restrainer gap or by taking other similar measures because such modification would not address the fundamental shortcoming of the method, which is the computation of the relative hinge displacements. It is apparent that an alternate design method that more accurately accounts for the nonlinearity of the elements needs to be developed.

Conclusions

1. In analysis and design of hinge restrainers it is necessary to consider the performance of the restrainer system and not merely the restrainers. The system includes (a) the connection between the restrainers and the superstructure, including any diaphragms, (b) the superstructure adjacent to the hinge, and (c) the restrainers.
2. The weak link in the restrainer system in bridges with narrow hinge seats needs to be the superstructure, because yielding of the restrainers or the failure of the connections could lead to collapse. In bridges with wide hinge seats, by allowing the restrainers to experience limited yielding, the integrity of the bridge can still be maintained. A minimum level of strain hardening would be required for the restrainers.
3. The Loma Prieta earthquake activated the hinge restrainers in the majority of the bridges investigated in the present study. Except for a few instances, the restrainers and their supporting systems performed well.
4. The most critical case for restrainer design corresponds to the condition when the restrainer gap is zero, whereas the critical abutment forces during the earthquake may occur when the restrainer gap is maximum. As a result, in a refined analysis both conditions would need to be considered.

ACKNOWLEDGMENTS

The study presented in this paper was part of a project funded by Caltrans, the National Science Foundation, and the Nevada Department of Transportation. S. Chi Liu, Jim Roberts, Jim Gates, Mark Yashinsky, Floyd Marcucci, and Richard Obisanya are thanked for their support and comments. Other members of the project team at the University of Nevada, Reno, Saber Abdel-Ghaffar and Dan O'Connor, provided valuable input.

A shortened version of this article was published in the proceedings of the Fifth U.S. Conference on Earthquake Engineering held in Chicago, Illinois, in July 1994.

REFERENCES

1. Jennings, P. C. *Engineering Features of the San Fernando Earthquake of February 9, 1971*. Report EERL 71-02. California Institute of Technology, Pasadena, 1971.
2. Gates, J. H. Seismic Resistant Bridge Design in California. *Proc., U.S.-Japan Conference on Seismic Research for Highway Bridges*, Department of Civil Engineering, University of Pittsburgh, Pittsburgh, Pa. 1984, pp. 1–14.
3. Yashinsky, M. Performance of Retrofit Measures on Existing Older Bridges. *Proc., Structural Engineers Association of California Meeting*, Lake Tahoe, Nev. 1990.
4. Housner, G. W. *Competing Against Time*. A Report to Governor George Deukmejian from the Governor's Board of Inquiry on the 1989 Loma Prieta Earthquake, Office of Planning and Research, State of California, Sacramento, 1990.
5. Saiidi, M. Current Bridge Seismic Retrofit Practice in the United States. *ACI Concrete International*, Vol. 14, 1992, pp. 64–67.
6. Saiidi, M., E. Maragakis, S. Abdel-Ghaffar, S. Feng, and D. O'Connor. *Response of Bridge Hinge Restrainers During Earthquakes—Field Performance, Analysis, and Design*. Report CCEER-93-6. Civil Engineering Department, University of Nevada, Reno, 1993.
7. *Seismic Design References (Bridge Design Aids and Memos to Designers)*. Division of Structures, Department of Transportation, State of California, Sacramento, 1990.
8. American Concrete Institute Committee 318. *Building Code Requirements for Reinforced Concrete and Commentary*. American Concrete Institute, Detroit, Mich. 1989.
9. Todd, D., N. Carino, R. Chung, H. Lew, A. Taylor, W. Walton, J. Cooper, and R. Nimis. *1994 Northridge Earthquake—Performance of Structures, Lifelines, and Fire Protection Systems*. NIST Special Publication 862. U.S. Department of Commerce, 1994.

Application of Base Isolation to Single-Span Bridge in a Zone with High Seismicity

James Kwong, Richard K. Lindsay, and Arthur J. Woodworth,
A-N West, Inc.
David M. Jones and Richard P. Knight, *Dynamic Isolation Systems, Inc.*

The Carlson Boulevard Overcrossing is part of the 23rd Street Grade Separation Project, a major reconstruction of a complex intersection in the city of Richmond, California. The design of this bridge was based on a recommended, site-specific response spectrum because the project site is 3 km from the Hayward fault. The response spectrum values are very high over a broad range of periods. Also, because of the proximity of the structure to the fault, large displacements occur at the longer periods. The initial design approach was to use a two-span concrete structure with a center bent. It was then determined that the entire grade separation could be spanned with a single-span structure and the cost of the center bent could be saved. The single-span, multicell concrete box girder structure is 153 ft long, varies in width from 49 to 57 ft, and is on a skew of approximately 40 degrees. With the single-span structure, the lateral earthquake forces are required to be resisted by only the abutments. However, the tall seat-type abutments used for this project were not able to resist the large accelerations required by the response spectrum. Therefore, isolation bearings were selected to reduce the lateral seismic forces and to accommodate the large displacements at the abutments. The joints between the abutments and superstructure consist of 2-in. joint seals for everyday service use and short knock-off walls that give way for the large seismic movements. The analysis, design, and construction of the Carlson Boulevard Overcrossing are described in detail.

The 23rd Street Grade Separation Project (Figure 1) is designed to carry 23rd Street under the Southern Pacific Railroad mainline and the adjacent Carlson Boulevard. The completed project maintains—with much better geometrics—the traffic pattern that existed before underpass construction, but it eliminates a complicated six-point intersection crossing the railroad's main route to the Pacific Northwest, Central Valley, and eastern connections. Twenty-third Street is a major thoroughfare that currently carries an average of more than 25,000 vehicles per day, with traffic volume expected to increase to 40,000 vehicles per day once the work on nearby Interstate Highways 580 and 80 is completed.

Other project features include the removal of an abandoned Santa Fe Railway bridge, the relocation of utilities and petroleum project pipelines, and the design of a storm water pumping station, traffic signals, street lighting, landscaping, and a double-track railroad shoofly. The completed project will conduct traffic through

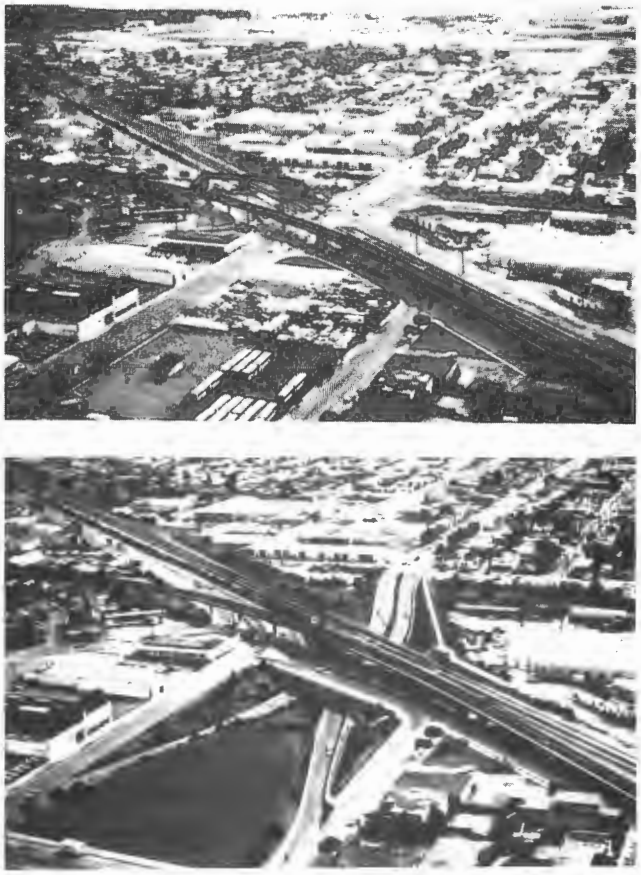

FIGURE 1 Aerial photographs of project site: (*top*) project site before construction, looking south; (*bottom*) artist's conception of finished project, looking South (Carlson Boulevard Overcrossing in foreground).

the area more efficiently and will create developable land that should invigorate existing businesses and enhance the neighborhood overall.

History and Design of Carlson Boulevard Overcrossing

The 23rd Street Grade Separation Project was planned and designed in the mid-1960s, but it was shelved before the project went out for bid. The Carlson Boulevard Overcrossing was originally designed as a four-span, reinforced concrete box girder bridge. However, in the late 1980s, when the project was resurrected, the geometrics had to be modified and retaining walls had to be added. To take advantage of these changes to the project, the Carlson Boulevard Overcrossing was shortened from 239 to 153 ft. With the shortened length, it became feasible to cross over 23rd Street with a single span.

In the period between the 1960s and the 1980s, the Bay Area Rapid Transit (BART) built an aerial structure between the Southern Pacific Railroad mainline and Carlson Boulevard. Subsequently, the design of the Carlson Boulevard Overcrossing in the 1980s had to address issues related to the construction of the new overcrossing structure in the vicinity of the existing BART aerial structure. One such site constraint imposed by BART was a vibration limit for the existing aerial structure throughout the construction period. Therefore, to reduce or eliminate vibration, the pile-supported substructure components of the project were changed from driven 12-in. precast, prestressed concrete piles to 30-in.-diameter, cast-in-drilled-hole (CIDH) concrete piles.

The Carlson Boulevard Overcrossing is a single-span, cast-in-place, prestressed concrete box girder, at-grade structure on an approximate 40-degree skew. At Abutment 1 one of the exterior girders is curved to parallel the horizontal curve of the roadway. The abutments are of the pile-supported, tall-seat type. The overcrossing is designed according to the State of California Department of Transportation (Caltrans) Bridge Design Specifications and 1983 AASHTO guidelines with revisions by Caltrans (*1*). The design concrete strength, f'_c, is 4,500 lb/in.^{2} for the superstructure and 4,000 lb/in.^{2} for the abutments. The total jacking force, with low relaxation strands, is 11,900 kips, or 1,983 kips per girder. All of the preceding design values are fairly typical of a regular Caltrans-type bridge. What is not regular, however, is the seismic design input and the subsequent method of design to accommodate the seismicity criteria.

Seismicity Criteria

The project site is located approximately 3 km from the active Hayward fault. Because of its proximity to this fault, Geospectra (in Richmond, California), the geotechnical engineer for this project, developed site-specific spectra for the project. To establish design earthquake ground motions at the site, Geospectra performed an in-depth seismic risk analysis (*2*). The seismic risk for the site was evaluated by using probabilistic assessments of ground motions. In general, it involved the use of a model for the seismic activities of pertinent seismic sources, the Hayward, Calaveras, San Andreas, Seal Cove-San Gregorio, Rodgers Creek-Healdsburg, and Green Valley-Concord faults, and a model for the attenuation of the ground motion, from source to site, to evaluate exposure to seismic activity and to estimate the probability that peak ground motion parameters would be exceeded during the estimated life of the structure. A more detailed description of the approach

taken by the geotechnical engineer to conduct the seismic risk analysis and develop the site-specific spectra is beyond the scope of this paper.

For large return periods, the seismic risk analysis yielded a peak ground acceleration value of 0.7 *g* for the site. See Figure 2 for the site-specific elastic response spectra for both 5 and 10 percent dampings.

Seismic Design

The seismic design for a single-span bridge is not complicated. Normally, an equivalent static analysis is performed to determine the seismic load to be applied to the system. However, the results from an equivalent static analysis for the Carlson Boulevard Overcrossing yielded lateral loads greater than 1.6 times the weight of the superstructure, because the period placed the structure only slightly off the peak on the downslope side of the response spectrum.

A dynamic analysis was then done, modeling the abutment stiffness to see if the structure response could be brought down farther from the peak. Because of the nature of the response spectrum, somewhat flat at and near the peak, the dynamic loads were not much less than the previously calculated equivalent static load.

For a single-span structure, the seismic load due to the inertia of the superstructure is resisted only by the two abutments. The longitudinal forces (in the direction of traffic) are resisted by one abutment at a time. The transverse forces are shared by the two abutments. Caltrans seismic design criteria restrict longitudinal seismic forces above the abutment seat by allowing the abutment back wall (from the top of bridge deck to the soffit) to fail and mobilize the soil behind (Figure 3) to an ultimate pressure of 7.7 ksf. Transverse seismic forces are resisted by abutment shear keys (limited to 75 percent of the lateral capacity of the abutment piles) plus the shear capacity of one abutment wing wall (Figure 4). The design criteria for resisting longitudinal and transverse seismic loads is intended to keep all damage above the footing level.

The seismic design forces, as calculated by equivalent static or dynamic analysis, exceeded the ultimate longitudinal pressure of 7.7 ksf and indicated the need for additional CIDH concrete piles to resist the transverse forces. Adding these piles was considered only a partial solution, because it did not address the longitudinal force problem.

Ideas to modify the abutments to accommodate the seismic forces were numerous and varied. One idea was to design a friction slab under the approaches and behind the back walls (Figure 5) to use the weight of overburden to resist the longitudinal forces. A friction slab, however, would have had such substantial dimensions that use of a friction slab would not have been economical or feasible. To provide additional transverse resistance, interior shear walls located behind the abutment wall and below the seat were considered (Figure 6). Again, this led to another problem: the abutment dimensions did not allow for the required number and size of shear walls to be constructed.

Another idea was to provide restrainer cables (Figure 5) at each abutment so that both abutments could resist the seismic forces simultaneously in the longitudinal direction. This mechanism was determined to be undependable, however. Even the idea of reintroducing an intermediate bent was entertained. This bent would have provided another lateral load-resisting system, but it also would have cluttered the grade separation by adding columns to the median of the separation (although this was the original concept in the 1960s). The bottom line, however, was that an intermediate bent was not cost-effective. At a meeting with Geospectra to discuss the development and consequences of the site-specific response spectrum, the question of how to design for the large load magnitudes generated by the response spectrum was considered. At this point the geotechnical engineer suggested investigating the use of base isolation to absorb the forces produced by the superstructure impacting the abutments. He further explained that for structures in close proximity to a main causative fault, displacement is as important a design consideration as ground acceleration due to ground motion, and base isolation would be a good candidate that could be used to accommodate both considerations. Preliminary calculations were run to determine if lower levels of superstructure acceleration could be achieved without increasing superstructure displacement to unacceptable values. The calculations showed that it was attainable. Dynamic Isolation Systems, Inc. (DIS), was then contacted for support and to provide a detailed analysis and design of the base isolators for the superstructure.

Isolation System Design

A successful seismic activity isolation system must provide a horizontal plane of flexibility to lengthen the period of response, substantial amounts of energy dissipation to control displacements, restoring force for centering after an earthquake, and high initial stiffness to resist lateral service loads such as wind and traffic loads. The lead-core rubber isolation bearing designed by DIS (Figure 7) provides all of these features in a single component.

The first step in the design process was to conduct a feasibility study to assess the benefits of introducing isolation bearings at the abutment seats. DIS was presented

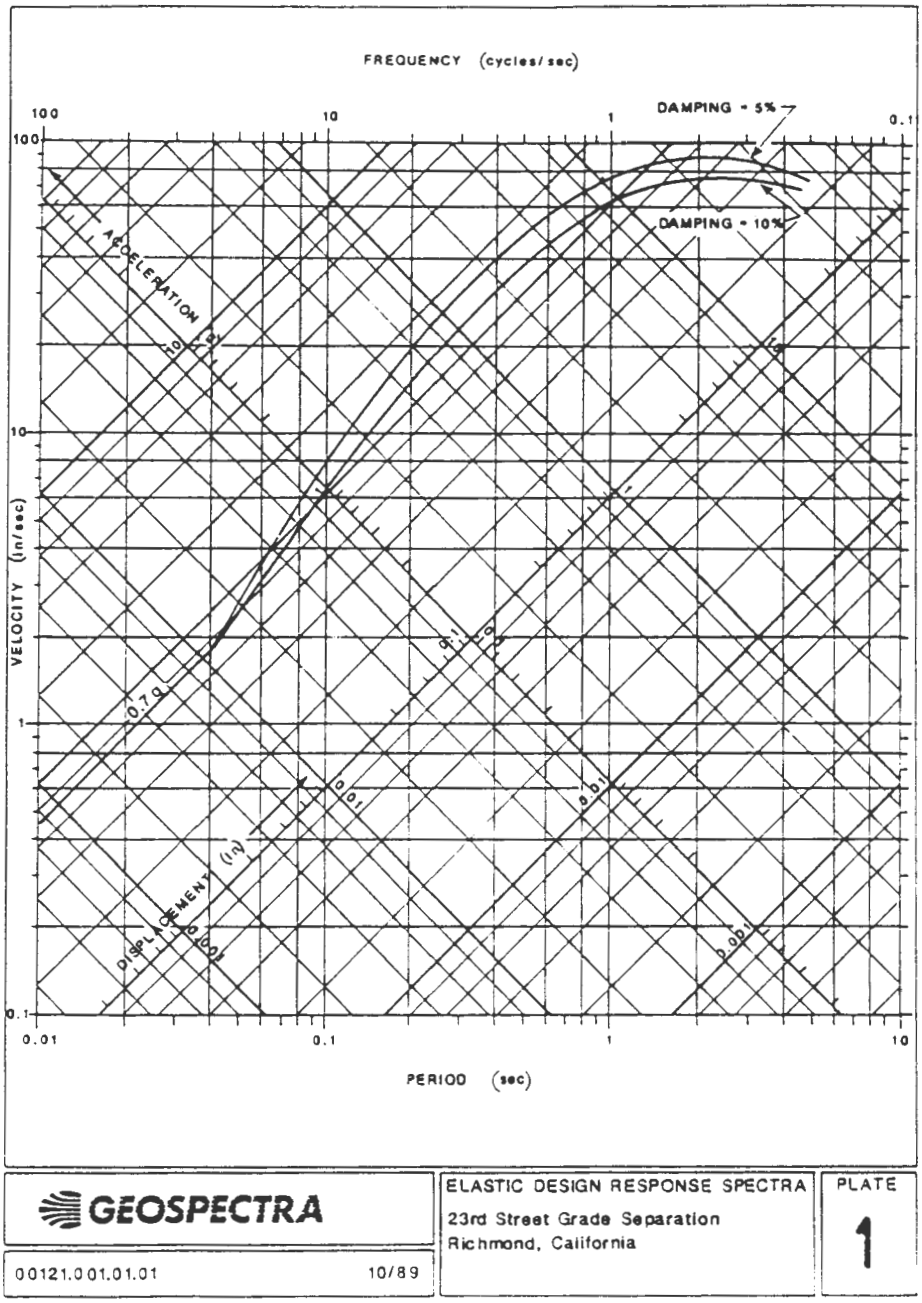

FIGURE 2 Response spectra (*continued on next page*).

with the necessary information, including a general plan, site-specific design response spectra, and dead and live load reactions for each abutment. Usually, it would be important to provide information regarding wind and traffic loads and thermal and creep movements. This information is needed to ensure that the design of the seismic isolators can also accommodate these service load conditions. However, it was clear from the site-specific spectrum that seismic criteria would govern the design, which could be checked for adequacy against service loads.

The DIS software program LEADeR was used to design the lead-core rubber isolators. LEADeR performs the two interrelated parts of the design process: sizing the isolators to ensure adequate factors of safety under all seismic and nonseismic load combinations and evaluating the seismic performance of the isolators so designed. The Caltrans curve for 0.7 *g* and 80 to 150 ft of alluvium was used to design the isolators, because this provided a good match with the site-specific spectrum for isolated periods greater than 1.25 sec (Figure 2).

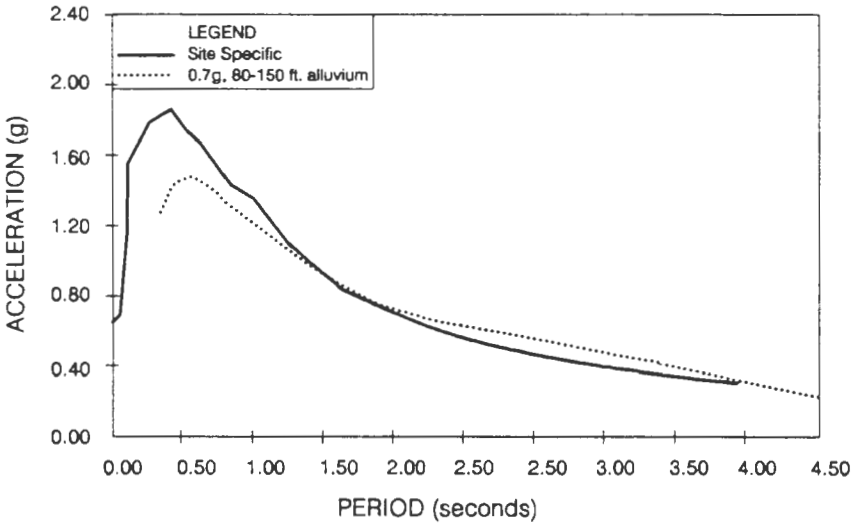

Site-Specific Response Spectrum: Caltrans 0.7g, 80-150 ft. alluvium

FIGURE 2 (*continued*).

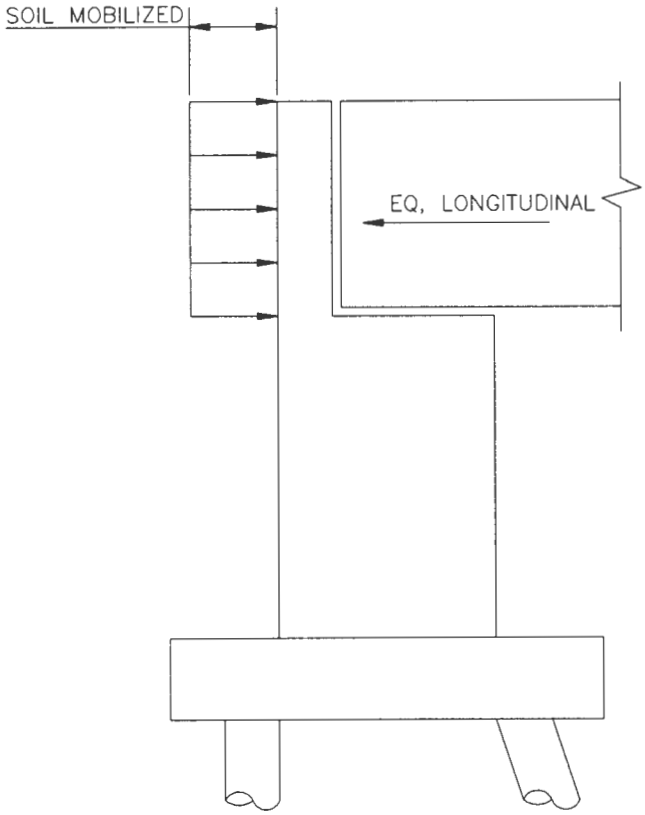

FIGURE 3 Abutment section.

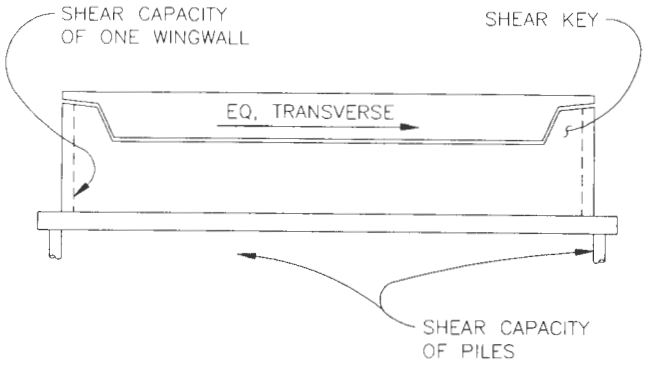

FIGURE 4 Abutment front section (*3*).

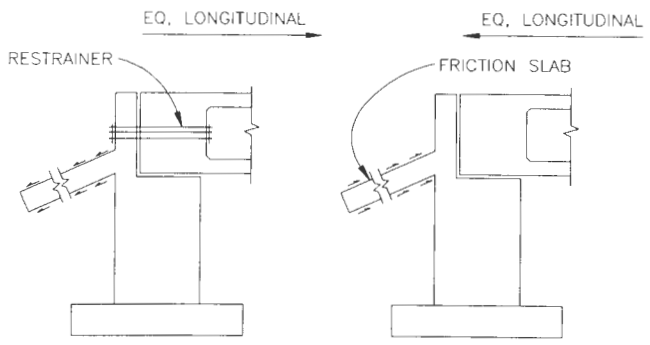

FIGURE 5 Abutment sections with friction slab and restrainers (*3*).

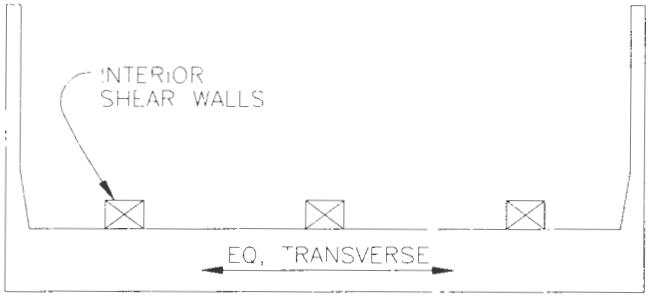

FIGURE 6 Abutment plan with interior shear walls (*3*).

The study assumed four isolators at each abutment, requiring the end diaphragm to span approximately 15 ft between isolators. For the total vertical load at each abutment, the maximum dead and live loads per isolator were 325 and 48 kips, respectively. By using the LEADeR program, the design called for isolators 29 in. square in plan, nominally 12 in. high, with a 7.25-in.-diameter lead core. A plan size of only 21 in. square was adequate to support dead and live loads; however, in this case, the plan size was controlled by the requirement to carry the dead load safely at the seismic displacement under the maximum credible earthquake. The lead cores, as dimensioned, provided a yield level of $0.15W$ (where W is the weight of structure above the isolators), which resulted in an elastic lateral load capacity per isolator of 43 kips, which was more than sufficient to resist the applied wind and traffic loads. The isolator height was also more than that required to accommodate creep and thermal movements.

The square isolators were to be oriented parallel to the skewed superstructure alignment. Because of the oversized masonry plate required to anchor the isolators, the abutment seat was inordinately wide. It was decided to use circular isolators to reduce this width. The final design produced a 31-in.-diameter isolator, nominally 13 in. high, with the same 7.25-in.-diameter lead core. The effective period is approximately 1.6 sec, and the elastic force coefficient is 0.46, which represents a reduction factor of approximately 3.5 from the conventional coefficient of 1.6. The maximum displacement is 11.6 in.

Isolator Specification and Testing

The final design was implemented with a performance specification that included tabulation of the required performance characteristics on the isolator plan sheet (Table 1). The essence of the performance specification is embodied in the testing requirements, which are designed to ensure that the properties of the isolators installed in the structure are those on which the engineer's global design is based. Prototype tests of isolators are required to confirm the design properties used for the analysis and performance evaluation of the structure. Quality control tests are performed on isolators intended for installation and are a means of verifying the consistency of properties over a large number of units, as well as allowing visual inspection of each unit under compressive and shearing load conditions.

Four prototype tests were performed. The first checked nonseismic displacement, under repeated service loading, against the specified maximum of 0.13 in. The two intermediate tests checked isolator performance at various increments of the specified maximum seismic displacement of 12 in. The final test subjected the isolators to three fully reversed cycles of loading at 1.5 times the seismic displacement, or 18 in. Throughout these tests, the isolators remained stable and exhibited the desired force-deflection and energy-dissipation characteristics.

The quality control tests included those performed in accordance with relevant ASTM standards for the re-

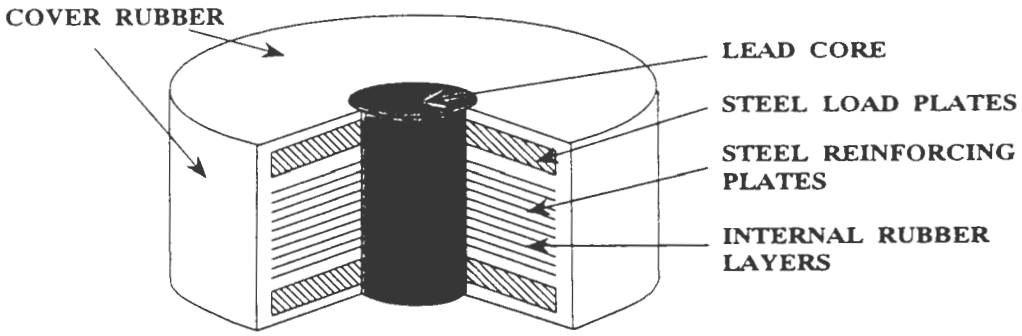

FIGURE 7 Seismic isolation bearing.

TABLE 1 Isolation Performance Specifications

Seismic Isolation Bearing Performance and Test Data, Based on Site-Specific Spectra		
Acceleration Level	0.7g	
Effective Period (secs)	1.6	
Maximum Displacement (inches)	12	
Maximum Lateral Non-Seismic Displacement (inches)	0.13	
Elastic Force Coefficient	0.45	
Effective Damping, %, at 12 inches Displacement	20	
Shape	circular	
Maximum Baseplate Size (circular or square)	3'-0"	
Dead Load	1300^{k} (1)	325^{k} (2)
Live Load	220^{k}	55^{k}
Maximum Lateral Non-Seismic Force (kips - total at each abutment)	50^{k}	12.5^{k}

Notes: (1) Kips - Total load at each abutment
(2) Kips - Load per bearing; with 4 bearings per abutment

Required Hysteretic Behavior of the Seismic Isolation System at 1.6 Seconds per Cycle Period of Vibration			
Each Bridge			Tolerance (Prototype Test)
K_{eff}	K_r	EDC	$K_{eff} \pm$ 10% K_{eff} (Table)
kips/inch	kips/inch	kip-inch	$K_r \geq$ 90% K_r (Table)
12.5	8.5	2095	EDC $\geq$ 90% EDC (Table)

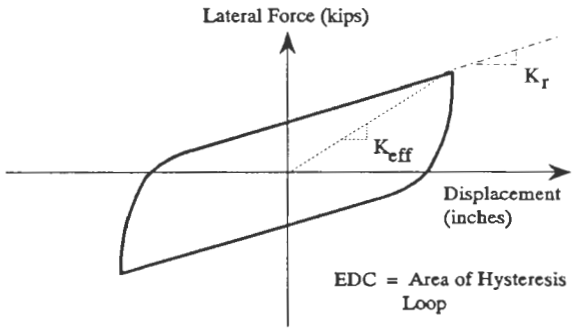

HYSTERESIS LOOP

N.T.S.

quired material properties of the isolator's components (rubber, steel, and lead). The completed isolators were tested under sustained compression, compression stiffness, and combined compression and shear conditions. In addition, a sample taken from a prototype isolator was tested in accordance with the provisions of California Test 663, which requires a minimum fatigue life of the rubber bond of 10,000 cycles at ±50 percent shear strain.

Practical Aspects

The use of isolation bearings led to some special design considerations. Because the lead-core rubber isolation bearings were designed to safely provide up to 12 in. of displacement in any lateral direction, a detail allowing this amount of movement at the superstructure-abutment interface had to be developed. The final design is shown in Figure 8. The knock-off concrete block at the top of

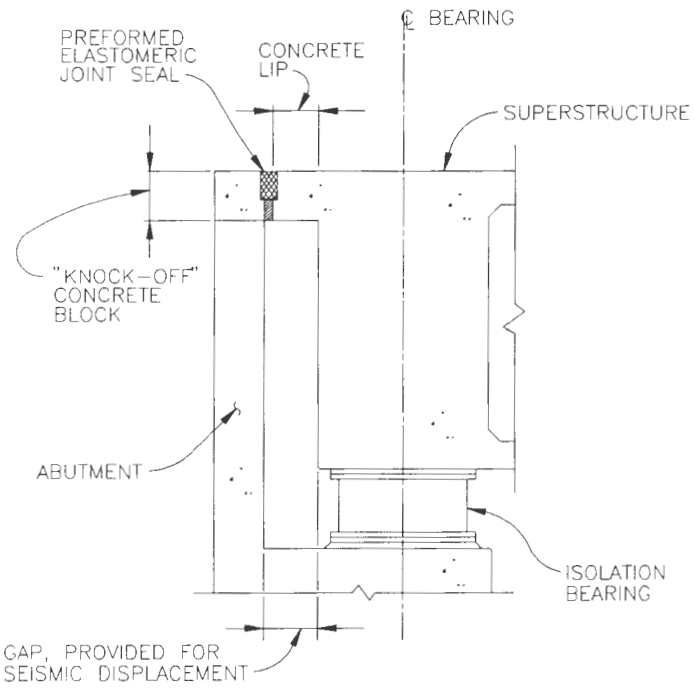

FIGURE 8 Superstructure-abutment interface.

the abutment back wall is intended to break away when it is struck by the concrete lip hanging off the end diaphragm; this will provide for the anticipated seismic movement. Everyday movements are accommodated by the preformed elastomeric joint seal detail. At the barriers and sidewalk, a 12-in. gap was detailed into the superstructure-abutment interface for seismic displacements. Steel plates were used at the barriers and tread plates were used at the sidewalk to produce a continuous surface across the gap. Finally, the abutment seat had to be widened to support the rather large circular isolation bearings, but not as much as would have been needed to accommodate the square bearings.

As for any special construction aspects, the use of isolation bearings had no impact on the schedule other than that they be manufactured and tested early in the project—earlier than use of regular elastomeric bearings would have required.

The postseismic aspect of the isolation bearing design compares favorably with the only possible and workable alternative discussed previously in the Seismic Design section: the addition of an intermediate bent. The base isolated design would require the replacement of the knock-off wall and, on either side of this wall, the repair of the roadway and possibly the overhanging concrete lip. During reconstruction, traffic access across the overcrossing may still be maintained by placing steel plates over the damaged sections of the approaches.

Conclusions

The single-span Carlson Boulevard Overcrossing presented many different interesting design facets to the project: from being a redesign of a project completed 20 years earlier and having to be constructed close to an existing aerial structure to having to be designed for site-specific spectra because of its proximity to an active fault. The seismic design required investigating several provocative alternatives, the most provoking being a return to the original design concept of using multiple spans. Fortunately, for the cleaner design concept of the late 1980s, the use of isolation bearings prevented the design direction from being reversed to the use of multiple spans visualized in the 1960s. Because isolation bearings are specified to be tested individually, they can be relied on to perform their intended function for everyday service loads and the infrequent seismic loads over the life of the overcrossing. The examination of numerous seismic design strategies led to a simple, cost-effective solution that uses seismic isolation. This retained the open, single-span design and provided a simple solution to an otherwise frustrating and complicated problem.

ACKNOWLEDGMENT

The authors thank Sandi Fischer for advice and support in preparing this paper.

REFERENCES

1. *Standard Specifications for Highway Bridges*, 13th ed., 1983, and Interim Specifications, 1986, AASHTO, Washington, D.C., with revisions by Office of Structure Design, Department of Transportation, State of California.
2. *Geotechnical Investigation and Seismic Design Criteria, 23rd Street Grade Separation, Richmond, California, March 1989*. Geospectra, Inc., 1989. (Letter Addenda to November 1989.)
3. Memo to Designers Manual. Division of Structures, State of California Department of Transportation.

Seismic Retrofit of Southern Freeway Viaduct, Route 280 (Single-Level Segment), San Francisco, California

Roy A. Imbsen and Robert A. Schamber, *Imbsen & Associates, Inc.*
A. A. (Frank) Abugattas, *Brown & Root, Inc.*

The Loma Prieta earthquake of 1989 generated the need to strengthen the single-level Southern Freeway Viaduct. The double-deck portion just south of this project was damaged, and the whole viaduct was closed to traffic. The Southern Freeway Viaduct is a continuous reinforced concrete box girder bridge built in 1964 in accordance with the AASHO standard specifications. The viaduct is composed of three main lines, as follows: ES Line, SE/A Line, and R1 Line. The columns are rectangular with inadequate tied reinforcement. The columns at most multicolumn bents are pinned at the bottom. Several of the fixed-base columns have lap splices. The majority of footings are supported on steel HP piles; however, some are spread footings. The footings do not have top mat and shear reinforcing. Several of the A-Line bents north of 25th Street are outriggers. Soil conditions at the southern section (south of Bent 73 on the main lines) can be classified as soft bay mud sites, whereas more generally, the site has a combination of a thick soft bay mud layer and a large depth to bedrock. The northern segment is founded on bedrock or stiff soils. Most of the deficiencies found in the viaduct are related to the original design of the hinges, columns, footings, and outriggers. Solutions to retrofitting the viaduct were limited by the existing conditions and existing features (i.e., railroad lines, streets, leased airspace below the viaduct, utilities, etc.) within the project limits. The retrofit strengthening concepts used on the project included the following: hinge retrofits, separation of two level bents, steel column casings, column strengthenings (additional vertical steel encased within a steel casing), grade beam retrofit, new drop caps (bent replacements), elimination or retrofit of outriggers, and footing retrofits. This final retrofit strategy met the required seismic performance goals established by the California Department of Transportation for this project to prevent collapse and provide serviceability after a maximum credible earthquake.

The Loma Prieta earthquake of 1989 generated the need to strengthen the single-level Southern Freeway Viaduct. The double-deck portion just south of this project was damaged, and the whole viaduct was closed to traffic.

This paper describes the seismic retrofit of the single-level segment of the Southern Freeway Viaduct in San Francisco, California, which was under contract to Imbsen & Associates, Inc. (IAI), and Brown & Root, Inc. (B&R), from the California Department of Transportation (Caltrans) between 1990 and 1993. In addition, DRC Consultants, Inc., and Earth Mechanics, Inc. (EMI), provided retrofit design and geotechnical support, respectively. Anatech Research Corporation per-

formed an analysis of joint shear. The design efforts culminated with a final set of plans, specifications, estimates, and construction contracts.

The objective was to seismically retrofit the single-level portion of the Southern Freeway Viaduct, Route 280, in San Francisco to prevent collapse or major damage in an earthquake with the maximum intensity expected to occur at this site. The structure's serviceability performance goals are that it will be repairable and that there will be access beneath the viaduct for emergency services and repair.

The single-level segment of Route 280 in San Francisco branches into the following viaduct lines (Figures 1 and 2):

- ES Line: beginning at the hinge adjacent to Bent ES-59 near Evans Street and extending to Bent ES-90 between 23rd and 25th Streets.
- R1 Line: beginning at the hinge adjacent to Bent R1-50 near Innes Street and extending to Abutment R1-72 near Main Street.
- SE/A Lines: beginning at the hinge adjacent to Bent SE-53 near Galvez Avenue and extending to Abutment A-111 north of 22nd Street.
- B and C Lines: all bents on both of these ramps between 23rd and 25th Streets.

For the purpose of facilitating construction contracts that expedite opening the bridge to traffic, the project was divided into three separate design projects.

- Project 1 included any retrofit work that would cause significant interference with traffic on Route 280. Completion of construction of this work was scheduled for the end of 1992 to allow opening the structure to traffic (SR-637).
- Project 2 included the retrofit of all bents south of Army Street that were not retrofitted in Project 1 (SR-605).
- Project 3 included the retrofit of the remaining Southern Freeway Viaduct north of Army Street. This project was eventually divided into two separate projects for construction (SR-604 and SR-641).

IAI was under prime consultant contract to complete Project 1, and B&R was under prime consultant contract to complete Projects 2 and 3. IAI, B&R, and EMI were teamed and involved in the retrofit design of all projects. DRC was involved in the retrofit design of Projects 1 and 2. Figures 1 and 2 show the locations of these lines and project limits.

Description of Existing Bridge

The Southern Freeway Viaduct is a continuous reinforced concrete box girder bridge built in 1964 in accordance with the AASHO Standard 1961 Specifications for Highway Bridges and subsequent interims. The columns are rectangular with vertical reinforcement and 12-mm bar ties typically at 305-mm spacing (no. 4 ties typically at 12-in. spacing). The columns at most multicolumn bents are pinned at the bottom with four 35-mm bars (no. 11 dowels). Most of the fixed-base columns have lap splice connections. The majority of footings are supported on steel HP piles, whereas others

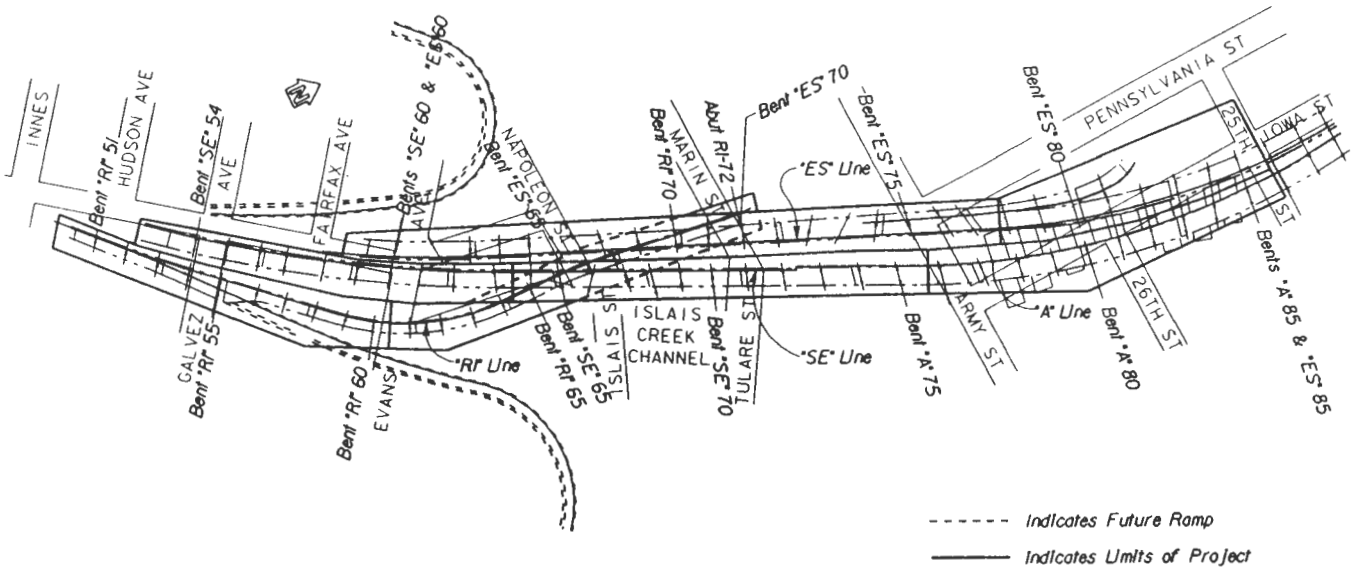

FIGURE 1 Projects 1 and 2, plan view.

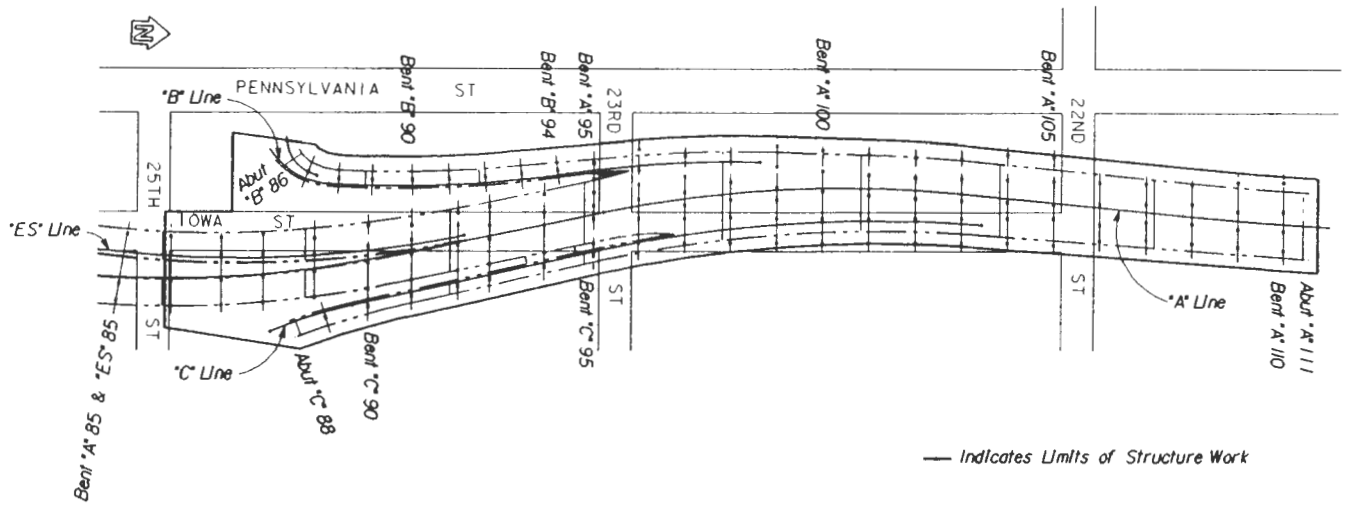

FIGURE 2 Project 3, plan view.

are spread footings. The footings do not have top mat and shear reinforcing. The HP piles are connected to the footings with one 20-mm bar (no. 6 rebar). Many of the A-Line bents north of 25th Street are outriggers. The outriggers were constructed to allow the viaduct to span over Iowa Street and existing and future railroad tracks beneath the structure.

The behavior of the single-level viaduct is complicated by the fact that the ES, SE, and R1 Lines intersect at three locations. The R1 and SE Lines intersect at Bent R1-66/SE-65, and the ES and R1 Lines intersect at Bents R1-69/ES-67 and R1-70/ES-68. At two of these intersections (i.e., R1-66/SE-65 and R1-70/ES-68) the supporting bent is a two-level frame. At these two locations the preferred retrofit was to separate the lower level from the upper level.

Following the San Fernando earthquake in 1971, Caltrans initiated the Phase One earthquake retrofit program. Seismic restrainers were installed at the intermediate expansion hinges on the Southern Freeway Viaduct in 1973. The cable units consisted of 14 cable restrainer units that are similar to the current Caltrans C1-Type restrainers [i.e., cable drum units, bolsters, 19-mm-diameter (3/4-in. diameter) cables]. The hinge seats are approximately 152 mm (6 in.) in length. Access holes for the cable restrainer units were placed in the top deck of the Southern Freeway Viaduct and were sealed with concrete. There are no access holes in the soffits.

The consultants divided the viaduct into five segments for analysis and design. A general description of each stage is provided in Table 1.

TABLE 1 General Description of Existing Bridge

Line	No. Spans	Span Length Ranges (ft)	No. Cells	Minimum Curb-to-Curb Width (ft)	No. Hinges	Single Column Bents	2 Column Bents	3 Column Bents	4 Column Bents	>4 Column Bents	Outrigger Bents	Shared Bents with Adjacent Superstructure
SE/A Line (Stage 2)	33	80-121	6-7	49	12	3	29	0	0	0	3	1
R1 Line (Stage 1)	22	80-104	4-8	28	8	17	4	0	0	0	2	3
ES Line (Stage 3);	26	70-132	6-12	49	10	7	16	3	0	0	0	2
Ramp R4	2	85-97	5	36	0	1	0	0	0	0	0	0
A Line (Stage 4);	13	66-113	13-25	52	4	0	0	0	9	4	12	0
Ramp B;	9	51-80	4-5	32	3	8	0	0	0	0	0	0
Ramp C	9	60-113	3-4	24	2	7	0	0	0	0	0	0
A Line (stage 5)	12	40-93	16-22	120	4	0	0	0	5	7	15	0
Total	126	N/A	N/A	N/A	43	43	49	3	14	11	32	N/A

Soil Profile and Response Spectra

The soil profile along much of the Southern Freeway Viaduct includes three major soil layers:

- Layer 1: a surficial fill layer of gravel, sand, and silt of moderate stiffness and strength;
- Layer 2: a second layer of very soft bay mud; and
- Layer 3: a layer of very dense sand or stiff clay above bedrock consisting of sandstones, referred to as the San Franciscan formation.

Soil conditions at the southern section (south of Bent 73 on the main lines) are classified as soft bay mud sites, whereas elsewhere there is a combination of a thick soft bay mud layer and a large depth to bedrock. The northern segment is founded on bedrock or stiff soils where the depth to bedrock is less than 15.25 m (50 ft), and the thickness of the soft clay layer is less than 1.53 m (5 ft). The soft bay mud layer is nonexistent in some areas.

On November 26, 1991, our project team and Caltrans adopted for Project 1 the Seed and Sun 8+ spectrum (1989) and a bedrock spectrum provided by Translab for the southern (soft soil site) and the northern (firm-ground site) portions of the Southern Freeway Viaduct, respectively.

On December 24, 1991, Translab provided four response spectra: (a) DeLeuw Cather's deep bay mud spectrum, (b) Curve A, (c) Curve B, and (d) a new bedrock spectrum (*1*). The three soft soil spectra, including Curves A and B and the DeLeuw Cather deep bay mud curves, were considered appropriate for the southern portion of the project sites. The new bedrock spectrum was considered appropriate for the northern portion (north of Bent 72). See Figure 3 for the response spectra used.

To meet the schedule for the plans, specifications, and estimate (PS&E) submittal for Project 1, the project team and Caltrans decided to continue Project 1 work with the Seed and Sun 8+ spectrum and the unrevised Translab bedrock spectrum of November 26, 1991. However, it was agreed that the new bedrock spectrum and Translab's three soft soil spectra be adopted for Projects 2 and 3.

Discrepancies between the response spectrum criteria used in Project 1 and the revised response spectrum criteria are relatively small considering the level of uncer-

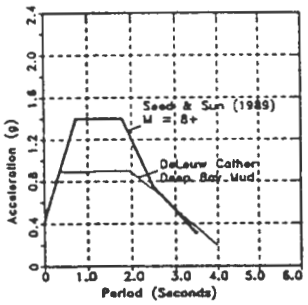

a. **DeLeuw Cather – Deep Bay Mud (South of Bent 61)**

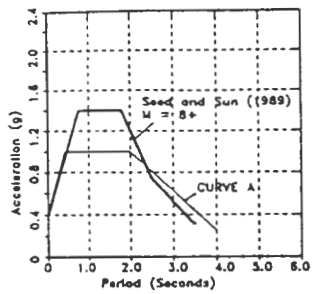

b. **Curve A (Bent 61 to 66)**

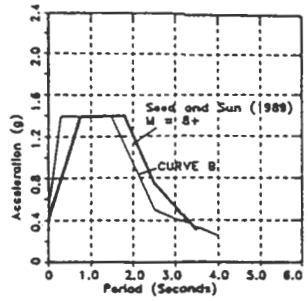

c. **Curve B (Bent 66 to 72)**

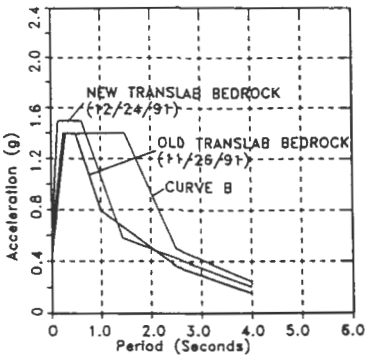

d. **New Translab Bedrock Curve (North of Bent 72)**

FIGURE 3 Response spectra for Southern Freeway.

tainty on earthquake ground motion; therefore, no changes were made to the Project 1 design.

Retrofit Design Criteria

The design criteria were in conformance with Caltrans's procedures for retrofitting (2). Seismic retrofit analysis techniques and retrofit schemes were continuously developed during the project. The project team maintained close coordination with the Caltrans contract administrator to ensure that the very latest criteria were used. Demand/capacity ratios were obtained for all bridge components.

The retrofit was based on the following criteria:

- Material strengths. The columns are composed of reinforced concrete that are typically rectangular in shape. The reinforced concrete strengths specified on the plans for the bridge were f_s of 137 800 kPa (20,000 lb/in.^{2}) for rebar and f'_c of 20 670 kPa (3,000 lb/in.^{2}) for Class A concrete and f_s of 137 800 kPa (20,000 lb/in.^{2}) and f'_c of 31 005 kPa (4,500 lb/in.^{2}) for high-strength concrete. Based on recent tests conducted by Caltrans and recognizing that higher strengths are appropriate for retrofitting measures, f'_c was increased to 37 895 kPa (5,500 lb/in.^{2}) for the single-level portion of the Southern Freeway Viaduct. The steel strength was chosen as f_y of 275 600 kPa (40,000 lb/in.^{2}) for the reinforcement.
- Hinges. Caltrans's simplified procedures for designing restrainer hinges were used. Pipe seat extenders and long cable restrainers were proposed. The pipe seat extenders are designed with 203-mm-diameter (8-in.-diameter) double-extra-strong pipes and a maximum vertical load of 445 kN (100 kips), based on tests at Cypress Street Viaduct.
- Columns. Procedures outlined by Caltrans's Memo-to-Designers 20-4 (2) were used to obtain ductility demands for single and multicolumn bents. The moment ductility demand on existing columns was limited to 1.0 in single-column bents (tied) and 2.0 in multicolumn bents (tied). The moment ductility demand for retrofitted columns with steel casing was limited to 6-in. single-column bents and 8-in. multicolumn bents. For ductilities that exceeded those values, a pin was forced at the tops of the columns to approximate a plastic hinge.

The thicknesses of the column steel casings were designed by using the procedures from lecture materials obtained at the retrofit seminar at the University of California, San Diego (3). Casings were full height, and thicknesses varied, being thicker within the plastic hinge zones.

- Footings. Pile loads were determined by conventional analysis methods (i.e., linear elastic). The majority of existing columns in multicolumn bents are pinned at the base; therefore, only axial loads for uplift and compression were checked in the as-built condition. For the retrofitted condition several columns were made fixed to the footing by using a column-strengthening retrofit measure. A steel pipe pile was chosen as the pile for retrofitting. Capacity curves, based on the as-built log-of-test borings, were provided by EMI to determine the additional number of piles required. In some instances the footing size needed to be reduced to avoid utilities or adjacent footings, so nonlinear analysis was provided by EMI to design the footing. The footing was assumed to be infinitely rigid. A moment-rotation analysis was used by assuming a neutral axis, and pile deflections were calculated. These deflections were used to determine pile reactions from nonlinear force deflection curves. The analysis was iterated on the neutral axis location until the sum of vertical forces was zero. The applied moment was determined by summing the pile reactions.
- Outriggers. Outrigger bents were evaluated with the latest criteria from Caltrans, including the Terminal Separation Design Criteria dated December 4, 1991.
- Superstructure. The superstructure capacity was checked on the as-built structure by distributing the plastic column moment in the longitudinal direction of the nominal moment [1.3 times (M_n)] to each face in the superstructure and adding the dead load moment effects. Both top and bottom fibers in the superstructure were checked in the deck and soffit, respectively.

Seismic Analysis

Four computer programs were used to analyze the Southern Freeway Viaduct: SEISAB (4), GTSTRUDL (5), MSTRUDL (6), and IAI-NEABS (7). SEISAB was used to generate the model coordinates along the alignment. Various widths in the superstructure were accounted for in the model.

With the coordinates generated from SEISAB, various GTSTRUDL, MSTRUDL, or IAI-NEABS models were developed. Consideration was given to modeling a limited number of frames for analysis, but with the line intersections being located in the middle of the segment, it was determined that the level of production time would be of the same order as that for a full-scale model or a limited number of frame models. In addition, IAI provided a postprocessor for the GTSTRUDL and IAI-NEABS programs, and DRC provided a postprocessor for the MSTRUDL program to calculate ductility demands in the columns at the tops and bottoms for both moment and shear.

The computer program PILECAP was provided by EMI and was used to determine the foundation soil spring stiffness matrices. The program performs the analysis for a pile group foundation considering the interaction between soil, individual piles, and the pile cap. Individual pile head stiffness matrices and pile head-to-pile cap connectivities were included in the analyses. The resulting foundation stiffness matrices were input into the structural models at every column.

Both tension and compression models were used to evaluate the proposed retrofit strategies. The following are the main features of the structural model:

- Space frame members (linear elastic analysis), a minimum of three interior nodes per superstructure span, and a minimum of two interior nodes per column were incorporated into the model.
- Linear springs to model the soil-foundation stiffness, both piles and pile cap, were used.
- Additional frames plus one bent were modeled at each end. Lumped masses and springs were placed at the end of the model.
- Ninety percent or more of the mass participated in each of the horizontal directions.
- Gross member sections were used for all sections except for outriggers (20 percent gross for torsion in the as-built model).
- Spring constants to model soil-foundation interaction were modified to reflect any eccentricity between the columns and the footings.
- Finite size joints between the superstructure's center of gravity and the top of the column were used.

As-Built Structural Deficiencies

Review of the as-built plans and results of the as-built dynamic analysis provided information on the structural deficiencies of the existing structures. In reviewing this information the following conclusions were reached.

Hinges

The as-built structure contained a minimum number of cable restrainers per hinge. These cables are similar to Caltrans C-1-Type restrainers. The typical seat width was only 152 mm (6 in.) and required pipe seat ex-

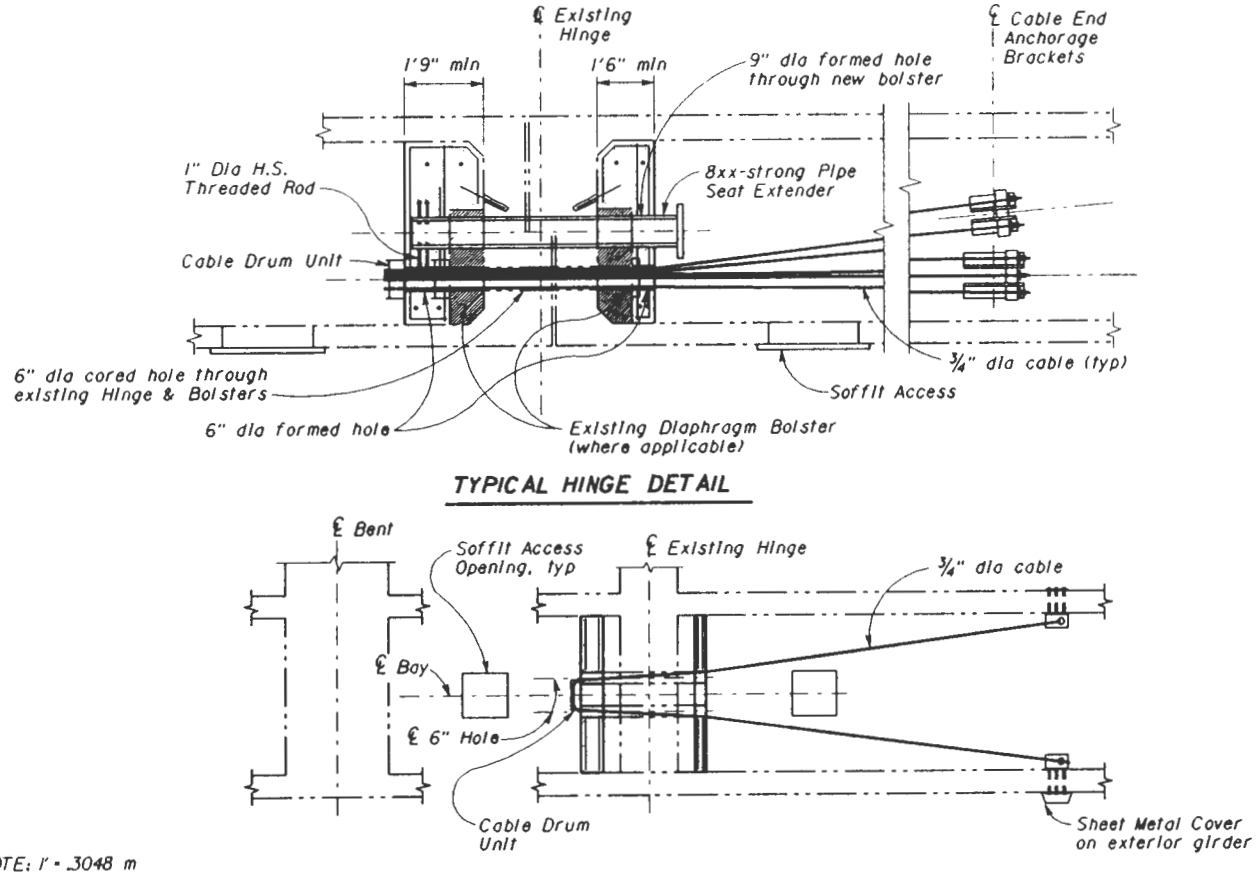

FIGURE 4 Typical hinge retrofit.

tenders to prevent the seat from dislodging. Caltrans's simplified procedure was used to determine the number of cables required incorporating 203-mm-diameter (8-in. diameter) double-extra-strong pipe seat extenders and longer cables (*8*).

Columns

- The percentage of main reinforcement was inadequate in some cases.
- All columns have ties of 12-mm bar at 305 mm (no. 4 bars at 12 in.), which was inadequate.
- A weak connection was the pinned connection between the column and footings four 35-mm bar dowels (four no. 11 dowels). The development length of reinforcement dowels at this joint was inadequate.
- Column tension capacity was exceeded in many columns.
- The connection between the column and the bent cap was deficient for the development length of longitudinal reinforcement, with 45-mm bar (no. 14 bars), and 60-mm bar (no. 18 bars) being most critical.
- The lap splice for fixed columns at the base was inadequately confined and insufficient in length.
- Moment ductility demand/capacity ratios were high in many cases.
- The demand/capacity ratios for shear exceeded 1.0 in most of the columns.

Footings

- There was no top mat of steel and shear steel.
- There were inadequate pile connections to the footing: one 20-mm bar (no. 6 bar) per pile.
- The footings were inadequate to resist column plastic moments.

Superstructure

- There was limited moment capacity in the superstructure for positive moments at support locations.

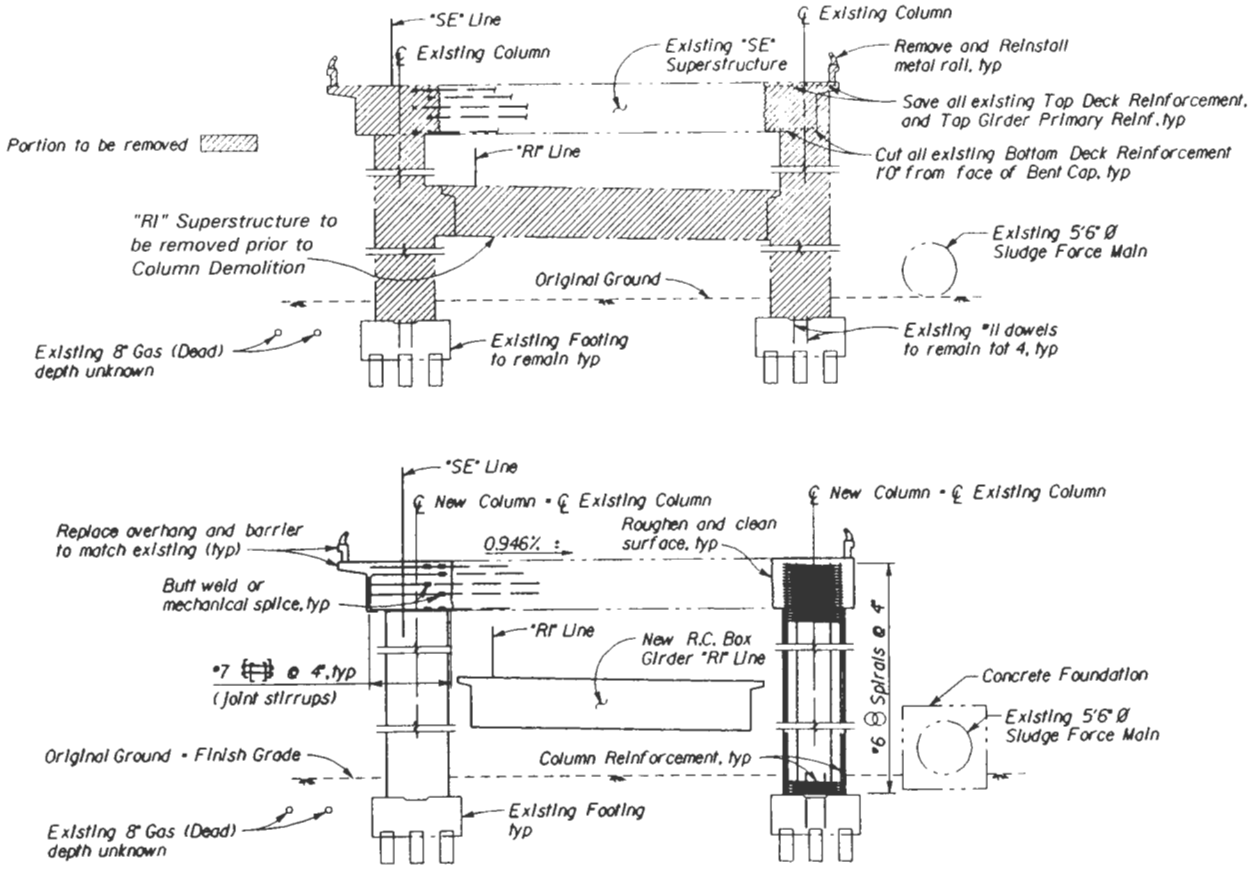

FIGURE 5 Separation of two-level bent (SE-65).

Outriggers

- Torsional capacity in the outriggers was limited because of inadequate cross-section sizes, lack of closed torsion stirrups, inadequate longitudinal reinforcement for torsion, and insufficient stirrups.
- Shear capacity in the outriggers was inadequate. Additional shear stirrups were required.
- Bending capacity in the outriggers for positive and negative moments at both ends of the outrigger cap was inadequate.
- Joint confinement within the outrigger-to-column connection was insufficient.

Retrofit Solutions

The existing structure was deficient in several areas. The final retrofit solutions addressed these deficiencies as well as other concerns related to utilities, roadway traffic, leased airspace, and railroads.

Several retrofit schemes that addressed these items and that improved the structure's response to earthquake forces were studied. The following is a discussion of some of the retrofit schemes evaluated and the final retrofit strategy selected for the various bridge components.

Hinges

New hinge restrainers will be placed at all hinges. Caltrans's Simplified procedure was used to determine the numbers and lengths of new restrainers. Pipe seat extenders were also used to transmit lateral force and to support the structure if seismic movements exceeded the small existing hinge seat width (Figure 4).

Columns and Bents

One of the major problems of the structure was its flexibility, primarily in the longitudinal direction. Several retrofit schemes were analyzed. The use of superbents was studied. Superbents are retrofits to selected bents to make them very stiff and strong, and therefore they resist most of the seismic force, thus reducing the ret-

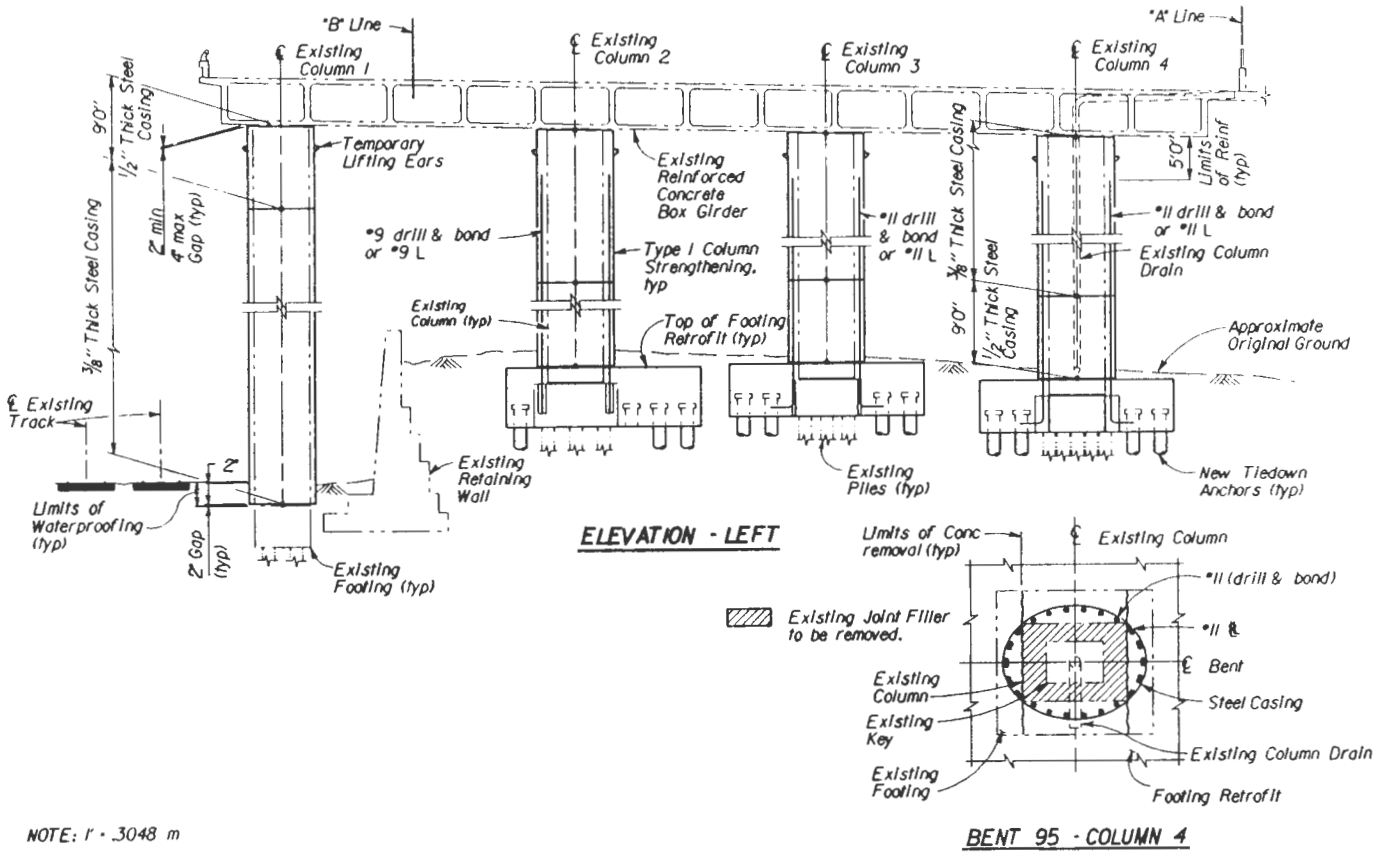

FIGURE 6 Column casing and column strengthening (A-95).

rofit work on other adjacent bents. It was determined that the use of a few superbents was not feasible. The bents could not be made strong enough to eliminate the retrofit work on the adjacent bents.

At intersecting Bents R1-66/SE-65 and R1-70/ES-68 the preferred retrofit was to separate the upper-level and lower-level superstructures. Columns were placed under each superstructure (Figure 5).

The use of column strengthenings was also studied in an attempt to increase the stiffness of the structure. This concept was eventually used extensively on the project. A column strengthening involves placing a steel casing around an existing column and placing vertical reinforcing steel in the void between the casing and the column. The voided area is then filled with concrete. The new rebar is anchored in the footing. This concept allowed the transformation of an existing pinned column base into a fixed column base and thus increased the stiffness of the structure in response to seismic forces. The live load carrying capacity of columns needed to be evaluated when column fixities were changed. Footing retrofit was required when a column strengthening was used. The top of column connection to the superstructure remained unchanged from the as-built condition by using this concept (Figure 6).

Grade beam retrofits were also used on this project. A grade beam retrofit involves constructing a concrete member connecting the columns of a two-column bent at the column base, just above the top of the existing footing. This concept provides frame action to resist transverse earthquakes forces without the need to retrofit the footing for column moments (a pinned connection still exists between the column frame and the footings). This concept was used in an area where the limits of footing work were restricted and the transverse bent stiffness was weak (Figure 7).

Another method of improving transverse stiffness was the use of bent replacements. The use of bent replacements involves building a new drop cap beneath the superstructure and supporting the drop cap on new columns and footings. This concept provided higher capacity at the top of column and bent cap connection and was used at bents weak in transverse stiffness that had minimal conflicts with the existing features below (Figure 8).

Every effort was made to eliminate outriggers by removing existing columns and reconstructing them un-

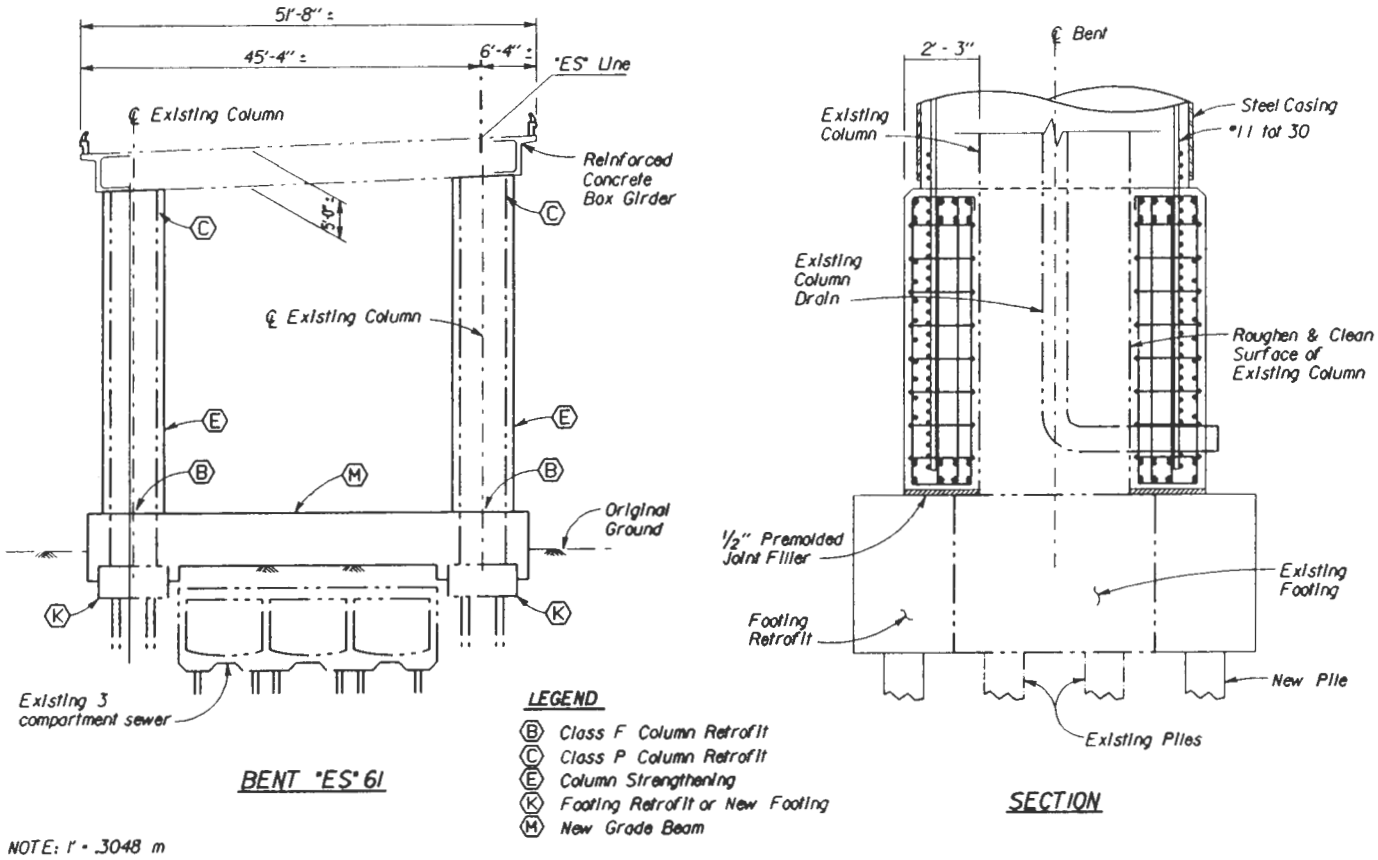

FIGURE 7 Grade beam retrofit (ES-61).

der the edge of the superstructure. Outriggers that could not be eliminated were reconfigured into pinned connections on top if the resulting forces could be handled in the remaining bent frame. At those locations where the pinning at the top of the outrigger resulted in excessive forces in the remaining bent frame, the outrigger column and portions of the cap were removed and replaced to provide higher capacity (Figures 9 and 10).

Steel casings were placed around all existing columns not being replaced or strengthened with longitudinal steel and a steel casing. The casings provide confinement and shear capacity.

Superstructure

The superstructure capacity was checked on the as-built structure by distributing one-half of the plastic column moment in the longitudinal direction (1.3 times the M_n) to each face in the superstructure and adding the dead load moment effects. Both top and bottom fibers in the superstructure were checked in the deck slab and soffit slab, respectively. Initially, an effective width of D (depth of the superstructure) on each side of the column was added to the column width to check the longitudinal capacity of the superstructure. The results indi-

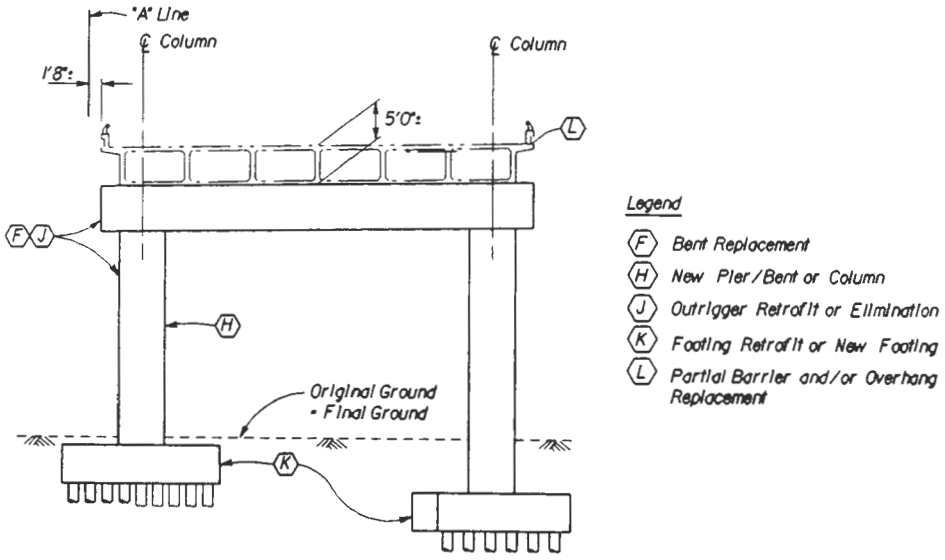

TYPICAL SECTION BENT "A" 76

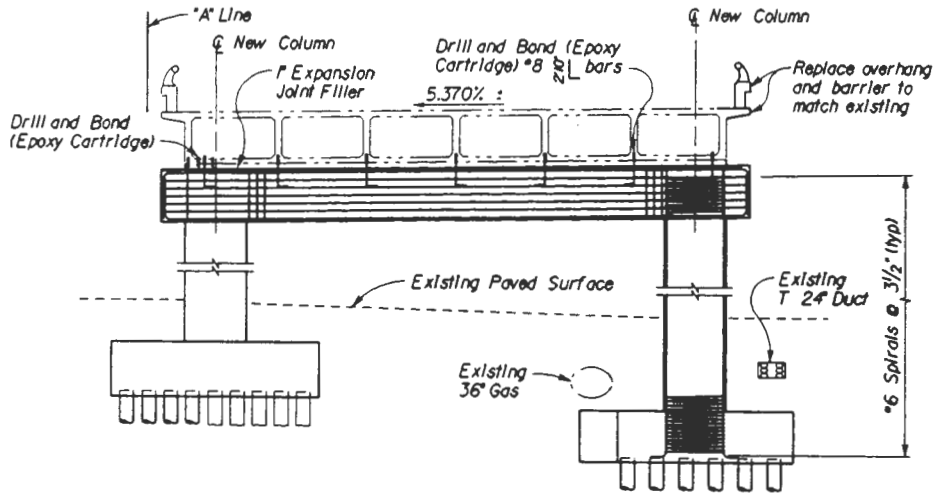

ELEVATION BENT "A" 76

NOTE: 1' = .3048 m

FIGURE 8 New drop cap (A-76).

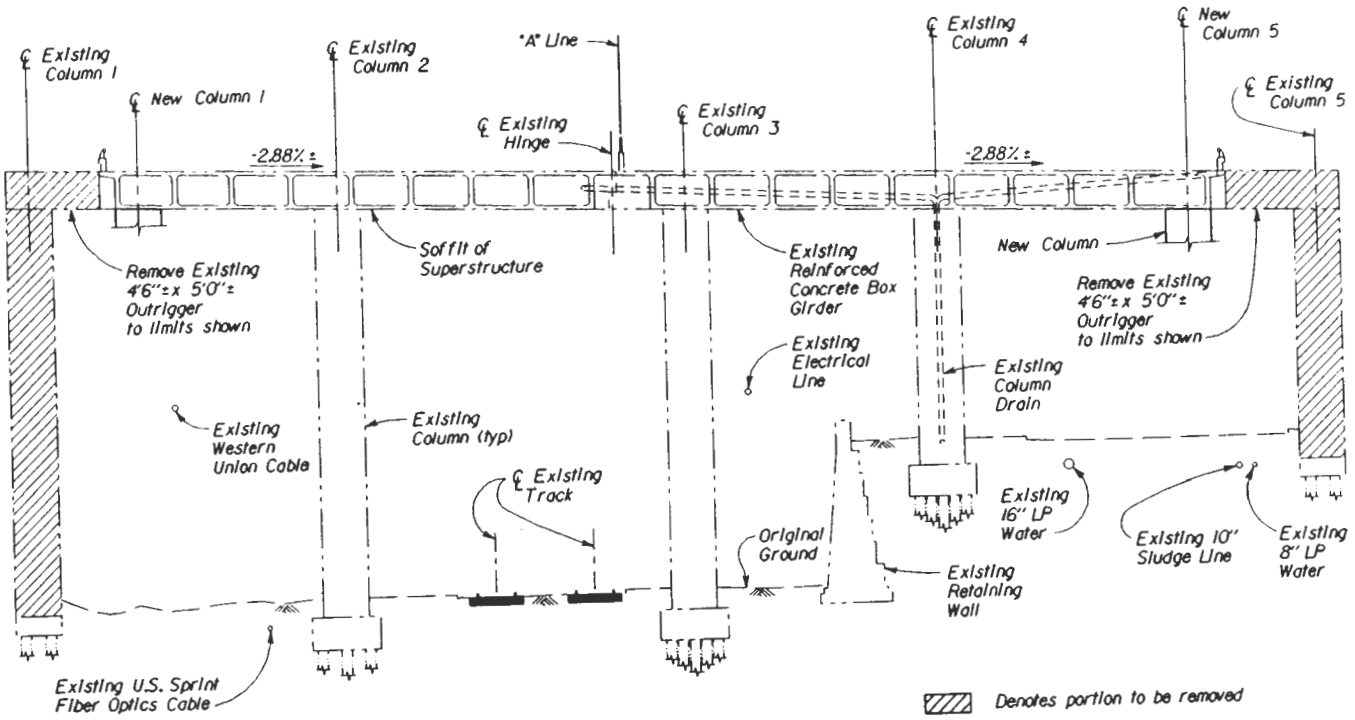

ELEVATION

BENT "A" 104

NOTE: r • .3048 m

FIGURE 9 Outrigger elimination (A-104).

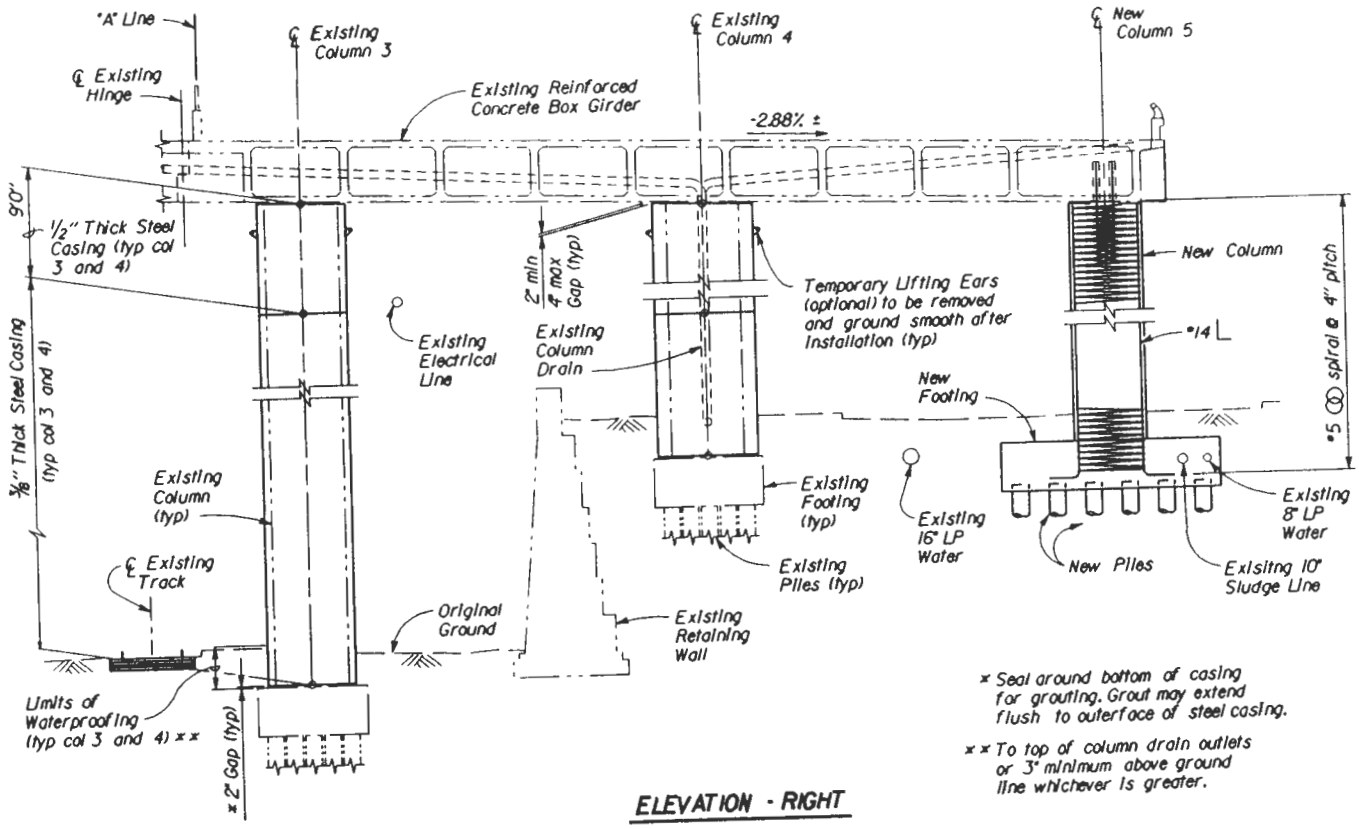

ELEVATION - RIGHT

NOTE: 1' • .3048 m

FIGURE 10 Reconstruction of outrigger bent (A-104).

cated that at a few single bents (i.e., R1-63 and ES-64), the capacity of the superstructure was exceeded. It was believed that the full width of the superstructure would be mobilized during an earthquake, and on the basis of that rationale the capacity was rechecked. Capacities were checked at bents in Projects 1 and 2 at R1-51, R1-63, R1-55, SE-54, SE-56, SE-59, SE-70, A-73, A-75, A-78, A-80, A-84, SE-60, ES-64, ES-71, and ES-78. The results gave capacity/demand ratios of greater than 1. Studies were also conducted by using a full-width effective section at selected bents in Project 3, and the results indicate that adequate superstructure capacity was achieved.

Joint Shear

Many of the bents of the Southern Freeway Viaduct are not of the outrigger configuration, and so their bent cap to column joints are relatively inaccessible for retrofitting. In a major seismic event, joint shear and the overall performance of these joints are still concerns.

Anatech Research Corporation performed an analysis of the joint shear concern as part of B&R's retrofit contract with Caltrans. Anatech constructed a three-dimensional continuum, finite-element model to evaluate joint shear behavior and ultimate strength, ductility, and potential failure modes under seismic motion. They modeled a typical two-column bent (Bent A-78) in the single-level portion of the viaduct.

Anatech's report states that two incremental analyses were performed, one for primarily transverse motion and one for primarily longitudinal motion, but in each case smaller orthogonal motions were applied to create a realistic biaxial response (9).

Implementation of Anatech's report as a design guide has not been completed to date. Further review of the results of the present study is needed to determine a general design memorandum that would cover all bridges with joint designs similar to those of Southern Freeway Viaduct joints. We were informed by Caltrans that any retrofit recommendations required for joint shear would be part of a later contract.

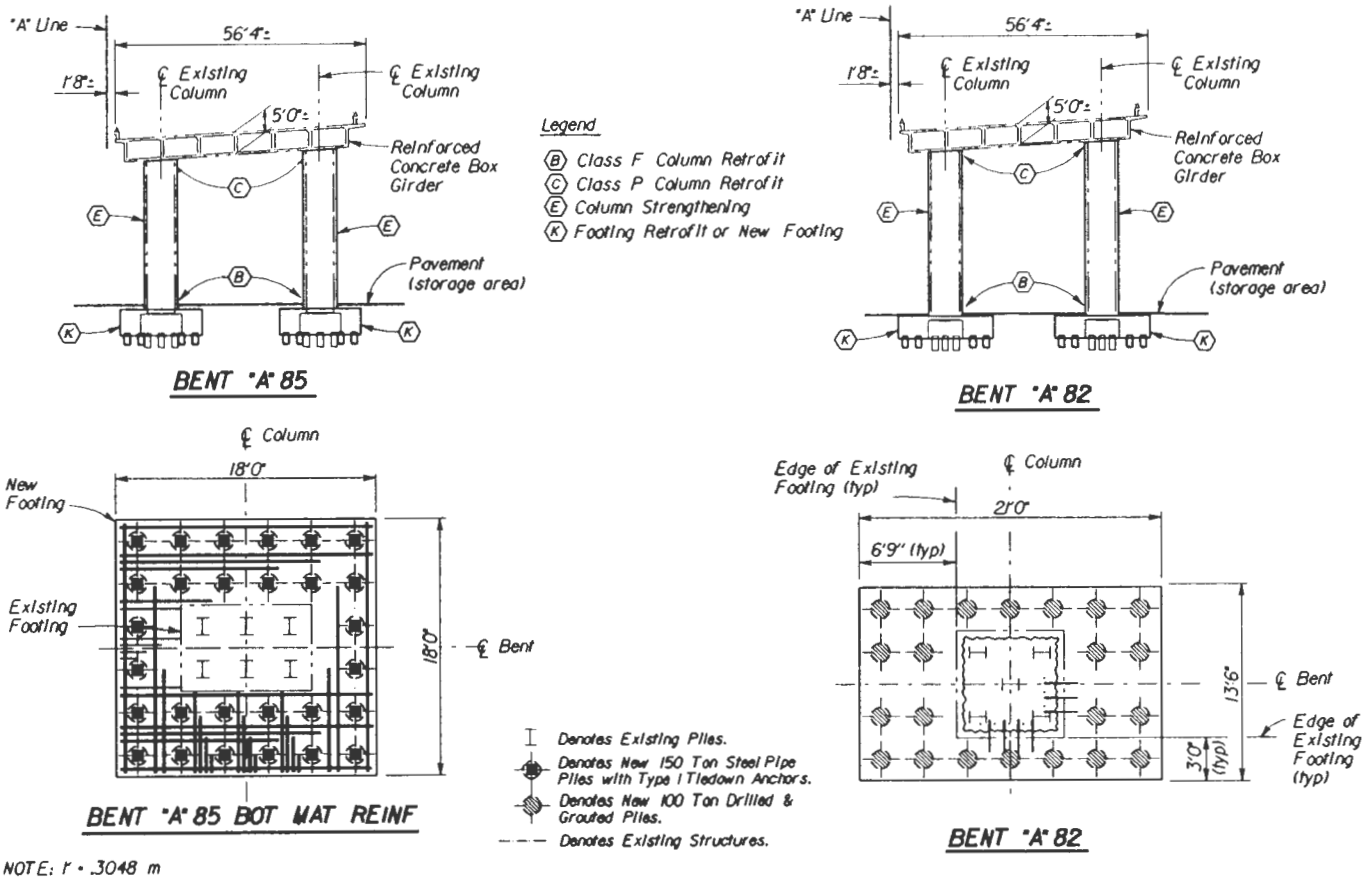

FIGURE 11 Footing retrofit.

Footings

Footing retrofits were required primarily at those locations where a pinned base column was retrofitted to be a fixed base column (column strengthenings). The moment capacity of the footing had to be increased at these locations (Figure 11).

The variable soil conditions along the length of the viaduct resulted in several footing retrofit solutions. The south end of the project consisted of deep bay mud with bedrock at a depth of approximately 42.7 m (140 ft). Long steel pipe piles were used to provide the tension and compression resistance at these bents. The northern end of the project consisted of thinner deposits of bay mud with depths to bedrock in some cases of only 6.10 m (20 ft). Steel pipe piles were used again, but tiedowns were installed inside the piles. The tiedowns were drilled into the bedrock to provide the required uplift resistance.

Some existing footings at the north end of the project are spread footings placed near or on bedrock. As part of the retrofit program, the footings are to be enlarged and tiedowns are to be placed to provide the required uplift resistance.

Noise and vibration concerns in the leased airspace occupied by mini-warehouses led to the development of a drilled and grouted pile for footing retrofits in that area. A hole is to be drilled through the soil and into the bedrock layer. A steel pipe pile is to be placed in the hole, and the void between the pile and the soil-bedrock is filled with grout. The pile interior is then filled with concrete. The embedment of the pile into the bedrock provides the required uplift resistance. By this method, the noise and vibration of pile-driving operations are eliminated.

ACKNOWLEDGMENTS

Robert M. Jones, who was the contract administrator from Caltrans, provided oversight throughout the project. James Gates from Caltrans provided guidance during the retrofit strategy phase of the project. Other personnel contributing substantially were Tim McGrady of B&R, Richard J. LeBeau of IAI, and Erich Aigner of DRC, who were project managers. Also, Eli M. Aramouni of IAI and M. A. Ravanpour and Dan Copps of B&R were lead project engineers on the job. Thomas G. Tracy of IAI provided the specifications for the project. Po Lam and Lino Cheng of EMI provided geotechnical support throughout the project.

REFERENCES

1. *Southern Freeway Viaduct.* Final Retrofit Strategy Report. Imbsen & Associates, Inc., Sacramento, Calif., Jan. 23, 1992.
2. Memo-to-Designers 20-4. California Department of Transportation, Sacramento, April 6, 1992.
3. *Seismic Assessment and Retrofit of Bridges.* University of California, San Diego, La Jolla, July 1991.
4. *Seismic Analysis of Bridges.: User Manual.* Imbsen & Associates, Inc., Sacramento, Calif., 1993.
5. *GTSTRUDL, User's Manual.* GTICES Systems Laboratory, Georgia Institute of Technology, Atlanta, 1990.
6. *MSTRUDL—Users Manual,* Version 2.7.2. CAST Corporation, Fremont, Calif.
7. *Linear and Nonlinear Earthquake Analysis of Bridge Systems.* Imbsen & Associates, Inc., Sacramento, Calif., Dec. 1993.
8. *Caltrans Bridge Design Aids 14.* California Department of Transportation, Sacramento, Dec. 31, 1992.
9. Dameron, R. A. *Detailed 3D Analysis of Shear in Unretrofitted Joints of Bent A-78 on the Southern Viaduct.* Anatech Research Corporation, June 5, 1992.

Earthquake Retrofit of California Bridge: Route 242/680 Separation

Robert C. Fish, *HDR Engineering, Inc.*
George L. Rowe, *Dokken Engineering*

The California Department of Transportation is currently implementing a statewide earthquake retrofit program. The goals of the program are to improve structural ductility and to provide corrective measures to the factors that contributed to the major damage and collapse of bridges during the San Fernando and Loma Prieta earthquakes. A case study of a retrofit design project of a bridge located in the San Francisco Bay area, in proximity of the Concord fault, is described. The structure type, geometry, traffic volumes, and maximum credible earthquake led to many difficulties in the analysis and resulted in solutions that were complex and unique for a bridge structure. The bridge investigated consists of two very different structure types joined by a voided pier that serves as a central abutment for both. The focus is primarily on the south structure, where base isolation was used, in contrast to the more conventional retrofit techniques used for the north structure.

The Route 242/680 separation carries Route 242 traffic over six lanes of Route 680 and Walnut Creek. This facility was designed in 1960, constructed in 1964, and seismically retrofitted in 1984 (prior to the Loma Prieta earthquake). The bridge is 12 spans, totaling 373 m (1,222 ft), with the longest span of 65 m (214 ft) crossing over Route 680. The structure is made up of two different types of bridges joined at Bent 4, which acts as a common seat abutment.

The south structure has a width of 12 m (39 ft 8 in.) and a depth of 2.44 m (8 ft) and is a continuous three-span prestressed concrete box girder supported by steel rocker bearings at Abutment 1 and Bent 4. At Abutment 1 and Bent 4 there is a gallery that is 0.92 m (3 ft) wide. Spanning this gallery and supporting vehicle traffic is a short flat concrete deck slab with a 0.15-m (6-in.) seat. At Bents 2 and 3 the superstructure rests on fixed steel bearings. These bents have five square columns, each with external bent caps. The abutment and bents of this section of the structure are on a 69-degree skew.

The north structure has a width of 12 m (39 ft 8 in.) and a depth of 1.22 m (4 ft) and is a continuous concrete box girder. Bent 4 is on a 69-degree skew, and Bent 5 through Abutment 13 are on a 54-degree skew. Steel rocker bearings support the superstructure at Bent 4 and Abutment 13. The bridge is composed of three frames with hinges located in Spans 6 and 9, near Bents 7 and 10, respectively. Bents 5 through 12 are two square-column bents, with the bent caps cast monolithically with the superstructure. The bridge spans Walnut Creek between Bents 9 and 10. To protect the columns within the channel during flood stages, concrete debris walls were constructed at Bents 7, 8, 9, 10, and 11 and were slightly slotted into column sides for support.

The abutments are of the seat type and are supported by two rows of piles. Bent 4 is a 9.14-m (30-ft)-high

voided pier that acts as a seat abutment for both structures and is also supported by two rows of piles (Figure 1). The other bents are supported on pile footings. All piles are concrete with a compressive design load of 400 kN (45 tons).

The bridge had previously been retrofitted during the initial phase of the earthquake retrofit program of the California Department of Transportation (Caltrans) (Phase I). The goals of this phase were to provide continuity to the superstructure by connecting all narrow hinge seats with longitudinal cable restrainers and to place additional supports (concrete catcher blocks) at bearing locations to eliminate the chance of the superstructure losing elevation if the bearings fail. Bents 2 and 3 additionally have 19-mm (3/4-in.) cables connecting the soffit to the external bent caps to restrain longitudinal movement, also in case of bearing failure.

The closest fault is the Concord fault, which is 1.77 km (1.1 mi) from the bridge site. The maximum credible earthquake (MCE), as determined by a site-specific study, is a magnitude 6.5 on the Richter scale. The depth to rock-like material is about 45 m (150 ft), with a maximum horizontal bedrock acceleration of 0.53 *g*.

Analysis with As-Built Computer Model

A global three-dimensional linear response spectrum analysis was performed on the structure by using STRUDL. The following assumptions and methods were used in modeling the structure:

1. The superstructure was modeled by using a single line of elements.
2. A lumped mass model was used. Mass was placed at quarter points along the superstructure spans.
3. The bases of the footings were assumed to be fixed points in the model. The effects of the soil stiffness were accounted for only through application of the chosen response spectrum curve (see item 10).
4. For aged concrete a value of 34.47 MPa (5,000 lb/in.^{2}) for compressive strength was used according to the recommendation of Caltrans.
5. Gross (uncracked) section properties were used for the columns to obtain maximum force demand.
6. Cracked section properties were used for the columns to obtain maximum displacements.
7. Steel rocker and fixed bearings were assumed to fail during the design seismic event for a subsequent analysis. To represent friction contact between the soffit and catcher blocks, bearing locations were modeled with relatively soft spring elements. The spring stiffness was adjusted after the initial run to equal the dead load times the friction coefficient.
8. The hinges were modeled as short, rigid elements to allow for the proper member end force and moment releases to simulate actual hinge movement. Longitudinal cable restrainers across the hinges were modeled as short-space truss members of equivalent stiffness, parallel to and connecting to the same joints as the rigid hinge elements. To model the nonlinearity of the hinges with cable restrainers, two models were created. The first, a tension model, allowed relative longitudinal movement between adjacent frames by releasing the longitudinal force in the rigid hinge element and activating the cable restrainer elements. The second, a compression model, locked the longitudinal hinge force and allowed only moments about the vertical and horizontal centerlines of a hinge to be released.
9. Each cable restrainer unit (1984 seismic retrofit) at Bents 2 and 3 was modeled as an individual space truss element. Since only one side of the cable is in tension at any given point in time, each side is modeled with half of its equivalent stiffness. This resulted in the correct stiffness for longitudinal movements.
10. The response spectrum used was a standard Caltrans' elastic site spectrum (*ARS*) curve (*1*) with a depth of alluvium of 25 to 45 m (80 to 150 ft), acceleration of 0.6 *g*, and 5 percent damping, where *A* represents the base rock acceleration of 0.6 *g*, *R* represents the structure damping, which is assumed to be 5 percent, and *S* represents the effects of the depth of alluvium over the bedrock of from 25 to 45 m (80 to 150 ft).
11. Earthquake forces were applied independently along the centerline of the superstructure and perpendicular to the centerline. Forces were combined by using the standard Caltrans method (100 percent longitudinal plus 30 percent transverse and 100 percent transverse plus 30 percent longitudinal).

Summary of Structural Deficiencies

The plans were reviewed, and the results of the dynamic analysis obtained by using STRUDL, displacement ductility analysis (*2*), and hand calculation were evaluated. The following structural deficiencies were found:

1. All columns were designed with very little transverse steel. The columns in Bents 2 and 3 have No. 5 hoops at 0.3 m (12 in.). The other columns have No. 4 hoops at 0.3 m (12 in.). Because of this minimal transverse reinforcing of the ultimate curvature of the potential, plastic hinge zones are limited by the strain that causes the concrete cover to spall.
2. At each column ductility demands exceeded the allowable flexural ductility ratio of 1.5 (*2*), and the rotational ductility in the plastic hinge zone was also exceeded.

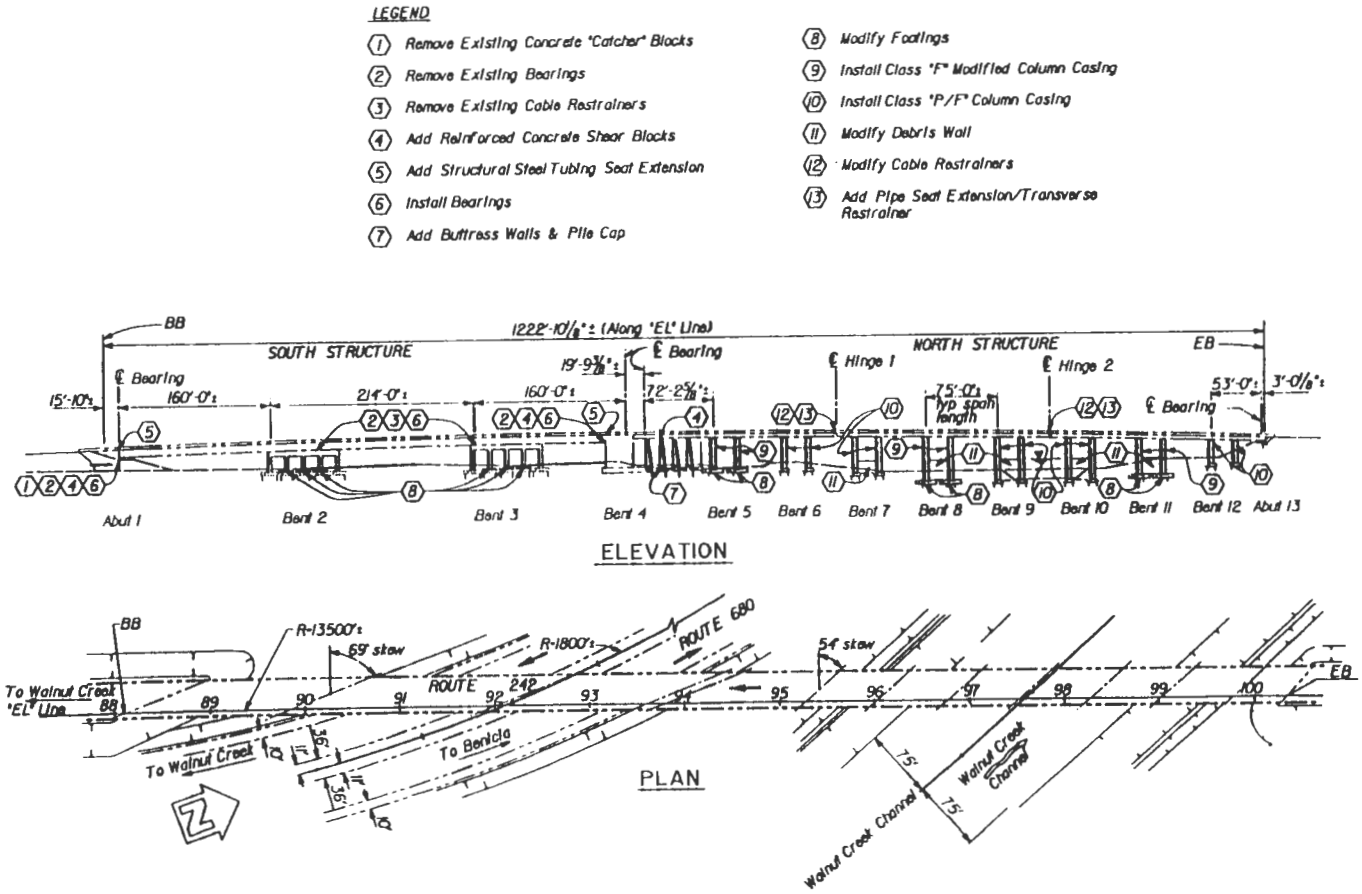

FIGURE 1 Elevation and plan of south and north structures.

3. Footings had insufficient moment capacity to resist the column's plastic hinging moments. This deficiency was due to the lack of top mat steel in the footing and insufficient pile tension capacity.

4. As assumed previously, rocker and fixed steel bearings would fail under the large lateral inertial forces.

5. The debris walls resulted in an unintended change in stiffness along the centerline of the bent that could force plastic hinging in the columns near the top of the wall. This would create an unstable situation if plastic hinges also occurred at the bases and tops of the columns.

6. The south structure exhibited unacceptably large displacements in both transverse and longitudinal directions that could cause the short concrete deck slabs spanning the gallery area to collapse, leaving a large gap in the roadway surface.

Retrofit Strategy Alternatives

The condition of the north structure posed no major obstacles to the use of a conventional bridge retrofit. The as-built condition of the structure was analyzed, and the minimum possible numbers of columns and footings were selected to be modified. The selection process was based on Caltrans criteria (2) to provide the minimum amount of modifications required to prevent collapse of the structure.

The retrofit of the north structure (Figure 2) consisted mainly of providing 9.5-mm (3/8-in.)-thick steel casings, to be installed around the columns, which are pressure grouted to provide confinement for increased ductility, and modifying the footings to withstand the plastic moments of these modified columns. Additional retrofit measures were to install casings at other columns ungrouted for twice the column width above the footing or below the soffit to protect against shear failure (2). The intent at these locations is to ensure a flexural failure at the tops or bottoms of the columns at a seismic demand level below that required for a shear failure. At these columns rotational capacity is lost either by failure in flexure of the column or failure of the footings or piles. Therefore, it is assumed that these columns have no lateral restraint and are only capable of carrying vertical loads after the seismic event. To reat-

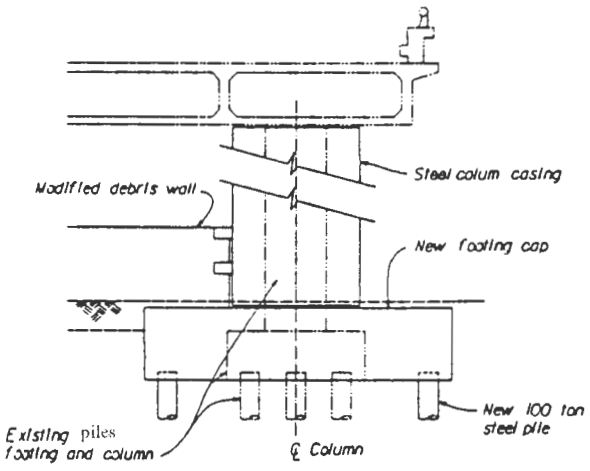

FIGURE 2 Column and footing retrofit.

tach the debris walls that were vertically saw cut and partially removed adjacent to each column for installation of the casing, a slotted steel debris wall-to-column casing connection with steel plates was designed. A small gap was left to prevent the columns from impacting the wall. This eliminated the potential for plastic hinging to occur in the column at the top of the wall height. In addition, the superstructure hinges adjacent to Bents 7 and 10 received pipe seat extensions (2). These 216-mm (8-in.)-steel pipes are installed in holes cored through the hinge diaphragms, parallel to the superstructure, to provide additional seat length and transfer transverse forces across the hinge.

The south structure provided some interesting challenges. Four possible retrofit strategies were investigated. The first two, Alternatives A and B, are termed the "resistive" solutions. The other two, Alternatives C and D, are termed the "isolated" solutions.

The resistive solutions involved standard modifications to the columns, footings, and bent caps of Bents 2 and 3. Both required steel column casings and complete footing modifications, including a reinforced concrete footing cap and additional 890-kN (100-ton) piles. In addition, Alternative A required removal of the bearings at Bents 2 and 3 and extension of the bent cap up into the superstructure to be monolithic with the internal diaphragm of the superstructure. Alternative B left the bearings in place, but it relied on modifications at Abutment 1 and Bent 4 to restrict the superstructure movement.

Both of these strategies met the goals of the design criteria and were therefore acceptable. However, several concerns arose. The cost (including that of the north structure, but not that of traffic control) of either of these strategies is approximately \$3.5 million or \$840/m^2 (\$78/ft^2) of deck. This is nearing the cost of replacement of the structure of about \$915/m^2 (\$85/ft^2) of deck. Also, with the major work required at Bent 3 (which lies in the median of Route 680), traffic handling would be a major concern. The closure of one lane on each side of the bent would be required for approximately 60 days. With high peak-hour traffic volumes (average daily traffic, 183,000; peak-hour traffic, 20,100) at this location, any lane closures would have a significant negative impact on the public.

The isolated solutions were then investigated. The first isolation strategy, Alternative C, simply involved allowing the steel bearings to fail at Abutment 1 and Bents 2, 3, and 4 (all points of support for the south structure). This would result in the superstructure dropping approximately 1 in. onto the existing concrete catcher blocks of the previous retrofit (Caltrans Phase I seismic retrofit program, 1984). It was anticipated that the friction that would develop between the concrete surfaces of the superstructure soffit and catcher blocks would result in forces and displacements at the tops of Bents 2 and 3 below their capacity. However, this did not hold to be true. The frictional force was assumed to be approximately 50 percent of the dead load, according to Caltrans recommendations. A static analysis of the bents by using the frictional forces applied at the top of the catcher blocks and a dynamic analysis by using STRUDL, with spring elements (similar to those used in the as-built model) used to approximate this frictional force, were performed. Both of these analyses indicated that the frictional force resulted in flexural stresses and displacements that exceeded the ultimate capacities of both the columns and the bent caps. The large horizontal displacements would also allow the short concrete spans to drop into the galleries. Furthermore, the locations of the existing catcher blocks are such that upon bearing failure the redistribution of dead load stresses in the bent caps and internal superstructure diaphragms exceeded their ultimate capacities. Because of these predicted failures and the unpredictability of the maximum lateral displacement of the superstructure, this alternative was not pursued further.

Final South Structure Strategy

The second isolated, and final, strategy, Alternative D, was developed. This strategy uses lead-core rubber seismic isolation bearings (3) (Figure 3) at Abutment 1 and Bent 4, and polytetrafluoroethylene (PTFE) spherical bearings (4) (Figure 4) at Bents 2 and 3.

This strategy provides some very distinct advantages over the other alternatives:

1. Increased system damping and, therefore, lower force demands. The lead-core rubber bearings act in

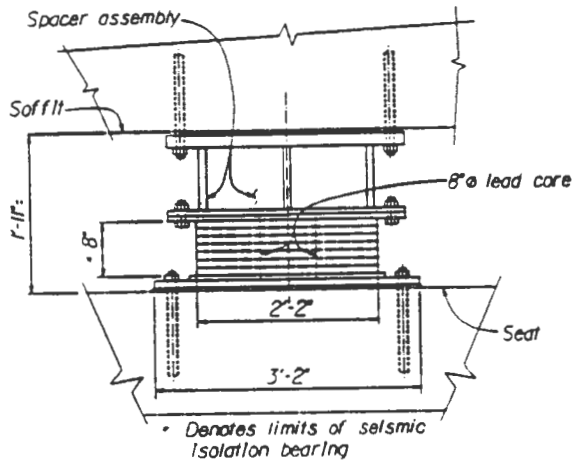

FIGURE 3 Seismic isolation bearing detail.

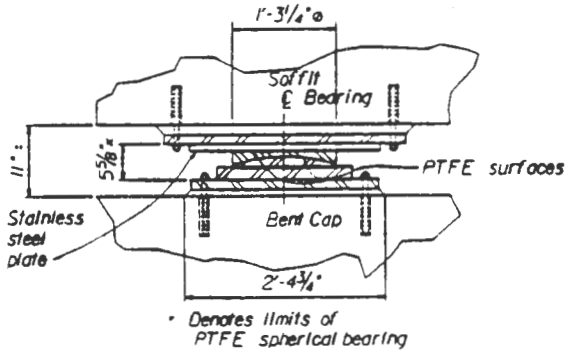

FIGURE 4 Elevation of PTFE spherical bearings.

two important ways to achieve this. First, the bearings add a soft stiffness component to the support points. This, combined in series with the more rigid stiffness of the existing substructure, results in a lower overall system stiffness and, therefore, a period shift to a region of lower demand on the response spectrum curve (Figure 5).

Second, the lead-core component of the bearing acts to raise the damping from the commonly assumed 5 percent to nearly 20 percent, based on the bearing size used and the configuration of the bridge structure. This is predicted to occur for modes with periods greater than 1.33 sec, at which point the lead core is predicted to begin plastic shear deformation.

Although a lead-core elastomeric isolation bearing was used for this project because of specific energy dissipation and displacement limitation requirements, other types of isolation bearings (such as friction pendulum, nonlinear elastomeric, etc.) are available. One or more types of isolation bearings may be acceptable for use in a particular project.

2. Dramatically reduced force demand at Bents 2 and 3. In addition to the beneficial effects of the lead-core rubber bearings given above, the PTFE-to-stainless steel contact of the PTFE spherical bearings reduces the frictional forces to less than 10 percent of the concrete-to-concrete friction forces from the as-built seismic forces (Figure 6).

3. Predictable displacement of the superstructure. Isolation bearings, including the lead-core rubber bearings used for this project, are designed to produce a hysteresis loop (Figure 7), which results in predictable displacement behavior. This was particularly critical for retrofitting the seat length of the short [length, 0.92 m (3 ft)] slab spans crossing the galleries at the ends of the south superstructure. Alternatives A and B also offered predictable displacement; however, Alternative C, which relied on concrete-to-concrete friction to resist lateral movement, did not.

4. Construction cost. The total construction cost, including that of the north structure, is estimated to be \$1.97 million, or \$474/m^2 (\$44/ft^2) of deck. This is a 43.6 percent reduction (\$1.53 million savings) from the typical resistive alternatives (Figure 8).

5. Traffic handling. This structure carries Route 242 over six lanes of Route 680. For approximately 6 hr per day the commuter traffic on Route 680, as well as Route 242, is stop-and-go, with an emphasis on stop. Any lane closures other than temporary night closures would have a significant adverse impact on this already poor traffic service level. The retrofit work required in the median of Route 680 at Bent 3, including the footing caps, can be accomplished from within the shoulder limits of the median. The result is a minor impact on traffic.

Additional retrofits required for this alternative are as follows:

- Remove existing cable restrainers at Bents 2 and 3 to allow for freer superstructure movement and less

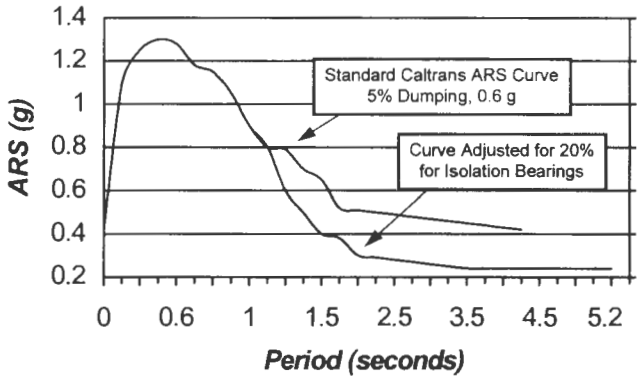

FIGURE 5 Composite response spectrum.

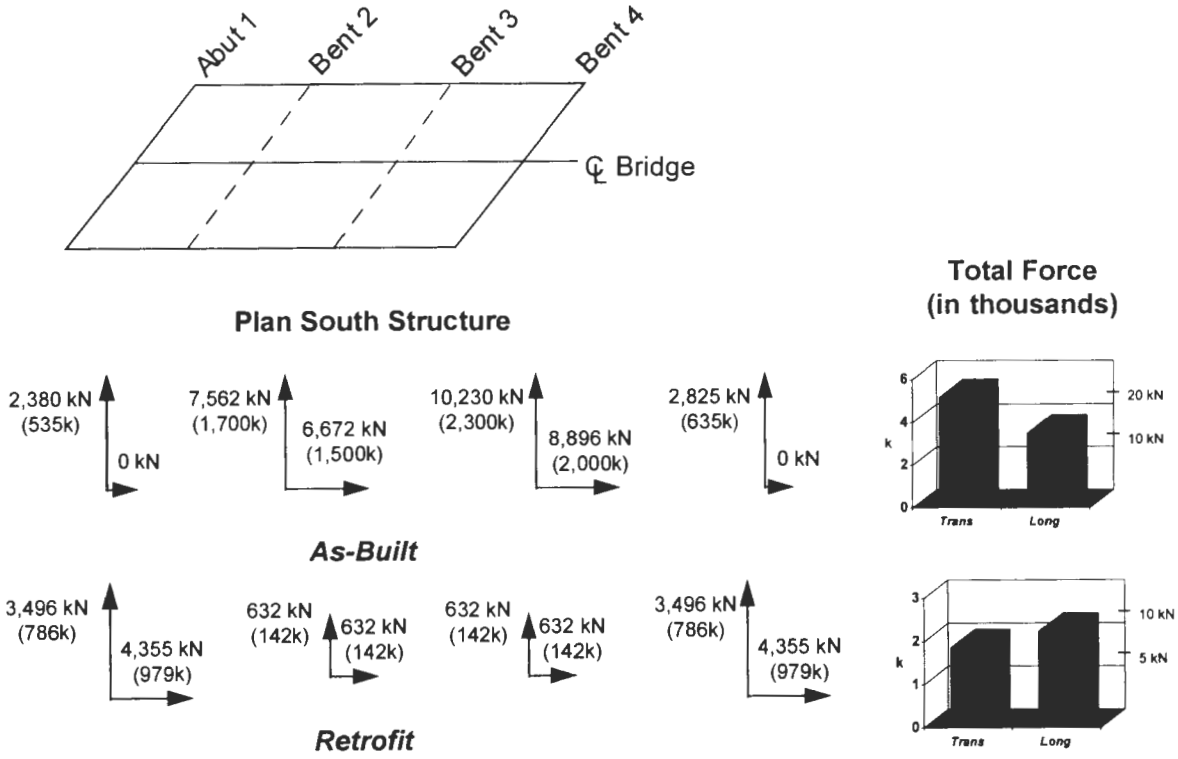

FIGURE 6 Redistribution of force.

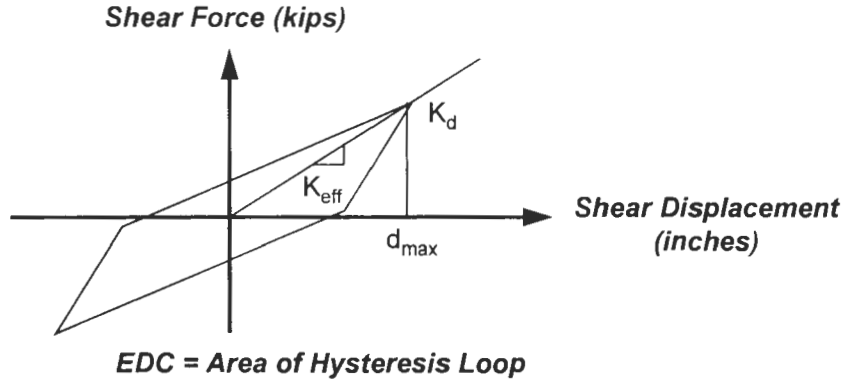

Location		d_{max}	K_{eff}	K_d	EDC
Abut or Bent	Bearing Location	mm (inches)	kN/mm (kip/inch)	kN/mm (kip/inch)	kN/mm (kip-inch)
Abut 1 and Bent 4	All	275 (10.83)	3.22 (18.4)	2.22 (12.7)	289 (2560)

Force - Deflection characteristics, per isolator

FIGURE 7 Hysteresis loop.

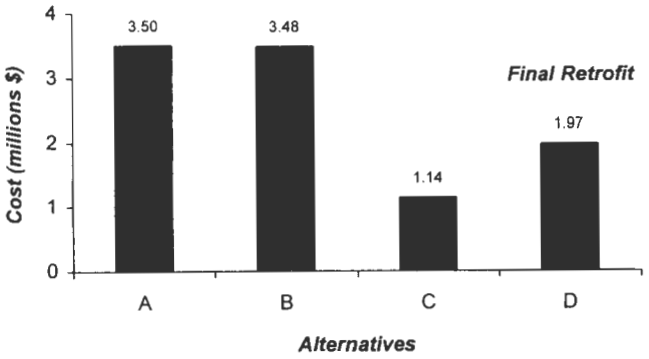

FIGURE 8 Cost of each alternative.

force delivered to the bents after installation of the new PTFE bearings.

- Install reinforced concrete shear or thrust blocks behind each lead-core isolation bearing at Abutment 1 and Bent 4 to prevent the superstructure from moving into the gallery area and crushing the short concrete slabs.
- Install a structural tube steel seat extension on the end diaphragms at both ends of the superstructure (Abutment 1 and Bent 4) to prevent the short concrete slab from dropping into the gallery.
- Reinforce Bent 4 (serving as a raised abutment) with a series of four buttress walls and pile-supported grade beam to prevent overturning of the bent and failure of the existing piles.

Conclusion

Before 1971 (San Fernando earthquake) bridge and building design codes required minimal attention to earthquake forces and seismic detailing. Demand forces were often only a small fraction of that required under current codes. Therefore, many structures of that era are potentially dangerous to the public and provide an economic liability to the owner. In most cases the cost of replacement is prohibitive, and thus, replacement is not a viable solution.

With any structure there may be many viable retrofit alternatives. It is the engineers' responsibility to fully understand the behavior of the structure, the impacts of the proposed retrofit, and the requirements of the owner. As a minimum all retrofits must prevent loss of life. Beyond this the owner's requirements must be fully understood, such as the level of structural damage an owner is willing to accept. On the basis of minimum life and costly safety criteria, this can vary from developing a retrofit that may leave the client with a condemned structure after an earthquake to developing one that results in little or no damage and no interruption to the use of the structure.

The case study presented here shows the benefit of investigating various solutions. For the south structure, Alternatives A and B met the required design criteria and may have been acceptable to the client. However, both would have been very costly to construct and the damage to the retrofitted structure during a large earthquake could still be very extensive. Alternative C, on the other hand, was the least expensive but was also the strategy that would most likely endanger the public and therefore was eliminated.

The selected alternative, Alternative D, not only provided a significant reduction in construction costs over those of resistive alternatives and would have a minimal impact on traffic, but also only minor damage, such as concrete spalling at thrust blocks, should result from an MCE.

In contrast, the north structure resulted in a very routine retrofit by using standard Caltrans (2) retrofit practice. For this more conventional (in California) portion of the structure, these standard retrofit procedures also resulted in the most economical solution

Acknowledgments

The authors express their gratitude to David Jones and Richard Knight of Dynamic Isolation System Inc.; Roland Anderson and Peter Johnson of Merriman; and Roberto Lacalle, senior bridge engineer and bearing specialist of Caltrans, for providing valuable design information and guidance.

References

1. *Bridge Design Specifications for Highway Bridges*, 13th ed. Department of Transportation, State of California, 1983.
2. *Division of Structures Seismic Design References.* Memos to Designers Manual, Interim 20-4. Department of Transportation, State of California, 1991.
3. *AASHTO Design Procedures for Seismically Isolated Bridges.* Dynamic Isolation System Inc., March 1992.
4. Design Guide for Lubrite Bearings, *Lubrite Bearing Catalog.* Merriman, June 1991.

BRIDGE BEARINGS, JOINTS, AND DETAILS

Field Measurements of Large Modular Expansion Joint

Charles W. Roeder, *University of Washington, Seattle*
Mark Hildahl, *David Goodyear Engineering Services*
John A. Van Lund, *Department of Transportation*

Modular expansion joints are sometimes used on bridges with large movement potential. Single-support-bar modular expansion joints with 1200 mm of movement capability were used at each end of the third Lake Washington Bridge between Seattle and Mercer Island on Interstate 90. Fatigue cracks were observed in these joints within the first few years of service, and an extensive research program was undertaken. An initial study used a range of analyses, which showed that the behavior of the joint was influenced by the dynamic wheel loading and the characteristics of the joint. Field measurements were performed to verify the analytical conclusions, and the results are summarized. The field measurements included measurements of strains, bending moments, and deflections for a series of controlled truck loadings on a large modular joint. Braking and acceleration of vehicles produce the largest horizontal wheel forces and joint movement. The horizontal forces produced by overrolling (nonbraking and nonaccelerating vehicles) are small. Impact and rebound due to vertical loading are significant. Measurements are compared with fatigue design recommendations and correlated with analytical results. Recommended vertical and horizontal fatigue design loads are given for large-movement single-support-bar expansion joints.

Modular expansion joints are used on bridges with large movements, and fatigue cracks have been noted on these systems. At present there is no specific AASHTO fatigue design procedure for modular joints; however, a relatively simple procedure has been proposed by Tschemmernegg and colleagues (*1–3*). The nominal stress range, $\Delta\sigma_{max}$, at critical locations in the joint components are computed for the fatigue design wheel loads, including impact. These fatigue design loads (gravity load of +91.0 kN, vertical rebound of −27.3 kN, and horizontal load of ±18.2 kN in either direction, all including impact) are based on field measurements on modular joints in Europe (*3*).

Recent research (*4–6*) has suggested that although the Tschemmernegg fatigue design method is easy to use and complete, it may not accurately represent the fatigue behavior of all modular joints because of their widely varying dynamic properties and stiffness characteristics. Single-support-bar modular expansion joints with 1200 mm of movement capability were used at each end of the third Lake Washington Bridge between Seattle and Mercer Island on Interstate 90 (*7*). Fatigue cracks were observed in these joints within the first few years of service. Figure 1 is a photograph of one of these cracks.

The joints (Figure 2 and 3) use a single transverse beam or support bar that supports all of the center-

FIGURE 1 Fatigue cracking.

beams at each point. The support bar is a stiff, strong steel section, which is pinned at one end of the bridge superstructure, whereas it slides on a low-friction sliding surface at the other end. Elastomeric bearings are used to help cushion components of the joint and assist in the accommodation of movement and the control of spacing and geometry of joint components. The centerbeams must have a moveable attachment with stirrups, elastomeric springs, and low-friction sliders between the centerbeam and support bar.

Experimental Program and Measurements

An experimental study was started to examine the behavior of modular joints and to correlate this measured behavior to the prior analytical study (*4*). The large modular expansion joint at the east end of the high-occupancy vehicle (HOV) reversible lanes of the I-90 third Lake Washington Floating Bridge were instrumented (*5*) during the summer of 1993. The general objectives of the measurements were to

1. Verify the results of the earlier (*4*) computer analysis.
2. Verify the dynamic characteristics of the modular joint system including impact and damping.
3. Determine the stresses and strains of critical joint components under the applied loads.

Two types of instrumentation were used on this joint. The first type of instrumentation included eight groups of four strain gauges that were connected as full Wheatstone bridges to measure bending. All eight bending measurements were placed at various positions under the outside southernmost lane of traffic (Figure 4). Six of these channels measured bending in the vertical load plane, but two measured bending in the horizontal load plane. Six of the bending gauge groups (four vertical and two horizontal) were located on centerbeam CB13, which was the second centerbeam from the east edge of the joint. The remaining two bending groups were at-

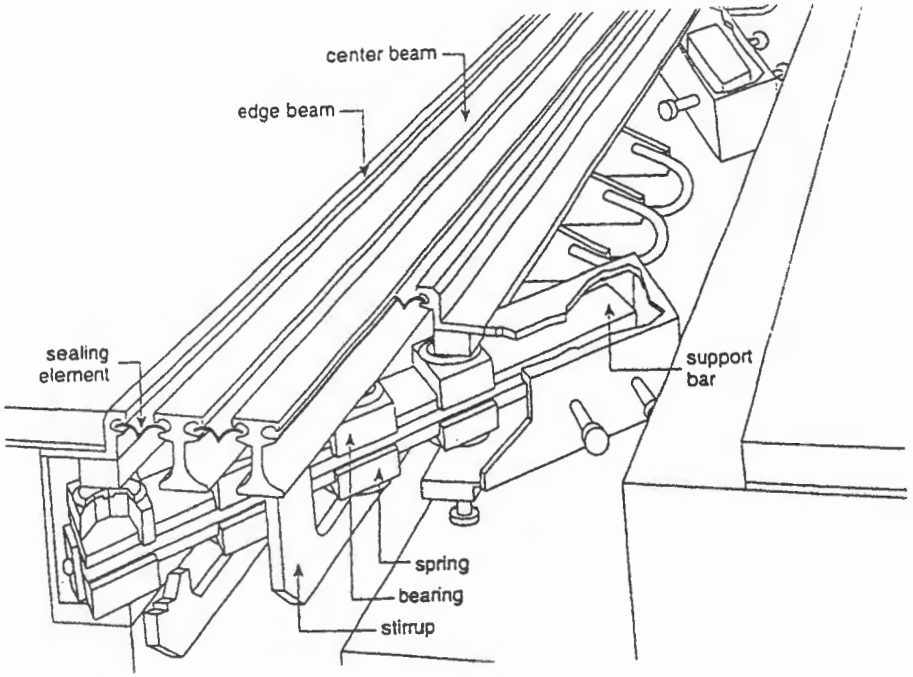

FIGURE 2 Single-support-bar system.

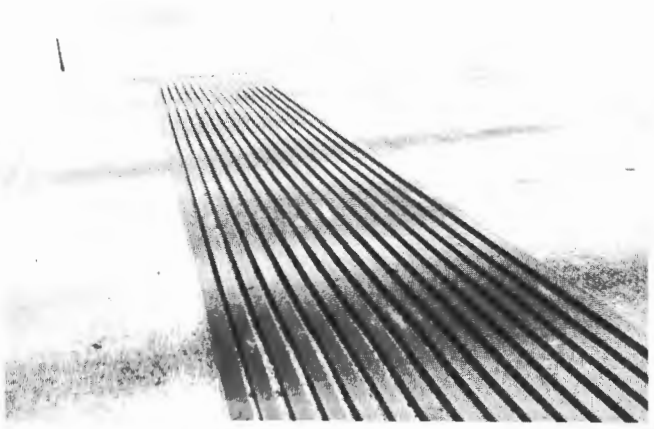

FIGURE 3 Road surface of modular expansion joint.

tached to adjacent centerbeams, centerbeams CB12 and CB14. Comparison of the bending moments measured in CB12, CB13, and CB14 gave a measure of the wheel load distribution between centerbeams as a function of time. The four vertical gauges on CB13 provided a redundancy of measurements so that the magnitude of the truck wheel load and the position of the truck could be estimated with the aid of influence lines for the measurement locations. The instrumentation also included two linear variable differential transformers that were used to measure the horizontal displacements of the centerbeams. The horizontal displacements were measured at the center of a long span and at the adjacent support bar of CB13. These horizontal displacement measurements approximately coincided with two of the more critical bending moment measurements.

All measurements were recorded as voltage differentials. For bending moments the voltage measurements were multiplied by a calibration factor to obtain curvature, and the curvature was multiplied by the stiffness to obtain the bending moment. Deflections were directly determined by multiplying the calibration factor by the voltage. The six bending channels of centerbeam CB13 were measured for nearly all of the controlled and uncontrolled field tests. The horizontal displacements and the bending channels on CB12 and CB14 were measured only for selective measurements during the controlled tests. HP5813A waveform recorders were used to record most of the data, and additional data were recorded with an HP3852A data acquisition system. The waveform recorders are capable of recording up to 4,000,000 samples per second of data per channel, but they are sampling at the rate of 2,000 samples per second for these tests since this was more than ample to measure the joint response. The recorders were coupled together, and they were self-triggering and continually sampled data. They only recorded data when a big enough measurement was noted, and then only a short burst (approximately 2 sec) of data was recorded. Data for a number of trucks were recorded in this manner until the internal memory was full. The data were then transferred to an HP9816 computer and stored in a compact binary format in an IEM 5300 disk drive. The data were transferred again by an HPUX 700-340 computer and were analyzed by the normal research computer facilities.

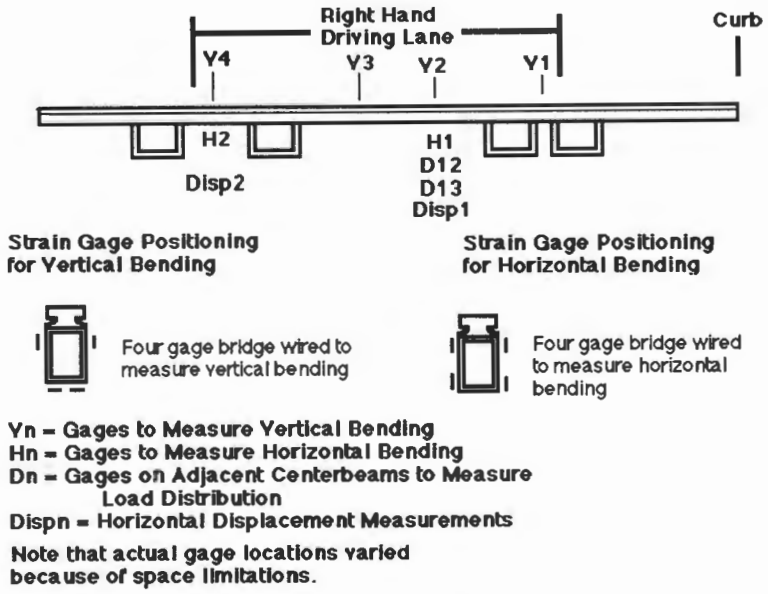

FIGURE 4 Instrumentation on expansion joint.

Test Program

Two series of controlled tests were performed (*5,6*). During August 17 to 19, 1993, the right lane of traffic was shut down for several hours each day, and loads were applied by a moderately heavy, three-axle dump truck. The dimensions and the static wheel loads of the truck were measured before testing. Figure 5 shows the static wheel loads and dimensions of the test truck. The truck passed over the joint at known speeds and locations 24 different times during the 2-day period. The position of the vehicle relative to the joint was measured by the tire track observed on strategically placed tape markers on the joint. The truck was at constant speed, braking, accelerating, or at rest. A second series of controlled tests was performed during February 1 and 2, 1994. This second series of controlled tests was performed when the bridge was closed to other traffic. This allowed many more options in the speed and placement of the vehicle on the joint. Forty-two load passes were made with the same truck and loading used in the earlier tests. Nearly all of the truck passes were made at various points within the outside (southernmost) lane. Most of the tests were performed with eastbound truck traffic, but a few passes were performed with a westbound truck. Two tests were performed with the truck passing in the center lane so that the effect of such a truck passing on the measured results could be determined. The results of these tests were used to establish basic elements of joint behavior such as the effect of truck position, truck braking or acceleration, and distribution of load between centerbeams.

Test Results

Figure 6 shows the typical measured bending moments due to the controlled test truck passing over the joint with nearly the same path very slowly and at 90 km/hr. The trucks were maintaining a constant speed with no vehicle braking or acceleration. The dynamic load experienced by the centerbeam is proportional to the maximum bending moment. Comparison of the two truck crossings shows that there is 30 to 45 percent amplification of the vertical loads (and moments) for the high-speed vehicle over that for the static loading. This measured amplification is typical of other values obtained at similar vehicle speeds. Figure 6 shows that a peak centerbeam bending moment is achieved as the wheel crosses directly over the centerbeam and a dynamic rebound occurs as the wheel leaves the centerbeam. Tschemmernegg (*1,2*) uses fatigue design loads that imply a dynamic rebound that is 30 percent of the maximum direct load on the joint. Rebound on the order of 30 to 50 percent of the direct-impact loading was noted with the truck traveling at 90 km/hr. There is no rebound, however, with the static loading, and this suggests that the rebound effect is smaller with slower-moving vehicles.

After the wheel leaves the centerbeam the centerbeam tends to vibrate in a mode of free vibration. Examination of the period of this vibration gives a measure of the period of the excited mode of vibration, and the free vibration response illustrated in Figure 6 suggests that the period of the centerbeam vibration is approximately 0.015 sec. Prior computer analyses (*4,5*) showed that many closely spaced modes of vibration contributed to the dynamic responses of these joints in both the horizontal and the vertical planes. The computed periods ranged from 0.05 to 0.005 sec, with 0.015 sec being an approximate average value. Thus, it appears that the measured period for vertical vibration of the centerbeam is consistent with that predicted in the theoretical calculations. Furthermore, it can be noted that the duration of loading on an individual centerbeam with the truck traveling at 90 km/hr is approximately 0.0125 sec. The ratio of this duration to the period of vibration is approximately 0.85, and the theoretical dynamic amplification predicted is approximately 50 percent. These combined observations suggest that there is a good correlation between earlier (*4–6*) theoretical predictions and experimental measurements. The decay of the free vibration after the rebound cycle can be used to estimate the damping in the joint, and damping on the order of 6 to 13 percent of critical was noted for trucks crossing the joint without significant acceleration or braking. A comparison of theoretical and measured dynamic characteristics is shown in Table 1.

Figure 7 shows the horizontal plane bending moments measured with the same trucks used to obtain the data given in Figure 6. The vehicle is crossing the joint at constant speed. However, it should be noted that the joint is on a slight 2 to 3 percent grade, and this grade requires some minimal acceleration to maintain constant driving speed. The bending moments again are theoretically proportional to the dynamic force felt by the centerbeam. Earlier dynamic analyses (*4,5*) suggested that this joint system would be very flexible in horizontal loading, and as a result it was postulated that the centerbeam could not experience a large horizontal load. On the other hand, the Tschemmernegg fatigue evaluation procedure (*1–3*) requires a horizontal design force that is approximately 30 percent of the basic vertical (static) design force, and the method also postulates that the elastic support points be modeled as rigid connection for the horizontal loading. Comparison of the moments in Figure 7 with those shown in Figure 6 suggest that the dynamic force acting in the horizontal direction is approximately 10 percent of the vertical load.

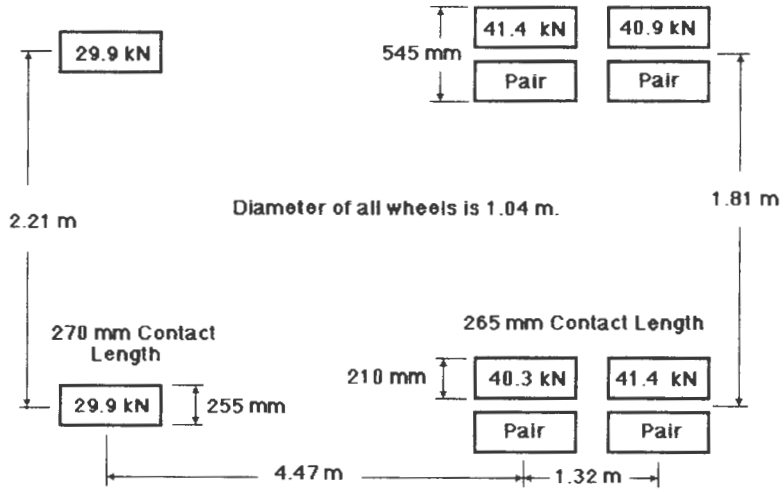

FIGURE 5 Wheel loads and geometry of test truck.

Figure 8 shows a typical comparison with the data in Figure 7 with the truck traveling at a slower speed (approximately 50 km/hr). The dynamic amplification is in the range of 25 to 35 percent of the static load for this reduced speed. The duration of loading is longer at this reduced speed, and the ratio of the duration to the period of vibration for the centerbeam is also proportionally larger (1.55 as opposed to 0.85). The dynamic rebound is on the order of 40 to 50 percent of the vertical load at 90 km/hr, approximately half this amount at 50 km/hr, and zero when the vehicle is at rest.

Figure 9 shows the horizontal bending moments for the truck crossing for which data are given in Figure 8. Comparison of Figures 7 and 9 shows that the horizontal force of the vehicle traveling at 50 km/hr is somewhat larger than that noted for the vehicle traveling at 90 km/hr. However, in both cases the bending moment and horizontal force are much smaller than the vertical load. The majority of the participating masses in the horizontal modes of vibration were resident in modes with periods in the range of between 0.16 and 0.035 sec. Therefore, the ratio of the duration of load to the period varies between a high of approximately 0.6 when the vehicle is traveling at 50 km/hr and a possible low of 0.3 to 0.0 when the vehicle is traveling at 90 km/hr.

The horizontal loads are much smaller than suggested by the Tschemmernegg fatigue design procedure

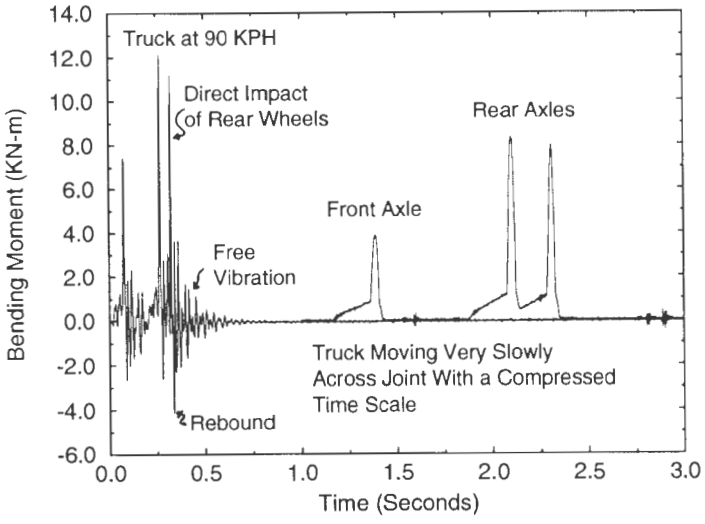

FIGURE 6 Measured bending moment in centerbeam due to vertical wheel loads at 90 km/hr and static conditions.

TABLE 1 Typical and Measured Dynamic Characteristics

Dynamic Characteristics	Estimated From Field Measurements	Estimated from Past Theoretical Calculations	Tschemmernegg Estimates from Field Measurements
Periods for Vertical Modes of Vibration	0.0125 to 0.015 seconds for Normal Vibration	0.005 to 0.05 secs. with Averages Approx. 0.015 seconds	Approx. 0.015 secs.
Periods for Horizontal Modes of Vibration	0.03 to 0.05 seconds for Normal Vibration and 0.12 seconds for severe braking	0.015 to 0.15 secs with Average Approx. 0.03 to 0.05 seconds and 0.15 secs associated with global movements	Approx 0.048 secs.
Damping	6 to 13% of Critical Under Normal Vibration	No Estimate	Approx. 7.1 %

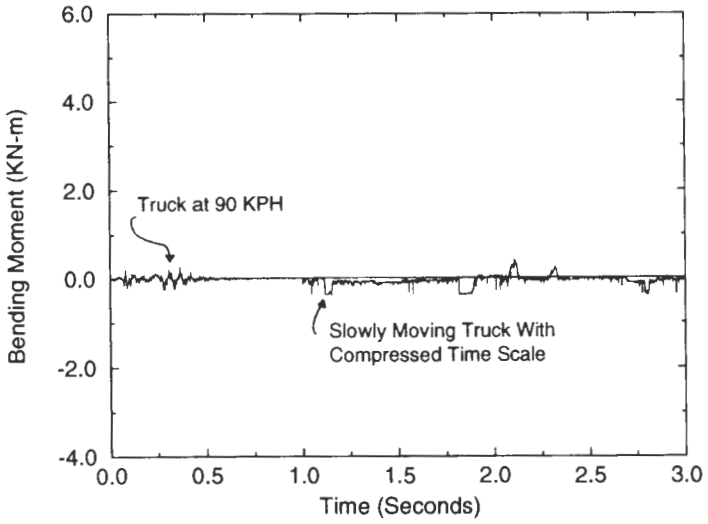

FIGURE 7 Measured bending moment in centerbeam due to horizontal wheel loads at 90 km/hr and static conditions.

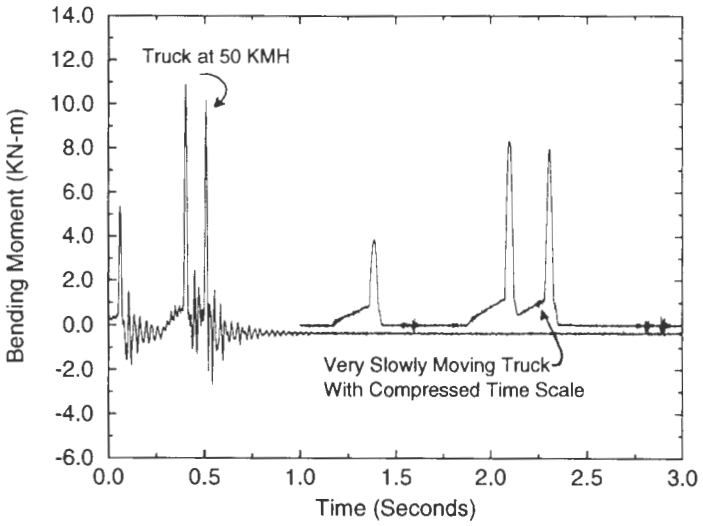

FIGURE 8 Measured bending moment in centerbeam due to vertical wheel loads at 50 km/hr and static conditions.

under normal driving conditions. If the vehicle is braking or accelerating as it crosses the modular joint, the horizontal forces are much larger. Figure 10 shows the moments due to horizontal loading with emergency braking for a vehicle originally traveling at 90 km/hr. Comparison of Figures 7, 9, and 10 shows that vehicle braking causes much larger horizontal dynamic loads. These dynamic loads due to braking may be even larger than those suggested by Tschemmernegg (*1–3*).

Horizontal movements were also measured for some cases. No horizontal movement of the centerbeam was noted if the truck was not braking or accelerating to gain speed over the joint. However, Figure 11 shows typical centerbeam movement if the truck is braking to an emergency stop. It can be seen that a substantial horizontal deflection occurs under this severe braking condition. The maximum movement is approximately 10 mm, and there is a permanent set of approximately 3 mm. The largest centerbeam movements appeared to occur at slower speeds because of the dynamic characteristics of the joint. This is consistent with the observations made in an analysis that greater dynamic amplification of horizontal loads occurred at slower speeds because the duration of loading more closely matches

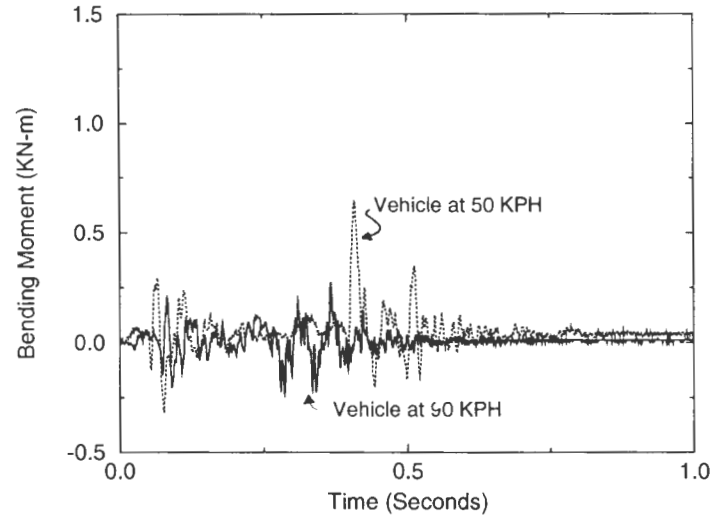

FIGURE 9 Measured bending moment in centerbeam due to horizontal wheel loads at 50 and 90 km/hr.

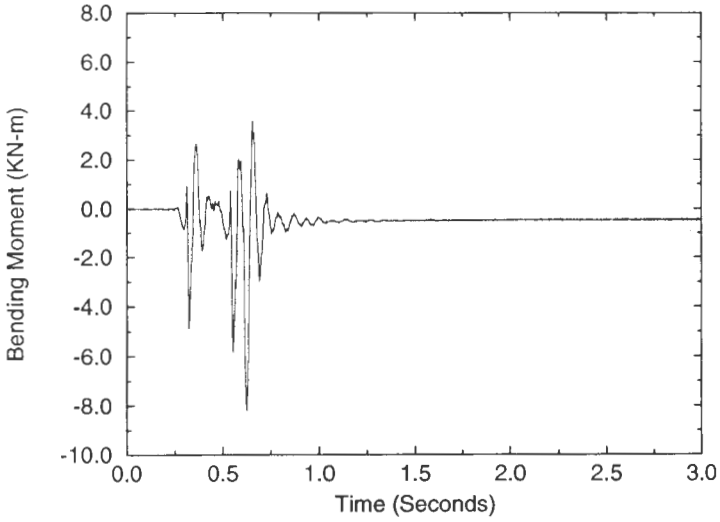

FIGURE 10 Measured bending moment in centerbeam due to horizontal wheel loads at 90 km/hr with emergency braking.

the longer periods noted for horizontal displacement. The major portion of the deflection is causing deformation and sliding of the elastomeric springs. That is, the centerbeam moves approximately as a rigid body. Some of the horizontal displacement is recovered after the load is removed, but that due to sliding results in permanent set and is not immediately recovered. The permanent set is recovered after time because of vibrations of the joint due to lighter traffic and the geometry of the joint system. These measurements indicate that horizontal loads on this particular joint system are significant only when the vehicle is braking or accelerating. This is consistent with some observations (*8*) of past joint fatigue behavior.

Design Implications

The results of the controlled tests performed in August and February were compared, and the results were similar except that it was noted that a given truck crossing on a specific path caused a larger centerbeam bending

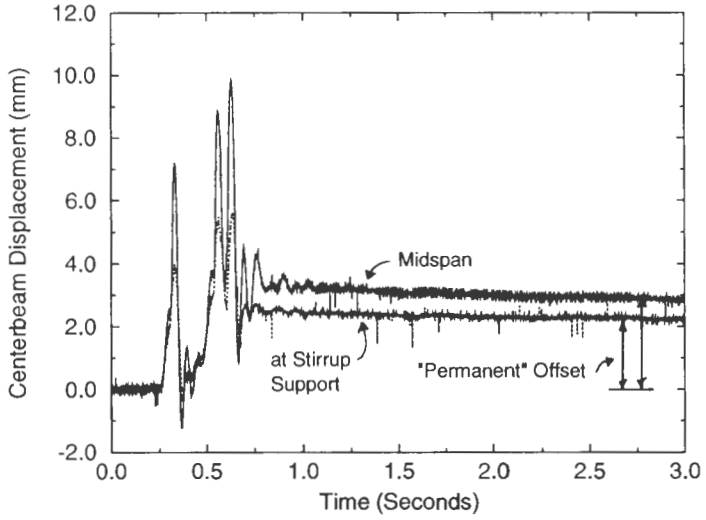

FIGURE 11 Measured horizontal displacement of centerbeam due to horizontal wheel loads at 90 km/hr with emergency braking.

moment in the tests in February than in the tests in August. The difference was small and clearly indicated that the data recorded during the two different time periods were comparable and permitted an evaluation of the load distribution between centerbeams. The joint geometry was measured, and the application of Tschemmernegg's graphical wheel distribution model suggested that less than 50 percent of the total wheel load should be applied to a single centerbeam in August and that 50 percent would be appropriate in February. Bending moments obtained for adjacent centerbeams, centerbeams CB12, CB13, and CB14, were compared to examine the load distributions between centerbeams. These measurements indicated that a larger portion of the vertical load was carried by an individual centerbeam than suggested by the Tschemmernegg method. For this joint system it appears that the load distribution to the most heavily loaded centerbeam should be increased by 10 percent over that recommended by the Tschemmernegg method.

An examination of the fatigue design load spectrum was another important goal of this research. The uncontrolled truck measurements provide insight into these load data when they were combined with the controlled test results. The dynamic responses of nearly 20,000 truck wheel crossings were measured during these uncontrolled tests, and summary data on the peak response for each wheel, the maximum rebound, and free vibration cycles were developed. However, the responses of only the very heaviest trucks were measured. That is, trucks with vertical dynamic wheel loads of less than approximately 30 kN were neglected. The Tschemmernegg load spectrum and statistical distribution (*3*) suggest that this limit includes only the heaviest 16 percent of the truck wheels.

The speed of the truck crossing the joint, the position of the truck on the joint, the geometry of the truck wheels, the distribution of loads between centerbeams, and the actual static wheel loads of the truck all affect the uncontrolled measurements. None of these variables are known with certainty for any one truck measurement. However, substantial information can be theoretically inferred (*6*) on the basis of comparison of the measured data with theoretical influence lines for each measurement location. Therefore, the data were analyzed to examine the effects of these different parameters. Measurement of typical truck axles indicate that a spacing of approximately 1.8 m is appropriate for most dual-wheel rear axles, and this was used in the design load evaluation since the largest wheel loads produce the greatest fatigue damage. Front wheels have larger and more variable wheel spacings, but the wheel loads are usually lighter.

Given the wheel spacing, the position of the truck crossing the joint and the magnitude of the dynamic load can be theoretically predicted from the influence lines generated for each measurement location. The controlled truck measurements were used to evaluate the location and load estimation procedure. There were enough measurements to provide redundancy and checks of the data evaluation. It was determined that some channels of data produced inherently more useful data than others. Furthermore, it was determined that there was relatively little sensitivity to position if the truck was near the middle of the travel lane. There was great sensitivity if it was changing lanes or was close to the curb. Finally, it was determined that vehicles that are outside the middle portion of the travel lane were identifiable, because of the ratios and relative magnitudes of critical measurements.

As a result data for crossings by trucks that were changing lanes or driving out of the right-hand lane were identified and removed from the statistical sample. The dynamic wheel loads were then estimated for direct-impact loading, vertical rebound, and horizontal loading with the vehicle in the middle portion of the lane. The most reliable channels of measured data were used to estimate the dynamic wheel load, and the average of these most reliable estimates was used. The dynamic wheel loads considered the distribution of load between centerbeams and the distribution of the wheel loads on the centerbeam. Figures 12 and 13 show the measured load spectra for vertical and horizontal wheel loads, respectively, from statistical analysis of the uncontrolled truck measurements compared with the Tschemmernegg design spectrum. Again, it should be emphasized that responses for only the heaviest 16 percent of truck traffic were measured in these tests. It can be seen that a substantial number of trucks exceeded the maximum vertical load in the Tschemmernegg design spectrum, but the maximum horizontal wheel loads achieved in this study were very similar to those reported by Tschemmernegg. There were a larger number of large vertical dynamic loads and fewer large horizontal dynamic loads than recommended by Tschemmernegg. These larger vertical loads cause the largest amount of fatigue damage. Thus, the Tschemmernegg load spectrum was viewed as unconservative for vertical loads and overly conservative for horizontal loads on this joint. It should be emphasized that these recommendations are joint specific. Different recommendations must be expected for other joint systems because of the variations in the dynamic characteristics of the joints. Therefore, it is recommended that the vertical dynamic wheel load for this joint system be increased to 110 kN. The vertical rebound load should be increased to 45 kN. When these increased vertical loads are used, it is appropriate to recognize the smaller horizontal loads present in the joint. Therefore, a horizontal load of 10 kN is suggested for this joint system and traffic pattern.

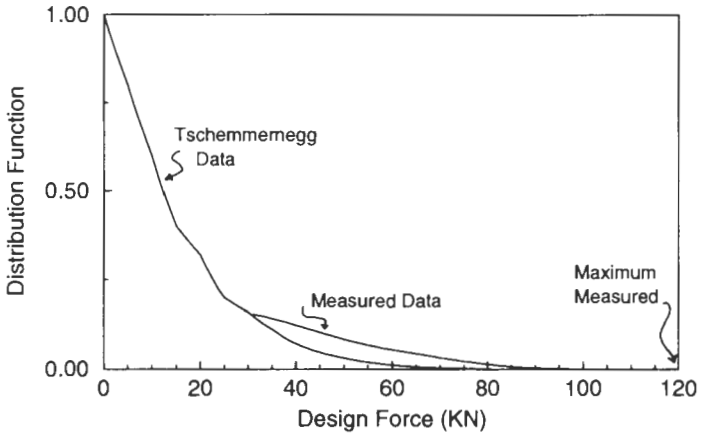

FIGURE 12 Cumulative distribution functions for vertical dynamic wheel loading.

These fatigue design load and load distribution recommendations are summarized in Table 2.

Summary and Conclusions

This paper has described a series of field measurements performed on a single-support-bar modular joint system under dynamic truck loading. The measurements were performed in response to fatigue cracks noted on the joint and a series of calculations completed after the first cracks were noted. The experimental methods and the results are summarized in this paper.

A few general conclusions can be noted:

1. The experimental observations appear to be consistent with earlier theoretical calculations (*4,5*). The dynamic periods measured in the experiments are consistent with the theoretical predictions.

2. The vertical loading due to the direct impact of the truck is amplified through a wide range of vehicle speeds, with dynamic amplification on the order of 50 percent expected at normal interstate vehicle driving speeds of 90 km/hr.

3. The vertical rebound load is larger with higher-speed vehicles and smaller with slower traffic.

4. The horizontal loads under ordinary traffic on this particular joint system are much smaller than those suggested by the Tschemmernegg fatigue design method. This occurs because of the horizontal flexibility and potential for slip noted with this type of modular joint. This supports the prior theoretical calculations that indicated that joint behavior is very dependent on the joint type. Horizontal forces are likely to be much more significant with some very stiff modular joint systems.

5. Bending moments due to horizontal loads under vehicle braking may be very large. These moments may

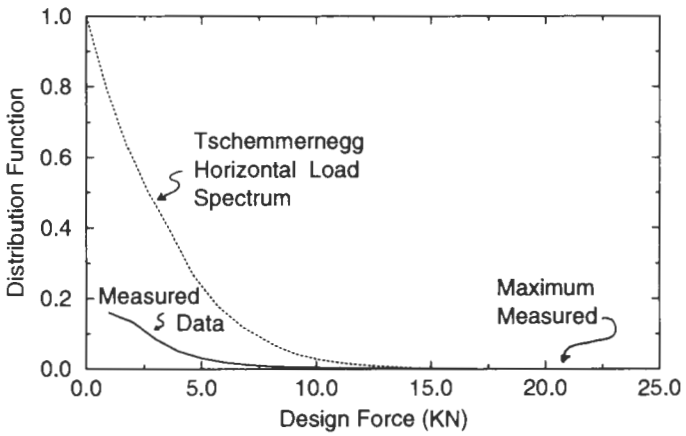

FIGURE 13 Cumulative distribution functions for horizontal dynamic wheel loading.

TABLE 2 Fatigue Design Load Recommendations

	Recommendations From This Research	Tschemmernegg Recommendations
Direct Vertical Dynamic Load	110 KN	91 KN
Rebound Vertical Dynamic Load	45 KN	27.3 KN
Positive Horizontal Dynamic Load	+10 KN	+18.2 KN
Negative Horizontal Dynamic Load	-10 KN	-18.2 KN
Load Distribution to Centerbeams	0.1 + Graphical Procedure	Graphical Procedure Provided

exceed those suggested by the Tschemmernegg fatigue design method. For this joint system horizontal movements occur in the joint when the braking vehicles cross the joint. The movements involve multiple spans of centerbeams accompanied by shear deformation of the elastomeric springs and sliding of the low-friction surfaces. The large moments are caused by the increased effective centerbeam span induced by support movement as well as by increased load.

6. Load distribution between centerbeams is also evaluated, and these measurements suggest that the load distribution between individual centerbeams produces a somewhat larger force on individual centerbeams than suggested by the Tschemmernegg fatigue evaluation method. Fatigue design loads are recommended for direct-impact, rebound, and horizontal loadings for this type of single-support-bar modular joint.

ACKNOWLEDGMENTS

This research was funded by the Washington State Transportation Center and the Washington State Department of Transportation. The assistance of John Van Lund, Myint M. Lwin, and Alan H. Walley is gratefully acknowledged.

REFERENCES

1. Pattis, A., and F. Tschemmernegg. *Fatigue Testing and Design of Modular Expansion Joints*. University of Innsbruck and The D. S. Brown Co., Innsbruck, Austria, March 1992.
2. Fatigue Design and Testing for Expansion Joints. *Technology Bulletin for Bridge Bearings, Expansion Joints and Components*, No. 1. The D. S. Brown Co., North Baltimore, Ohio, Oct. 1991, 2 pp.
3. Tschemmernegg, F. The Design of Modular Expansion Joints. *Joints and Sealants*. Vol. 1, preprint. *Proc., Third World Congress on Joint Sealing and Bearing Systems for Concrete Structures*, Toronto, American Concrete Institute, Detroit, Mich., Oct. 1991, pp. 67–86.
4. Roeder, C. W., M. Hildahl, and J. A. Van Lund. Fatigue Cracking in Modular Expansion Joints. In *Transportation Research Record 1460*, TRB, National Research Council, Washington, D.C., 1994.
5. Hildahl, M. *Fatigue Cracking of Modular Expansion Joints*. M.S. thesis. University of Washington, Seattle, 1993.
6. Roeder, C. W. *Field Measurements of Dynamic Wheel Loads on Modular Expansion Joints*. Report WA-RD 369.1. Washington State Transportation Center, Jan. 1995.
7. Brown, S., and U. Haerle. Design of a Sealed Expansion Joint for the 3rd Lake Washington Bridge. *Joint Sealing and Bearing Systems for Concrete Structures*, vol. 2, SP-94. American Concrete Institute, Detroit, Mich., 1986, pp. 967–974.
8. Mayrbaurl, R. M. Analysis of the Manhattan Bridge Modular Expansion Joints. Presented at 73rd Annual Meeting of the Transportation Research Board, Washington, D.C., Jan. 1994.

The opinions and conclusions expressed or implied in this paper are those of the authors and are not necessarily those of the funding agency.

Bridge Bearing Replacement

John A. Van Lund, *Washington State Department of Transportation*

The Washington State Department of Transportation (WSDOT) has removed and replaced nonfunctioning bridge bearings to extend the service lives of existing bridges. Inoperable roller nests and seismically vulnerable steel rocker bearings with excessive tipping have been removed and replaced to restore expansion capability. The superstructure must be raised to replace bridge bearings. Case studies that show three recent bridge bearing replacement projects designed by WSDOT are presented. In the first case study, a 113.0-m single-span truss built in 1925 was raised from below by placing two hydraulic jacks and the upper steel distribution plates directly under the bearing pin gusset plates. The unreinforced pier cap was posttensioned to prevent spalling. A sliding disc bearing was installed in place of the frozen roller nest. In the second case study, the bearings were removed and were replaced as part of an overall structural rehabilitation project. The existing concrete deck was removed and the ends of seven 54.9-m single-span trusses were lifted sequentially from above with a pair of jacking beams consisting of two W36 × 245 steel beams. Hanger rods were attached directly to the jacking beams and the floor beam top flange. Four 50-metric-ton jacks (two per jacking beam) simultaneously raised the ends of the trusses. Sliding fabric pad bearings were used to replace the frozen expansion roller nests. In the final case study, seismically vulnerable tipping rocker bearings were replaced with elastomeric bearings. Jacking diaphragms were located in the exterior bays at the girder centerline of bearings so that the lifting loads would not cause tipping of the pier. Additional shelf width was provided by adding a continuous corbel to the pier cap. Superstructure lifting recommendations are given. Jacks are sized for at least 1.5 times the calculated lifting loads. Bearing design loads, replacement bearing costs, and costs for lifting bridge superstructures are presented.

The Washington State Department of Transportation (WSDOT) has removed and replaced nonfunctioning bridge bearings on older steel truss bridges. After 60 to 70 years of service, the steel roller nests, which were used to provide for expansion and contraction, are inoperable because of excessive tipping and extensive corrosion. In addition, tipping rocker bearings are seismically vulnerable and are replaced with more stable bearings. As shown in the second case study, removal and replacement of nonfunctioning bearings can be included as part of bridge rehabilitation or seismic retrofit projects. Replacement bearings include multirotational disc bearings, fabric pads with polytetrafluoroethylene (TFE) and stainless steel sliding surfaces, elastomeric bearings, and lead-core isolation bearings. It is WSDOT's policy to remove and replace defective or seismically vulnerable bearings to extend the service lives of existing bridges.

To replace bridge bearings, the superstructure must be raised. Hydraulic jacks have been used to raise existing bridge superstructures so that defective pot bearings could be removed and replaced (*1*). In Washington State jacks were used to raise one bridge superstructure by as much as 6.3 m so that avalanches could pass below the bridge without hitting the girders. On another

project jacking was used as a means of transferring the dead load of the superstructure from one existing substructure to another. Jacks with a capacity of 1.5 to 2 times the calculated lifting loads are used (2). Generally, jacking under a live load is not recommended. However, traffic is permitted on the bridge after the girders have been safely blocked. Blocking and member connections must be designed for the total dead and live loads. On one recent WSDOT project, jacking was done under a live load. Initially, jacking was done at night, and later the operation was expanded to permit jacking under traffic during daylight hours.

WSDOT shares responsibility with the contractor for the success of the lifting operation by designing the most practical lifting procedure based on past experience. As the owner, WSDOT is concerned that no damage to the bridge should occur during a lifting operation. In most cases the WSDOT-designed lifting procedure is used, but the contractor may propose an alternate procedure. In either case the contractor submits working plans and independent calculations, which are stamped by a registered professional engineer.

The following case studies show three recent bridge bearing replacement projects designed by WSDOT.

Case Study 1: Puyallup River Bridge, Bridge No. 167/20E, Pierce County, Washington

The Puyallup River Bridge, originally the Meridian Street Bridge, was built in 1925. The bridge consists of a 113.0-m single-span steel truss that spans the river and two 5.8-m timber approach spans at each end of the main span (Figure 1). The two trusses are narrowly spaced at 7.3 m and are 19.0 m high at the midspan.

In 1991 the bridge was closed to traffic and was rehabilitated. Part of the rehabilitation effort involved removing and replacing the frozen roller nests at the expansion end of the truss span. The trusses were raised by jacking from the top of the existing pier cap. Before raising the bridge, the unreinforced pier cap was post-tensioned with two 35-mm-diameter high-strength bars to prevent spalling of the pier cap concrete. The post-tensioning bars were located directly under the truss gusset plates and jacks (Figure 2).

The end of each truss was raised individually to prevent possible lateral movements that might have occurred if both trusses were raised simultaneously. Analysis showed that there was no overstress in the end portal and connections when the trusses were lifted independently. The differential vertical deflection between the jacked and the unjacked bearing was not to exceed 25 mm, and no jacking was permitted when the wind speed exceeded 40 km/hr. Two 180-metric-ton locknut jacks were placed as close as possible to the bearing pin. Locknut jacks were used because no suitable blocking points were available. The jacking cylinders were centered directly under the gusset plates. A steel distribution plate and an epoxy leveling course were used to provide a level jacking surface, because the bottoms of the gusset plates were uneven (Figure 3). The purpose of the epoxy leveling course was to distribute the lifting load uniformly to the gusset plates and to prevent overstressing of individual gusset plates during the lifting operation. The epoxy leveling course was a two-component epoxy consisting of a resin and a catalyst similar to that used in the wire rope industry for resin socketing. The resin-catalyst was pourable and hardened within 15 min with a fully cured compressive strength of 131 MPa. The lifting load, based on hydraulic pressure gauge readings, was approximately 150 percent greater than the calculated dead load, which may be attributed to heavy rusting of the roller nests, internal friction forces in the jacks caused by binding,

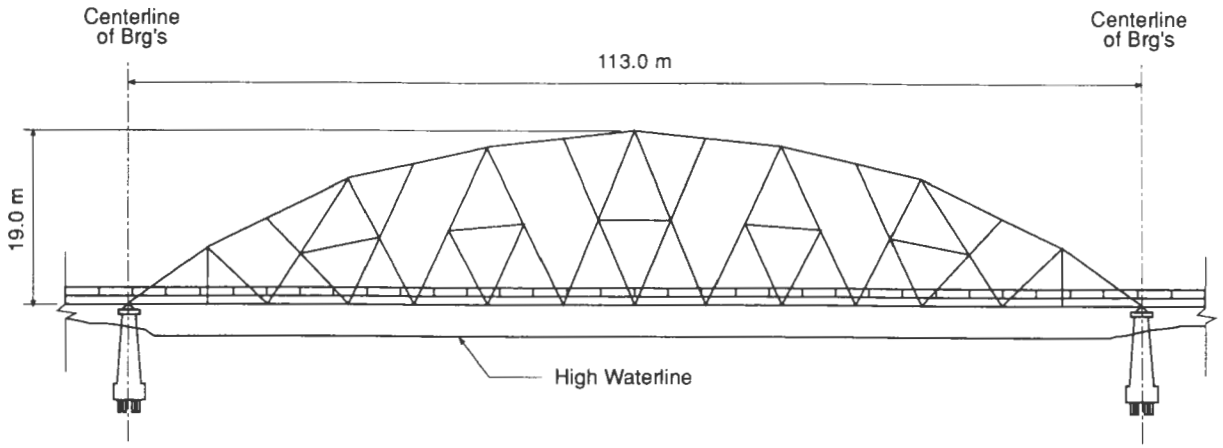

FIGURE 1 Case Study 1: elevation, Puyallup River Bridge.

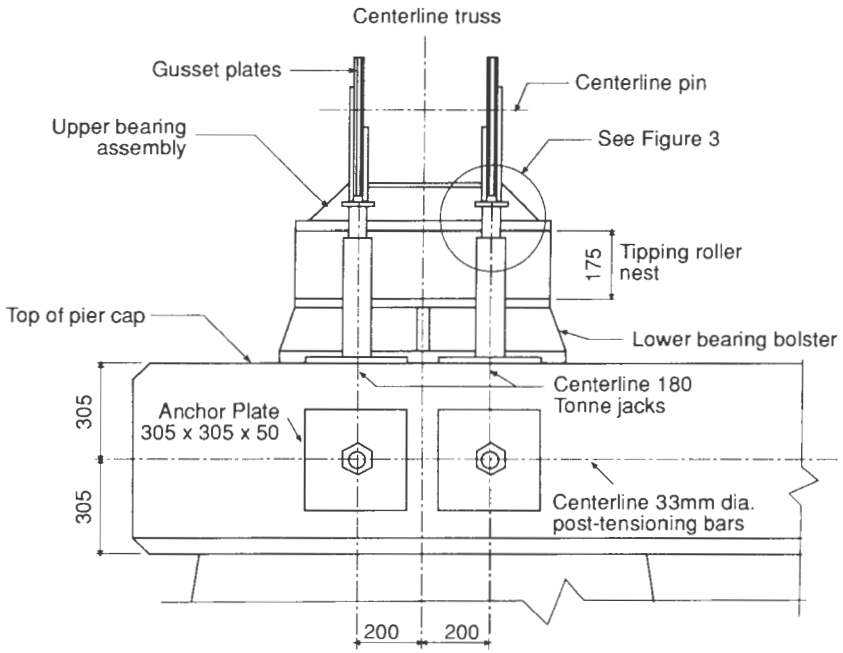

FIGURE 2 Case Study 1: pier cap post-tensioning and jack location, Puyallup River Bridge.

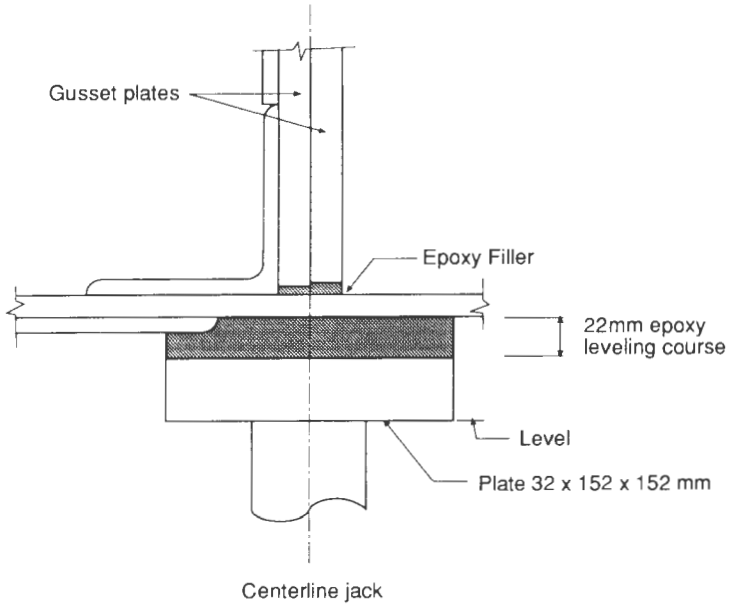

FIGURE 3 Case Study 1: epoxy leveling course.

or faulty gauges. During the lifting operation, the pier was monitored for potential tipping because the jacks were positioned 560 mm from the pier centerline. No tipping from the eccentric lifting loads was observed. However, just as the truss started to rise, the epoxy leveling course cracked but supported the truss without failing. The roller nests were removed, the new sliding disc bearings were installed.

If epoxy is used as a leveling course for uneven gusset plates, it should be confined along each side to prevent failure. Steel confinement bars can be welded to the upper load distribution plate. The depth of confinement should be equal to one-half the height of the leveling course to prevent spalling. It is also important to have temporary blocking available to be installed in the space formerly occupied by the bearing in case the epoxy leveling course fails. Steel shims, which require careful machining, could also be used in lieu of epoxies to obtain a level bearing surface for uneven gusset plates.

Case Study 2: Snohomish River Bridge, Bridge No. 529/10E, Snohomish County, Washington

The Snohomish River Bridge was built in 1926 and consists of a 44.5-m steel lift span, eight single-span steel trusses (seven with spans of 54.9 m and one with a span of 42.9 m), and numerous reinforced concrete approach spans. The overall length of the bridge is 816.8 m. In 1994 the bridge was closed to traffic and rehabilitated at a cost of $6.0 million. The concrete deck, steel stringers and floor beams, and truss panel point gusset plates were removed and replaced.

The expansion ends of the trusses were raised sequentially with a pair of steel jacking beams so that the frozen expansion bearing roller nests could be removed and replaced (Figure 4). The jacking beams consisted of two W36 × 245 steel beams placed side by side and had a mechanical advantage of 2 to 1. Each jacking beam weighed 11.5 metric tons and could be placed anywhere on the bridge by an overhead crane, which was supported by rails attached to the upper chords of the trusses.

Four 25.4-mm-diameter high-strength hanger rods connected the jacking beam and the floor beam (Figure 5). Four 50-metric-ton jacks (two per jacking beam) simultaneously raised the ends of the jacking beams 50 mm. Adequate space was provided between the jacks to install blocking so that the jack's cylinders could be lowered. The roller nests were removed, and new fabric pad bearings with TFE and stainless steel sliding surfaces were installed. The maximum lifting load was 91.0 metric tons, and the maximum jacking beam deflection was approximately 8 to 10 mm.

Raising trusses from above is a practical lifting technique during rehabilitation projects after the existing deck slab has been removed. In this case study, the weight of the deck slab accounted for 70 percent of the truss dead load. Smaller jacking beams and jacks were used because of this reduction in dead load. Raising these trusses from above with the deck slab in place was not feasible because the end floor beams and floor beam-to-truss connections would be overstressed and would require extensive reinforcement.

Case Study 3: Kalama River Bridge, Bridge No. 5/113, Cowlitz County, Washington

The Kalama River Bridge, which was built in 1970, is a two-span steel plate girder bridge that spans over Interstate 5. There are four plate girders with simple spans of 44.5 m, and fixity is provided at the end abutments. Two sets of rocker bearings permit expansion at the intermediate pier. Shortly after construction it was observed that the rocker bearings at the intermediate pier had tipped toward the west. The tipping occurred because of 0.3 to 0.6 m of settlement of the west approach fill, which continued after construction because of underlying organic soil. In early 1972 the bridge was jacked, the base plates were slotted, and the rocker bearings were plumbed. The tipping continued and was monitored for the next two decades until the settlement stabilized.

In 1995 the tipping rocker bearings were replaced with reinforced elastomeric bearings. Plate girder diaphragms, which had been installed to raise the bridge in 1972 and which had been left in place as permanent bracing, were again used to raise the ends of the girders (Figure 6). The jacking diaphragms were located in the exterior bays at the girder centerline of bearings so that the lifting loads would not cause tipping of the pier. Additional shelf width was provided by post-tensioning a new 305-mm-thick continuous corbel to the pier cap. The bridge was raised 25 mm by four 90-metric-ton jacks located adjacent to each girder. The existing rocker bearing was removed, and the upper bearing block, which was welded to the bottom flange of the plate girder, was cut free by arc gouging and was ground smooth to remove any excess weld metal. A concrete pedestal, which was integral with the continuous corbel, was constructed because the height of the new elastomeric bearing is 230 mm less than that of the original rocker bearing. The plan dimensions of the new elastomeric bearing are 305 by 650 mm, and the height is 78 mm. Six 14-gauge steel shims reinforce the 12.7-mm-thick internal elastomer layers. The external elastomer thickness is 6.4 mm.

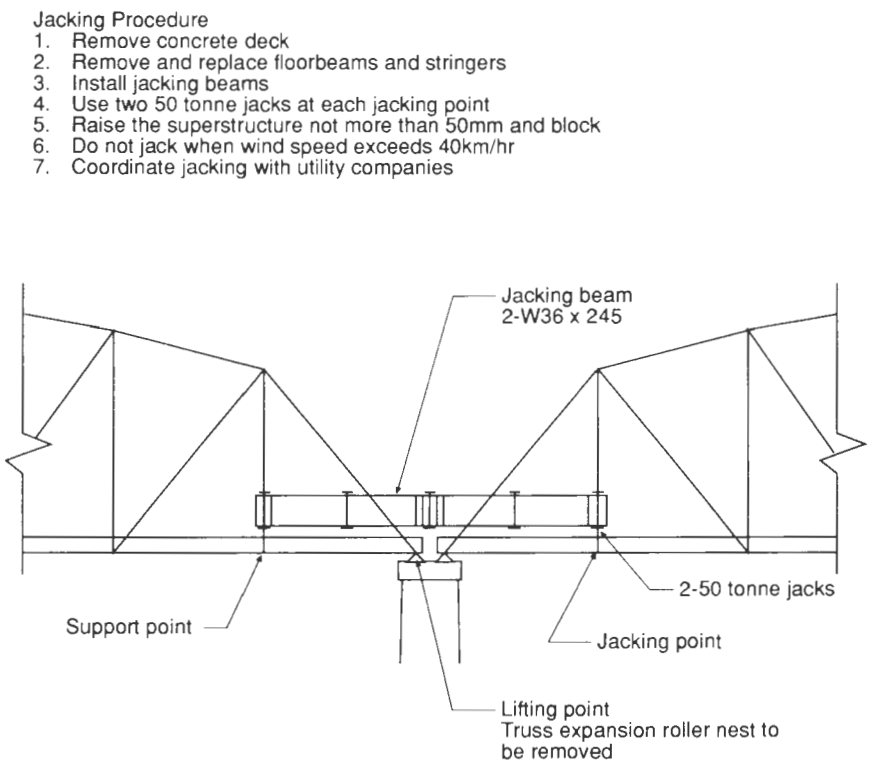

FIGURE 4 Case Study 2: elevation of jacking scheme, Snohomish River Bridge.

Superstructure Lifting Recommendations

Lifting recommendations based on WSDOT's experience (*2,3*) and on guidelines from Orr (*4*) are as follows:

1. Show details in the plans for the most practical lifting procedure, and permit the contractor to propose an alternate procedure. Show the lifting points and indicate the lifting loads in the contract plans. The effects of wind loading, construction loading, and live loading, if any, should be included in the calculated lifting loads.

2. Size jacks for at least 1.5 times the calculated lifting load and require backup jacks. If a jack fails, it can readily be replaced if backup jacks are available. The manufacturer's nameplate and the rated capacity of the jack should be attached to each jack. The schematic hydraulic layout, including gauges, valves, manifolds, and other equipment, should be shown in the contractor's working drawings.

3. Control relative vertical displacements so as not to overstress the existing structural members and connections during lifting. Indicate the maximum vertical displacement and the relative vertical displacements permitted between adjacent lifting points and between adjacent girders.

4. Determine maximum permissible deflections. Prevent excessive longitudinal and lateral movement by providing positive restraining systems and by adding temporary cross bracing to prevent member distortion. This may be particularly important for bridges on steep grades, in wind-prone areas, or with high superelevations. Targets and tilt meters can be placed on the structure to monitor any movement.

5. Block and shim during the lifting operation. WSDOT uses locknut jacks whenever space is not available to block the structure. Generally, the structure is shimmed tight or the locknuts are secured after incremental lifts of 3 mm. In the event of a jack failure, there will be no significant differential settlement and a backup jack can be quickly installed.

6. For safety reasons do not permit traffic on the bridge or the presence of any unnecessary construction personnel near the bridge during lifting. Occasionally, WSDOT has permitted jacking under traffic. Extreme care, advance planning, careful coordination, cribbing, and locknut jacks are required when lifting under traffic. A temporary ramp, usually constructed of asphalt, may be required at the approaches if the total height of the lift exceeds 20 mm.

7. Disconnect any utilities, railing, traffic barrier cover plates, and sliding expansion joint plates that will prevent the lifting of the structure.

8. The working drawings, jacking procedures, and calculations should be prepared, stamped, and signed

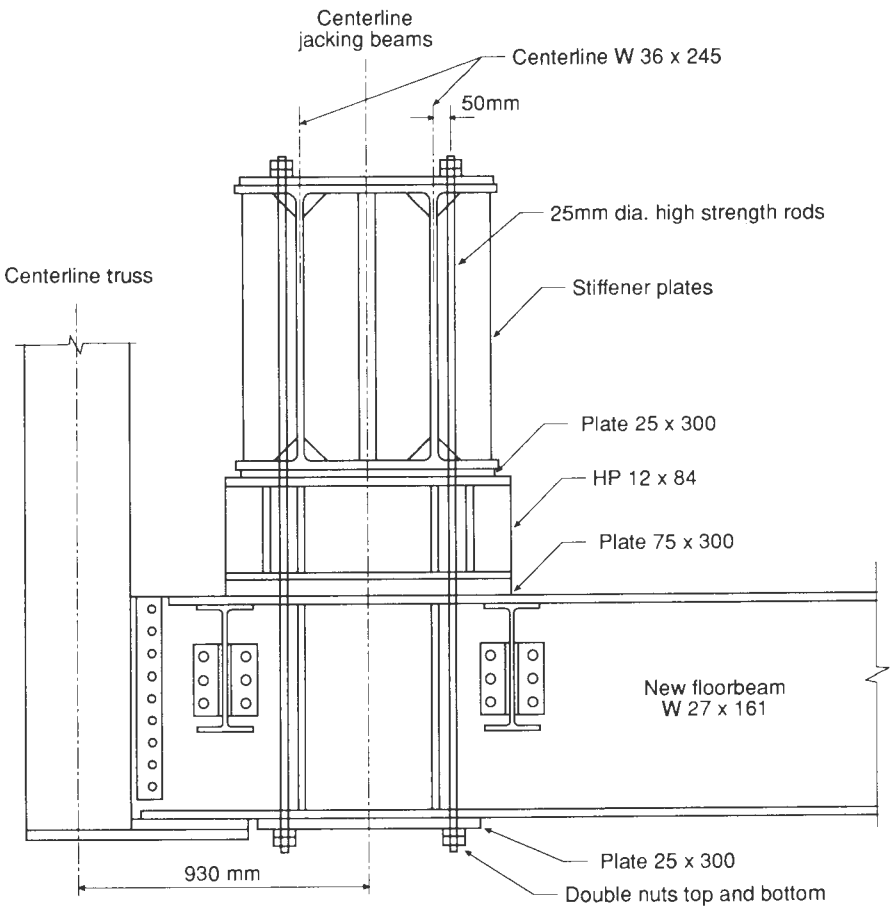

FIGURE 5 Case Study 2: details at lifting point, Snohomish River Bridge.

by a professional engineer licensed in the state where the lifting is to take place. The engineer should inspect all aspects of the lifting operation and be present during the lifting.

Replacement Bearing and Lifting Costs

The design service load limits and costs for various bearing types used by WSDOT are given in Table 1. These costs are per metric ton of the design service load. The lowest cost of \$3 to \$5/metric ton is for elastomeric bearings, and the highest cost of \$13 to \$20/metric ton is for multirotational and seismic isolation bearings. Since 1987 WSDOT has not permitted the use of pot bearings because of poor performance, which may be related to overrotation during construction. WSDOT has used fabric pad bearings with a TFE and stainless steel sliding surface and multirotational disc bearings as replacement bearings for frozen truss expansion roller nests. Elastomeric bearings have been used as replacement bearings for steel girder bridges with tipping rocker bearings when the expansion and contraction are less than ± 50 mm.

High-load elastomeric bearings can also be used for expansion bearings for trusses, provided that the load and expansion limits are not exceeded. For new bridges WSDOT has designed high-load elastomeric bearings with a maximum elastomer height of 150 mm and for service loads of up to 360 metric tons in accordance with AASHTO's Method B (*5*). Elastomeric bearings can also be designed as isolation bearings that will reduce the seismic forces acting between the superstructure and substructure. Elastomeric bearings show excellent promise as replacement bearings because they are corrosion resistant, durable, easy to install, maintenance-free, and more economical than any other bearing type.

Table 2 provides the lifting costs per bearing per metric ton for the three case studies. The costs range from a low of \$22 to a high of \$78/metric ton. The figure of \$22/metric ton is low because the contractor had unbalanced the bid by overpricing the disc bearings. When the bearing unit price is decreased to reflect a reasonable price for disc bearings, the lifting cost would be ap-

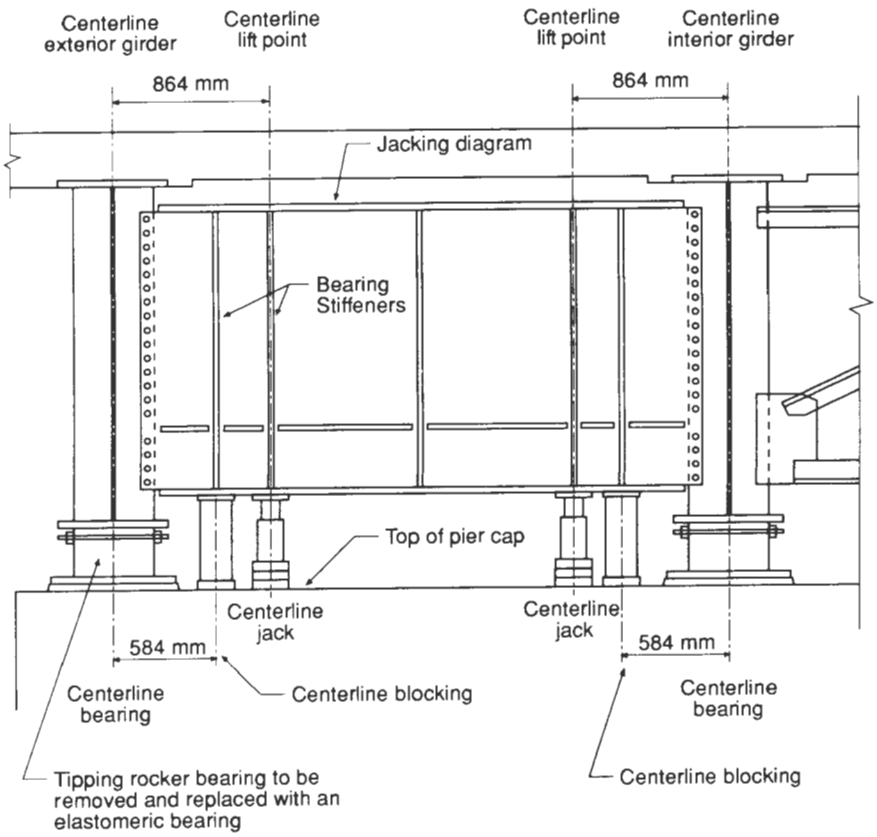

FIGURE 6 Case Study 3: jacking details, Kalama River Road Overcrossing.

proximately $50/metric ton. The high cost of $78/metric ton included the fabrication of the jacking beams used for raising the Snohomish River Bridge.

Summary

1. It is WSDOT's policy to remove and replace nonfunctioning or seismically vulnerable tipping rocker bearings to extend the service lives of existing bridges.
2. Details of three recent bearing replacement projects in Washington State are presented. Case studies describe three different lifting approaches: direct bearing on truss gusset plates, the use of a jacking beam as a pry bar with a mechanical advantage of 2 to 1, and the use of jacking diaphragms placed between the ends of plate girders.
3. WSDOT shares responsibility for the success of the lifting operation by including details in the plans for the most practical lifting procedure on the basis of past experience. As the owner WSDOT is concerned that no damage to the bridge should occur during a lifting operation. The contractor may propose an alternate lifting procedure. Generally, jacking under live load traffic is not recommended.
4. Hydraulic jacks are used as a means of lifting bridges so that defective or frozen bearings can be removed. Jacks should be sized for a minimum of 1.5 times the calculated lifting loads to account for discrepancies between hydraulic gauge readings and calculated

TABLE 1 Bearing Design Loads and Costs, 1991 to 1995

Bearing Type	Design Service Load (tonnes)[a]	Cost/tonne ($ U.S.)
Elastomeric[b]	<360	3-5
Fabric Pad[b]	<270	5-10
Steel Pin	>270	6-20
Disc or Spherical[b]	>360	10-20
Seismic Isolation[b]	<360	13-20

[a] All loads are in tonnes (metric tons).
[b] Replacement bearing types used by WSDOT.

TABLE 2 Superstructure Lifting Costs, 1991 to 1995

Case Study	Bridge	Description	Cost/tonne ($ U.S.)
1	Puyallup River Bridge Br. No. 167/20E	Jacking against truss gusset plates	22[a]
2	Snohomish River Bridge Br. No. 529/10E	Jacking beams 2-W36X245	78[b]
3	Kalama River Bridge Br. No. 5/113	Jacking diaphragms between girders	58

[a]Contractor unbalanced bid by overpricing the disc bearings. When a reasonable disc bearing price is used, the lifting cost is increased to $50/tonne.

[b]Includes fabrication of jacking beams.

lifting loads. The gauge readings indicate that heavier lifting loads occur and may be attributed to the increased force required to break the bond caused by heavy rusting of the roller nests, internal friction in the jacks caused by binding, or faulty gauges.

5. In the first case study, epoxy was used as a leveling course for uneven gusset plates. This was the first time that WSDOT specified an epoxy as a means of uniformly distributing lifting loads. To prevent spalling, the epoxy leveling course should be confined by steel bars along each side for a depth equal to one-half height of the leveling course.

6. Bridge bearing replacement is simplified if it is coordinated with rehabilitation projects. As shown in the second case study, it was easier to lift the bridge from above with jacking beams after the concrete deck was removed because the deck accounted for 70 percent of the dead load. Smaller jacking beams and jacks were used because of the reduced dead load.

7. Replacement bearings include multirotational disc bearings, fabric pads with TFE and stainless steel sliding surfaces, elastomeric bearings, and lead-core isolation bearings. Elastomeric bearings show promise as replacement bearings because they are corrosion resistant, durable, easy to install, maintenance-free, and more economical than other bearing types.

8. Maximum design loads for replacement bearings, costs for replacement bearings, and costs for lifting bridges are given.

ACKNOWLEDGMENTS

The Puyallup River and Kalama River bearing replacement projects were designed by Munindra Talukdar, WSDOT, and were checked by the author. The Snohomish River lifting and bearing replacement project was designed by Jugesh Kapur and was checked by John LaBranche, WSDOT. Rick Liptak, WSDOT, was the Bridge Technical Advisor for the Snohomish River Bridge project. Progressive Contractors, Inc., did the lifting and bearing replacement on the Puyallup River and Snohomish River bridges. Mowat Construction Company was the contractor for the Kalama River Bridge bearing replacement.

The author thanks WSDOT for support in preparing this paper. The bearing replacement designs were prepared under the direction of Allan H. Walley, former WSDOT Bridge and Structures Engineer, and M. Myint Lwin, current WSDOT Bridge and Structures Engineer. Their support and encouragement are very much appreciated.

REFERENCES

1. Redfield, C., and C. Seim. Pot Bearing Replacements—Two Case Studies: Cline Avenue Interchange and I-285/I-85 Interchange. *Joint Sealing and Bearing Systems for Concrete Structures*, Vol. 2, SP-94. American Concrete Institute, Detroit, Mich., 1986, pp. 817–823.
2. Van Lund, J. A. Jacking Steel Bridge Superstructures in Washington State. In *Transportation Research Record 1319*, TRB, National Research Council, Washington, D.C., 1991, pp. 94–101.
3. Structural Lifting Operations. *Bridge Special Provision*, Washington State Department of Transportation, Jan. 1991.
4. Orr, J. Planning, Knowledge Keys to Safe Bridge Lifting. *Roads & Bridges*, Vol. 26, No. 4, April 1988, pp. 85–87.
5. *Standard Specifications for Highway Bridges*, 15th ed. AASHTO, Washington, D.C., 1992, pp. 294–299.

Behavior of Bearing Plate Type Bridge Bearings Under Traveling Load

Toshihiko Naganuma and Koretada Seki, *Hanshin Expressway Public Corporation, Japan*
Masanori Iwasaki and Koichi Tokuda, *Yokogawa Bridge Corporation, Japan*

Although bridge bearings are important parts in bridges, they are subject to severe conditions for long periods of time. This might lead to damage, particularly if maintenance is poor. Macroscopic analysis of the inspection data on the Hanshin Expressway is provided. Then, the dynamic behaviors of bridge bearings under traveling loads were measured both before and after new bridge bearings were installed. Model tests with full-size bridge bearings were conducted to improve the functions of the bridge bearings. The major results are as follows. (a) Approximately 70 percent of the bearings on the Hanshin Expressway are plate bearings, and the number of damaged bridge bearings increases after 20 years of service. (b) Plate bearings that had been used for about 20 years no longer functioned well under traveling loads. The sliding function could not be fully restored, even by replacing the existing bridge bearings with identical new ones. (c) Rubber bearings (particularly pot bearings) are suitable for improving bridge bearing function.

The principal functions of bridge bearings are

1. To support the dead load of the bridge and the repetitive traveling load.
2. To prevent the constraint of the repetitive displacement of the girders caused by vehicle loads and temperature changes.
3. To prevent the unusual displacement produced in the substructure of a bridge during an earthquake from being transmitted to the superstructure of the bridge.

However, bridge bearings are often used for long periods of time under severe environmental conditions, and they are prone to corrosion caused by the accumulation of rainwater and dust leaking from the expansion joints. Bridge bearings are susceptible to damage because they are installed at the last stage of the erection process. In fact, considerable damage is inflicted on the body of bridge bearings and near bridge bearings in bridges that have been in service for a long time.

Replacing the bridge bearings is the best way to restore the bridge bearing function of an existing bridge in such a condition. However, it is difficult to replace bridge bearings when the bridge is in use, and it is not economical to replace them frequently, such as for a consumable item. In the future there will be a growing need for practical bridge bearings with durability. To date much of the research conducted to make bridge bearings more durable has been concentrated on the

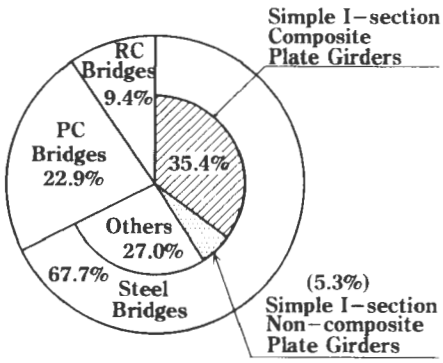

FIGURE 1 Assortment of bridges in Hanshin Expressway.

body of the bearing itself; almost nothing has been done to examine the influence on the main girders.

First, we analyzed the actual state of maintenance on the Hanshin Expressway. Second, we conducted a field test to study the behavior of bridge bearings before and after replacement of the plate bearings. Third, we conducted comparative laboratory tests using full-size model girders to compare the functions of various kinds of bridge bearings. These tests clarified the types of bridge bearings that are suitable for steel bridges.

Maintenance on the Hanshin Expressway

The Hanshin Expressway has been in service as a trunk road in the Kansai Region since 1964. Most of the approximately 160 km was constructed between 1964 and early 1994 and consists of urban elevated expressway. Figure 1 shows the assortment of bridges on the Hanshin Expressway.

Approximately two-thirds of these are steel bridges. A large proportion of those are simple I-section steel bridges with spans of approximately 30 m that were constructed in the 1970s. Furthermore, many of the bridge bearings installed in these bridges are plate bearings with capacities of about 100 metric tons.

Figure 2 summarizes the results of periodic visual inspections of the entire structures of the bridges except for the decks conducted at intervals of once every several years. Ranks AA to C in Part 1 in Figure 2 were determined by third parties or by the importance of each structure (Table 1). Figure 2 shows that about 20 percent of all damage is classified as Rank A, and most of the damage consists of both damage to the bridge bearings and fatigue cracks.

Table 2 summarizes the actual conditions of the abnormalities in bridge bearings. There is considerable damage to plate bearings, which account for approximately 67 percent of all bearing stock.

In particular, a large number of set bolts used for assembling were damaged. These bolts were attached to provide temporary bearing when the bridges were erected and have no effect on the bridge bearing functions. Other damage that was identified was unusual spacing and contact with the side block, but these problems revealed functional deterioration caused by temperature changes. The deterioration of the functions of the bridge bearings themselves and the subsequent effects on the girders were not, in fact, inspected because of the structural details. Fatigue cracks, on the other hand, were mostly confined to the intersection between the main girder and the cross beam or sway bracing. Recently, however, the fatigue cracks shown in Figure 3 have developed on a frequent basis. This evidence indicates that the causes of the fatigue cracks are secondary stress and repetition accompanying a decline in the bridge bearing function under traveling loads and that

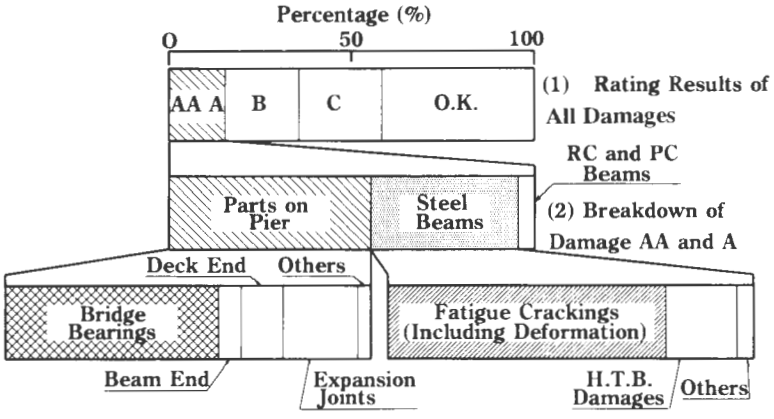

FIGURE 2 Results of bridge inspections.

TABLE 1 Ranking of Damages

Ranking of Damages	Criteria for rating of damage
AA	The damage is very serious, and emergency repair is needed.
A	The damage is serious, and repair is required.
B	The damage requires repair as needed.
C	The damage is minor but should be repaired as needed.
O.K.	For cases other than those mentioned above.

these bridge bearings should be replaced to eliminate risk.

Field Tests on Functions of Bridge Bearings

Method of Field Testing

In many cases old bridge bearings are replaced with identical bearings to restore the bridge to its original condition, but because this replacement work is done under service conditions, it is not easy to restore the bridge to its original quality and performance potential. For these reasons we conducted a field study on the behaviors near bridge bearings before and after replacement. Figure 4 is a general view of the target bridges that we studied, and Table 3 describes the structures of the old and new plate bearings. The bridges are continuous, standard simple I-section bridges that have been in service for 22 years. During this period the bridge bearings had not been replaced. However, all bridge bearings in several spans including those of the target bridge were replaced because some of the bridge bearings developed damage such as cracks in the mortar bed or contact with the side block. The field study involved dynamic measurements with both a wire strain gauge and a contact-type deflection sensor at three stages: before the replacement, just after the replacement, and 1 year later.

Field Test Results

Figure 5 provides examples of the field measurement results. Each axis is the amplitude of dynamically measured data by through traffic vehicles. The stress σc in the center of the span of the external main girder is stress that is believed to be proportional to the weight of the vehicles. The measurement values were scattered broadly according to the crossing position of the vehicles and their speed, although the regression line is provided in Figure 5. The closed symbols in Figure 5 represent the result of F.E.M. analysis; the actual bridge was modeled by using three-dimensional shell elements, and the design load was loaded (T-20, equivalent to a two-axle vehicle weighing 20 metric tons). Our results are summarized below.

1. The movable bearing must move horizontally by deflection of the main girder, but there was almost no

TABLE 2 Conditions of Abnormalities in Bearings (Rank A)

	Type of Bearing*								
Type of damage	LB	PB	Ro	Pi	Pv	PiR	PvR	Others	Total
Substance of bearing	13	138	50	1		4	1	12	219
Subsidence of bearing	33	112		8					153
Cracking on base concrete	18	18	3					1	40
Edge of bearing	3								3
Set bolts for assembling	8	1,273	46	16	2	5	2		1,352
Anchor bolts	4	13	2	1					20
Corrosion Inside		2	10			2	4	1	19
Corrosion Outside	14	29	1	2					46
Unusual spacing of bearing	48	266	11			2	2		329
Contact with side block	19	257	322			14	29	6	647
Abnormal noise			4				3		7
Others	2	27			2	4	1		36
Total Number of Rank A	146	2,039	407	27	4	20	38	18	2,699
(%)	(3.2)	(8.7)	(12.4)	(1.1)	(1.4)	(10.0)	(18.3)	(11.5)	(7.7)
Total Number	4,587	23,501	3,289	2,518	296	201	208	391	35,001

*: LB:Linear Bearing, PB:Plate Bearing, Ro:Single Roller Bearing, Pi:Pin Bearing
Pv:Pivot Bearing, PiR:Pin and Multi-Roller Bearing, PvR:Pivot Roller Bearing

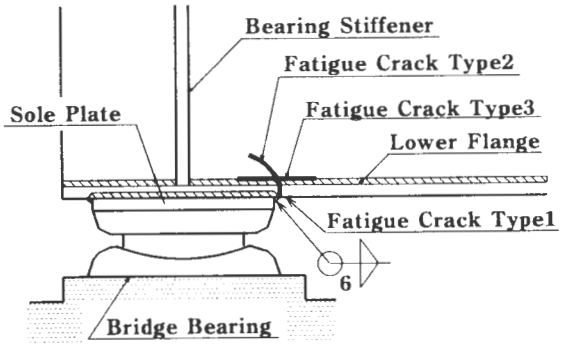

FIGURE 3 Fatigue cracks near bridge bearings.

horizontal movement of the movable bearing before replacement. It increased threefold after replacement and by about eight times 1 year after replacement, and it tended to approach the analytical values. However, it was still only about 44 percent of the analytical value even 1 year later.

2. The rotation angle on the movable bearing fell about 58 percent just after replacement in comparison with that before replacement, but it was 1.5 times the original value after 1 year. A comparison of these results with the analysis results indicates that the value for the fixed bearing is almost identical to the analysis value just after replacement and that the value for the movable bearing point is almost identical to the analysis value before replacement and 1 year after replacement. The rotation angle on the fixed bearing was reduced to a value identical to the analysis results, provided that there is complete constraint by replacement, and it remained unchanged 1 year later.

3. The stress σf on the movable bearing was changed little by the replacement, and its value was identical to the analysis value for the fixed bearing.

Experiment with Full-Scale Model Bearings

Experimental Method

We conducted a series of comparative laboratory tests on various types of full-size bridge bearings on the basis of the results of the field study. Figure 6 shows the test mock-up. The dimensions and specifications of the model girder were matched to those of the target bridge. At the same time a reaction force of 50 metric tons equivalent to a dead load was continuously loaded at the bearing point by PC rods, and a force equal to the traveling load was loaded at the center. Table 4 shows the specifications of the bridge bearing used in the test. For comparison, a pin-roller bearing was used as a model under an ideal condition. During the tests a pin bearing was fixed as the bridge bearing.

Experimental Results

Figure 7 shows examples of the relationship between P1 and the amount of horizontal movement or the rotation angle. At a low load horizontal movement is constrained in the rubber bearing. When the amount of horizontal movement per unit of load in the high-load area (15 to 25 metric tonf) was compared by taking the pin-roller bearing load as 100 percent, the following results were obtained: approximately 60 percent for BP-A1 and BP-A2, in which the horizontal sliding surface was equipped with fixed lubricants; between 66 and 75 percent for BP-A3, in which the horizontal sliding surface was a polytetrafluoroethylene (PTFE) plate, and for BP-A4 and a pot bearing case; and approximately 85 percent for the rubber bearing. The rotation angle of the plate bearing was, in all cases, smaller than that of the pin-roller bearing. However, the rotation angles of

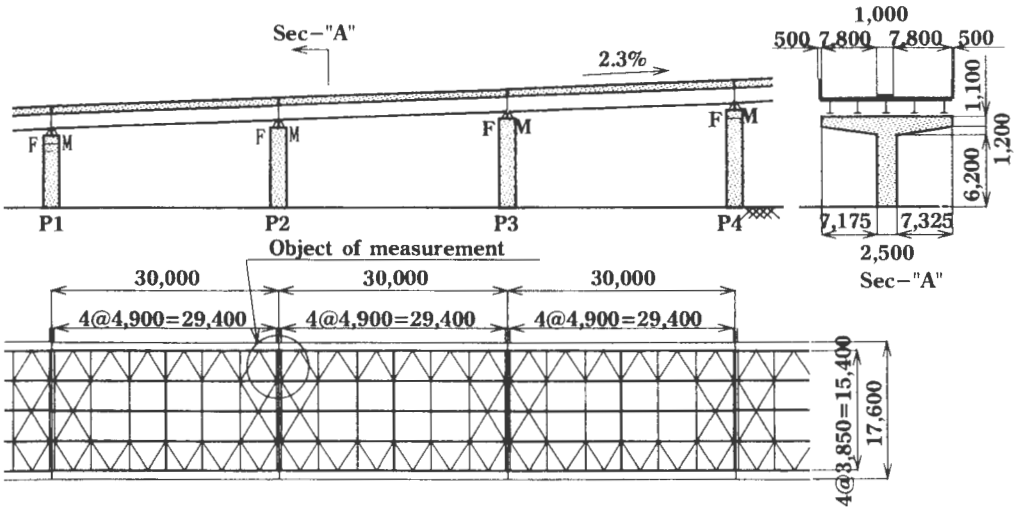

FIGURE 4 General view of target bridges.

TABLE 3 Comparison of Bearings Before and After Renewal

Bearing	Radius of Curvature r(mm)	Surface Condition* Hu	Hl	Ru	Rl
Existing Bearing	500	M.D.	G	G	M.D.
Renewal Bearing	210	SUS	PTF	G	M.D.

* :See Ap.Fig
M.D.:Molybdenous Disulfide Coating
G:Inlaid with Graphite
SUS:Welded with SUS316 Thin Plate(2mm)
PTF:Set on PTFE Plate(4mm)

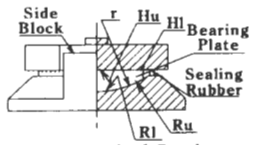

AP.FIG. Typical Section

the pot bearing and the rubber bearing were larger. Figure 8 presents the longitudinal-direction strain distribution of the lower flange at the front of the sole plate and the vertical-direction strain distribution of the girder web per unit of load (stress at right angles to Type 3 cracks in Figure 3). In both cases strain convergence is seen in the front surface of the sole plate. Although overall the plate bearing provided higher values than the pin-roller bearing, those of the pot bearing and the rubber bearing were either the same or lower. In the case of the pot bearing in particular, the value was low (ϵ = 56 percent and ν = 96 percent).

Conclusion

The actual state of maintenance of bridge bearings on the Hanshin Expressway was investigated by a field study of

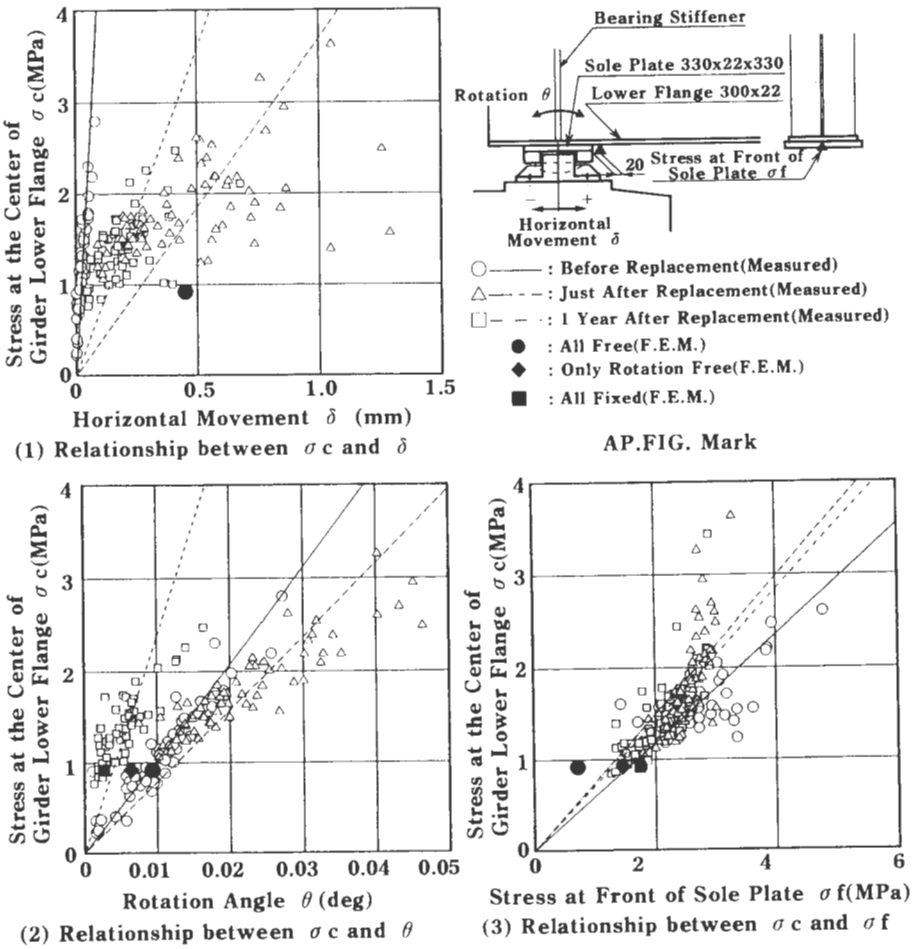

FIGURE 5 Field measurement results on movable support.

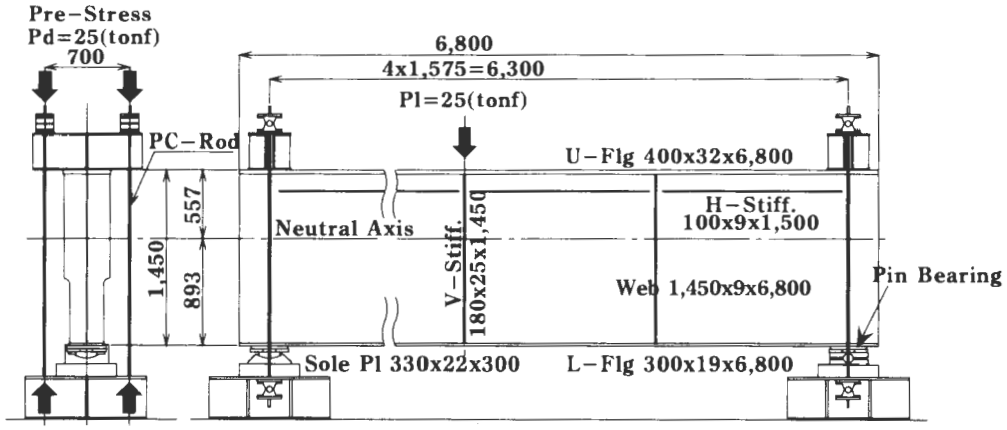

FIGURE 6 Test mock-up.

TABLE 4 Comparison with Characters of Test Bearings

Mark		BP-A1*	BP-A2*	BP-A3*	BP-A4*	PB**	RB***
Radius of Curvature r(mm)		500	210	210	210		
Surface Condition	Hu	M.D.	M.D.	SUS	SUS	SUS	Rubber
	Hu	G	G	PTFP	PTFP	PTFP	
	Ru	G	G	G	PTFC	Rubber	
	Rl	M.D.	M.D.	M.D.	PTFC		

*,**,***:See AP.FIG
M.D.:Molybdenous Disulfide
G :Inlaid with Graphite
SUS :Welded with SUS316 Thin Plate(2mm)
PTFP:Set on PTFE Plate
PTFC:PTFE Powder Coat

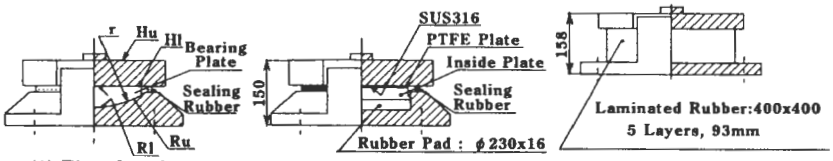

(1) Plate Bearing (2) Pot Bearing (3) Rubber Bearing

AP.FIG Typical Section

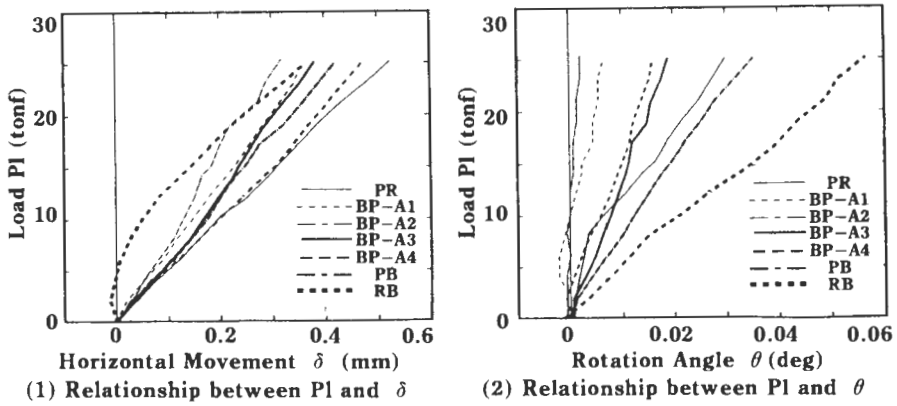

(1) Relationship between Pl and δ (2) Relationship between Pl and θ

FIGURE 7 Test results for movable support.

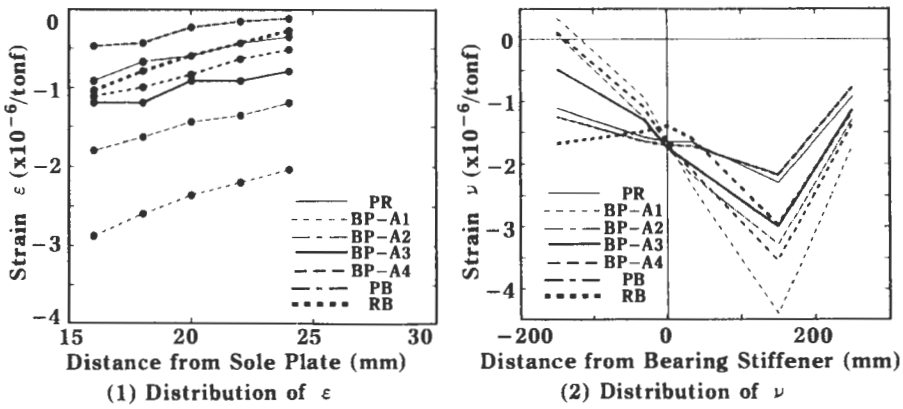

FIGURE 8 Strain distribution near sole plate on movable support.

the behavior near the bridge bearing before and after replacement of the plate bearings. We performed comparative tests on models equipped with various types of full-size bridge bearings. The results are summarized below.

1. Periodic inspections revealed damage to the plate bearings, which accounted for about 70 percent of all the bridge bearings, and extensive fatigue cracks in the steel girders.

The sliding function of the bridge bearings has not been fully inspected because of problems with structural details.

2. The horizontal sliding function of plate bearings inlaid with graphites that have been in use for roughly 20 years had declined sharply.

3. Replacing bridge bearings with plate bearings with a PTFE plate as their horizontal sliding surface improved their horizontal sliding function. However, those bridge bearings are not sufficient to deal with the minute displacement caused by the traveling load, as would be expected from the design.

4. There were cases in which it was impossible to improve the rotation function of plate bearings by replacing the bridge bearings.

5. Stress in the bridge axial direction of the lower flange near sole plates was reduced little by replacement.

6. The function of the plate bearings subject to a traveling load can be improved by using PTFE plates on their sliding surfaces, but it is still insufficient.

7. Tight rubber bearings or pot bearings provide excellent performance under traveling loads. In particular, tight rubber bearings are effective at preventing fatigue cracks in the main girders.

It will be necessary to develop both a method of inspecting the sliding functions of bridge bearings and bridge bearings with superior durabilities.

Development and Testing of a New Shear Connector for Steel Concrete Composite Bridges

Wayne S. Roberts and Robert J. Heywood, *Queensland University of Technology, Australia*

A new cross section has been developed for steel concrete composite bridges that eliminates the top steel girder flange. This is made possible by utilizing a recently developed shear connector known as the Perfobond Strip. This shear connector provides a stiff connection between steel and concrete and reportedly has excellent resistance to fatigue. Because the success of this new cross section and numerous other applications depends on the performance characteristics of the shear connector, the present design models were investigated. Some inconsistencies were found between current design models and experimental results; the results of a series of shearbox tests that have led to the development of a new design model are included. This new design model is compared with current models. Some details of a full-scale bridge test are also included to examine the fatigue behavior and overall performance of the new bridge cross section.

Steel concrete composite construction is re-emerging as a competitive form of construction for bridges. This is because of the availability of higher yield strength steels, automated fabrication methods, and the development of new coating systems to resist corrosion (*1*). Permitting tensile stresses in the concrete deck provided crack widths are controlled and research into the behavior of shear connectors have encouraged production of more cost-efficient designs (*2*). The focus of current research in composite structures is to increase the understanding of shear connector behavior and to develop designs that are more cost-effective through efficient use of materials.

A new shear connector known as the Perfobond Strip has been developed by Leonhardt and Partners in Germany (*3*). It consists of a steel strip with holes punched in it that can be welded to the top flange of steel I-sections. Concrete is cast through the holes, forming a series of concrete dowels that resist the shear flow.

The top steel girder flange contributes little to the strength of the composite section because of its proximity to the neutral axis. Its main function is to provide stability during the construction process and a location for the attachment of shear studs. Although designers have minimized the size of the top flange, it would be more efficient for fabrication if it were eliminated. Knowles has stated that this would be possible if researchers could find a suitable method of shear connection that did not require a top flange for the shear connection to function effectively (*4*).

The Perfobond Strip shear connector can be incorporated into a composite cross section that eliminates the top steel girder flange and the shear studs (*5*). This

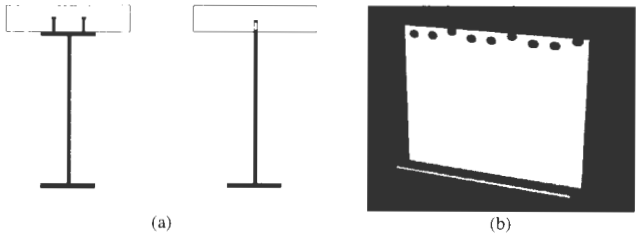

FIGURE 1 (*a*) **Comparison of traditional and new composite cross sections;** (*b*) **inverted steel T-section used in the new cross section.**

cross section, illustrated in Figure 1, leads to savings in steel fabrication costs because there is no top flange and no weld between the top flange and web plate. Although the web plate is a little deeper in the new cross section, fabrication time is significantly reduced. Instead of shear connectors being welded to the top flange, holes are punched in the top of the web. Figure 1 compares the traditional composite cross section with the inverted T cross section.

The inverted T cross section requires appropriate handling and construction techniques because the T section is unstable before the concrete deck is complete. While the inverted T alone is sufficiently stable during handling, it is not able to carry construction loads. Construction methods involving erecting the section with the concrete deck precast onto the steel girder have been investigated and found to be feasible. A new bridge cross section has been developed using precast steel and concrete composite T-beams (*6*). Incremental launching with the concrete deck cast in place is also a feasible option.

One disadvantage of the inverted T cross section is that deck replacement would be more difficult. This is not a problem in Australia as the climatic conditions are not as severe as they are elsewhere and deck replacement is unusual.

For the inverted T cross section to be successful, the performance of the shear connection in this application is vital. This paper reports research aimed at verifying the performance of this new method of shear connection in the absence of the steel girder top flange.

Perfobond Strip

Figure 2 illustrates the typical dimensions of the Perfobond Strip. The advantage of the Perfobond Strip shear connector is that it behaves like a rigid connector at working stress levels and it does not deform like shear studs. A comparison of the static performance of shear studs and the Perfobond Strip, both with steel girder flanges, is presented in Figure 3 (*7*). The comparison is based on pushout test results using six shear studs 19 mm in diameter and ten holes 30 mm in diameter at 80-mm centers. The strip provides a slightly stiffer connection before the ultimate load is reached and maintains up to 80 percent of its load after 15 mm of slip. The load for the shear studs begins to fall off after 10 mm of slip as individual studs shear off. The fatigue performance of the Perfobond Strip has also been investigated by Leonhardt et al. (*3*). After 2 million load cycles at 40 percent of ultimate load, the recorded slip for the Perfobond Strip shear connector was 0.14 mm, whereas the slip for the shear stud was significantly higher at 1.5 mm. At working stress levels the Perfobond Strip shear connector does not deform and is therefore a rigid means of shear connection. Therefore, it is not as prone to fatigue problems, which limit the

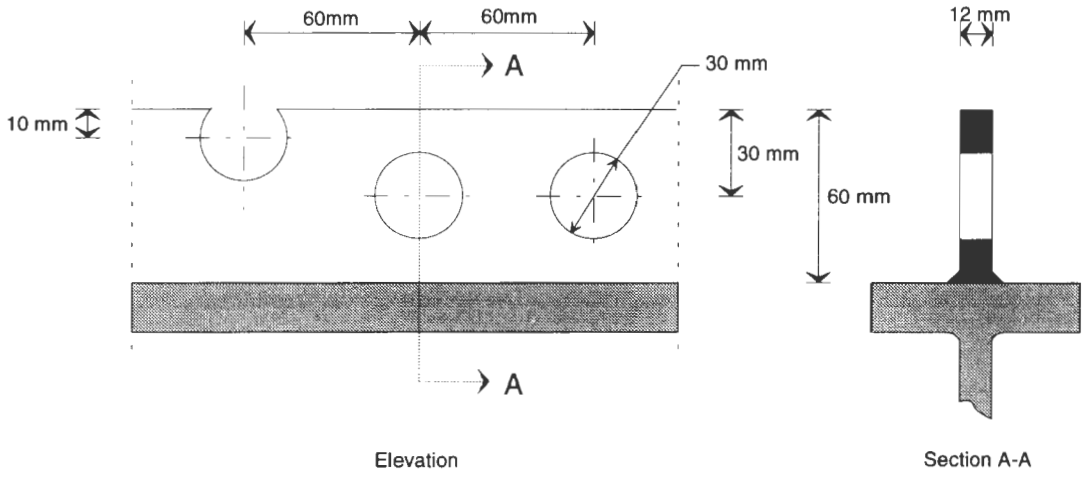

FIGURE 2 The Perfobond Strip.

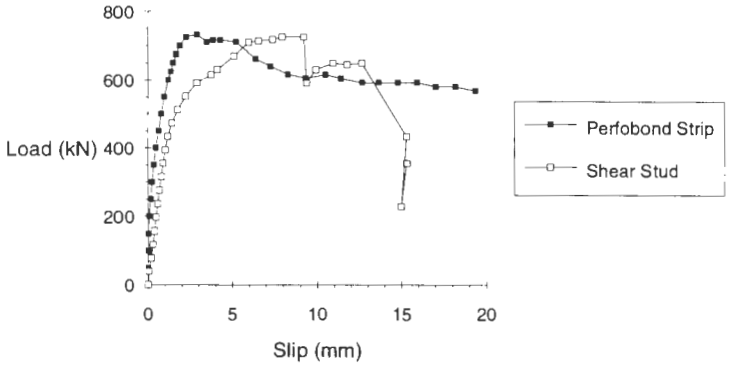

FIGURE 3 Comparison of shear studs and the Perfobond Strip (7).

service loads carried by shear studs. Figure 4 illustrates the fatigue test results.

Present Design Equations

Leonhardt et al. have presented design equations for the Perfobond Strip (3). The desired failure mode is by shearing of the concrete dowels, and the resulting ultimate capacity is given by Equation 1. *SF* is the ultimate shear force per hole.

$$SF = 2 \times \frac{\pi D^2}{4} \times 1.6 f_c' \tag{1}$$

The equation is essentially the hole area where D is the diameter, multiplied by the shear strength developed in the concrete, which is given by the constant 1.6 (shear strength parameter) times the concrete strength (f_c'). This value was given as 1.3 in Leonhardt's paper but has been converted to 1.6 so that the cylinder strength can be used instead of the cube strength. This is multiplied by two as there are two shear planes per hole. A strength reduction factor $\phi = 0.7$ is applied to calculate the design shear force SF^*. Other modes of failure include failure of the concrete dowels by bearing and shearing of the steel strip between the holes; these can be avoided by ensuring appropriate hole sizes and spacings for the plate thickness used.

There is also a requirement that reinforcing steel be provided transverse to the strip to confine the concrete around the strip to ensure that the concrete in the hole is confined in three dimensions. The requirement for this transverse steel is further illustrated using a strut tie analogy in Figure 5. The amount of reinforcing required is calculated using Equation 2 where A_{st} is the area of steel required, SF^* is the design shear force per concrete dowel, and f_{sy} is the yield strength of the reinforcing:

$$A_{st} \geq \frac{0.8 \times SF^*}{f_{sy}} \tag{2}$$

Oguejiofor and Hosain have also presented a design equation (Equation 3) for the Perfobond Strip (8). It is based on an application for beams using 375-mm

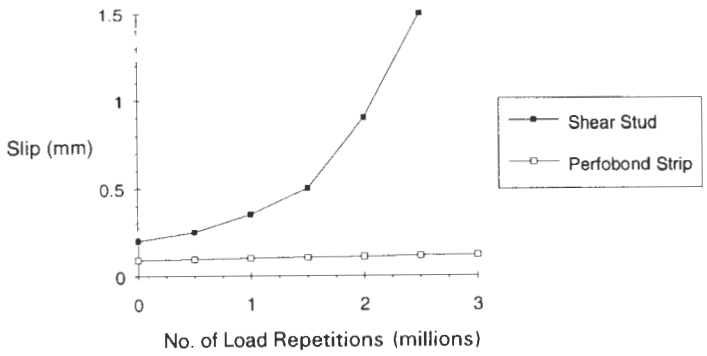

FIGURE 4 Fatigue comparison between shear studs and the Perfobond Strip (3).

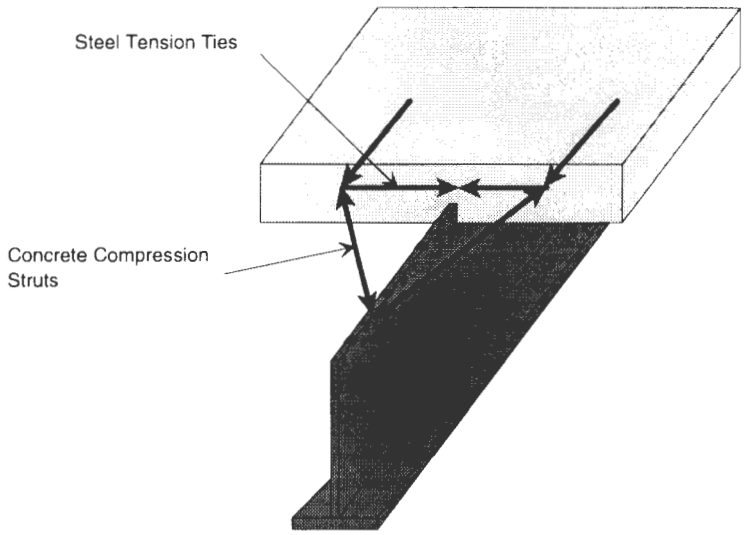

FIGURE 5 Internal forces associated with the Perfobond Strip shear connector.

lengths of strip. Consequently it allows for end bearing of the strip on the concrete. Their equation is based on the results of pushout tests that failed because of splitting of the slab along the line of the connector. This failure mode resulted from the use of lighter transverse reinforcing typical of building applications. The first term is related to the splitting of the concrete where A_{cc} is area of concrete in the plane of the connector. The second term accounts for the degree of confinement from the transverse reinforcement where A_{rt} and f_y are the area and yield strength, and the last term gives the shear strength of the concrete dowels where A_{bs} is the total area of the dowels in shear. In this case SF is the ultimate shear force per connector, as follows:

$$SF = 0.6348A_{cc}\sqrt{f'_c} + 1.1673A_{rt}f_y + 1.6396A_{bs}\sqrt{f'_c} \quad (3)$$

The differences between the methods of Leonhardt (*3*) and Oguejiofor and Hosain (*8*) revolve around the various failure modes that result from the differences in the transverse reinforcing used. Leonhardt et al. use the concrete strength, whereas Oguejiofor and Hosain use the square root of the concrete strength. Clearly there are some inconsistencies in the methods available for the design and prediction of the Perfobond Strip capacity. This is to be expected as the current theories are based on the results of pushout tests of varying configurations.

Pushout Testing

A series of pushout tests was conducted to verify the performance of the Perfobond Strip and to investigate the performance of the connector without a top steel girder flange. The configurations used in the program are illustrated in Figure 6. Tests 1 and 2 consisted of two strips with holes 30 mm in diameter at 80-mm centers with the strips welded to a top flange in Test 1 and with no flange in Test 2. Test 3 consisted of holes 30 mm in diameter at 50-mm centers with no flange. The transverse reinforcing was typical of Leonhardt's requirements. The strain in the transverse reinforcing was recorded during the tests.

The results of the testing program are illustrated in Figure 7. The initial data recorded were load slip data, which have been converted to shear strength parameter versus slip. The shear strength parameter was outlined in reference to Equation 1. Plotting the shear strength parameter permits the comparison of test results with various concrete strengths and hole diameters. The shear strength parameter is representative of the shear strength being developed in the concrete dowels. The straight line on the graph represents Leonhardt's value of the shear strength parameter at ultimate, which is used in Equation 1.

A number of conclusions can be drawn from the results of this test series. By comparing the results of Tests 1 and 2 it is clear that the Perfobond Strip remains functional without the top flange. The initial stiffness is similar, but there is some reduction in ultimate strength that could be allowed for in the design process. This is because the concrete is not confined around the strip by the flange. Comparing the results of Tests 2 and 3, in which the same number and size of holes were used, showed that there was a drop-off in load when the holes were closer together. However the area of steel in the

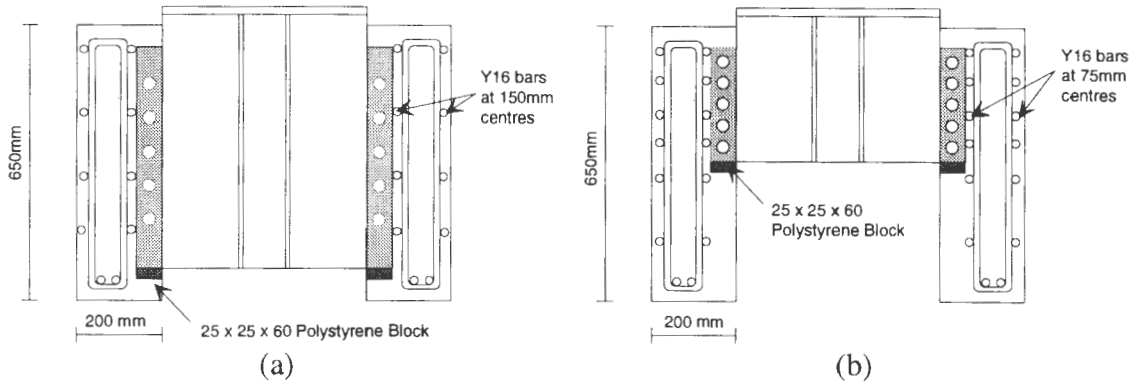

FIGURE 6 Pushout test configuration (*a*) for Test 1 (with flange) and Test 2 (without flange) and (*b*) for Test 3.

TABLE 1 Pushout Test Failure Loads and Calculated Failure Loads

Test No.	Concrete Strength (MPa)	Experimental Failure Load (kN)	Calculated Failure Load (kN) (Experimental Failure Load as a percentage of calculated load) Leonhardt et al	Oguejiofor and Hosain	Shearbox Equation
1	30	732	678 (107%)	2686 (27%)	471 (155%)
2	33.5	640	758 (84%)	2724 (23%)	451 (142%)
2A	34	640	769 (83%)	2729 (23%)	361 (177%)
3	36	470	814 (57%)	2866 (16%)	384 (122%)

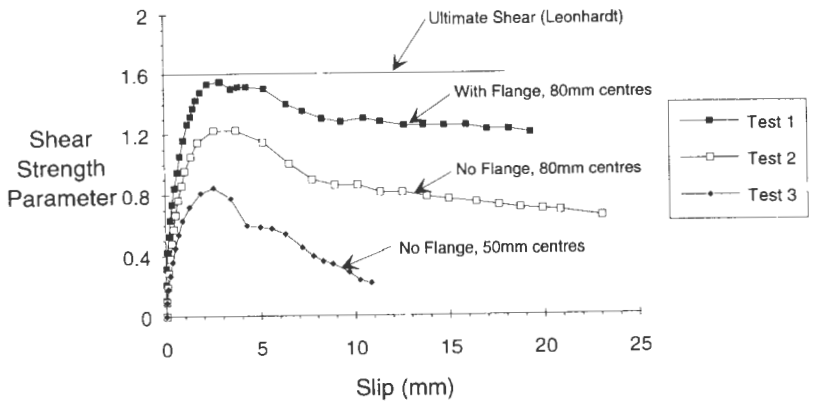

FIGURE 7 Graph of shear strength parameter versus slip for Perfobond Strip pushout tests.

strip without holes in it also decreases. This result highlights a problem with both of the currently used equations in that they do not consider the effect of friction between the surrounding plate and concrete.

Shear Box Testing

To investigate some of the inconsistencies highlighted by the pushout testing program, a series of shear box tests was undertaken. The principal aims of these tests were to investigate whether friction between the plate and concrete contributed to the strength of the shear connection, the effect of varying hole diameters, and the influence of the confining force provided by the transverse reinforcement. The test specimens consisted of plates 12 mm thick with varying hole diameters cast into concrete. The specimens were then sheared along one interface between the plate and the concrete. Figure 8*a* illustrates the different plates used in the investigation. The shaded area indicates the area of plate in contact with the concrete. Figure 8*b* illustrates a test specimen.

The investigation involved a total of 60 samples in five sets. Hole diameter was varied between 0 and 40 mm. The confining force was varied between 0 and 60 kN (0 and 4 MPa). Some typical shear force (load) versus slip curves are presented in Figures 9 and 10. The legend code describes the sample and test characteristics. D30CF0S3 denotes a diameter of 30 mm, a confining force of 0 kN, and that the test was from Series 3. Figure 9 illustrates tests with a common diameter of 30 mm with varying confining forces, whereas Figure 10 presents the results for varying hole diameters with constant confining force. In general, shear strength increases with increasing hole diameter and increasing confining force. The bond between the plate and concrete contributes to the strength indicated by result D0CF40S5 and the connector produces some strength with no confining force, which indicates a cohesion effect.

Analysis of Results

The factorial method of analysis is a method used to evaluate experiments in which interaction between variables is expected in experiments (*9*). A factorial analysis on the shear box test data indicated that both confining force and hole diameter influenced the results but no interaction occurred between the two.

A suitable strength model was required to describe the results from the shear box testing. The Mohr Coulomb soil shear strength model summarized by Equation 4 was chosen because it describes the shear strength of materials that have cohesion and friction components. This model allows the shear strength to vary with the applied stress normal to the shear plane, which was typical of the results from the shear box tests.

$$SF = C + \sigma_n \tan \phi \tag{4}$$

The results were segregated into the four different hole diameters so that the principal variable was the stress normal to the shear plane. To account for various concrete strengths the shear strengths have been divided by the square root of the concrete strength. The square root was used as shear failures and is related to the tensile strength of the concrete, which is related to the square root of the concrete strength. The data were plotted with shear force on the vertical axis and normal stress on the horizontal axis. Using linear regression

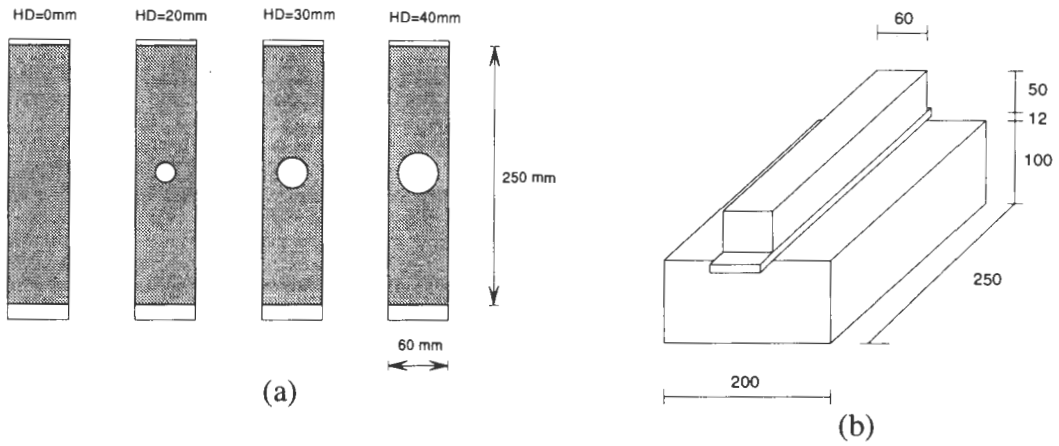

FIGURE 8 (*a*) **Steel plates with varying hole diameters;** (*b*) **sample use in shear box investigation.**

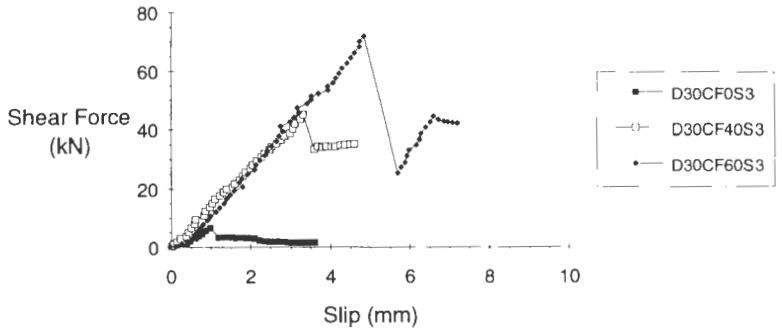

FIGURE 9 Typical shear force versus slip curves for Series 3.

analysis, four lines were plotted for each of the hole diameters. These lines are illustrated in Figure 10. Although there is some variation in the data, all regression lines fitted the data with an r^2 value of 0.9 or higher. The result for the hole 20 mm in diameter appears to be inconsistent with expected results. This inconsistency may be related to the influence of concrete aggregate in the hole. More testing would confirm the influence of aggregate in the hole. The ratio of hole area to plate area is also not typical of applications using the Perfobond Strip. A smaller plate size should be used for any subsequent testing.

Equation 5 represents the results of the tests on the basis of the regression lines in Figure 11 except for the 20-mm-diameter hole. The equation consists of a cohesion and friction angle component for the bond between the concrete and the steel plate and for the concrete to concrete interface in the concrete dowel as follows:

$$SF = \sqrt{f'_c}[A_p(0.046 + 0.15\sigma_n) + A_h\{(2.1 - 0.00055A_h) + (-0.079 + 0.00029A_h)\sigma_n\}] \quad (5)$$

here

A_h = the hole area;
A_p = the plate area in contact with the concrete less the hole area;
σ_n = the stress normal to the plate; and
f'_c = the concrete strength.

The quantities A_h and A_p are illustrated in Figure 12. *SF* in this case is the shear force per shear plane. The units are in millimeters, megapascals, and newtons. This equation allows the calculation of the shear strengths for hole sizes between 30 and 40 mm at any spacing. Further verification is required before this equation could be used for any size hole. The effect of hole spacing on the shear strength has not been considered in this investigation.

To equate the results of the shear box testing program back to the pushout testing results, it is necessary to quantify the stress normal to the plate (σ_n), which in the case of pushout tests is developed by the transverse reinforcing (see Figure 5). Using the average strain measured in the reinforcing bars, a stress normal to the connector was calculated and used in Equation 5 to derive a failure load for the pushout tests. The results are included in Table 1 along with calculated loads from Leonhardt's Equation 1 and Oguejiofor and Hosain's Equation 3. Equation 3 has been used out of context in this situation as the tests in this study used polystyrene blocks to prevent end bearing. Test 2A was identical in configuration and failure load to Test 2 but lower strains were recorded in the reinforcing bars. With the

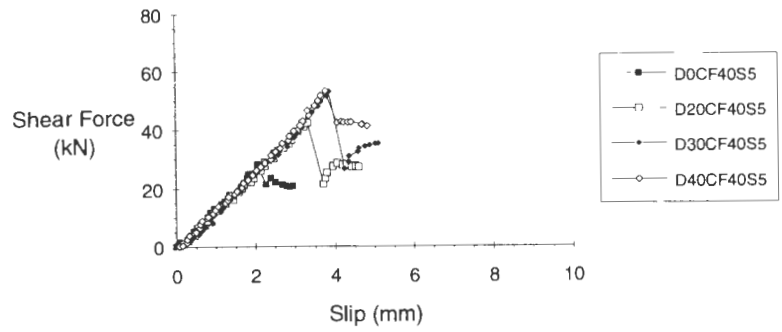

FIGURE 10 Typical shear force versus slip curves for Series 5.

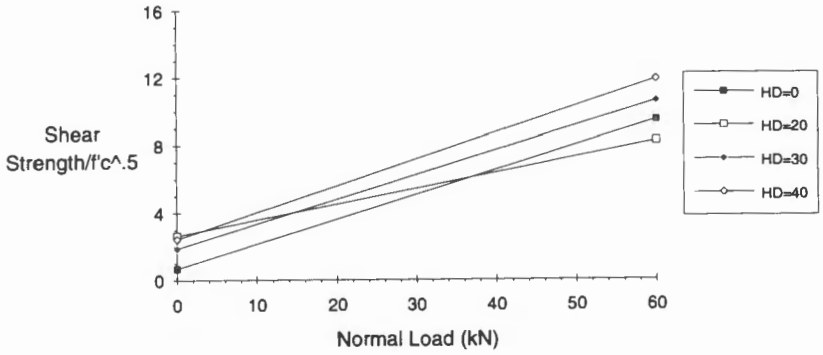

FIGURE 11 Results of linear regression.

shear box method this leads to a lower calculated value for failure load. The actual failure load as a percentage of the calculated load is indicated in brackets.

These results indicate that Equation 1 is inadequate for Test 3, and Equation 2 should not be used for heavily reinforced applications typical of the tests in this paper. The results from Tests 2 and 3 are encouraging for the shearbox equation. In all cases the shearbox equation underestimates the failure load. Further investigation into the relationship between confining force and reinforcement quantities should lead to a more accurate method for the design of the Perfobond Strip.

This work has illustrated the difficulty of extrapolating the results of shear connection test data outside the limits of experimental data. In this exercise methods have been compared with less accuracy than is desired, and it has shown the importance of operating within the confines of experimental data when considering shear connector behavior.

Full-Scale Bridge Test

Although the results of pushout tests and other small-scale tests are an ideal method for comparing the performance of various methods of shear connection and for investigating the effect of various parameters on the performance of shear connection, pushout tests do not reproduce the behavior of shear connectors in a structure because of the presence of more complex stress states.

To investigate this and to answer some questions about the performance of the Perfobond Strip without a top flange in a structure, a full-scale bridge section was constructed. The principal aims of this test are to verify the claimed fatigue performance of the Perfobond Strip and to examine the effects of stress concentrations in the tension zone of the girder because of the strip holes. Other issues to be examined are the overall performance of the concept, the performance of the deck slab without a top steel girder flange, and the performance of the shear connector particularly in negative moment regions where the slab is transversely cracked. Figure 13 illustrates the bridge that was designed. The deck slab was designed in accordance with the requirements of the Ontario Highway Bridge Design Code (*10*). The shaded section indicates the section that was constructed for testing. Figure 14 illustrates the cross section that represents one design lane of the structure. This section was subjected to 500,000 cycles of loading, with each cycle equivalent to a T44 design truck plus impact allowance, which is the AUSTROADS requirement for fatigue testing (*11*). The bridge section showed

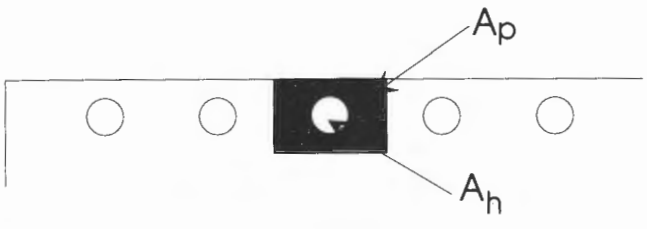

FIGURE 12 Plate and hole areas used in Equation 5.

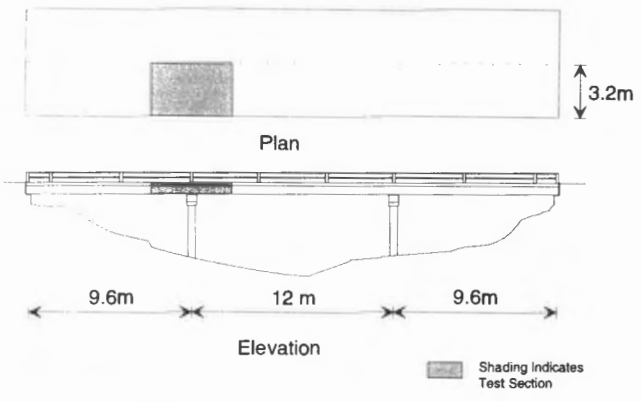

FIGURE 13 Details of full-scale bridge test.

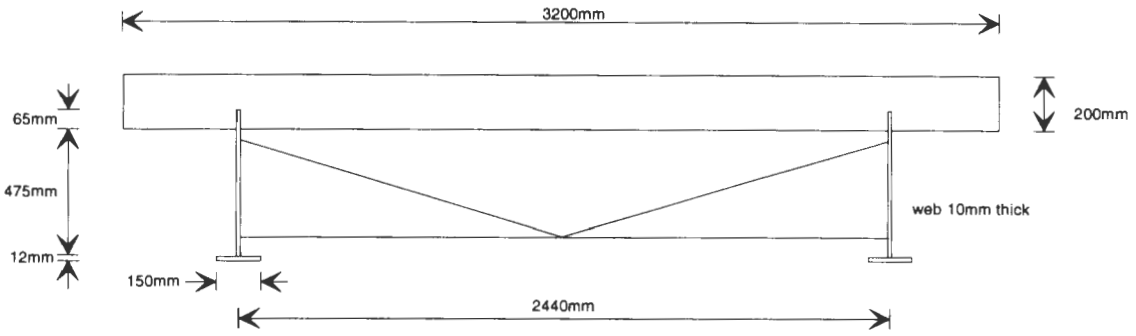

FIGURE 14 Cross section of full-scale bridge test.

no measurable signs of deterioration during the 500,000 cycles. The section also performed satisfactorily under ultimate design loads. An ultimate wheel load was also applied to the slab during testing to investigate load transferral from the slab into the web. No relative displacement occurred between the slab and the girder during this test.

Conclusion

This paper has introduced an innovative bridge cross section that utilizes a new shear connector and eliminates the top steel girder flange. An evaluation of the currently existing design theories for the Perfobond Strip has indicated inconsistencies with these design methods related to the transverse reinforcing used and the resulting failure modes. A series of pushout tests concluded that the shear connector was functional without a top steel girder flange and highlighted the fact that the strength of the concrete to plate bond does contribute to the strength of the shear connection.

A series of shear box tests was conducted and a design equation was developed that takes into account the strength of the concrete to plate bond as well as the strength of the concrete dowels in shear. This equation was related to the pushout tests using the recorded strain in the reinforcing bars to calculate a stress normal to the connector, which illustrated that more work is required in relating the reinforcing to the normal stress that it produces.

With the results of the completed work and the findings from the full-scale bridge test, an innovative new steel concrete composite bridge design, as outlined in this paper, should be feasible. This design will lead to more economically competitive composite designs, which should be more competitive in the market against existing prestressed concrete solutions.

References

1. Abe, H., H-P. Andra, R. Gruter, J. Haensel, P. Ramondenc, and R. Saul. Steel Composite Railway Bridges. *Structural Engineering International*, Vol. 2, No. 4, 1992, pp. 259–267.
2. Zellner, W. Recent Designs of Composite Bridges and a New Type of Shear Connector. *Proc., Engineering Foundation Conference Composite Construction in Steel and Concrete* (C. Buckner and I. Viest, eds., New Hampshire, 1987, pp. 241–252.
3. Leonhardt, E. F., W. Andra, H-P. Andra, and W. Harre. New Improved Shear Connector With High Fatigue Strength For Composite Structures (in German). *Beton—Und Stahlbetonbau*, Vol. 12, 1987, pp. 325–331.
4. Knowles, P. R. *Composite Steel and Concrete Construction*, Butterworths, London, 1973.
5. Roberts, W. S., and R. J. Heywood. An Innovation To Increase The Competitiveness Of Short Span Steel Concrete Composite Bridges. *Proc., 4th International Conference on Short and Medium Span Bridges. Developments In Short and Medium Span Bridge Engineering '94* (A. A. Mufti, B. Bakht, and L. G. Jaeger, eds.), Halifax, Nova Scotia, Canada, 1994, pp. 1161–1171.
6. Roberts, W. S., and R. J. Heywood. Innovations in Short Span Steel and Concrete Composite Bridges. *Proc., AUSTROADS Bridge Conference on Bridges Essential To Our Economy*, Melbourne, Australia, 1994, pp. 40(1)–40(10).
7. Roberts, W. S., and R. J. Heywood. Shear Connector For Composite Structures. *Physical Infrastructure Centre Digest*, Vol. 3, No. 2, 1992, pp. 1–3.
8. Oguejiofor, E. C., and M. U. Hosain. Perfobond Rib Connectors For Composite Beams. *Proc., Engineering Foundation Conference on Composite Construction in Steel and Concrete II* (W. S. Easterling and W. M. Roddis, eds.). Potosi, Mo. 1992, pp. 883–898.
9. Orr, D. M. F. Factorial Experiments in Concrete Research. *ACI Journal*, Vol. 69, No. 5, 1972, pp. 619–624.
10. Ontario Ministry of Transport and Communication. *Ontario Highway Bridge Design Code*, Toronto, 1983.
11. *Bridge Design Code*. AUSTROADS, Sydney, Australia, 1992.

Application of Precast, Prestressed Concrete Piles in Integral Abutment Bridges

Mounir R. Kamel, Joseph V. Benak, and Maher K. Tadros, *University of Nebraska-Lincoln*
Mostafa Jamshidi, *Nebraska Department of Roads*

In jointless integral abutment bridge superstructures, thermally induced movements must be absorbed by the abutments, which in most cases are supported on piles. Most states in the United States use steel piles in their integral abutment bridges. Research was undertaken to compare the flexibility of steel and concrete piles to determine whether concrete piles may be used in integral abutment bridges and, if not, to modify the pile abutment joint detail currently used with steel piles for possible use with concrete piles. Load-deflection tests on one steel and two concrete piles were conducted to evaluate and compare their stiffnesses. The computer program LPILE was used to analyze both concrete and steel piles in various types of soil. The results of the analysis and tests showed that concrete piles have limited flexibility for lateral loads with current pile abutment details; therefore, they can be used only in short span integral abutment bridges. For concrete piles, a new pile abutment joint was investigated. The joint consists of a neoprene bearing pad with a Teflon layer. It allows for controlled movement or rotation of the pile relative to the abutment, or both. Laboratory tests were conducted to study the behavior of the proposed joint under axial and lateral loads. The test results showed that the proposed joint would allow the use of concrete piles in integral abutment bridges of lengths comparable to those with steel piles.

Historically, a system of expansion joints, roller supports, and other structural releases was provided in long bridges to permit thermal expansion and contraction (Figure 1*a*). Providing expansion joints in a bridge, however, leads to a substantial increase in initial cost. In addition, expansion joints are sources of deterioration and frequently do not operate as intended, thus resulting in high maintenance costs. Integral abutment bridges provide an attractive design alternative (Figure 1*b*). These are defined as bridges with no movement joints at the abutments. The supporting foundation, in most cases piles, therefore has to be flexible enough to accommodate all lateral movements that develop from thermal expansion and contraction of the bridge superstructure. The maximum thermal expansion that can be allowed by the piles without significantly decreasing their vertical load capacity or integrity is of primary importance.

Currently, most states, including Nebraska, use steel H-piles in integral abutment bridges. When used as friction piles, steel H-piles must be driven deeper than concrete piles to attain their required vertical load capacity. This is because of higher concrete/soil friction than steel/soil friction and because a concrete pile has a larger cross-sectional area. A smaller number of shorter concrete piles could provide the same amount of vertical

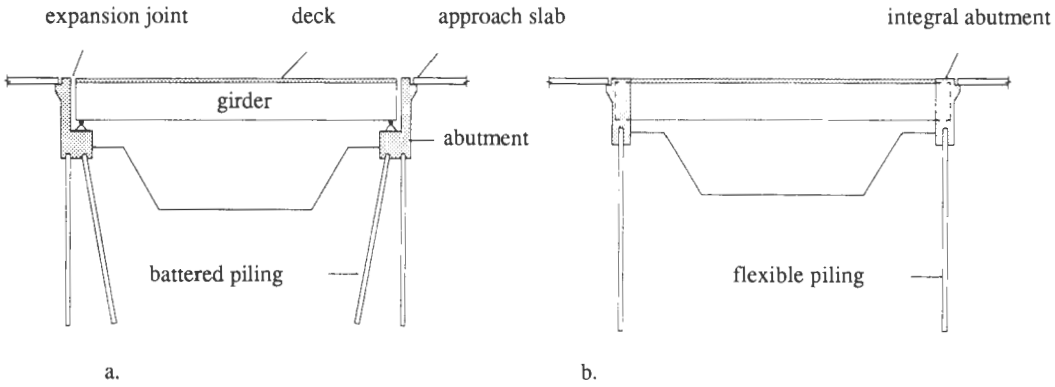

FIGURE 1 Types of bridge abutments: (*a*) bridge with expansion joints; (*b*) jointless bridge with integral abutments.

capacity as a given number of steel piles. This is true when pile loads are governed by soil bearing capacities rather than pile material properties, which is likely to happen in most practical cases.

Research Objectives

The main objectives of this research were (*a*) to evaluate the current design practices of agencies using integral abutments supported on concrete piles, especially precast concrete piles; (*b*) to determine whether precast concrete piles are feasible for use in integral bridges and if they are not; (*c*) to modify the current details that are used by various bridge designers for possible use in Nebraska.

Current Practice

A survey was conducted among highway agencies in the United States to identify those agencies that use precast, prestressed concrete piles in integral abutment bridges. The survey showed that steel, timber, concrete cast in drilled holes, concrete cast in thin steel shells, and precast concrete piles are all used in integral abutment bridges. However, most of the states prefer to use steel H-piles (Figure 2). States that use integral abutments rely on their own experience, empirical formulas, and simplified design assumptions to place span limits, instead of depending on theoretical calculations.

Many states use predrilled oversized holes filled with granular soil. It is assumed that pile stresses are relieved and allowable lengths of integral abutment bridges are increased accordingly. Various depths of these holes are required by different states. An additional feature of predrilled oversized holes is reduction of downdrag forces when compressible soil is present or minimization of the effects of elastic shortening when prestressed concrete superstructures are used, or both.

In most states where steel H-piles are used, the effect of thermal movement of the superstructure on the piles is not considered as long as bridges are designed according to their span limits and details. From a review of the literature, it was found that there is no reported specific research conducted on prestressed concrete piles in integral abutment bridges. The review included research on piles in integral abutment bridges (*1–3*), laterally loaded piles (*4–6*), and seismic design and ductility of prestressed concrete piles (*7–9*).

Laboratory Testing

Laboratory tests were conducted on three pile to pile cap specimens. The specimens were tested as cantilevers to obtain the load-deflection relationship. The objectives of the tests were to compare the stiffness of concrete piles with the stiffness of steel piles and to evaluate the stiffness S (equivalent EI) versus bending moment for concrete piles. In addition, it was necessary to study the behavior of the pile to pile cap joint in terms of whether the current joint detail provides full or partial fixity for the pile head and whether there is any relative rotation, movement, or slippage occurring at the pile to pile cap interface.

Three pile specimens were tested: one steel H-pile and two prestressed concrete piles. The steel H-pile (Specimen 1) was A36 steel 10 in. × 42 lb/ft (25.44 mm × 0.61 kN/m). The two concrete piles were 12 in. (305 mm) square, one with 9-in. (228 mm) pitch spiral reinforcement (Specimen 2) and the other with 3-in. (76-mm) pitch spiral reinforcement (Specimen 3). Pile Unit 3 represents the standard detail used in Nebraska for 12-in. (305-mm) concrete piles. The concrete pile cap dimensions and details were prepared with the same

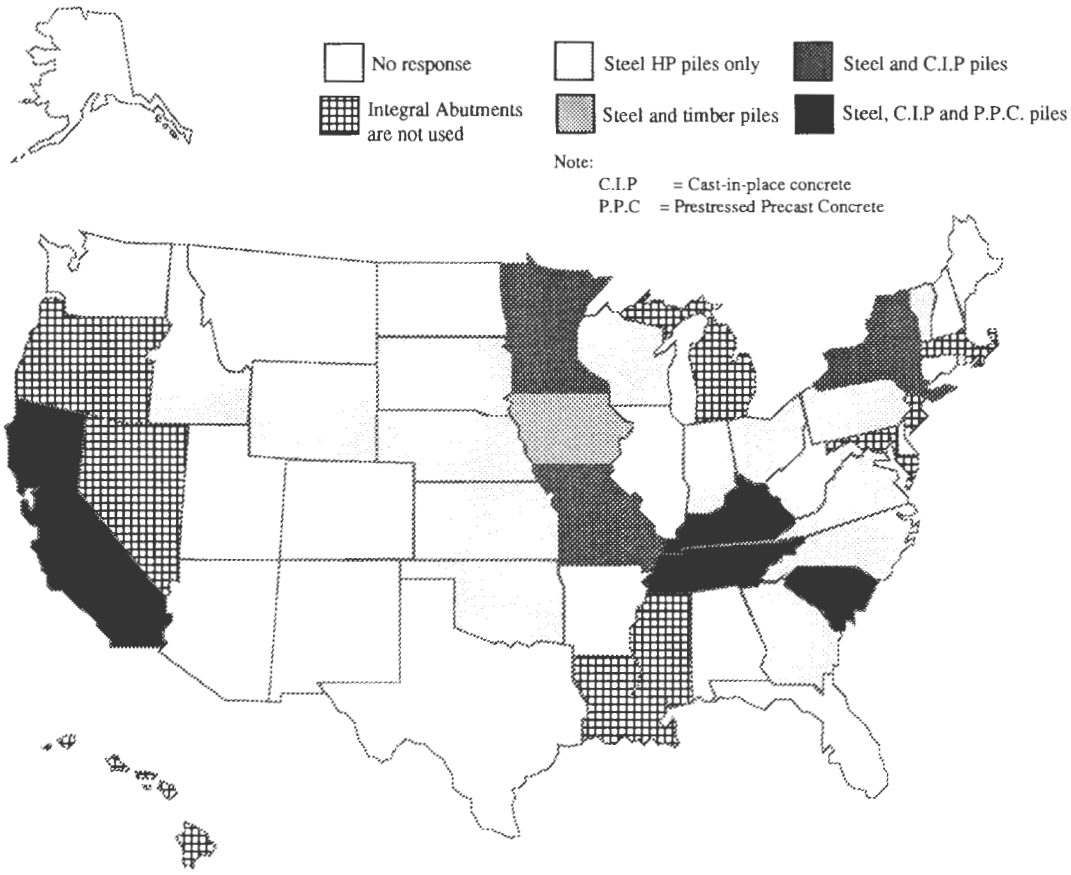

FIGURE 2 Types of piles in integral abutment bridges in various states.

standards as those currently used by the Nebraska Department of Roads so as to simulate the bridge abutment. The embedded length of both concrete and steel piles was 24 in. (610 mm). Test results are shown in Figure 3.

Stiffness of Prestressed Concrete Piles

To predict the behavior of the concrete pile at different loading stages, a nonlinear analysis was used to calculate the moment versus stiffness of the piles. The stiffness of a cracked section varies along the pile length according to the magnitude of bending moment the section is subjected to and, hence, varies according to the stage of loading. The basis of the nonlinear solution is to calculate the proper depth of compression zone for a section at a given concrete strain value. Once both the depth of compression zone and the strain distribution are obtained, all forces at the section can be calculated. These are the forces in the concrete and in the top and bottom strands as well as an applied axial load, if it exists. In these analyses, the axial applied load is 0. With a trial-and-error procedure, the proper depth of the compression zone can be obtained, and all strains and stresses at the section are known. The stiffness of the section is defined by the following equation:

$$\text{Stiffness } S, \text{ equivalent } EI = \frac{M}{\theta} \tag{1}$$

where θ is the curvature of the section, which is equal to the slope of the strain diagram and M is the moment at the section. Figure 4 shows the assumed stress and strain distribution diagrams of a pile section in a cracked stage. The nonlinear concrete stress-strain relationship is represented by Equation 2. This analytical approximation of concrete stress-strain relationship was given by Hognested (*10, 11*), as a result of his experimental study on the behavior of concrete members under combined bending and axial loads.

$$f_c = f'_c \left[2\left(\frac{\epsilon}{\epsilon_o}\right) - \left(\frac{\epsilon}{\epsilon_o}\right)^2 \right] \tag{2}$$

The integration of Equation 2 over the depth of compression zone, Figure 4, gives the total of compression

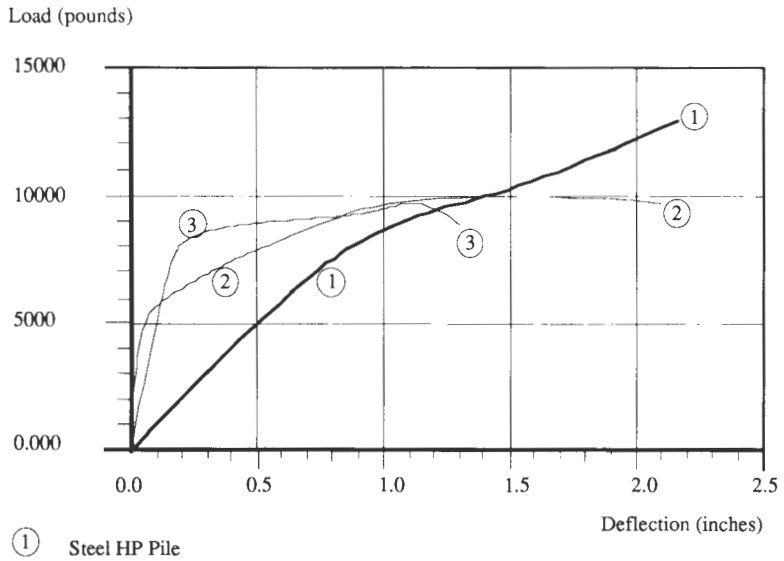

① Steel HP Pile
② 12" Prestressed Concrete Pile with 9" Pitch Spiral Reinforcement
③ 12" Prestressed Concrete Pile with 3" Pitch Spiral Reinforcement

FIGURE 3 Combined load deflection test results for steel and concrete piles.

force F_c in the concrete block as follows:

$$F_c = t \int_{x=0}^{x=c} f_c d_x \tag{3}$$

substituting ϵ by (θx) in Equation 2, where $\theta = \epsilon_c/c$, and integrating gives the total compression force F_c:

$$F_c = t f'_c \left[\left(\frac{\theta}{\epsilon_o} c^2 - \frac{1}{3} \left(\frac{\theta}{\epsilon_o} \right)^2 c^3 \right] \right. \tag{4}$$

The moment of F_c about the neutral axis can be given by the following equation:

$$M_{cNA} = t \int_{x=0}^{x=c} f_c \times d_x \tag{5}$$

Using the same substitutions as in Equation 4, the moment of the concrete force about the neutral axis is given by the following equation:

$$M_{cNA} = t f'_c \left[\frac{2}{3} \left(\frac{\theta}{\epsilon_o} \right) c^3 - \frac{1}{4} \left(\frac{\theta}{\epsilon_o} \right)^2 c^4 \right] \tag{6}$$

The stress in the strands f_{ps} can be calculated from their strain values using the following equation:

$$f_{ps} = \epsilon_{ps} \left[A + \frac{B}{\{1 + (C\epsilon_{ps})^D\}^{1/D}} \right] < f_{pu} \tag{7}$$

where

ϵ_{ps} = the strain in prestressing steel and
f_{pu} = ultimate stress of prestressing steel.

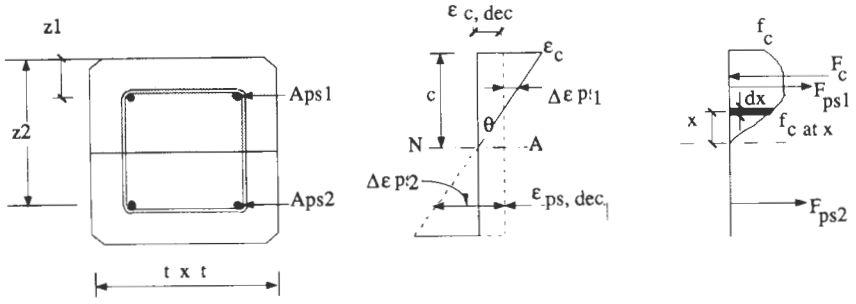

a. Cracked section b. Strain distribution c. Stress distribution

FIGURE 4 Properties of prestressed cracked pile section.

A, B, C, and D are constants presented with the details of the equation by Devalapura and Tadros (*12*). After all losses, the strain in the strands, $\epsilon_{ps,dec}$, the decompression strain caused by the effective prestressing, is calculated from the following equation:

$$\epsilon_{ps,dec} = \frac{P_{se}}{A_{ps}E_{ps}} \tag{8}$$

where

P_{se} = effective prestressing force,
A_{ps} = area of the prestressing steel, and
E_{ps} = modulus of elasticity of prestressing steel.

The initial strain in the concrete, ϵ_{ci}, before applying any bending moment, is calculated from the following equation:

$$\epsilon_{ci} = \epsilon_{c,dec} = \frac{P_{se}}{A_cE_c} \tag{9}$$

When the section is subjected to applied moment causing compression in the concrete top fibers and tension in the bottom fibers, the top strands will be subjected to a certain compression strain, $\Delta\epsilon_{ps1}$, and the bottom strand will be subjected to a tension strain, $\Delta\epsilon_{ps2}$. Flexural moment decreases the tension strain in the top strands and increases the strain in the bottom strands. The final strain in the strands is calculated by the summation of $\epsilon_{ps,dec}$ and $\Delta\epsilon_{ps}$. A spreadsheet program was used for the calculations. Figure 5 shows the calculated moment versus stiffness relationship.

Calculation of Deflection

The predicted test deflections were calculated using the variable stiffness by nonlinear analysis (*13*). The method of virtual work was used to calculate the deflections by dividing the span into 16 equal segments. The step-by-step method of calculating both the stiffness by nonlinear analysis and the deflections corresponding to each increment of load is given by Kamel (*14*). Figure 6 compares the calculated and the experimental deflection curves. The test curves represent the results of the second cycle of loading for both concrete pile tests. The second cycle is chosen to represent the behavior of the pile after the concrete is initially cracked at the first loading cycle. This assumption was used in this study and was believed to represent the case of slow cyclically laterally loaded concrete piles.

Analysis of Pile/Soil System Behavior

The LPILE computer program of Reese and Wang (*6*) was used to solve the problem of laterally loaded piles using the method of finite difference. Reese's soil *p-y* curves were used in the program and were included as a subroutine. The program provides deflection, moment

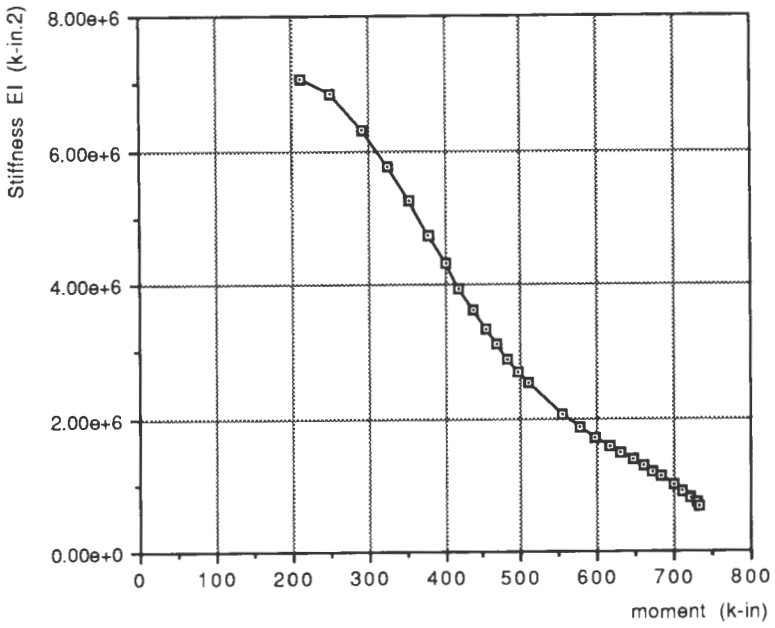

FIGURE 5 Calculated bending moment versus stiffness of 12-in. concrete pile.

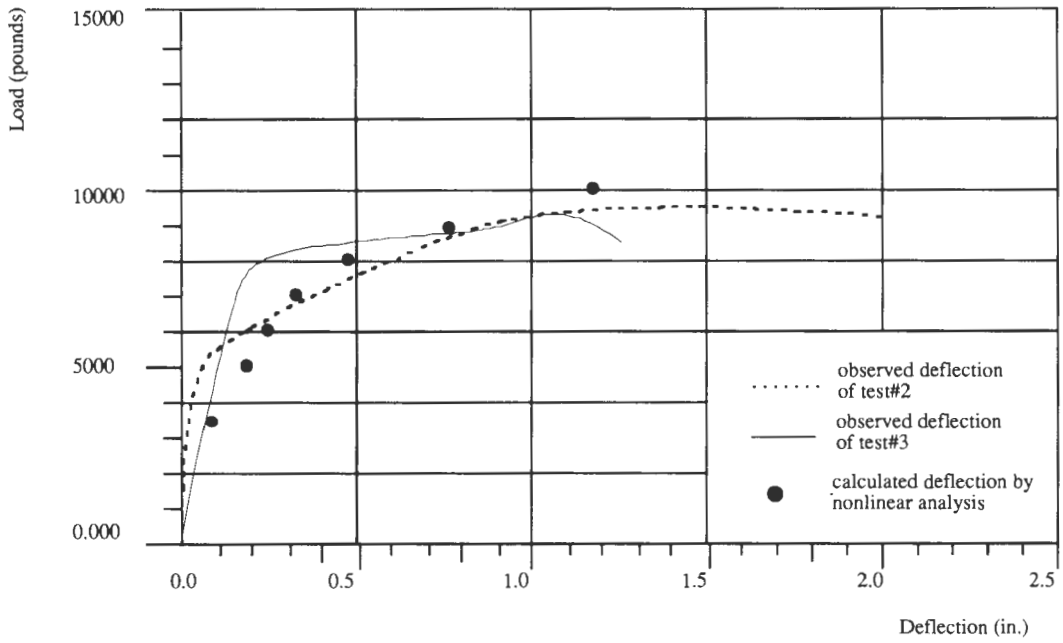

FIGURE 6 Evaluation of deflection calculation by nonlinear analysis.

diagrams, soil response, and *p-y* curves for laterally loaded piles. Reese verified the program by comparing results with a number of full-scale tests of piles under lateral loads, and these results were generally satisfactory. The program was used in this study to determine the maximum allowable horizontal deflection that a single pile can undergo without exceeding its service moment capacity.

Parametric Study

A total of 12 cases were run with the LPILE program for various types of soil and parameters. Parameters of the first five cases as an example are presented in Table 1. Cases 1, 2, 2*, 3, and 4 represent prestressed concrete piles 12 in. (305 mm) square in loose sand, loose sand followed by dense sand, dense sand, loose sand followed by soft clay, and loose sand followed by stiff clay, respectively. Cases 5 through 8 represent 10-in. (254-mm) steel H-piles with the same soils as those in Cases 1 through 4. Cases 9 through 12 represent concrete piles with a reduced modulus of elasticity of 50 percent with the same soils as those in Cases 1 through 4. The concept of using a reduced modulus of elasticity to account for creep action in laterally loaded concrete piles is being investigated by several researchers (*3,5*). Reese's *p-y* curves were used to represent soil stiffness for various types of soil.

All twelve cases were assumed to be 60 ft long (18.30 m) driven through 10 ft (3.05 m) of loose sand underlain by different types of soil, except in Case 2*. The top loose sandy layer was used to simulate the condition of using predrilled holes filled with loose sand. Case 2* was for a concrete pile driven into dense sand without a top layer of loose sand. This case is used for comparison with the case of a top loose sandy layer. In prestressed concrete piles, a constant flexural rigidity is used along the pile length. For piles subjected to large axial loads and relatively small bending moments, the section generally remains uncracked before compression stresses reach their maximum allowable limits under service loads (*14*). Both fixed and hinged pile head joints were represented in all cases. Axial loads of concrete piles were chosen to be 190 kips (845 kN) of which 100 kips (445 kN) is an effective prestressing force and 90 kips (400 kN) is applied load. Axial loads on steel piles were chosen to be 110 kips (489 kN), which represents the currently used allowable applied service load on steel piles in Nebraska.

Results of Analysis

Figures 7 and 8 show the horizontal force versus bending moment and horizontal deflection, respectively, for Cases 1, 2, and 2*. Maximum moments are determined regardless of their positions along the pile. In the case of fixed top joints, the maximum moment occurs immediately below the pile to pile cap interface. In the case of hinged joints, maximum moment occurs at a distance between 4 and 6 ft (1.2 and 1.8 m) from the pile to cap

TABLE 1 Cases of Pile/Soil Systems Run by LPILE Program

Case	Properties	Soil Layers
1 12" concrete pile in loose sand	pile properties and axial load concrete strength = 5.50 ksi modulus of elasticity = 4230 ksi effective prestressing force = 100 k applied axial load = 90 kips soil properties: loose sand soil modulus of subgrade = 25 pci density = 0.063 lb/in3 angle of internal friction = 30°	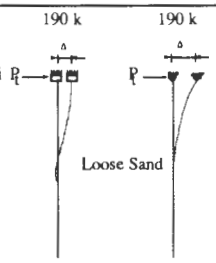
2 12" concrete pile in dense sand with 10' predrilled hole filled with loose sand	pile properties and axial load as case 1 soil properties: loose sand properties as case 1 dense sand properties: modulus of subgrade = 225 pci density = 0.075 lb/in3 angle of internal friction = 40°	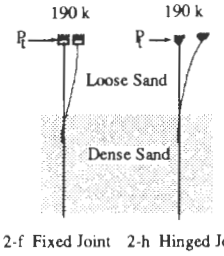
2* 12" concrete pile in dense sand without predrilled hole	Pile Properties and Axial Load as case 1 Soil Properties: loose sand properties as case 1 dense sand properties as case 2	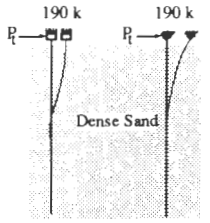
3 12" concrete pile in soft clay with 10' predrilled hole filled with loose sand	pile properties and axial load as case 1 soil properties: loose sand properties: as case 1 soft clay properties: modulus of subgrade = 30 pci density = 0.063 lb/in3 cohesion = 3.0 lb/in strain at 50% = 0.02	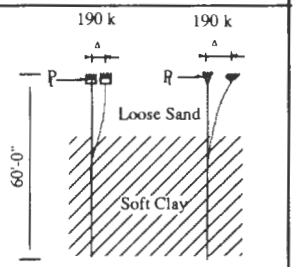
4 12" concrete pile in stiff clay with 10' predrilled hole filled with loose sand	pile properties and axial load as case 1 soil properties: loose sand properties: as case 1 stiff clay properties: modulus of subgrade = 200 pci density = 0.069 lb/in3 cohesion = 13.0 lb/in strain at 50% = 0.007	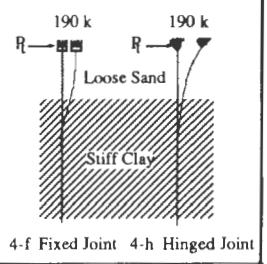
5 10x42 steel pile in loose sand	Pile Properties and Axial Load section 10x42 HP steel pile cross-sectional area = 12.4 in section modulus = 14.2 in. steel A 36 ksi soil properties: loose sand properties: as case 1	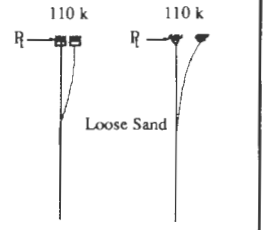

interface. Allowable moment was calculated for concrete and steel piles on the basis of their allowable compressive stress as 335 kip-in. (37.86 kN-m) and 180 kip-in. (20.34 kN-m), respectively. The corresponding lateral loads were determined from the lateral load versus moment curves, and the corresponding lateral deflections were determined from lateral load versus lateral deflection curves. A summary of the results is presented in Table 2.

Discussion of Results

Concrete Pile Versus Steel Pile

In all cases steel piles showed more capacity to accommodate lateral deflection than concrete piles, but the difference was not very significant. For example, in loose sand a steel pile with a hinged top joint could deflect up to 0.40 in. (10.2 mm) compared with 0.34 in. (8.6 mm) for a concrete pile under the same conditions. Similar behavior was obtained under other conditions. However, in the case of concrete piles, a lateral force of 7.8 kips (34.69 kN) was needed to deflect the pile 8.6 mm (0.34 in.), whereas only 5.1 kips (22.68 kN) was needed to deflect the steel pile 0.40 in (10.1 mm). This result agreed with laboratory test results in which the steel pile showed more flexibility than concrete piles.

Effect of Predrilled Hole

The common practice of using a predrilled hole filled with loose sand was studied by introducing a layer of loose sand at the top 10 ft (3.05 m) of embedment. Table 2 and the resulting curves show that the loose sandy layer has a significant effect on the behavior of the examined cases. Because most of the deflections and moments occur within the top 10 to 12 ft (3.05 to 3.66 m) of the pile, the soil type in this region will have a significant influence on the behavior of the pile under lateral loads. This result is clearly shown in Case 2* when loose sand was not used. In this case a very small

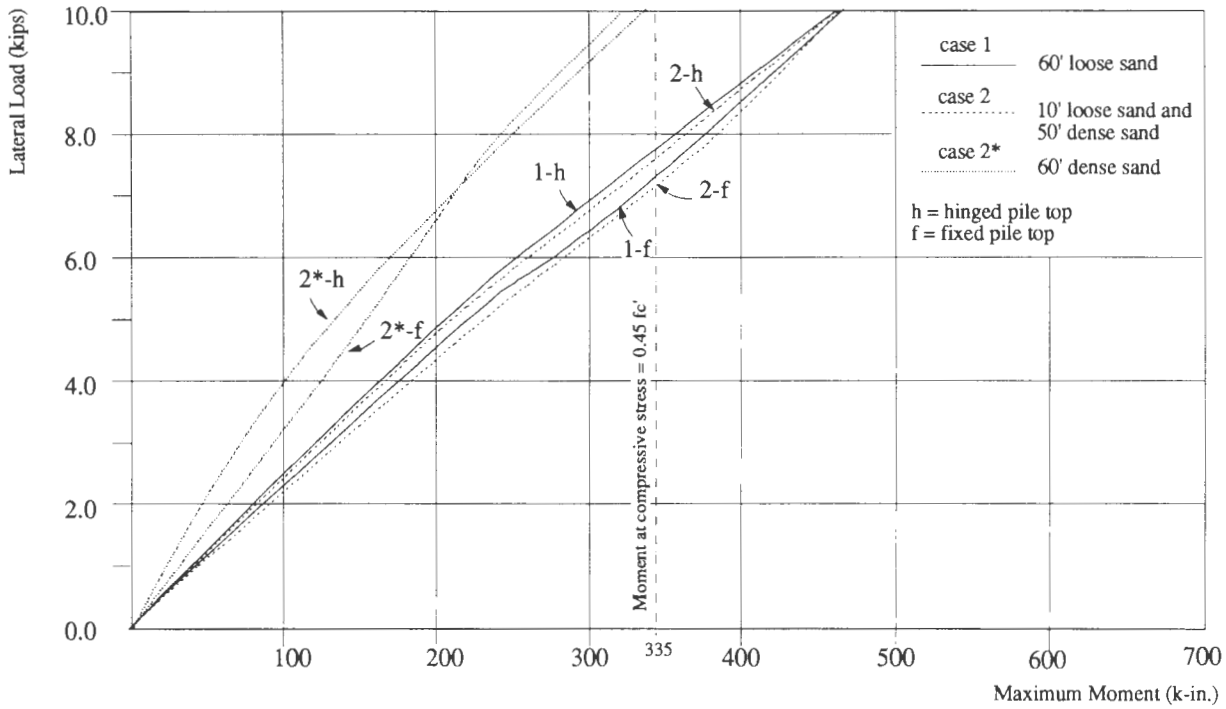

FIGURE 7 Horizontal force versus maximum bending moment for 12-in. concrete pile in sand.

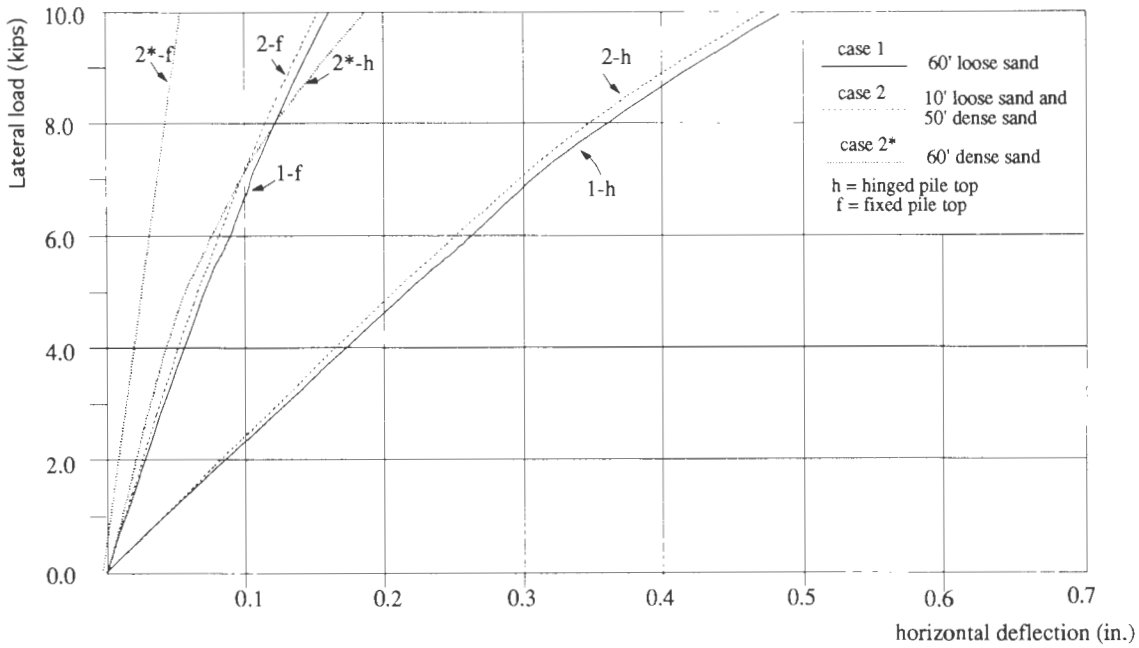

FIGURE 8 Horizontal force versus horizontal deflection for 12-in. concrete pile in sand.

TABLE 2 Summary of Analytical Results

Case	Lateral load corresponding to max. moment kip (KN)	Deflection corresponding to max. load in. (mm)	Case	Lateral load corresponding to max. moment kip (KN)	Deflection corresponding to max. load in. (mm)	Case	Lateral load corresponding to max. moment kip (KN)	Deflection corresponding to max. load in. (mm)
1-h	7.8 (34.69)	0.34 (8.6)	5-h	7.0 (31.14)	0.65(16.5)	9-h	7.8 (34.69)	0.51 (12.9)
1-f	7.2 (32.02)	0.11 (2.8)	5-f	8.0 (35.58)	0.25 (6.3)	9-f	8.1 (36.03)	0.18 (4.6))
2-h	7.8 (34.69)	0.31 (7.9)	6-h	7.0 (31.14)	0.64 (16.2)	10-h	7.8 (34.69)	0.48 (12.2)
2-f	7.2 (32.02)	0.10 (2.5)	6-f	8.0 (35.58)	0.24 (6.1)	10-f	8.1 (36.02)	0.17 (4.3)
2*-h	10.5 (46.70)	0.2 (5.1)	7-h	7.0 (31.14)	0.7 (17.8)	11-h	7.8 (34.69)	0.53 (13.5)
2*-f	10.5 (46.70)	0.05 (1.3)	7-f	8.0 (35.58)	0.22 (5.6)	11-f	8.1 (36.03)	0.18 (4.6)
3-h	7.8 (34.69)	0.34 (8.6)	8-h	7.0 (31.14)	0.65 (16.5)	12-h	7.8 (34.69)	0.51 (12.9)
3-f	7.2 (32.02)	0.12 (3.0)	8-f	8.0 (35.58)	0.21 (5.3)	12-f	8.1 (36.03)	0.18 (4.6)
4-h	7.7 (34.25)	0.32 (8.1)						
4-f	7.2 (32.02)	0.1 (2.5)	*f* = *fixed joint*			*h* = *hinged joint*		

amount of deflection was sufficient to cause the maximum allowable lateral load. In addition, very close results were obtained in all cases when using an upper 10-ft (3.05-m) loose sand layer, regardless of the type of soil below this depth.

Effect of Reduced Modulus of Elasticity

Reducing the modulus of elasticity has a significant effect on the deflection of the concrete piles. In Cases 9 through 12, maximum deflections were increased by about 50 percent when using a reduced modulus of elasticity.

Proposed Pile Abutment Joint

The feasibility of using a sliding joint for pile/abutment connection was investigated. A joint capable of allowing the abutment to slide and rotate over the top of the pile would allow for more lateral expansion than would a rotationally restrained pile top connection. Figure 9 shows a proposed joint detail. A bearing pad was used at the top of the pile. The pad consists of a layer of random-oriented reinforced-fiber neoprene coated with a Teflon layer. The Teflon layer allows lateral movement against an embedded steel plate that is connected to the cast-in-place concrete abutment by welded studs or rebars. The four sides of the pile top were covered by compressible material such as expanded polystyrene or urethane Styrofoam. The compressible material at the two sides, in the direction of deflection, allows lateral movements. On the other two faces (front and rear) the compressible material was used to break the bond between the abutment poured concrete and the pile head when the abutment moves laterally. The joint could be manufactured in one piece and placed on the pile top once the pile is driven to its final position. In cases where the pile top is damaged as a result of driving, the damaged part should be either cut or cast with rich cement grout to keep the original dimensions of the pile. If the damage is not serious, the pile top may not require further treatment before placing the joint.

Testing of Proposed Joint

A prototype of pile abutment joint was tested in the laboratory to verify its behavior. The bearing elastomer pad should have the following capabilities:

1. Carry an applied axial load of the pile, which is about 90 kips (400 kN) for a 12-in. (305-mm) concrete pile,
2. Allow some rotation between upper and lower faces of the pad; and
3. Have minimum coefficient of friction to allow sliding against the upper steel plate.

There are many bearing pad producers, and each one provides its own design guides. Any bearing pad that meets the above requirements could be used. The chosen pad for the test was manufactured by JVI, Inc., and designed according to their Design Guide Handbook (7). A sliding pad was chosen with a thickness of ½ in. (12.7 mm) and a dimension of 8 × 8 in. (203 × 203 mm). The JVI "MASTICORD" pad was coated with a Teflon layer 3/32 in. (2.4 mm) thick. The pad has an allowable compressive stress of 2.50 ksi (17.23 Mpa) and a coefficient of friction of less than 5 percent against smooth stainless steel surface (2B or mirror finish (7)).

Figure 10 shows the schematic test setup as well as the test results. Vertical loads as well as lateral loads were applied to the joint. Lateral deflections were measured for various lateral loads acting under constant

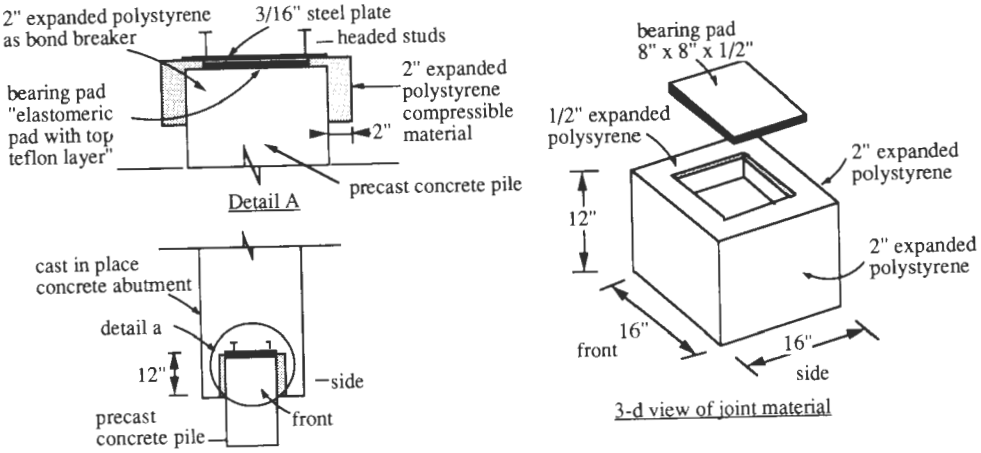

FIGURE 9 Proposed concrete pile abutment joint.

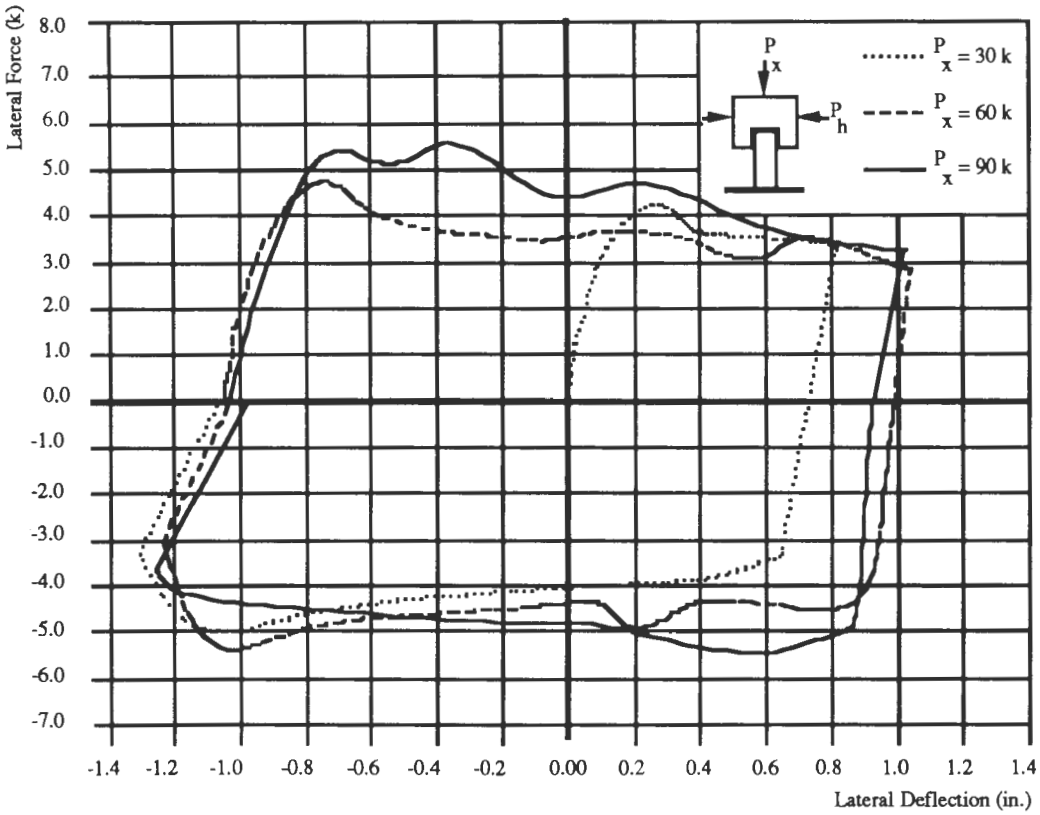

FIGURE 10 Test results of the proposed pile to pile cap joint.

vertical loads. The vertical loads were 30, 60, and 90 kips (133, 266, and 400 kN). Lateral loads were applied until the cap moved against the pile head unit for about 1 in. (25.4 mm); then the load was reversed.

The results show the capability of the proposed joint to allow lateral movements of about 1 in. (25.4 mm) in each direction under sustained vertical loads up to 90 kips (400 kN). The lateral force that overcomes the friction and the resistance of the compressible material was about 5 kips (22.3 kN). The observed maximum vertical deflections caused by the compressibility of the joint system were 0.1, 0.17, and 0.2 in. (2.5, 4.3, 5 mm), corresponding to 30, 60, and 90 kips (133, 266, and 400 kN) vertical loads.

Longitudinal Stability

According to AASHTO (*15*), braking force is estimated as 5 percent of the bridge live load. In bridges, live load normally does not exceed 40 percent of the total vertical load. Therefore, the maximum horizontal longitudinal breaking force on the pile is estimated to be 1.8 kips (8.0 kN). Testing of the proposed joint showed that it could resist up to 5 kips (22 kN) before sliding occurs.

Cost Analysis

The total material cost of the proposed joint was $25. The cost of the bearing pad was $18, and the rest of the cost was for the steel plate and the compressible material. This cost is equivalent to the approximate cost of 2 ft (0.6 m) of pile. When the proposed joint is used, it will not be necessary to use the predrilled holes filled with loose sand unless they are needed for other purposes.

Conclusion

The detail of the pile abutment connection that is currently used in Nebraska and other states for steel piles needs to be modified for possible use with concrete piles. Allowable lateral deflections of concrete piles with rotationally restrained pile abutment joints would be small; hence, the use of such joints with concrete piles would be limited to short integral abutment bridges.

Using the uncracked stiffness properties for prestressed concrete piles is a proper assumption for calculating lateral deflections of a fully loaded pile. Attempting to take advantage of a reduced cracked section stiffness in calculating lateral deflections is not an appropriate assumption.

The 10-in. (254-mm) HP steel pile is more flexible than the prestressed 12-in. (305-mm) concrete pile. The capacity of steel piles to accommodate lateral deflections is greater than that of concrete piles. However, the difference is not significant when compression stresses are limited to their allowable values.

The common practice of using a predrilled hole filled with loose sand has a significant effect on the behavior of laterally loaded piles. Because most of the deflections and moments occur within the top 10 ft (3.05 m) of the pile, soil type in this region will always control the behavior of the pile regardless of the type of soil below this depth.

A new type of joint is proposed for use at the top of concrete piles. The joint allows relative lateral movement up to 1 in. (25.4 mm), with a maximum generated lateral load of 5 kips (135 kN). In most soil types the concrete piles deflect elastically about 0.15 in. (3.8 mm) under this lateral load. The proposed joint would allow the prestressed concrete piles to be used in integral abutment bridges with a total allowable movement of at least 2.3 in. (58.4 mm). Therefore, concrete piles could provide an alternative design solution in integral abutment bridges where steel piles are currently used.

ACKNOWLEDGMENTS

The authors wish to thank the Nebraska Department of Roads, the Precast Concrete Association of Nebraska, and the Center for Infrastructure Research, University of Nebraska, for sponsoring this project. Special thanks are due to Morrie Workman of the Wilson Concrete Company and his staff for their assistance during the pile testing. Thanks go to Amin Einea for his valuable input in reviewing this paper. Deborah Derrick was helpful in proofreading and providing editorial input.

REFERENCES

1. Greimann, L. F., R. E. Abendroth, D. E. Johnson, and P. B. Ebner. *Pile Design and Tests for Integral Abutment Bridges*. Final Report. Iowa DOT Project HR-273, ISU-ERI-Ames 88060. Dec. 1987.
2. Greimann, L. F., D. D. Girton, and T. R. Hawkinson. *Validation of Design Recommendations for Integral Abutment Piles*. Report. Iowa DOT Project HR-292, Ames, Sept. 1989.
3. Wasserman, E. P. Jointless Bridge Decks. *Engineering Journal*, American Institute of Steel Construction, 3rd quarter, 1987.
4. Evans, L. T., Jr., and J. M. Duncan. *Simplified Analysis of Laterally Loaded Piles*. Report UCB-GT/82-04. De-

partment of Civil Engineering, University of California, Berkeley, July 1982.
5. Reese, L. C. Behavior of Piles and Pile Groups Under Lateral Load. Research Report. FHWA/RD-85/106. U.S. Department of Transportation, Washington, D.C., 1985.
6. Reese, L. C., and S.-T. Wang. *Documentation of Computer Program LPILE, Version 3*. University of Texas, Austin, 1989.
7. *Masticord Structural Bearing Pad, Design Guide*, 3rd ed. JVI Inc., Skokie, Ill.
8. Sheppard, D. A. Seismic Design of Prestressed Concrete Piling. *PCI Journal*, Vol. 28, No. 2, March–April 1983.
9. Pam, H. J., and R. Park. Flexural Strength and Ductility Analysis of Spirally Reinforced Prestressed Concrete Piles. *PCI Journal*, Vol. 35, No. 4, pp. 64–83, July–August 1990.
10. Hognestad, E. *A Study of Combined Bending and Axial Load in Reinforced Concrete Members*. Bulletin 399. University of Illinois Engineering Experiment Station, Urbana, Nov. 1951.
11. Lin, T. Y. *Design of Prestressed Concrete Structures*, 3rd ed., p. 5.29, 1981.
12. Devalapura, R., and M. K. Tadros. Stress-Strain Modeling of 270 ksi Low-Relaxation Prestressing Strands. *PCI Journal*, Vol. 37, No. 2, March–April 1992.
13. Tadros, M. K. Expedient Service Load Analysis of Cracked Prestressed Concrete Sections. *PCI Journal*, Vol. 27, No. 6, Nov.–Dec. 1982.
14. Kamel, M. Precast Prestressed Concrete Piles in Integral Abutment Bridges. Master's thesis. University of Nebraska, 1992.
15. *Standard Specifications for Highway Bridges*, 13th ed. AASHTO, Washington, D.C., 1983.

PRESTRESSED CONCRETE BRIDGES

Development Length of Prestressing Strand in Bridge Members

Susan N. Lane, *Federal Highway Administration*

FHWA is undertaking a research study on the development length of prestressing strand. The objective is to investigate the validity of AASHTO Equation 9-32 for predicting both the transfer length and flexural bond length components of development length for fully bonded, straight, uncoated, and epoxy-coated prestressing strand. Toward this end, the effects of strand diameter [9.5, 12.7, and 15.2 mm (3/8, 0.5, and 0.6 in.)], concrete strength, strand coating (uncoated or epoxy coated), and strand spacing on development length will be evaluated. The phase of the research study involves full-size prestressed concrete bridge members. A total of 32 AASHTO Type II prestressed concrete bridge girders and 32 prestressed concrete deck panels were fabricated at a precast concrete plant in Winchester, Virginia. All of the members will undergo transfer and development length experimentation. The fabrication, instrumentation, and experimentation procedures, as well as partial results, are described. Experimentation is scheduled to be finished in the spring of 1995.

The bond of prestressing strands in pretensioned concrete members has been studied by many researchers over the last few years. Much of this research was initiated as a result of FHWA's October 1988 memorandum. The memorandum increased the required development length for fully bonded uncoated strand by 1.6 times the development length specified by AASHTO in Equation 9-32 (*1*). For debonded strand, this factor was specified as 2.0. The memorandum also disallowed the use of a strand 15.2 mm (0.6 in.) in diameter in a pretensioned application and restricted the minimum strand spacing (center-to-center of strand) to four times the nominal strand diameter. The FHWA memorandum indicated that its restrictions were adopted only as an interim measure, until research results indicate otherwise and AASHTO adopts the results.

The advent of epoxy-coated prestressing strand has also prompted research on bond of prestressing strand. Epoxy-coated strand was developed by a manufacturer to provide corrosion protection for prestressing strand. This epoxy coating has a chemical formulation that is different from that of the epoxy coating found on reinforcing bars, and it is also much thicker. The thickness of the epoxy coating on prestressing strands is 0.64 to 1.14 mm (0.025 to 0.45 in.) thick, whereas the epoxy coating on reinforcing bars is 0.18 to 0.30 mm (0.007 to 0.012 in.) thick (ASTM A 882-92 and ASTM A 775-93a). For pretensioned applications, particles of grit are embedded in the surface of the epoxy coating to enhance the bond of the coated strand to the concrete. Questions arose as to the applicability of the AASHTO equation for development length to pretensioned members containing epoxy-coated strand.

FHWA initiated its research effort in the spring of 1990 in an effort to answer questions concerning bond for both uncoated and epoxy-coated prestressing

strand. The research effort is in two phases: Phase 1 involves rectangular prestressed concrete specimens, whereas Phase 2 uses full-size prestressed concrete deck panels and girders.

Rectangular prestressed concrete specimens for Phase 1 were fabricated and evaluated at the FHWA Structures Laboratory in the Turner-Fairbank Highway Research Center in McLean, Virginia. A total of 50 rectangular specimens were fabricated: 24 had concentric uncoated or epoxy-coated strands, 24 had eccentric uncoated or epoxy-coated strands, and 2 were used to monitor shrinkage of the concrete. The specimens ranged in size from 102 × 102 × 3658 mm (4 in. × 4 in. × 12 ft) to 356 × 356 × 8534 mm (14 in. × 14 in. × 28 ft). Three strand sizes were used in the following diameters, namely 9.5, 12.7, and 15.2 mm (3/8, 0.5, and 0.6 in.), and the specimens contained either one strand or four strands. The details of this phase of the study are provided elsewhere (*2–4*). The rectangular specimens containing concentric strands underwent transfer length experimentation only. Both transfer and development length experimentation were performed for the rectangular specimens containing eccentric strands. The broad conclusions from the first phase of the study were as follows:

- The AASHTO transfer and development length expressions were unconservative for specimens with multiple uncoated strands of all diameters;
- The AASHTO transfer length expression was conservative for specimens containing epoxy-coated strands, except for the specimens containing four strands 12.7 mm (0.5 in.) in diameter; and
- The AASHTO development length expression was conservative for all specimens containing epoxy-coated strands.

Full-size members for Phase 2 of the study were fabricated at Shockey Bros., Inc., precast concrete plant in Winchester, Virginia. A total of 32 AASHTO Type II prestressed concrete I-girders and 32 prestressed concrete subdeck panels (hereafter called deck panels) were fabricated from February through May 1994. Development length experimentation began in May 1994 and is still ongoing at the time this paper was written.

This paper describes the fabrication, instrumentation, and methods of experimentation for Phase 2 of the study. Because the experimentation is ongoing as of the writing of this paper, limited results will be presented here.

Background

In a pretensioned member, the prestressing force in a prestressing strand is transferred from the strand to the concrete by bond. A certain distance is needed to achieve bonding at ultimate load between the steel strand and the concrete to attain the capacity of the member. This distance, measured from the end of the member, is called the development length.

The development length consists of two components: transfer length and flexural bond length. The transfer length is the distance from the end of the member needed to fully transfer the effective prestress (f_{se}) by bond from the steel strand to the concrete. The flexural bond length is the additional embedment length needed beyond the transfer length to achieve bonding between the strand and the concrete to attain the stress in the strand at the ultimate load of the member (f_{su}^*) (*5–7*).

In Article 9.27 of the AASHTO specifications (*1*), the development length of a member is given by Equation 9-32 as

$$(f_{su}^* - \frac{2}{3} f_{se})D \tag{1}$$

where D equals the nominal diameter of the strand in inches.

This expression can be rewritten in terms of its constituent parts (*6*) as

$$L_d = \frac{f_{se}D}{3} + (f_{su}^* - f_{se})D \tag{2}$$

where

L_d = development length,
$\frac{f_{se}D}{3}$ = transfer length, and
$(f_{su}^* - f_{se})D$ = flexural bond length.

In Article 9.20.2.4 of the AASHTO specifications (*1*), it is stated that the transfer length component of the development length may be assumed to be equal to 50 times the nominal diameter of the strand. The multipliers specified in the FHWA memorandum referred to previously would be applied to equation 1 or 2 mentioned earlier.

Description of Members

Girders

A total of 32 AASHTO Type II prestressed concrete I-girders were fabricated as part of this study. Half of the girders contained epoxy-coated strand, whereas the other half contained uncoated strand. Three different strand patterns were used in the girders, as shown in Figure 1. Strand Pattern A contained eight strands 12.7

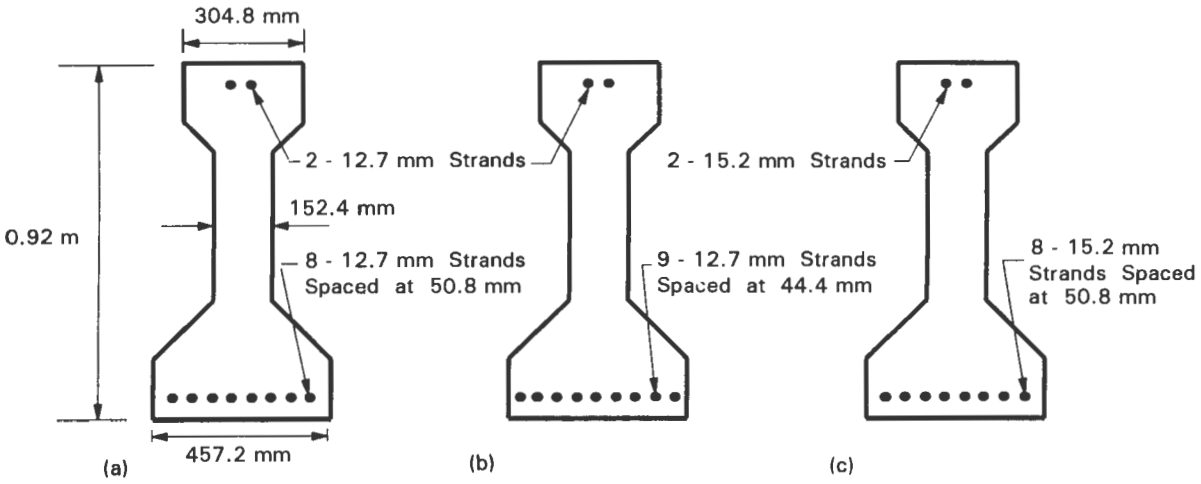

FIGURE 1 AASHTO Type II girder with various strand patterns: (*a*) Strand Pattern A; (*b*) Strand Pattern B; and (*c*) Strand Pattern C. (1 m = 3.28 ft; 1 mm = 0.039 in.)

mm (0.5 in.) in diameter spaced at 50.8 mm (2 in.) in one row in the bottom flange and two strands 12.7 mm (0.5 in.) in diameter in the top flange (Figure 1*a*). Strand Pattern B is shown in Figure 1*b*; it contained nine strands 12.7 mm (0.5 in.) in diameter spaced at 44.4 mm (1.75 in.) in one row in the bottom flange and two strands 12.7 mm (0.5 in.) in diameter in the top flange. Strand Pattern C contained eight strands 15.2 mm (0.6 in.) in diameter spaced at 50.8 mm (2 in.) in one row in the bottom flange and two strands 15.2 mm (0.6 in.) in diameter in the top flange (Figure 1*c*). All of the strands were fully stressed.

All of the girders were 9.46 m (31 ft) long. A total of 24 of the girders had a 28-day design concrete compressive strength of 34.4 MPa (5 ksi), with a specified maximum 28-day compressive strength of 44.8 MPa (6.5 ksi). The remaining eight had a 28-day design compressive strength of 68.9 MPa (10 ksi), with a specified maximum 28-day compressive strength of 89.6 MPa (13 ksi). These limits, or windows, of concrete strength were specified to differentiate between the two strengths of concrete. A matrix of the makeup of the girders is given in Table 1.

As can be seen from Table 1, 12 of the girders will be made composite with a cast-in-place slab. This will be done in an attempt to increase the strain in the bottom strands at failure. In a report for FHWA (*8*, pp. 56–57) Buckner stated the following:

> . . . specimens proportioned to have strains at failure near yield (0.010) have usually achieved their predicted moment strengths at strand embedments calculated by the current ACI/AASHTO [development length] expression. Specimens proportioned to achieve strains at failure of about 0.035 have typically failed to reach their expected moment capacities due to premature bond failure.

In an attempt to verify this observation, the FHWA research program has included girders with and without composite slabs. This will provide a range of strand strain values at failure of the girders.

All of the girders contained single-leg stirrups, spaced at 76.2 mm (3 in.), which alternated sides of the cross section at each spacing. Confinement reinforcement was placed in the top and bottom flanges for the first 0.92 m (3 ft) on each end of a girder.

Deck Panels

A total of 32 prestressed concrete deck panels were fabricated as part of this study. Half of the deck panels contained epoxy-coated strand, whereas the other half contained uncoated strand. The deck panels were designed and fabricated in four different sizes, as shown in Figure 2.

Two different deck panel thicknesses were chosen, namely 76.2 mm (3 in.) and 88.9 mm (3.5 in.). This was done to determine whether there is any difference in bond behavior between deck panels of these thicknesses. Currently, FHWA specifies an 88.9-mm (3.5-in.) subdeck panel thickness for bridges built with federal-aid monies, whereas the Precast/Prestressed Concrete Institute (PCI) recommends a minimum deck panel thickness of 76.2 mm (3 in.) (*9*).

Two different panel lengths were selected. Deck panel types A and B were 2.52 m (8.25 ft) long, whereas deck panel Types C and D were 3.05 m (10 ft) long. This was done to provide varying embedment lengths

TABLE 1 AASHTO Type II Girders

Girder No.	Design f'_c (MPa)	Strand Pattern	Strand Epoxy Coated (E) or Uncoated (U)	Made Composite With Slab?
33, 34	34.4	A	U	No
35, 36	34.4	A	E	No
37, 38	68.9	A	U	No
89, 90	68.9	A	E	No
41, 42	34.4	A	U	Yes
43, 44	34.4	A	E	Yes
57, 58	34.4	B	U	No
59, 60	34.4	B	E	No
61, 62	34.4	B	U	Yes
63, 64	34.4	B	E	Yes
45, 46	34.4	C	U	No
47, 48	34.4	C	E	No
49, 50	68.9	C	U	No
51, 52	68.9	C	E	No
53, 54	34.4	C	U	Yes
55, 56	34.4	C	E	Yes

1 MPa = 0.145 ksi

for the development length experimentation. The 2.52-m (8.25-ft) length represents an overall length less than twice the calculated AASHTO development length; the 3.05-m (10-ft) length represents an overall length greater than twice the calculated AASHTO development length.

All of the deck panels had a 28-day design concrete compressive strength of 34.3 MPa (5 ksi), and they all contained strands 9.5 mm (3/8 in.) in diameter strands. A matrix of the makeup of the deck panels is given in Table 2. As can be seen from Table 2, half of the deck panels will be made composite with a cast-in-place slab. This will be done in an attempt to increase the strain in the strands at failure. All deck panels contained a layer of intermittently spaced reinforcing bars on top of the strands and perpendicular to them. The reinforcing bars functioned as a means of distributing the load and met the minimum reinforcement requirement specified in Article 9.23.2 of the AASHTO specifications (*1*).

Materials

Prestressing Strand

All of the uncoated prestressing steel was seven-wire, Grade 270 [1,860 MPa (270 ksi) guaranteed ultimate tensile strength], low-relaxation strand, conforming to ASTM Standard A 416-90a. The strand was used in the as-received condition, with occasional surface rust visible but no pitting. Tests were run to determine any phosphate residue left on the strand surface. Also, concrete blocks containing untensioned, uncoated, and epoxy-coated strands were cast with samples from the as-

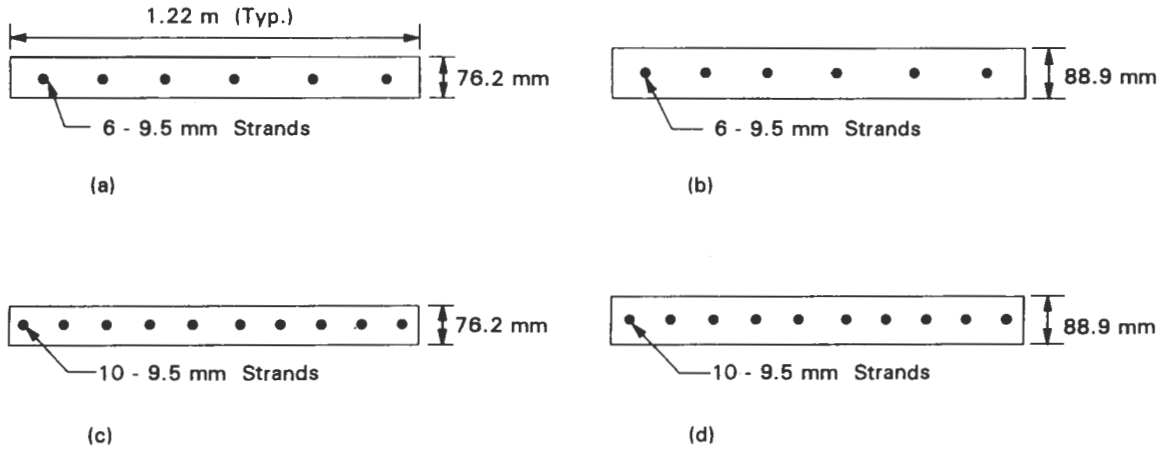

FIGURE 2 Deck panels (*a*) Type A; (*b*) Type B; (*c*) Type C; and (*d*) Type D. (1 m = 3.28 ft; 1 mm = 0.039 in.)

TABLE 2 Deck Panels

Deck Panel No.	Design f_c' (MPa)	Deck Panel Type	No. Of Strands	Length of Panel (m)	Strand Epoxy Coated (E) or Uncoated (U)	Made Composite With Slab?
1, 2	34.4	A	6	2.52	U	No
3, 4	34.4	A	6	2.52	U	Yes
5, 6	34.4	A	6	2.52	E	No
7, 8	34.4	A	6	2.52	E	Yes
9, 10	34.4	B	6	2.52	U	No
11, 12	34.4	B	6	2.52	U	Yes
13, 14	34.4	B	6	2.52	E	No
15, 16	34.4	B	6	2.52	E	Yes
17, 18	34.4	C	10	3.05	U	No
19, 20	34.4	C	10	3.05	U	Yes
21, 22	34.4	C	10	3.05	E	No
23, 24	34.4	C	10	3.05	E	Yes
25, 26	34.4	D	10	3.05	U	No
27, 28	34.4	D	10	3.05	U	Yes
29, 30	34.4	D	10	3.05	E	No
31, 32	34.4	D	10	3.05	E	Yes

1 MPa = 0.145 ksi
1 m = 3.28 ft

received strand reels. Pull-out tests were later conducted on the strands in these blocks in an attempt to identify a possible measure of strand surface condition. The pull-out tests will also be used to investigate a possible correlation between pull-out values and transfer length. The results and analysis from the phosphate residue test and pull-out tests are beyond the scope of this paper.

The epoxy-coated prestressing steel was seven-wire, Grade 270, low-relaxation strand, conforming to ASTM Standard A 882-92. This strand had small aluminum oxide particles called "grit" embedded in the surface of the epoxy coating.

Concrete

The same concrete mix was used for the deck panels and for the normal-strength [34.4-MPa (5-ksi)] girders. This concrete mix was designed to obtain a 28-day compressive strength (f_c'), which was greater than or equal to 34.4 MPa (5 ksi) and less than or equal to 44.8 MPa (6.5 ksi). The mixture was also designed to have a compressive strength of 27.6 MPa (4 ksi) for prestress release in approximately 24 hr. This concrete mix consisted of Type III portland cement, sand, crushed limestone aggregate, water, an air-entraining admixture, a retarder, and a superplasticizer. The average water/cement ratio for the 16 batches was 0.44.

The precast concrete plant used cylinders 101.6 × 203.2 mm (4 × 8 in.) to determine concrete compressive strength. These cylinders measuring 101.6 × 203.2 mm (4 × 8 in.) were cured in heated containers where the temperature matched that of the heat applied to the prestressing bed for curing. When the compressive strength of these cylinders met or exceeded 27.6 MPa (4 ksi), the strands were detensioned. At that time, researchers tested cylinders 152.4 × 304.8 mm (6 × 12 in.), cured at the prestressing bed, for a corresponding concrete compressive strength at the time of prestress release. The 28-day concrete compressive strengths were determined by testing two sets of cylinders 152.4 × 304.8 mm (6 × 12 in.): one set was cured in a moist room and one set was cured in air with the members.

The average compressive strength for the normal-strength concrete mix at the time of prestress release was 31.5 MPa (4.57 ksi). The average 28-day compressive strength for this concrete was 44.2 MPa (6.42 ksi) for the set of cylinders that was air cured, and 49.2 MPa (7.15 ksi) for the set of cylinders that was moist cured.

The concrete mix used in the high-strength girders was designed to obtain a 28-day compressive strength that was greater than or equal to 68.9 MPa (10 ksi) and less than or equal to 89.6 MPa (13 ksi). The mixture was also designed to have a compressive strength of 48.2 MPa (7 ksi) for prestress release in approximately 24 hr. This concrete mix consisted of Type III portland cement, microsilica, sand, crushed traprock aggregate, water, an air-entraining admixture, a retarder, and a superplasticizer. The average water/cementitious material ratio for the four batches was 0.33.

The average compressive strength for the high-strength concrete mix at the time of prestress release was 54.3 MPa (7.88 ksi). The average 28-day compressive strength for this concrete was 71.3 MPa (10.35 ksi) for the set of cylinders that was air cured and 74.2 MPa (10.77 ksi) for the set of cylinders that was moist cured.

Fabrication

The fabrication process consisted of the following: stressing the strand, mixing the concrete at an on-site batch plant, transporting the concrete to the stressing bed via a ready-mix truck, casting the concrete, curing the concrete, and detensioning (releasing) the strand. This process was successfully repeated four times for the deck panels and 10 times for the girders.

After the stressing of the epoxy-coated strands, a few strands slipped out of their anchorages. Because of safety concerns and the lack of time available to obtain new anchorages, the decision was made by the precast plant to strip the epoxy coating off of all of the epoxy-coated strands in the anchorage areas. The tensioning was then completed as for uncoated strands.

Accelerated curing was used for all members. Steam pipes running underneath the stressing beds heated the members, which were covered with moisture retention covers. Curing continued until compression tests on concrete cylinders indicated the desired strength for prestress release. Detensioning was accomplished by flame cutting the strands for the girders and by flame cutting the strand or cutting the strand with wire cutters for the deck panels.

Instrumentation

Mechanical Gauge Points

Every member was instrumented with gauge points for measuring surface strains (called Whittemore points) at regularly spaced intervals on the concrete. Most girders had gauge points running along both sides of the top flange for the full length of the girder and along both sides of the bottom flange at the ends of the girder. A few girders had only gauge points along the bottom flange at the ends of the girders. The spacing of the gauge points was 100 mm (3.94 in.) at the girder ends and 200 mm (7.87 in.) along the midspan regions of the top flange. Each deck panel had gauge points spaced at 100 mm (3.94 in.) along the full length of both sides of the panel. The gauge points for all members were placed at the level of the strands. Because of the large number of gauge points involved, threaded brass inserts were preattached to thin steel strips. The strips were then attached with screws to the inside surface of the framework, and the points were embedded in the concrete as the concrete was cast.

Once the concrete attained a compressive strength of 27.6 MPa (4 ksi), the screws attaching the thin steel strips to the formwork were removed. The formwork was then stripped, and the mechanical strain gauge (Whittemore gauge) was used to measure the distances between the gauge points. Portable data loggers were used to collect the numerous Whittemore gauge measurements directly from the Whittemore gauge. The measurements were then downloaded into a computer. Immediately after detensioning, another set of readings was taken using the same equipment. The differences in values between the two sets of readings were used to determine the strains in the concrete after detensioning. A full set of readings was also taken at concrete ages of 7, 14, and 28 days and immediately before development length experimentation.

End Slip

The end slip of every strand at both ends of every member was measured. A small channel-shaped fixture was attached to a strand adjacent to the end of a member. Holes were bored in the legs of the fixture to accept a digital depth gauge, which was used to measure the distance from the outer leg of the fixture to the concrete surface. This distance was measured both before and after detensioning; the difference between these two values was the end slip of the strand. A full set of readings was taken at each of the intervals mentioned above.

Concrete Temperature

Thermocouples to measure concrete temperature were installed at each end and at midspan of one girder for each cast. A total of 15 thermocouples were used for a girder, spread around the cross section at each of the three aforementioned locations. The thermocouples were monitored during curing and throughout the period when the Whittemore gauge measurements were taken after detensioning.

Three thermocouples were installed at each end of one deck panel for each cast. These thermocouples were monitored in a fashion similar to that for the girders.

Other Measurements

Camber was measured for each of the girders using standard surveying equipment. Shrinkage of the concrete was monitored using cylinders 152.4 × 304.8 mm (6 × 12 in.) cast for each batch of concrete. Freeze-thaw testing was performed using prisms cast from the high-strength concrete. The coefficient of thermal expansion was also determined for both the normal and high-strength concretes.

Experimentation

All girders and deck panels were transported to the FHWA Structures Laboratory in McLean, Virginia. The

composite decks for 12 of the girders and 16 of the deck panels will be cast there. Experimentation was also performed there.

Transfer Length

The transfer length of each end of each member was determined by plotting the strains calculated from the Whittemore gauge readings. The transfer length can be defined as the distance from the end of the beam to the point on the curve equal to the average value of strain for the plateau portion of the plot. Transfer lengths were determined for average values of strain equal to 100 percent of the plateau value and for average values of strain equal to 95 percent of the plateau value. This was done in an effort to compare transfer length values with other researchers who use varying definitions of transfer length. Transfer lengths were determined for each of the intervals mentioned for the Whittemore gauge measurements.

Development Length

Development length experimentation will be performed for each end of each girder. The estimated development length is first calculated and is called the embedment length. A single point load is applied at a distance from the end of a girder equal to this embedment length. This point load is increased in intervals up to failure. Failure can be one of two types: flexural failure or bond failure. Flexural failure occurs when the concrete crushes in compression or the strands break in tension. Bond failure occurs when the strands lose their bond and slip in toward the member. In I-shaped members, bond failure is usually accompanied by shear cracks. A flexural failure signifies adequate embedment length, whereas a bond failure signifies inadequate embedment length.

The type of failure for one end of the girder dictates the embedment length for the opposite end of the girder. If a flexural failure occurs, the embedment length is decreased for the next test. If a bond failure occurs, the embedment length is increased for the next test. This iterative approach is employed until the development length is determined.

Point loads were applied by use of a hydraulic jack and were measured using a load cell. During the experimentation, vertical deflections under the load and at midspan were measured. Linear variable displacement transducers (LVDTs) were used to measure slip of each strand. All of these measuring devices were connected to a data acquisition system and were read continuously during the experiments.

Development length experimentation also will be performed for each deck panel. A line load will be applied along the full width of the panel at the midspan of the panel. This load is increased incrementally to failure, and is measured using a load cell. LVDTs attached to the end of each strand at both ends of the panel will be used to measure strand slip. Deflection at midspan will also be measured.

Results and Conclusions

Because the experimentation is ongoing as of this writing, only a limited number of results are presented here. Additional results and conclusions will be presented later.

TABLE 3 Transfer Length Results for Girders

Girder Description	Average Transfer Length (in)
0.5" Uncoated Strand @ 2", N.S.C.	46.5*
0.5" Uncoated Strand @ 2", H.S.C.	19.2
0.5" Epoxy-Coated Strand @ 2", N.S.C.	18.6
0.5" Epoxy-Coated Strand @ 2", H.S.C.	13.0
0.5" Uncoated Strand @ 1.75", N.S.C.	44.6
0.5" Epoxy-Coated Strand @ 1.75",N.S.C.	19.4
0.6" Uncoated Strand @ 2", N.S.C.	56.0
0.6" Uncoated Strand @ 2", H.S.C.	23.7
0.6" Epoxy-Coated Strand @ 2", N.S.C.	21.8
0.6" Epoxy-Coated Strand @ 2", H.S.C.	18.7

N.S.C. = Normal Strength Concrete
H.S.C. = High Strength Concrete

1 inch = 25.4 mm

* Approximate average; two values of transfer length exceeded 56 in (the limit of instrumentation), but were taken as 56 in to compute the average.

As previously described, the transfer lengths for each end of each girder and deck panel were determined from the Whittemore readings at certain intervals. Table 3 gives some of these results. Specifically, it lists average transfer lengths for girders at a concrete age of 28 days. These transfer length values represent the average of all ends of particular groups of girders, such as girders containing strands 12.7 mm (0.5 in.) in diameter and fabricated with normal-strength concrete. The values listed are those determined using average values of strain equal to 95 percent of the plateau values.

Several conclusions can be drawn from the results shown in Table 3. First, the transfer lengths of epoxy-coated strands with grit were considerably shorter than those of uncoated strands for a given strand diameter and spacing. For normal strength concrete, the transfer lengths for epoxy-coated strands were less than half those of their respective uncoated strands.

Second, the use of high-strength concrete resulted in a reduction in transfer length. The reduction was much more pronounced for uncoated strand than it was for epoxy-coated strand.

Third, the transfer lengths for uncoated strands in normal-strength concrete were considerably longer than those predicted by the AASHTO approximation of 50 times the strand diameter. For uncoated strands 12.7 mm (0.5 in.) in diameter, the transfer lengths were approximately equal to 90 times the strand diameter. For uncoated strands 15.2 mm (0.6 in.) in diameter, the values were longer than 110 times the strand diameter.

Fourth and finally, the transfer lengths for strands 12.7 mm (0.5 in.) in diameter spaced at 44.4 mm (1.75 in.) were approximately equal to those for the same diameter strands spaced at 50.8 mm (2 in.). This conclusion held for both uncoated and epoxy-coated strands.

ACKNOWLEDGMENTS

The author would like to express her appreciation to the research teams of FHWA and of Construction Technology Laboratories, who worked together during the fabrication of the members. The teamwork of the staff of Shockey Bros. precast concrete plant, as well as the work of a review committee of prestressed concrete specialists for this study, is also gratefully acknowledged. It should be noted that the contents of this paper reflect the views of the author and do not necessarily reflect the official views or policies of FHWA.

REFERENCES

1. *Standard Specifications for Highway Bridges*, 15th ed. AASHTO, Washington, D.C., 1992.
2. Lane, S. N. Transfer Lengths in Rectangular Prestressed Concrete Concentric Specimens. *Public Roads*, Vol. 56, No. 2, Sept. 1992, pp. 67–71.
3. Lane, S. N. Development Length of Uncoated Prestressing Strand. *Proc., 12th Structures Congress*, Vol. 1, American Society of Civil Engineers, Atlanta, April 1994, pp. 624–629.
4. Lane, S. N. Development Length of Epoxy-Coated Prestressing Strand. *Proc., 12th FIP Congress*, Vol. 2, Federation Internationale De La Precontrainte, Washington, D.C., May/June 1994, pp. J12–J15.
5. Lane, S. N. Development Length of Prestressing Strand. *Public Roads*, Vol. 54, No. 2, Sept. 1990, pp. 200–205.
6. *Building Code Requirements for Reinforced Concrete (ACI 318) (Revised 1992) and Commentary.* ACI 318R-89 (Revised 1992). American Concrete Institute, Detroit, 1993.
7. Nilson, A. H. *Design of Prestressed Concrete*, John Wiley and Sons, Inc., New York, 1978.
8. Buckner, C. D. *An Analysis of Transfer and Development Lengths for Pretensioned Concrete Structures.* Report FHWA-RD-94-049. FHWA, U.S. Department of Transportation, 1994.
9. PCI Bridge Producers Committee. Recommended Practice for Precast Prestressed Concrete Composite Bridge Deck Panels. *PCI Journal*, Vol. 33, No. 2, March–April 1988, pp. 67–109.

Applications and Limitations of High-Strength Concrete in Prestressed Bridge Girders

Henry G. Russell, *Henry G. Russell, Inc.*
Jeffery S. Volz, *Construction Technology Laboratories, Inc.*
Robert N. Bruce, *Tulane University*

High-strength concrete provides a higher compressive strength, a higher modulus of elasticity, a higher tensile strength, reduced creep, and greater durability than normal-strength concrete. For the same cross section and span length, a high-strength concrete girder will have less initial deflection, a higher permissible tensile stress, less prestress loss, less camber change, and longer life than a similar girder made with normal-strength concrete. Structurally, the benefits of using high-strength concrete are fewer girders for the same width bridge, longer span lengths or reduced dead load. The limitations of existing prestressed concrete girders relative to the use of high-strength concrete and several options to more effectively utilize high-strength concrete are described. Analytical results indicate that the use of existing girder cross sections with concrete compressive strengths up to 69 MPa (10,000 psi) allow longer span lengths and more economical structures. However, to effectively utilize concrete with compressive strengths greater than 69 MPa (10,000 psi), additional prestressing force must be applied to the cross section through the use of smaller strand spacings, larger strand sizes, higher-strength strands or post-tensioning.

For over 25 years, concretes with compressive strengths in excess of 41 MPa (6000 psi) have been used in the construction of columns of high-rise buildings (*1*). Initially, the availability of high-strength concretes was limited to a few geographic locations. However, over the years, opportunities have developed to utilize these concretes at more locations across the United States. As opportunities have developed, material producers have accepted the challenge to produce concretes with higher compressive strengths.

In the precast prestressed concrete bridge field, a specified compressive strength of 41 MPa (6,000 psi) has been used for many years. However, strengths at release frequently control the concrete mix design so that actual strengths at 28 days are often in excess of 41 MPa (6,000 psi). It is only in recent years that a strong interest in the utilization of concrete with higher compressive strengths has emerged. This interest has developed at a few geographic locations in a manner similar to that in the building industry. Several research studies (*2–9*) have addressed the application of high-strength concrete in bridge girders. These studies have suggested that there may be a limit at which the higher-strength concretes can no longer be effectively utilized.

This paper examines the use of high-strength concrete in precast prestressed solid-section girders. The ob-

jective of the research is to define the limits at which the utilization of higher-strength concretes may no longer be structurally or cost effective. The paper then describes some solutions to overcome the limitations so that higher-strength concretes can be effectively utilized in bridge construction.

High-Strength Concrete

Concretes with compressive strengths in excess of 69 MPa (10,000 psi) have been produced commercially utilizing ready-mixed concrete at many geographic locations around the United States (*1*), including Illinois, Minnesota, New York, Ohio, South Carolina, Texas, and Washington. These concretes have been produced with a high decree of workability and pumpability. However in bridge design, a design strength in excess of 41 MPa (6,000 psi) at 28 days is hardly ever utilized. Rarely has concrete with a specified strength in excess of 69 MPa (10,000 psi) been utilized in a highway bridge structure. Consequently, here is a need to seek ways in which high-strength concrete can be effectively utilized.

Several investigations (*2–9*) have identified the advantages of using high-strength concrete in prestressed bridge girders. These advantages include fewer girders for the same width bridge, longer span lengths, or reduced dead load. The girders also will have increased durability. Studies (*5,7*) have also shown that these advantages more than offset the increased costs of high-strength concrete.

In addition to providing a higher compressive strength, high-strength concrete provides a higher modulus of elasticity, a higher tensile strength, reduced creep, and greater durability than normal-strength concrete. For the same cross section and span length, a high-strength concrete will result in less axial shortening and less short-term and long-term deflections. The higher tensile strength provides a small advantage where the allowable stress in tension controls the design. High tensile and compressive strength may be beneficial in reducing the transfer length at the ends of girders (*10*). The reduced creep will result in less prestress losses, which can be beneficial in reducing the number of strands and reducing the change in camber. Improved durability, particularly when silica fume is used, will result in a longer life for bridge girders.

Optimized Cross Sections

In the early applications of prestressed concrete, designers developed their own ideas of the "best" girder cross section to utilize. "As a result, each bridge utilized a different girder shape. Consequently, the reuse of girder formwork on subsequent contracts was not possible. As a result, girder shapes were standardized in the interest of improving economy of construction. This led to the development of the standard AASHTO-Prestressed Concrete Institute (PCI) sections for bridge girders. Types I through IV were developed in the late 1950s and Types V and VI were developed in the 1960s.

Adoption of the AASHTO standard bridge girders simplified design practice and led to wider use of prestressed concrete for bridges. Standardization resulted in considerable cost savings in the construction of bridges. However, following the original adoption of the standard AASHTO-PCI shapes, individual states again developed their own standard sections for improved efficiency and economy. In 1980, FHWA initiated an investigation to identify new optimized sections for major prestressed concrete girders.

In an FHWA study (*2,3*), Construction Technology Laboratories (CTL) found that the most structurally efficient sections were the Bulb-Tee, Washington, and Colorado girders. In an analysis for cost-effectiveness, the Bulb-Tee girder with a 152-mm (6-in.) web was recommended for use as a national standard for precast, prestressed concrete bridge girders in the United States for span lengths from 24 to 43 m (80 to 140 ft).

Subsequently, the PCI Committee on Concrete Bridges developed a modified section for use as a national standard. The modifications resulted in a slightly heavier section that was easier to produce and handle. This cross section was subsequently adopted by several states and is identified as the PCI Bulb-Tee in this paper. Several other versions of the Bulb-Tee also have been developed in various geographic locations (*11,12*).

Analyses of Existing Cross Sections

In the present analysis, the following specific cross sections were selected for analysis of their cost efficiency:

1. PCI Bulb-Tee BT-72, identified as BT-72.
2. Florida Bulb-Tee BT-72 (*11*), identified as FL BT-72.
3. AASHTO Type VI with a web 152 mm (6 in.) thick, identified as Type VI.
4. Washington Series 14/6, which is similar to a Washington Series 14 but with a web 152 mm (6 in.) thick and is identified as WA 14/6.
5. Colorado Series G68/6, which is a Colorado G68 but with a web 152 mm (6 in.) thick and is identified as CO G68/6.
6. Nebraska Section (*12*) with a depth of 1800 mm and a web thickness of 150 mm and is identified as NU 1800.

The girder depths were selected on the basis that they are suitable for similar span lengths. Dimensions of all sections are shown in Figure 1.

Method of Analysis

The majority of the cost-effectiveness analyses were performed using computer program BRIDGE. BRIDGE was written as part of the previous investigation for the Optimized Sections for Precast, Prestressed Bridge Girders (2). The required input of BRIDGE consists of girder span, spacing, and cross section; concrete and strand characteristics; and relative costs of materials. The program determines deck thickness and deck reinforcement, required number of prestressing strands, and cost index per unit surface area of bridge deck. The program also provides section properties, moments, stress levels, and deflections. Comparisons were made on the basis of relative costs.

For purposes of making the cost comparisons, the relative unit cost for in-place materials was assumed to be the same as that used in the previous report (2).

- Concrete (girders and deck): 1 unit/unit weight of concrete;

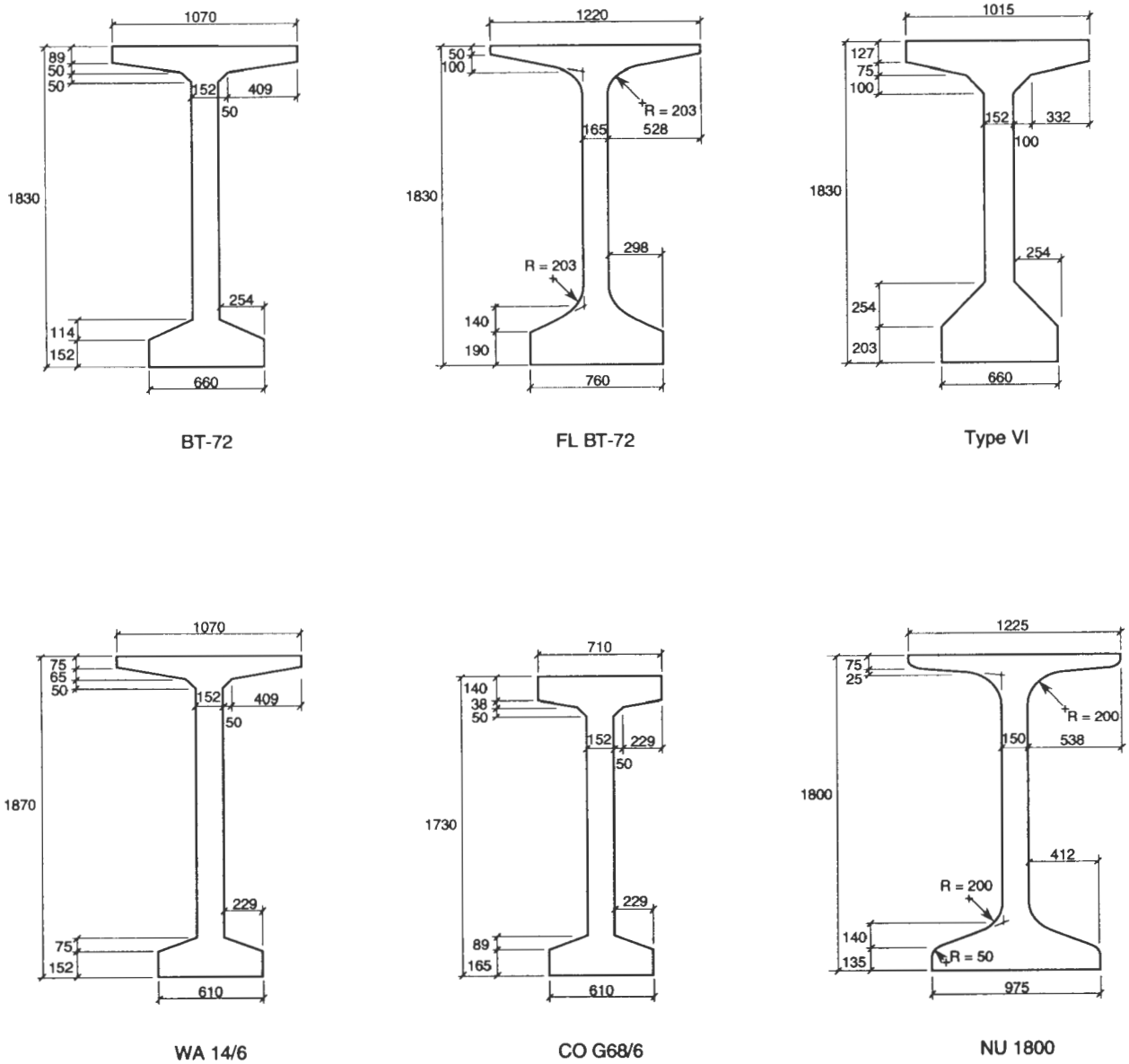

FIGURE 1 Cross sections of girders analyzed (dimensions in millimeters).

- Strands: 8 units/unit weight of strands;
- Reinforcing steel: 9 units/unit weight of reinforcing; and
- Epoxy-coated reinforcing steel: 12 units/unit weight of epoxy-coated reinforcing.

The relative costs of materials were taken as the product of material weight and the relative unit cost. The summation of relative cost of materials was then divided by deck area to give cost index per unit area.

It is recognized that shipping lengths, girder weights, lateral stability of girders, and prestressing bed capacities that exist today could limit the type of girders that can be produced. In addition, design information for use with very high-strength concretes may not be available. However, these limitations were not used as a means to restrict potential applications. The intent of the project was to look beyond current design and production capabilities.

Cost-Effectiveness

Computer program BRIDGE was used to perform cost-efficiency analyses of the various cross sections. Full details of the analyses were given previously (*13*). As shown in Figure 2, the cost index per unit surface area of bridge deck can be plotted versus span length for a given cross section. At various girder spacings, different cost curves result, as shown by the solid lines in Figure 2.

An "optimum cost curve" is obtained if the end points of each individual cost curve are joined, as shown by the dashed line in Figure 2. This "optimum cost curve" indicates the least cost index for a particular span and varies as a function of girder spacing. As shown in Figure 2 and discussed by Rabbat and Russell (*2*), for a given span, cost index per unit area of bridge deck decreases as girder spacing increases.

Optimum cost curves are generated for a constant girder concrete strength. The cost chart in Figure 2 is for a 28-day girder concrete strength of 41 MPa (6,000 psi). Additional optimum cost curves can be generated at other girder concrete strengths for the same girder cross section. Figure 3 is a plot of the optimum cost curves for a BT-72 at 41, 55, 69, and 83 MPa (6,000, 8,000, 10,000, and 12,000 psi). The compressive strength of the concrete in the deck was assumed to be 28 MPa (4,000 psi) for all girder concrete strengths.

Figure 3 illustrates the benefits and limitations of higher-strength concrete for existing cross sections of precast, prestressed bridge girders. Although Figure 3 represents one particular cross section (BT-72), the results and relationships are consistent with those of other sections analyzed within this investigation (*13*) and will be used as a basis for discussion. To examine the benefits and limitations, the curves must be studied at three separate locations.

The first location is for spans less than 27.4 m (90 ft). For these spans, the controlling condition is initial prestress at transfer. For a given span, there is a point at which additional prestressing will cause tension in the top fibers regardless of the concrete strength. Although this tension would be offset in the service load condition, the dead load at prestress transfer is constant for a given span and cross section and independent of the final in-place girder spacing. As a result, there is no benefit realized for higher-strength concrete at these span lengths.

The second location is for spans between 27.4 and 30.5 m (90 and 100 ft) when concrete strengths are between 41 and 55 MPa (6,000 and 8,000 psi) and spans between 27.4 and 33.5 m (90 and 110 ft) for strengths of 55 MPa (8,000 psi) and greater. As previously discussed, Rabbat and Russell (*2*) found that for a given span, cost index per unit area of bridge deck decreases as girder spacing increases. With the use of higher-strength concrete, additional prestressing will allow larger girder spacings for a given cross section and span length. However, there is a point at which the increase in the unit deck costs begins to offset the savings in unit girder costs associated with larger spacings. This effect is discussed in more detail elsewhere (*13*).

The third location to examine in Figure 3 is for spans exceeding 30.5 m (100 ft) when concrete strengths are between 41 and 55 MPa (6,000 and 8,000 psi) and spans exceeding 33.5 m (110 ft) when concrete strengths exceed 55 MPa (8,000 psi). These areas represent the optimization of benefits of high-strength concrete for the cross sections analyzed. The higher-strength concrete allows larger prestressing forces and, as a result, greater girder spacings for a given span length, thus reducing unit cost. For these span lengths, the original conclusion of Rabbat and Russell (*2*) is confirmed: for a given span length, cost index per unit area of bridge deck decreases as girder spacing increases.

At these longer span lengths, the optimum girder spacings that result in lowest possible cost for a given cross section are not reached. In other words, the cost index as a function of girder spacing is still decreasing when the girder capacity is reached. For example, at a span length of 42.7 m (140 ft) with a 41-MPa (6,000-psi) girder, the maximum spacing is 1.8 m (5.9 ft), whereas a 55 MPa (8,000 psi) girder can be spaced at 2.5 m (8.3 ft). Although the deck costs will be greater for the 55-MPa (8,000-psi) girder, the savings in girder costs far outweigh increased deck costs and result in a more cost-effective superstructure.

Figure 3 also indicates that cost benefits vary as a function of span length and girder concrete strength.

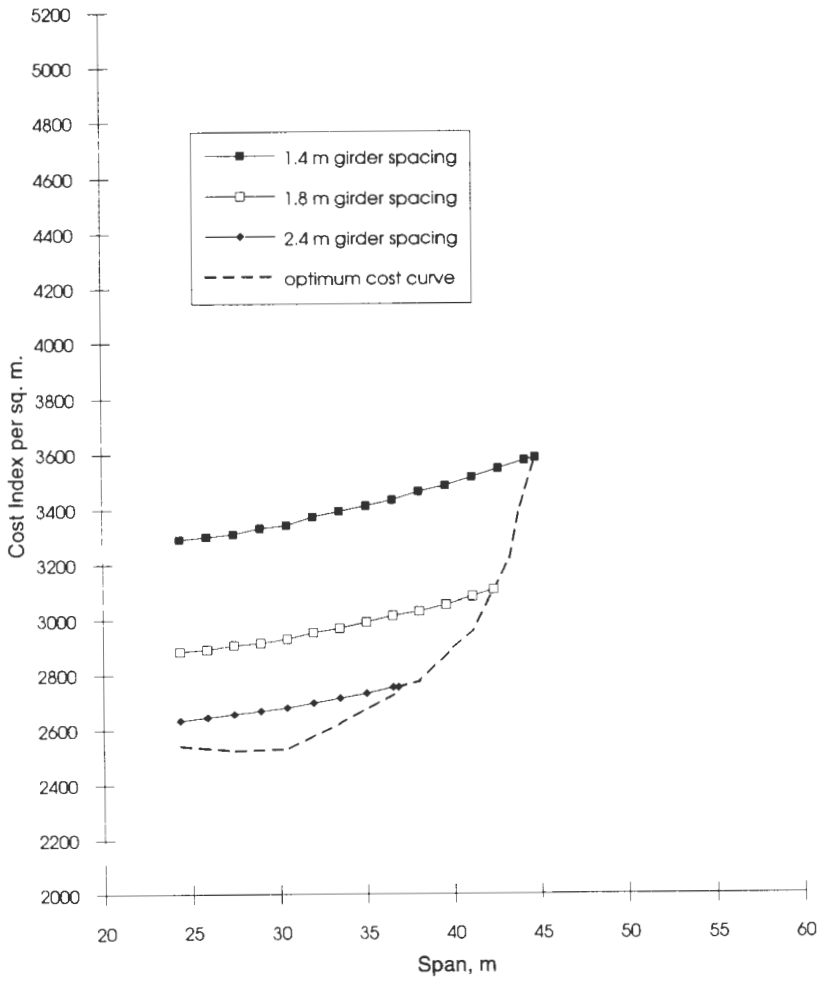

FIGURE 2 Cost chart for a BT-72, 41 MPa (6,000 psi).

For example, a 55-MPa (8,000-psi) girder has a 3 percent lower cost index than a corresponding 41-MPa (6,000-psi) girder at a span length of 33.5 m (110 ft), but a 10 percent lower unit cost at a span length of 42.7 m (140 ft). These cost benefits continue to increase as the span length increases, reaching a maximum of 18 percent at a span length of 44.8 m (147 ft). At this point, the lower-strength girder has reached its maximum span length, whereas the higher-strength girder still has additional capacity. In other words, another benefit of high-strength concrete is the ability to achieve greater span lengths.

Figure 3 also indicates another important point: the diminishing returns realized with the use of high-strength concrete for existing cross sections. The shift in the optimum cost curve decreases for each succeeding 13-MPa (2,000-psi) increase in girder compressive strength. For example, at a girder spacing of 1.5 m (5 ft), the maximum span length increases by 4.6 m (15 ft) when girder compressive strength is increased from 41 to 55 MPa (6,000 to 8,000 psi); however, the maximum span length increases by only 2.7 m (9 ft) when girder compressive strength is increased from 55 to 69 MPa (8,000 to 10,000 psi). Furthermore, the span length increases fall off dramatically at girder compressive strengths exceeding 69 MPa (10,000 psi).

The primary cause of these diminishing returns is the decreasing strand eccentricity. Once strands are placed within the web, the efficiency of a particular section begins to decrease rapidly. The incremental benefit of each succeeding strand decreases when sufficient room within the flange does not exist. Once additional prestressing force cannot be induced in the girder, the beneficial effects are limited to the increase in concrete tensile strength, which only increases as the square root of compressive strength (*1*).

In general, increases in the girder concrete strength result in the following:

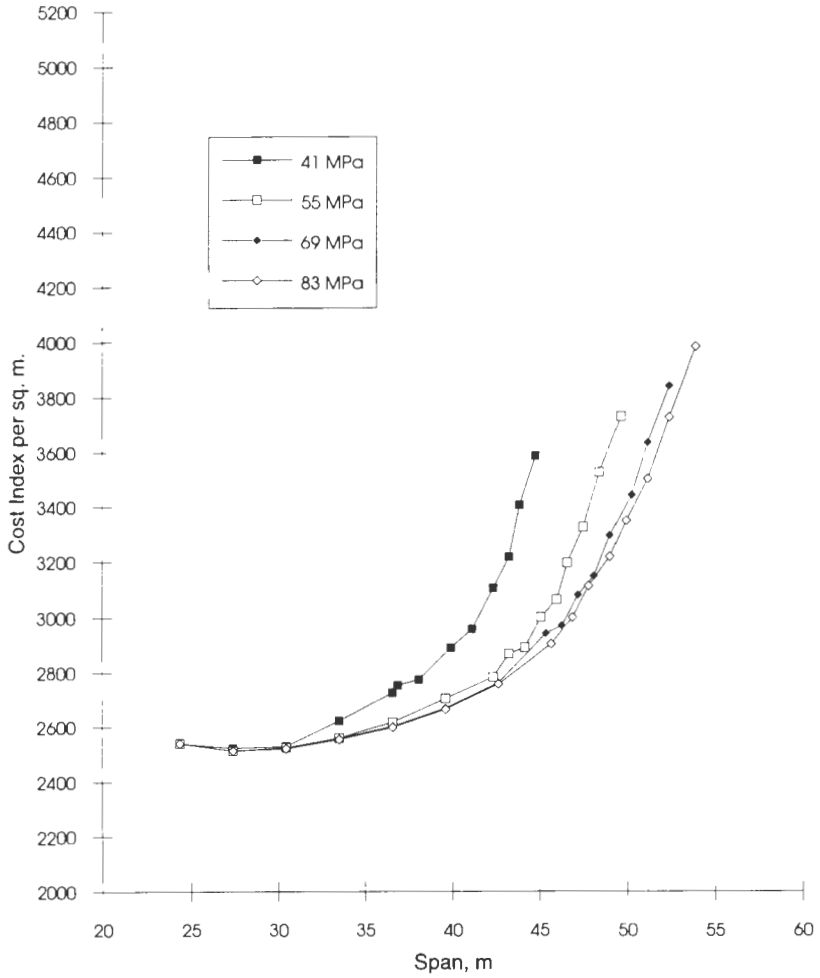

FIGURE 3 Optimum cost curves for a BT-72.

1. A shift in the optimum cost curve to the right for each succeeding increase in girder concrete strength. This is beneficial because longer span lengths can be achieved without an increase in the unit cost.
2. Decreasing incremental benefits for each incremental increase in concrete strength.
3. Minimal benefits beyond a girder concrete strength of about 69 MPa (10,000 psi).
4. No benefit from higher concrete strength for the horizontal portion (shorter span lengths) of the optimum cost curve.

Cost comparisons for the other analyzed sections of similar depths are shown in Figure 4 for concrete strengths of 41 and 83 MPa (6,000 and 12,000 psi). Optimum cost curves for the BT-72, WA 14/6 and CO G68/6 are shown in Figure 4*a*. Important observations from this figure consist of the following:

1. The curves are essentially identical for the shorter span lengths.
2. The curves vary at the longer span lengths. However, this variation is greatest for the CO G68/6 and is attributable to the shallower depth and thinner top flange. The BT-72 and WA 14/6 are similar within the vertical portions.
3. Incremental shifts in the optimum cost curve for increasing girder strength vary for each section. The BT-72 undergoes the largest shifts, whereas the WA 14/6 undergoes the smallest. This fact is due primarily to the number of prestressing strands that can be placed within the flange. The BT-72, WA 14/6 and CO G68/6 can accommodate 39, 30, and 35 strands, respectively, within the bottom flange. Strand placement within the flange is more efficient than that in the web and allows the CO G68/6 to gradually gain on the WA 14/6 as girder strength is incrementally increased.

Optimum cost curves for the NU 1800 and FL BT-72 are shown in Figure 4*b*. No cost advantage existed for one section over the other as the curves are almost identical.

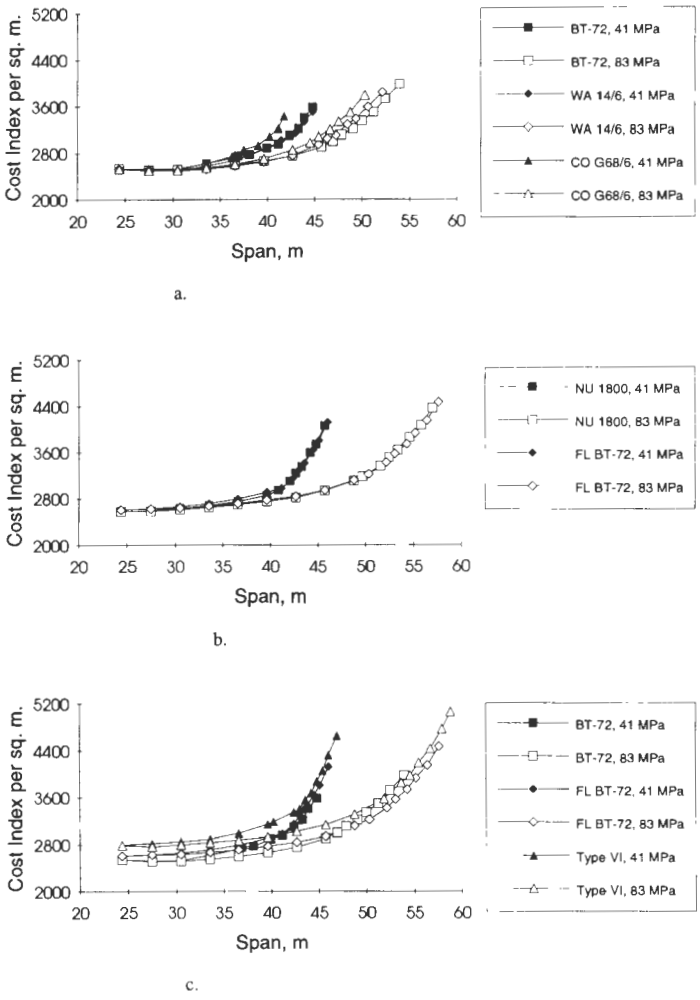

FIGURE 4 Comparison of different cross sections: (*a*) BT-72, WA 14/6, CO8/6; (*b*) NU 1800, FL BT-72; (*c*) BT-72, FL BT-72, Type VI.

Figure 4*c* contains plots of the optimum cost curves for the BT-72, FL BT-72, and Type VI at concrete strengths of 41 and 83 MPa (6,000 and 12,000 psi), respectively. Important observations from this figure consist of the following:

1. At a girder strength of 41 MPa (6,000 psi), the BT-72 is the most cost-effective cross section, with savings of 1 to 6 percent over the FL BT-72 and 5 to 13 percent over the Type VI.
2. At all girder strengths, the BT-72 is the most cost-effective cross section for span lengths up to about 45.7 m (150 ft), with savings of 3 to 6 percent over the FL BT-72 and 8 to 13 percent over the Type VI.
3. Incremental shifts in the optimum cost curve for increasing girder strength vary for each section. The FL BT-72 undergoes the largest shift, whereas the BT-72 undergoes the smallest. This fact is primarily because of the number of prestressing strands that can be placed within the bottom flange. However, it is also a function of the efficiency in which the strands are placed in the bottom flange. For instance, the FL BT-72 and BT-72 have wide rectangular bottom flanges, whereas the Type VI has a more squarish bottom flange. Although the Type VI can accommodate significantly more strands than the FL BT-72 (81 versus 59), their placement is not as efficient (less eccentricity) and, as a result, shifts in the FL BT-72 curve are greater than those for the Type VI.
4. As a result of the incremental shifts in the optimum cost curve as discussed in Item 3, the FL BT-72 becomes the most cost-effective cross section for span lengths exceeding about 45.7 m (150 ft) and girder strengths of 55 MPa (8,000 psi) and greater.
5. Although the FL BT-72 and Type VI enjoy greater horizontal shifts in their optimum cost curve than the

BT-72 as a result of larger bottom flanges, they pay a price at smaller span lengths. For these spans, the BT-72 is the more cost-effective cross section at all girder concrete strengths.

Comparisons were also made to determine the effect of the premium cost for higher-strength concretes on the cost index per unit area. The following ratios were assumed for the premium costs of higher-strength concrete (1 MPa = 145 psi):

Strength (MPa)	*Minimum Ratio*	*Intermediate Ratio*	*Maximum Ratio*
41	1.00	1.00	1.00
55	1.00	1.05	1.10
69	1.00	1.13	1.25
83	1.00	1.25	1.50

The comparisons of optimum cost curves were made for the BT-72 for compressive strengths from 41 to 83 MPa (6,000 to 12,000 psi). Data from the three sets of cost index curves are shown in Figure 5. The effect of the premium costs is to displace the relative positions of the curves for the various concrete strengths. These data indicate that as the premium for the higher-strength concretes increases, it becomes more economical to utilize a lower-strength concrete for longer span lengths. For example, with no premium concrete costs, the 55-MPa (8,000-psi) compressive strength concrete is the most economical up to a span length of approximately 36 m (120 ft). However, with the maximum premium costs, it is more economical to use 41 MPa (6,000 psi) up to a span length of approximately 36 m (120 ft) and then to utilize 55 MPa (8,000 psi) up to a span length of 46 m (150 ft). However, on a relative basis, when comparing different cross sections, the effect of the premium concrete costs is to displace cost index curves by a similar amount. Consequently, although the premium costs are important when comparing concrete strengths for the same girder cross section, they are less significant when comparing different cross sections with the same concrete strength.

Limited analyses were made to investigate the sensitivity of the cost index per unit area to the assumed relative unit costs of the different materials. On the basis of an industry survey, a range of relative unit costs was obtained. Comparisons of optimum cost curves for BT-72 were made for this range. It was concluded (*13*) that the cost index per unit area on a comparative basis is relatively insensitive to the assumed relative costs of the in-place materials.

Analyses of Modified Cross Sections

The analysis of existing sections indicated that the utilization of high-strength concrete was limited by the amount of prestressing force that can be applied to a girder cross section and the eccentricity of the force. Consequently several alternatives were investigated to increase the amount of prestressing force that can be applied at maximum distance from the neutral axis. The alternatives included decreasing strand spacing, increasing strand size, increasing strand strength, and increasing bottom flange size.

Strand Spacing and Size

Previous analyses in this investigation were based on a strand diameter of 12.7 mm (0.5 in.) at a spacing of 51 mm (2 in.). The effect of decreasing the strand spacing to 38 mm (1.5 in.) and providing strands 15.2 mm (0.6 in.) in diameter spaced at 51 mm (2 in.) and 64 mm (2.5 in.) was investigated. The results are shown in Figure 6 for a BT-72. The most cost-efficient solution occurs with the largest amount of prestressing force that can be accommodated within the section. The benefits are more pronounced at the longer span lengths and illustrate one way to increase the effectiveness of high-strength concrete.

Strand Strength

The possibility of using a higher grade prestressing strand was also investigated. A limited benefit was obtained by using a 2,070-MPa (300-ksi) strand compared with a 1,860-MPa (270-ksi) strand.

Section Geometry

Two modifications of the bottom flange were studied. Modification 1 consisted of increasing the bottom flange edge thickness from 152 mm (6 in.) to 203 mm (8 in.) while maintaining the overall 1830-mm (72-in.) section depth. Modification 2 consisted of increasing the bottom flange thickness from 152 mm (6 in.) to 203 mm (8 in.) by increasing the section's overall depth from 1830 to 1880 mm (72 to 74 in.).

Figure 7 compares optimum cost curves at concrete strengths of 41 and 83 MPa (6,000 and 12,000 psi), respectively. As can be seen from this figure, the modifications have a larger impact on the 83 MPa (12,000 psi) girders than on the 41 MPa (6,000 psi) girders.

The behavior of the optimum cost curve for the modifications is consistent with the previous conclusion that the bottom flange limited the effectiveness of higher concrete strengths; however, the behavior is slightly different from that which was experienced with modifications to strand size, spacing, and strength. A penalty

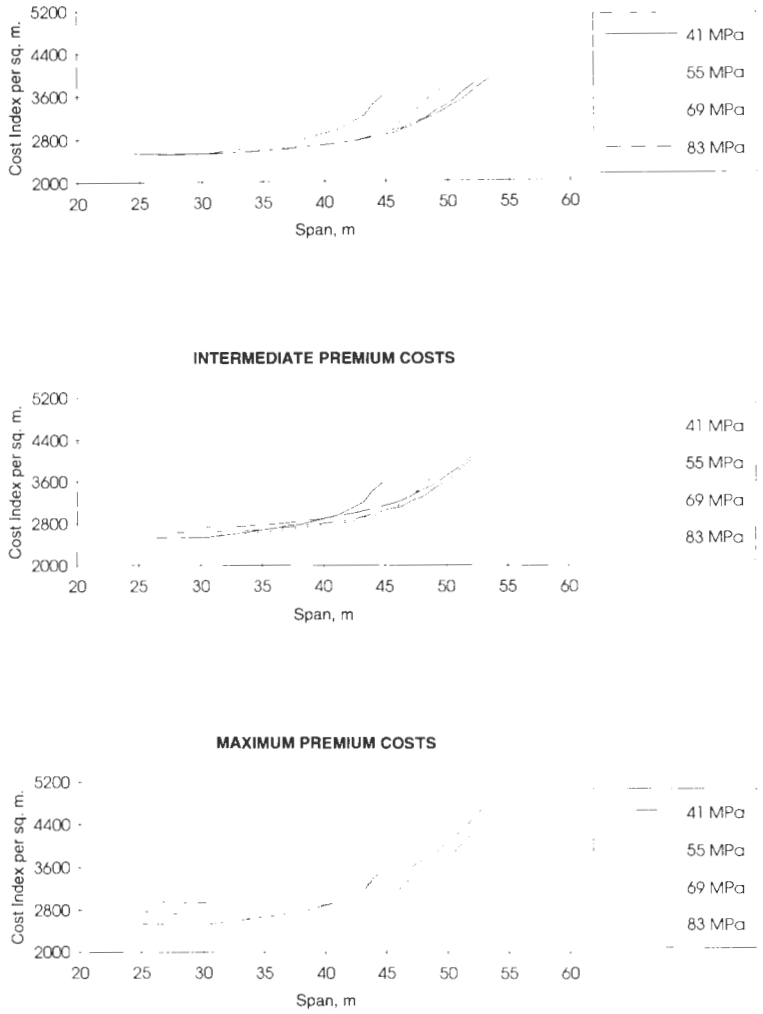

FIGURE 5 Effect of premium concrete costs for a BT-72.

is paid in the form of increased volume of concrete and corresponding weight when the bottom flange size is increased to incorporate more prestressing, as opposed to reducing strand spacing to obtain the same result. This penalty offsets some of the potential benefits of more prestressing with the bottom flange, and, consequently, cost benefits are not realized until concrete strengths exceed 55 MPa (8,000 psi). In addition, this penalty results in the original BT-72 being more cost-effective at all concrete strengths for span lengths of 42.7 m (140 ft) and less.

Modification 2 is a slightly more cost-effective alternative then Modification 1. However, it is interesting to note that the shift in the optimum cost curve between Modification 1 and Modification 2 is virtually identical at both concrete strengths. This fact occurs because the benefit of Modification 2 over Modification 1 is only a slightly deeper section. Both revised sections accommodate the same maximum number of prestressing strands within their larger bottom flange.

Conclusions

On the basis of the cost analyses described in this paper, the following conclusions are made:

1. For existing cross sections designed using Grade 270 strand 12.7 mm (0.5 in.) in diameter at 51-mm (2-in.) centers with 51 mm (2 in.) of cover, the BT-72 was the most cost-effective cross section for span lengths up to 45.7 m (150 ft) at all concrete compressive strengths. However, the WA 14/6 and CO G68/6 were equally cost-effective for span lengths up to about 36.6 m (120 ft). For span lengths greater than 45.7 m (150 ft) and all concrete compressive strengths, the FL BT-72 and NU 1800 were the most cost-effective.
2. For all existing sections designed using Grade 270 strand 12.7 mm (0.5 in.) in diameter at 51-mm (2-in.) centers with 51 mm (2 in.) of cover, the maximum useful concrete compressive strength was in the range of 62 to 69 MPa (9,000 to 10,000 psi). Above this

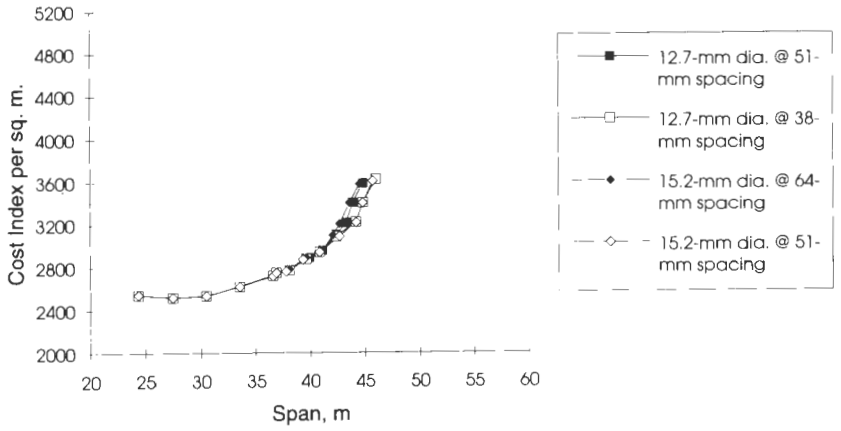

a.

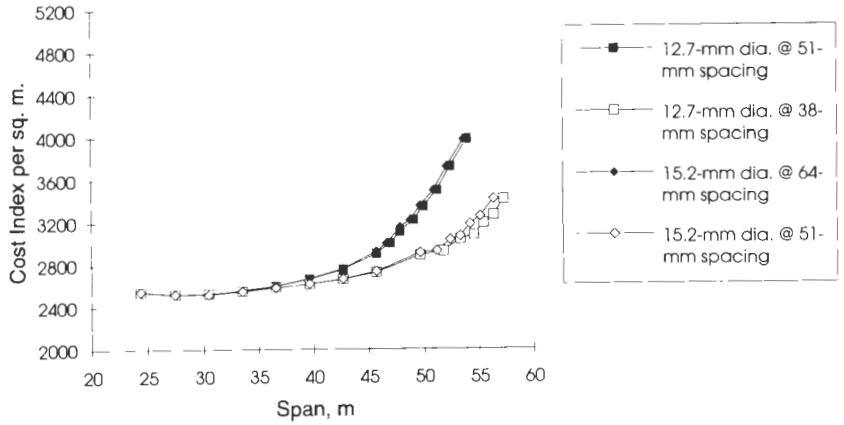

b.

FIGURE 6 Effect of strand spacing and size for a BT-72: (*a*) BT-72 with 41 MPa of specified girder concrete strength; (*b*) BT-72 with 83 MPa of specified girder concrete strength.

strength level, sufficient prestressing force cannot be introduced into the cross section to take advantage of any higher concrete compressive strengths.

3. For all the cross sections analyzed, the use of a higher-strength concrete enabled a given section to be designed for a longer span length. The increase in span length with compressive strength is greater when additional prestress force can be applied to the cross section. However, if additional prestressing force cannot be included, the beneficial effects are limited to the increase in allowable tensile stress at midspan. Because this increase is limited to the increase in the square root of the compressive strength, the incremental benefits decrease with each incremental increase in compressive strength.

4. A shallower section with a higher-strength concrete can be more cost-effective than utilizing a deeper section with a lower-strength concrete. Depending on the premium for the higher-strength concrete, the unit cost of the superstructure may be lower with the shallower section than with the deeper section. In addition, there will be other savings from the reduced substructure height. This concept is worthy of further study with regard to replacement of existing bridges.

5. As the premium for high-strength concrete increases, it becomes more economical to use lower-strength concretes for longer span lengths. The unit cost of the superstructure is relatively insensitive to changes in the premium costs as the cost of the girder concrete is only one component of the total cost.

6. The use of smaller-strand spacing, larger-diameter strand, or higher-strength strand in the BT-72 was beneficial at the higher concrete strength levels where additional prestressing force was needed to take advantage of the higher compressive strength of the concrete. Ad-

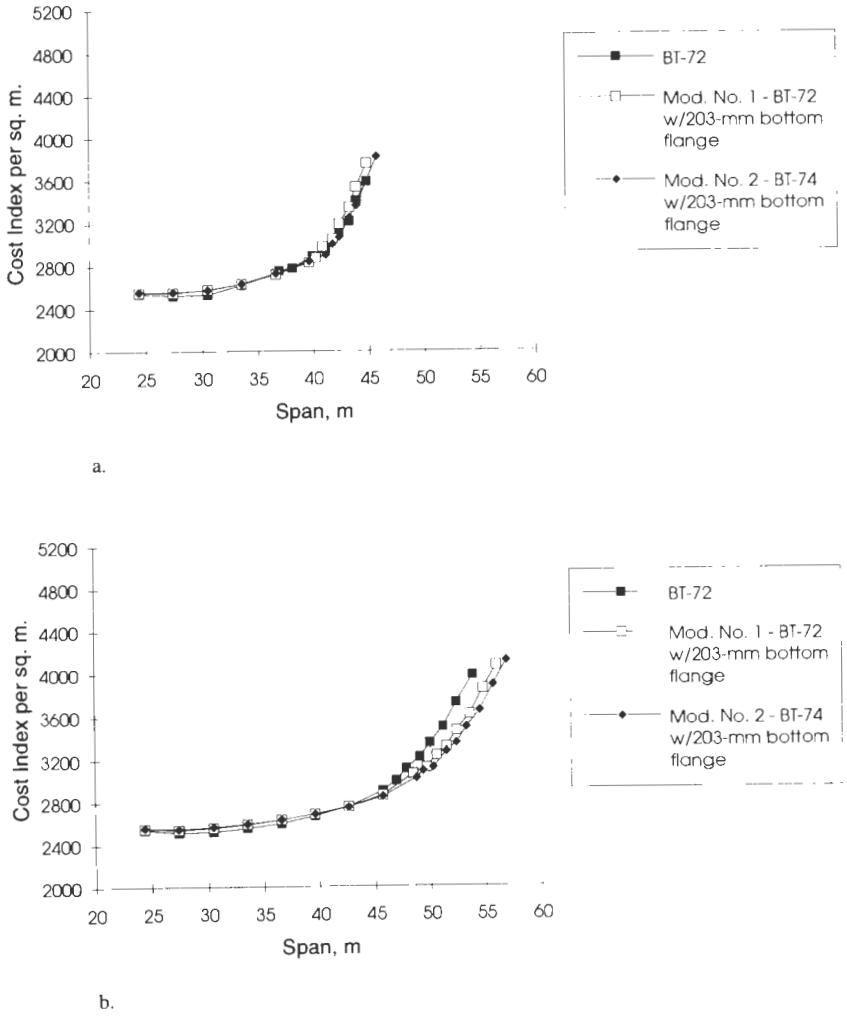

FIGURE 7 Effect of section geometry for a BT-72: (*a*) BT-72 modifications with 41 MPa of specified girder concrete strength; (*b*) BT-72 modifications with 83 MPa of specified girder concrete strength.

ditional research is needed on transfer and development lengths in high-strength concrete before the beneficial effects can be implemented.

7. The effect of increasing the bottom flange thickness of the BT-72 so that an additional row of prestressing strands can be added had little benefit when the girder concrete compressive strength was 41 MPa (6,000 psi) and a benefit of less than 5 percent when the concrete strength was 83 MPa (12,000 psi).

Recommendations

1. In the near future, the industry should concentrate on the usage of concrete with specified compressive strengths up to 69 MPa (10,000 psi). For existing girder cross sections designed with Grade 270 strands 12.7 mm (0.5 in.) in diameter at 51-mm (2-in.) centers and 51 mm (2 in.) of cover, the use of concrete with compressive strengths up to 69 MPa (10,000 psi) will allow longer span girders and, depending on the premium cost for the higher-strength concrete, more economical structures. As a minimum, all highway departments should adopt 53-MPa (8,000 psi) compressive strength concrete as the normal design strength for longer span girders. It should be recognized that many precasters are already producing girders at this strength level.

2. To effectively utilize concretes with compressive strengths in excess of 69 MPa (10,000 psi), the industry must develop methods to apply additional prestressing force to the cross section. This can be achieved either by the utilization of strands 12.7 mm (0.5 in.) in diameter at 38-mm (1.5-in.) centers or strands 15.2 mm (0.6 in.) in diameter at 51-mm (2.0 in.) centers. The use

of the closer spacing for the strand 12.7 mm (0.5 in.) in diameter may be feasible with the higher-strength concretes.

3. The PCI Bulb-Tee (BT-72) should continue to be considered as a national standard for span lengths from 24.4 to 61.0 m (80 to 200 ft). However, the WA 14/6 and CO G68/6 are equivalent at span lengths up to 36.6 m (120 ft). For span lengths greater than 45.7 m (150 ft), the FL BT-72 and NU 1800 are slightly more economical.

4. Before concrete with compressive strengths in excess of 69 MPa (10,000 psi) can be successfully used, additional research is needed on transfer and development lengths; deflection, lateral stability, and dynamic characteristics of girders; prestress losses; shear strength of girders; design age strength; and alternative deck systems.

ACKNOWLEDGMENTS

The information described in this paper was developed under a grant from FHWA. The authors express their appreciation to Susan N. Lane, James Hoblitzell, and Thomas J. Pasko of FHWA for their review of the final report and to the following individuals who contributed information to this project: Joseph S. Balik of W. R. Grace & Co.; W. Vincent Campbell of Bayshore Concrete Products Corporation; Reid W. Castrodale of Portland Cement Association; James E. Cook of Gifford-Hill, Inc; Z. T. George of Texas Concrete Company; Howard W. Knapp of Rocky Mountain Prestress, Inc.; Robert P. McCrossen of Florida Wire and Cable, Inc.; Walter Podolny, Jr., of FHWA; Basile G. Rabbat of Portland Cement Association; Bradley K. Violetta of Master Builders Technology; and Max J. Williams of Gulf Coast Pre-Stress, Inc.

REFERENCES

1. ACI Committee 363. *State of the Art Report on High-Strength Concrete* (ACI 363R-92). American Concrete Institute, Detroit, 1992.
2. Rabbat, B. G., T. Takayanagi, and H. G. Russell. *Optimized Sections for Major Prestressed Concrete Bridge Girders.* Report FHWA/RD-82/005. FHWA, U.S. Department of Transportation, 1982.
3. Rabbat, B. G., and H. G. Russell. Optimized Sections for Precast, Prestressed Bridge Girders. *Journal of the Prestressed Concrete Institute*, Vol. 27, No. 4, July/Aug. 1982, pp. 88–104. (Also reprinted as PCA Research and Development Bulletin RD080.01E, 1982, Portland Cement Association, 10 pp.)
4. Carpenter, J. E. Applications of High Strength Concrete for Highway Bridges. *Public Roads*, Vol. 44, No. 2, Sept. 1980, pp. 76-83.
5. Zia, P., J. J. Schemmel, and T. E. Tallman. *Structural Applications of High Strength Concrete.* Report FHWA/NC/89-006. North Carolina Center for Transportation Engineering Studies, 1989.
6. Castrodale, R. W., M. E. Kreger, and N. E. Burns. *A Study of Pretensioned High Strength Concrete Girders in Composite Highway Bridges—Design Considerations.* Report 381-4. University of Texas Center for Transportation Research, 1988.
7. Bruce, R. N., B. T. Martin, H. G. Russell, and J. J. Roller. *Feasibility Evaluation of Utilizing High Strength Concrete in Design and Construction of Highway Bridge Structures.* Report FHWA/LA-92/282. Louisiana Transportation Research Center, 1994, 219 pp.
8. Russell, B. W. Impact of High Strength Concrete on the Design and Construction of Pretensioned Girder Bridges. *Journal of the Precast/Prestressed Concrete Institute*, Vol. 39. No. 4, July/Aug. 1994, pp. 76–89.
9. Mokhtarzadeh, A., T. Ahlborn, C. French, and R. Leon. Applications of High Strength Concrete to the Prestressed Bridge Girder Industry. *Proc., 3rd International Conference on Utilization of High Strength Concrete*, Lillehammer, Norway, June 1993, pp. 163–174.
10. Cousins, T. E., J. M. Stallings, and M. B. Simmons. Reduced Strand Spacing in Pretensioned, Prestressed Members. *ACI Structural Journal*, Vol. 91, No. 3, May-June 1994, pp. 277–286.
11. Garcia, A. M. Florida's Long Span Bridges: New Forms, New Horizons. *Journal of the Precast/Prestressed Concrete Institute*, Vol. 38, No. 4, July/Aug. 1993, pp. 34–49.
12. Geren, K. L., and M. K. Tadros. The NU Precast/Prestressed Concrete Bridge I—Girder Series. *Journal of the Precast/Prestressed Concrete Institute*, Vol. 39, No. 3, May/June 1994, pp. 26–39.
13. Russell, H. G., J. S. Volz, and R. N. Bruce. *Optimized Sections for High-Strength Concrete Bridge Girders.* FHWA, U.S. Department of Transportation, 1994.

Serviceability Criteria for Prestressed Concrete Bridge Girders

Andrzej S. Nowak and Hassan H. El-Hor, *University of Michigan*

Serviceability limit states often govern in the design of prestressed concrete bridge girders, yet the corresponding acceptability criteria are not clearly justified. The paper deals with allowable stresses and ultimate moment. The requirements of the AASHTO standard specifications are demonstrated on pretensioned bridge girders AASHTO Types III through VI. Moments are calculated for the considered limit states and for various spans. It is observed that the ratio of these moments varies with regard to span length. In most cases, the final tension stress (after the final loss of prestress) determines the minimum required number of prestressing strands. On the other hand, the important limit state is compression stress in concrete, as overloading may lead to unacceptable permanent deformations. Revision of the serviceability limit states, consistent in format with the new AASHTO load and resistance factor design specifications, is suggested. The formulation of a compression limit state in concrete that is based on the elastic limit and tension limit states in concrete and the modulus of rupture is proposed.

Design of prestressed concrete bridges specified by the AASHTO (*1*) is a combination of working stress design and ultimate strength design. Prestressed concrete girders are designed to satisfy the allowable stress requirements at service load conditions. Then, the ultimate flexural capacity of the section is also checked. In most cases the allowable tension stress governs. However, most of the code calibration effort was directed to the development of the ultimate load criteria (*2*). Therefore, there is a need to consider the allowable stress design.

The objective of this paper is to review and compare the design criteria for prestressed concrete bridge girders, with regard to the ultimate limit states (ULS) and serviceability limit states (SLS), as specified in AASHTO standard specifications and AASHTO Load and Resistant Factor Design (LRFD). In particular, the analysis was focused on ultimate moment and allowable stresses in tension and compression.

Limit States

A structural component can be in a safe state or a failure state. The limit state is defined as the boundary condition separating these two states. In general, failure is considered as the inability to perform a function(s), such as, carrying the loads, providing a shelter, or satisfying certain deformation criteria (deflection or vibration). The limit states can be put into categories, depending on the following functions:

- ULS,
- SLS, and
- Fatigue limit states.

ULS is related to load-carrying capacity. A structure that reaches a ULS is on the brink of failure, in the form of a collapse, overturning, or rupture. ULS for a beam is defined as reaching the ultimate moment carrying capacity, or shear capacity, but also loss of stability. The limit state can be considered for a component or for the whole structure (bridge). In general, a bridge reaches a ULS only after several components (girders) have reached their ULSs. If moment in a girder is equal to the ultimate moment, the girder cannot take any more loading, but it does not necessarily mean a failure. In most cases, the bridge loading still can be increased until several girders reach their ULSs.

SLS's are related to bridge performance under load levels lower than those used at ULS. Examples of SLS include cracking, deflection, vibration, and excessive permanent deformation. In general, the consequences of reaching an SLS are much less severe than that for ULS. Cracking is undesirable; it may lead to corrosion of reinforcement or prestressing steel or both. However, opening of a crack once in a while may be acceptable. Deflection and vibration are two limit states that are difficult to define. The acceptability criteria are not clear and appear to be subjective. Compression stress in concrete may exceed the elastic limit, and this may result in a permanent deformation. Therefore, there is a need to control stress at the top fibers of the girder at transfer (after the wires are cut) and bottom part of the composite girder after the final loss of prestress.

FLSs are related to load-carrying capacity under repeated loads. Multiple application of load, even at a level that is lower than the ultimate load, can lead to rupture. Bridge structures often carry millions of trucks, and each passage can be considered as a load cycle. Welded steel components in tension are vulnerable to fatigue failure.

In practice, the limit states are formulated using various load and resistance parameters, $x_1, \ldots x_n$, in form of the so-called limit state functions, $f(x_1, \ldots x_n)$. Limit state function is an equation:

$$f(x_1, \ldots x_n) = 0 \tag{1}$$

so that if $f(x_1, \ldots x_n) > 0$, the structure (or component) is in a safe state, and if $f(x_1, \ldots x_n) < 0$, the structure (or component) is in a failure state.

Safe realization of structures requires that the probability of reaching a limit state be kept at an acceptable low level. That probability is often called the probability of failure (P_F) and it depends on cost of investment (C_I), and consequences of failure (C_F). The cost (C_I) includes the costs of design, construction, and operation (use). The optimum probability of failure corresponds to the minimum total expected cost:

$$\min C_T = C_I + \Sigma(P_{Fi}\, C_{Fi}) \tag{2}$$

where

P_{Fi} = probability of failure for limit state i and
C_{Fi} = cost of failure for limit state i.

The consequences of failure vary depending on limit state; therefore, the products of P_{Fi} and C_{Fi} are calculated for all limit states involved in the design.

In the design codes, the acceptability criteria are also formulated in terms of limit state functions. Safety reserve is ensured by specifying conservative values of load and resistance parameters. The probability-based approach has been used to derive the optimum load and resistance factors for the ULS (*2*). However, for the SLS, the consequences of failure (reaching the limit state) are usually an order of magnitude (or more) lower than for ULS. Therefore, there is a need for quantification of the load and resistance parameters for SLS and the development of a basis for calibration.

Design Criteria

The design of prestressed concrete bridge girders on the basis of AASHTO (*1*) is based on the calculation of stresses under the so-called service loads and their comparison with specified allowable stresses. Stresses are calculated at midspan. Service loads are determined as unfactored effects of dead load, live load, and impact. The prestressing force is also considered and its effect is reduced by estimated prestress losses. The ultimate moment carrying capacity is calculated and compared with the total factored load. The design requirements are reviewed by considering AASHTO girders Types III through VI.

The calculation of dead load (DL) does not involve much uncertainty. The statistical parameters of DL are available (*2*). On average, DL exceeds the design values by about 3 to 5 percent. The coefficient of variation is 0.08 to 0.10.

Design live load (LL) is calculated using HS20 truck or lane loading. It was found that the actual truck traffic can produce much higher load effects (*3*). The expected maximum 75-year lane moments can be as large as 2.10 of HS20 moment for about a 150-ft (45-m) span or about 1.60 of HS20 moment for a 20-ft (6-m) span. Design dynamic load (impact) (IL) is specified as a function of span length:

$$\text{IL} = [50/(125 + L)]\ \text{LL} \tag{3}$$

where L = span length (1 ft = 0.3 m). The actual dynamic load is a function of bridge span, roughness of the surface and vehicle dynamics (*4*). It has been observed that IL decreases with increasing truck weight,

and for very heavy vehicles IL = 0.15 LL. The coefficient of variation for (LL + IL) is about 0.18.

The girder distribution factor (GDF) specified by AASHTO (*1*) for prestressed concrete girders is $s/5.5$, where s = girder spacing in feet (1 ft = 0.3 m). The resulting GDFs are conservative in most cases. A recent study by Zokaie et al. (*5*) indicated that the current AASHTO specifications are overly conservative for longer spans and girder spacings (by about 50 percent) but are too liberal for shorter spans and girder spacings.

Prestressing force is the major design consideration. The stress level is controlled by the number of strands and initial prestressing force. Prestress loss is estimated at two stages: immediately after the wires are cut (initial loss of prestressing force) and at the end of economic life (final loss of prestressing force).

The design stresses under service load are calculated for unfactored dead load and HS20 truck plus impact (Equation 3), with GDF equal to $s/5.5$. The calculations are carried out to determine the maximum stresses in compression and tension. Tension stress at the top fibers of the girder is considered after the wires are cut (after initial loss of prestressing force). It is calculated using the following formula:

$$\sigma_{ti} = F_i/A_c - F_i e_o/Z_t + M_{\min}/Z_t \quad (4)$$

and corresponding compression stress at the bottom is calculated as follows:

$$\sigma_{ci} = F_i/A_c + F_i e_o/Z_b - M_{\min}/Z_b \quad (5)$$

where

A_c = area of concrete,
F_i = initial prestressing force,
e_o = eccentricity of strands,
Z_t = section modulus with respect to top fibers for noncomposite section,
Z_b = section modulus with respect to bottom fibers for noncomposite section, and
$M_{\min}$ = moment caused by self-weight of the girder.

Other stresses are calculated for a composite section. Maximum compression in the top fibers is checked under live load and after the final loss of prestressing force. Maximum tension stress (if any) is calculated at the bottom fibers, also after the final loss of prestressing force. The compression stress is calculated as follows:

$$\sigma_{cs} = F_s/F_c(1 - e_o/K_b) + M_p/Z_t + M_c/Z'_{tc} \quad (6)$$

and tension stress:

$$\sigma_{ts} = F_s/A_c(1 - e_o/K_t) - M_p/Z_b - M_c/Z_{bc} \quad (7)$$

where

F_s = final prestressing force,
Z_{bc} = section modulus with respect to bottom fibers for composite section,
Z'_{tc} = section modulus with respect to extreme top fibers for composite section,
$K_t = -Z_b/A_c$,
$K_b = Z_t/A_c$,
$M_c = M_{sD} + M_{LL}$,
$M_p = M_g + M_s$,
M_s = moment caused by slab weight,
M_{sD} = superimposed moment,
M_g = moment caused by girder weight, and
M_{LL} = moment caused by LL and impact.

The specified allowable stresses are listed in Table 1 (*1*). Prestressed concrete bridge girders designed by AASHTO are required to satisfy the initial and final concrete stresses shown in Table 1 at any section along the girder. It is assumed that the considered stresses are exposed to a corrosive environment; therefore, the allowable tension stress is $3\sqrt{f'_c}$. The specifications allow a maximum of 75 percent of ultimate prestressing steel stress, f'_s, to be applied initially at transfer for low relaxation strands. The resistance reduction factor for prestressed concrete sections in flexure is $\phi = 1.0$.

The allowable tension stress is specified to control the occurrence of cracking. Tension may occur at the top of the beam immediately after the wires are cut. It may also be present at the bottom, as the result of LL. Then, the maximum tension can be expected after the final loss of prestressing force (at the end of economical life). A cracked girder requires a different analytical model than an uncracked section. Cracking may cause an accelerated corrosion of reinforcement or prestressing steel. However, the problem can be controlled by ordinary reinforcement. The physical limit is the tensile strength of concrete (moment corresponding to the modulus of rupture in concrete), or, after the initial

TABLE 1 Allowable Stresses Specified by AASHTO (*1*)

Types of Stress		Stress (psi)
Initial stress in concrete at transfer	Tension	$6\sqrt{f'_{ci}}$
	Compression	$0.6f'_{ci}$
Final stress in concrete	Tension *	$3\sqrt{f'_c}$
	Compression	$0.4f'_c$

* severe corrosive environment

(1 psi = 6.894 kPa)

crack occurred, the decompression moment. Therefore, the limit state function can be formulated as

$$M_r - M_{DL} - M_{LL} - M_{IL} = 0 \quad (8)$$

where

M_r = moment corresponding to the tensile strength limit in concrete and includes the prestressing effect and loss of prestressing force, if any;
M_{DL} = moment caused by dead load;
M_{LL} = moment caused by live load; and
M_{IL} = moment caused by dynamic load (impact).

The cracking moment M_{cr} can be determined as a function of the tensile strength of concrete (f_r). The mean modulus of rupture is about 700 psi (4.8 MPa) for concrete with f'_c = 5,000 psi (34.5 MPa); this compares with allowable tension stress of 530 psi (3.6 MPa) (6).

The allowable compression stress is specified to avoid excessive permanent deformation. As in the case of tension stress, two cases are considered. Immediately after transfer, maximum compression occurs at the bottom of the girder. After the final prestress loss, the maximum compression stress must be checked at the top. The physical limit for permanent deformation is elastic limit, which is assumed to correspond to about 0.6 f'_c. Therefore, the limit state function for compression can be formulated as follows:

$$M_{el} - M_{DL} - M_{LL} - M_{IL} = 0 \quad (9)$$

where M_{el} = elastic moment (moment corresponding to elastic stress limit in concrete) and includes the prestressing effect and loss of prestressing force, if any.

The ultimate moment for a prestressed concrete girder, M_n, is calculated from the following formula:

$$M_n = A_{ps} f_{ps} d_p (1 - 0.6\rho) \quad (10)$$

where

A_{ps} = area of prestressing steel;
f_{ps} = yield strength;
d_p = effective depth;
$\rho = A_{ps} f_{ps}/(b d_p f'_c)$ (reinforcement ratio);
b = width of the section (effective slab width); and
f'_c = strength of concrete.

The actual moment carrying capacity is a random variable. The mean value is about 5 percent larger than the design value calculated using Equation 10, and the coefficient of variation is 0.075 (2).

The ultimate moment (M_n) is compared with the factored load effect (M_u) calculated as follows:

$$M_u = 1.3\, M_{DL} + 2.17\, (0.5)\, (GDF)\, (M_{LL} + M_{IL}) \quad (11)$$

where

M_{DL} = moment caused by dead load;
M_{LL} = moment caused by live load (per lane);
GDF = girder distribution factor; and
M_{IL} = moment caused by dynamic load (impact).

In addition to the ultimate moment, AASHTO (*1*) requires that the cracking moment (M_{cr}) be checked and defined as

$$M_{cr} = (Z_{bc}/Z_b)[F_{pe} A_{ps} (e_o - K_t)] - f_r Z_{bc} \quad (12)$$

where f_r = modulus of rupture.

Analysis of AASHTO Girders

The calculations are performed for prestressed concrete AASHTO-type Girders III through VI. The cross sections are shown in Figure 1. Simple spans are considered from 40 through 120 ft (12 through 36 m). It is assumed that all the considered bridges carry at least two traffic lanes, that girders are composite with concrete deck slab, and that strands are draped at the third points.

Further it is assumed that dead load, in addition to the girder weight, includes two normal-size parapets, a 1-in. (25-mm) haunch, diaphragms 1 ft (0.3 m) wide, a wearing surface of 30 psf (1.44 kN/m^2) and a stay-in-place form work of 15 psf (0.72 kN/m^2). The thickness of the cast-in-place concrete deck varies with the girder spacing. It is assumed that the nominal final concrete strength in the pretensioned girder is 6,500 psi (45 MPa) and in the deck it is 4,500 psi (31 MPa). Concrete strength at transfer is considered to be 5,500 psi (38 MPa). The prestressing steel is composed of 0.5-in. (12-mm) low relaxation strands with an ultimate strength of 270 ksi (1860 MPa).

The number of prestressing strands is the single most important parameter that determines the resistance for ULS and SLS. For each limit state, i, the number of required strands (n_i) is determined. The calculations are carried out for the following limit states considered in the design: allowable initial tension stress for concrete, allowable initial compression stress for concrete, allowable final tension stress for concrete, allowable final compression stress for concrete, and ultimate moment. The number of strands required for the ultimate load-carrying capacity is denoted by n_u. For tension stress, the number of strands required is denoted by n_{ti} for the initial stage (after transfer), and n_{ts} for the final stage (after final prestress loss). Similarly, for compression stress, the number of strands required is denoted by n_{ci} for the initial stage (after transfer), and n_{cs} for the final stage (after final prestress loss).

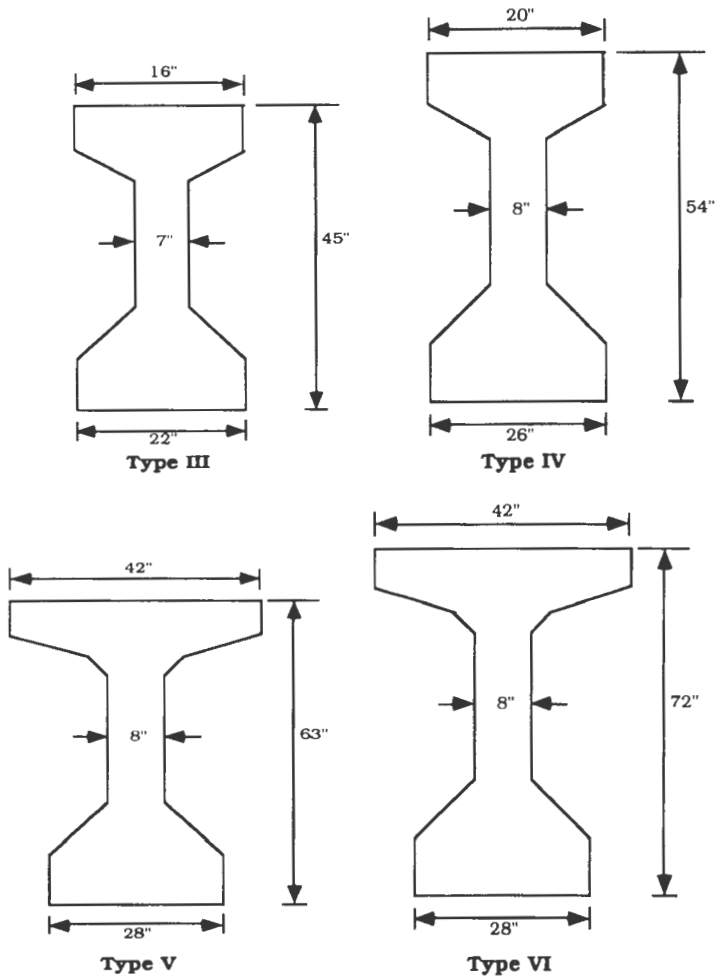

FIGURE 1 AASHTO girders Types III through VI. All dimensions are in inches (1 in. = 25 mm).

Only one limit state is considered at a time. If, for example, the ultimate moment is considered, then the number of strands is determined only with regard to the required moment carrying capacity. The results are shown in Figure 2. The presented numbers of strands are calculated for girder spacing of 8 ft (2.4 m) and slab thickness of 8 in. (200 mm). The size of the AASHTO-type girder is selected depending on the span length: for spans 40 to 60 ft (12 to 18 m) AASHTO Type III, for spans 60 to 80 ft (18 to 24 m) AASHTO Type IV, for spans 80 to 100 ft (24 to 30 m) AASHTO Type V, and for spans 100 to 120 ft (30 to 36 m) AASHTO Type VI.

The sign of expected stress at the initial stage and final stage are opposite. Immediately after transfer, prestressing force is the major factor that increases the critical tension and compression stresses. Therefore, an upper bound is imposed on the required number of strands. For spans up to about 70 ft (21 m), tension in the top fibers of the girder govern, and for longer spans, compression at the bottom governs. In the final stage, after the final loss of prestress, prestressing force decreases the critical stresses. Therefore, a lower bound is determined for the required number of strands. The feasible domain is shown as the shaded area in Figure 2. There is a considerable variation of the required numbers of strands. However, it is clear that the design is governed by the allowable tension stress (in the final stage).

The effect of the allowable tension stress on the required number of strands is shown in Figure 3. Various limits are considered from 0 (no tension allowed) to 10 times the square root of f'_c.

For the considered AASHTO girders, moments are calculated for various limit states, in particular:

- Moment corresponding to the allowable tensile stress in noncomposite girder,
- Moment corresponding to the allowable compression stress in noncomposite girder,

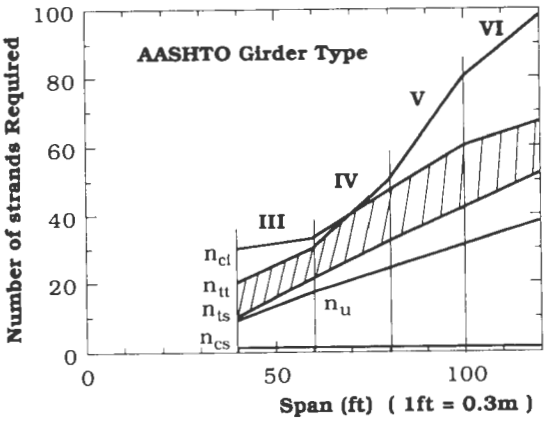

FIGURE 2 Required number of strands: n_u = ultimate moment, n_{ti} = tension at the initial stage (after transfer), n_{ci} = compression at the initial stage, n_{ts} = tension at the final stage (after final prestress loss), and n_{cs} = compression at the final stage.

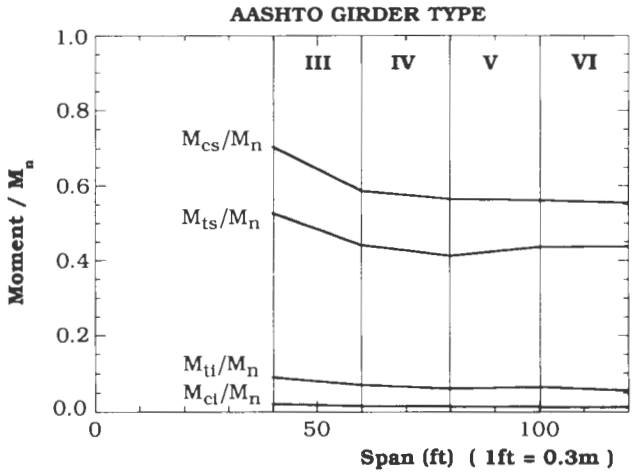

FIGURE 4 Moment ratios calculated for allowable tension and compression stresses.

- Moment corresponding to the allowable tensile stress in composite girder,
- Moment corresponding to the allowable tensile stress in composite girder, and
- Moment corresponding to the ultimate load-carrying capacity in composite girder.

Each moment is determined with regard to only one limit state (other limit states are disregarded). The ratios of these moments and the ultimate moment are plotted in Figure 4 for AASHTO girder Types III through VI.

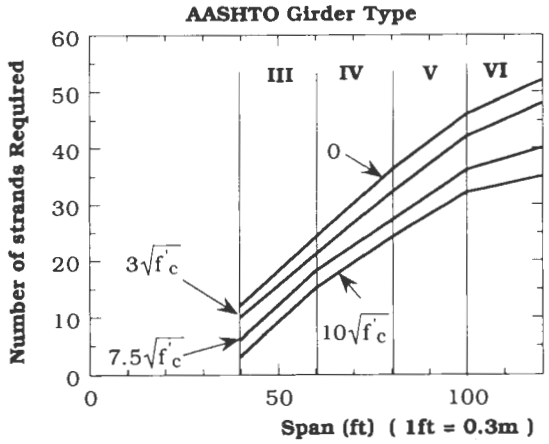

FIGURE 3 Required number of strands for various values of the allowable tension stress at the final stage.

The nominal moment, M_n, is calculated for the composite section using Equation 10. The ratios of moments M_{cs}/M_n, M_{ts}/M_n, M_{ti}/M_n, and M_{ci}/M_n vary with span length. Moments M_{ti} and M_{ci} are applied to a non-composite section and, therefore, they appear to be small compared with M_n.

Conclusions

Ultimate limit states and serviceability limit states are considered for prestressed concrete girders. The minimum required number of strands is calculated for various limit states, including allowable initial tension stress, initial compression stress, final tension stress, final compression stress, and ultimate moment. The results confirm that the final tension stress governs the design.

Serviceability limit states based on allowable stress in concrete require further consideration. Design resistance and loads are not realistic and, therefore, the calculated stress have no physical meaning. The actual concern is an excessive permanent deformation of the girder. Therefore, it is suggested that the elastic limit stress in compression be checked. Furthermore, because the live loads are unrealistic, the use of factored loads specified in the new LRFD AASHTO (*1*) is suggested. Tension stress can be controlled by additional reinforcement. The girder distribution factors are overly conservative in most cases.

It is suggested that the design be based on the following limit states:

- Tension stress in concrete (initial and final),
- Elastic limit for compression stress in concrete, and
- Ultimate moment.

ACKNOWLEDGMENTS

The research presented was carried out in conjunction with the development of the LRFD AASHTO Code (NCHRP Project 12-33, Calibration). It was also partially sponsored by a National Science Foundation grant managed by Ken Chong, which is gratefully acknowledged. The opinions and conclusions expressed or implied in the paper are those of the author and are not necessarily those of the sponsoring organizations.

REFERENCES

1. *Standard Specifications for Highway Bridges*. AASHTO, Washington, D.C., 1992.
2. Nowak, A. S. *Calibration of LRFD Bridge Design Code*. Report submitted to NCHRP, University of Michigan, Ann Arbor, 1994 (in press).
3. Nowak, A. S., and Y-K. Hong. Bridge Live Load Models. *ASCE Journal of Structural Engineering*, Vol. 117, No. 9, 1991, pp. 2757–2767.
4. Hwang, E.-S., and A. S. Nowak. Simulation of Dynamic Load for Bridges. *ASCE Journal of Structural Engineering*, Vol. 117, No. 5, 1991, pp. 1413–1434.
5. Zokaie, T., T. A. Osterkamp, and R. A. Imbsen. *Distribution of Wheel Loads on Highway Bridges*. NCHRP Project 12-26(1). Imbsen and Associates, Sacramento, Calif., 1994.
6. Nowak, A. S., and H. N. Grouni. Serviceability Criteria in Prestressed Concrete Bridges. *ACI Journal, Proc.*, Vol. 83, No. 6, Jan.–Feb. 1986, pp. 43–49.

Structural Safety of Prestressed Concrete and Composite Steel Highway Bridges

Sami W. Tabsh, *University of Houston*

Traditionally, the safety evaluation of existing bridges and code calibration of newly developed structural design specifications for the ultimate limit states are usually based on the maximum factored design loads. The advantage of this approach is that it does not require detailed design computations. Past experience with prestressed concrete girder bridges indicates that the design of such bridges is governed by the allowable stresses requirement at release or under service load effects. Similarly, the design of composite steel beam bridges is generally controlled by overloading for compact sections and by the maximum stress criterion for noncompact sections. The reliability of bridges designed according to AASHTO's Load Factor Design code is evaluated on the basis of actual designs. Reliability is measured in terms of the reliability index for the ultimate flexural capacity limit state. The statistical data on strength are generated starting from statistics on material properties and using simulation methods. Statistical data on load components are compiled from the available literature. The scope of the study covers a wide range of precast sections and rolled beams, span lengths, and beam spacings.

Highway bridges traditionally have been designed on the basis of deterministic values of load and resistance. The use of minimum material properties, specified load intensities, and prescribed computational procedures serves the important role of ensuring uniformity in the nominal performance of bridges. The deterministic approach has been reinforced by the large extent to which structural engineering design is codified and by the lack of feedback about actual performance of structures. The lack of information about actual behavior of bridges combined with the use of codes embodying relatively high safety factors can lead to the view that absolute safety can be achieved. Absolute safety is unattainable; in addition, the use of very high levels of safety can be undesirable because it may require the deployment of almost infinite resources.

Conventional methods of computing the safety of existing bridges and calibration of newly developed structural design codes for an ultimate limit state usually assume that the maximum factored design load effect governs the design. The advantage of this approach is that it does not require detailed design computations, such as the selection of the precast or rolled section and determination of the thickness of the concrete deck. The nominal capacity in this case is assumed to be equal to the applied factored load and divided by the capacity reduction factor. This approach neglects the effect of other design requirements, such as serviceability and overloading, on the final capacity of the structure.

Past experience with prestressed concrete I-girder and box beam bridges indicates that the design of such bridges is governed by the allowable stresses requirement at release of the prestress and under service load effects. The magnitude of the allowable stresses under

service load effects is a function of the exposure condition (corrosive versus noncorrosive environments). Similarly, the design of composite steel beam bridges is generally controlled by overloading for compact sections and by the maximum stress criterion for noncompact sections.

In 1994, AASHTO published its Load Resistance Factor Design (LRFD) specifications (*1*) for the design of highway bridges. The first edition of the specifications was intended to provide a framework for future versions. The limit states that could be calibrated for prestressed concrete, structural steel, and composite structures were mainly related to strength. Other limit states, such as serviceability and overloading, were made equivalent to the standard Load Factor Design (LFD) specifications until enough data are available to be able to calibrate them reliably.

In this paper, the reliability of prestressed concrete girders and composite steel beams is evaluated on the basis of actual designs. The bridges are designed in accordance with the current AASHTO's LFD specifications (*2*). Simply supported prestressed concrete I-girders, as well as compact and noncompact composite steel beams, are considered in this study. The limit state function considered is the flexural capacity at ultimate. The structural reliability is measured in terms of the reliability index. The statistical data on strength are generated starting from statistics on material properties and using simulation methods. Statistical data on load components are compiled from the available literature. The scope of the study covers a wide range of precast sections and rolled beams, span lengths, and beam spacings.

Statement of the Problem

Traditionally, the safety of prestressed concrete and composite steel bridges has been generally based on considering the mean value of the resistance (μ_R) to be to the following (*3*):

$$\mu_R = \lambda[\alpha_D(D) + \alpha_{L+I}(L + I)]\left(\frac{1}{\phi}\right) \quad (1)$$

where

α_D and α_{L+I} = dead load and live load (including impact) factors, respectively;
D and $L + I$ = nominal dead load and live load plus impact effects, respectively;
λ = mean-to-nominal ratio; and
ϕ = resistance reduction factor.

The use of Equation 1 to compute the safety of prestressed concrete girders at ultimate can be erroneous because this equation assumes that the factored moment capacity governs the design of the section over the allowable stress requirement. For illustration, Figure 1 shows the required number of strands versus the simple span length for a 28/63 I-girder (the first and second numbers represent respectively the bottom flange width and the total beam depth, in inches). The girders are

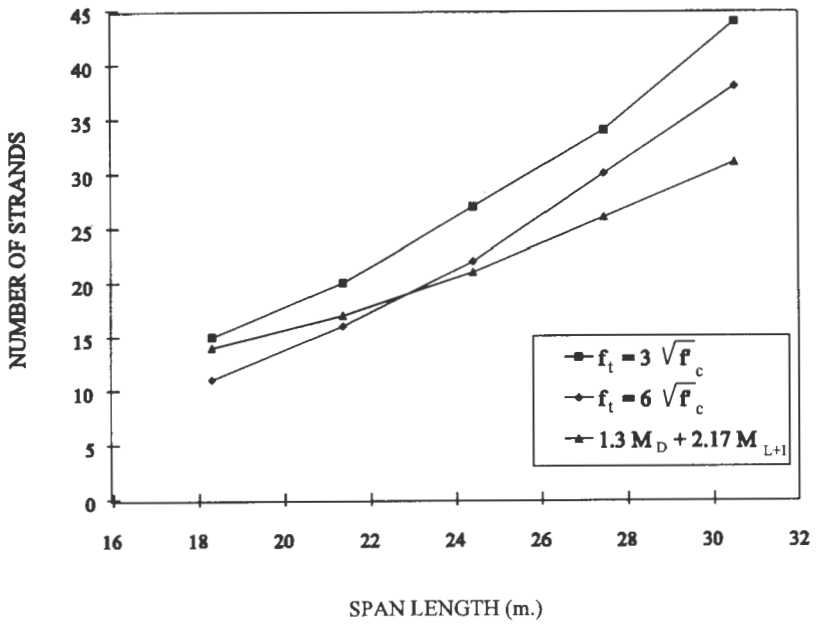

FIGURE 1 Number of strands versus simple span length for 28/63 P/S concrete I-girder.

designed according to the AASHTO code and have a spacing of 2.44 m (8 ft.). Two separate limit states are considered in the design: (*a*) serviceability (with a maximum allowable final tensile concrete stress, f_t, limited to $3\sqrt{f'_c}$ or $6\sqrt{f'_c}$, where f'_c is the nominal strength of concrete at 28 days), and (*b*) ultimate strength. In the useful range of application, the curves representing the allowable stress condition are consistently above the one representing ultimate strength requirement, thus indicating that the serviceability limit state governs the design of the girder.

Similarly, code calibration based on Equation 1 alone can be inadequate when applied to steel bridges in flexure because it assumes that the steel beam is compact and that the capacity is based on the plastic stress distribution. In general, some wide-flange rolled steel beams do not satisfy AASHTO's ductility requirement for compactness and, therefore, the capacity should be based on the moment at first yield. Further, the maximum stress and overloading conditions usually control the design of noncompact sections for the practical range of application. For example, Figure 2 shows the maximum simple span length versus the girder spacing for a W36 × 210 composite beam designed in accordance with the AASHTO code. Analysis of the section in plastic bending for beam spacings in the range of 1.83 to 3.66 m (6 to 12 ft) showed that it does not satisfy AASHTO's ductility requirement (Equation 10-128a of the specifications). Therefore, the section is classified as noncompact according to the specifications. The design of the composite beams in Figure 2 is based on three different and separate conditions. These conditions include the (*a*) plastic moment capacity, (*b*) yield moment capacity, and (*c*) overloading. The analysis shows that the design of the composite beams for the considered beam spacings is governed by the yield moment requirement (i.e., maximum stress in the bottom flange limited to the specified yield stress). The maximum simple span lengths based on the maximum stress condition for the considered beam spacings are about 25 percent less than the corresponding designs that are based on the plastic moment capacity. For this reason, the use of Equation 1 can underestimate the actual safety of steel bridges designed by AASHTO.

AASHTO's General Design Requirements

AASHTO's specifications are used for the design of typical simple span I-girder and spread box beam bridges. The AASHTO code requires interior girders to have an ultimate capacity in flexure (ϕM_n) at least equal to the factored load effect (M_u):

$$\phi M_n \geq M_u \tag{2}$$

in which M_u is computed according to AASHTO's Group I load combination:

$$M_u = 1.3[M_{DL1} + M_{DL2} + (5/3)\, M_{L+I}] \tag{3}$$

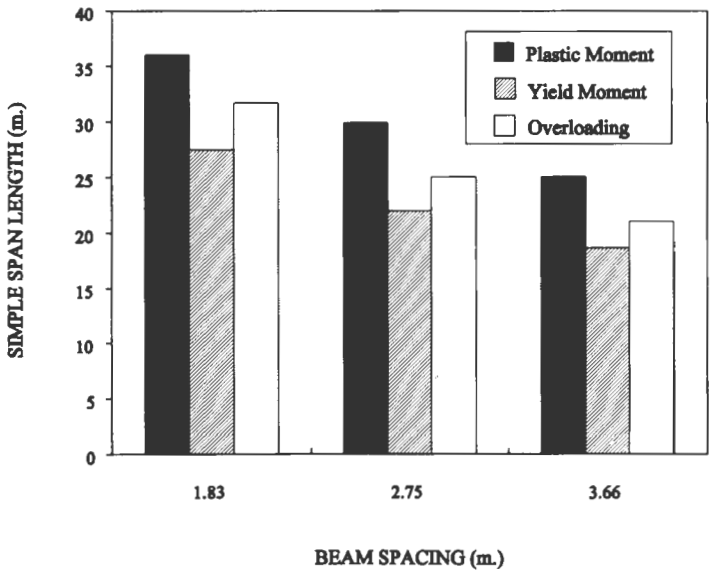

FIGURE 2 Span capability of W36 × 210 composite steel beams.

TABLE 1 Allowable Initial and Final Concrete Stresses by AASHTO

TYPES OF PRESTRESS		ALLOWABLE STRESS
INITIAL STRESS AT TRANSFER OF P/S	TENSION	$3\sqrt{f'_{ci}}$
	COMPRESSION	$0.6\, f'_{ci}$
FINAL STRESS UNDER DESIGN LOADS	TENSION	$3\sqrt{f'_c}$ OR $6\sqrt{f'_c}$
	COMPRESSION	$0.4\, f'_c$

where

M_{DL1} = dead load moment on the noncomposite beam
M_{DL2} = superimposed dead load moment on the composite beam, and
M_{L+I} = live load plus impact moment on the composite section.

M_{DL1} is estimated by selecting deck dimensions, girder section, and stay-in-place forms; M_{DL2} is caused by the effect of the weight of concrete barriers, railing, and future wearing surface; and M_{L+I} is based on AASHTO's girder distribution factors, the HS20-44 (truck or lane) or alternate military loading, and AASHTO's impact coefficient. Additional specific requirements for prestressed concrete and composite steel bridges are listed below.

Prestressed Concrete Girders

The ultimate flexural capacity of under-reinforced pretensioned concrete girders having a rectangular section behavior is based on the following expression:

$$\phi M_n = \phi A_s^* f_{su}^* d\left(1 - \frac{0.6\rho^* f_{su}^*}{f'_c}\right) \tag{4}$$

where

ϕ = capacity reduction factor of 1.0;
A^* = area of prestressing steel strands;
f_{su}^* = stress in the prestressing steel strands at ultimate;
d = depth of prestressing steel strands;
ρ^* = reinforcement ratio (equal to A^*/bd); and
b = effective width of section.

Prestressed concrete bridge girders are also required to satisfy the initial and final concrete stresses shown in Table 1 at any section along the girder, where f'_c and all stresses are in pounds per square inch. AASHTO allows a maximum stress of 70 percent of the ultimate prestressing steel stress (f'_s) to be applied initially at transfer for stress relieved strands. The corresponding stress at transfer for low relaxation strands is 75 percent of f'_s. Slight overstressing up to 85 percent of f'_s for a short period is permitted to offset seating losses.

Composite Steel Beams

The ultimate strength of compact composite steel beams designed by AASHTO is based on the fully plastic stress distribution shown in Figure 3. Composite beams in positive bending qualify as compact when their steel section meets two requirements. First, the depth of the

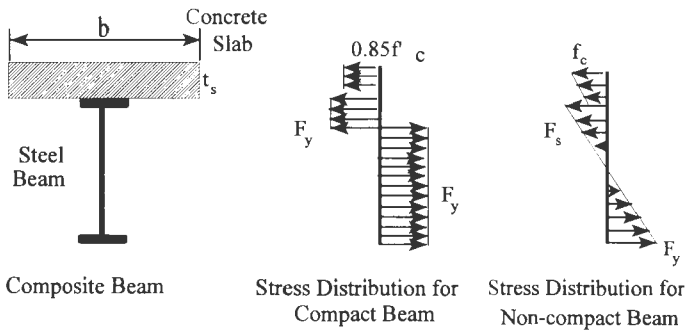

FIGURE 3 Plastic stress distribution for compact composite steel beams.

web in compression at the plastic moment (D_{cp}) should satisfy the following inequality:

$$\frac{2D_{cp}}{t_w} \leq \frac{19230}{\sqrt{F_y}} \tag{5}$$

where t_w is the web thickness and F_y is the specified minimum yield strength in pounds per square inch. The second requirement limits the depth from the top of the concrete slab to the neutral axis in plastic bending (D_p) to the following value:

$$D_p \leq \frac{(d + t_s + t_h)}{7.5} \tag{6}$$

where

d = depth of steel section,
t_s = thickness of concrete slab, and
t_h = average thickness of the concrete haunch above the top flange (in.).

Also, the AASHTO code requires the ratio of the projecting top compression flange width, b', to its thickness (t) not to exceed the value determined by

$$\frac{b'}{t} = \frac{2200}{\sqrt{1.3(f_{DL1})_{tf}}} \tag{7}$$

where $(f_{DL1})_{tf}$ is the top flange compressive stress caused by noncomposite dead load (in pounds per square inch). This expression should be satisfied by both compact and noncompact composite beams.

When the steel section does not satisfy the compactness requirements of Equations 5 and 6, AASHTO requires that the maximum strength of the section be taken as the moment capacity at first yield, M_y. In this case, the maximum factored moment caused by the applied loading, M_u, as given by Equation 3, will be smaller than or equal to ϕM_y, where ϕ is equal to 1.0. AASHTO also requires the sum of stresses produced by the applied loading on the noncompact beam to be below the yield stress at any point. For unshored construction, the total stress must satisfy the following expression:

$$1.3[f_{DL1} + f_{DL2} + (5/3)f_{L+I}] \leq F_y \tag{8}$$

where f_{DL1}, f_{DL2}, and f_{L+I} were defined earlier. For shored construction, the stress f_{DL2} in Equation 8 is 0.

Finally, the design of composite steel beams should satisfy AASHTO's overloading requirement regarding the stress in the steel section:

$$f_{DL1} + f_{DL2} + (5/3)f_{L+I} \leq 0.95F_y \tag{9}$$

The above requirement applies to all composite sections, whether compact or noncompact.

Reliability Models

Reliability-based safety evaluation of structures starts with the formulation of the limit state functions. These limit states are conditions under which a structure can no longer serve its intended purpose during its life span. In general, the reliability of a structural member or system for the ultimate flexural capacity limit state can be expressed by the use of a failure function, G, as

$$G(R, Q) = R - Q \tag{10}$$

where R is the resistance and Q is the total load effect. Failure occurs if G is less than or equal to 0. Load components and resistance are random by nature because of the inherent variability in material and load, lack of statistical data, mathematical idealization, approximate design procedures, and human error. Therefore, G is a random variable because it is a combination of random variables, as indicated by Equation 10. Structural safety can be measured in terms of a reliability index (*4*), β, as in the following:

$$\beta = \frac{\mu_G}{\sigma_G} \tag{11}$$

in which μ_G and σ_G denote the mean and standard deviation of G, respectively. The relationship between the probability of failure (P_f) and reliability index is expressed as the following:

$$P_f = 1 - \Phi(\beta) \tag{12}$$

where Φ is the cumulative standard normal distribution function of $G(\mu = 0$ and $\sigma = 1)$. Figure 4 shows a typical probability distribution of G and a graphical definition of the reliability index and probability of failure.

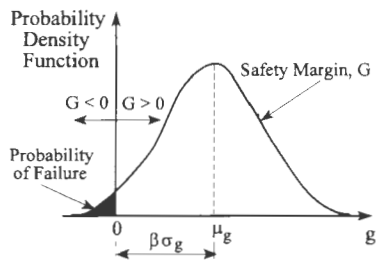

FIGURE 4 Random representation of the safety margin.

In this study the reliability index is computed using the Rackwitz-Fiessler method (*5*) because R and Q do not have the same probability distributions. This iterative procedure is based on approximating the true probability density functions of the random variables by normal distributions at the point of maximum probability (design point).

Bridge Load Models

The statistical parameters of load and resistance are needed for evaluating the reliability index. The maximum load effects on a highway bridge are mainly caused by dead load, live load, dynamic load, environmental loads, and accidental loads (braking forces, vehicle collision, etc.). Environmental loads do not govern for short and medium span bridge superstructures and, hence, they are not treated in this study. Therefore, the total load effect (Q) for a bridge girder can be represented by the following:

$$Q = [D + L + I] \tag{13}$$

where D is dead load, L is live load, and I is the dynamic load effect. The statistical parameters of the total load effect (Q) are determined using Turkstra's rule (*6*), and the probability distribution is approximated by a normal distribution.

It is convenient to consider four components of dead load, according to quality control measures. These components are weight of precast members (D_1), cast-in-place concrete elements (D_2), asphalt (D_3), and miscellaneous items (D_4). The bias (mean-to-nominal) ratios and coefficients of variation (COV) of dead load components are shown in Table 2 (*7*).

Nowak's live load model (*8*) is used in this study. The live load model is based on truck surveys in North America. It was shown that the governing combination for multiple-lane short and medium span bridges is caused by two trucks traveling side-by-side on the bridge. Actual or "more accurate" girder distribution factors (GDFs) are needed for evaluating the live load means per girder. The following expression for GDF for I-girders is considered (*9*):

$$\text{GDF} = 0.15 + \left(\frac{S}{3}\right)^{0.6}\left(\frac{S}{l}\right)^{0.2}\left(\frac{k_g}{lt_s^3}\right)^{0.1} \tag{14}$$

where

S = girder spacing (ft),
l = span length (ft),
t_s = concrete slab thickness (ft), and
k_g = (ft^3) is evaluated from the following:

$$k_g = n(I + Ae_g^2) \tag{15}$$

where

n = modular ratio
I and A = moment of inertia and the area of the beam or girder, respectively, and
e_g = eccentricity of the beam with respect to the slab. The statistics of the live load model include professional factors to account for uncertainties in the value of the GDF.

The dynamic load on bridges is generally caused by the dynamic properties of the structure, the suspension system of the vehicle, and surface roughness and bumps. The mean value of impact is considered to be 15 percent of live load with a high coefficient of variation of 0.80 (*8*).

Bridge Resistance Models

The component strength for most highway bridges depends on the bridge type, girder layout and geometry, material properties, and section dimensions. The random nature of the strength is mainly a result of the variability of material strength, accuracy of strength prediction theories, and fabrication. The statistical properties of the material strengths that are used in the study are compiled from the available literature (*10*) and presented in Table 3.

TABLE 2 Statistical Parameters of Dead Load

Class	Description	Bias	C.O.V
D_1	Factory-made Members	1.03	0.04
D_2	Cast-in-place Members	1.05	0.08
D_3	Wearing Surface	1.00	0.15
D_4	Miscellaneous Items	1.03	0.04

TABLE 3 Statistics of Materials Used in the Study

Material Variable	Mean-to-Nominal Ratio	Coefficient of Variation
Yield Stress for Flanges	1.05	0.10
Yield Stress for Webs	1.10	0.11
Modulus of Elasticity of Steel	1.00	0.06
Poisson's Ratio of Steel	1.00	0.03
Tensile Strength of Steel	1.00	0.11
Concrete Compressive Strength	0.99	0.18
Concrete Tensile Strength	1.04	0.10
Strength of Prestressing Strands	1.04	0.04

The flexural strength of concrete girders and composite steel beams is studied in terms of the moment-curvature relationship. The Monte Carlo simulation method is used to evaluate the statistical parameters of the ultimate moment capacity. Several pretensioned concrete girders with different reinforcement ratios are analyzed. A typical probabilistic moment-curvature relationship for an AASHTO Type III I-section at the mean and one standard deviation above and below the mean is shown in Figure 5. The analysis showed that the mean-to-nominal ratio and coefficient of variation of the moment capacity at ultimate are governed by the statistics of the prestressing strands and are equal to 1.04 and 0.08, respectively.

Similarly, several composite steel beams of various sizes are analyzed in flexure with consideration of material statistics. Typical probabilistic moment-curvature relationship for a composite beam having a W36 × 210 rolled section is shown in Figure 6. The analysis showed that the ultimate moment carrying capacity has a mean-to-nominal ratio of 1.10 and a coefficient of variation equal to 0.12. These statistical properties include professional factors to account for uncertainties in the analysis, that is, the difference between theory and experiment.

The results of the analysis indicate that the probability distribution of the ultimate moment capacity of concrete and steel girders can be approximated by a lognormal model.

Findings

The AASHTO specifications are used for the design of simply supported prestressed concrete I-girders and composite steel beams. The live load is composed of the HS20-44 or alternate military loading, whichever governs. The girder spacing ranges between 1.82 and 3.65 m (6 and 12 ft). All bridges have two normal size parapets, an average haunch above the top flange 25.4 mm thick (1 in.), future wearing surface of 1.44 kN/m^2 (30 psf), and stay-in-place formwork of 0.72 kN/m^2 (15 psf). The specified 28-day concrete compressive strength in the cast-in-place deck is 27.6 MPa (4,000 psi). The thickness of the deck varies with the girder spacing.

Prestressed Concrete Girders

Nominal final concrete strength of 44.8 MPa (6,500 psi) is specified for the pretensioned girder. Concrete strength in the girder at transfer is considered to be 37.9 MPa (5,500 psi). The prestressing steel is composed of 12.7-mm (0.5-in.) low relaxation strands with 1862 MPa (270 ksi) ultimate strength. The steel strands are draped at the third points.

Figure 7 shows the ratio of the number of strands to satisfy serviceability to the number of strands required for strength, denoted by h, versus the span length. The plots are generated for allowable concrete stresses on the basis of corrosive and noncorrosive environments. The shaded areas represent designs that have different girder spacings. This deterministic analysis shows that allowable stresses govern the design for the spans and girder spacings considered. Figure 7 indicates that the number of strands to satisfy serviceability is about 1.15 to 1.45 times larger than the number of strands needed for strength.

Figure 8 shows the range of reliability indexes for the flexural capacity limit state based on designs to satisfy strength or allowable stresses. The range of reliability indexes for AASHTO designs is 5 to 6 for noncorrosive environments and 6 to 8 for corrosive environments. The range of reliability indexes based on the limit state (1.3 M_D + 2.17 M_{L+I}) lies between 3.2 and 4.3.

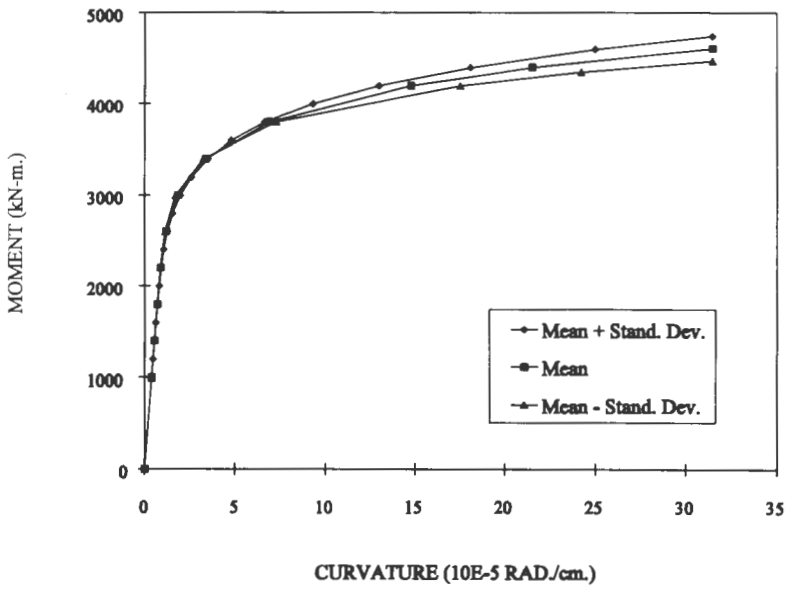

FIGURE 5 Probabilistic moment-curvature relationship for AASHTO type III P/S concrete I-girder.

Composite Steel Beams

The design of the composite steel beams covers 10 wide-flange rolled sections. AASHTO M270 grade 36 (248 MPa) structural steel is specified for the wide-flange sections.

Figure 9 shows the maximum simple span length of composite beams with rolled sections for a profile of girder spacings. Most of the considered steel beams are not compact because they do not satisfy AASHTO's ductility requirement (Equation 6). The study showed that the design of the noncompact beams was governed by the maximum stress requirement (Equation 8), whereas the overloading condition controlled the design of the compact beams (Equation 9). The reliability indexes for the composite steel beams in Figure 9 are pre-

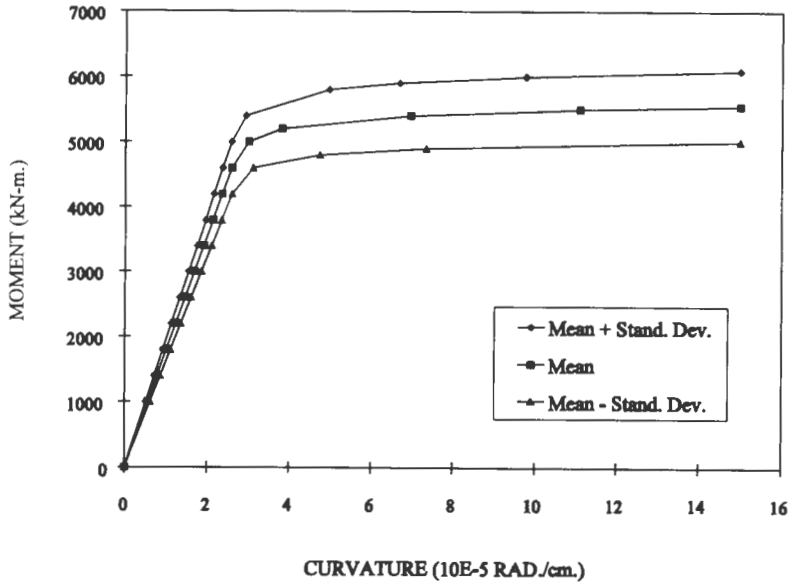

FIGURE 6 Probabilistic moment-curvature relationship for a W36 × 210 composite steel beam.

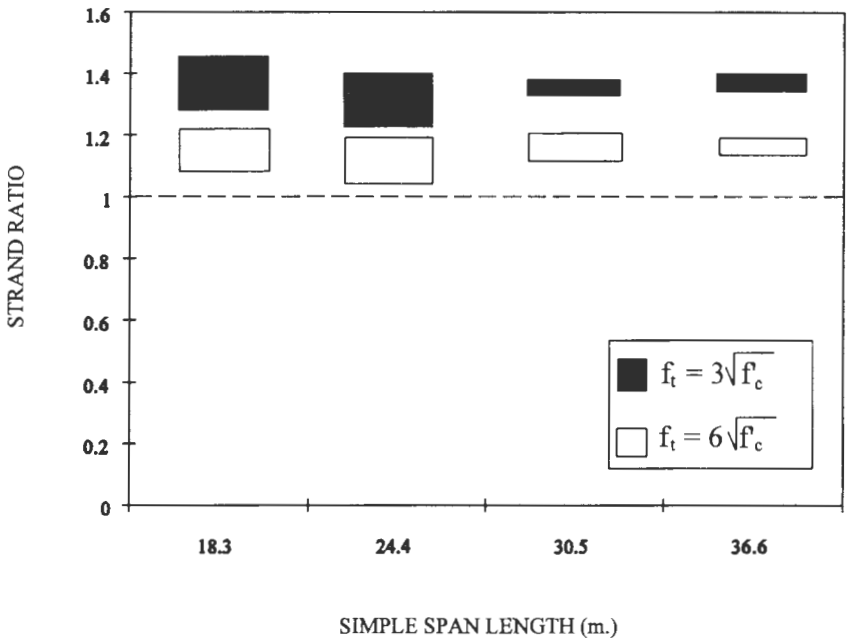

FIGURE 7 Strand ratio versus simple span length for P/S concrete I-girders.

sented in Figure 10. Also shown in Figure 10 is the range of the reliability indexes for bridges having the same beam spacings but assuming that the design is governed by (1.3 M_D + 2.17 M_{L+I}). The results of the reliability study indicate non-uniformity in the safety of steel bridges that are designed in accordance with the current AASHTO code. In general, the reliability index varies between 5 and 7, depending on the beam spacing, span length, and section size. The corresponding reliability indexes for designs based on the factored moments are between 2.7 and 4. The main reasons for the non-uniformity in the reliability are because of

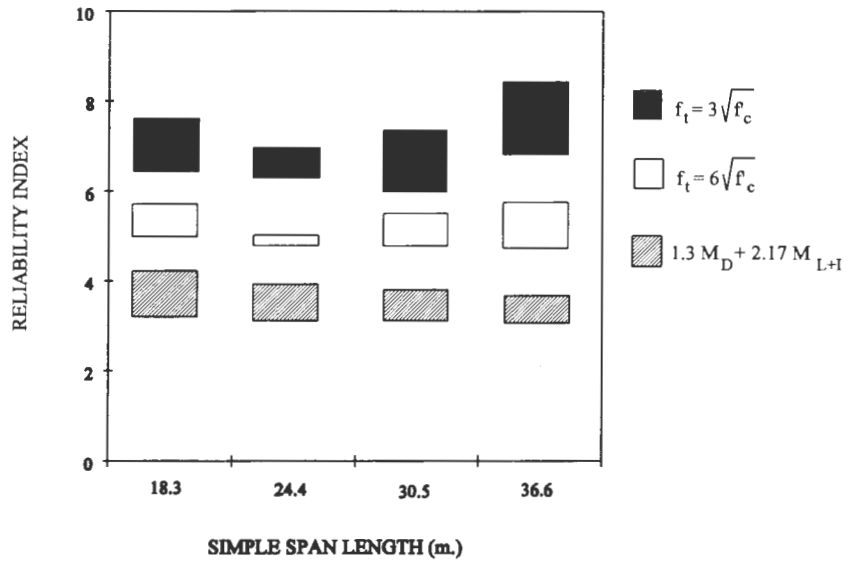

FIGURE 8 Reliability index versus simple span length for P/S concrete I-girders.

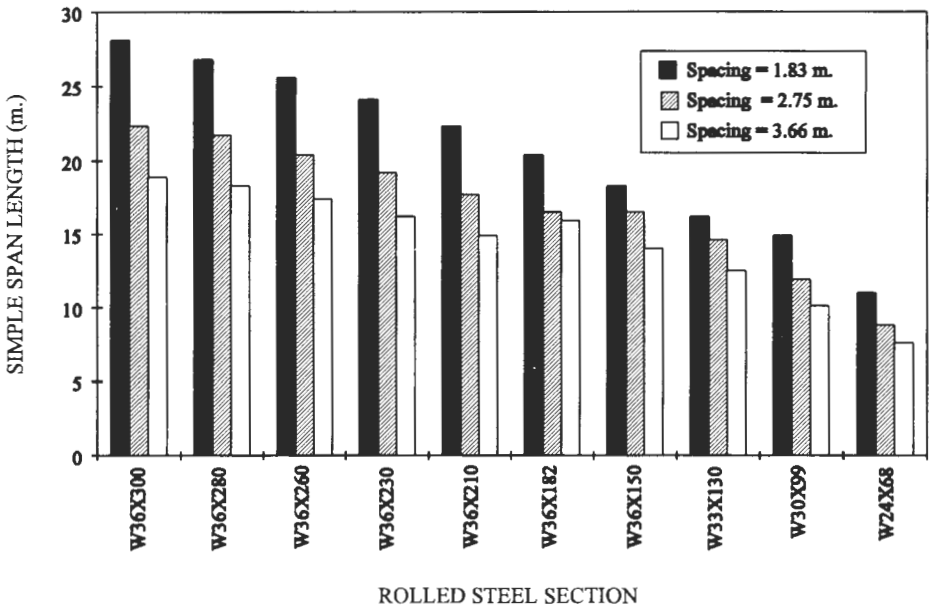

FIGURE 9 Maximum simple span length for composite steel beams.

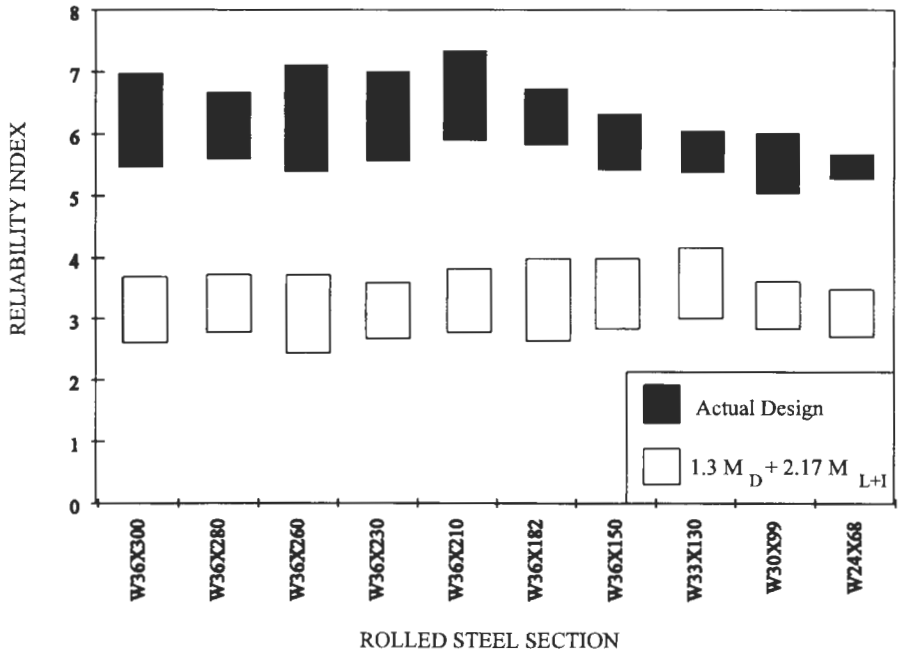

FIGURE 10 Reliability indexes for composite steel beams.

AASHTO's approximate live load girder distribution factor, which overestimates the live load for larger girder spacings, and the fact that the AASHTO is not a reliability-based code. The study also indicates that noncompact beams have higher reliability indexes than do compact beams because noncompact beams are more conservatively designed than compact ones using the current specifications.

Conclusions

Simply supported pretensioned concrete girders and composite steel beams designed according to AASHTO specifications are investigated using reliability methods. Reliability indexes are computed on the basis of actual designs for a range of span lengths, girder spacings, and precast/rolled sections. The results of this study about bridge girders in flexure at ultimate lead to the following conclusions:

1. Current LFD-based specifications for concrete and steel bridges result in non-uniform safety for different spans and girder spacings.
2. Prestressed concrete girder design is usually governed by allowable service stress requirements. In most practical cases, the actual ultimate flexural capacity is 15 to 45 percent higher than the required strength because of the applied factored loads. Higher values are for designs that limit allowable concrete tensile stresses to $3\sqrt{f'_c}$ instead of $6\sqrt{f'_c}$.
3. The design of noncompact composite steel beams that do not satisfy AASHTO's ductility requirement is governed by the maximum stress requirement. The design of compact beams is usually controlled by overloading.
4. The actual reliability prestressed concrete I-girders are in the range of 5 to 6 for noncorrosive environments and 6 to 8 for corrosive environments. The range of reliability indexes based on the $(1.3\ M_D + 2.17\ M_{L+I})$ limit state lies between 3.2 and 4.3.
5. The reliability index of composite steel beams varies between 5 and 7. Lower values of the reliability index are associated with compact beams and smaller girder spacings.

References

1. *LRFD Bridge Design Specifications*, 1st ed., AASHTO, Washington, D.C., 1994.
2. *Standard Specifications for Highway Bridges*, 15th ed., AASHTO, Washington, D.C., 1992 and 1994 interim.
3. Ghosn, M., and F. Moses. Reliability Calibration of Bridge Design Code. *Journal of the Structural Division*, ASCE, Vol. 112, No. 4, April 1986, pp. 745–763.
4. Thoft-Christensen, P., and M. J. Baker. *Structural Reliability Theory and Its Applications*. Springer-Verlag, New York, 1982.
5. Rackwitz, R., and B. Fiessler. Structural Reliability Under Combined Random Load Sequence. *Computer and Structures*, No. 9, 1978.
6. Turkstra, C. J. *Theory of Structural Design Decisions, Study No. 2*. Solid Mechanics Division, University of Waterloo, Ontario, Canada, 1970.
7. Tabsh, S. W., and A. S. Nowak. Reliability of Highway Bridges. *Journal of the Structural Division, ASCE*, Vol. 117, No. 8, Aug. 1991, pp. 2372–2388.
8. Nowak, A. S., Y-K. Hong, and E-S. Hwang. Modeling Live Load and Dynamic Load for Bridges. In *Transportation Research Record 1290*, TRB, National Research Council, Washington, D.C., 1991, pp. 119–126.
9. Zokai, T., R. A. Imbsen, and T. A. Osterkemp. Distribution of Wheel Loads on Highway Bridges. In *Transportation Research Record 1290*, TRB, National Research Council, Washington, D.C., 1991, pp. 110–118.
10. Ellingwood, B., T. V. Galambos, J. G. MacGregor, and C. A. Cornell. *Development of a Probability Based Load Criterion for American National Standard A58*. NBS Special Publication 577. National Bureau of Standards, Washington, D.C., 1980.

Bangkok Second-Stage Expressway System Segmental Structures

Brian Dodson, *J. Muller International*

In December 1988, the Expressway and Rapid Transit Authority of Thailand entered into an agreement with the Bangkok Expressway Consortium, Ltd., to build and operate the Bangkok Second-Stage Expressway for a period of 30 years. The project includes 66 km (41 mi) of elevated structures to be built in two phases. The precast segmental structures consist of over 2,000 spans with an average length of 42 m (138 ft). A gigantic precasting yard was designed to produce a total of 20,500 superstructure segments. New construction engineering procedures had to be developed to accommodate production of as many as 1,000 superstructure segments per month.

With less than half of the road density of similarly sized developed cities, Bangkok is notorious for its heavily congested roadways (*1*). To help alleviate this situation, in December 1988, the Expressway and Rapid Transit Authority of Thailand entered into an agreement with the Bangkok Expressway Consortium, Ltd. (BECL), to build and operate the Second-Stage Expressway. The contract was a build-operate transfer contract. BECL would provide the financing of the project in exchange for tax breaks and a 30-year operation concession. At the end of 30 years, the ownership of the expressway would revert to the Rapid Transit Authority of Thailand (*1*). This toll facility would be the world's second largest public utilities concession project. The firm Kumagai Gumi Co., Ltd., Project Manager for BECL, chose Freeman Fox Intercom to design the elevated expressway. J. Muller International (JMI) was hired to provide detailed engineering for production of the segmental bridge structure.

The Second Expressway System (SES) is a network of elevated express lanes through the Bangkok metropolis and suburban areas. The project includes a north–south route (Bangklo-Chaeng Watthana) and an east route (Phyathai–Srinakarin).

The project is built in two stages: (*a*) initial SES with a total length of 47 km (29 mi) completed in February 1993 and (*b*) incremental SES with a length of 19 km (12 mi), currently under construction and expected to be completed in 1995. The total cost of construction will exceed 1.2 billion U.S. dollars.

The initial SES includes the Chaeng Watthana Road to Middle Ring Road segment on the north–south route and the Phayathai to Rama IX Road segment on the east route. The initial SES is composed of 1,131 spans.

The incremental SES includes a north–south segment extending from Phayathai to the southern portion of the First-Stage Expressway. This section of the SES is composed of over 700 spans.

Description of Segmental Structures

The original concept for the Second-Stage Expressway utilized a U-beam section. Under the urging of JMI, the

project manager, Kumagai Gumi decided to convert a large portion of the project, 770,000 m^2, to a precast segmental box girder. The decision to convert to segmental was based on speed of construction in this dense urban environment. The precast segmental superstructures are built from the top with almost no concrete cast in situ to minimize traffic interruptions. In addition, precasting allows for good quality control, and the concrete box girder provides pleasing aesthetics.

The segmental structures for the Bangkok SES consist of over 2,000 spans with an average length of 42.25 m (140 ft). Span length varied from a minimum of 24.9 m (82 ft) to a maximum 48.75 m (160 ft). To accommodate box girder width variations, two different sections were used for the project: (*a*) Section D2 for width up to 12.2 m (40 ft) and (*b*) Section D3 for width up to 15.6 m (51 ft). Both sections are 2.4 m (7 ft 10 in.) deep. In some areas two box girders are connected by a cast-in-place closure joint between the wing tips. The top slab of the box girder is transversely post-tensioned. The spans are simply supported to take into account potential differential settlements; however, the box girders are linked through continuity of the top slabs to provide good rideability. An in-situ slab was placed between adjoining spans' segments. The "link slab" restricted differential movement between the two adjacent spans. Expansion joints are placed approximately every four spans. The spans are divided into concrete segments with an average length of 3.40 m (11 ft 2 in.). Diaphragm segments are used at each end of the spans to receive post-tensioning tendon anchorages and distribute bearing reactions. The post-tensioning tendons are placed inside the box girders but outside of the concrete. They are typically draped and deviated at three locations within the span. The deviator segments are reinforced with ribs along the webs and a bottom slab beam. To simplify the post-tensioning layout, "diabolos" were used to each tendon deviation. The diabolo is a pipe with bell-shaped extremities, which is cast into the segment. After casting, the diabolo is removed, leaving a bell-shaped void, which will accommodate the longitudinal post-tensioning. The radii of the bells are computed to accommodate all variations of tendon angles caused by span length and geometry. This design allows simplicity and standardization of the tendon geometry and accelerates the casting process, thereby reducing possible offset caused by pipe fabrication or placement errors. The superstructure is erected by the "span-by-span" method with dry joints. After erection, the top slab segment joints are sealed with an epoxy compound, and an asphalt overlay 30 m (1 in.) thick is placed on the deck.

The structures are designed according to the AASHTO standard specifications of 1983 (*3*) and the Guide Specifications of Design and Construction of Segmental Bridges of 1989 (*3*). The highway loading was based on AASHTO HS20-44 loads increased by 30 percent with an overload provision of 27.8-ton (61.3-kips) trucks, centered at 11.15 m (36 ft 7 in.) and occupying a single lane.

Precasting

The production goal of the precasting yard for the initial SES was ambitious: all 14,400 segments were to be completed within a 2-year period.

Precasting Yard Design

General

The project manager had the precasting yard built and equipped under a separate contract. After completion of this task the project manager selected the casting yard "operator," a joint venture of Bilfinger & Berger and CH. Karnchang, for manufacturing segments. The segments are then delivered to three erection contractors.

As previously stated, the production goal for the precasting yard was ambitious: a total of 20,500 superstructure segments had to be produced, of which 14,400 segments were for the initial SES and 6,000 segments were for the incremental SES.

Production of the 14,400 segments began in January 1991 and was completed in November 1992. The average monthly production was 630 segments, including the learning curve. The maximum monthly production reached a high of 1,013 segments.

The "short cell" casting method was chosen over the long bench method because of the necessity to build spans with variable curvatures in plan and elevation. In addition, a limited amount of space was available for the casting yard (200,000 m^2). It was necessary to install a total of 50 casting cells (34 for typical segments, 16 for pier segments), making the casting yard the largest of its kind in the world (see Figures 1 through 3). Because of poor soil quality, the casting yard is totally covered with a concrete slab, supported on piles in high load areas.

To ease the management of the casting operations, the yard was divided into four distinct production zones. However, reinforcing bars were produced at a single location, and concrete was produced at two concrete plants. Because of the high cost of imported equipment, the yard had to be designed to minimize the equipment requirements.

The following were other objectives of the casting yard design:

1. To maintain a continuous production flow (e.g., rebar → rebar cage → casting machine → segment → temporary storage → storage → erection);

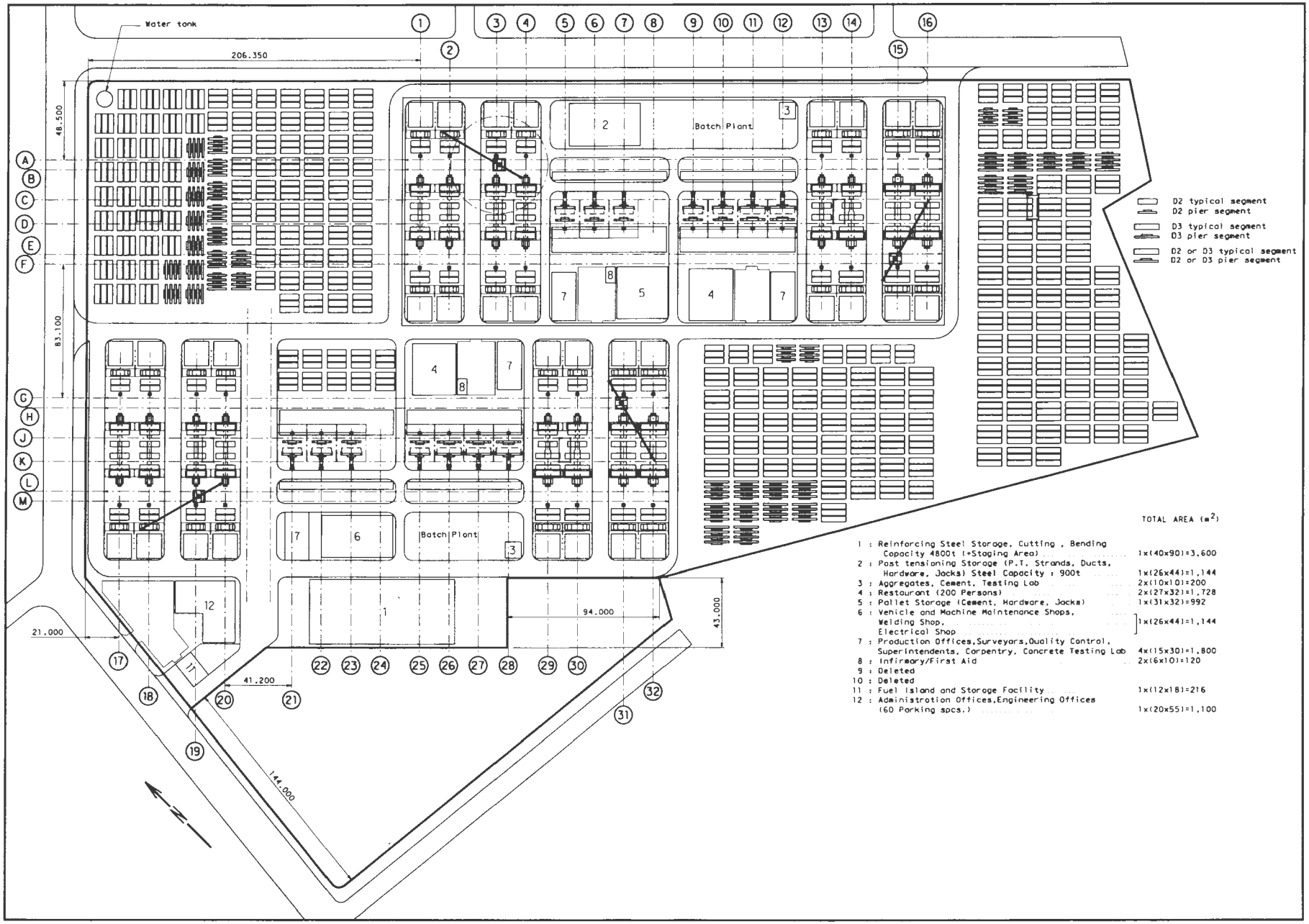

FIGURE 1 Layout of the Bang Pa-In casting yard.

FIGURE 2 Aerial view of casting yard.

2. Because of the layout of the production areas, to allow this flow to occur within a limited amount of space with minimum conflicts;
3. To separate the production areas from segment handling areas for safety reasons, and to reduce interruptions in the production process; and
4. To allow for the different levels of experience in segmental production by management and supervisors. The laborers had no experience in segmental production, and little or no experience in general construction.

Equipment

The casting machines were designed to accommodate the varying geometry characteristics of the superstructure: minimum radius 83 m (272 ft) and variable segment lengths and widths. Production requirements are one typical segment per machine per day and three diaphragm segments per machine per week. To accelerate operations, hydraulic systems were used to operate the collapsible core forms and adjust the soffits. Tight tolerances were given for fabrication of the casting machines—in particular for the form bulkheads—to ensure consistency of the concrete segment dimensions. Finally, the design of the casting machines had to take into account the high number of uses (approximately 450 uses per machine). Four tower cranes were placed on rails to service the four different production areas. They are used mainly to rotate form soffits and handle rebar cages, which were produced in jigs close to the forms.

Six travel lifts are used to carry the segments from the production area to storage. They are also used to load trucks transporting the segments to the erection site. The casting machines are equipped with three soffits, the wet cast, match cast, and a temporary storage. With this layout of the segment loading, storage operations are removed from the critical path and travel lift usage is optimized. For additional simplicity, the casting machines were aligned such that the segments produced were stored within the path of the shuttle lift.

The concrete is produced in two mixing plants at 80 m^3/hr (105 CY/hr) and delivered to the casting machines with concrete trucks. Adjustable conveyor belts are used to place the concrete in the forms. Conveyor belts were selected over concrete pumps because of their lower cost and simplicity of operation. In addition, limited amounts of concrete were wasted with this system. Special measures were taken to ensure that the segment production would not be affected by the rainy season; in particular, all working areas, including rebar cage assembly and casting machines, were protected with rolling sheds.

FIGURE 3 Typical D2 casting machine.

Supervision—Personnel

A crew was assigned to each casting machine to work on forms and assembly of rebar cages. Concrete crews rotate between forms to handle concrete pours. Each of the four production areas was organized with an independent engineering and supervision staff that included the following:

- Production superintendent,
- Quality control engineers, and
- Survey crews.

In addition, independent crews are used for handling of the segments and finishing work on the segments. Work is performed 20 hr/day with staggered shifts allowing for optimum use of the equipment.

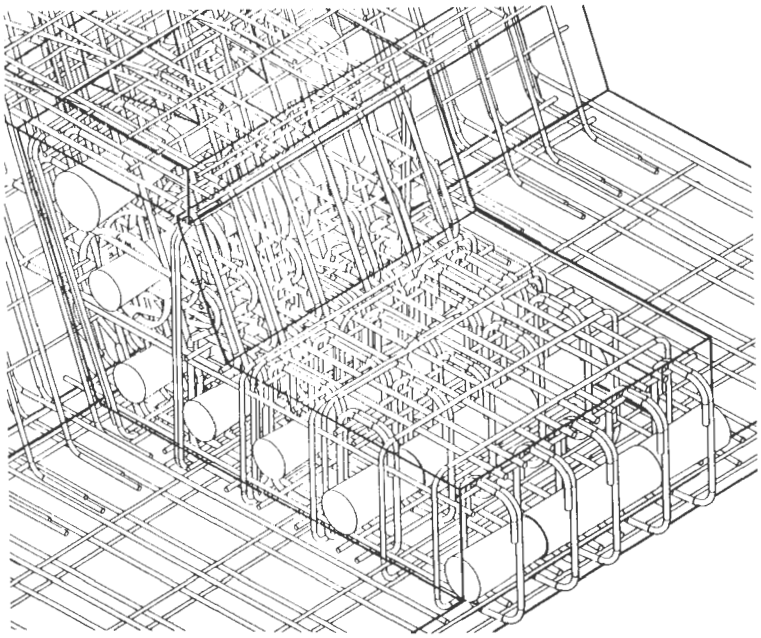

FIGURE 4 Reinforcement detail of typical deviation segment; note voids for diabolos.

Geometry Control

The short cell casting method was somewhat sophisticated. It relied on an accurate placement of the match cast segment in the casting machine for proper geometry control. It was necessary to check with great accuracy the relative positions of matching segments after each pour. The information obtained from these measurements was then used to compute the adjustment of the next match cast segment in the casting machine. This method had never been used before in a casting yard of this size.

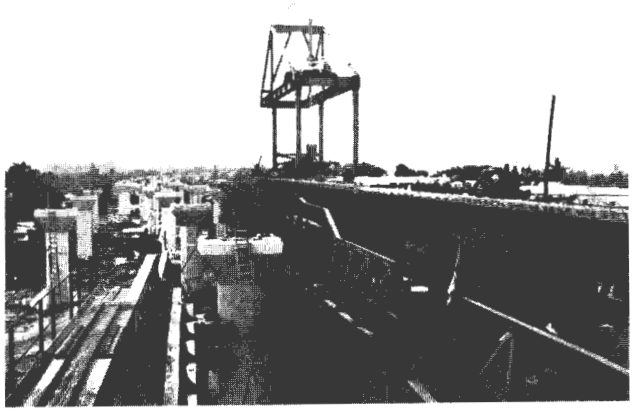

FIGURE 5 Underslung truss; note portal frame on existing structure.

It was necessary to develop an iterative computer program to ensure that proper geometry control would be achieved for all casting machines. The three-dimensional computer program Precast-SC computed casting curves, provided setup values for the match cast segments before each pour, and "as-cast" coordinates for all control points after the segments are cast. These final coordinates are used to adjust segment positions during erection. The program works from theoretical three-dimensional coordinates of three control points at each segment joint and takes into account actual survey readings after each segment pour.

Superstructure Shop Drawings

Detailed drawings were required for all the superstructure segments to facilitate production. A span layout drawing was produced for each span. It provided the following information:

- Dimensions of all segments of the span,
- Three-dimensional coordinates of the control points at each segment joint,
- Orientation of segment joints at the extremities of the span,
- Coordinates of span supports to verify consistency with pier locations, and
- Location of embedded items such as access holes, drain holes or gullies, sleeves and blockouts necessary for the erection equipment.

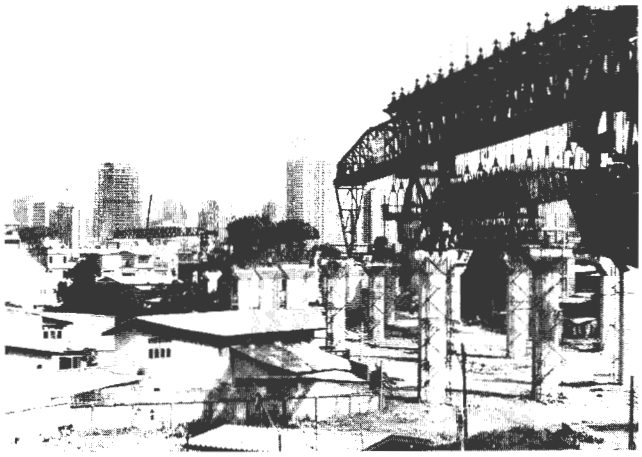

FIGURE 6 Six overhead trusses converging at construction of interchange.

Drawings showing post-tensioning and reinforcing details for all segments were also developed along with bending diagrams, dimensions, and quantities for all reinforcing bars. As mentioned earlier, the post-tensioning layouts were simplified by deviating all the tendons at only three locations. Further simplification was achieved through the use of diabolos at each tendon deviation.

Three-dimensional computer-assisted design models were developed for all typical rebar cages (Figure 4). These models were useful for detecting potential conflicts between rebar and other embedded items. JMI produced approximately 10,000 shop drawings in a period of 1.5 years.

Erection Systems

The segments were assembled by the span-by-span method with ten erection trusses: four pairs of underslung triangle trusses and six overhead trusses. In unobstructed areas with ground access, the contractor used self-launching twin triangular trusses, equipped with a launching nose and tail, which supported the segment under the wing. The segments were delivered from the top, traveling over the previously erected spans, and placed on the truss with a specifically designed steel portal frame. Once the longitudinal post-tensioning was stressed, the trusses were lowered until the span rested on the bearing pads of the columns. Then the self-launching truss was advanced to the next span. In full production, the contractor was able to erect one span per truss per day (Figure 5).

In areas over waterways or existing roadways (including a three-level interchange with 83-m (272-ft) radii and 10 percent cross slope), the spans were erected with a self-launching overhead truss, which required no access to the ground level. The truss was supported entirely on the pier cap. The segments were delivered over the previously completed structure and suspended from the overhead truss until post-tensioning was completed. Once the post-tensioning is complete, the truss would advance to the next successive span. In full production, the contractor was able to erect one span per truss every 2 days (Figure 6). The first span of the initial SES project was erected in May 1991. The last span was completed in March 1993.

Conclusion

The precast segmental method of construction was successfully applied to this gigantic project built in a dense urban environment. Two of the casting yard production areas were opened in February 1991 and two more were opened in May 1991. In August 1991, the production reached 750 segments, which was the goal assigned for this project. The maximum monthly production actually reached over 1,000 segments.

The erection of the 1,131 spans of the initial SES was accomplished with a total of 10 trusses. It started at the end of June 1991 and was completed in March 1993.

ACKNOWLEDGMENT

To all the individuals involved in the SES project the author expresses his appreciation, especially to Kumagai Gumi and the JMI Bangkok office.

REFERENCES

1. Reina, P. Bangkok Builds BOT Mega Projects. *Engineering News Record*, June 15, 1992.
2. *Standard Specifications for Highway Bridges*, 13th ed. AASHTO, Washington, D.C., 1983.
3. *Guide Specifications of Design and Construction of Segmental Bridges*. AASHTO, Washington, D.C., 1989.

BRIDGE STRUCTURAL SYSTEMS

High-Performance Concrete U-Beam Bridge: From Research to Construction

Mary Lou Ralls, *Texas Department of Transportation*

The Louetta Road Overpass on State Highway 249 in Houston, Texas, is a high-performance concrete bridge design and construction project that is sponsored by FHWA and the Texas Department of Transportation in cooperation with the Center for Transportation Research at The University of Texas at Austin. The overpass, being constructed in 1995, incorporates high-performance concrete in the precast pretensioned U-beams, the composite precast/cast-in-place deck, and the precast posttensioned substructure. Beam concrete design strengths reach 90 MPa (13,000 lb/in.^{2}), with 15.2-mm (0.6-in.)-diameter, 1862-MPa (270-ksi) prestressing strands required to fully use the higher concrete capacity. The use of high-performance concrete in bridge construction is anticipated to be cost-effective at the time of construction and during the life of the structure. Implementing its use in bridge construction is a dynamic process that requires flexibility as new information and concerns arise. The ability of all parties involved to work as a team, with open lines of communication, is of extreme importance.

Bringing state-of-the-art materials and methods to bridge construction is a dynamic process and involves effecting changes in the ways in which a diverse group of people do business. Specifically, high-performance concrete is a state-of-the-art material that is engineered to have both high strength and improved durability. With these improved properties, its use in bridge construction is anticipated to be cost-effective not only at the time of construction but also during the life of the structure. The process of going from research to construction, that is, implementing high-performance concrete in Texas bridge construction, is discussed.

In July 1993 a cooperative agreement was initiated between FHWA and the Texas Department of Transportation (TxDOT), in cooperation with the Center for Transportation Research at The University of Texas at Austin. The 3-year research study, entitled Design and Construction of Extra-High Strength Concrete Bridges, includes development of design and construction standards and specifications for the use of high-performance concrete in bridges and construction of a bridge that optimally uses the improved properties of high-performance concrete.

The bridge in this project, the Louetta Road Overpass on State Highway 249 in Houston, was placed under contract in February 1994 and will be constructed during 1995. It incorporates high-performance concrete in the precast pretensioned U-beams, the composite precast/cast-in-place deck, and the precast posttensioned pier segments. Figure 1 is a perspective of the southbound main lanes of the bridge (*1*).

Structural Details

The Louetta Road Overpass, as shown in Figure 2, consists of two adjacent three-span bridges. The spans

range from 37.0 to 41.3 m (121.5 to 135.5 ft). They consist of simply supported beams and continuous composite decks that have construction joints at the interior supports.

A transverse section of the superstructure is shown in Figure 3. The beams are 1372-mm (54-in.)-deep U-beams, the open-top trapezoidal beams recently developed by TxDOT. The beams are uniformly spaced at each support, with average spacings of 3.6 to 4.8 m (11.7 to 15.8 ft) because of the varying roadway widths.

In this project the U-beam is designed to fully use concrete with design strengths from 69 to 90 MPa (10,000 to 13,000 lb/in.^{2}). This requires the use of 15.2-mm (0.6-in.)-diameter, 1862-MPa (270-ksi) prestressing strands on a 50-mm (1.97-in.) grid spacing, which provides the large prestressing force at the maximum eccentricity needed to use the high allowable compressive stress for the high-performance concrete. A maximum number of strands (87), shown in Figure 3, is required in the outside beams of the 41.3-m (135.5-ft) middle span. The strands are straight, with the prestress force reduced at the ends through debonding of a portion of the strands. Debonding extended a maximum of 9 m (30 ft) from the ends of a few of the beams, including the beam shown in Figure 3. The researchers will be observing the behaviors of these beams, since the typical maximum debonded length used in design is 6 m (20 ft) for this beam length.

The southbound main lanes of the bridge are designed with a 55-MPa (8,000-lb/in.^{2}) deck. The northbound main lanes of the bridge deck are designed with 28-MPa (4,000-lb/in.^{2}) cast-in-place concrete, TxDOT's standard strength for cast-in-place decks. Both bridges have composite precast/cast-in-place concrete decks with 55-MPa (8,000-lb/in.^{2}) precast concrete panels. The researchers are experimenting with mix designs to achieve improved durability in both decks.

The long-term benefits of the increased strength and durability of high-performance concrete in service are undocumented. The presence of adjacent bridge decks with significantly different cast-in-place concretes not only allows comparison of the placing and curing of the two different concrete mixes during construction but also allows a comparison of deck behavior during the lives of the structures. Monitoring for a period of 20 to 30 years, similar to pavement evaluations, may be required to fully document the long-term cost-effectiveness of high-performance concrete in bridges.

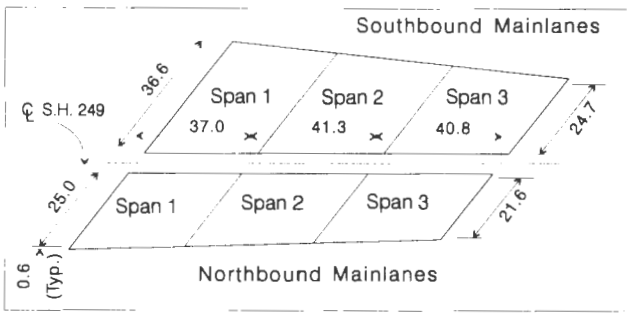

FIGURE 2 Plan view of Louetta Road Overpass (dimensions are in meters; 1 ft = 0.305 m).

The tapered, slender precast pier substructure was created to complement the shape of the U-beam superstructure for a unified aesthetic appearance. The individual piers, to be cast by the contractor, are precast hollow-core posttensioned 69-MPa (10,000-lb/in.^{2}) concrete segments. The piers are designed to consist of 1.2- to 1.8-m (4- to 6-ft)-long, match-cast segments on a drilled shaft foundation and with a tapered capital for the beam support, as shown in Figure 1. The column cross section is a 1.0-m (3.25-ft) square with clipped corners. The wall thickness is 100 mm (4 in.) on the walls opposite the two 190-mm (7.5-in.)-thick walls that each hold three posttensioned bars. Cast-in-place concrete will provide a shallow 1.2-m (4-ft)-diameter base for the transition from drilled shaft to precast segment and will also fill the lower column segments to a height of 1.5 m (5 ft) to resist vehicular impacts.

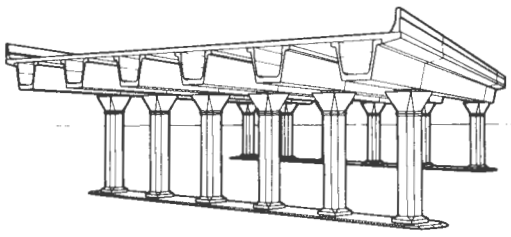

FIGURE 1 Southbound main lane of Louetta Road Overpass.

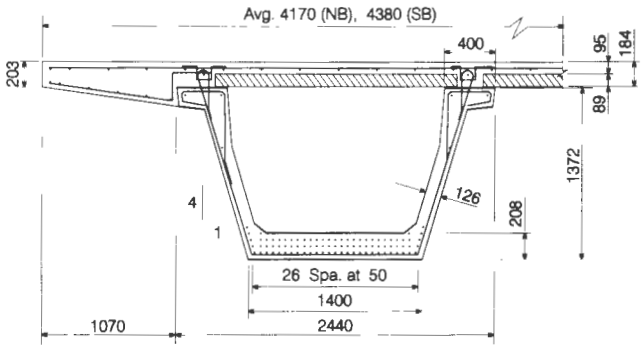

FIGURE 3 Cross section of Louetta Road Overpass (dimensions are in millimeters; 1 in. = 25.4 mm).

Bridge Costs

The use of high-performance concrete in bridges is expected to decrease construction costs because its higher strength allows for faster construction and designs with fewer beams than is possible with normal-strength concrete. Its use is also expected to decrease long-term maintenance costs because of the improved durability characteristics.

Cost comparison of the Louetta Road Overpass with similar normal-strength concrete U-beam construction is limited because of the recent development of the U-beam and, therefore, the lack of historical data. Comparison of construction costs can, however, be made with the construction costs of typical pretensioned concrete I-shaped beam bridges in Texas, which are averaging $\$290/m^2$ $(\$27/ft)^2$ of deck area for the total structure. The Louetta Road Overpass, which is part of the third large U-beam bridge project, received the low bid of $\$260/m^2$ $(\$24/ft)^2$ of deck area for the total structure. This cost is the same as that for the 12 normal-strength concrete U-beam bridges on the project and slightly lower than those of the other U-beam bridge projects let to date.

Significant construction cost reductions may not become apparent until use of the new high-performance materials and methods becomes more standard practice. In addition, studies of 20 to 30 years in duration may be needed to fully document the decreased maintenance costs anticipated with high-performance concrete bridges.

Beam Design

Typical methods were used in the design of the Louetta Road Overpass, except that the properties of high-strength concrete were used in the design of the U-beams. Design loading was the standard HS20 truck. Allowable stresses controlled the design, with ultimate state also checked. The standard AASHTO prestress loss equations were used for the design, with subsequent creep and shrinkage tests initiated to obtain a more accurate indication of losses in high-performance concrete.

Preliminary deflection measurements with a stretched-wire system attached to the sides of the U-beams indicate actual camber in the range of 60 to 90 mm (2.3 to 3.5 in.) at transfer compared with a calculated camber in the range of 65 to 100 mm (2.6 to 3.9 in.). Therefore, actual camber at transfer appears to be approximately 10 percent lower than the camber predicted by using suggested multipliers from the *PCI Design Handbook* (2) on the basis of the limited data obtained to date.

Camber growth with time is also being monitored, and limited preliminary data reduction indicates a 20 to 30 percent decrease in actual versus calculated values when the suggested multipliers at erection are used. The lower measured cambers are similar to values previously measured in closed-top box beams, which, like the U-beams, have greater stiffness than I-beams.

An interesting phenomenon due to thermal effects has been observed. The actual camber measurements in the limited data available to date have shown as much as a 20-mm (0.8-in.) variation in camber in 1 day, between the morning and afternoon readings, as the sun passes over the open-top U-beam.

As previously shown by research, the flexural tension cracking capacity of high-strength concrete is greater than that of normal-strength concrete. In the present study the U-beams were designed for a maximum tensile stress of $10(f'_{c_i})$ instead of $7.5(f'_{c_i})$ for release conditions and a maximum tensile stress of $8(f'_c)$ instead of $6(f'_c)$ for 28-day conditions. Testing of the actual concrete mix design shows that these values are adequate.

An early, relatively high modulus of elasticity is required to provide adequate beam stiffness to resist the potential for excessive camber resulting from the large prestress forces at release. The beams were therefore designed for a modulus of elasticity of 41 GPa (6 million $lb/in.^2$) at release and 28 days. Modulus of elasticity tests of the actual concrete mix used in the beams in the Louetta Road Overpass averaged 44 GPa (6.4 million $lb/in.^2$).

Concrete

The researchers are taking an active role in supporting the contractor and subcontractors in all aspects of high-performance concrete bridge construction. They provide technical expertise in developing and evaluating the high-performance concrete mix designs, working with the producers to show them what is needed and why. This method gives the producers the knowledge that they will need to independently produce high-performance concrete in future jobs.

As an example the researchers made more than 80 trial batches of beam concrete in their laboratory and at the precast plant, varying the curing methods and the types, sources, and amounts of cement, fly ash, and admixtures. This enabled the researchers to guide the precaster in the selection of materials and in the development of the actual mix design for the beams, shown in Table 1, and in achieving the required properties. Table 2 shows the actual compressive strengths of the control cylinders for the first 19 U-beams.

TABLE 1 Concrete Mix Design for U-Beams of Louetta Road Overpass

Component	Quantity	Type
Coarse Aggregate	1138 kg/m^3	Crushed dolomitic limestone, $^1/_2$" max, ASTM GR 7
Fine Aggregate	610 kg/m^3	Sand
Water	147 kg/m^3	
Cement	398 kg/m^3	Type III, Alamo
Fly Ash	187 kg/m^3	ASTM Class C
Retarder	1045 mL/m^3	Pozzolith 300R
Superplasticizer	6885-8780 mL/m^3	Rheobuild 1000

Note: 1 pcy= 0.593 kg/m^3 1 oz/cy= 38.7 mL/m^3

Prestressing Steel

During the course of the study the need for experimental verification that transfer and development lengths were adequate for 15.2-m (0.6-in.)-diameter strands on a 50-mm (1.97-in.) grid became apparent. The larger strands were found to be necessary to fully use concrete strengths greater than about 69 MPa (10,000 lb/in.^{2}).

However, in October 1988 FHWA placed a moratorium on the use of 15.2-mm (0.6-in.)-diameter strands in pretensioned concrete applications. In addition, the 50-mm (1.97-in.) grid spacing, considered essential for optimum use of the larger strands, results in a clear spacing between strands that is less than that currently allowed by AASHTO code. Approval was therefore requested from FHWA to use 15.2-m (0.6-in.)-diameter strands with 50-mm (1.97-in.) grid spacing in the project described here. Conditional approval pending results from experimental testing was received from FHWA.

Testing included casting two full-scale models of one of the U-beam designs. These beams were then instrumented with detachable mechanical strain gauges (DEMEC gauges) on both sides of the beam length to obtain strain measurements at release. Observations at release indicated that no significant strand slip or concrete cracking occurred and that the transfer length was between 457 and 610 mm (18 and 24 in.) for strands with a somewhat rusty surface condition. No testing to ultimate state was done on these U-beams.

Also cast were two 356-mm (14-in.)-wide, 1067-mm (42-in.)-deep rectangular beams, each with six 15.2-mm (0.6-in.)-diameter, 1862-MPa (270-ksi) strands on a 50-mm (1.97-in.) spacing and with a concrete strength of 90 MPa (13,000 lb/in.^{2}). The same shipment of 15.2-mm (0.6-in.)-diameter strands with a rusty surface condition was used to build these beams. These beams were also instrumented with DEMEC gauges on both sides of the beam length to obtain strain measurements. Observations at release again indicated that no significant strand slip or concrete cracking occurred and that the transfer length was approximately 457 mm (18 in.). These beams were tested to ultimate state, with one test conducted on each beam end with development lengths of 4140, 3023, 2591, and 1981 mm (163, 119, 102, and 78 in.) Even with the shortest development length of 1981 mm (78 in.), failure was in flexure, and no strand slip was observed. The use of a 15.2-mm (0.6-in.)-diameter strand on a 50-mm (1.97-in.) grid in the beams used in the Louetta Road Overpass was therefore considered acceptable and was given final approval by FHWA.

TABLE 2 Control Cylinder Strengths for U-Beams of Louetta Road Overpass

	Compressive Strength	
Time	Avg.	Range
Release (16-21 hrs.)	60.7	55.9 - 66.7
28 days	96.0	85.7 - 100.3
56 days	104.8	97.1 - 110.2

Note: Dimensions shown in megapascals: 1 ksi = 6.89 MPa

Quality Control and Quality Assurance

As the project progresses research needs evolve. One example is related to heat of hydration. Temperature measurements of the concrete in the U-beams used in the Louetta Road Overpass indicated that heat of hydration temperatures in the solid end block were in excess of 93°C (200°F); thus, this is higher than the maximum temperature typical in normal-strength concrete. As a result the researchers are conducting independent temperature studies on high-strength concrete specimens to determine the effects of high temperatures on the quality of the concrete. In addition, temperature-measuring instrumentation is being installed and monitored in the U-beams used in the Louetta Road Overpass, and corresponding controlled-temperature cylinders are being cast to determine whether deleterious effects occur because of these high temperatures.

A related aspect of concern has to do with TxDOT's specifications on the fabricator's release of prestress. The fabricators break concrete cylinders to verify that they have obtained concrete strengths to meet or exceed design release strengths. By obtaining timely acceptable release strengths, the fabricators can transfer the prestress to the beams and have optimum prestress bed turnaround times. The fabricators place the control cylinders near the webs of the beams so that they are covered with the beams and are exposed to similar temperatures. These cylinders are then tested to check

concrete strengths before the release of prestress is approved.

The concern arises because these control cylinders may not attain the high, and possibly deleterious, temperatures that have been measured in the various regions of the beams and therefore may not be an adequate measure of the concrete strengths actually achieved in the beams. Limited preliminary measurements indicate that the beam concrete strength could be 10 percent lower than the control cylinder strength because of the detrimental effects of the high heat of hydration temperatures.

Therefore, additional experimental studies have been initiated to evaluate the adequacy of current specifications and develop new specifications as they are required. Additional studies are also addressing the durability aspects specified in the current definition of high-performance concrete.

Teamwork

The need for adequate communication among all parties involved is extremely important when new materials and methods are being implemented. Appropriate scheduling of meetings with all of the right people leads to fewer oversights and erroneous assumptions.

Several weeks before the February 1994 letting, a prebid meeting was scheduled by the TxDOT Houston district office and required the attendance of all contractors planning to bid on the Louetta Road Overpass project. The agenda included a presentation on the innovations included in the Louetta Road Overpass project, a discussion by the researchers on their involvement with the project, comments by FHWA, and a question-and-answer period that allowed the contractors to discuss their concerns.

After the contract was let, a partnering workshop was held in April 1994. Partnering is a new emphasis that has been implemented at TxDOT to encourage the team concept between TxDOT and the contractor and other parties. Partnering workshops are typically done on a voluntary basis, but they are encouraged by TxDOT when it is deemed necessary, for example, for unique projects. The contractor coordinates the workshop, including setting up the facility and hiring an outside facilitator. Selection of the facilitator is usually based on the contractor's previous experience with the facilitator or on recommendations received from others. Expenses for the workshop are paid by the contractor, who then submits a change order to TxDOT for reimbursement for half of the expenses.

The contractor, subcontractors, researchers, FHWA, and TxDOT personnel attend the 1- to 2-day partnering workshop. The outside facilitator leads the discussions, which include a mission statement for the project. Also included are brainstorming on issues. Possible solutions and action plans are then developed, showing the proposed activity, the party responsible for doing the activity, and the time frame in which the action is to be accomplished.

An example of the issues addressed in the Louetta Road Overpass partnering workshop was a proposal made by the contractor to use mortar joints rather than match casting for the pier segments. A representative from the contractor was designated the party responsible for developing a proposal to submit to FHWA and TxDOT, and a deadline was set for submission and response.

Following the partnering workshop, a preconstruction meeting was held in May 1994. The meeting was coordinated by the TxDOT Houston district office, with an invitation to attend the meeting extended to the contractor, subcontractors, researchers, and FHWA and TxDOT personnel. The purpose of the meeting was to discuss in detail the researchers' involvement in the project, including activities and time frames. The items discussed included the researchers' instrumentation plan and its impact on the construction schedule.

Ongoing weekly meetings between the contractor and TxDOT district personnel are occurring throughout the duration of the project. The researchers, FHWA personnel, and other TxDOT personnel are invited as needed to address the issues of concern discussed at that meeting.

The researchers and the TxDOT research project director are continually in contact. In addition, a monthly summary report of project activity is sent to the Project Advisors Committee, which is a group of local technical experts; to the project's National Peer Advisory Group, which is a diverse group of experts from around the United States; and to various other individuals, such as the contractor and FHWA personnel. The individuals receiving the monthly summary report have been extremely helpful in pointing out various aspects that should be considered in carrying out this innovative construction project.

Conclusion

Innovations in bridge construction require the ability to adapt as new information and concerns develop and the ability of all parties to work together as a team to meet the challenges. In Texas the challenges are being met, and work continues in the effort to bring high-performance concrete to the bridge-building industry.

During the course of the study various means of facilitating the implementation of research findings became apparent, and these are as follows:

1. Comparison studies of adjacent bridges, one built with and one built without the new materials or by the new methods, will better define the cost-effectiveness of the innovation in bridge construction.
2. Long-term monitoring of high-performance concrete bridges, for example, for 20 to 30 years, will be initiated immediately after construction to adequately document the actual benefits of the improved durability characteristics.
3. Studies of cost-effectiveness will be publicized to show the economic benefits of implementing the research. For example, the cost savings due to the use of longer spans with fewer beams and reductions in long-term maintenance can be documented and publicized to encourage the use of high-performance concrete in bridge construction.
4. Flexibility in the research study will allow additional experimental or analytical studies to be done as the need for them becomes apparent.
5. Research studies done in conjunction with actual construction projects allow the researchers to act as coaches, providing technical expertise in developing and evaluating the new materials and methods. Thus, the producers gain experience so that they can independently continue the innovations.
6. Research tasks include evaluation of the adequacy of current state department of transportation design and construction specifications and development of new specifications as required.
7. Emphasis is being placed on partnering with all parties involved in the implementation of the new materials and methods. A mandatory prebid meeting, a partnering workshop, and a preconstruction meeting can be included as part of the contract package.

ACKNOWLEDGMENTS

The researchers on this project are Ramon L. Carrasquillo, Ned H. Burns, and David W. Fowler, who are with the University of Texas at Austin. Experimental testing was conducted with the assistance of the graduate students at the Construction Materials Research Group and at the Phil M. Ferguson Structural Engineering Laboratory of The University of Texas at Austin. The Texas Concrete Company in Victoria, Texas, cast specimens for the experimental studies and is the precast U-beam subcontractor on the project. Funding is provided through FHWA's Office of Advanced Research and through its Office of Technology Applications as part of the Strategic Highway Research Program Implementation Program. Technical assistance is received from the FHWA Bridge Division, Structures Division, Region 6 Office of Engineering, and Texas Division. The author appreciates the efforts and teamwork demonstrated by each of the above and by all others participating in the project.

REFERENCES

1. Ralls, M. L., and R. L. Carasquillo. Texas High-Strength Concrete Bridge Project. *Public Roads*, Vol. 57, No. 4, Spring 1994, pp. 1–7.
2. *PCI Design Handbook*, 4th ed. Precast/Prestressed Concrete Institute, 1992, pp. 4–44.

External Prestressing for Bridge Rehabilitation in Italy

Mario P. Petrangeli, *University of Rome "La Sapienza," Italy*

The Italian motorway network was built about 20 to 30 years ago; it has a large number of prestressed concrete viaducts often located in mountain regions where deicing salts are used. Most of these bridges must now be rehabilitated. The main reasons for the rehabilitation, besides the use of salts, are (a) the increased live loads, (b) the insufficient knowledge of seismic problems at the time that the bridges were built, (c) underestimation at the time of building of the effects of time on the concrete, and in some cases, (d) the poor quality of the construction. External prestressing has been found to be a powerful tool for repair work; therefore, it is used extensively in Italy. Three stages in the evolution of this technique can be focused: (a) the additional cables are embedded in new concrete and are added and attached to the old concrete, (b) the cables remain external to the original section with few points of contact with the deck; the wires or the strands are encased in high-density polyethylene pipes that are grouted with cement mortar (no petroleum wax or grease has been used in Italy until now), and (c) the cables are composed of single sheeted and greased strands located inside a high-density polyethylene pipe that is not grouted. Each strand acts as a unit and can be easily replaced. Three examples, one for each of the techniques, are provided.

Most of the Italian motorway network, which is more than 8000 km long, was built about 25 years ago. A large number of prestressed concrete (p.c.) viaducts and tunnels were needed to cross the Apennines Mountains running along the whole length of the peninsula: the 440-km A3 Motorway linking Naples to Sicily has 264 p.c. main viaducts whose total length is about 56 km, that is, 13 percent of the length of the entire motorway.

A number of these viaducts now need to be rehabilitated, with the main causes of deterioration being (a) the aging of the concrete and subsequent corrosion of p.c. cables and rebars, which occurs frequently where deicing salts are used; (b) the lack of seismic strength because of insufficient design knowledge at the time that the bridges were built; (c) the underestimation at the time of building of the effects of time on the concrete; and (d) deficiencies in the construction.

The two public agencies managing all of the main roads in Italy, Autostrade for toll motorways and ANAS for all of the remaining roads, are now carrying out an extensive program of inspection and rehabilitation of these bridges.

Bridge Assessment

Inspection

A program of instrumentation tests and controls was planned for each bridge, as a rule, on the basis of qualified visual inspections. These tests concerned (a) the geometry, (b) the foundations, (c) the materials, and (d) the overall behavior of the bridge. Neglecting here the wide range of problems that often arise in the foun-

dations because of ground instability, the relevant tests of the p.c. decks can be summarized as follows.

Materials

Boring of 100-mm-diameter cores with stress release, ultrasonic pulse velocity measures in conjunction with the surface hardness, and Windsor penetration tests were commonly used to assess the concrete. The efficiency of the grouting as well as the possible corrosion of the prestressing cables were systematically inspected with an endoscope (fiber optics), which proved to be a powerful tool (Figure 1). The 3-mm-diameter holes, which were needed to thread the instrument head to the cable, were easily drilled at single points.

Overall Behavior of Bridge

The most complete information about the soundness of the bridges was obtained by appropriate static load tests, although these tests required the interruption of traffic. To reduce the number of these tests, alternative dynamic tests were carried out extensively. In this case the traffic was not stopped and the transit of heavy trucks was used as the external stimulus. The free vibrations of the structure after the transit of the truck were recorded and analyzed.

Numerical nonlinear analyses were carried out to check the behaviors of the bridges in the case of strong earthquakes. The requested ductility was compared with the available ductility; the available ductility was derived theoretically by using the original drawings together with the results of the materials tests.

FIGURE 1 Control with an endoscope of a prestressing cable embedded into a beam. Photographic images of cables can also be obtained by this technique.

Level of Repair

A wide range of situations were identified. For the most common type of p.c. viaducts, that is, those composed of a number of simply supported T- or V-shaped beams, some typical situations can be described, as follows.

Low-Level Damage

Bearing devices and the deck joints need to be changed. Some parts of the concrete surface must be restored. This was the situation for most of the viaducts examined.

Need for Seismic Retrofitting

A number of viaducts built in the south of Italy between 1965 and 1975 do not comply with today's Italian seismic code. This may be due to an initial insufficiency of the structure or to a revised and more severe classification of the site with respect to seismic action.

A change in the static scheme was the solution often adopted for decks originally joined on each pier. The deck slab has been made continuous over 8 to 10 piers, that is, over a length of 300 to 400 m, so that all of the horizontal forces are transmitted to a new abutment to be built behind the original one (Figure 2).

Special energy-dissipating devices have been placed at the new abutment to reduce the seismic forces (Figure 3).

Need for Serious Repair Work

Serious repair work was necessary when the controls and the analysis showed a lack of strength with respect to the ultimate or serviceability limit states.

Appropriate solutions to these problems were offered in many cases by adding external prestressing tendons (*1–3*), as in the examples illustrated later.

Removal of Existing Decks

In some extreme cases replacement of the old decks with new ones offered the most economical solution.

FIGURE 2 New abutment built to withstand longitudinal horizontal forces; in front, deck with continuous slab.

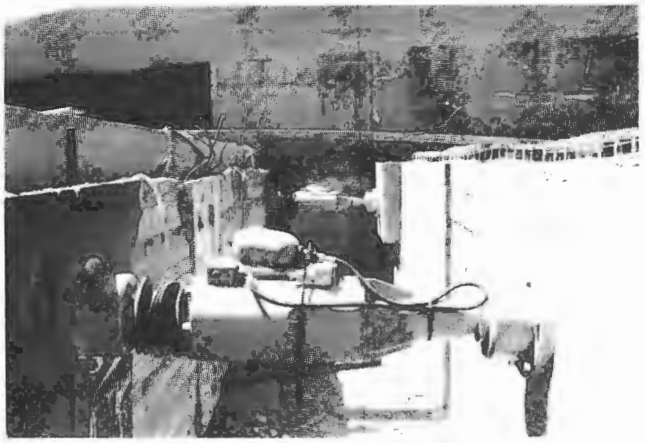

FIGURE 3 Energy-dissipating devices for strong earthquakes: (*left*) modified old deck; (*right*) new abutment.

External Prestressing

General Features

Three stages in the development of the external prestressing technique for bridge retrofitting in Italy can be recognized.

Embedded Cables

In the very first application the new cables were embedded in new reinforced concrete that was added to the old concrete. The tendons were external to the original section, but they acted as traditional p.c. cables with respect to the final section.

External Grouted Cables

The use of external grouted cables is the most common application in Italy. The new cables are external to the concrete section that is not modified. They are placed inside a duct, generally made of high-density polyethylene (HDPE), and are grouted with ordinary cement mortar. To date no petroleum wax has been used in Italy.

External Nongrouted Cables

In the last application the new cables were composed of single sheeted and greased strands. In some cases the wires or the strands are zinc coated. These units are placed in HDPE ducts without grouting except to the lengths of the anchorages and the crossings of the deviation blocks.

These cables are similar to the stays of the cable-stayed bridges of the last generation.

Deviation Blocks

The deviation blocks have usually been cast in situ with ready-mixed concrete with a minimum compressive strength of 45 MPa. The blocks are joined to the original section by steel dowels (20 to 24 mm in diameter) embedded with resin in 30- to 40-mm-diameter holes drilled in the old concrete (Figure 4).

Some tests carried out in box girder bridges (Figure 5) showed that a pullout force of 100 kN can be easily reached with a 20-mm-diameter dowel and an anchorage length of 16 to 18 cm, provided that the old concrete can offer a strength of about 35 MPa. Maximum working loads of 20 kN (axial) and 40 kN (shear) per dowel were generally accepted at the stressing of the cables.

FIGURE 4 Dowels ready to connect new anchor blocks to existing p.c. box deck.

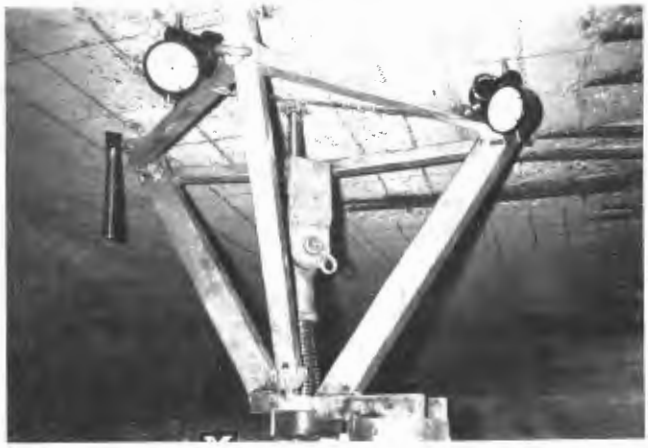

FIGURE 5 Device for a pullout test on a 20-mm-diameter, 170-mm anchored connector. The test was stopped at a force of 100 kN.

Anchor Blocks

Both concrete blocks or steel frames placed at the beam ends have been adopted. When no room was available behind the end of the deck, interior anchor blocks similar to the deviation blocks, but with more dowels, were adopted. Steel frames, although more expensive in Italy, were found to be the best solution when time savings was fundamental.

Three Examples

A3 Motorway Viaducts

Seven 25-year-old viaducts of a mountain section of the A3 Motorway had serious problems because of deficiencies in the construction and the effects of deicing salts. All of the viaducts have simply supported decks (32 in total) spanning over 32 m (Figure 6). Every carriageway had four double T-beams, that is, 256 in total, most of which were seriously damaged because of the lack of grouting in the prestressing cables.

When the results of dynamic and static tests found prestress losses greater than 60 percent with respect to the theoretical prestress loss, the removal of the old deck and the construction of a new one were found to be the best solution (*4*).

When the prestress losses were supposed to be between 60 and 10 percent, appropriate new cables were added to the beams. In this case the new cables were embedded in concrete cast around the lower flange of the beam. Rebars sealed in holes drilled in the existing beams guaranteed the connection between the old and the new concrete. The anchorages of these cables were made with concrete blocks or steel frames according to each situation (Figure 7).

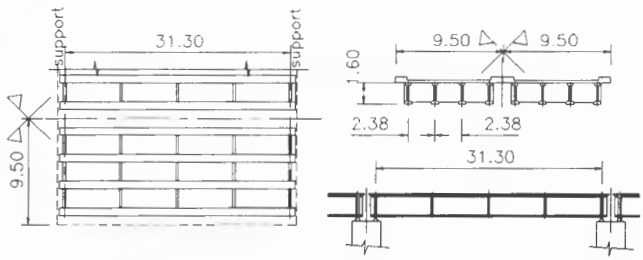

FIGURE 6 Typical simply supported p.c. deck built 20 to 30 years ago.

Stupino and Ruiz Viaducts

The Stupino and Ruiz viaducts were built by the cantilever method. Spanning over 120 m and with piers with heights of up to 150 m, they can be considered among the most important of the A3 Motorway.

According to the solutions adopted at the time, no rigid connection was made at the end of the opposite cantilevers: a short dropped span (9 m) was built at the midspan of the Ruiz Viaduct, whereas a simple hinge connected the two facing cantilevers of the Stupino Viaduct at midspan (Figure 8). The large creep, developed over the 20 years of the bridge's life, caused unacceptable deflections at midspan (*5*).

The prestressing cables added inside the box girder, at the bottom of the upper slab, allowed a reduction in the deflections and the addition of a lightweight aggregate wearing course to make the road profile acceptable. This is a classic example of external prestressing with grouted cables. The prestressing forces were trans-

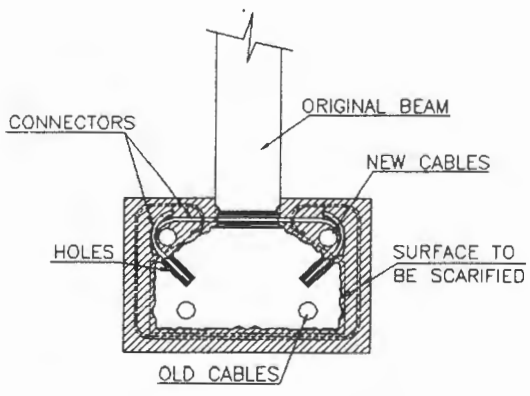

FIGURE 7 In early applications new cables were incorporated into concrete pour added to original section.

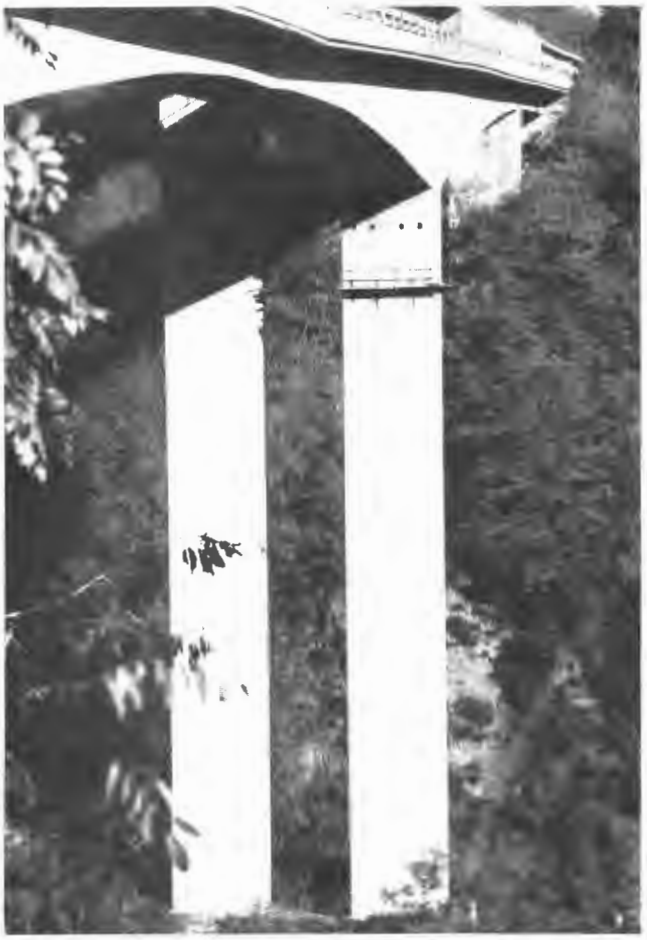

FIGURE 8 Ruiz Viaduct before repair. A large deflection at midspan is visible to the naked eye.

FIGURE 10 External cables added inside Stupino Viaduct. HDPE sheets were grouted with cement-mortar.

ferred to the existing section with concrete anchor blocks and shear connectors (Figures 9 and 10).

E45 Viaduct

Rehabilitation work was done on five viaduct with a total of 142 simply supported decks composed of two V-shaped beams for each carriageway (Figure 11). The decks had just been finished when some shear cracks appeared in a number of beams. The beams were initially prestressed with pretensioned strands, and the cracks were probably due to the insufficient strength of

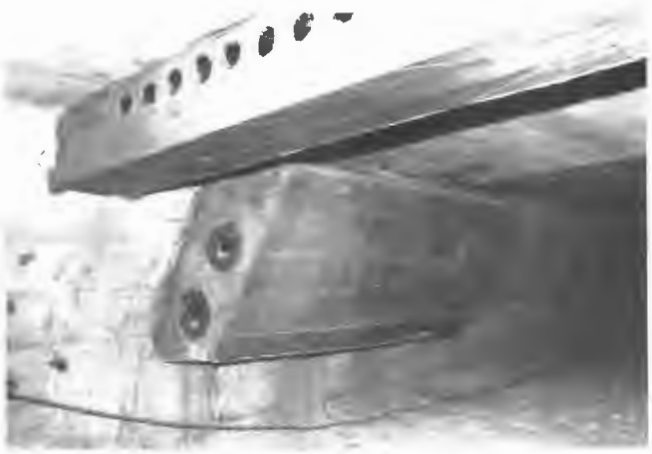

FIGURE 9 Deviation block (upper slab) and anchor block (web) ready to receive cables.

FIGURE 11 Deviation block added inside box girder. The external prestressing cables are composed of single sheeted strands. They will not be grouted.

FIGURE 12 Steel frame placed at end of each beam to anchor new cables.

the concrete at the time of release of the prestress. Slippage of the strands near the beam ends occurred, and the sections in this zone behaved as nonprestressed ones.

In this case external cables formed with single sheeted and greased strands were used. The strands were encased in an HDPE tube without any injection, and the anchorages have been designed in such a way that a single unit can also be replaced. A steel frame that transfers the force to the p.c. beam at its ends was chosen because of the narrow distance between two adjacent beams (Figure 12).

Conclusion

In the coming years in Italy, as well as in all of Europe, large amounts of economic resources will be necessary to rehabilitate road bridges mainly built 20 to 30 years ago with p.c. This budget is expected to be greater than the one for the construction of new bridges in the future.

The situation will require (a) reliable assessment criteria and (b) economical and efficient repairs.

The external prestressing offers in many cases an adequate answer, and it is expected to be used more and more frequently in future applications.

REFERENCES

1. Petrangeli, M. P. The Use of External Prestressing for Bridge Repair and Retrofitting (in Italian). *L'Industria Italiana del Cemeto*, Vol. 680, Sept. 1993.
2. Virlogeux, M. La Précontrainte Extérieure. *Annales de LTTBTP*, Vol. 420, Dec. 1983.
3. Wicke, M., and M. Ostermann. Bridge Rehabilitation with External Prestressing. *Proc., International Workshop on Bridge Rehabilitation*, Darmstadt, Germany, June 1992.
4. Petraneli, M. P. Inspection and Repair of Some Highway Bridges in Italy. In *Bridge Management* (J. E. Harding, G. A. R. Parke, and M. J. Ryall, eds.), Elsevier, London, 1991.
5. Del Papa, M., M. P. Petrangeli and A. Bajo. Rehabilitation of Prestressed Concrete Bridges Built by the Cantilever Method in Italy. In *Bridge Management*, Vol. 2 (J. E. Harding, G. A. R. Parke, and M. J. Ryal, eds.), Thomas Telford, London, 1993.

Precast Arches as Innovative Alternative to Short-Span Bridges

Pierre Segrestin, *Terre Armee Internationale, France*
William J. Brockbank, *Reinforced Earth Company Ltd., Canada*

As the transportation infrastructure ages in many countries around the world, there is a growing number of bridges that are structurally deficient or functionally obsolete and require either major repair or replacement. There are estimated to be hundreds of thousands of bridges in this condition in North America alone. A cost-effective option for replacement of bridges with short spans (from 10 to 20 m) is the construction of a precast arch. The growing popularity of the precast arch can be attributed to its combination of the age-old structural efficiency of the arch shape and the modern-day cost-effectiveness of precasting. Rapid construction of approximately 15 m of arch per day keeps erection costs low. Not only is the construction cost-effective, but it also can be accomplished without disturbance to the stream, road, or rail it crosses. With no bearings or expansion joints, a precast arch will function for its entire service life virtually maintenance free. Construction is carried out in three basic operations: preparation of footing, erection of precast elements, and finally the simultaneous placement of backfill and end walls. The precasting is made economical with simple repetitive casting and stripping cycles utilizing high-production steel forms.

This paper was written to provide an understanding of precast arches, including design, precasting, and construction. It starts by comparing precast arches with short-span bridges in several ways and points out the advantages that a precast arch may have over a short-span bridge. The paper is written on the basis of the authors' knowledge of the TechSpan arch, which is designed and supplied by Reinforced Earth Company, Inc. (Terre Armee International). Because of this most of the detailed information is specific to the TechSpan precast arch. This, however, does not detract from the ability to point out comparisons between bridges and precast arches in general. No quantitative cost comparisons have been given since they are extremely project specific and are best left for the reader to do with a given project in mind.

Although the precast arch is already quite popular in Europe, it is still in an early stage of acceptance in other countries around the world. This point is clearly shown by the number of TechSpan installations to date, which total more than 300 in Europe but which total only 20 in Australia, Canada, Japan, United States, and Venezuela combined.

Comparison of Precast Arches and Short-Span Bridges

Advantages of Precast Arches

The main advantage of the precast arch is the high speed at which it can be constructed. Three basic operations are required to complete an installation: (a) site preparation and footing construction, (b) erection of the

arch, and (c) backfilling. The first and third operations are basic construction practices that can be performed by even the most unspecialized of contractors, and the construction rates for these operations are predictable. The only operation whose construction rate is not commonly known is the erection of the arch itself. Experience has shown that this operation is in fact the quickest of all three and is usually accomplished in 1 week or less, yielding average construction rates of 15 m/day or more.

Since the arch has no bearings or expansion joints, long-term maintenance requirements are low. The only item requiring maintenance is the concrete itself. Since the concrete of the arch is cast in a controlled precast plant, its quality will be inherently better than that of cast-in-place concrete, which often is poured during extreme weather or on a hurried schedule. The use of a steel form also produces a smoother and more durable surface than use of a temporary form, which is often made of wood.

Reduced use of these items that require long-term maintenance is being considered more often by highway departments as they focus their efforts on selecting structures with the lowest life cycle cost rather than structures with the lowest capital cost.

In regions where freezing temperatures occur in winter, precast arches have two advantages. The first is the reduction of the icing potential that occurs on bridges during rapid drops in temperature. The earth cover over the arch not only insulates against the freezing air underneath but it also acts as a source of heat to slow the freezing process. The second advantage for locations with freezing temperatures is a reduced level of exposure to deicing chemicals or salts used above the structure. Salts that lay in solution on bridge decks attack the concrete, but they have a much more difficult time reaching the arch because they will be diverted and diffused by the soil cover. If a salt solution eventually reaches the arch, it will be drawn by gravity around the outside of the arch and down to the drainage system.

Arches also perform well during earthquakes. With the memories of both the Loma Prieta and Northridge earthquakes in California still fresh in the minds of civil engineers, much attention is being paid to using more earthquake-resistant designs for bridges. The evidence to date in California has been excellent for the performance of what the California Department of Transportation categorizes as "buried structures." In fact state-of-the-art design code ATC-6, which has recently been adopted by AASHTO, does not require that any specific seismic design be considered on such structures because they do not appear to be susceptible to earthquakes (*1*).

This opinion was supported by a study conducted at the University of British Columbia under the direction of Peter Byrne on a TechSpan arch constructed in Vancouver, British Columbia, Canada, in 1990 (*2*).

One of the situations in which an arch has an obvious cost advantage over a bridge is in the case of a short span and a high grade separation. In this case the question is not whether to use an arch or a bridge but rather what length the arch should be. By "daylighting" the arch tunnel just beyond the shoulder of the upper road, the cost of the arch and the volume of backfill are both reduced. This reduced cost is offset by the requirement for higher end walls, however. By running several cost comparisons for various arch lengths, the optimum arch length can be selected for a given project.

A precast arch can be built without disturbance to the service that it is spanning. Examples of this include numerous installations in Europe in which rail lines were kept open with several trains per day; a twin arch conveyor underpass in Fort McMurrary, Alberta, Canada; and river crossings such as the one shown in Figure 1 on the Illecillewaet River, British Columbia, Canada.

For applications in which the underpass is on a shallow grade, an arch can be sloped to match this grade. On the other hand a bridge would have to be designed for the point of minimum clearance at the uphill end of the underpass, thus resulting in an extra height of the abutment at the downhill end.

Advantages of Short-Span Bridges

An advantage of a bridge over a precast arch is that the bridge can span greater distances. For practical reasons the range of the market for precast arches is under about 20 m of span, that is, in the category of bridges with very short spans.

A second advantage of a bridge is that the depth between the upper road surface and the top of the clear-

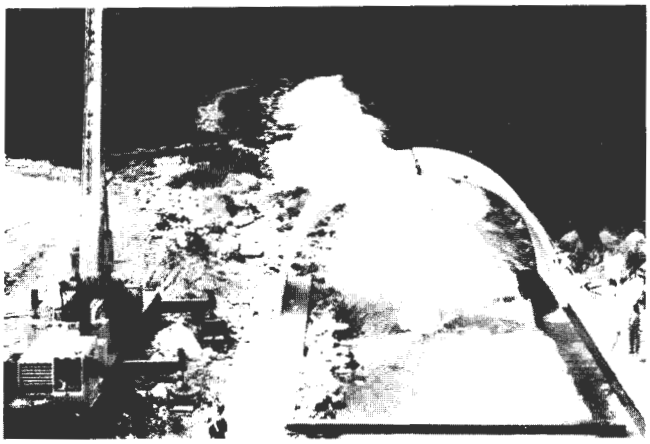

FIGURE 1 Precast arch construction over a river.

ance box for the underpass road can often be less than what is required for an arch. The reason for this is that an arch must account for (a) 1-m recommended earth cover over the arch, (b) the thickness of the arch, and (c) the amount of curvature of the arch above the top of the clearance box. When all three dimensions are added together the clearance for an arch is usually slightly greater than the depth of the girders plus the deck. This situation can be improved, however, if the arch is allowed to cut off the corners of the underpass clearance box.

General Design Characteristics

Other items that do not appear to be advantages for either structure type but that affect design are

- Application to very high skews; both types of structures must be extended to accommodate the skew.
- Application to curves of an underpass; both types of structures can accommodate curves with large radii. For curves with smaller radii it is preferred to construct the arch straight and increase the span to allow for the offset between the centerline of the arch and the centerline of the clearance box.
- Application on poor foundation; both types of structures will require foundation improvements or a deep foundation. A possible exception is if the bridge is built on mechanically stabilized earth.
- Requirements for select backfill; both types of structures require roughly the same quantity of clean granular backfill within a drainage zone behind an arch or cast-in-place abutment wall.

Construction of Precast Arches

By using a simple repetitive procedure contractors are able to achieve average production rates of between 10 and 20 lineal meters per 8-hr shift with the TechSpan arch. The range in production rates is due to variations in site access and the sizes of elements. This section describes the basic construction procedure for TechSpan arches, from the casting of the footing to the erection of elements and, finally, the placement of backfill and the concurrent construction of the head wall and wing wall. The basic components of a TechSpan arch are shown in Figure 2.

Footing

The first item constructed is the footing. After inspection of the foundation by a geotechnical engineer the footing is cast on either competent native material or structural fill. The footing is constructed to conform to the grade requirements of the arch. Tolerances for the width and thickness of the footing are in accordance with standard construction practices for footings, but tolerances for the recess that the arch sits in must be tighter to ensure good alignment and rapid erection. The recess is usually designed to be 100 mm wider than the thickness of the arch so that it can accommodate wood wedging for aligning of the elements.

Installation of Arch Elements

The crew and equipment needed to install the arch generally consist of three laborers, one crane and one crane

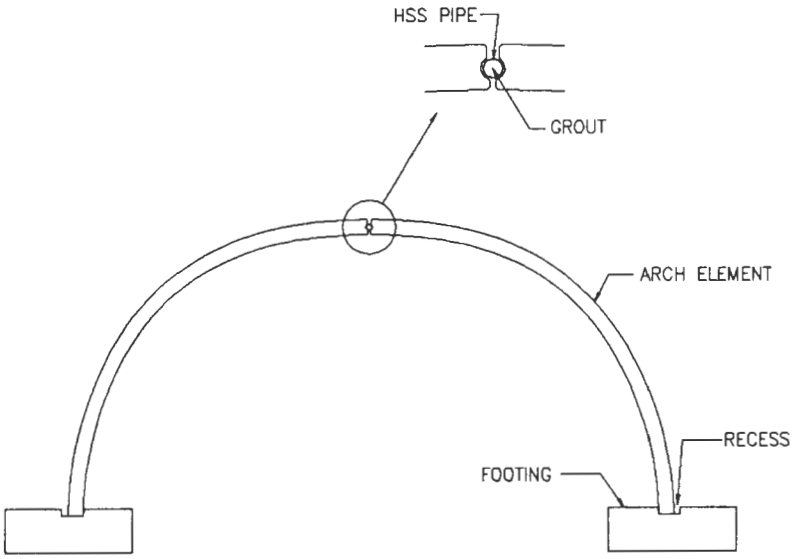

FIGURE 2 Typical cross section of an arch.

operator, and one foreman. A second crane is needed to erect the first two pieces and remains on site to position the first four pieces. Once the elements arrive on site they either can be installed on the same day or can be stored in a designated area until they are needed. The best means of production is accomplished when the elements can be transported directly to the leading edge of the arch and then off-loaded and immediately installed. If stockpiling is required, a front-end loader can be used to carry the elements from the stockpile to the leading edge of the arch. The crown pipe is bolted to the top of each element just before the crane lifts it. This pipe is used to provide a temporary gap at the crown that will be filled with a 40-MPa grout to provide uniform bearing to transfer axial forces from one element to another. Four cables complete with rolling blocks attached to the backface of the elements are used to give good control during the lift. Appropriate cable lengths are selected so that each element will need to rotate only slightly once it has been inserted in the footing recess.

The staggered installation pattern used is shown in Figure 3. This has the advantage of requiring only one crane, as opposed to the two cranes that would be necessary if opposing elements were in line with each other. Once all elements have been erected, including half panels on each end, the crown and footing recess are grouted. The last item to be installed is a membrane that covers all exterior joints. This membrane is usually self-adhesive for ease of installation. On some projects the project's owner may require that the entire outside surface be covered with a membrane and protective board; however, this is usually not necessary, and in fact on some stream crossing projects only a geotextile across the joints has been used.

Backfilling

The backfill placed around the arch is of two types. Fill placed nearest to the arch (in about the first meter from the outside of the arch) is a clean granular backfill. This is to allow free drainage of any water. Beyond this small zone any material suitable for embankment construction (as defined by most highway departments) can be used. Compaction requirements are (a) that the first 400 mm not be compacted; (b) that the next 600 mm be compacted to 95 percent of the standard proctor density with light (walk-behind) equipment; (c) beyond that large compactors can be used to achieve the same 95 percent requirement.

Collar Walls and Wing Walls

Many types of retaining walls can be used at the ends of a precast arch. The system most often used with the TechSpan arch is a reinforced earth wall.

The facing of the collar wall is constructed of either precast concrete panels or a temporary wire facing, which is in turn covered with cast-in-place concrete. The placement of backfill for the walls and the arch is done simultaneously.

Precasting of Arches

Precasting operations will vary depending on the type of system or manufacturer, but several items are common to all operations. As with all precasting it is the efficiency achieved through repetitive operations that

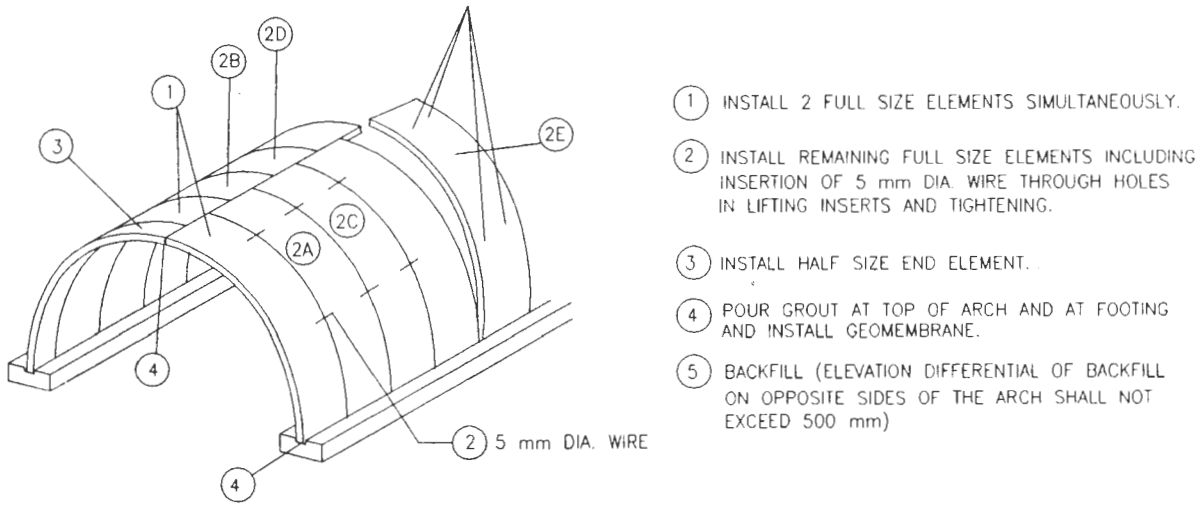

FIGURE 3 Suggested construction procedure.

makes precasting economical. The forms that are used play a key role in this operation because they must be able to be used easily and quickly and must be durable to withstand hundreds of casting and stripping cycles.

The following describes briefly the setup operation of the TechSpan system.

A steel base plate on which the elements are cast is set up, ensuring that the plate is sufficiently supported to avoid excessive bending under the weight of the forms and concrete (alternately, a concrete slab can be used). A plywood template cut to the exact shape of the arch is then secured to the base plate.

The forms are made from the three basic components of flexible skin, adjustable-length screws (to change the curvature of the skin), and a fixed steel frame. The skins are then bent to conform to the shape of the template by slowly turning the adjustment screws. With the forms now in position it is necessary to fabricate the reinforcing steel cage. The longitudinal bars are radially bent nearly to the shape of the arch and are tied to the stirrups with the assistance of a jig.

Once the reinforcement is given appropriate cover with plastic chairs, lifting anchors are secured and the top and bottom bulkheads are positioned. After this the element is cast. Quality control checks should be done on the resulting elements, including thickness at the top, bottom, and middle; internal cord lengths for cords on both sides; and lengths of both internal diagonal cords.

A dimensional record should be kept for each element including the form number from which it was cast so that any minor differences can be traced back to the source.

After each casting the forms are cleaned and new release oil is applied. One casting is done per day; therefore, the number of forms in production will govern the number of casting days to complete a project. Only 18 hr of curing before form stripping and lifting of the element is required because all early lifts on the elements are done while the element is on its edge, a position in which it acts as a very stiff beam supporting its own weight.

Analysis

Theory of Arches

The development of the arch was probably the most significant event in the history of structural design. It allowed people to support a load yet still have an open area beneath the load. For many years this was the only structural tool that could be used by people, and it was used in all buildings to span windows and doorways and as a three-dimensional arch (or, more properly named, a dome) to span interior rooms. At this same time similar principles were being used to create spans for roadway bridges in the form of the stone arches shown in Figure 4. Figure 4 illustrates how a vertical load can be converted to a compression force simply through the shape of the arch, and stone, brick or concrete can take compression loads very well. How is it, however, that arches are capable of working such magic? The answer is best illustrated not by looking at compression structures but by looking at tension structures and something called a funicular curve. The word *funicular* is defined by the dictionary as "of a rope or its tension." Since rope cannot support compression or bending loads it takes all of its load in tension, as shown in the first three cases in Figure 5. Of particular interest to arches is Case 3, which shows a rope supporting both vertical and horizontal loads all in tension. If the shape from Case 3 is inverted while maintaining its exact shape and if the exact vertical and horizontal forces were applied to the same points to which they were applied in Case 3, this new structure would support its load completely in compression (Case 4). This loading shown in Case 4 is the type of load that an arch in soil is required to support, that is, primarily vertical loads with some horizontal loads.

This simple example gives some insight into why an arch is structurally efficient.

Numerical Analysis

Because it is necessary to consider the relative stiffness between the soil and arch, this is best done with the assistance of some numerical analysis. The idea of relative stiffness can best be illustrated by Figure 6, in which a very flexible and a very stiff arch are shown side by side. The flexible arch avoids load by deforming, causing the soil to take the load by "arching." The stiff arch, on the other hand, not only supports the soil above it but also attacks the load from the adjacent soil settling around it.

Most finite-element methods (FEM) programs use a series of beam elements to model an arch, but the

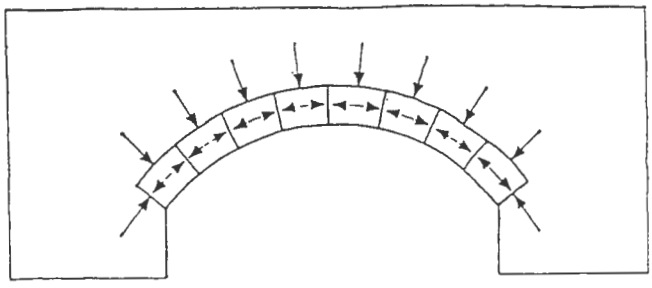

FIGURE 4 Simple stone arch in compression.

BOPRE program developed by Terre Armee Internationale defines the arch as a separate material with the properties of concrete and the actual thickness of the arch. A FEM mesh is generated (Figure 7) on the basis of the best arch shape, as chosen by an algorithm written with criteria for minimizing the total cost of the arch.

Materials

Six different materials are analyzed by the program:

- Concrete arch,
- Foundation soil,
- General backfill around the arch,
- Backfill immediately surrounding the arch,
- Soil-concrete contact elements, and
- Hinge elements (at the footing and crown).

The material characteristics of the three main materials are as follows.

Concrete

The concrete of the arch is assumed to behave entirely elastically and is defined by three basic parameters: Young's modulus, Poisson's ratio, and unit weight. The values of the three parameters usually used are 20,000 MPa and 0.2 and 25 kN/m^3, respectively.

Foundation Soil

The same three parameters are used to define the foundation soil, but the additional properties of cohesion, friction angle, and dilatancy angle are added. These parameters can be varied from project to project to help model the actual conditions of the foundation. In fact, different materials can even be used under the footings; for example, on one project it was necessary to define the foundation material as concrete for the zone immediately beneath the footing to simulate a concrete caisson foundation.

Backfill

By far the most complicated material to model is the backfill around the arch. This is understandable since it is constructed by incremental lifts with compaction. It is also this material surrounding the arch that has the greatest effect not only on the loading of the arch but also on the lateral support of the arch, and because of this the more detailed modeling of this material is justified. To best model this material the relationship defined by Duncan et al. (3) is used.

BOPRE Program

The BOPRE program is a nonlinear elasto-plastic program with the ability to incorporate strain hardening of the backfill. It has been found that the strain hardening changes the results very little, so it is routinely eliminated, making the stress path purely elastic at first and then purely plastic after the yield point.

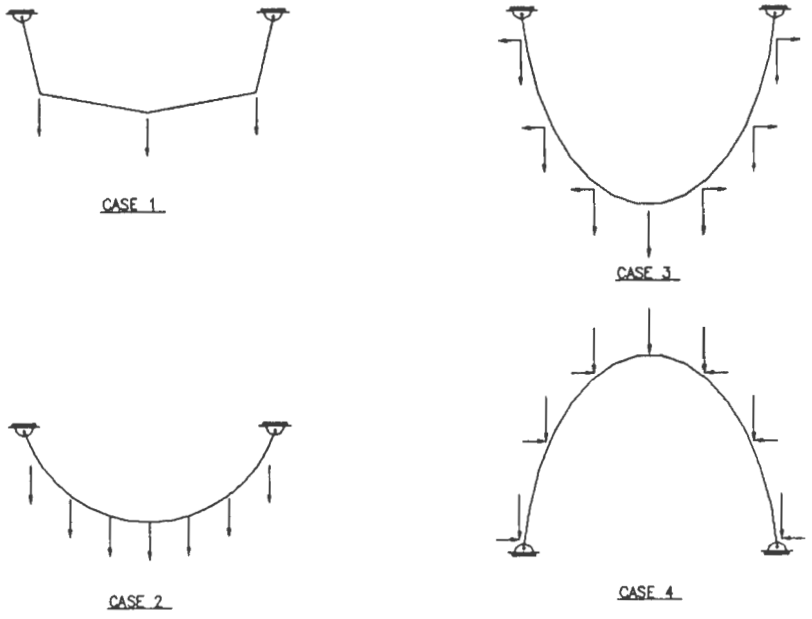

FIGURE 5 Funicular curves.

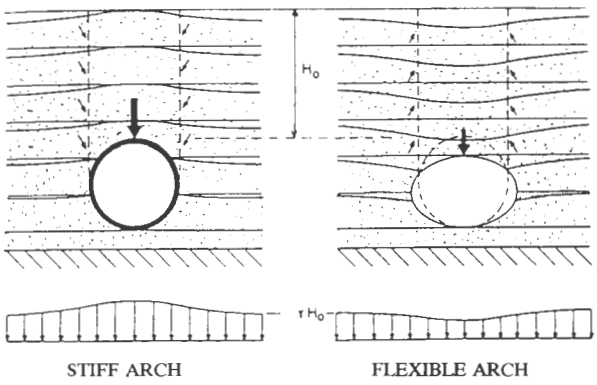

FIGURE 6 Soil-arch interaction.

The method used for solving the nonlinear stiffness matrices is the visco-plastic method, which is based directly on the initial strain method.

The BOPRE program goes through many steps before the final loading condition is reached (Figure 8). The first step is for the arch alone with no backfill. Subsequent steps apply approximately 2 m of fill at a time, alternating from one side of the arch to the other until the fill has reached the crown. From this point on the layers of fill are placed simultaneously on both sides until the final grade is reached. The last step is the application of a uniform surcharge, which is applied on only one side of the arch because this gives a more critical loading than application on both sides.

To simulate a compaction effort and the corresponding strains that result, each step contains three load increments. The first is the application of the thickness of backfill. The second is the application of a 10-kPa surcharge (to simulate compaction). The third is the application of a negative 10-kPa surcharge (to simulate the removal of the compaction equipment). During this last increment any elastic strains that occurred in the second increment will be removed, but the plastic strains will remain. This is in agreement with intuitive knowledge of the behavior of soil during compaction.

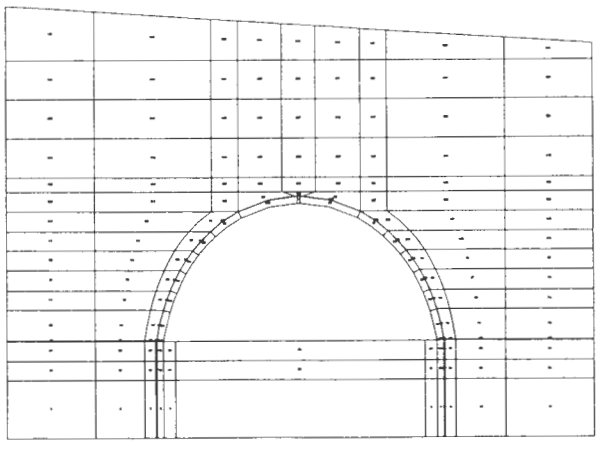

FIGURE 7 Finite-element mesh.

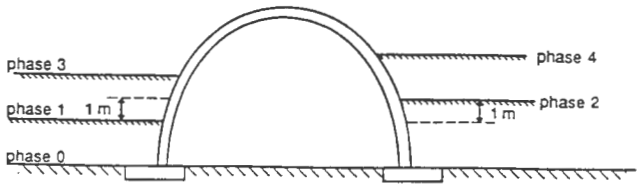

FIGURE 8 Alternative loading.

Soil-Arch Interaction Summary

After analysis of many different projects a few trends are evident. Although the deformations of the arch are very small, the FEM program indicates that the arch is slightly pushed from side to side with the application of the asymmetric backfill lifts, but this movement is generally less than 10 mm. The crown of the arch rises slightly as the sides are squeezed in during the backfilling below the crown. As backfill is placed above the crown, the crown is forced down again, although not as far down as its initial starting position. This movement of the crown was substantiated by survey monitoring performed by Syncrude Canada Ltd. on their Twin Arch Conveyor Underpass (*4*), in which the initial maximum movement of the crown was approximately 30 mm.

On many projects the stress on the outside of the arch is in excess of the soil's unit weight times the overburden height, indicating that the arch is acting like a hard point, with the softer backfill settling around it, which is behavior opposite that of corrugated steel pipe arches. On such projects the arch is more flexible than the soil in the horizontal direction but is stiffer than the soil in the vertical direction. This pattern is dependent on the geometry of the arch and, in particular, on the stiffness of the foundation soils and backfill.

Structural Design of Foundation System

Several types of acceptable foundations support an arch structure. In general, depending on foundation soil conditions, the span, the function of the structure, and many other factors, a certain type of support system will be selected. Some of the options include

1. Continuous strip footings with or without pedestals,

2. A full-width, continuous reinforced concrete slab, with or without pedestals,
3. Continuous grade beams supported on reinforced concrete caissons or drilled shafts, and
4. Continuous reinforced concrete pile caps supported on driven H-piling.

The most common foundation system is continuous strip footing with or without pedestals.

The decision of whether to use a pedestal depends on the required headroom (or crown height) required for a given span. If a lot of headroom is required, such as for a train rail application, then pedestals on top of the footings will be used to raise the crown of the arch. The structural design of the strip footings is conventional except that significant overburden pressure is present on the top of the footing on the outside of the arch. The footing is sized so that less than the allowable bearing pressure for the foundation soils can be applied. The FEM results provide the reactions for the arch elements, the applied bearing pressure beneath the footing, and the applied overburden pressure on top of the footings. By using these data the design of the footing reinforcement is straightforward.

Structural Design of TechSpan Elements

The structural design of the arch elements must consider all of the stresses to which the element will be subjected, including stripping and handling in the precast yard, shipping and transportation to the project site, all of the conditions of erection and backfilling, and the final loading conditions in service.

The arch elements need to be designed or checked both as a bending beam and as a column, subject to combined bending and axial load. All of the loading conditions outlined earlier need to be considered and tabulated in a summary table so that the most severe combinations of conditions can be used to design the concrete reinforcement. In general, the arch elements are designed for the maximum moment that cause tension on the inside and outside faces. The arch is then checked as an eccentrically loaded column by using moment interaction diagrams to check that the elements are adequate for the applied axial loads. The arch elements are also designed for the maximum shear forces, although these are generally small.

As with most concrete designs there is the traditional trade-off between a thinner section that is highly reinforced or a thicker section that has less reinforcement.

ACKNOWLEDGMENTS

The authors thank the many employees of the Terre Armee Internationale group of companies for their work in the development of the TechSpan precast arch and in particular Santiago Muelas of the Spanish Terre Armee Internationale company.

REFERENCES

1. *ATC-6 Seismic Design Guidelines for Highways Bridges.* FHWA, U.S. Department of Transportation, Oct. 1981.
2. Anderson, D. L., P. M. Bryne, and T. Srithar. *Seismic Analysis of TechSpan Soil-Arch Structure Cassiar Connector Project, Vancouver, British Columbia.* British Columbia Ministry of Transportation, Victoria, July 23, 1990.
3. Duncan, J. M., P. Byrne, K. Wong, and P. Mabry. *Strength, Stress-Strain and Bulk Modulus Parameters for Finite Element Analysis of Stresses and Movements in Soil Masses.* Report UCB/GT/80-01. Department of Civil Engineering, University of California, Berkeley, Aug. 1980.
4. Brockbank, B., R. Dunphy, and L. Yasinko. Innovative Underpass for Highway 63, Syncrude, Alberta. *Proc., International Road Federation Conference and Exposition*, Vol. 9. Transportation Association of Canada, Ottawa, Ontario, Canada, July 1994.

Impact of Load and Resistance Factor Design Specifications on Short- to Medium-Span Steel Bridges

Dennis R. Mertz, *University of Delaware*
John M. Kulicki, *Modjeski and Masters, Inc.*

In 1993, AASHTO adopted the *Load and Resistance Factor Design Bridge Design Specifications* (LRFD specifications) as an alternative to the *Standard Specifications for Highway Bridges* (standard specifications). Its adoption raises many questions regarding the specification's impact on the resultant bridge members' proportions and the design process itself. The implication of the provisions of the LRFD specifications on the design of steel highway bridges relative to those of the load factor design (LFD) provisions of the standard specifications is investigated through a dissection of the specifications into the load and resistance sides of the LRFD equation. A simple design example illustrates the impact of the LRFD specifications. Finally, the design process and effort required to apply each set of provisions, LRFD and LFD, are discussed on the basis of the example. Through the dissection of the LRFD specifications into the load and resistance sides of the LRFD equation and the discussion of the design process, the general impact of the specifications on the economy of short- to medium-span steel bridges and on the design community in general is assessed.

At the spring meeting of 1993 the AASHTO Subcommittee on Bridges and Structures adopted the *Load and Resistance Factor Bridge Design Specifications* (*1*) (LRFD specifications) as an equal alternative to the *Standard Specifications for Highway Bridges* (*2*) (standard specifications).

The LRFD specifications are the product of NCHRP Project 12-33, Development of Comprehensive Bridge Design Specifications and Commentary, a 5-year, 50-person research effort led by Modjeski and Masters, Inc. The intent of NCHRP Project 12-33 was to develop a structural reliability-based, technically state-of-the-art bridge design code to replace the standard specifications.

Bridges designed to the standard specifications were not deemed to be performing unsatisfactorily. The provisions of the standard specifications, however, were deemed to contain gaps, in which coverage is missing, and inconsistencies, in which internal conflicts or contradictions in wording or philosophy exist. Bridges designed to the code developed by NCHRP Project 12-33 are not to be specifically stronger or weaker but more rationally designed.

Furthermore, NCHRP Project 12-33 was charged with integrating existing research findings into the code

but not to develop new findings, because funding was not adequate to do both.

Reliability-based design methodologies seek to account for the statistical variations in loads and resistances in the design process. The theory of structural reliability can be used to directly compute the level of safety, quantified as the reliability index, inherent to a given set of nominal loads, the designer's estimate of the nominal resistance of the component being designed, and statistical data quantifying the variation of load and resistance. Thus, it is possible to vary the nominal resistance to achieve the level of safety for the component (or system) that is acceptable to society.

Alternatively, the process can be worked backwards to calibrate a combination of the load and resistance factors required to achieve a general targeted reliability index. In this manner the combination of load and resistance factors was derived for the LRFD specifications. The design process then proceeds analogously to load factor design (LFD) in the standard specifications, and the designer needs to know little, if anything, of structural reliability theory. Bridges designed to the LRFD specifications are not to be specifically stronger or weaker than those designed to the standard specifications but more uniformly reliable.

Reliability indexes inherent in the standard specifications were calculated for existing bridges and a supplemental set of virtual bridges studied during the calibration of load and resistance factors. The resultant ranges of the reliability indexes for both moment and shear are given in Figure 1. The wide range of values indicates the inconsistent levels of safety inherent in the standard specifications.

Reliability indexes were recalculated for each of the bridges on the basis of the provisions of the LRFD specifications. The resulting ranges of the reliability index are given in Figure 2.

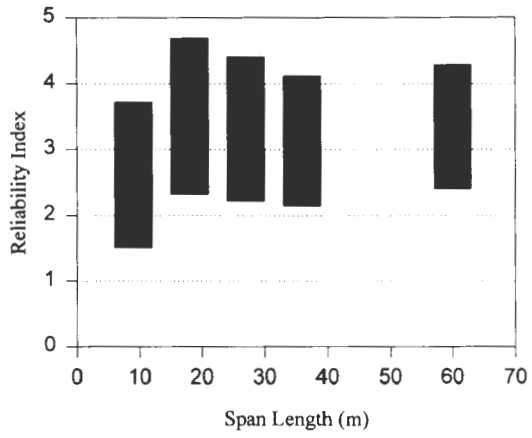

FIGURE 1 Reliability indexes by standard specifications.

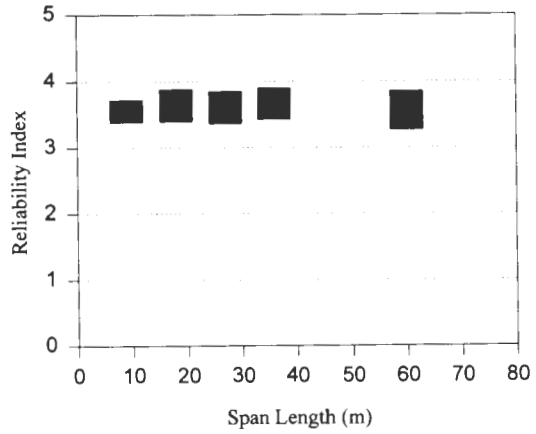

FIGURE 2 Reliability indexes by LRFD specifications.

Figure 1 suggests that a reliability index of 3.5 is indicative of past practice. Hence, this value was selected as a target for the calibration of the LRFD specifications.

Figure 2 suggests that the LRFD specifications achieve this level of reliability or safety consistently, with considerable improvement in the clustering of reliability indexes around the target value. This is a direct result of the integration of the load factors, resistance factors, accurate load models, and suitable resistance models of the LRFD specifications.

NCHRP Project 12-33 was not charged with making a wholesale readjustment of the inherent safety in the nation's highway system but to achieve a more uniform level of safety. The resultant uniformity of structural safety is evident in Figure 2.

The provisions of the LRFD specifications can be subdivided according to the general LRFD equation given in Article 1.3.2.1 of these specifications:

$$\eta \Sigma_i \gamma_i Q_i \leq \phi R_n \quad (1)$$

where

η = a factor relating to ductility, redundancy, and operational importance;
γ_i = load factor;
Q_i = force effect;
ϕ = resistance factor; and
R_n = nominal resistance.

The discussion of the impact of the LRFD specifications on the design of steel bridges is divided into two parts:

- Those provisions relating to the load side of the LRFD equation (the left-hand side), and

- Those relating to the resistance side of the LRFD equation (the right-hand side).

Load Side of LRFD Equation

The provisions relating to the load side of the LRFD equation that have an impact on the design of steel bridges are those relating to

- The live-load model,
- The dynamic load allowance,
- Lateral live-load distribution, and
- The load factors.

Live-Load Model

As a result of the evolution of the vehicles traveling on the nation's highways, the HS 20 loading of the standard specifications, originally developed in 1944, no longer bears a uniform relationship to these vehicles. In developing a new design specification providing more uniform and consistent safety for bridges, a new live load is necessary.

Figure 3 compares the various moment-type force effects for span lengths of 6 to 45 m generated by a set of vehicles currently using the nation's highways with those of the HS 20 live-load model. This set of vehicles was determined to be that which routinely produces the most severe moments and shears. These vehicles represent state grandfather exceptions to the federal axle weight limits or gross vehicle weight limits and travel without special permits (these are referred to here as grandfather vehicles). The ratio of the force effect from the envelope of grandfather vehicles divided by the corresponding force effect from the HS 20 model is plotted on the verticle axis versus the span length on the horizontal axis. Thus, a complete match of force effects, suggesting that the HS 20 model is an accurate and representative model of the loads of grandfather vehicles, would be indicated by a horizontal line passing through the vertical axis at a value of 1.0. Corresponding information for the shear force effects has also been developed. These comparisons illustrate that the HS 20 model is not representative of current loads on the nation's highways.

A combination of the various elements of the live-load model of the standard specifications adequately represents the current loads on the nation's highways and was chosen as the new notional design live load in the LRFD specifications. These elements are

- The HS 20 truck, or
- A slight variation of the Alternate Military Loading in combination with
- The HS 20 uniform load without the concentrated loads.

For the case of negative moment over a pier a special provision is included for two closely spaced HS 20 trucks in one lane. The live-load model is specified in Article 3.6.1.2 of the LRFD specifications and is termed the HL 93 loading.

A summary of the moment-type force effect ratios for the grandfather vehicles divided by that for the new LRFD live-load model is shown in Figure 4. The results for moment-type force effects are tightly clustered and form bands of data that are essentially horizontal. This tight clustering of data results in a comparison of shear-type force effects also, indicating that one notional

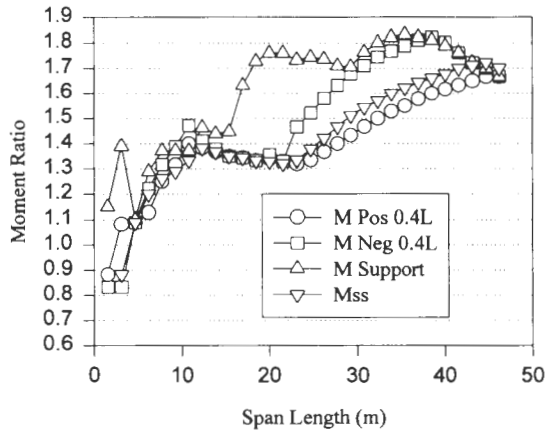

FIGURE 3 Moment ratios comparing grandfather vehicle loads versus HS 20 loads.

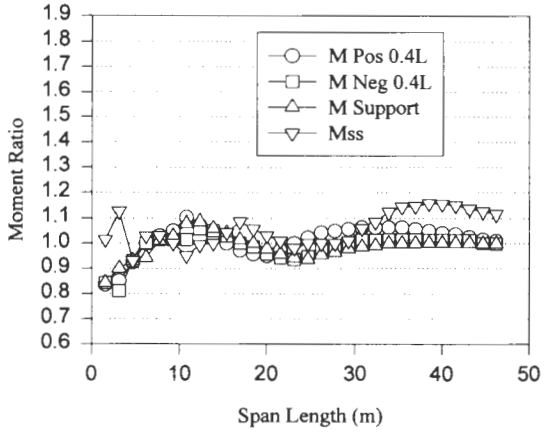

FIGURE 4 Moment ratios comparing grandfather vehicle loads versus HL 93 loads.

model can be developed for both moment and shear. The fact that the data are essentially horizontal indicates that both the model and the load factor applied to live load are independent of span length. The tight clustering of all the data for all force effects further indicates that a single live-load factor will also be sufficient for both moment and shear.

A comparison of Figures 3 and 4 reveals the change in live-load requirements inherent in the implementation of the LRFD specifications. Since, for the most part, the curves of Figure 4 all fall below those of Figure 3, the unfactored live-load requirements of the LRFD specifications are greater than those of the standard specifications.

In the special case of the fatigue limit state, a single HS 20 truck is specified as the live load to be considered on the bridge (i.e., multiple lanes of loading are not considered). Neither the tandem nor the design lane load is applied in this limit state. Furthermore, the distance between the two large axles on the truck is a constant 9 m rather than the variable spacing used for strength design. The reason for this simplification is that the majority, and therefore the statistically significant number, of vehicles on the road are relatively long 3S-2 configurations. It would be unduly severe to assume that all of the fatigue stress ranges result from the smaller numbers of relatively short trucks. In addition to the size of the vehicle, the number of single-lane occurrences is necessary to predict the number of cycles of fatigue loading. This is referred to in the LRFD specifications as a single-lane average daily truck traffic. In the absence of site-specific information, this may be related to the typically tabulated average daily truck traffic volume through a factor ranging from 100 percent for a single lane available to truck traffic to as low as 80 percent when three or more lanes are available.

Calculated stress ranges by the LRFD specifications are lower than those by the standard specifications because of the reduced fatigue live-load model, but the numbers of cycles by the LRFD specifications are much increased. The net result is that both specifications are essentially equivalent. The cumulative fatigue damage due to the lower stress range for a larger number of cycles according to the LRFD specifications is essentially equal to that due to the higher stress range for a smaller number of cycles according to the standard specifications.

Since multilane loading and lane loading are not considered for fatigue design, the fatigue limit state controls less often in the LRFD specifications than in the standard specifications. This is not a liberalization of the fatigue requirements but an acknowledgment that the requirements of the standard specifications are not rational.

Dynamic Load Allowance

In the standard specifications the specified amplification of static load to replicate dynamic response is termed *impact* and is a function of span length alone.

The LRFD specifications terms the amplification the *dynamic load allowance* and in general simply requires that a constant amplification of 33 percent be applied to the design vehicle only. Initially, this may seem like a step backwards, but research suggests that this simple approach is warranted.

The simple approach of the LRFD specifications is based on a study of dynamic effects reported by Nowak (*3*). In that study the dynamic effect was quantified by investigating deflection. The study concludes that

- As the gross vehicle weight increases, naturally the static deflection increases,
- As the gross vehicle weight increases, the dynamic amplification as a percentage of the gross vehicle weight decreases, yet
- Throughout the range of gross vehicle weights, the magnitude of the increment between static and dynamic deflections remains constant.

The study revealed that the most influential factor on dynamic load allowance is roadway surface roughness.

Since roadway surface roughness during the service life of the bridge is beyond the control of the designer, it is foolhardy to specify a precise value of dynamic load allowance including the functionalities beyond surface roughness.

In consideration of that study the general dynamic load allowance in the LRFD specifications is taken as one-third of the weight of the design truck or tandem, with no dynamic load allowance applied to the design lane load. Nowak's study (*3*) indicates that the dynamic load allowance for a 325-kN truck is about one-fourth. Since the specified superposition of the design truck and lane loads is intended to represent a truck with a weight greater than 325 kN, the dynamic load allowance is taken as one-third of the weight of the design truck. Furthermore, as the span length of the bridge increases, the lane load models not only a single truck heavier than the design truck but also the presence of other traffic around the design truck. The study indicates that increased traffic decreases the dynamic effects; therefore, no dynamic load allowance is applied to the design lane portion of the live-load model.

For comparisons with the standard specifications, the dynamic load allowance should be considered one-fourth, since the one-third on the truck is to replicate one-fourth on the whole live load, as discussed earlier. Therefore, for the strength and service limit states the LRFD specifications require

- Less impact or dynamic load allowance for span lengths less than 22.9 m, and
- More impact for span lengths greater than 22.9 m.

For the fatigue limit state the LRFD specifications require 15 percent impact, a more average value, resulting in

- Less impact or dynamic load allowance for span lengths less than 63.5 m, and
- More impact for span lengths greater than 63.5 m.

Lateral Live-Load Distribution

New lateral live-load distribution factors have been developed by Imbsen and Associates, Inc., under NCHRP Project 12-26 (*4*). The distribution factors developed in that study are reported to be typically accurate to within 5 percent of the results obtained by more refined methods of analysis. These new distribution factors form the basis for those included in the LRFD specifications and are included in the recently published AASHTO *Guide Specifications for Distribution of Loads for Highway Bridges* (*5*).

Their study (*4*) reveals that beam spacing is the most significant parameter. However, span length, longitudinal stiffness, and transverse stiffness also affect the load distribution factor. Ignoring the effects of parameters other than beam spacing can result in highly inaccurate results. Even when they are properly applied, the simple distribution factors of the standard specifications can result in both highly unconservative and highly conservative designs.

Thus, new load distribution factors are provided for the design of bridges. These factors are more realistic than the traditional values of the standard specifications. The distribution factors in the LRFD specifications yield less moment per girder for larger girder spacings, say greater than 2.75 m, for all span lengths and more moment per girder for very short span lengths, say less than 9 m, when the girder spacing is less than 2.5 m.

Load Factors

The basic strength load combination in the LRFD specifications, called Strength Load Combination I, is

$$\Sigma_i \gamma_i Q_i \quad 1.25DC + 1.50DW + 1.75LL \tag{2}$$

where

DC = dead load due to components and attachments,
DW = dead load due to wearing surfaces and utilities, and
LL = live load.

In the standard specifications, the comparable load combination appears as

$$\Sigma_i \gamma_i Q_i = 1.3D + 2.17LL \tag{3}$$

where D is equal to all components of the dead load.

The differences in dead-load factor are insignificant, because the slight decrease in load factor for components and attachments compensates for the larger increase in the load factor for wearing surfaces and utilities.

The change in the live-load factor is much more significant, representing an across-the-board decrease of 24 percent for the LRFD specifications.

Resistance Side of LRFD Equation

Unlike other sections of the LRFD specifications such as that dealing with concrete structures, Section 5 (Concrete Structures), the section dealing with steel structures, Section 6 (Steel Structures), offers no major changes. For the most part this is due to the steel industry's involvement in the AASHTO Bridge Subcommittee's Technical Committee system. This involvement ensures that recent research findings quickly get adopted as interim changes to the standard specifications.

Nonetheless, new provisions that do not appear in the standard specifications are included in the LRFD specifications. They relate to

- Replacement of deflection limitations with flange-stress control of permanent deformation at overload,
- Removal of the arbitrary 7.6-m diaphragm spacing,
- Inclusion of reduction factor on tensile resistance to account for shear lag,
- New equations for combined flexure and compressive resistance,
- Updating of provisions for flexural resistance of I-sections,
- Updating of shear resistance provisions,
- New constructability provisions, and
- Inelastic analysis procedures.

The changes represented by this list, other than the inclusion of resistance factors, evolve from the LFD provisions of the standard specifications and do not consist of the implementation of new design philosophies or methodologies. With time these changes need to be incorporated into the standard specifications. As such their impact should not be considered as part of the implementation of the LRFD methodology.

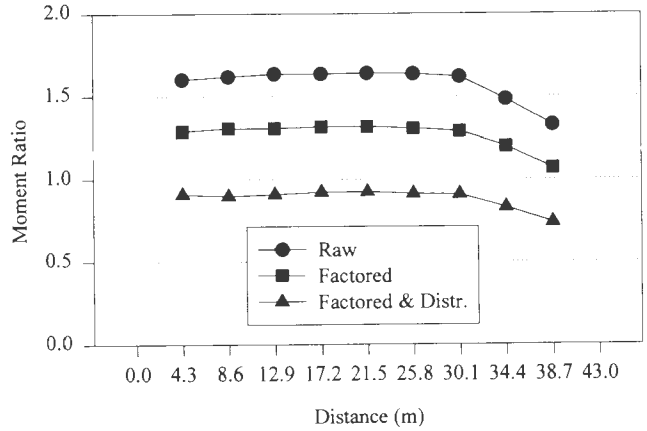

FIGURE 5 Positive live-load moment ratios.

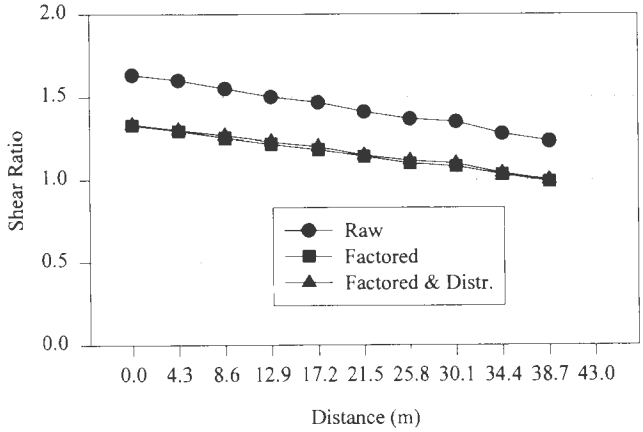

FIGURE 7 Positive live-load shear ratios.

Resistance Factors

The explicit specification of resistance factors does represent a part of the implementation of the LRFD methodology. The resistance factors specified in the LRFD specifications for flexure and shear of steel members are both specified as 1.0. Although the LFD provisions of the standard specifications do not contain resistance factors or capacity reduction factors, since the specified values are unity, these represent no net change between the two specifications.

Conclusions

If it is accepted that the resistance side of the LRFD equation for steel bridges represents an evolution of the LFD provisions of the standard specifications and not new design methodologies, the impact of the LRFD specifications on short- to medium-span steel bridges can be assessed on the basis of mainly the load side of the LRFD equation.

A typical design example illustrates the impacts that changes on the load side of the LRFD equation have on the design of steel bridges. The results shown in Figures 5 through 8 are based on a two-span unit of equal 43-m span lengths. The girder spacing is 3.7 m. An interior girder loaded with two or more lanes of live load is chosen for comparison.

The figures show comparisons between the load provisions of the LRFD specifications and those of the standard specifications. The vertical axes of the figures represent the ratio of moments or shears obtained by applying the provisions of the LRFD specifications to those obtained by applying the standard specifications. The horizontal axes represent longitudinal distance along the girder. Datum points representing values at the ten 0.1 points along the girder have been plotted. The moments or shears, including the dynamic load allowance or impact, indicated as raw data are unfac-

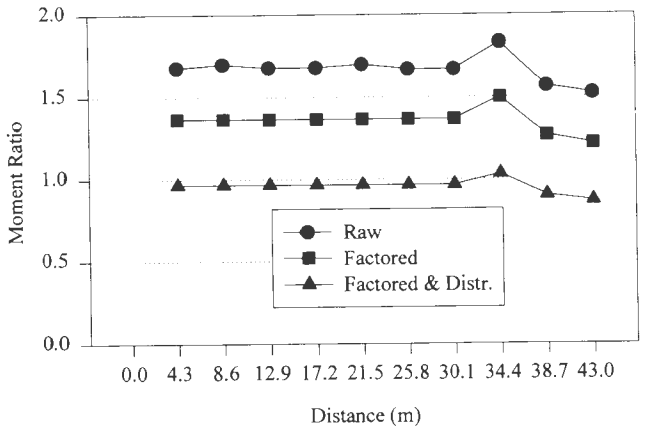

FIGURE 6 Negative live-load moment ratios.

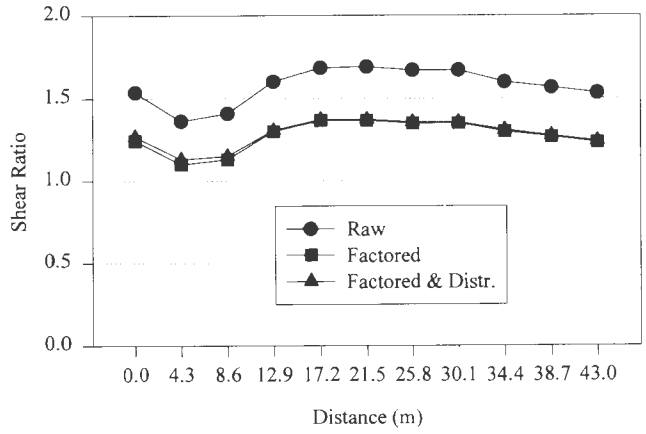

FIGURE 8 Negative live-load shear ratios.

tored. The factored data are the product of the raw data and the appropriate load factors. The factored and distributed data are the product of the factored data and the appropriate distribution factors. Since the resistance factors for moment and shear of steel members are both unity, this final ratio, factored and distributed data, represents the change in live-load demand required on the basis of the implementation of the LRFD specifications.

Figure 5 shows the positive live-load moment ratios. The impact of combining the truck and lane loads in the HL 93 loading of the LRFD specifications in comparison with considering them independently according to the standard specifications is indicated by the datum points representing unfactored moment and is labeled raw data. Most of the live-load moments at the various 0.1 points according to the LRFD specifications are approximately 1.6 times the moments according to the standard specifications. Once the unfactored moments are factored by the respective live-load factors, 1.75 for the LRFD specifications and 2.17 for the standard specifications, the factored moments are somewhat closer, with typical ratios of about 1.3. Distribution of these factored moments per lane to the girders brings the factored moments per girder to approximately the same level in the two specifications, with the demand according to the LRFD specification being approximately 90 percent of that according to the standard specifications for this steel bridge example. The refined distribution factor of the LRFD specification is significantly lower than the distribution factor of the standard specifications. The close comparison in factored and distributed moments is very dependent on the individual structure type. For the same span length and girder spacing configuration, a prestressed concrete girder example resulted in a demand of 110 percent of that of the standard specifications.

Figure 6 shows similar ratios of negative live-load moment, with the spike in raw data at the 0.8 point indicating the place where the two closely spaced trucks in one lane of the HL 93 loading began to govern negative moment.

Figures 7 and 8 show positive and negative live-load shear ratios, respectively. The refined distribution factor for shear according to the LRFD specifications is relatively larger than that for bending moment in this example. The effect of this can be seen in Figures 7 and 8. There is almost no difference between the ratios of the factored shears and those of the factored and distributed shears according to the LRFD specifications and the standard specifications; in others words the distribution factors were essentially the same for each specification. The increased live load of the LRFD specifications results in more shear demand than the shear demand from the live load of the standard specifications for this steel bridge example.

The development of this design example illustrated the relative effort required in the application of each specification. This design example suggests that a small amount of increased design effort is required when applying the LRFD specifications. The calculation of the live-load distribution factor is more complex. Although the HL 93 load is merely a superposition of existing HS 20 loads, additional bookkeeping is required. The special provision for two closely spaced trucks for negative moment near a support definitely requires additional effort. Furthermore, the fatigue load with its fixed rear axle spacing requires additional bookkeeping. The increased effort, however, brings with it increased designer confidence in the relative precision of the calculations.

As was intended by the subcommittee, the LRFD specifications do not alter the basic safety or reliability inherent in the standard specifications. As Figure 1 indicated, however, the inherent safety is not uniform. The implementation of the LRFD specifications provides more uniform safety, as indicated in Figure 2. Some bridges require slightly additional strength, such as very short spans with close girder spacings, whereas others require less strength. In general, the impact on short- to medium-span steel superstructures is minimal.

ACKNOWLEDGMENTS

AASHTO, in cooperation with the FHWA, sponsored the effort to develop a new probability-based bridge design code, which became the *Load and Resistance Factor Bridge Design Specifications*, 1st ed. TRB of the National Research Council administered the effort, conducted in NCHRP.

REFERENCES

1. *Load and Resistance Factor Bridge Design Specifications*, 1st ed. AASHTO, Washington, D.C., 1994.
2. *Standard Specifications for Highway Bridges*, 15th ed. AASHTO, Washington, D.C., 1992.
3. Nowak, A. S. *Calibration of LRFD Bridge Design Code*. NCHRP Project 12-33. TRB, National Research Council, Washington, D.C., 1992.
4. Zokaie, T., T. A. Osterkamp, and R. A. Imbsen. *Distribution of Wheel Loads on Highway Bridges*. Final Report, NCHRP 12-26. TRB, National Research Council, Washington, D.C., 1991.
5. *Guide Specifications for Distribution of Loads for Highway Bridges*. AASHTO, Washington, D.C., 1994.

BRIDGE SUBSTRUCTURES: SCOUR AND SHIP IMPACT

Florida Department of Transportation Bridge Scour Evaluation Program

P. F. Lagasse and E. V. Richardson, *Ayres Associates*
K. E. Weldon, *Florida Department of Transportation*

Following the catastrophic failure of the Schoharie Creek bridge in April 1987 FHWA established a national bridge scour evaluation program under the National Bridge Inspection Standards to be implemented by state highway and transportation departments. Initial scour susceptibility screening was completed for the most part by October 1992, and FHWA has established January 1997 as the completion date for scour evaluations of all existing bridges identified as scour susceptible. The procedures that were developed and the results to date of scour evaluation of bridges in Florida are highlighted. The Florida Department of Transportation guidelines contain a four-phase approach to scour evaluations: Phase I is data collection and qualitative analysis, Phase II is hydrologic and hydraulic assessment for scour analysis, Phase III is geotechnical and structural scour assessment, and Phase IV is a recommended plan of action. The checklists and field procedures developed to complete Phases I and II of the evaluation are presented, and the results of the scour evaluations to date are summarized.

Following the catastrophic failure of the Schoharie Creek bridge in April 1987 FHWA established a national bridge scour evaluation program to be implemented by state highway and transportation departments. Initial scour susceptibility screening was completed for the most part by October 1992, and FHWA has established January 1997 as the completion date for scour evaluations of all existing bridges identified as scour susceptible. With almost 8,000 bridges under the National Bridge Inspection Standards (NBIS), Florida is facing a formidable task. The procedures that were developed and the results to date from scour evaluation of bridges in Florida by the Florida Department of Transportation (FDOT) are highlighted. The checklists and field procedures developed to complete the initial phases of the evaluation are presented and discussed. This paper expands on and updates a description of the scour evaluation program developed initially for a single district of FDOT (*1*).

FDOT Guidelines

Technical Advisory 5140.23, *Evaluating Scour at Bridges* (*2*), issued by FHWA in 1991 to supersede Technical Advisory 5140.20, provides guidance on the development and implementation of procedures for evaluating bridge scour. The technical advisory indicates that every bridge over a waterway, whether existing or under design, should be evaluated for scour to determine prudent measures to be taken for its protection. The evaluations are to be conducted by an interdisciplinary team (hydraulic, geotechnical, and struc-

tural engineers) and are to include hydraulic studies and scour evaluation.

The scour evaluation procedures implemented in Florida are based on FDOT guidelines for scour evaluation studies (*3*), which are supported by FHWA guidance in Technical Advisory 5140.23 and FHWA's Hydraulic Engineering Circulars 18 (HEC-18) (*4*) and 20 (HEC-20) (*5*). FDOT guidelines contain a four-phase approach to scour evaluations:

- Phase I: data collection and qualitative analysis,
- Phase II: hydrologic and hydraulic assessment for scour analysis,
- Phase III: geotechnical and structural scour assessment, and
- Phase IV: recommended plan of action.

The site data analysis for Phase I is qualitative. It involves preliminary conclusions and findings based on the application of simple geomorphic concepts and reconnaissance-level evaluation of office data, field data, and site conditions. This phase relies heavily on the stepwise procedure and techniques presented in HEC-20 (*5*). Phase II involves basic engineering analysis techniques and development of quantitative information for bridge scour assessment. Guidance in specific areas of the evaluation and the level of detail required are based on the results of Phase I. Again, a stepwise analysis procedure presented in HEC-20 (*5*) provides guidance for the Phase II effort, and scour analyses are completed in accordance with the detailed procedures presented in HEC-18 (*4*).

Phases III and IV of the FDOT procedure, which will not be discussed further, involve the structural and geotechnical disciplines represented on the scour evaluation team (Phase III) and the development of a conceptual plan for scour countermeasures for protecting structural elements considered at risk as a result of scour (Phase IV). Phase IV involves the entire multidisciplinary evaluation team and relies on the countermeasure guidance contained in HEC-18 (*4*) and HEC-20 (*5*).

Evaluation Criteria

In HEC-18 (*4*) the recommendation is made that states screen their bridges and place them into three categories: low risk, scour susceptible, and unknown foundations. If the evaluation team detects an immediate scour threat to a bridge during Phase I, the responsible department of transportation district should be notified. Consequently, the Phase I procedure developed for FDOT includes an additional scour-critical category. The following guidelines are provided to assist the evaluation team in making consistent ratings. A high, medium, and low priority is also included to assist the FDOT district in prioritizing Phase II and follow-on activities.

Category	*Rating*
Scour critical	Yes or no
Scour susceptible	High, medium, low
Low risk	High, medium, low
Foundations	Known or unknown

Scour critical

- Evidence of structural damage due to scour,
- Aggressive stream or tidal waterway (high velocity, steep slope, deep flow),
- Exposed footing in erodible material,
- Exposed piles with unknown or insufficient embedment,
- Countermeasures needed immediately, and
- Actively degrading channel.

Scour susceptible (high priority)

- Aggressive stream or tidal waterway,
- Foundations are spread footings on erodible soil, shallow piles, or embedment unknown,
- Tidal flows have high velocities (surface velocity, >0.9 m/sec) and large tidal amplitudes (>0.6 m),
- Bed material is easily eroded,
- Evidence of scour or degradation,
- Scour is below top of footing,
- Large angle of attack (>10 degrees),
- No countermeasures or countermeasures in poor condition,
- Clear water scour mode (e.g., relief bridge on floodplain),
- Significant flow over the bank (potential for contraction scour), and
- Possibility of bridge overtopping (potential for pressure flow).

Scour susceptible (medium priority)

- Characteristics fall between high and low.

Scour susceptible (low priority)

- Stream is not aggressive (low velocities) or other factors mitigate the high velocities,
- Foundations are on piles but of unknown embedment,
- Tidal flows have low velocities and tidal amplitudes,
- Bed material is erodible,

- Some evidence of scour or degradation,
- Scour is not below top of spread footings,
- Stream is degrading but foundations are known, and
- Countermeasures are in fair to good condition.

Low risk (high priority)

- Stream is not aggressive (low velocity), or other factors mitigate the high velocity,
- Foundations on piles of known embedment,
- Stream is aggressive or the tidal range is large, but foundations are known and cross section is stable,
- Stream is aggrading or stable, and
- Countermeasures are in fair condition.

Low risk (medium priority)

- Characteristics fall between high and low.

Low risk (low priority)

- Stream is not aggressive or other factors mitigate high velocity,
- Foundation is in bedrock,
- Stream is aggrading or stable,
- Pile foundations are deep,
- Cross section is stable,
- No evidence of scour,
- Tidal flows have low velocities and ranges,
- Countermeasures are in good condition,
- No possibility of overtopping bridge,
- Foundations are designed using current technology,
- Channel is heavily vegetated, and
- No flow over the bank.

Unknown foundations

- No record of foundation type (i.e., spread footing versus piles) or condition of foundation or pile embedment is unknown (generally rated a minimum of scour susceptible, low priority, unless there are significant mitigating factors, e.g., a long history of significant aggradation).

These criteria are intended to serve as guidelines in the Phase I scour evaluation. Although a numerical rating scheme could be developed, Phase I is intended to be a qualitative evaluation based heavily on experience and engineering judgment. It is not necessary that all factors in a given category be present to justify a specific rating, but the observance of several factors in a given category would guide the rating toward that category, considering all other office review and field reconnaissance data available. As noted in FDOT guidelines (*3*), the engineer must use good judgment in the evaluation process and is encouraged to use ingenuity in applying the recommended concepts and procedures.

Standardized Forms

Phase I: Qualitative Analysis

To support the Phase I office and field evaluation, a set of standardized forms was developed (Figure 1). The form consists of 11 categories that systematically address structural components affected by scour, abutments and piers, lateral and vertical channel stability, geomorphology, other considerations (watershed, tidal, and tributary factors), and additional comments (such as unique characteristics and a standard set of photographs), which can be evaluated on a qualitative basis during office and field inspections. The appropriate data collected in the office for Sections 4 through 11 (Figure 1) are considered during the Phase I field evaluation and review. Each of these categories is tied closely to the FHWA guidelines and procedures presented in HEC-18 (*4*) and HEC-20 (*5*). Initially, field site visits were scheduled before the office review, but experience has shown that many questions in the field can be avoided if adequate time has been taken to assemble and review all available file information first.

The specific conclusions reached following the office and field review are summarized in Sections 1 through 3, which outline the Scour Vulnerability Rating (rating and reasons for rating), FDOT Scour Index (based on a preliminary screening by FDOT), and recommendations (including countermeasures and the need for a Phase II analysis). A standard cover sheet (Figure 1) identifies the bridge by number and location, provides a scour vulnerability summary (scour mode and rating), and provides a recommendation regarding the need for a Phase II quantitative analysis.

The forms are arranged to guide the inspector or reviewer through a standard evaluation process. Several areas of the form allow alternative choices in each of the categories. These areas are intended to be appropriately marked or circled in the field for further evaluation in the office. The scope of Phase I qualitative analysis is designed to develop an informed opinion of scour susceptibility based on available site-specific data and good engineering judgment.

The countermeasures identified on the form represent recommendations of the inspector or reviewer. If scour monitoring is specified as a countermeasure, this would require installation on the bridge of a device designed to continuously or periodically measure scour. If inspections are recommended as a countermeasure, the frequency is specified (i.e., during routine bridge inspec-

Prepared For:

SCOUR EVALUATION REPORT

Prepared By:

AYRES ASSOCIATES

3901 Coconut Palm Drive
Suite 100
Tampa Florida
(813) 628-0742

REPORT IDENTIFICATION

■ PHASE 1 — Qualitative Evaluation/ Assessment — Date: _____

☐ PHASE 2 — Hydraulic/Hydrologic Assessment — Date: _____

☐ PHASE 3 — Structural/Geotechnical Assessment — Date: _____

☐ PHASE 4 — Plan of Action — Date: _____

Bridge Number: _____ Name: _____

Location: _____ County: _____

SCOUR VULNERABILITY

SCOUR MODE: ☐ Riverine ☐ Tidal ☐ Both

SCOUR RATING:

Scour Critical: ☐ Yes ☐ No

Scour Susceptible:

☐ High ☐ Medium ☐ Low

Low Risk:

☐ High ☐ Medium ☐ Low

Foundations: ☐ Known ☐ Unknown

RECOMMENDATION:

Name of Engineer	Initials	Engineering Registration Number	Discipline

Reviewing Bridge Engineer/Supervisor	Confirming Registered Professional Engineer
Name _____ P.E. No. _____ Initials _____	Name _____ P.E. No. _____ Signature/Seal _____

a

SCOUR EVALUATION - FIELD / OFFICE REVIEW REPORT

Bridge #:	County:	Route:	Over:

1. SCOUR VULNERABILITY RATING (PER FHWA)

a. Scour Critical:	☐ Yes	☐ No	
Scour Susceptible:	☐ High	☐ Medium	☐ Low
Low Risk:	☐ High	☐ Medium	☐ Low
Foundations:	☐ Known	☐ Unknown	
Structure Type:	☐ Bridge	☐ Bridge Culvert	

b. Reasons for Rating:

2. FLORIDA DOT SCOUR INDEX NUMBER Initial____ Secondary ____

3. RECOMMENDATIONS

a. Countermeasures:

- ☐ Riprap
- ☐ Scour Monitor
- ☐ Inspection
- ☐ Other

b. Phase Two Analysis Recommended: ☐ Yes ☐ No

c. Phase Two Priority: ☐ High ☐ Medium ☐ Low ☐ None

d. Remarks:

b

FIGURE 1 Scour Evaluation Report cover sheet and Phase I qualitative evaluation Field/Office Review Report forms.

SCOUR EVALUATION - FIELD / OFFICE REVIEW REPORT

4. SITE FIELD REVIEW

a. Evidence of Scour at Structure

1) Abutment Tilting / Moving in:	☐ Yes	☐ No
2) Slopes Washing in / Sloughing:	☐ Yes	☐ No
3) Scour Holes Near Abutments / Bents:	☐ Yes	☐ No
4) Bed Deposits Downstream:	☐ Yes	☐ No
5) Bridge Railing Sagging:	☐ Yes	☐ No
6) Debris:	☐ Yes	☐ No
7) Highwater Mark:	☐ Yes	☐ No

b. Feasibility of Monitoring During High Flow

1) Rod / Pole / Weight from Deck:	☐ Yes	☐ No
2) Fixed Monitoring Device:	☐ Yes	☐ No

c. Feasibility of Adding Riprap or Other Scour Countermeasures: ☐ Yes ☐ No

5. ABUTMENTS

a. Type:

☐ Spill Through ☐ Vertical Wall ☐ Wing Walls
☐ Bridge ☐ Concrete Box Culvert ☐ Seawalls

b. Foundation:	Dimensions (L,W,D,) (ft)	Embedment (ft)	Scour Exposure (ft)
☐ Spread Footings			
☐ Pile Caps			
☐ Piles			
☐ Drilled Shaft			

Source of Data: ☐ Field Review ☐ Design Plans ☐ As-built Drawings ☐ Pile Driving Records ☐ Inspection Reports ☐ Other

c. Location from Bank:	Left (ft)	Right (ft)
☐ Set back		
☐ In Channel		
☐ At Bank		

d. Protection

1) Riprap: ☐ Sand Cement ☐ Rubble ☐ Commercial Block ☐ Grouted ☐ Seawall ☐ None ☐ Other

2) Condition:	Good	Fair	Poor
Left	☐	☐	☐
Right	☐	☐	☐

c

SCOUR EVALUATION - FIELD / OFFICE REVIEW REPORT

6. PIER

a. Type:

☐ Concrete Wall ☐ Pile Bent ☐ Column Type

b. Shape: ☐ Square ☐ Rounded ☐ Sharp Nose

c. Width: ft. Length ft.

d. Foundation (worst pier)	Dimensions (L,W,D,) (ft)	Embedment (ft)	Scour Exposure (ft)
☐ Spread Footing			
☐ Pile Cap			
☐ Piles			
☐ Drilled Shaft			

Source of Data: ☐ Field Review ☐ Design Plans ☐ As-built Drawings ☐ Pile Driving Records ☐ Inspection Reports ☐ Other

e. Protection

1) Riprap: ☐ Sand Cement ☐ Rubble ☐ Commercial Block ☐ Grouted ☐ Seawall ☐ None ☐ None Apparent ☐ Other

2) Condition: ☐ Good ☐ Fair ☐ Poor

7. CHANNEL LATERAL STABILITY

a. Bends

1) Bridge Location:	☐ Upstream of Bend	☐ Downstream of Bend	☐ In Bend
2) Migration:	☐ Yes	☐ No	
3) Countermeasures:	☐ Yes	☐ No	Type:

b. Bank Condition:	Upstream	Downstream
1) Eroding	☐	☐
2) Stable	☐	☐
3) Vegetated	☐	☐
4) Seawall	☐	☐

5) Countermeasures: ☐ Yes ☐ No Type:

c. Angle of Attack: Flood Flow Normal Flow

d. Point Bar Under Bridge: ☐ Yes ☐ No

e. Islands or Bars

1) Upstream:	☐ Yes	☐ No
2) Downstream:	☐ Yes	☐ No

d

FIGURE 1 (*continued*)

SCOUR EVALUATION - FIELD / OFFICE REVIEW REPORT

8. CHANNEL VERTICAL STABILITY

a. Exposed Footing: ☐ Yes ☐ No ☐ Unknown ☐ Not Applicable

b. Exposed Piles: ☐ Yes ☐ No ☐ Unknown ☐ Not Applicable

c. Contraction Scour (Encroachment)

1) Overbank Flow: ☐ Left ☐ Right

2) Relief Bridge: ☐ Yes ☐ No

3) Roadway Over Topping: ☐ Yes ☐ No ☐ Unknown ☐ Possible

4) Bridge Over Topping: ☐ Yes ☐ No ☐ Unknown ☐ Possible

d. Long Term

1) Aggradation: ☐ Yes ☐ No ☐ Unknown

2) Degradation: ☐ Yes ☐ No ☐ Unknown

e. Bed Material

☐ Sand

☐ Gravel

☐ Cobbles

☐ Other

9. GEOMORPHOLOGY

a. Alluvial Fan: ☐ Yes ☐ No

b. Dam or Reservoir: ☐ Yes ☐ No

c. River Form: ☐ Straight ☐ Meandering ☐ Braided ☐ Man Made

d. Instream Mining/Dredging: ☐ Yes ☐ No

e. Headcuts or Nickpoints: ☐ Yes ☐ No

f. Diversions: ☐ Yes ☐ No

g. Channel Modification: ☐ Yes ☐ No

h. Stream Size: ☐ Small (< 100 ft) ☐ Medium (100 - 500 ft) ☐ Large (> 500 ft)

i. Flow Characteristics: ☐ Intermittent ☐ Perennial ☐ Tidal

e

SCOUR EVALUATION - FIELD / OFFICE REVIEW REPORT

10. OTHER CONSIDERATIONS

a. Sediment Transport:

1) ☐ Live Bed Condition ☐ Clear Water Condition ☐ Unknown

2) Armored Bed: ☐ Yes ☐ No ☐ Unknown

b. Watershed: ☐ Agricultural ☐ Forested ☐ Swamp ☐ Urban

c. Tidal Influence: ☐ Yes ☐ No ☐ Possibly

d. Tidal Features: ☐ Bay ☐ Estuary ☐ Inlet ☐ Barrier Island

1) Normal Range (amplitude): ☐ Field Observation ☐ Tide Table

2) Observed Surface Velocity: fps

3) Seiching (wind set up): ☐ Yes ☐ No ☐ Possible

4) Distance to coast miles (along thalweg miles)

5) Traffic: ☐ Ship ☐ Recreation ☐ Commercial ☐ Barge ☐ ICW

e. Tributaries:

☐ Upstream ☐ Downstream ☐ No Factor

Distance to confluence of next stream/waterbody:

f. Observed Stream Velocity: fps

g. Mannings n: Channel Overbank

11. ADDITIONAL COMMENTS

a. Photographs: ☐ Bridge Number ☐ Upstream Channel ☐ Upstream Face ☐ Downstream Channel ☐ Downstream Face

b. Remarks:

Field Inspectors:

Date of Field Review: Time of Field Review:

f

FIGURE 1 (*continued*)

tions, frequent seasonal inspections, or inspections made following storm events or tidal surges).

The basic forms are combined with a single page of text and selected bridge sketches to provide a standardized Phase I report on each bridge. The one-page report summary includes a summary of findings (and recommendations), the basis for the evaluation (discussion), and a listing of the materials and documentation used to develop the report. A bridge location map and plan, profile, and boring logs are also included when they are available. The bridge profile (elevation) includes an as-built streambed cross section (profile) at the bridge and, when they are available, successive cross sections taken by bridge inspectors during the standard biennial bridge inspection under the FHWA NBIS. These successive cross sections are compared with point soundings taken by lead line, pole, or sonic sounder during the Phase I field site visit and constitute a critical component of the Phase I qualitative evaluation. Both long-term aggradation or degradation trends and any recent local scour problems are generally readily apparent from this time-sequenced cross section comparison.

Phase II: Hydrologic and Hydraulic Assessment for Scour

Phase II of the FDOT program is somewhat less structured than Phase I, but it follows the recommended procedures of HEC-20 (*4*) and HEC-18 (*5*). In Florida the selection of the hydraulic analysis approach requires consideration of both riverine and tidal flow conditions. Phase II analysis has three basic components: hydrology, hydraulics, and scour computations. The majority of the effort in Phase II is in quantifying the discharge conditions (hydrology) and modeling the corresponding flow conditions at the bridge (hydraulic analysis). Given the hydraulic variables, the scour computations are relatively simple and straightforward. If the hydrologic and hydraulic analyses can be simplified without a significant loss in the accuracy of the scour results, a major cost savings will be realized.

In the interests of economy, then, a simplified riverine or tidal analysis generally is considered first. For riverine flow conditions use of a very conservative estimate of discharge and a simple FHWA WSPRO (*6*) water surface profile model obtained by using a limited number of cross sections of the stream usually represents the simplest approach to the problem. If these prove inadequate for the complexities of the bridge reach (e.g., complex cross sections, flow bifurcation, multiple openings, or multiple bridge crossings in the reach), then a more complex (detailed) WSPRO model with more refined discharge estimates must be developed or, perhaps, a two-dimensional hydrodynamic model must be applied.

Similarly, for tidal conditions the simplified procedures presented in HEC-18 (*4*) (e.g., a tidal prism or constricted waterway approach) are considered first. If these simplified techniques prove inadequate, then more complex (detailed) one- or two-dimensional unsteady flow modeling approaches are used. Regardless of the approach used to develop hydraulic parameters for the bridge reach, the equations presented in HEC-18 (*4*) are applied to evaluate potential scour conditions. For scour evaluations very conservative assumptions are made to support the simplified analysis techniques for both riverine and tidal conditions. Thus, if a bridge can be shown to be at low risk for scour by the simplified approaches, more complex techniques should not be required. However, if a bridge is rated marginally susceptible for scour by simplified techniques, more complex techniques with less conservative assumptions could refine the evaluation and could possibly result in a lower risk rating. This approach ensures that an appropriate level of effort is applied to support a quantitative scour evaluation, resulting in overall program economy. For both riverine and tidal conditions, the results of a simplified analysis provide a point of departure for a more detailed analysis if one is necessary.

To support the simplified or detailed Phase II quantitative analysis, a standard format has been developed. The Phase II Field/Office Review Report is shown in Figure 2. A standard cover sheet (Figure 1) is used to summarize the scour evaluation and update the analysis from the Phase I rating. This is followed by several pages of text with the following sections:

- 1.0 Summary of Findings
- 2.0 Hydrologic Analysis
- 3.0 Hydraulic Analysis
- 4.0 Scour Analysis
- 5.0 Materials and Documentation

Typically, two figures are included in the summary section: a bridge location map and bridge profile (elevation) showing the 100-year and 500-year scour prism or the scour prism from the overtopping flood, if that puts the most stress on the bridge. Several attachments complete the report:

- Attachment A: Phase II Field/Office Review Report (Figure 2).
- Attachment B: hydrologic calculations,
- Attachment C: WSPRO (or other computer model) input and output files,
- Attachment D: scour calculations, and
- Attachment E: original Phase I Scour Evaluation Report.

SCOUR EVALUATION – PHASE 2

FIELD / OFFICE REVIEW REPORT

Bridge #:	County:	Route:	Over:

1. SCOUR VULNERABILITY RATING (PER FHWA)

a Scour Critical

Scour Susceptible	☐ High	☐ Medium	☐ Low
Low Risk	☐ High	☐ Medium	☐ Low
Foundations	☐ Known	☐ Unknown	

b Method of Analysis ☐ Simplified ☐ Detailed

c. Reasons for Rating:

2. PHASE 1 RATING

3. FLORIDA DOT SCOUR INDEX NUMBER Initial _____ Secondary _____

4. RECOMMENDATIONS

a Countermeasures

- ☐ Riprap
- ☐ Scour Monitor
- ☐ Inspection
- ☐ Other

b Phase 3 Analysis ☐ Required ☐ Not Required

c Phase 4 Analysis ☐ Required ☐ Not Required

a

5. SCOUR IMPACT ASSESSMENT FOR DESIGN FLOOD EVENT

a.* Reported Design / Constructed Embedment _____

b.* Current Remaining Embedment _____

c. Estimated Embedment Remaining After Scour _____

* Based on 19__ Pile Driving Records

6. EVALUATION OF METHODS

a. Method of Analysis

☐ Simplified ☐ Detailed

b. Do results of analysis provide reasonable prediction of scour depths for this structure?

☐ Yes ☐ No

c. If 6b is NO, perform Detailed Analysis.

d. If 6b is YES, does the predicted scour suggest instability of structure, based on existing knowledge of the bridge?

☐ Yes (Phase 3 or Phase 4 is recommended) ☐ No (No further action required)

b

FIGURE 2 Phase II Field/Office Review Report forms.

7. FLOOD HISTORY

a Drainage Area _____ sq. mi.

b Scour Mode: ☐ Riverine ☐ Tidal ☐ Both

c Riverine Flow

Q_{100} Discharge From:

☐ Gage Analysis ☐ Regression Analysis ☐ Rational Method ☐ Other _____

$Q_{OVERTOPPING}$ Discharge From (____ Yr):

☐ Gage Analysis ☐ Regression Analysis ☐ Rational Method ☐ Other _____

Q_{500} Discharge From:

☐ Gage Analysis ☐ Regression Analysis ☐ Rational Method ☐ Other _____

Q_{100} = _____ cfs $Q_{OVERTOPPING}$ = _____ cfs Q_{500} = _____ cfs

d Tidal Flow:

Q_{DAILY} Discharge (Tidal Flow) _____ cfs ☐ Tide Table ☐ HEC 18 Procedure

Q_{100} Discharge (Surge) _____ cfs ☐ Historic Data ☐ HEC 18 Procedure

Q_{500} Discharge (Surge) _____ cfs ☐ Historic Data ☐ HEC 18 Procedure

8. CHANNEL STABILITY CONSIDERATIONS

a Natural Channel Aggradation/Degradation Expected Over Remaining Life of Structure ____ ft

b Channel Migration Anticipated During Life of Structure ☐ Left ____ ft ☐ Right ____ ft

c Armoring Potential ☐ Yes ☐ No

d Depth to Armoring for Q ___ of cfs ____ ft

e Discussion:

c

9. DESIGN FLOOD - SCOUR EVENT

a. Worst Case Flood Event (≤ 100 yr): ☐ 100 yr ☐ overtopping	Discharge	_____ CFS
	Frequency	_____ YR
b. Contraction Scour:	Left Over Bank	_____ FT
	Main Channel	_____ FT
	Right Over Bank	_____ FT
c. Maximum Pier Scour Location at:	Scour Depth	_____ FT
	Minimum Remaining Pile Tip / Pier Footing Embedment	_____ FT
☐ Worst Pier ☐ Typical Pier	Maximum Approach Velocity	_____ FPS
Pier No: ____ Bent No: ____	Approach Froude Number	_____
d. Abutment Scour:	Left Abutment	_____ FT
	Right Abutment	_____ FT
e. Maximum Total Scour: (8a + 9b + (9c or 9d))	Left Abutment	_____ FT
	Main Channel Pier	_____ FT
	Flood Plain Pier	_____ FT
	Right Abutment	_____ FT

10. CHECK FLOOD - SCOUR EVENT

a. Worst Case Flood Event (≤ yr): ☐ 500 yr ☐ overtopping	Discharge	_____ CFS
	Frequency	_____ YR
b. Contraction Scour:	Left Over Bank	_____ FT
	Main Channel	_____ FT
	Right Over Bank	_____ FT
c. Maximum Pier Scour Location:	Scour Depth	_____ FT
	Minimum Remaining Pile Tip / Pier Footing Embedment	_____ FT
☐ Worst Pier ☐ Typical Pier	Maximum Approach Velocity	_____ FPS
Pier No: ____ Bent No: ____	Approach Froude Number	_____ FT
d. Abutment Scour:	Left Abutment	_____ FT
	Channel	_____ FT
	Right Abutment	_____ FT
e. Maximum Total Scour: (8a + 10b + (10c or 10d))	Left Abutment	_____ FT
	Main Channel Pier	_____ FT
	Flood Plain Pier	_____ FT
	Right Abutment	_____ FT

d

FIGURE 2 (*continued*)

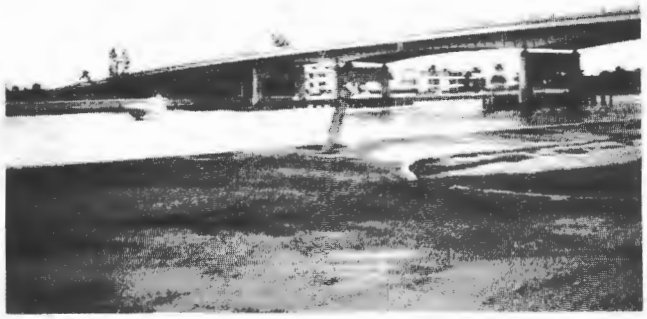

FIGURE 3 Bridge over Baker's Haulover inlet, Biscayne Bay, District 6, FDOT.

FIGURE 5 Bridge over Shad Creek, just above confluence with St. John's River, Jacksonville, District 2, FDOT.

The standardized approach to scour evaluations adopted by FDOT for both Phase I and Phase II evaluations will lend itself to development of a statewide database on bridge scour vulnerability.

Results

The Phase I and Phase II procedures outlined above have been applied to scour evaluations of a wide variety of bridges in Florida. These range from large bridges over aggressive tidal inlets (Figure 3) and bascule bridges over the Intracoastal Waterway (Figure 4) or small tidal waterway bridges (Figure 5) to small riverine bridges in rural northeastern Florida (see Figure 6).

FDOT has 7,948 bridges in the inventory, with 4,395 bridges in the federal aid program and 3,553 not in the federal aid program. As of March 1994 preliminary scour screening resulted in the ratings shown in Table 1. Table 2 provides a more detailed summary of results of Phase I scour evaluations for a small population of bridges in District 2 (Lake City/Jacksonville), District 6 (Miami/Florida Keys), and District 7 (Tampa Bay). Thus, a wide range of tidal, riverine, urban, and rural conditions are represented by the bridges in this sample (Figures 3 to 6). It should be noted that these bridges do not represent a random sample. Most districts in FDOT have chosen to focus on bridges that were considered potentially scour susceptible on the basis of a very preliminary screening by FDOT that primarily used office records (Table 1). As would be expected in

FIGURE 4 Bascule bridge over Intracoastal Waterway, Indian Rocks, District 7, FDOT.

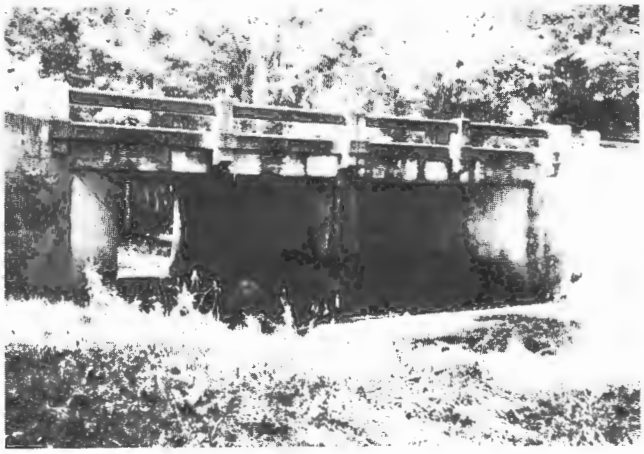

FIGURE 6 U.S. Highway 17 Bridge over Unnamed Tributary to Lofton Creek, Nassau County, District 2, FDOT.

TABLE 1 FDOT Preliminary Bridge Scour Screening

Category	Federal Aid	Non-Federal Aid	Total
Scour-Susceptible	2,377	2,006	4,383
Low Risk	1,539	726	2,265

Florida many of the bridges are tidal or tidally influenced (Table 2). Although no bridges in this small population were scour critical, 61 percent were considered scour susceptible with either a high, a medium, or a low priority, and a Phase II quantitative analysis was recommended for almost all of these bridges. Exceptions were bridges on which remedial actions or replacement planning was under way.

It is significant that 49 percent of the bridges in this group were found to have unknown foundations; that is, after the office and field reviews it was uncertain what the structural foundation condition was or what the pile lengths were for pile-supported foundations. This is not a problem unique to Florida. As of February 1995, of the 481,708 bridges over water in the NBIS, 22 percent had unknown foundations. Consequently, FHWA has removed the requirement for in-depth scour evaluations to be completed by January 1997 for structures except Interstate bridges with unknown foundations (unknown pile tips). The bridges to which this exemption applies are to be monitored until such time as technology becomes available to determine foundation conditions in situ.

Conclusions

To meet the requirements of FHWA Technical Advisory 5140.23 for bridge scour evaluations, FDOT has adopted a four-phase approach. Although a numerical rating scheme could be developed, Phase I of the FDOT procedure is intended to be a qualitative evaluation based heavily on experience and engineering judgment. The approach is consistent with FHWA procedures presented in HEC-18 (*4*) and HEC-20 (*5*) and provides meaningful results on which to base decisions for monitoring, the use of countermeasures, or replacement for scour-susceptible bridges. Since all FDOT bridges will be evaluated by the procedures highlighted here, a consistent database on bridge scour vulnerability will be developed for all bridges in Florida.

The Phase I forms ensure that numerous qualitative geomorphic factors, related primarily to stream instability concerns, are considered in the evaluation. The Phase I evaluations, including office and field review for each bridge, were estimated to require a level of effort of about 40 hr for an average bridge, and the results of the first group of Phase I evaluations support this estimate.

The approach to Phase II evaluations adopted by FDOT, which considers, first, a simplified tidal or riverine scour analysis before proceeding to more detailed or complex computational techniques, should result in significant cost savings for the statewide scour evaluation program. As of this writing, simplified techniques have been satisfactory for most of the bridges requiring a Phase II scour analysis.

References

1. Lagasse, P. F., E. V. Richardson, and N. Jetha. Implementation of the NBIS Scour Evaluation Program, District 2, Florida. *Proc., 1993 Hydraulic Engineering Specialty Conference*, ASCE, New York, N.Y., 1993.
2. *Evaluating Scour at Bridges*. Technical Advisory 5140.23. FHWA, U.S. Department of Transportation, 1991.

TABLE 2 Phase I Scour Evaluation Results for 330 Bridges in Florida

	Riverine	Tidal	Riverine/ Tidal	Total	Scour Critical	Scour Susceptible	Low Risk	Known Foundation	Unknown Foundation	Phase II Recommended
District 2 (Lake City/ Jacksonville)	76	34	14	124	0	70	54	72	52	70
District 6 (Miami/ Florida Keys	0	27	4	31	0	28	3	4	27	28
District 7 (Tampa Bay)	73	71	31	175	0	102	73	92	83	102
Total	149	132	49	330	0	200	130	168	162	200
Percent (%)	45	40	15			61	39	51	49	61

3. *Guidelines for Scour Evaluation Studies*. Tallahassee, Florida Department of Transportation, 1991.
4. Richardson, E. V., L. J. Harrison, J. R. Richardson, and S. R. Davis. *Evaluating Scour at Bridges*. FHWA Report No. FHWA-IP-90-017, Hydraulic Engineering Circular 18. Office of Research and Development, McLean, Va., 1993.
5. Lagasse, P. F., J. D. Schall, F. Johnson, E. V. Richardson, J. R. Richardson, and F. Chang. *Stream Stability at Highway Structures*. FHWA Report FHWA-IP-90-014, Hydraulic Engineering Circular 20. Office of Research and Development, McLean, Va., 1991.
6. Shearman, J. O. *Bridge Waterways Analysis Model for Mainframe and Microcomputers*. WSPRO/HY-7. FHWA, U.S. Department of Transportation, 1987.

Bridge Scour in the Coastal Regions

J. R. Richardson, *University of Missouri at Kansas City*
E. V. Richardson, *Owen Ayres & Associates, Inc.*
B. L. Edge, *Texas A&M University*

Bridge scour and waterway instability in the coastal region where waterways are subjected to tidal flow can be subjected to mass density stratification, water salinity, sedimentation (littoral drift or riverine transport), and unsteady reversible flows from astronomical tides and storm surges, as well as riverine flows. Nevertheless, bridge foundation scour depths can be determined and waterway instability can be countered by using existing scour equations and geomorphology techniques. A major difference for nontidal (riverine) streams is that the design discharge (50-, 100-, or 500-year return period flows) has a constant value, whereas with tidal waterways the design discharge for the same return periods may increase because it is dependent on the design storm surge elevation, the volume of water in the tidal prism upstream of the bridge, and the area of the waterway under the bridge at mean tide. If there is erosion of the waterway from the constant daily flow from the astronomical tides that increase the area of the waterway, the discharges can increase. An existing clear-water scour equation can be used to predict the magnitude of this scour, but not its time history. Recent experience indicates that this long-term degradation can be as large as 0.2 to 0.9 m/year.

Scour (erosion) of the foundations of bridges over tidal waterways in the coastal region that are subjected to the effects of astronomical tides and storm surges is a combination of long-term degradation, contraction scour, local scour, and waterway instability. These are the same scour mechanisms that affect nontidal (riverine) streams. Although many of the flow conditions are different in tidal waterways, the equations used to determine riverine scour are applicable if the hydraulic forces are carefully evaluated.

Bridge scour in the coastal region results from the unsteady diurnal and semidiurnal flows resulting from astronomical tides, large flows that can result from storm surges (hurricanes, northeasters, and tsunamis), and the combination of riverine and tidal flows. Also, the small size of the bed material (normally fine sand) as well as silts and clays with cohesion and littoral drift (transport of beach sand along the coast resulting from wave action) affect the magnitude of bridge scour. Mass density stratification and water salinity have a minor effect on bridge scour. The hydraulic variables (discharge, velocity, and depths) and bridge scour in the coastal region can be determined with as much precision as riverine flows. These determinations are conservative, and research is needed for both cases to improve scour determinations. Determining the magnitude of the combined flows can be accomplished by simply adding riverine flood flow to the maximum tidal flow, if the drainage basin is small, or routing the design riverine flows to the crossing and adding them to the storm surge flows.

Although tidal flows are unsteady, peak flows from storm surges have durations long enough that the time is sufficient for fine sand in most coastal zones to reach scour depths determined from existing scour equations.

Astronomical tides, with their daily or twice-daily inflows and outflows, can and do cause long-term degradation if there is no source of sediment except at the crossing. This has resulted in long-term degradation of 0.2 to 0.9 m (0.8 to 3.0 ft) per year with no indication of stopping (*1,2*). The Indian River inlet in Delaware went from a depth of 3.7 m (12 ft) in 1938 to 15.8 m (52 ft) in 1986 (*1*).

Mass density stratification (saltwater wedges), which can result when the denser, more saline ocean water enters an estuary or tidal inlet with significant freshwater inflow, can result in larger velocities near the bottom than the average velocity in the vertical. With careful evaluation the correct velocity can be determined for use in the scour equations. With storm surges, mass density stratification will not normally occur. The density difference between saltwater and freshwater, except as it causes saltwater wedges, is not significant enough to affect scour equations. Density and viscosity differences between freshwater and sediment-laden water can be much larger in riverine flows than their differences between saltwater and freshwater. Salinity can affect the transport of silts and clays by causing them to flocculate and possibly deposit, which may affect stream stability and which must be evaluated. Salinity may affect the erodibility of cohesive sediments, but this will affect only the rate of scour, not the ultimate scour. Littoral drift is a source of sediment to a tidal waterway (*3*), and its availability can decrease contraction and possible local scour and may result in a stable or aggrading waterway. The lack of sediment from littoral drift can increase long-term degradation, contraction scour, and local scour. Evaluating the effect of littoral drift is a sediment transport problem involving historical information, future plans (dredging, jetties, etc.) for the waterway or the coast, sources of sediment, and other factors.

One major difference exists between riverine scour at highway structures and scour resulting from tidal forces. In determining scour depths of riverine conditions, a design discharge is used (discharge associated with a 50-, 100-, and 500-year return period). For tidal conditions a design storm surge elevation is used, and from that the discharge is determined. That is, for the riverine case the discharge is fixed, whereas for the tidal case the discharge may not be. In the riverine case, as the area of the stream increases the velocity and shear stress on the bed decrease because of the fixed discharge. In the tidal case, as the area of the waterway increases the discharge may also increase and the velocity and shear stress on the bed may not decrease appreciably. Thus, long-term degradation and contraction scour can continue until sediment inflow equals sediment outflow or the discharge driving force (difference in elevation across a highway crossing an inlet, estuary, or channel between islands or islands and the mainland) reduces to a value that the discharge no longer increases (*4,5*). Hydraulic Engineering Circular 18 (HEC-18) (*4*) and Richardson et al. (*5*) present a method for determining the potential long-term degradation, but not its time history, when the sediment supply is cut off or decreased at an inlet.

An overview of tidal hydraulics, a three-level method of scour analysis for tidal waterways, and scour equations for determining scour depths as given by FHWA is presented in the following section (*4*). Level 1 is a qualitative evaluation of the stability of a tidal waterway, estimating the magnitude of the tides, storm surges, littoral drift, and flow in the tidal waterway and attempting to determine whether the hydraulic analysis depends on tidal or river conditions, or both. Level 2 represents the engineering analysis necessary to obtain the velocity, depths, and discharge for tidal waterways to be used in determining long-term aggradation or degradation, contraction scour, and local scour by using existing scour equations. Level 3 analysis is for complex tidal situations that require physical or one- or two-dimensional computer models.

Overview of Tidal Processes

Glossary

Bay: a body of water connected to the ocean with an inlet.
Estuary: tidal reach at the mouth of a river.
Flood or flood tide: flow of water from the ocean into the bay or estuary.
Ebb or ebb tide: flow of water from the bay or estuary to the ocean.
Littoral drift: transport of beach material along a shoreline by wave action.
Run-up: height to which water rises above still-water level when waves meet a beach or wall.
Storm surge (hurricane surge, storm tide): tidelike phenomenon resulting from wind and barometric pressure changes.
Tidal amplitude: generally, half of tidal range.
Tidal cycle: one complete rise and fall of the tide.
Tidal inlet: a channel connecting a bay or estuary to the ocean.
Tidal passage: a tidal channel connected with the ocean at both ends.
Tidal period: duration of one complete tidal cycle.
Tidal prism: volume of water contained in a tidal bay, inlet, or estuary between low and high tide levels.
Tidal range: vertical distance between specified low and high tide levels.

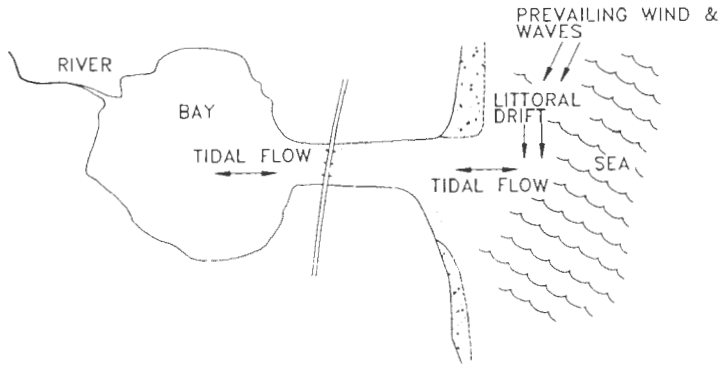

1. Inlets between the open sea and an enclosed lagoon or bay, where most of the discharge results from tidal flows. Tidal inlet fed by littoral drift.

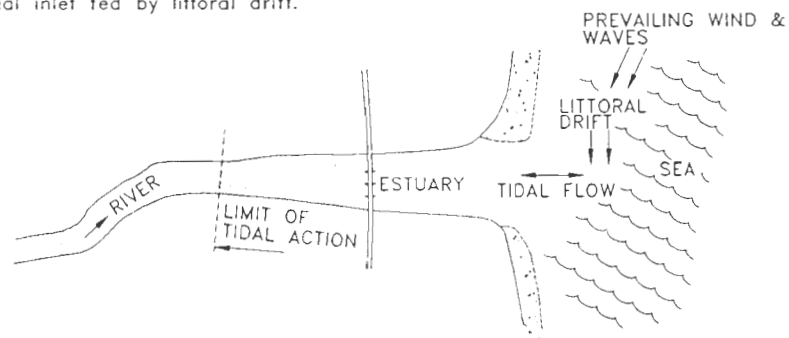

2. River estuaries where the net discharge comprises river flow as well as tidal flow components.

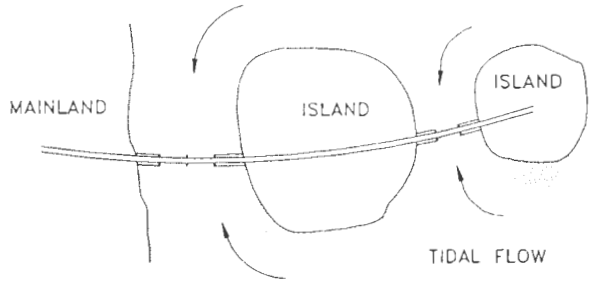

3. Passages between islands, or between an island and the mainland, where a route to the open sea exists in both directions.

FIGURE 1 Types of tidal waterway crossings (6).

Tidal waterways: a generic term that includes tidal inlets, estuaries, bridge crossings to islands or between islands, crossings between bays, tidally affected streams, and so forth.

Tides, astronomical: rhythmic diurnal or semidiurnal variations in sea level that result from gravitational attraction of the moon and sun and other astronomical bodies acting on the rotating earth.

Tsunami: long-period ocean wave resulting from earthquake, other seismic disturbances, or submarine landslides.

Waterway opening: width or area of bridge opening at a specific elevation, measured normal to principal direction of flow.

Wave period: time interval between arrivals of successive wave crests at a point.

Definition of Tidal and Coastal Processes

Typical bridge crossings of tidal waterways are diagrammed in Figure 1 (6). Tidal flows are defined as being between the ocean and a bay (or lagoon), from the ocean into an estuary, or through passages between islands or islands and the mainland. Idealized astronomical tidal conditions and tidal terms are illustrated in Figure 2 (6).

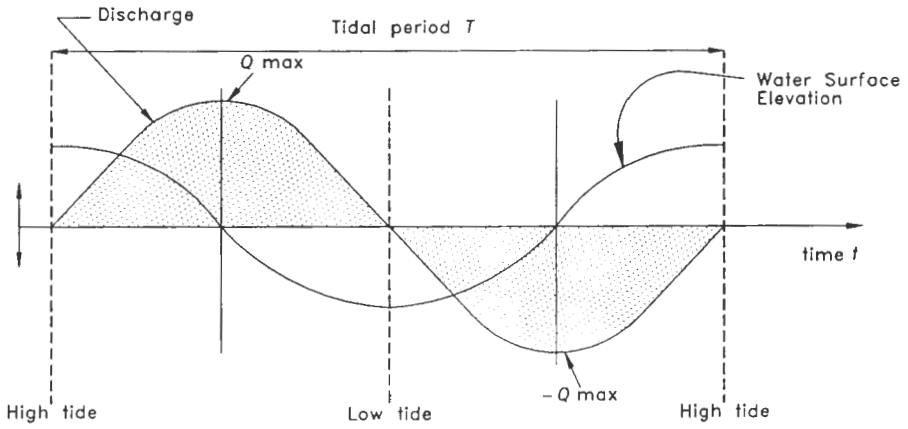

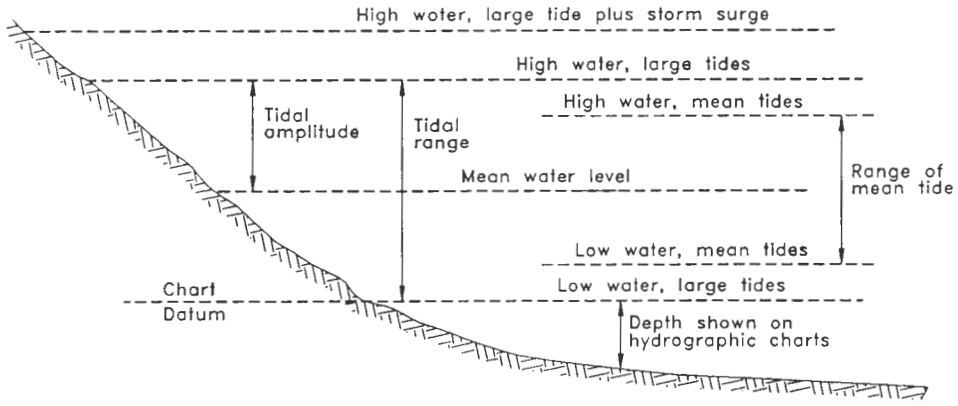

FIGURE 2 Principal tidal terms (6).

The forces that drive tidal fluctuations are primarily the result of the gravitational attraction of the sun and moon on the rotating earth (astronomical tides), wind and storm setup or seiching (storm surges), and geologic disturbances (tsunamis). As illustrated in Figure 2 the maximum discharge (Q_{max}) at the flood or ebb tide occurs often (but not always) at the crossing from high to low or low to high tide. The continuous rise and fall of astronomical tides will usually influence long-term trends of aggradation and degradation. Conversely, when storm surges or tsunamis occur, the short-term contraction and local scour can be significant. These storm surges and tsunamis are infrequent events with much longer tidal periods, elevations, and discharges than astronomical tides. Storm surges and tsunamis are a single-event phenomenon that, because of their magnitudes, can cause significant scour at a bridge crossing.

Although the hydraulics of flow for tidal waterways is complicated by the presence of two-directional flow, the basic concept of sediment continuity is valid. Consequently, a clear understanding of the principle of sediment continuity is essential for evaluating scour at bridges spanning waterways influenced by tidal fluctuations. The sediment continuity concept states that the sediment inflow minus the sediment outflow equals the time rate of change of sediment volume in a given reach.

In addition to sediments from upland areas, littoral drift (Figure 3) is a source of sediment supply to the inlet, bay or estuary, or tidal passage. During the flood tide these sediments can be transported and deposited into the bay or estuary. During the ebb tide these sediments can be remobilized and transported out of the inlet or estuary and can be either deposited on shoals or moved farther down the coast as littoral drift.

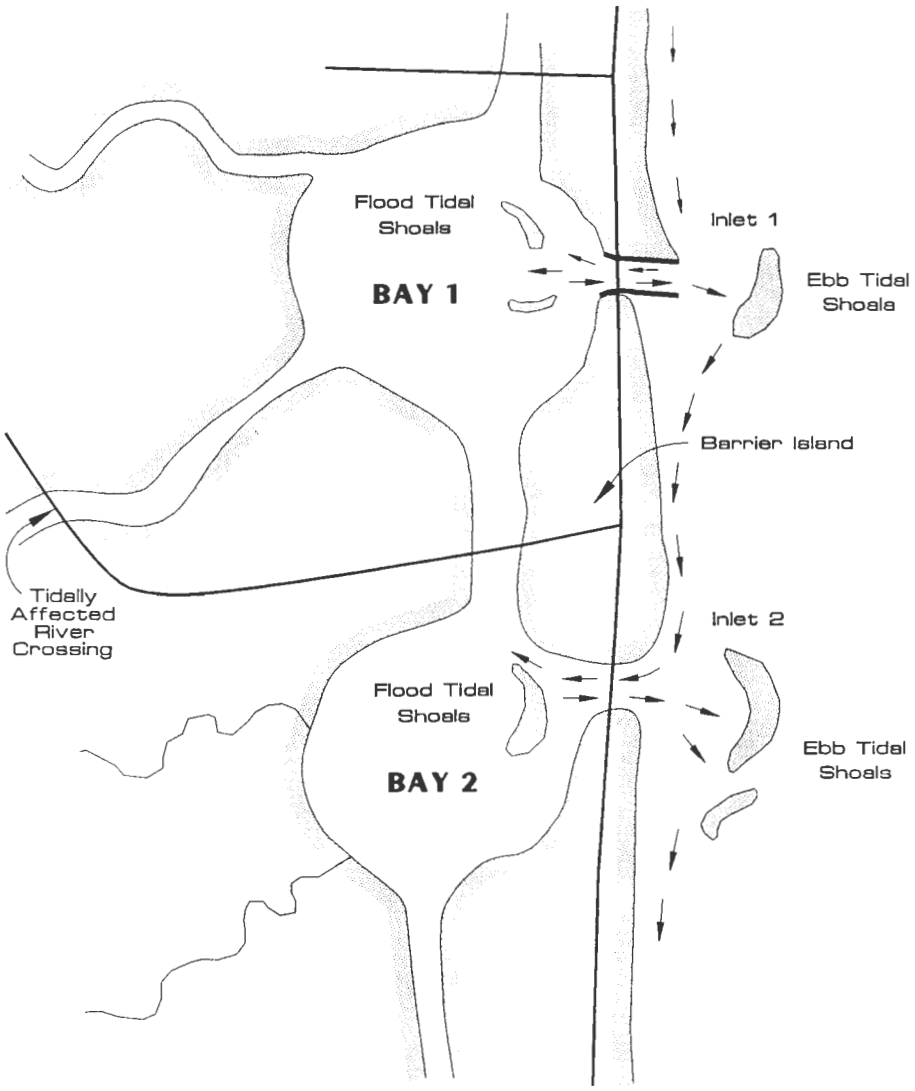

FIGURE 3 Sediment transport in tidal inlets (3).

Sediment transported to the bay or estuary from the upland river system can also be deposited in the bay or estuary during the flood tide and can be remobilized and transported through the inlet or estuary during the ebb tide. However, if the bay or estuary is large, sediments derived from the upland river system can deposit in the bay or estuary in areas where the velocities are low and may not contribute to the supply of sediment to the bridge crossing. The result is clear-water scour unless sediment transported on the flood tide (ocean shoals, littoral drift) is available on the ebb. Sediments transported from upland rivers into an estuary may be stored there on the floor and transported out during ebb tide. This would produce live-bed scour conditions unless the sediment source in the estuary was disrupted. Dredging, jetties, or other coastal engineering activities can limit sediment supply to the reach and influence live-bed and clear-water scour conditions.

A net loss of sediment discharge into the tidal waterway could be the result of cutting off littoral drift by means of a jetty projecting into the ocean (Figure 3) or dredging. Because the availability of sediment for transport into the bay or estuary is reduced, highway crossing degradation could result. As discussed earlier, as the cross-sectional area of the crossing increases, the flow velocities during the ebb and flood tides may not decrease, resulting in further degradation of the inlet.

Level 1 Analysis

Level 1 analysis is the qualitative determination of the (a) classification of the tidal crossing, (b) tidal charac-

teristics, (c) lateral, vertical, and overall stabilities of the waterway and bridge foundations, and (d) characteristics of the riverine and tidal flows. Design plans; boring logs; inspection and maintenance reports; fluvial geomorphology; historical flood, scour, and tidal information; 100- and 500-year return period storm surge elevations; riverine flows; and so forth are collected and analyzed. Field reconnaissance, office review, and contact with relevant agencies such as the Federal Emergency Management Agency (FEMA), National Oceanic and Atmospheric Administration (NOAA), U.S. Geological Survey, U.S. Coast Guard, U.S. Corps of Engineers (USCOE), state agencies, and so forth are used.

The crossing is classified as an inlet, bay, estuary, or passage between islands or islands and the mainland (Figure 1). The crossing may be tidally affected or tidally controlled. Tidally affected crossings do not have flow reversal, but the tides act as a downstream control. Tidally controlled crossings have flow reversal. The limiting case for a tidally affected crossing is when the magnitude of the tide is large enough to reduce the discharge through the bridge to zero.

The objectives of a Level 1 analysis are to determine the magnitudes of the tidal effects on the crossing, the overall long-term vertical and lateral stabilities of the waterway and bridge crossing, and the potential for the waterway and the crossing to change.

Level 2 Analysis

Level 2 analysis is the basic engineering assessment of scour and stream stability at an existing bridge for the design of a new or replacement bridge or the design of countermeasures for waterway instability or bridge scour. The general procedure is to determine (a) design flows (100- and 500-year storm tides and riverine floods) and (b) hydraulic characteristics (discharge, velocity, and depths) and scour components (depths of degradation, contraction scour, pier scour, and abutment scour) and (c) to evaluate the results.

Design Flows and Hydraulic Variables

The riverine 100- and 500-year return period storm discharge is determined by standard hydrology frequency analysis procedures. The magnitude of the 100- and 500-year return period discharge for a tidal surge depends on the elevation of the surge at the crossing, the volume of water in the tidal prism above the crossing, the area of the bridge waterway at the water surface elevation between high and low tides (ebb) or low and high tides (flood), and the tidal period (time between successive high or low tides).

The elevation of the 100- and 500-year storm surge, tidal period, and surge hydrographs for storm surges can be obtained from FEMA, NOAA, and USCOE. From this information the volume of the tidal prism above the crossing, the area of the waterway at the bridge and the elevation of the crossing between high and low tides, the design storm surge discharges, and hydraulic variables for use in the scour equations can be determined for an unconstricted waterway by a method given by Neill (*6*) and for a constricted waterway by a method given by Chang et al. (*7*).

Design Flows and Hydraulic Variables for Unconstricted Waterways

FHWA's HEC-18 (*4*) presents an example problem by Neill's method (*6*). The steps are as follows:

Step 1. Determine and plot the net waterway area at the crossing as a function of elevation. Net area is the gross waterway area between abutments minus the area of the piers.

Step 2. Determine and plot tidal prism volumes as a function of elevation. The tidal prism is the volume of water between low- and high-tide levels or between the high-tide elevation and the bottom of the tidal waterway.

Step 3. Determine the elevation-versus-time relation for the 100- and 500-year storm tides. The relation can be approximated by a sine curve, which starts at the mean water level, or a cosine curve, which starts at the maximum tide level. The cosine equation is

$$y = A \cos \theta + Z \tag{1}$$

where

y = amplitude or elevation of the tide above mean water level (m) at time t;
A = maximum amplitude of the tide or storm surge (m), defined as half the tidal range or half the height of the storm surge; and
θ = angle subdividing the tidal cycle (degrees); one tidal cycle is equal to 360 degrees.

$$\theta = 360 \left(\frac{t}{T}\right)$$

where

t = time from beginning of total cycle (min),
T = total time for one complete tidal cycle (min), and
Z = vertical offset to datum (m).

To determine the elevation-versus-time relation for the 100- and 500-year storm tides, the tidal range and period must be known. FEMA, USCOE, NOAA, and other federal or state agencies compile records that can be used to estimate the 100- and 500-year storm surge elevation, mean sea level elevation, low-tide elevation, and time period.

Tides, and in particular storm tides, may have periods different from those of astronomical semidiurnal and diurnal tides, which have periods of approximately 12.5 and 25 hr, respectively. This is because storm tides are influenced by factors other than the gravitational forces of the sun, moon, and other celestial bodies. Factors such as the wind, the path of the hurricane or storm creating the storm tide, freshwater inflow, and shape of the bay or estuary influence the storm tide amplitude and period.

Step 4. Determine the discharge, velocities, and depth. The maximum discharge, in an ideal tidal estuary, may be approximated by the following equation (6):

$$Q_{max} = \frac{3.14\ VOL}{T} \tag{2}$$

where

Q_{max} = maximum discharge in the tidal cycle (m^3/sec),
VOL = volume of water in the tidal prism between high- and low-tide levels (m^3), and
T = tidal period between successive high or low tides (sec).

In the idealized case Q_{max} occurs in the estuary or bay at the mean water elevation and at a time midway between high and low tides, when the slope of the tidal energy gradient is steepest (Figure 2). In many cases in the field Q_{max} occurs 1 or 2 hr before or after the crossing, but any error caused by this is diminutive. The corresponding maximum average velocity in the waterway is

$$V_{max} = \frac{Q_{max}}{A'} \tag{3}$$

where V_{max} is the maximum average velocity in the cross section at Q_{max} (m/sec) and A' is the cross-sectional area of the waterway at mean tide elevation, halfway between high and low tides (m^2).

The average velocity must be adjusted to determine the velocities at individual piers to account for the nonuniformity of velocity in the cross section. As for inland rivers local velocities can range from 0.9 to approximately 1.7 times the average velocity, depending on whether the location in the cross section is near the bank or near the flow thalweg. The calculated velocities should be compared with any measured velocities for the bridge site or adjacent tidal waterways to evaluate the reasonableness of the results.

The discharge at any time t in the tidal cycle (Q_t) is given by

$$Q_t = Q_{max} \sin\left(360\ \frac{t}{T}\right) \tag{4}$$

Step 5. Include any riverine flows. This may range from simply neglecting the riverine flow into a bay (which is so large that the riverine flow is insignificant in comparison with the tidal flows) to routing the riverine flow through the crossing.

Step 6. Evaluate the discharge, velocities, and depths that were determined in Steps 4 and 5.

Step 7. Determine scour depths for the bridge by using the values of the discharge, velocity, and depths determined from the earlier analysis.

Design Flows and Hydraulic Variables for Constricted Waterways

To determine the hydraulic variables at a constricted waterway (constricted either by the bridge or the channel) the tidal flow may be treated as orifice flow and the following equation taken from van de Kreeke (*8*) and Bruun (*9*) can be used:

$$V_{max} = C_d(2g\ \Delta H)^{1/2} \tag{5}$$

$$Q_{max} = A'\ V \tag{6}$$

where

V_{max} = maximum velocity in the inlet (m/sec),
Q_{max} = maximum discharge in the inlet (m^3/sec),
C_d = coefficient of discharge ($C_d < 1.0$),
g = acceleration due to gravity (9.81 m/sec^2),
ΔH = difference in water surface elevation between the upstream and downstream sides of a crossing or channel for the 100- and 500-year return period storm surge as well as for the normal astronomical average tides; the latter is used to determine the average normal discharge on a daily basis to determine potential long-term degradation at the crossing of a tidal waterway if it becomes unstable (*4*) (m), and
A' = net cross-sectional area at the crossing, at the mean water surface elevation (m^2).

The coefficient of discharge (C_d) is

$$C_d = (1/R)^{1/2} \tag{7}$$

where

$$R = K_u + K_d + \frac{2g\,n^2\,L_c}{h_c^{4/3}} \tag{8}$$

and

R = coefficient of resistance,
K_d = velocity head loss coefficient on downstream side of the waterway,
K_u = velocity head loss coefficient on upstream side of the waterway,
n = Manning's roughness coefficient,
L_c = length of the waterway or bridge opening (m), and
h_c = average depth of flow at the bridge at mean water elevation (m).

If ΔH is not known, the following method developed by Chang et al. (*7*), which combines the orifice equation with the continuity equation, can be used. The total flow approaching the bridge crossing at any time (t) is the sum of the riverine flow (Q) and tidal flow. The tidal flow is calculated by multiplying the surface area of the upstream tidal basin (A_s) by the drop in elevation (H_s) over the specified time ($Q_{tide} = A_s\,dH_s/dt$). This total flow approaching the bridge is set equal to the flow calculated from the orifice equation.

$$Q + A_s\frac{dH_s}{dt} = C_d A_c\sqrt{2g\,\Delta\bar{H}} \tag{9}$$

where A_c is the bridge waterway cross-sectional area (m^2) and the other variables have been defined previously.

Equation 9 may be rearranged into the form of Equation 10 for the time interval $\Delta t = t_2 - t_1$, where subscripts 2 and 1 represent the end and beginning of the time interval, respectively:

$$\frac{Q_1 + Q_2}{2} + \frac{A_{S1} + A_{S2}}{2}\frac{H_{S1} - H_{S2}}{\Delta t} = C_d\left(\frac{A_{C1} + A_{C2}}{2}\right)\sqrt{2g\left(\frac{H_{S1} + H_{S2}}{2} - \frac{H_{t1} + H_{t2}}{2}\right)} \tag{10}$$

For a given initial condition, t_1, all terms with the subscript 1 are known. For $t = t_2$ the downstream tidal elevation (H_{t2}), riverine discharge (Q_2), and waterway cross-sectional area (A_{c2}) are also known or can be calculated from the tidal elevation. Only the water-surface elevation (H_{s2}) and the surface area (A_{s2}) of the upstream tidal basin remain to be determined. Because the surface area of the tidal basin is a function of the water-surface elevation, the elevation of the tidal basin at time t_2 (H_{s2}) is the only unknown term in Equation 10, which can be determined by trial and error to balance the values on the right and left sides.

Chang et al. (*7*) suggest the following steps for computing the flow:

Step 1. Determine the period and amplitude of the design tide(s) to establish the time rate of change of the water surface on the downstream side of the bridge.

Step 2. Determine the surface area of the tidal basin upstream of the bridge as a function of elevation by planimetering successive contour intervals and plotting the surface area versus the elevation.

Step 3. Plot bridge waterway area versus elevation.

Step 4. Determine the quantity of riverine flow that is expected to occur during passage of the storm tide through the bridge.

Step 5. Route the flows through the contracted waterway by using Equation 10 and determine the maximum velocity of flow. Chang et al. (*7*) and Richardson et al. (*4*) give an example problem using a spreadsheet and have developed a computer program to aid in using this method.

Level 3 Analysis

Level 3 analysis involves the use of physical models or computer programs for complex situations in which a Level 2 analysis appears to be inadequate. Many computer programs are available. A study of computer models (*10*) for analyzing the hydraulic conditions of tidal streams at highway structures recommended the one-dimensional unsteady flow model entitled UNET (*11*) and two two-dimensional models entitled FESWMS-2D (*12*) and the TABS/FastTABS system with RMA-2V (*13*).

Scour Calculations

By using the information and hydraulic variables developed in the Level 2 or 3 analysis, long-term degradation, contraction scour, and local scour at piers and abutments are determined. The methods and equations given in HEC-18 (*4*) are summarized in the following sections.

Long-Term Aggradation or Degradation

From a study of site conditions, fluvial geomorphology, historical data of changes in waterway bed elevation,

and potential future changes in the tidal waterway or coastal conditions, determine if the waterway is aggrading or degrading. If the waterway from that study is degrading an estimate of the amount of degradation that will occur in the future is made and is added to the other scour components. Historical data sources could be maps, soundings, tide gauge records, and bridge inspection reports for the site and in the area. Determine if there are plans to construct jetties or breakwaters, dredge the channel, construct piers, and so forth that could affect waterway stability. Also, determine changes in the riverine environment, such as dams, which would change flow conditions.

Long-term degradation can occur if there is little or no sediment supply to an inlet or estuary or if it is decreased (*1,2*). HEC-18 (*4*) presents an example problem that estimates potential long-term degradation.

Contraction Scour

Contraction scour can occur at a tidal inlet, estuary, or passage between islands or islands and the mainland. It may be live-bed or clear-water scour. It would be considered live-bed scour if there is a substantial quantity of bed material moving in contact with the bed. Contraction scour can occur if the tidal waterway constricts the flow or if only the bridge constricts the flow. Also, because the discharge in a contracted tidal waterway depends on the area of the waterway for a given tidal or storm surge amplitude, the discharge will need to be recalculated after the area has increased from contraction scour.

Live-Bed or Clear-Water Scour

To determine if the flow in the tidal waterway is transporting bed material, compare the critical velocity for beginning of motion (V_c) with the mean flow velocity (V) in the tidal waterway. If the critical velocity of the bed material is larger than the mean velocity ($V_c > V$), then clear-water contraction scour will exist. If the critical velocity is less than the mean velocity ($V_c < V$), then live-bed scour may exist. To calculate the critical velocity Equation 17 can be rearranged into the following:

$$V_c = \frac{K_s^{1/2}(S_s - 1)^{1/2} D^{1/2} y^{1/6}}{n} \tag{11}$$

By using S_s equal to 2.65 and n equal to $0.041\ D^{1/6}$, Equation 11 for critical velocity (V_c) for fine bed material ($D_{50} < 2$ mm, $K_s = 0.047$) becomes

$$V_c = 6.79\ y^{1/6} D^{1/3} \tag{12}$$

for medium coarse-bed material (2 mm $< D_{50} <$ 40 mm, $K_s = 0.03$) Equation 11 becomes

$$V_c = 5.43\ y^{1/6} D^{1/3} \tag{13}$$

and for coarse-bed material ($D_{50} > 40$ mm, $K_s = 0.02$) Equation 11 becomes

$$V_c = 4.43\ y^{1/6} D^{1/3} \tag{14}$$

where

V_c = critical velocity above which bed material of size D and smaller will be transported (m/sec),
K_s = shields parameter,
S_s = specific gravity of the bed material,
y = depth of flow (m),
D = partial size for V_c (m), and
n = Manning's n roughness coefficient.

Live-Bed Scour

To calculate live-bed contraction scour a modified Laursen's equation (*14*) is recommended in HEC-18 (*4*):

$$\frac{y_2}{y_1} = \left(\frac{Q_2}{Q_1}\right)^{6/7} \left(\frac{W_1}{W_2}\right)^{K_1} \tag{15}$$

$$y_s = y_2 - y_1 = \text{(average scour depth)} \tag{16}$$

where

y_1 = average depth in the upstream main channel (m),
y_2 = average depth in the contracted section (m),
W_1 = bottom width of the upstream main channel (m),
W_2 = bottom width of the main channel in the contracted section (m),
Q_1 = flow in the upstream channel transporting sediment (m^3/sec),
Q_2 = flow in the contracted channel or bridge opening (m^3/sec),
k_1 = exponent determined from below,
$V_* = (\tau_0/\rho)^{1/2} = (g y_1 S_1)^{1/2}$, shear velocity in the upstream section (m/sec),
ω = fall velocity of bed material based on the D_{50} (m/sec),
g = acceleration of gravity (9.81 m/sec^2),
S_1 = slope of energy grade line of main channel (m/m),
τ_0 = shear stress on the bed (N/m^2), and
ρ = density of water (freshwater = 1,000 kg/m^3).

Exponent k_1 is as follows:

TABLE 1 Correction Factor K_1 for Pier Nose Shape

	Shape of Pier Nose	K_1
(a)	Square nose	1.1
(b)	Round nose	1.0
(c)	Circular cylinder	1.0
(d)	Sharp nose	0.9
(e)	Group of cylinders	1.0

TABLE 3 Correction Factor K_4 for Armoring by D_{90} Size (Froude number ≤ 0.8)

	D_{50} (mm)	$D_{90}/D_{50} \geq$	Maximum V_1	K_4
Sand	< 2.0	--	--	1.0
Gravel	2 - 32	--	--	1.0
Gravel	32 - 64	4 - 3	$V_1 \leq 0.7\ V_c$	0.95
Cobbles	64 - 250	3 - 2	$V_1 \leq 0.8\ V_c$	0.90
	250 - 500	2 - 1	$V_1 \leq 0.8\ V_c$	0.85
	> 500	1	$V_1 \leq 0.9\ V_c$	0.80

V_c from equations 11 through 14 using the D_{90} particle size.

V_*/w	k_1	*Mode of Bed Material Transport*
<0.50	0.59	Mostly contact bed material discharge
0.50 to 2.0	0.64	Some suspended bed material discharge
>2.0	0.69	Mostly suspended bed material discharge

If the bed material is moving as suspended sediment discharge or if there are large particles in the bed material, the use of the clear-water scour equation should be investigated. If the bed material is moving mostly in suspension, clear-water scour may occur, which could increase contraction scour. Large particles in the bed material may decrease the contraction scour by armoring the bed.

Clear-Water Scour

To calculate clear-water scour, the following equations based on Laursen's method (*15*) for relief bridge scour were developed:

$$y = \left[\frac{n^2 V^2}{K_s(S_s - 1)D}\right]^3 \tag{17}$$

In terms of discharge (Q) the depth (y) is

$$y = \left[\frac{n^2 Q^2}{K_s(S_s - 1)D_m W^2}\right]^{3/7} \tag{18}$$

With Manning's n given by Stricklers in metric form as n equal to $0.040\ D_m^{1/6}$, with S_s equal to 2.65, and the indicated values for Shields coefficient (K_s) for the indicated bed material size range, the equations are as follows:

For fine bed material (D_{50} < 2 mm, K_s = 0.047):

$$y = \left(\frac{0.0206\ Q^2}{D_m^{2/3} W^2}\right)^{3/7} \tag{19}$$

For medium coarse-bed material (2 mm < D_{50} < 40 mm, K_s = 0.03):

$$y = \left(\frac{0.0323\ Q^2}{D_m^{2/3} W^2}\right)^{3/7} \tag{20}$$

For coarse-bed material (D_{50} > 40 mm, K_s = 0.02):

$$y = \left(\frac{0.0485\ Q^2}{D_m^{2/3} W^2}\right)^{3/7} \tag{21}$$

TABLE 2 Increase in Equilibrium Pier Scour Depths (K_3) for Bed Condition

Bed Condition	Dune Height (m)	K_3
Clear-Water Scour	N/A	1.1
Plane bed and Antidune flow	N/A	1.1
Small Dunes	3> H > 0.6	1.1
Medium Dunes	9> H >3	1.1 to 1.2
Large Dunes	H >9	1.3

$$y_s = y - y_o = \text{(average scour depth)} \quad (22)$$

where

y = average depth in the contracted section (m),
n = Manning's roughness coefficient,
Q = discharge through the bridge associated with the width W (m^3/sec),
K_s = Shield's coefficient,
S_s = specific gravity (2.65 for quartz),
D_m = effective mean diameter of the smallest non-transportable particle in the bed material (1.25 D_{50}) in the contracted section (m),
D_{50} = median diameter of bed material (m),
W = bottom width of the contracted section less pier widths (m),
y_s = depth of scour in the contracted section (m), and
y_o = original depth in the contracted section before scour (m).

For stratified bed material the depth of scour can be determined by using the appropriate clear-water scour equation sequentially with successive D_m values of the bed material layers.

Local Scour at Piers

HEC-18 (*4*) on the basis of a study by Jones (*16*), recommends the following equation for computing local live-bed and clear-water scour at piers in tidal waterways:

$$\frac{y_s}{a} = 2.0\, K_1 K_2 K_3 K_4 \left(\frac{y_1}{a}\right)^{0.35} Fr_1^{0.43} \quad (23)$$

where

y_s = scour depth (m),
y_1 = flow depth directly upstream of the pier (m),
K_1 = correction factor for pier nose shape (Table 1),
K_2 = correction factor for angle of attack of flow, $(\cos\theta + L/a \sin\theta)^{0.65}$,
K_3 = correction factor for bed condition (Table 2),
K_4 = correction factor for bed material size (Table 3),
a = pier width (m),
L = length of pier (m),
Fr_1 = Froude number = $V_1/(gy_1)^{1/2}$,
V_1 = mean velocity of flow directly upstream of the pier (m/sec), and
θ = angle between velocity vector and pier.

Scour depths are limited to y_s/a equal to 2.4 when the Froude number is less than 0.8 and to y_s/a equal to 3.0 when the Froude number is greater than 0.8.

HEC-18 (*4*) gives methods and recommendations on determining pier scour for exposed footings, exposed pile groups, pile caps in the flow, multiple columns, pressure flow, and debris on a pier.

Abutment Scour

Abutment scour equations are based almost entirely on laboratory data, and experience has indicated that they predict excessive scour depths. This results because the equations use abutment and approach embankment length as a major variable. Richardson and Richardson (*17*) state, "The reason the equations in the literature predict excessively conservative abutment scour depths for the field situation is that, in the laboratory flume, the discharge intercepted by the abutment is directly related to the abutment length; whereas, in the field, this is rarely the case." Thus, "predictive abutment scour equations, based soley on the available laboratory studies are flawed" (*18*). Therefore, foundations can be designed with shallower depths than predicted by the equations when the foundations are protected with rock riprap or a guide bank placed upstream of the abutment (*4*). Design of riprap and guide banks is given in HEC-18 (*4*), and design of guide banks is given in HEC-20 (*19*).

Conclusions

Bridge scour at tidally affected waterways is very complex because of unsteady diurnal and semidiurnal flows resulting from astronomical tides, large flows from storm surges (hurricanes, northeasters, and tsunamis), mass density stratification, water salinity, sand-size bed material as well as silts and clays with cohesion, littoral drift, and the combination of riverine and tidal flows. However, by using the available methods to determine the hydraulic variables of discharge, velocity, and depth resulting from the tides and storm surges, the total scour at bridges can be calculated by using the available scour equations. A major difference between scour at a riverine highway crossing and that at a tidal bridge crossing is that the flow at a riverine crossing has a fixed discharge for a given return period, whereas a tidal bridge crossing may have an increase in the discharge for a given return period because it is based on the storm surge elevation and period, the volume of water in the tidal prism, and the cross-sectional area of the waterway opening. If the area of the waterway opening increases, the design discharge may increase for a given storm surge elevation and period. Thus, there is no (or only a small decrease in) velocity or boundary shear stress in the tidal crossing with an increase in area due

to scour. In such a case an equilibrium condition between the erosional and resisting forces is not reached.

REFERENCES

1. Butler, H. L., and J. Lillycrop. Indian River Inlet: Is There a Solution? *Hydraulic Engineering, Proc., 1993 National Conference*, ASCE, Vol. 2, 1983, pp. 1218–1224.
2. Vincent, M. S., M. A. Ross, and B. E. Ross. Tidal Inlet Bridge Scour Assessment Model. A. In *Transportation Research Record 1420*, TRB, National Research Council, Washington, D.C., 1993, pp. 7–13.
3. Sheppard, D. M. Bridge Scour in Tidal Waters. In *Transportation Research Record 1420*, TRB, National Research Council, Washington, D.C., 1993, pp. 1–6.
4. Richardson, E. V., L. J. Harrison, J. R. Richardson, and S. R. Davis. *Evaluating Scour at Bridges*. Report FHWA-IP-90-017. FHWA, U.S. Department of Transportation, 1993.
5. Richardson, E. V., J. R. Richardson, and B. E. Edge. Scour at Highway Structures in Tidal Waters. *Hydraulic Engineering, Proc., 1993 National Conference*, ASCE, Vol. 2, 1993, pp. 1206–1212.
6. Neill, C. R. (ed.). *Guide to Bridge Hydraulics*. Roads and Transportation Association of Canada. University of Toronto Press, Toronto, Ontario, Canada, 1973.
7. Chang, F., S. R. Davis, and R. Veeramanchaneni. *Tidal Flow Through Contracted Bridge Openings*. Miscellaneous Report. Bridge Section, Maryland Department of Transportation, Baltimore, 1994.
8. van de Kreeke, J. Water-Level Fluctuations and Flow in Tidal Inlets. *Journal of the Hydraulics Division*, ASCE, Vol. 93, HY4, 1967.
9. Bruun, P. Tidal Inlets on Alluvial Shores. *Port Engineering*, 4th ed. Vol. 2, Gulf Publishing, Houston, Tex., 1990, Chap. 9.
10. Ayres Associates. *Development of Hydraulic Computer Models to Analyze Tidal and Coastal Stream Hydraulic Conditions at Highway Structures*. Final Report, Phase I. South Carolina Department of Transportation, Columbia, 1994.
11. Barkau, R. L. *UNET—One Dimensional Unsteady Flow Through a Full Network of Open Channels*. Report CPD-66. Hydrologic Engineering Center, U.S. Army Corps of Engineers, Davis, Calif., 1993.
12. Lee, J. K., and D. C. Froehlich. *Two Dimensional Finite Element Modeling of Bridge Crossings*. Report FHWA-RD-88-149. FHWA, U.S. Department of Transportation, 1989.
13. *FastTABS Hydrodynamic Modeling Product Summary*. Engineering Computer Graphics Laboratory. Brigham Young University, Provo, Utah, 1993.
14. Laursen, E. M. Scour at Bridge Crossings. *Journal of the Hydraulics Division*, ASCE, Vol. 89, HY3, 1960.
15. Laursen, E. M. An Analysis of Relief Bridge Scour. *Journal of the Hydraulics Division*, ASCE, Vol. 92, HY3, 1963.
16. Jones, J. S. Comparison of Prediction Equations for Bridge Pier and Abutment Scour. In *Transportation Research Record 950*, TRB, National Research Council, Washington, D.C., 1983.
17. Richardson, J. R., and E. V. Richardson. Discussion of B. W. Melville, 1992 paper Local Scour at Bridge Abutments. *Journal of the Hydraulics Division*, ASCE, Vol. 119, HY9, 1993, pp. 1069–1071.
18. Richardson, J. R., and E. V. Richardson. The Fallacy of Local Abutment Scour Equations. *Hydraulic Engineering, Proc., 1993 National Conference*, ASCE, Vol. 2, 1993, pp. 749–755.
19. Lagasse, P. F., J. D. Schall, F. Johnson, E. V. Richardson, J. R. Richardson, and F. Chang. *Stream Stability at Highway Structures*. Report FHWA-IP-90-014. FHWA, U.S. Department of Transportation, 1991.

Alternatives to Riprap as a Scour Countermeasure

J. Sterling Jones, *Federal Highway Administration*
David Bertoldi and Stuart Stein, *GKY & Associates, Inc.*

Riprap is the most common and best documented method of protection against local scour at bridge piers. Alternatives to riprap vary in size, shape, and mass as well as flexibility of design. The overall performance of alternatives such as grout mats and grout bags, extended footings, tetrapods, cable-tied blocks, anchors (used in connection with countermeasures) and high-density particles is evaluated. In general, alternatives are used when riprap is hard to obtain, the size required for high-velocity streams is unreasonable, or riprap is difficult to place, among other reasons. Various tests were performed on all previously mentioned countermeasures with and without a pier on a fixed bed. An obstructed movable-bed condition was also tested to obtain qualitative data for each countermeasure. Recommendations for implementing these alternatives are based on laboratory results and include the effects of filter fabric, lateral extent of the countermeasure, sealing between the face of the pier and the countermeasure, and anchoring. The impact of the drag coefficients on the stability of the countermeasure was also examined. The results of these experiments provide some comparative conclusions among the countermeasures as well as criteria for the design and implementation of these devices in the field. Investigations at an FHWA hydraulics laboratory over several years are summarized, including results of the investigations of riprap and of alternatives to riprap. As a local scour countermeasure, each alternative has its unique attributes that, depending on the application, may provide superior protection over riprap.

State highway agencies are conducting a nationwide evaluation of existing bridges for vulnerability to failure due to scour. Of the 483,000 bridges over water, roughly 39 percent either are susceptible to scour or have unknown foundations. Of the scour-susceptible bridges that have been evaluated, about 17 percent have been identified as scour critical. These require monitoring, repair, or scour protection.

FHWA has dedicated much of the research activity in the Turner-Fairbank Highway Research Center hydraulics laboratory in support of the nationwide scour evaluation program. In particular, this laboratory has been a focal point for investigating the feasibility of various techniques for protecting bridge piers from local scour.

Rock riprap is the standard material that historically has been used to protect bridge piers from local scour, but it is not always readily available in sizes required to protect piers, nor is it always a practical option. FHWA initiated a graduate research fellowship study in 1991 that intended to look at various options for protecting bridge piers; these options ranged from rock riprap to the built-in scour arresting capability of footings and pile caps. Fotherby first reported on the use of alternatives to riprap as a local scour countermeasure in her original graduate research project (*1*). However, the investigation continued far beyond what was envisioned for Fotherby's study. This paper summarizes all tests conducted since the study began.

The study tested the following techniques for providing pier protection:

- Grout bags,
- Grout mats,
- Extended footings,
- Tetrapods,
- Cable-tied blocks,
- Anchors (used in conjunction with mats and cable-tied blocks),
- High-density particles, and
- Rock riprap with various apron sizes.

Grout mats and grout bags are fabric shells filled with concrete. The mat is a single continuous layer of fabric with pockets, or cells, filled with concrete; grout bags are individual pieces that, collectively, form a protective layer when placed side by side (Figures 1 and 2). The advantage of the grout mats is that the fabric between the cells acts as a filter, but the small-scale models used in these experiments were poor representations of the grout mats because the fabric, which was essentially the prototype fabric, overwhelmed the concrete cells.

Footings are often placed near the stream bed and appear to provide a measure of scour protection by protecting the sediment from the turbulence generated by the pier. Extended footings were investigated in this study to determine conditions necessary for them to provide significant scour reduction.

Tetrapods have long been used for shore protection because of their effectiveness in dissipating the energy of waves along shorelines. These tetrapods have four arms that are 120 degrees equilateral to each other. These devices have never been applied to fluvial systems or served as protection for bridge pier scour. A model tetrapod is shown in Figure 3.

Cable-tied blocks are composed of precast concrete blocks that are interconnected to form a continuous protection layer (Figure 4). Cable-tied blocks offer an advantage over riprap because the blocks subjected to the highest dynamic forces are stabilized by the surrounding blocks so that they act as a system rather than as individual particles.

Anchors are often recommended for mats and cable-tied block systems as a means of stabilizing the leading edge, at which failure is most likely to occur. Prototype anchors supplied by one of the manufacturers were tested for their resistance to uplift forces when placed in a fully saturated bed material (Figure 5).

High-density particles are individual armoring particles placed around a pier as a scour countermeasure. High-density particles can provide a stable protective layer around a pier without being much larger than the particles in the underlying bed material. Advantages

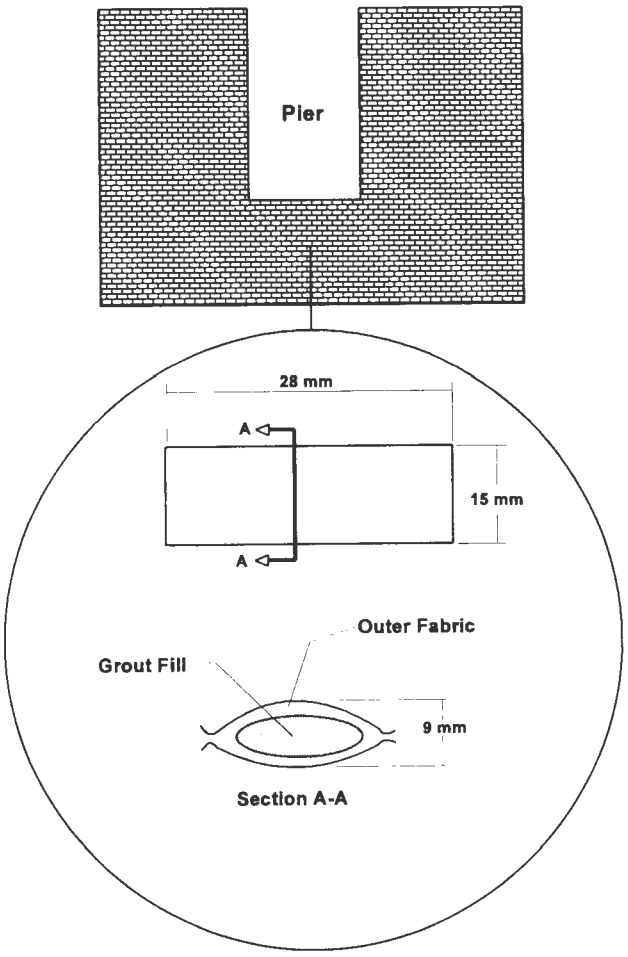

FIGURE 1 Grout mat plan view (*top*) and individual element detail (*bottom*).

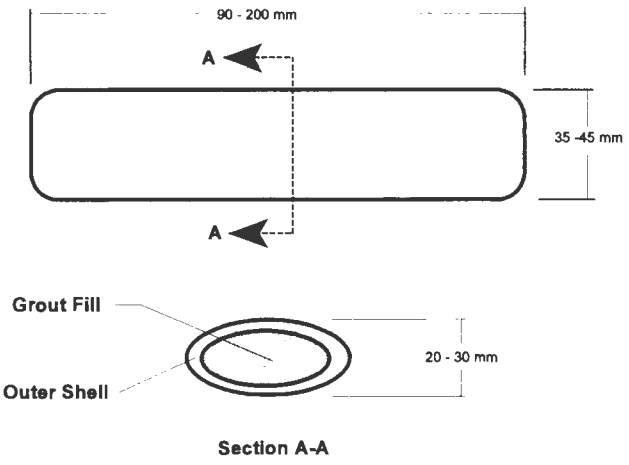

FIGURE 2 Grout bag detail.

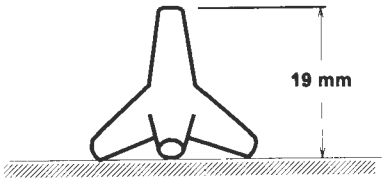

FIGURE 3 Model tetrapod.

over riprap include a reduced need for a filter layer and the possibility that the particles could be manufactured.

Framework for Experiments

Model experiments were conducted in a tilting flume 21.3 m long and 1.8 m wide equipped with a sediment recess (1.32 m long and 0.51 m deep), where the models were installed, located 9.3 m from the upstream end. The fixed bed upstream and downstream of the sediment recess consisted of a fine sand (D_{50} = 0.43 mm) glued to the flume deck (plywood), which helped establish a uniform surface roughness. The setup for the movable-bed experiments is shown in Figure 6. Most experiments were conducted under clear water conditions. Scour countermeasures can be modeled under clear water conditions because they are not the size particles that are normally transported by the stream.

The countermeasures were subjected to four basic tests:

- Scour reduction at incipient motion velocities for the underlying bed material,
- Scour reduction at higher velocities up to three times the incipient motion velocity,
- Failure criteria for the countermeasures when placed in unobstructed flow, and
- Failure criteria for the countermeasure when placed around a bridge pier in obstructed flow.

For the failure criteria, the flume was modified by covering the movable-bed section with a glued sand surface. This setup is shown in Figure 7 (*top*). The high-velocity experimental setup is shown in Figure 7 (*bottom*).

Most tests were allowed to run for 3.5 hr to accommodate two tests per normal work day. A 3.5-hr test duration is sufficient to ascertain the stability of countermeasures and establish a relative percentage scour re-

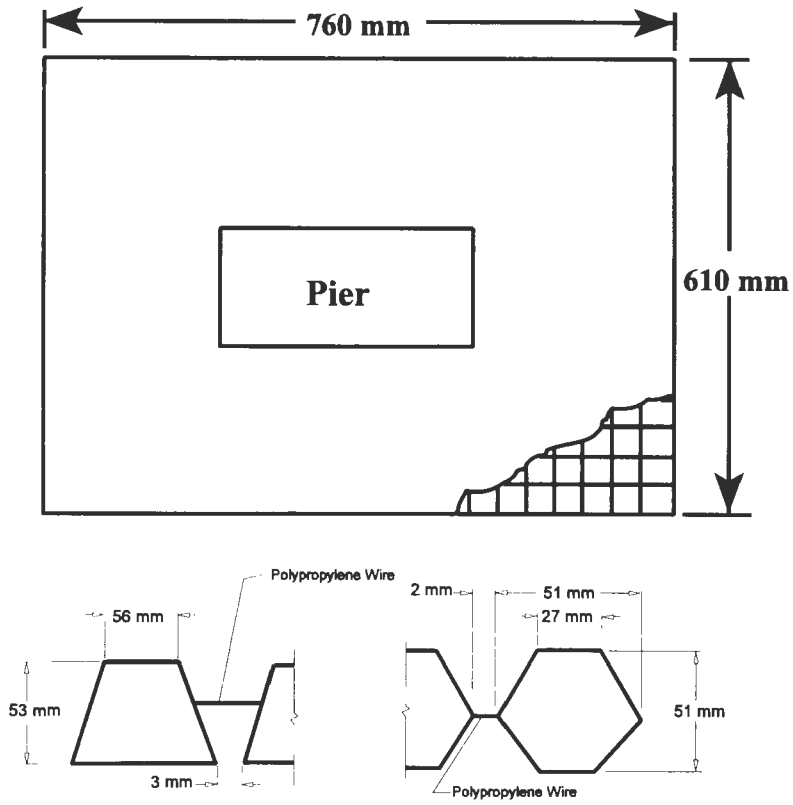

FIGURE 4 Cable-tied block plan view (*top*) and individual detail (*bottom*) for (*left*) trapezoidal and (*right*) hexagonal blocks.

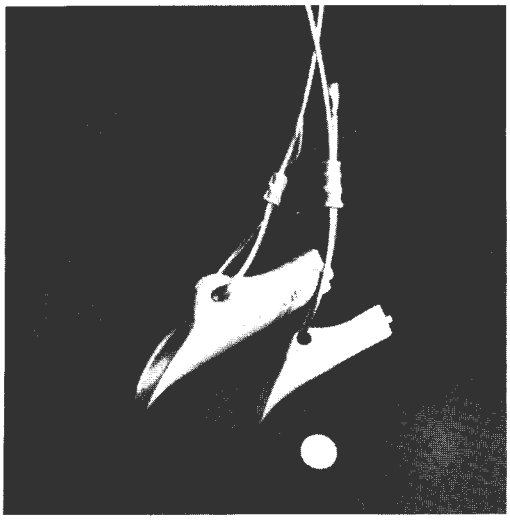

FIGURE 5 Prototype anchors tested for dislodging force.

duction. Some 24-hr tests were conducted throughout the research to evaluate the variation of scour over time.

Stability Paradigms

In designing scour countermeasures, the stability of the device in relation to the fluid forces imposing on it becomes the determining factor. The criteria that can be used to characterize the stability of a countermeasure depend in part on the failure mode that is envisioned. If the failure mode is overturning along the leading edge, the simplest way to characterize stability criteria is to specify an experimental drag coefficient. If, however, the failure mode is particle erosion or uplift on the internal parts of the apron, the most common ways of characterizing stability criteria are either Shields' shear velocity framework or Isbash's sediment number approach.

Shields Framework

A commonly used hydraulic characteristic for evaluating particle stability is shear stress. The shear stress on the channel bed due to the kinematic forces of the fluid can be defined as

$$\tau = \gamma_w y S_e \tag{1}$$

where

τ = shear stress due to fluid force (N/m^2),
γ_w = unit weight of water (9789 N/m^3 at 20°C),
y = depth of flow (m), and
S_e = energy slope.

For uniform flow, the energy slope can be calculated using Manning's equation as follows:

$$S_e = \frac{V^2 n^2}{y^{4/3}} \tag{2}$$

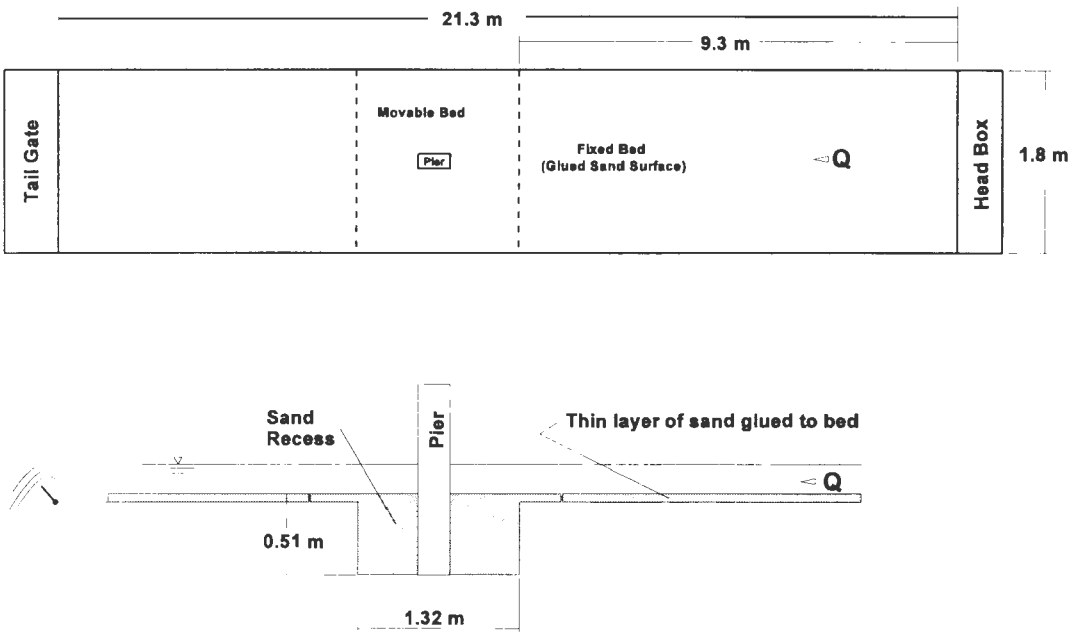

FIGURE 6 Sketch of flume plan view (*top*) and side profile (*bottom*) for movable-bed experiments.

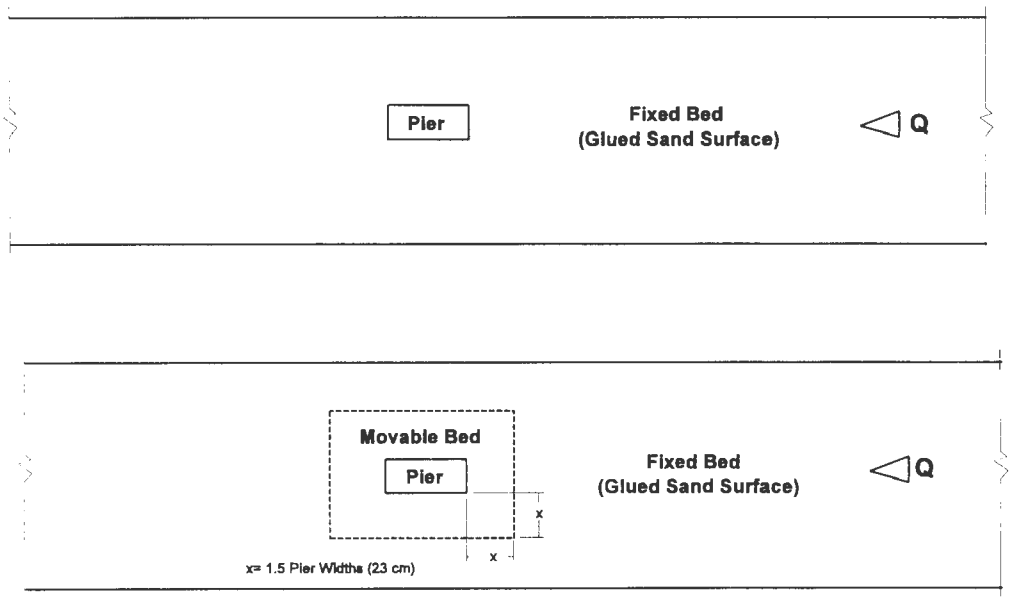

FIGURE 7 Flume setup for fixed-bed obstructed and unobstructed experiments (*top*) and for high-velocity movable-bed experiments (*bottom*).

where V equals velocity in meters per second and n equals Manning's n.

Shield's criteria for the shear stress, τ_c, required to move a particle can be represented as

$$\frac{\tau_c}{\rho_w g(\mathrm{SG} - 1)D_{50}} = \mathrm{SP} \tag{3}$$

where

ρ_w = density of water (kg/m^3),
SG = specific gravity of particle,
g = gravitational acceleration (9.81 m/sec^2), and
SP = Shields' parameter, which could be a function of Reynolds number or Froude number of approaching flow.

Shields represented the Shields parameter as a function of the Reynolds number only, but Kilgore observed that discrepancies in the Shields' parameter noted by various researchers can best be described by a Froude number relationship (*2,3*).

An alternative arrangement of this equation is

$$\frac{U_{*,c}^2}{g(\mathrm{SG} - 1)D_{50}} = \mathrm{SP} \tag{4}$$

where $U_{*,c}$ is the critical shear velocity in meters per second, or $(\tau_c/\rho_w)^{1/2}$.

Isbash Approach

Another approach is to consider the particle stability as presented by Isbash using the sediment number, N (*4*). The sediment number, also referred to as the stability number, is a dimensionless measure of stability calculated as follows:

$$N = \frac{V^2}{gD_{50}(\mathrm{SG} - 1)} = 2E^2 \tag{5}$$

where

V = average approach velocity (m/sec),
D_{50} = median armor unit size (spherical D_{50} is used to calculate spherical stability number) (m),
E = Isbash's coefficient (0.86 for stones that will not move at all and 1.20 for stones that can roll slightly until they become "seated").

The biggest challenge for applying the Shields or Isbash criteria for countermeasures other than rock riprap is selecting a representative D_{50}. This is handled for tetrapods and blocks by using an equivalent sphere diameter in lieu of D_{50}. The spherical diameter is a rough estimation for the diameter of a sphere that would have the same mass and specific gravity as the particle. The grout bags are more difficult because of their elongated shape, and attempts to represent them by a D_{50} gave a distorted comparison between grout bags and other countermeasures. For lack of a better choice, the height of the grout bags was selected for D_{50} in applying the Shields and Isbash criteria.

Overturning

The Shields and Isbash approaches provide a criterion for defining particle motion. However, for some coun-

termeasures the mode of failure is not erosion or uplift but an overturning induced by the protrusion of the countermeasure into the flow field. This type of failure can not be modeled using particle movement criteria. Another criterion for determining the characteristics of stability is to determine the drag coefficient, C_D, associated with overturning. This approach provides a criterion for the failure of various countermeasures, taking into account their geometries and relative positions in the flow field. The drag coefficient is derived by determining the force at which the device begins to overturn. This relation is given as

$$F_D = C_D A_o \rho \frac{V^2}{2g} \tag{6}$$

where

F_D = drag force (N),
C_D = drag coefficient,
A_o = area of obstruction (m^2), and
V = approach velocity (m/sec).

Here, the drag force, F_D, is assumed to act at the centroid of the device. Figure 8 shows an illustration of the forces acting on a grout bag oriented perpendicular to the flow. Calculating the drag force from Equation 8 will result in a drag coefficient for overturning the grout bag. Drag coefficients for the grout bags and cable-tied blocks are presented in Table 1.

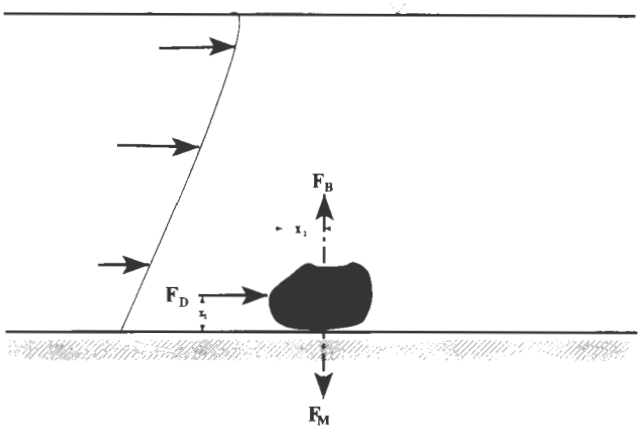

FIGURE 8 Forces acting on grout bag oriented perpendicular to approach flow.

Pier Model

The pier model used in this study was a 152- × 305-mm rectangular wooden column. Because the study is limited to one pier shape, the rectangular shape (as a conservative approach) was modeled because it tends to experience more severe scour than round-edged or circular piers. Two pier models were constructed for the experiments: one was a simple rectangular pier and the other was a special pier used only for the extended footing simulation. The pier for the extended footing had an 89- × 89-mm wooden support to allow for the lowering and raising of the pier (and its footing).

Unprotected Pier Scour

The flow conditions and resulting scour were examined for various sand and riprap configurations around a pier. Sand with a D_{50} of 0.43 mm was used to simulate local scour around the pier. Six unprotected experiments were conducted at incipient velocity conditions for 3.5 hr each. The maximum scour averaged 169 mm for the six experiments. These test results served as a reference standard for the evaluation of riprap alternatives.

TABLE 1 Drag Coefficients

Block Type	Configuration	Overturning Velocity (m/s)	Velocity at Mid- Block Height (m/s)	Flow Depth (mm)	Drag Coefficient C_d
Trapezoidal	3 Abreast	1.053	.890	237	3.96
Hexagonal	3 Abreast	.647	.578	320	1.40*
Grout Bag (A-size)	Perpendicular	.479	.398	308	3.21
Grout Bag (A-size)	Parallel	1.269	1.147	204	1.79

* Hexagonal blocks had a much lower apparent drag coefficient because of the small moment arm for the gravity forces tending to resist overturning.

As a point of reference, the laboratory-measured scour can be compared with an empirical scour equation based on laboratory data. For comparison, the Colorado State University (CSU) pier scour equation was used (*5*):

$$\frac{y_s}{y_1} = 2.0\ K_1K_2K_3\left(\frac{W}{y_1}\right)^{0.65} \mathrm{Fr}_1^{0.43} \tag{7}$$

where

y_s = scour depth (m),
y_1 = flow depth just upstream of pier (m),
K_1 = correction for pier nose shape (1.1 for square nose),
K_2 = correction for angle of attack of flow (1.0 for no skew),
K_3 = bed form factor,
W = pier width (m),
Fr_1 = approach Froude number = $V_1/(gy_1)^{0.5}$,
V_1 = average velocity just upstream of pier (m/sec).

Equation 7 predicts scour to be, on average, 203 mm for the unprotected pier experiments. This equation predicts the ultimate scour depths, and it is necessary to adjust for the duration of the experiments to compare measurements with predictions. For example, the scour depths for these tests were, on average, 169 mm, which corresponds to 83 percent of the ultimate scour predicted by Equation 7. Using Laursen's relationships between scour and time, in clear water conditions, the average scour depth of 169 mm after 3.5 hr corresponds to 80 percent (*6*). Extrapolating the results of the 3.5-hr experiments using Laursen's relationship yields a maximum scour depth of 211 mm. This value compares favorably with Equation 7. The effect of experiment duration should not change the relative results for these experiments.

Riprap Experiments

Many studies have examined the use of rock riprap for channel protection. Maynard et al. conducted a key study that is the basis for current U.S. Army Corps of Engineers riprap design procedures (*7*), and Wörman investigated the relationship between riprap layer thickness and filter requirements (*8*).

The pivotal study for use of riprap for bridge pier protection was done by Parola (*9*). Parola observed that riprap procedures developed for unobstructed channel flow could be used to size riprap for obstructed flow around bridge piers if the approach velocity is adjusted to account for vorticity and accelerations around a pier. The simplest expression derived by Parola is based on the Isbash equation to yield

$$\frac{(KV)^2}{g(\mathrm{SG} - 1)D_{50}} = 4.88 = 2(1.2)^2 \tag{8}$$

where K equals 1.7 for rectangular piers and 1.5 for round nose piers.

Parola's experiments were limited to full aprons that extended at least two pier widths on each side of the piers. He did not study the effect of reduced apron widths. Because the apron width was a variable for the alternative countermeasures included in this study, additional riprap tests were conducted to determine the scour reductions associated with various apron widths.

There was no scour when the riprap apron extended 1.5 to 2.0 times the pier width. For smaller aprons, scour occurred at the perimeter of the riprap apron, but it was much less severe than the maximum scour that would occur at the base of an unprotected pier. For example, the maximum scour depth at the perimeter of a riprap apron that extended only half a pier width on all sides was 58 mm, compared with 169 mm for the unprotected pier. The half-pier-width extension reduced the scour by 34 percent.

Grout Mats and Grout Bags

Various grout mats and grout bag configurations were evaluated for their effectiveness in protecting against pier scour. Both the mode of failure and degree of scour were observed.

The aim of these experiments was to determine the threshold of movement of the grout mat and the grout bags and then observe their effect on scour. Failure can be defined to be the point at which the device moves or "rolls" and the degree of scour that occurs underneath the device. Figure 9 shows a grout bag installation after a movable-bed experiment.

Grout Mats

The unobstructed incipient motion tests for the model grout mats exhibited two different failure modes at two ranges of bed shear stress. Grout mats placed loosely on the fixed bed failed by rolling up when the shear stress reached 0.17 N/m^2. The same mats, "toed in" at the upstream edge, required a greater shear stress, averaging 3.7 N/m^2, to induce failure. This greater shear stress is the result of the leading edge of the mat not being exposed to the flow field, thus creating a more stable device. These results demonstrate the effects of the bed shear stress. The mode of failure for these toed-in runs was for the mats to be "lifted up" off the bed,

FIGURE 9 Results of movable-bed grout bag test.

presumably by a low-pressure zone above the mats. The leading edge of the mat (the toed-in section) did not fail at all.

Obstructed fixed-bed incipient tests were also performed on the grout mat. The mats were placed around a rectangular pier on the surface of a fixed bed. The approach velocity was increased incrementally until failure occurred. Failure was obtained when the mat began to roll or flip up at the front edge. After this failure, velocity profiles and flow depths were recorded in the approach section. The mats failed by rolling up when the shear stress reached 0.18 N/m^2, which compares to the unobstructed failure bed shear stress of 0.17 N/m^2. Thus, this type of failure for the grout mat is independent of the obstruction created by the pier for the fixed-bed condition.

Scour with Grout Mat Protection

On the basis of the maximum scour depths for the grout mat experiments, the difference in scour depths between the runs appears to be due to the placement of the mat around the pier. That is, the proximity of the mat to the sides of the pier (tightness of fit) contributes greatly to the effectiveness of the mat. From the experiments, one of the runs had the highest velocity of all the runs but showed one of the lowest scour depths. This is primarily due to the subjective manner in which the mat was placed around the pier. Placement appears to be the difference between a successful and an unsuccessful protective measure. Approach velocity is a factor, but it is the placement of the protective grout mat that is the primary factor, assuming the lateral extent of this device is at least two pier widths. A silicon seal between the face of the pier and the grout mat was used for several runs, which reduced the scour depth at the face of the pier to zero. In the absence of such a seal, some runs showed significant scour (or undermining) beneath the mat. Similarly, when the mat was tucked up against the pier face, the resulting scour hole was less than if it was not tucked.

Observations

The grout mats provide a barrier through which flow cannot penetrate. The leading edge can sag when undermining occurs. This flexibility appears to provide protection against scour and to increase the mat's stability. Wider grout mats result in less sagging because the lateral extent is beyond the predominant near field vortices being shed by the pier. As with riprap mats, grout mats extending 1.5 pier widths provide significant protection for bridge piers.

Grout Bags

Unobstructed incipient motion tests were performed on various sizes of grout bags by placing the bags perpendicular and parallel to the approach flow. Similar to previous experiments, the velocity was increased slowly until failure was observed. Failure was obtained when the bags oriented perpendicular to the flow rolled over. Failure for the bags oriented parallel to the flow occurred when they moved or rolled in any direction, which required a much higher velocity.

Grout bags perpendicular to the flow failed by rolling over at an average bed shear stress of 0.5 N/m^2, and the grout bags oriented parallel to the flow failed at an average bed shear stress of 3.5 N/m^2. For the bags oriented parallel to the flow, failure appears to be independent of the bag length based on the similarities of the failure approach velocities for several different grout bag lengths.

Obstructed fixed-bed experiments were also performed using a grout bag apron around a rectangular pier. The mode of failure here was the displacement of any of the bags from around the edges of the pier; failure appears to depend on the positioning of the grout bags. That is, local positioning at the face and corners of the pier is an important part of their stability. The grout bags were tested using several placement techniques. Most were oriented parallel to the approach flow. Figure 10 demonstrates the placement of the bags around the pier. Failure of the grout bags at the edge of the pier appeared to depend on the position relative to the front corners of the pier, where the vorticity is the most intense. The positioning of the grout bags at the face of the pier dictates the stability of the individual bags relative to each other—when a bag overlapped the edge of the pier, it was less likely to fail than a bag that was aligned with the edge of the pier. The leftmost con-

figuration in Figure 10 has the highest probability of failure because its position coincides with the highest vorticity levels shed by the pier.

Scour with Grout Bag Protection

Failure with the grout bags usually occurred at the pier's leading edge, where a scour hole formed into which a grout bag would roll. For the higher-velocity experiments, the leading edge was not allowed to scour, causing the bags to fail by rolling because of the fixed-bed surface surrounding the pier. Experiments without filter fabric simply allowed flow to pass between bags and create a scour hole.

Grout bags depend on a filter fabric to prevent the underlying soil from seeping through the large voids between the bags. Experiments without filter fabric did not demonstrate any scour-reduction characteristics. A comparison of two similar experiments (one with and one without filter fabric) showed that without filter fabric, the scour is four times greater than it is with a filter.

Observations

The incipient motion experiments showed that the stability of a grout bag on a fixed bed depends on its position relative to the approach flow. However, from the practical standpoint of a movable bed with an obstruction, this positioning does not appear to be a factor. Typically, grout bags will be anchored to each other and to the bed, which will ensure stability. These experiments showed that their effectiveness as a scour countermeasure is dependent on the use of filter fabric, tightness of fit to the face of the pier, and lateral extent or width of the protective apron.

No conclusive comparative results can be made for grout mats and grout bags when tested on a fixed-bed surface because of their obvious differences in scale relative to the pier. Although the grout bags are more stable, on the basis of the bed shear stress, the incipient motion is an indicator not of its scour-reduction potential but of its measure of resistance to overturning.

Figure 11 provides a scour depth–to–velocity comparison for the grout bags and grout mats. The maximum scour depth with protection (d_s) over the maximum measured pier scour without protection (d_{so}) is plotted versus the average approach velocity (V_a) over the incipient failure velocity of the countermeasure (V_i). Figure 11 shows the reduction or increase in scour for the grout mats and grout bags at various ratios.

Extended Footings

The experimental setup consisted of a 152- × 305-mm rectangular pier placed on a rectangular footing installed over the sediment recess. Both footing width and footing location (elevation relative to the channel surface) were varied to determine the effect on scour. The footing width describes how far the footing extends from the pier in any direction. The height describes the vertical dimension of the footing, and the top location describes the elevation of the top of the footing relative to the sand surface. The setup for these experiments is shown in Figure 12. A total of 91 runs were performed at various footer widths, heights, and thicknesses for 3.5 hr each. The depth-averaged approach velocity was kept fairly constant within a range of 0.29 to 0.35 m/sec and a depth of 305 mm was maintained for all but two runs, which had depths of 152 mm.

Failure for extended footing runs is defined as the formation of a scour hole. Two types of local scour were identified for these experiments. The first was induced by the vertical position of the footing in the flow

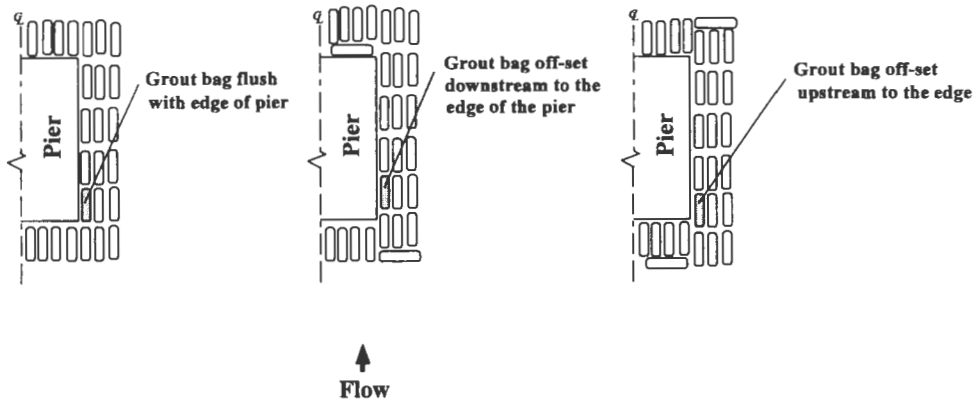

FIGURE 10 Test configurations for placement of grout bags relative to pier on obstructed fixed-bed surface.

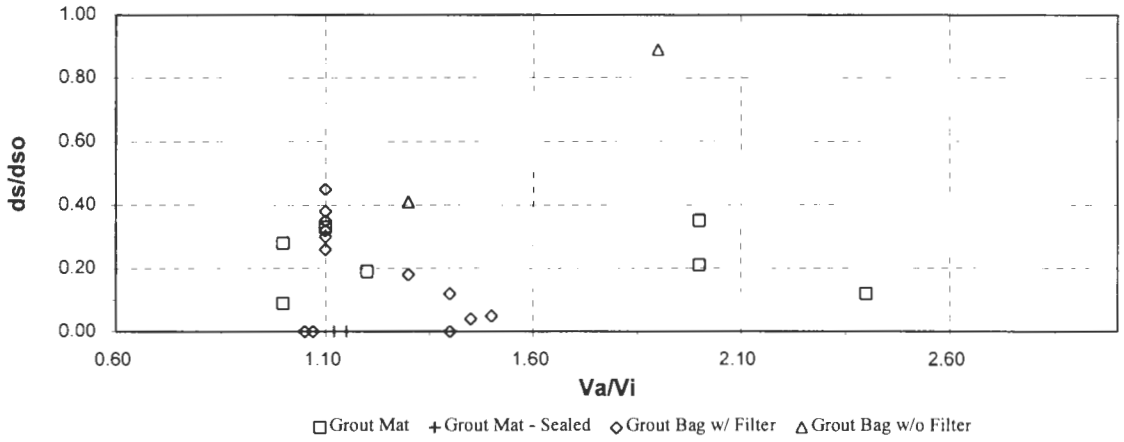

FIGURE 11 Scour reduction for grout bags and grout mats.

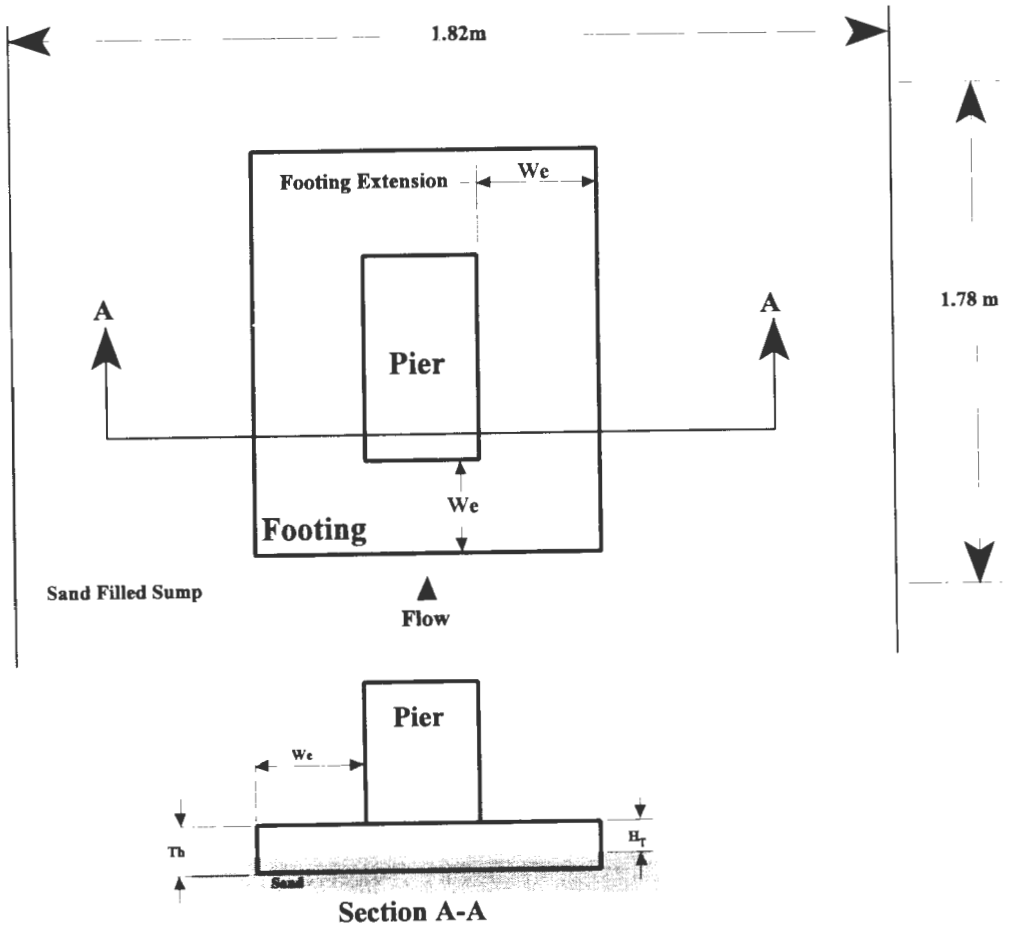

FIGURE 12 Configuration for extended footing experiments.

field. The scour depth was generally not as great for the deeper footing locations because the footing did not protrude high enough into the flow field. However, as the footing was raised, it protruded farther into the flow field, causing flow to be redirected down the face of the footing and resulting in greater scour. As the footing continued to be raised, a channel scoured out below the footing providing relief for the flow directed down the face of the footing, thus resulting in lower scour depths. The second type of scour was created by the near-field vortices being shed by the pier. For this case, the scour is related directly to the footing width. That is, the smallest footing width (76 mm) did not appear to extend far enough to provide protection against the local vorticity. The largest footing width (229 mm) showed no significant scour.

Tetrapods

The geometry of the tetrapod is believed to enhance its ability to resist movement and in turn increase its scour protection characteristics. The interlocking capability of the tetrapod is thought to account for greater stability than riprap. The results of these experiments show that tetrapods may exhibit a higher degree of stability, but the increase was slight and was within the scatter of riprap data.

Experimental Setup

A number of experiments were performed with various riprap and tetrapod configurations. In the first group of tests, conditions for tetrapod incipient motion were determined for unobstructed flow (no pier). The test section dimensions were 203 × 152 mm, and both recessed and surface placements of tetrapods were evaluated on a fixed bed.

There is a significant difference between placement of armor units on the surface and that on recessed. For riprap, the average Shields parameter for recessed placement is 0.096 versus 0.043 for surface placement. For tetrapods, the result is similar, with the recessed placement yielding an average Shields parameter of 0.075 and the surface placement, 0.042.

A comparison of tetrapods and riprap using the stability number versus relative roughness (D_{50}/y) for the recessed placement showed no obvious correlation. The riprap data of Parola and Neill are included to supplement these riprap data (*9,10*). Inspection reveals significant scatter in the data and no clear distribution in performance between the tetrapods and riprap.

Figure 13 summarizes a comparison of tetrapod and riprap data using the Shields parameter versus the Froude number for the recessed data only. The data from Neill and Parola are included in this comparison as well. The Shields parameter for tetrapods is higher, on average, than the riprap for a given Froude number. In addition, none of the tetrapod runs was conducted at Froude numbers greater than 0.8. The Pennsylvania Department of Transportation (PennDOT) is sponsoring additional research to expand this data base. However, there is enough scatter in the data to question whether the interlocking capability of the tetrapods represents a true increase in stability.

Obstructed Flow

Failure of the tetrapod armoring in obstructed flow runs typically occurred at the perimeter of the mats rather than at the pier. This suggests that the tetrapods are less vulnerable to diving currents at the pier than are other independent armoring units with less interlocking cap-

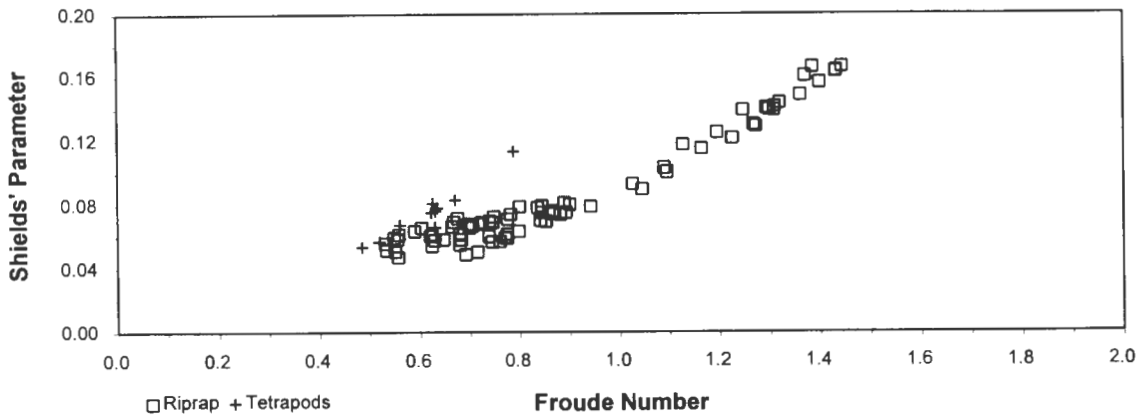

FIGURE 13 Shields parameter for riprap and tetrapods.

ability. However, the general turbulence in the flow field caused by the pier contributes to tetrapod failure.

For these tests, two mat widths were tested. As expected, the wider mat width (the pier width; 152 mm) resisted greater shear stress before failing than did the narrower width (76 mm). No runs were made with wider mats because there were insufficient tetrapod models and the PennDOT study was expected to expand on the experiments.

Results

Three tetrapod concentration variations were also evaluated. The lowest concentration of 3,300 tetrapods per square meter (or approximately a single layer) provided less protection than the medium concentration (4,900 tetrapod per square meter) for both mat widths. Greater concentrations, and therefore more opportunities for interlocking arms, apparently contribute to greater stability as well as less entrainment area for the flowing water. However, the highest concentration tested (5,700 tetrapods per square meter) resulted in earlier failure than the medium concentration for both mat widths. One explanation for this is that the higher concentration protruded farther up into the flow field, resulting in earlier failure. The higher-concentration experiments also had a higher percentage of the tetrapods that were not interlocking efficiently. That is, when a second layer of tetrapods is placed on top of the first, it will interlock better than a third layer on the second layer because there are fewer voids to allow interlocking. This situation caused the tetrapods to roll more easily.

The approach shear resisted by tetrapods in the obstructed cases should be less. In a comparison of the obstructed versus the unobstructed runs, the average shear stress was 2.4 N/m^2 for the 76-mm mat and 3.4 N/m^2 for the 152-mm mat. The unobstructed average shear stress was 5.4 N/m^2. For the obstructed runs, it is unclear if a larger mat would continue this trend and approach the unobstructed level of stability. Although no obstructed runs were conducted in a recessed test section, primarily because of time constraints, it is intuitive that tetrapods would demonstrate higher stability. Further experimentation would be required to verify this case. The fact that most failure is at the mat perimeter suggests that it would approach the unobstructed level.

Cable-Tied Blocks

Cable-tied blocks are continuous scour protection devices placed on the bed surface. This scour countermeasure consists of concrete blocks connected or joined by reinforcement cables. The blocks were evaluted for their stability on a fixed bed for both obstructed and unobstructed flow conditions and on an obstructed movable bed. High-velocity tests were performed for various sediment sizes to simulate live-bed conditions. Trapezoidal and hexagonal geometries were tested, and single trapezoidal and hexagonal blocks were also tested for their drag coefficients. These countermeasures are illustrated in Figure 4.

Trapezoidal Cable-Tied Blocks

Movable-bed experiments using the trapezoidal cable-tied block mats were performed under obstructed flow conditions. The first runs used the setup shown in Figure 6. The high-velocity runs, shown in Figure 6 (*bottom*), consisted of a movable bed underneath the mat in order to observe the performance of the mat at a high shear stress ratio, thus avoiding general bed scour. The mat was placed flush with the surrounding fixed bed. The mat used a filter fabric to prevent water entrainment. Here, no clear trend for scour depth versus velocity is apparent. The controlling factor appears to be the tightness of fit of the mat around the pier. Several experiments were performed at high velocities using a silicon seal between the face of the pier and the countermeasure. This scenario resulted in no scour.

The critical shear stresses, which represent incipient motion conditions, are considerably higher than the shear stresses for the unprotected sand experiments. This indicates that the cable-tied blocks are more stable than unprotected sand and could, therefore, mitigate scour in a live-bed situation. This finding is verified by the increased-velocity experiments, which show that approach velocities up to 3.4 times greater than the incipient motion velocity of the sand reduce scour even after equilibrium conditions are reached. The critical difference between significant scour and no scour regardless of the approach velocity appears to be the seal between the face of the pier and the countermeasure. Although some scour reduction is achieved without using a seal, sealing will greatly improve the effectiveness of the countermeasures.

Hexagonal Cable-Tied Blocks

Hexagonal cable-tied blocks are similar to the trapezoidal cable-tied blocks because they are interconnected by a network of plastic wire. Like the trapezoidal block experiments, hexagonal blocks were tested for their incipient motion as well as their scour-reduction capabilities.

The hexagonal cable-tied blocks were tested up to 2.5 times the incipient velocity motion of the sand. This indicates that the hexagonal blocks will remain effectively in place during flood events of that magnitude. The approach velocity and bed shear stress are greater for the unobstructed conditions than for the obstructed test conditions, which indicates that the incipient motion of the mat is partially dependent on the obstruction that the pier creates.

Results

The effectiveness of a cable-tied block mat in preventing scour depends on the surface roughness characteristics, its tightness of fit around the pier, and the lateral extent of the mat around the pier. The rougher surface of the cable-tied block mats provides better scour resistance, and the better fit of the mat around the pier reduces the scour potential. Regardless of the type of material, the most influential scour prevention characteristic is the lateral extent of the countermeasure and the tightness of fit. Securing the edges of the protective countermeasure to the river bed by using an anchoring system will decrease the countermeasures' natural tendency to overturn or flip up during large flood events. (Anchors and their application are discussed in greater detail in the next section.)

The use of filter fabric for such countermeasures is essential to their overall effectiveness. Without filter fabric, the erosive currents induced by the pier will penetrate between each block and eventually cause scour. Several experiments without filter fabric were performed, and observation indicated that the local scour progressed as if the mat were not there. This eventually led to a scour depth equal to that of an unprotected pier.

For the fixed-bed unobstructed incipient motion experiments, the trapezoidal block mat overturned at a lower bed shear stress than the hexagonal block mat. This occurrence indicates that the hexagonal blocks are more stable than the trapezoidal blocks. One observed phenomenon was that the calculated drag coefficients for the three-abreast hexagonal block experiments were lower than those for the trapezoidal three-abreast experiments. However, for the single block experiments this phenomenon appears to be reversed. One conclusion may be that stream-lining between the hexagonal blocks is more efficient than the trapezoidal blocks, thus creating a slightly more stable cable-tied block mat.

For the obstructed fixed-bed experiments, no clear advantage between either cable-tied block mat is evident. The bed shear stresses required to overturn the hexagonal and trapezoidal cable-tied block mats are 1.47 and 1.46 N/m^2, respectively. This similarity indicates that the incipient motion of an obstructed fixed-bed surface is dependent on the pier. That is, the stream-lining or local velocity gradients surrounding the pier dominate the stability of the mat.

From the results, it appears that the hexagonal and trapezoidal cable-tied blocks compare favorably to each other on the basis of their overall scour reduction potential. However, the incipient motion experiments showed that the hexagonal cable-tied block mat is slightly more stable for the unobstructed experiments. The stability of the countermeasure does not appear to control its scour reduction potential. The controlling factor for scour reduction appears to be how the countermeasure is anchored down and the tightness of fit between the face of the pier and the countermeasure. For example, two experiments were performed using a silicon seal between the face of the pier and the countermeasure. The result was no scour. When no seal was present, the scour depth increased proportionally with the velocity and as a function of the tightness of fit. This is based on both inductive reasoning and the fact that all of the observed scour throughout this research occurred at the face of the pier.

The trapezoidal cable-tied blocks are more stable than the hexagonal cable-tied blocks. This finding is verified by the trapezoidal block's lower drag coefficient and higher shear stress, which may be because the trapezoidal block has more surface area in contact with the bed surface, thus establishing a higher moment arm needed to overturn it. However, for a movable-bed situation, some attributes of the hexagonal blocks may be desirable—that is, the stability of a countermeasure does not necessarily dictate its scour protection potential. Assuming that the cable-tied block mat is stable relative to the underlying sediment, during a sizable flood event, the stream-lining between the individual blocks will most likely contribute to overall effectiveness against scour. The inherent shape of a hexagonal block will allow for channeling or diverting of the approach velocity forces between the blocks as opposed to the trapezoidal block mat, which may divert flow downward instead of around it. However, when used in conjunction with a filter fabric, this characteristic may not be a significant factor.

Anchors

Anchors are often recommended as an auxiliary device that adds stability to the leading edge of a countermeasure. They will improve the overall performance of the countermeasure for scour protection by anchoring to the bed. The anchor is designed to be prototypical in size and is to be implemented with various scour protection countermeasures. The anchor's cable is attached to the countermeasure at the surface and the anchor is

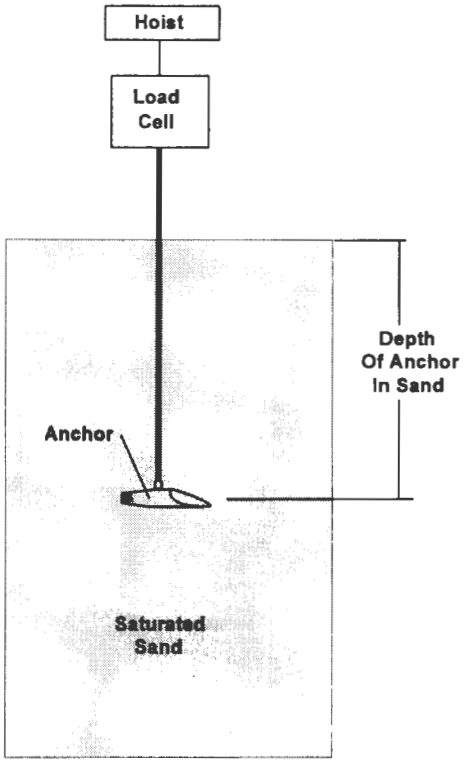

FIGURE 14 Configuration for anchor test.

driven into the bed to an appropriate depth. The setup for the experiments is shown in Figure 14. Intuitively, it can be seen that the anchor may work best with continuous scour devices such as the grout mat and cable-tied block mats.

These experiments were designed to determine the maximum force that an anchor, buried in sand, can withstand without being dislodged. This maximum resisted force becomes critical when the fluid forces acting on the anchor are equal to or greater than its resistance. The resistant forces of the anchor are reported as a function of the depth of the anchor embedded in the sand.

The large forces associated with dislodging the anchors for the different experiments vary considerably. These differences were due to inconsistencies in the sand settlement and saturation percentages. The force required to dislodge the anchor from the sand appears to be dependent on the location of the anchor within the barrel as well as the amount of time the sand had to settle between experiments. The compaction of the sand changed from one experiment to another.

An alternative design for an anchor might be one that is "duck-billed" on both ends. This design would enable the anchor to be driven into the bed material much easier. More important, it would provide a larger surface area when the anchor is in its horizontal position (i.e., once the anchor is in place, the force required to pull up the anchor would be greater since the obstruction area to uplift the anchor is greater). With respect to using anchors in conjunction with a countermeasure, the force required to dislodge the anchor from the bed can be combined with the force required to overturn the countermeasure: the drag force required to overturn the countermeasure can be recalculated using a larger force holding down the countermeasure. This can be used in sizing countermeasures for large flood events. The procedure for sizing the anchors and countermeasure would entail estimating the desired approach velocities and, in turn, the drag forces allied to the countermeasure for a large flood. The appropriate anchor can be determined from the drag force for a specifically sized countermeasure.

The experiments revealed that the performance of the anchor is dependent on soil characteristics such as consolidation and compaction. This conclusion is corroborated by the fluctuation of anchor strength from the first run to the second for the same depths. As can be expected, the larger anchor is more resistant to dislodging than the smaller for the same depth. Figure 15 summarizes the results for these experiments. Furthermore,

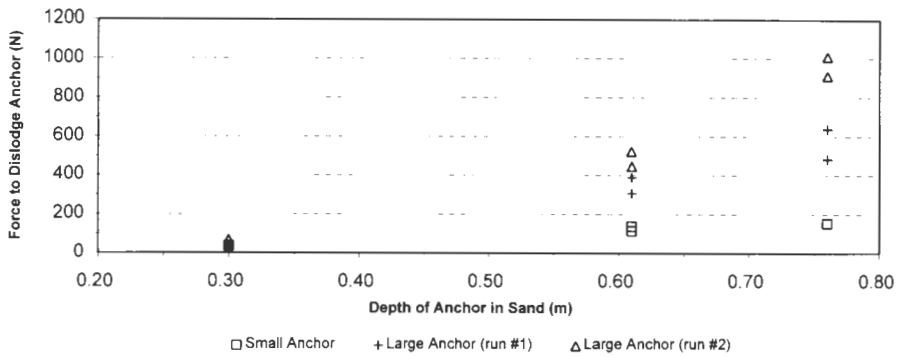

FIGURE 15 Anchor depth versus pullout force.

the resistance to dislodging increases as the sand consolidates. The influence of soil characteristics on the stability of the anchor is beyond the scope of this study. The performance, or pullout force, can be increased greatly by a design modification. Making the anchor duck-billed on both ends would significantly increase the resistance area and make installation easier.

High-Density Particles

High-density particles were tested for their performance as a local scour countermeasure. These particles may be less prone to turbulence around the pier because of their reduced size and their higher specific gravity. High-density particles are more than four times as dense as conventional riprap.

The purpose of these experiments is to evaluate this alternative to riprap as a scour countermeasure. Intuition suggests that high-density particles may provide a better protective apron around a pier than conventional riprap. These experiments are designed to give some insight into how high-density particles will perform as a local scour countermeasure.

Two sizes of high-density particles were tested. The particles were made from lead, were cylindrical in shape, and had diameters of 2.3 and 6.3 mm. Each particle size was tested on the high-velocity movable-bed surface shown in Figure 7 (*bottom*). A layer thickness of two to three diameters was used for the tests. No filter was used. The approach velocity averaged about 0.7 m/sec. Each experiment was allowed to run for about 4 hr, at which time the experiments were stopped and the scour depths recorded.

Although this countermeasure will provide an adequate protective layer, the size and specific weight of the high-density particles appear to have an important impact on its effectiveness. There appears to be a point at which these particles need to be sized according to the underlying bed material size. That is, if the high-density particles are smaller than the bed material that they are trying to protect, this type of countermeasure is inappropriate. When filter fabric is not used, the size of the particle must be larger than the bed material but small enough to close the spacing between each particle. In this manner, the water currents are prevented from entraining between the gaps, thus causing scour.

In general, high-density particles appear to be a more stable scour countermeasure, on the basis of their relative mass and size, than riprap. One advantage of high-density particles is the reduction in the size particles required to provide protection. Along with the size reduction are decreases in void size and the need for filters. Although the riprap experiments scoured less, these experiments were performed near incipient motion, whereas these tests achieved a velocity of 2.6 times that of the incipient motion of the underlying sediments. An increase in the velocity of about 500 percent was observed for these conditions, indicating the need for a thicker apron. With the riprap experiments, typically a two-layer-thick apron was used, which increased the ability of the countermeasures to withstand scour.

Conclusive results to validate this type of countermeasure could not be obtained because of the limited number of experiments performed. However, the Shields criteria and sediment number relations would apply for this type of protection if the appropriate specific gravity were used. Further research would enhance the understanding of this scour countermeasure.

Lead was used for these experiments only for convenience. The authors do not recommend using this countermeasure because of its environmental impact. A material that is more environmentally sound should be used instead.

Summary

The riprap experiments indicate that the protection increases substantially as the riprap apron width increases to 1.5 pier widths beyond the edge of the pier. From these experiments, the two-pier-widths extension criterion currently recommended in FHWA's Highway Engineering Circular 18 (*5*) is adequate.

Grout mats and grout bags also provide substantial protection, especially when they extend at least 1.5 pier widths. The grout mats and grout bags performed comparably to the riprap mats.

Footing configuration can have a profound effect on scour. Wide footings with the top of the footing level with the bed surface provide substantial protection against the strong near-field vortices being shed by a pier. Narrower footings might not extend far enough from the pier to provide protection against these vortices. As general bed scour occurs, the top of the footing is raised into the flow field and the flow is redirected down the face of the footing into the bed, increasing scour. As the footing continues to rise (or scour increases), a channel may be scoured out under the footing. This channel provides relief for the redirected flow and results in scour equilibrium being reached. The maximum protection is provided with wide footings (at least 1.5 pier widths) level with the bed surface, although this configuration does not appear to provide as much protection as equally wide riprap mats, grout mats, or grout bags because footings are rigid and cannot settle or roll into a scour hole. Another reason may be that the riprap sheds off, or breaks up, some of the dominating vortices that are present, whereas the extended footing only transfers them outward. The front

of the footing can also generate scouring vortices when raised into the flow field.

For both unobstructed and obstructed (pier) flow conditions, riprap and tetrapods behaved comparably when both stability number and spherical stability number were compared. These experiments also show that fixing the perimeter and varying the number of layers of tetrapods may affect stability. Therefore, economics should have a major role in choosing between riprap and tetrapods.

A direct comparison between the alternative protection measures is possible, but it must be done with care. The main reason is that the riprap, grout bags, grout mats, tetrapod models, high-density particles, and cable-tied blocks do not necessarily scale up to comparable prototype dimensions; equal scaling between the various models relative to the pier size could not be achieved. A measure such as the Shields parameter can reduce the importance of scaling for measures such as riprap and tetrapods but does not have the same utility for a continuous grout mat. The second problem in making direct comparisons derives from the unknown degree to which the presence of a protection measure changes local scour potential. This may be an issue in terms of both the location of the measure (i.e., whether it is extended into the flow field) and the extent to which the measure changes surface roughness locally (i.e., whether enough to change the flow field energy slope).

The countermeasures that act as a continuous apron can be compared. These include grout mats, grout bags, cable-tied blocks, and high-density particles. Figure 16 shows the effectiveness of these countermeasures relative to each other. The scour reduction ratio (d_s/d_{so}) versus the velocity ratio (V_a/V_i) is examined. Overall, the alternatives that used a seal between the pier and the countermeasure showed little or no scour regardless of the velocity ratio. None of the countermeasures appears to dominate in terms of its scour reduction capacity but the overall trend is that the scour increases proportionally with the velocity. The variability in scour for similar countermeasures at similar velocities may reflect the manner in which they were placed before the experiment. If, for instance, the grout mat was not tight enough around the pier, greater scour could result. From these experiments, there does not appear to be any correlation between the stability of a countermeasure and its scour reduction capability. The critical shear stress to overturn a hexagonal cable-tied block mat (1.9 N/m^2) on a fixed bed is almost 10 times that of a grout mat (0.2 N/m^2). However, from Figure 16, the grout mat experiments compare favorably to the hexagonal cable-tied block experiments.

Although comparing the scour protection alternatives is difficult at best, some relative comparisons are made from the perspective of inherent countermeasure stability and scour protection. The resisting critical shear stress and Shields parameter are measures of the resistance of the alternative to movement in a flow field. Since the Shields parameter is dimensionless, it is independent of scale. However, shear stress has units of force per area and is, therefore, scale dependent. Uniform sand with a D_{50} of 0.43 mm resists a shear stress of approximately 0.2 N/m^2 or less, and a sand with a D_{50} of 2.4 mm resists a shear stress of approximately 1.2 N/m^2. Any measure designed to protect the sand from scour should have a higher degree of resistance. This is true for all measures, except for grout mats laid

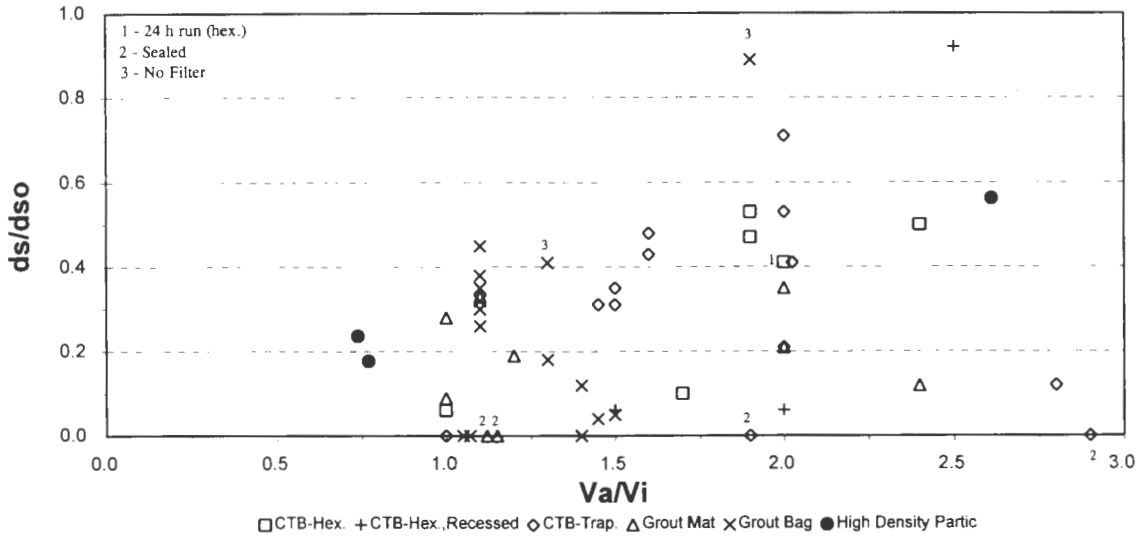

FIGURE 16 Combined scour reduction for countermeasures.

flat on the bed surface. It is also observed that the method of installation affects stability (compare grout mats laid flat and those toed-in, and tetrapods recessed and on the surface).

Another way to evaluate the countermeasures is to compare their effectiveness in scour protection. This is a function of both inherent stability and the ability to stop the base material from moving while underneath the countermeasure. The results show the range of scour allowed by each measure (as a percentage of the unprotected scour) and notes where that scour takes place. The riprap tests reduced maximum scour from 14 to 20 percent of the unprotected scour for a mat width of 152 mm and to 0 percent (no scour) for a mat width of 305 mm. Equally important is that the scour that did take place was found at the mat perimeter rather than at the pier and is, therefore, less of a threat. As expected, the other countermeasures show that a wider mat width improves scour protection. The results show that the installation technique for grout mats and grout bags affects not only the degree of scour, but also the location of scour.

Conclusions

This study provided some valuable insight into the overall behavior and effectiveness of various scour countermeasures. Two main areas of concern emerged: the first corroborated previous recommendations to extend at least two pier widths laterally from the pier in order to provide adequate protection from local scour, and the second addressed the use of filter fabric and sealing between the pier and countermeasure. Although each countermeasure has its own characteristics, the common bond between them is their ability to act as a continuation of the pier much like an extended footing. The following is a list of conclusions drawn from this study for each countermeasure:

- Countermeasures tested in this study are remedial measures to arrest local pier scour at existing bridges.
- Countermeasures were evaluated in terms of failure modes and techniques for analyzing expected stability. All of the alternatives to riprap merit another level of scrutiny for practicality and cost-effectiveness.
- Two techniques determined to be appropriate for analyzing stability were (a) particle displacement criteria patterned after Shields and Isbash incipient motion formulas and (b) drag coefficients to characterize overturning forces. Both of these techniques involve dimensionless parameters that can be transferred from laboratory to full-size conditions.
- Loose particle countermeasures such as rock riprap, tetrapods, or other precast concrete particles and high-density particles can be analyzed by particle displacement criteria and can be compared with one another by using an equivalent spherical diameter as a characteristic size.
- High-density particles can be formed into near-spherical shapes from scrap metal and crushed automobile bodies to serve as an effective countermeasure. Although they may pose environmental problems, they were tested because they are stable in much smaller diameters and in some situations can serve as their own filters for the underlying bed materials.
- Interconnected mats such as cable-tied blocks and grout mats have two failure modes. The first is overturning and rolling up the leading edge if it is not adequately anchored or toed in. The second usually occurs at much higher velocities if the leading edge is adequately anchored; it is uplift of the inner portion of the mat. This process is analogous to particle displacement.
- Anchor strengths of full-size, commercially available duck-billed anchors were measured in the laboratory by the forces required to dislodge them from a barrel of saturated sand. The forces depended on the depth of penetration and size of the anchor and varied from 200 N for the small anchors to 1000 N for the large anchors at 0.75-m penetration.
- Interconnected mats must be fitted around a pier and require a good seal between the mat and the pier to avoid being undermined by the diving currents along the upstream face of a pier.
- Grout bags formed into oblong shapes can be analyzed by particle displacement criteria, but the equivalent spherical diameter, which worked well for riprap, tetrapods, and high-density particles, was not an appropriate way to characterize the size of the grout bags. The authors selected the grout bag height as a characteristic size dimension.
- Extended footings can serve as scour arresters under favorable conditions, but they can become a major contributor rather than an arrester to scour if they are located above the stream bed.

Recommendations

The experiments reported in this paper provide valuable insight into some of the issues surrounding design and implementation of pier scour protection measures. However, additional model experimentation and field verification are necessary to produce defensible guidance for use in the field. More research is needed to address some of the issues that could not be resolved in these experiments of relatively small scale. These issues include

- Practical methods for placing filter fabric under water,

- Development of filter criteria for various prototype protective measures,
- Evaluation of the long-term integrity of cables and polyethylene ropes for cable-tied block systems,
- Evaluation of the long-term integrity of the fabric for grout mats,
- Performance of anchors used in conjunction with countermeasures,
- Consideration of environmental problems associated with the potential erosion of countermeasures and the corrosion of high-density particles,
- General verification testing at larger scales, and
- Evaluation of practical techniques for sealing countermeasures to piers on existing bridges.

Once their effectiveness is demonstrated, issues of cost, availability of materials, and installation will determine which measures are applied in the field.

REFERENCES

1. Fotherby, L. M. *Footings, Mats, Grout Bags, and Tetrapods; Protection Methods Against Local Scour at Bridge Piers*. Thesis. Colorado State University, Fort Collins, 1992.
2. Shields, I. A. *Application of the Theory of Similarity and Turbulence Research to Bed Load Movement*. (English Translation), 1936.
3. Kilgore, R. T. Riprap Incipient Motion and Shields' Parameter. *Proc., ASCE National Conference on Hydraulics Engineering*, San Francisco, Calif., July 1993.
4. Isbash, S. V. Construction of Dams by Depositing Rock in Running Water. *Transactions of 2nd Congress on Large Dams*, Vol. 5, Washington, D.C., 1936, pp. 123–136.
5. Richardson, E. V., L. J. Harrison, and S. S. Davis. *Highway Engineering Circular 18: Evaluating Scour at Bridges*. Report FHWA-IP-90-017, 2nd ed. FHWA, U.S. Department of Transportation, April 1993.
6. Laursen, E. M. An Analysis of Relief Bridge Scour. *Journal of the Hydraulics Division*, ASCE, Vol. 89, No. HY3, May 1963, pp. 106–109.
7. Maynard, S. T., J. F. Ruff, and S. R. Abt. Riprap Design. *Journal of Hydraulic Engineering*, ASCE, Vol. 115, No. 7, 1989.
8. Wörman, A. Riprap Protection Without Filter Layers. *Journal of Hydraulic Engineering*, ASCE, Vol. 115, No. 12, 1989.
9. Parola, A. *The Stability of Riprap Used to Protect Bridge Piers*. FHWA-RD-91-063. FHWA, U.S. Department of Transportation, 1991.
10. Neill, C. R. Mean Velocity Criterion for Scour of Coarse Uniform Bed Material. *Proc., 12th IAHR Congress*, Vol. 3, No. C-6, Fort Collins, 1967, C6.1–C6.9.

Bridge Pier Analysis for Ship Impact

M. I. Hoit, Mike McVay, and Scott E. Breneman, *University of Florida, Gainesville*

A comprehensive computer program that analyzes bridge piers including the pier structure, nonlinear piles, and nonlinear soil interaction is discussed. The program, LPGSTAN (laterally loaded pile group and structural analysis), includes pile group effects, missing and battered piles, and bridge connection effects. The program is unique in that the analysis models are defined by using the designer specifications such as pile spacing, number of columns, and soil layer information. All model definition and result review are performed in a graphical environment. The program has not been tested by comparisons with data in the literature on pile group tests and an extensive series of centrifuge tests performed at the University of Florida. The program is in use at the Florida Department of Transportation and consulting firms throughout Florida. An overview of the program's assumptions, modeling, and capabilities is given.

Over the past decades the abilities of general purpose analysis software have increased dramatically. With the increased abilities of these packages has come an increase in the complexity of using them for specific problems. A general purpose structural analysis package requires huge amounts of time to define and iterate on a complex structural design. These packages generally do not take advantage of the similarities of structures being repeatedly modeled by a particular individual or institution. Engineers must deal with the specifics of software modeling when it would be much more efficient to work with the structural design parameters directly. To allow this, structural analysis packages must be designed to fit the needs of specific types of analysis. For this reason the Department of Civil Engineering at the University of Florida, with major funding from the Florida Department of Transportation, has developed a structural analysis package that can be used to analyze bridge foundations that include a pile group and pier structure with nonlinear soil interaction under ship impact loading.

The analysis program that has been developed, LPGSTAN (laterally loaded pile group and structural analysis), is a nonlinear finite-element analysis program designed for analyzing bridge pier structures composed of a pier cap and columns supported on a pile cap and nonlinear piles with nonlinear soil. This analysis program couples standard structural finite-element analysis with current nonlinear static soil models for axial and lateral loading to provide a robust system of analysis of the coupled bridge pier structure and foundation system. LPGSTAN performs the generation of the finite-element model internally given the geometric definition of the structure and foundation system. This allows the engineer the opportunity to work with the design parameters directly and lessens the bookkeeping necessary to create and interpret a model. Coupled with the analysis program is a graphical preprocessor, LPGGEN, and a postprocessor, LPGPLOT. These programs allow the user of LPGSTAN to view the structure while generating the model and view the resulting deflections and

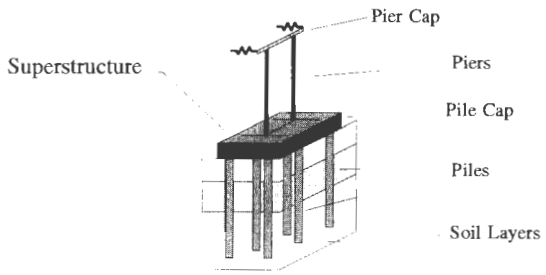

FIGURE 1 LPGSTAN model components.

internal forces in a graphical environment. LPGGEN provides an efficient method for defining the configuration of the structure to be analyzed. After analysis LPGPLOT can plot the undeflected shape, the deflected shape under the load conditions, and the internal stresses and forces in the members. The major components of the LPGSTAN model can be seen in Figure 1.

LPGSTAN is being used throughout the state of Florida for the design of bridge piers. Both the state department of transportation as well as consultants are using and verifying the program on active design projects. Five other states including Washington, Oregon, Oklahoma, Utah, and Louisiana are all testing the software for possible adoption. As the result of an FHWA workshop on the design of highway bridges for extreme events, LPGSTAN was selected as an acceptable analysis solution (*1*).

All of the programs in the LPGSTAN package have been developed to be portable. Working DOS and Unix versions are available. The analysis can be performed in a reasonable time (less than 10 min) on a personal computer with a minimum of 8 megabytes of memory and a 486-based central processing unit or better.

LPGSTAN Modeling

The structural components of the LPGSTAN model are all standard finite elements. The piles are modeled either linearly or nonlinearly by a discrete-element approach. The pile-soil interaction is modeled with lateral P-Y curves and axial T-Z curves. Also pile-soil-pile and group effects are modeled in two ways. The major structural components of the system are the piles, pile cap, pier columns, and pier cap. The piles, pier columns, and pier cap are all modeled by using three-dimensional beam elements. The pile cap is modeled by using three-dimensional flat shell elements. Additional beam elements are used in the modeling to connect the pier columns to the pile cap. These connector elements do not correspond to any true structural component of the bridge foundation structure but act to distribute the column load over an area and stiffen the cap. A view of a typical structure as show in LPGSTAN is given in Figure 2.

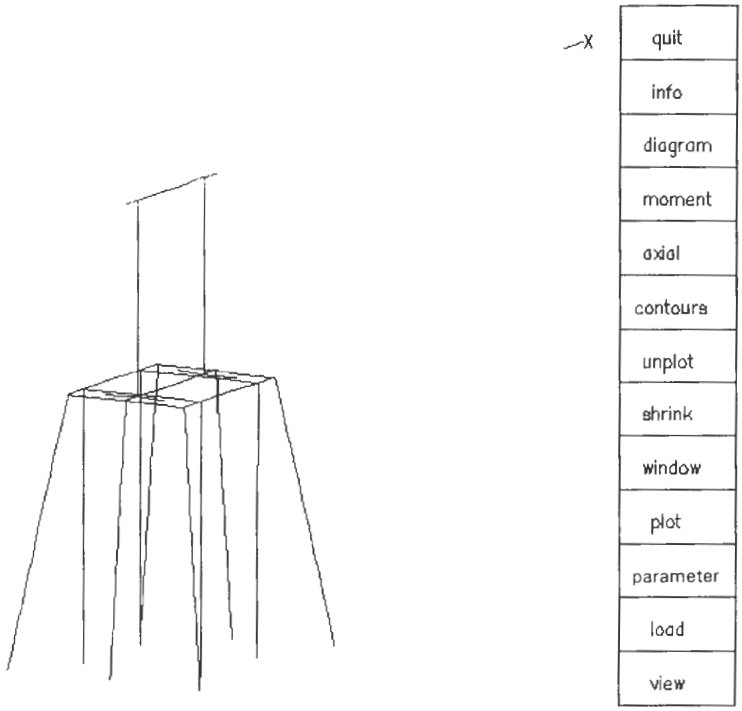

FIGURE 2 Example structure, three-dimensional view.

Pile Modeling

Each pile is modeled with 16 three-dimensional beam elements. These can be standard linear beams or nonlinear discrete-beam-element models (2). The nonlinear piles can model reinforced concrete for both square and round piles. Both elements model biaxial bending, torsion, and axial deformations. If the piles have a freestanding length above the soil layer, the first pile element connects from the pile cap to the top of the soil layer. For the nonlinear model the first element is composed of many subelements. This ensures the accuracy of the nonlinear behavior in the freestanding portion. The rest of the elements are of equal length down the remaining portion of the pile. If there is no freestanding length then all elements in the pile are the same length. For the linear elements the required properties are the moments of inertia, torsional constants (polar moment of inertia), material elasticities, and areas and diameters of the piles. The nonlinear elements require the concrete cross section, steel, and corresponding stress strain behaviors to be specified. The piles can be battered at angles from the plumb line in both the x and y directions. When the piles are battered the total length of the pile does not change but the total depth decreases. Additionally, the pile connection with the pile cap can be either a pinned or a fixed connection.

Pile Cap

The pile cap is modeled by using nine-node shell elements. The shell elements are based on Mindlin theory and include special reduced integration to account for shear deformations and to avoid zero-energy modes. In-plane torsion effects are also included. The pile positions make up the four corner nodes of each element. Additional nodes are placed at the midpoints of adjacent piles to give sufficient nodes for modeling the flexibility between piles. The shell element used can model both bending and shear in the pile cap. The shell elements require the thickness of the cap and the Poisson's ratio and Young's modulus of the cap material.

Pier Columns and Pier Cap

The pier columns and pier cap are modeled with the same linear beam elements as the linear piles. The pier cap connects adjacent pier columns and can have a cantilever length extending from the end pier columns. The pier columns and pier cap girders have independent sets of properties. The center of the girder that connects adjacent columns has its own independent set of properties. This center property can be set to zero to model unconnected pier columns. Each of these properties requires the moment of inertia, torsional inertia, cross-sectional area, material elasticity, and shear modulus.

LPGSTAN can also model the cross bracing between the pier columns, pile cap, or pier cap. Additional beam elements can be added between any nodes in the pile cap and pier columns. These additional elements have properties similar to those of the pier columns and pier cap.

Connectors

The top nodes of the pile elements are directly connected to the shell elements in the pile cap. Because of the general placement capabilities of the columns, the bottoms of the pier columns will not always match up with node locations in the pile cap. Because of this additional connector elements are placed between the nodes in the pile cap and the bottom node of the pier columns. These connectors eliminate the stress concentration in the pile cap and represent the pier column width. The connector elements are much stiffer than the pier columns to ensure the modeling of a stiff connection between the pier and the pile cap. LPGSTAN automatically sets the position and materials for these connector elements.

Deck Connectivity

In real structures the behavior of the foundation is not isolated from the behavior of the connected bridge deck and supports. The ability to include this interaction is provided by adding springs to the pier cap. In typical situations the springs would only be placed on the pier cap girders representing the bridge girders. It is acceptable to also place springs at any node in the pier columns and pile cap. Each spring can have a stiffness in each of the three translational and rotational directions. The values of these springs can be found through an analysis of the bridge deck by alternate static analysis methods or by considering the bridge deck as a large composite beam.

Soil Modeling

The soil modeling used by LPGSTAN includes the axial and lateral effects of pile displacements (3). Group effects are included through the use of P-Y multipliers for the pile rows or the use of pile-soil-pile springs.

When modeling the lateral soil-pile interaction the user has the choice of several P-Y curves, depending on the soil conditions at the site. For sand there is O'Neill's

recommended P-Y curve and the P-Y model from Reese, Cox, and Koop. The latter model for sand is included in FHWA's COM624P, which is a single-pile lateral load analysis program (*4*). For clay there is O'Neill's model, Matlock's representation for soft clays below the water table, Reese's model for stiff clays below the water table, and Reese and Welch's model for stiff clays above the water table. All of these clays except for O'Neill's are also included in FHWA's COM624P (*4*). A user-defined P-Y curve is also available.

The axial effects include soil properties along the length of the pile as well as a soil tip model. The axial soil along the length is given by the T-Z curves of McVay et al. (*3*). The soil tip model is based on similar T-Z curves and an ultimate tip resistance. If no soil is being used or the tip properties are not known, the tip can be either vertically constrained with a linear tip spring or constrained in all directions of motion.

One-way group effects are included in the analysis by using P-Y multipliers applied to the P-Y curves of individual piles. These multipliers reduce the resistance (P) of the soil to which they are applied. Experimental values for P-Y multipliers have been determined for only a few group configurations, and these have been for loading in the principal directions of the pile group (*5*). The choice of the P-Y multipliers is left to the users of LPGSTAN. When the net horizontal loading is not in one of the principal directions (x or y), the P-Y curves are superimposed for both directions.

As part of the research in developing the programs, centrifuge studies were performed on different pile group configurations. These studies had the dual purpose of (a) developing additional P-Y multipliers for different pile configurations and (b) verifying the program. The results of these tests are given by McVay et al. (*3*). Figure 3 provides a comparison of the results of the LPGSTAN program with those of the centrifuge study for an 18-in. round steel pipe pile that was 45 ft long in a medium-dense sand simulation. These results are typical for comparisons between the program and the centrifuge tests.

An alternate method of including group effects is to use pile-soil-pile springs. These are derived from considering the soil between the piles as a linearly elastic medium interconnecting the piles. This method is computationally expensive and is awaiting further advances. It is not recommended for use on microcomputers.

Loading

Structural loading consists of point loads applied to the superstructure. Multiple load cases can be defined in the program. Multiple loadings are treated separately as independent analyses. The multiple load specification is for user convenience. LPGSTAN was originally developed to handle ship impact loading. This type of loading is calculated following AASHTO, which results in a concentrated static load. Any type of static loading such as wind or traffic can be represented by an equivalent set of concentrated loads. However, these loads are currently not automatically defined.

Nonlinear Solution Method

Because the soil and pile models are nonlinear, LPGSTAN performs an iterative solution process. To minimize the work at each iteration the linear portions of the structure that include the pile cap and pier struc-

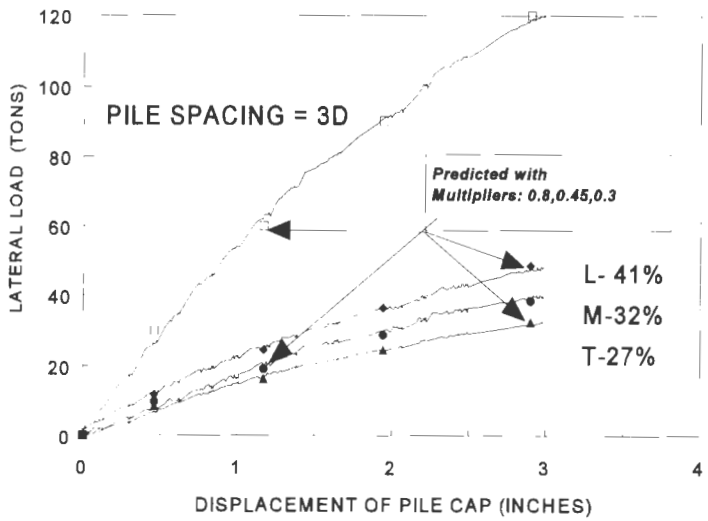

FIGURE 3 Typical comparison of centrifuge data and LPGSTAN.

ture are statically condensed before the iterative solution begins. The iterative method uses a secant method approach for the solution of the nonlinear equations. At each iteration, LPGSTAN finds the stiffness of the soil and piles (if nonlinear) for the current displacements, assembles the stiffness matrix, and solves for new displacement values. Convergence occurs when all nodes in the piles are in static equilibrium. Before this occurs the nodes will have out-of-balance forces. LPGSTAN uses the largest value of the out-of-balance forces as the measure of convergence. This maximum out-of-balance force should be a small percentage of the total load applied to the structure. The final converged displacements are then used to find the internal loads in the pile elements, and the forces in the superstructure are recovered. Users can check if the convergence tolerance is sufficiently small by looking at the printed out-of-balance forces at the pile nodes.

Analysis Procedures

To perform an analysis with LPGSTAN an engineer can follow this simple procedure. After having determined the desired configuration of piles, spacing, and soil, the engineer creates an input file that describes the structural configuration. This can be done graphically with the LPGGEN pre-processor. By using LPGGEN the structural properties and configuration as well as the soil and loading of the structure are defined.

Once the structure has been fully defined LPGSTAN is run. LPGSTAN analyzes the structure and writes the generation and solution information to the specified output file. By next running LPGPLOT the user can view the deflected structure and the resultant forces. Specific information about the internal forces and displacements at particular positions in the structure are contained in the output file. This information can be useful for finding the forces and displacements at particular locations of interest that have been located with LPGPLOT.

Both the LPGGEN preprocessor and the LPGPLOT postprocessor are graphical menu-driven programs that require the use of a pointing device. These programs show the current structure from a three-dimensional view that can be rotated and scaled to allow the user to visually inspect all of the components of the structural model.

Using LPGGEN

The graphical LPGGEN preprocessor is used to define the desired structure and to create the input file for LPGSTAN. While editing, LPGGEN displays the structure in a three-dimensional view. It also allows the user to zoom in on parts of interest. Most of the operations require the user to select an option from a menu and then type any required values. Many properties of the structure can be edited by clicking on the point of interest. A commonly used interface method of displaying a table of properties and their corresponding values is shown in Figure 4.

LPGGEN includes all of the menu commands required to make design modifications to the structure, including pile cap, pile configuration, pier columns and cap, soil, and loading. Figure 5 shows the starting screen of LPGGEN. This menu controls the flow of the problem definition.

Many of the structural properties can be edited while viewing the structure in a three-dimensional view, as seen in Figure 5. The notable exceptions to this are when editing the pile configuration and when defining the soil layers. For the configuration of the pile group, the piles and dimensions are displayed in the standard plan view of the group. An example of the plan view is provided in Figure 6. The batter, relative pile size, and cap overhang are shown.

The soil layers are defined while showing the layers graphically with a single representative plumb pile. An example of this can be seen in Figure 7. Here the user can graphically see the defined layers and can easily access the properties of each layer individually. The free length of the pile is shown proportionally to the true length of the pile.

Using LPGPLOT

The LPGPLOT postprocessor uses a three-dimensional view and interface similar to that used by LPGGEN. It allows the user to visually display a model that has been analyzed by LPGSTAN. Geometry, element and node numbering, and element connectivity can be checked visually by using LPGPLOT. In addition, frame element local coordinate systems, stress contours, displacement contours, deflected shapes, and pile moments of the model can be displayed. Stress and displacement contours can be plotted only for the pile cap. A screen similar to that in Figure 8 shows the main menu items when LPGPLOT is run.

LPGPLOT also plots the deflected shape for each of the load cases performed in the analysis. The magnitudes of the deflections are exaggerated to make them easily visible. Deflections of the individual nodes can be inspected to obtain numeric values. The same structure shown in Figure 8 but shown from a different point of view, including deflections, is given in Figure 9.

LPGPLOT can also show the relative axial forces and moments in each of the structural beam elements (piles,

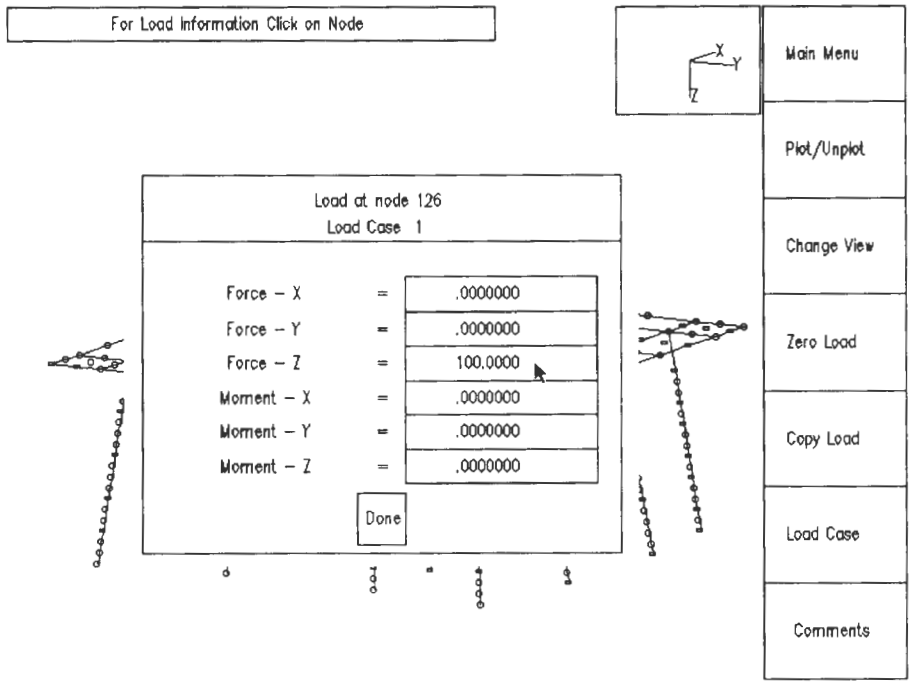

FIGURE 4 Example of table of values of LPGGEN.

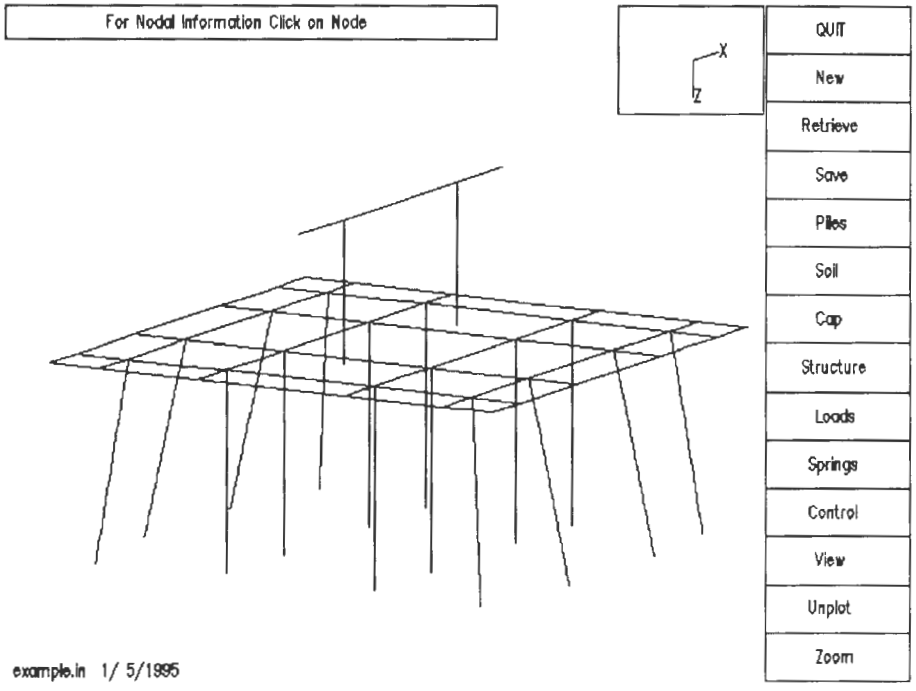

FIGURE 5 Main menu of LPGGEN.

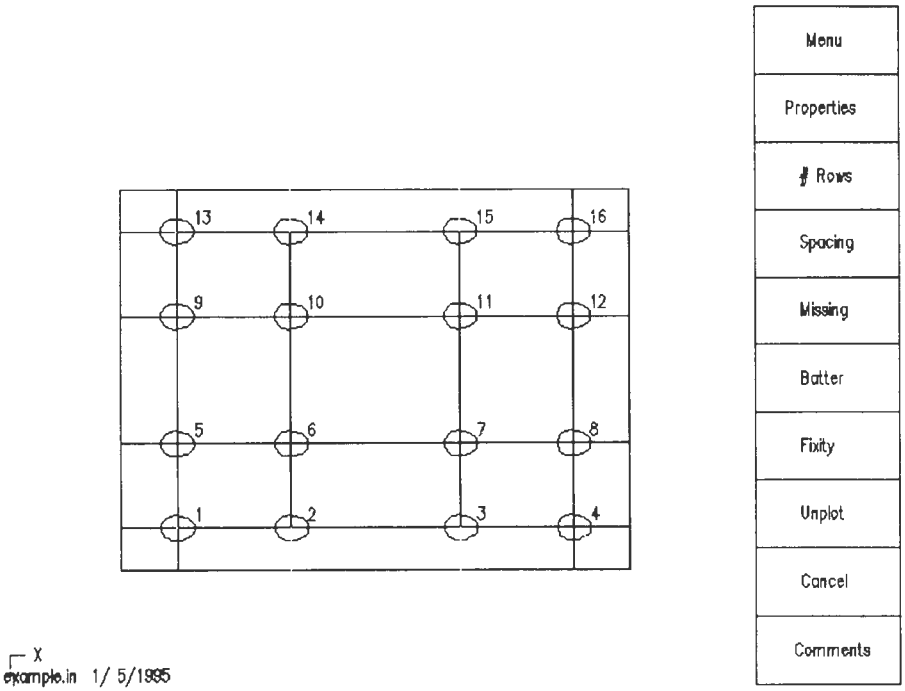

FIGURE 6 View of piles with batter.

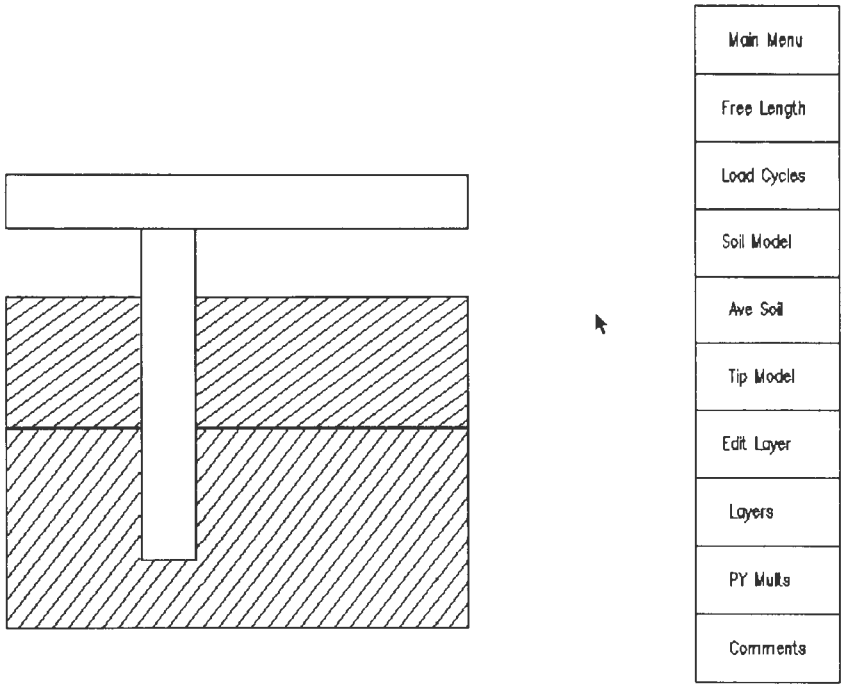

FIGURE 7 Example of soil menu view.

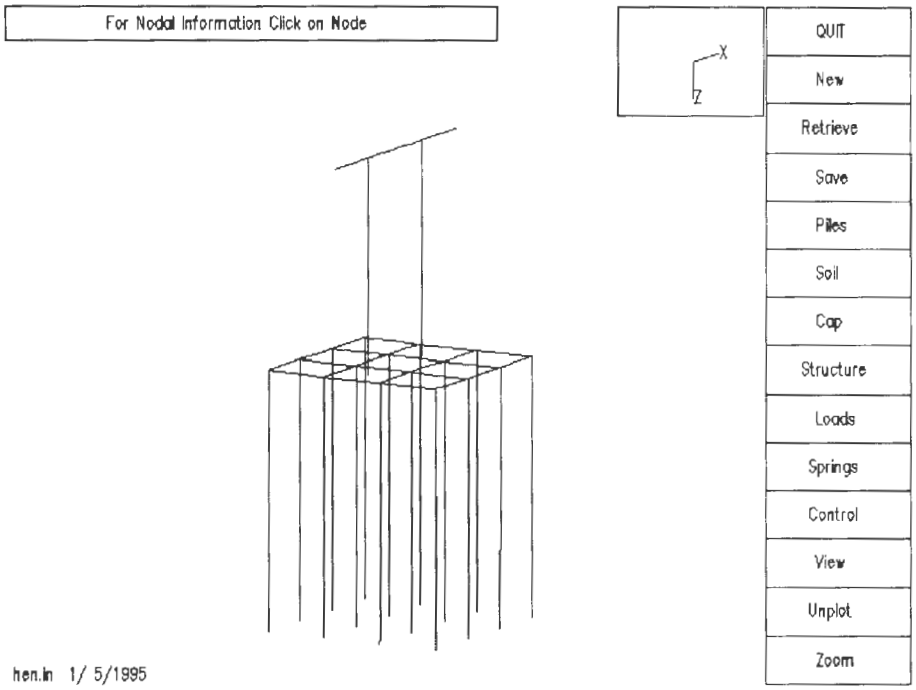

FIGURE 8 LPGPLOT initial view.

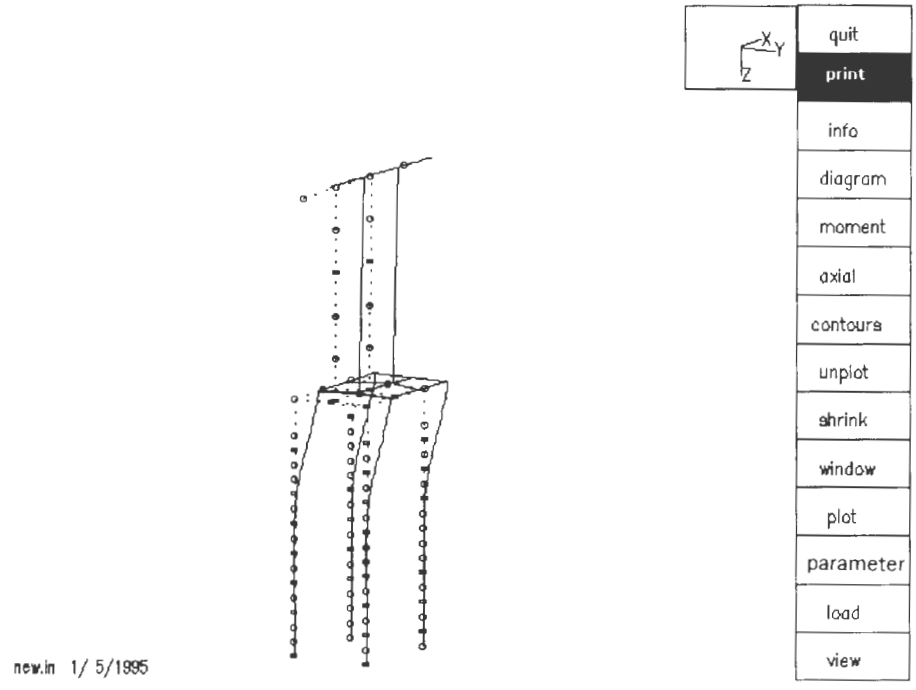

FIGURE 9 Deflected shape in LPGPLOT.

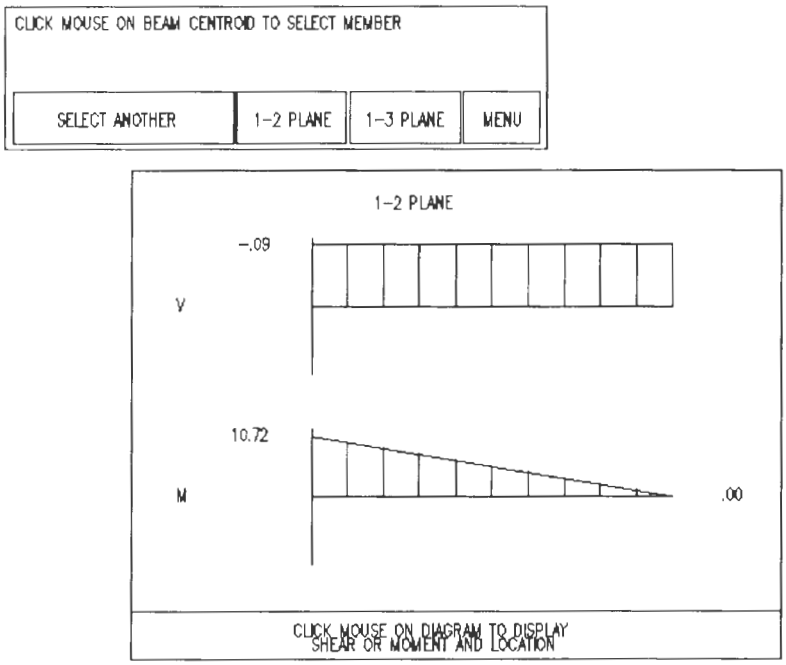

FIGURE 10 Moment diagram in LPGPLOT.

pier columns, and cap) or can give the shear and moment diagrams for individual elements, as shown in Figure 10.

Conclusions

The LPGSTAN bridge pier analysis package is an easy-to-use yet powerful analysis tool for engineers designing bridge pier foundation structures. Design parameters including the pile configuration and properties are changed directly, yielding fast iterations through the design process. The analysis is a highly accurate model of the structural foundation system and the soil interaction. The program has been verified by centrifuge studies and full-scale tests. The entire package runs efficiently on personal computers, making it accessible to all engineers working in bridge design.

Current extensions to the package being worked on are the ability to have automated or assisted pier column design and the automatic inclusion of AASHTO load conditions in the analysis. A grant from the Florida Department of Transportation involves the addition of concrete design check options for the pier columns and cap. The authors are also evaluating the proper design procedure for using AASHTO load combinations in preliminary design when using linear piles. Also being investigated is the use of nonlinear elements in the superstructure and when and how to switch to a complete design with nonlinear piles and superstructure.

Another needed extension is the complete coupling of the substructure to the superstructure (complete bridge). Although LPGSTAN handles the effects of bridge stiffness through the use of springs, this does not include the interaction between different piers. This coupling effect becomes even more important in dynamic analysis. Future extensions may also include multiple piers connected by a bridge span. The modeling of the bridge span can range from simple (a single beam) to a complete bridge model. In the long term use of a complete nonlinear finite-element bridge model connected to multiple piers with a time domain solution would give the most accurate dynamic analysis. However, for use as a design program this is not feasible because of the extremely large computational demands. A critical software need is in the area of bridge modeling.

LPGGEN provides an excellent designer interface for rapid design iterations in combination with the quick analysis capabilities of LPGSTAN. No such software exists for bridge modeling. The closest software for complete bridge modeling is the BRUFEM (Bridge Rating Using the Finite Element Method) system (*6*). BRUFEM is an interactive three-dimensional modeling system for bridges. Although BRUFEM is comprehensive and user friendly, it is not graphics based like LPGGEN. In addition, the analysis is only linear and static.

LPGSTAN is an excellent starting point for the pier portion of any software to be used as complete integrated analysis solution. Extending LPGSTAN to in-

clude multiple piers and a dynamic solution is a first step in developing a complete dynamic solution bridge system. Interim solutions for better bridge modeling range from simple beam models to the use of a complete BRUFEM-type model. Future bridge modeling requires a graphics interface (in the nature of LPGGEN) and inclusion of nonlinear modeling.

REFERENCES

1. Design of Highway Bridges for Extreme Events. FHWA Workshop, San Francisco, Sept. 1994.
2. Hoit, M. I., M. C. McVay, C. O. Hays, and P. W. Andrade. Nonlinear Bridge Pier Analysis Using LPGSTAN. *ASCE Journal of Structural Engineering*, submitted for publication.
3. McVay, M. C., M. O'Brien, F. C. Townsend, D. G. Bloomquist, and J. A. Caliendo. *Numerical Analysis of Vertically Loaded Pile Groups*. ASCE Foundation Engineering Congress, Northwestern University, Chicago, July 1989, pp. 675–690.
4. Wang, S.-T., and R. C. Reese, *COM624P—Laterally Loaded Pile Analysis Program for the Microcomputer*. FHWA Report FHWA-SA-94-048. FHWA, U.S. Department of Transportation, 1993.
5. McVay, M. C., R. Casper, and T. Shang. Lateral Response of Three Row Groups in Loose to Dense Sands at 3D and 5D Pile Spacing. *ASCE Journal of Geotechnical Engineering*, submitted for publication.
6. Hays, C. O., M. I. Hoit, M. Selvappalam, M. Vinayagamoorthy, and G. R. Consolazio. *Bridge Rating of Girder-Slab Bridges with Automated Finite Element Modeling Techniques*. Structures and Materials, Research Report 90-3. Engineering and Industrial Experiment Station, University of Florida, Gainesville, Oct. 1990.

BRIDGE FATIGUE AND REDUNDANCY

Evaluation of Fatigue-Sensitive Details Used in Moline Viaduct, Illinois

Richard A. Walther and Michael J. Koob, *Wiss, Janney, Elstner Associates, Inc.*

A comprehensive study was undertaken to assess the performance of fatigue-sensitive details used in the Moline Viaduct. This 26-span, 872-m (2,860-ft) structure constructed in 1973 is located on Interstate 74 in Rock Island County, Illinois. The complex bridge superstructure includes variations in span length and width along with curved and superelevated geometries. The superstructure is fabricated from ASTM A36 steel and includes longitudinal plate girders supported by box-shaped cross-girders at the mainline piers. The cross-girder extends continuously through the web plates of the longitudinal girders. Full-penetration welds are used to complete the girder to cross-girder connection. This detail is considered potentially fracture sensitive by an FHWA notice dated April 24, 1978. This notice was issued following the brittle fracture of several steel support bents of the Chicago Transit Authority's Dan Ryan Transit Structure in January 1978. A brief discussion of these brittle fractures is presented to introduce the fatigue behavior characteristics of slotted member bridge details. Examination of the structure revealed a number of cracking problems at the girder to cross-girder connection. In addition, various fatigue-sensitive conditions were identified in the cross-girder interior. Field testing indicated that nominal stress ranges in the vicinity of fatigue-sensitive details were below the crack growth threshold and crack growth should not occur. However, preventive retrofit recommendations and a surveillance program were recommended to address cracking and nonconformance items.

A comprehensive study of the Moline Viaduct was initiated in February 1990 for the Illinois Department of Transportation (IDOT) to address concerns regarding the fabrication of the box-shaped cross-girder and its connection to the longitudinal girders. The details used to complete the cross-girder to girder connection are considered potentially fracture sensitive by an FHWA notice dated April 24, 1978. This notice was issued to alert departments of transportation of potential cracking problems at locations where primary bridge members are slotted to receive other primary members and welding is used to complete the connection. Major brittle fractures that occurred in steel support bents of the Chicago Transit Authority's (CTA's) Dan Ryan Transit Structure in January 1978 prompted the FHWA notice. A brief discussion of these brittle fractures is presented here to introduce the fatigue behavior characteristics of slotted member details. Interestingly, the CTA structures that experienced brittle fracture were designed and fabricated in 1967–1970 by the same two firms that designed and fabricated the Moline Viaduct in 1970–1973.

The Moline Viaduct study included in-depth field inspection, instrumentation and field testing, structural analysis, and development of recommended retrofit procedures. Instrumentation and field testing was performed to determine live-load stress ranges in representative longitudinal girders, cross-girders, and adjacent cross-girder to longitudinal girder connections. This paper summarizes the information that was collected and outlines recommendations for retrofitting the Moline Viaduct.

Description of Moline Viaduct

The 26-span Moline Viaduct includes two separate mainline roadways, northbound and southbound, and four ramps along Interstate 74 in Rock Island County, Illinois. The 872-m (2,860-ft) structure carries traffic to and from the south end of the Twin Memorial Bridge that crosses the Mississippi River. The complex bridge superstructure includes variations in span length and width along with curved and superelevated geometries. The superstructure is fabricated from ASTM A36 steel and includes longitudinal plate girders and box-shaped cross-girders. The viaduct was designed in the early 1970s by using AASHO and IDOT specifications in effect at the time. Construction was completed in 1973. A view of the superstructure framing is shown in Figure 1.

The box-shaped cross-girders extend continuously through the longitudinal girder web plate and are supported by concrete piers to form bents. Cross-girder flange plates are typically 76.2 cm (30 in.) to 91.4 cm (36 in.) wide and 5.1 cm (2 in.) thick, whereas the web plates are typically 116.8 cm (46 in.) deep and 1.9 cm (0.75 in.) thick. Complete-penetration, single-bevel groove welds with backing bars are used to fabricate the box-shaped members. Backing bars are attached to the box interior with short intermittent fillet welds. Interior diaphragms are provided and align with longitudinal girders that frame into the box. Interior diaphragms and bearing stiffeners are fillet welded to the cross-girder web plates and compression flange. The cross-girder web plates and compression flange are connected to the longitudinal girder web with complete-penetration, double-V groove welds reinforced with fillet welds from both sides. A tight fit is provided between the cross-girder tension flange and girder web. A 2.5-cm (1-in.)-radius, half-circle stress relief hole is furnished in the girder web near the cross-girder tension flange. Note that stress relief holes for northbound Piers 1 through 4 were omitted during fabrication. Typical cross-girder fabrication details are shown in Figure 2.

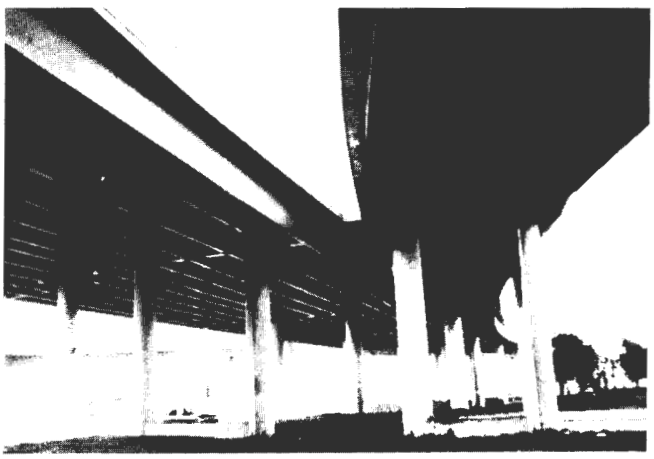

FIGURE 1 Superstructure framing.

The cross-girders were fabricated and shipped to the site with short segments (typically 5 ft beyond the web plate of the cross-girder) of the longitudinal girders attached. Longitudinal girders were then bolted to the shorter segments in the field. The number of longitudinal girders varies from 5 to 11 because of the changing roadway width. Girders occur in two-, three-, or four-span units between hinges, and in positive-moment regions girders are composite with the 20.3-cm (8-in.)-thick concrete deck. Interior girders are straight between bents, whereas fascia girders are curved.

Behavior of Slotted Member Details

Cracking in three rigid frame bents of the CTA Dan Ryan Transit Structure in January 1978 drew national attention to the poor fatigue characteristics associated with slotted member details. The brittle fracture in the Dan Ryan Transit Structure, shown in Figure 3, initiated at the welded junction of the longitudinal girder bottom flange tip and the box-shaped cross-girder. Cracking extended so as to completely fracture the cross-girder bottom flange and much of the web plates. The girder to cross-girder connection was fabricated such that the longitudinal girder bottom flange passed continuously through flame-cut slots in the cross-girder web. The flange to web connection was completed by groove welding around the perimeter of the bottom flange. Examination of the fracture surface indicated that brittle fracture had occurred after fatigue cracks had developed from unfused regions in the welded flange connection. The unfused regions form cracklike embedded defects that at very low stress range levels are sensitive to fatigue crack propagation. Poor-quality welds, fatigue crack growth, low temperatures, and stress concentrations at this highly restrained joint detail contributed to the brittle fractures (*1*).

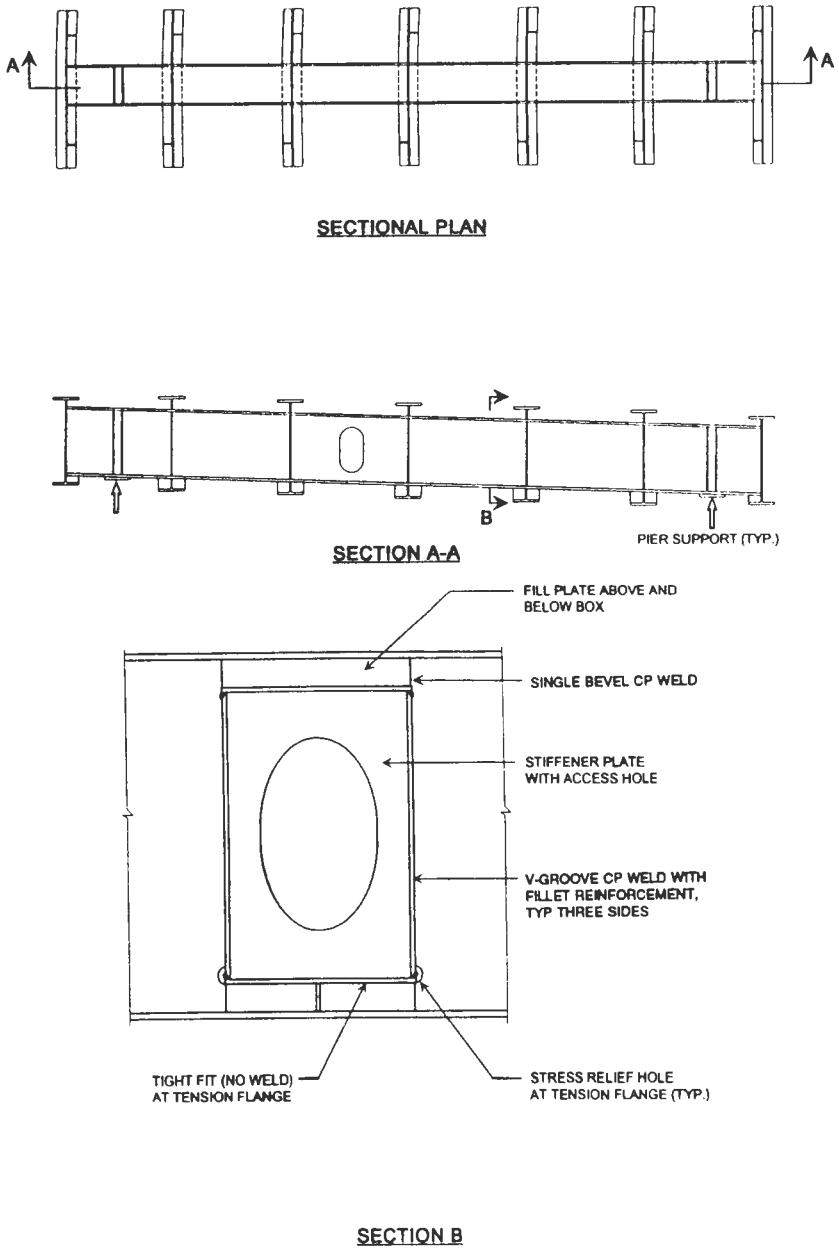

FIGURE 2 Typical cross-girder details.

Brittle fractures in the Dan Ryan Transit Structure, in addition to cracking found in other structures containing similar details, created a need for further research into the fatigue behavior of slotted member details. FHWA responded in April 1978 by issuing a warning to departments of transportation about the fracture-sensitive nature of slotted member details. The warning states that member penetrations located in a tension region exhibit a potential for fracture greater than a Category E detail. Slots that closely approximate the size of the member passing through the slot may contain flame-cut edges and sharp reentrant corners, which may result in high stress concentrations. At the points where welding is provided to close the gap, additional stress concentrations are imposed because of shrinkage of the highly restrained weld around the periphery of the slot. Furthermore, weld construction may result in embedded weld defects at the corners of the slot (*2*). These factors affect the fatigue sensitivity of this type of detail.

Research (*3–5*) reported that the fatigue resistance of slotted member details ranged from slightly better than Category E to approximately one-half of Category E′. Factors affecting the fatigue resistance classification

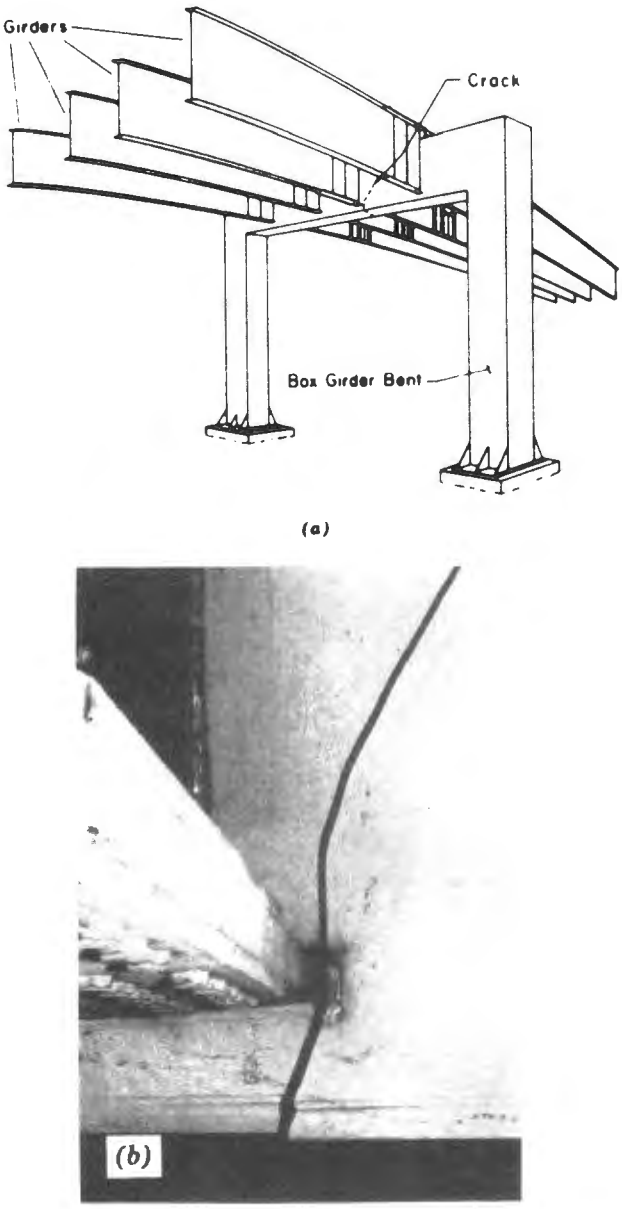

FIGURE 3 Fracture in CTA Dan Ryan Transit Structure, slotted member detail (*1*): (*a*) location of fracture; (*b*) close-up view of cracked box girder web.

of slotted member details include size of the connected components, quality and type of weld, and presence of a stress relief hole at the penetrating flange tip. The fatigue behavior for flanges framing into or piercing through girder webs is comparable to the fatigue resistance of a Category E′ detail when the flange thickness is equal to or greater than 2.5 cm (1 in.). For a flange thickness of less than 2.5 cm (1 in.) fatigue behavior more closely corresponds to a Category E detail. Fatigue resistance for member penetrations welded on each side is significantly improved over that for member penetrations welded from one side only. Member penetrations welded from one side only provide a fatigue resistance approximately one-half that of a Category E′ detail and should be avoided. The predicted fatigue behavior for member penetrations welded on one or both sides is illustrated in Figure 4. Fatigue resistance is also dependent on web plate thickness when fillet welds are used to complete the connection. The ability of achieving complete penetration with the base metal is greatly reduced when the thickness of the member being penetrated is greater than 0.6 cm (0.25 in.). The presence of weld discontinuities creates cracklike defects that are susceptible to fatigue crack growth at reduced stress levels. Providing stress relief holes at the tip of a flange penetration that is attached to the slotted member by fillet welds was found to result in a member fatigue behavior less than Category E′.

The poor performance of slotted member details used in the Dan Ryan Transit Structure, past research, and the similar details used in the Moline Viaduct led to IDOT's decision to carry out an in-depth evaluation of the girder to cross-girder connections.

In-Depth Inspection

The detailed field inspection of the Moline Viaduct superstructure was subdivided into two parts: (a) high-quality fatigue crack inspection of the welds used to connect longitudinal girders to the cross-girders and (b) inspection of the welds used to fabricate the cross-girders. Considerable time was also given to the inspection of other fatigue-sensitive details including lateral gusset plates and details susceptible to out-of-plane distortion, such as offset cross-frames.

Girder to Cross-Girder Connections

The inspection and nondestructive testing efforts concentrated on the girder to cross-girder connections in the vicinity of the cross-girder top and bottom flanges. At these locations vertical welds either terminate at a stress relief hole or intersect a horizontal weld [Figure 2(*b*)]. All 2,440 weld terminations or intersections were carefully inspected. For interior girders eight weld terminations or intersections, four on each side of the longitudinal girder, were inspected. At fascia girders four weld intersections were inspected. In general, the welds used to connect the longitudinal girders to cross-girders exhibit satisfactory workmanship. Typically, the vertical welds looked better than the horizontal welds.

A total of 82 (3 percent) of the 2,440 weld terminations or intersections exhibited cracking. The number of crack locations in the northbound bridge (52 cracks)

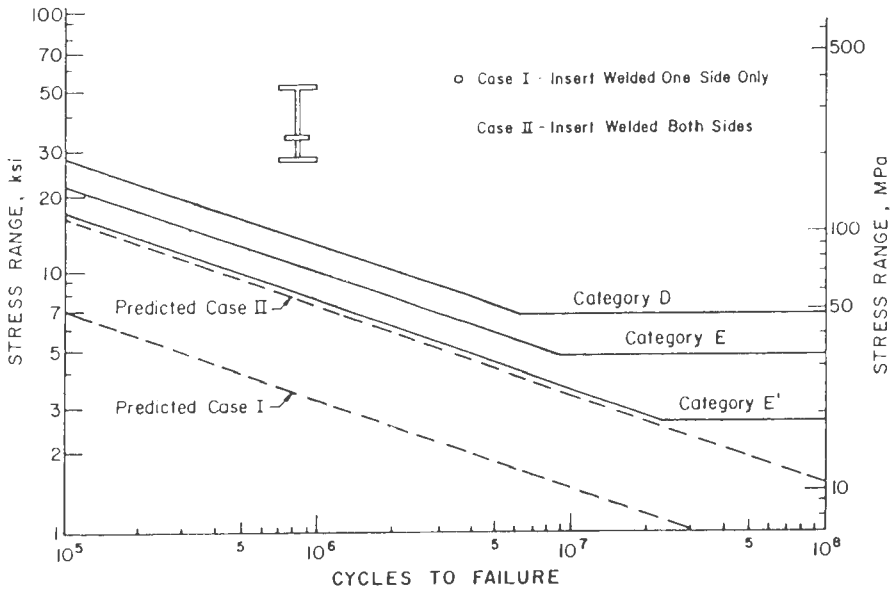

FIGURE 4 Comparison of fatigue life prediction of web penetration with unfused areas in the web (*5*).

was almost double that found in the southbound bridge (30 cracks). However, 21 of the 52 northbound bridge cracks were located at Piers 1 through 4, where stress relief holes had been omitted during fabrication. Excluding northbound Piers 1 through 4, cracking in the northbound and southbound bridges was almost equal; 31 cracks were observed in the northbound bridge, 23 at the cross-girder top flange and 8 at the bottom flange weld terminations or intersections, whereas 30 cracks were observed in the southbound bridge, 21 at the top flange locations and 9 at the bottom flange locations. A summary of the crack inspection findings is provided in Table 1.

Because many of the 82 cracks were similar in orientation and location, it was possible to categorize the cracks into several types. The most predominant cracking occurred at weld terminations (Figure 5) located at the top corners of the longitudinal girder to cross-girder connection or at weld intersections (Figure 6). In total, 50 of the 82 cracks were located at the top corner connection. Crack lengths varied from 0.3 cm (0.12 in.) to 5.1 cm (2 in.), with an average length of 1.3 cm (0.5 in.). Fifteen of the 32 cracks discovered at the bottom corner weld termination or intersection were located in northbound Piers 1 through 4, where prefabricated stress relief holes had been omitted (Figure 7). Cracks originated from the tight-fit gap between the cross-girder tension flange and girder web and extended horizontally along the groove weld toe. Several cracks were observed to turn and extend downward. Crack lengths ranged from 0.3 cm (0.12 in.) to 2.5 cm (1 in.) and averaged 1.6 cm (0.63-in.).

Subsequently drilled 1.6-cm (0.63-in.)-diameter stress relief holes were provided in northbound Piers 1 through 4. The holes were poorly positioned and did not intercept the crack tip. From Figure 7 it can be observed that crack propagation is not likely to intersect the drilled hole.

Interior Examination of Cross-Girders

All 49 cross-girders were opened and their interior surfaces were inspected. Several details used in the cross-girder fabrication including discontinuous backer bar joints and connecting tack welds, flame-cut gouges, weld remnants, and welded erection aids are categorized as fatigue sensitive. The objective of the inspection was to observe and identify any condition that potentially may have an adverse effect on the long-term performance of the bridge and to find evidence of crack growth if it existed. Heavy corrosion in 10 cross-girders impaired the inspection effort.

Discontinuous backer bars represent the most fatigue-sensitive condition observed. The full-penetration weld used to construct the box is fused to the backer bars on each side of the backer bar butt joint. The butt joint gap represents a built-in cracklike defect. Close inspection of this detail revealed no crack extension. Short intermittent fillet welds, used to hold the backer bar in position, exhibited poor profiles, porosity, and significant undercutting. In general, about 160 short fillet welds were present in 2.4 m (8 ft) of cross-girder (the space between two girder diaphragms). A

TABLE 1 Crack Inspection at Girder to Cross-Girder Connections

Northbound Bridge					Southbound Bridge				
	No. of Cracks					No. of Cracks			
Pier	Top	Bottom	Total	Max. Length cm (in.)	Pier	Top	Bottom	Total	Max. Length cm (in.)
1*	1	3	4	1.9 (¾)	1	2	0	2	1.3 (½)
2*	0	4	4	2.5 (1)	2	0	0	0	--
3*	3	7	10	5.1 (2)	3	3	1	4	1.9 (¾)
4*	2	1	3	1.3 (½)	4	1	2	3	1.3 (½)
5	0	4	4	2.5 (1)	5	2	0	2	2.5 (1)
6	0	0	0	--	6	2	0	2	0.3 (1/8)
7	1	1	2	1.6 (5/8)	7	1	0	1	2.5 (1)
8	2	0	2	1.9 (¾)	8	0	0	0	--
9	2	0	2	1.3 (½)	9	0	3	3	0.9 (3/8)
10	4	1	5	4.2 (1 5/8)	10	1	0	1	3.2 (1¼)
11	1	0	1	1.0 (3/8)	11	0	0	0	--
12	0	0	0	--	12	0	0	0	--
13	1	0	1	0.6 (¼)	13	0	0	0	--
14	0	0	0	--	14	0	0	0	--
15	0	0	0	--	15	1	1	2	1.3 (½)
16	0	0	0	--	16	0	0	0	--
17	1	0	1	1.3 (½)	17	1	0	1	1.0 (3/8)
18	0	1	1	5.1 (2)	18	0	0	0	1.0 (3/8)
19	1	0	1	2.5 (¼)	19	2	0	2	1.3 (½)
20	0	0	0	--	20	1	0	1	0.6 (¼)
21	1	0	1	1.3 (½)	21	0	0	0	--
22	2	1	3	3.8 (1½)	22	1	2	3	1.9 (¾)
23	0	0	0	--	23	3	0	3	2.5 (1)
24	7	0	7	1.3 (½)	24	0	0	0	--
25	0	0	0	--	25	0	0	0	--
TOTAL	29	23	52		TOTAL	21	9	30	

* Stress relief holes omitted during fabrication.

-- No crack found

number of these welds were cracked through the weld throat, with the cracks oriented parallel to the primary stress flow of the box.

Numerous welds that were made as a temporary aid during fabrication and without regard to good welding procedures were found. A number of these welds were cracked. Several cracks represented an extremely poor condition because the crack was oriented perpendicular to the primary stress flow of the box. No crack extension into the cross-girder plates was observed. In addition, flame-cut gouges were found throughout the cross-girders. Flame cutting was used to cut access holes and to remove defective welds and temporary welded attachments. Gouges and rough surfaces in areas subjected to tensile stress were carefully examined for signs of crack extensions; none were found.

Instrumentation and Field Testing

An instrumentation and field testing program was carried out to measure the Moline Viaduct's response to dynamic loadings provided by control vehicles and normal traffic. IDOT provided two 21,800-kg (48,000-lb) six-wheel dump trucks as the control vehicles and arranged a police escort to control traffic. The control vehicles were driven side-by-side across the bridge at 72 km/hr (45 mph). The test program objectives were as

FIGURE 5 Typical crack at top flange stress relief hole.

FIGURE 6 Typical crack at top flange weld intersection.

follows: (a) to measure strain levels to compare and verify the structural analysis, (b) to determine stress range at girder to cross-girder connections, and (c) to determine stress range in the box-shaped cross-girder.

Location of Instrumentation

A total of 54 single-element strain gauges were installed. Figures 8 and 9 show the gauge layout and numbering system. Strain gauges 1 through 6 and 49 through 54 were installed on cross-girders at southbound Pier 3 and northbound Pier 6, respectively, to measure the strains in the box-shaped member at maximum moment locations. Gauges 7 through 10 were installed on the girder web at southbound Pier 3 to measure strains in the vicinity of two cracks found at girder to cross-girder connections. Two longitudinal girders in northbound Spans 4–5, 5–6, and 6–7 were instrumented at maximum positive- and negative-moment locations. All gauges were aligned with the longitudinal axis of the member that was instrumented.

The measured stress ranges are summarized in Table 2. In general, the control loading produced the maximum stress ranges. The data obtained during 6 hr of normal traffic provided only a minimal number of vehicles that produced stress levels comparable to those from the control loading. Normal traffic data were recorded continuously during business hours on a typical weekday.

Measured Stresses in Cross-Girders

Representative strain gauge plots are given in Figure 10 for gauges installed on the northbound Pier 6 cross-girder. The maximum tensile stress ranges at the bottom flange of southbound Pier 3 and northbound Pier 6 cross-girder were 10.3 MPa (1.5 ksi) and 12.4 MPa (1.8 ksi), respectively. Gauge 3, located just below the flame-cut access opening, indicated a tensile stress range of 9.6 MPa (1.4 ksi). The strain gradient across the member cross section suggests that the neutral axis is located at the midheight of the member.

Measured Stresses Adjacent to Cracked Connections

Representative strain gauge responses for Gauges 7 and 10 are given in Figure 11. In general, these gauges indicated tensile stress ranges equal to or less than 3.4 MPa (0.5 ksi). However, Gauge 8 indicated a tensile stress range of 16.5 MPa (2.4 ksi). Additional strain gauge work is required to determine the reasons for this

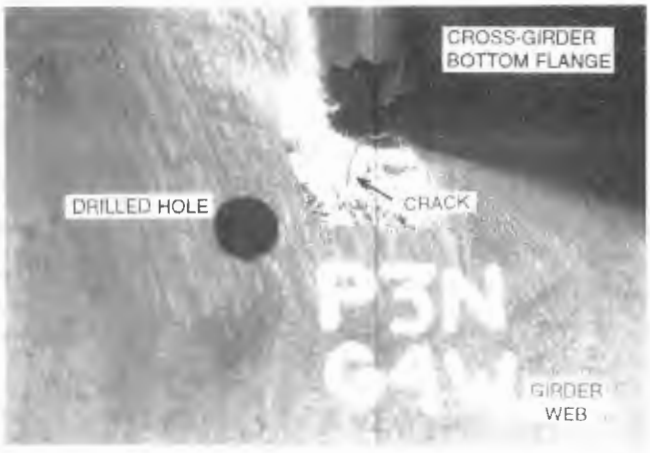

FIGURE 7 Typical crack at bottom flange stress relief hole.

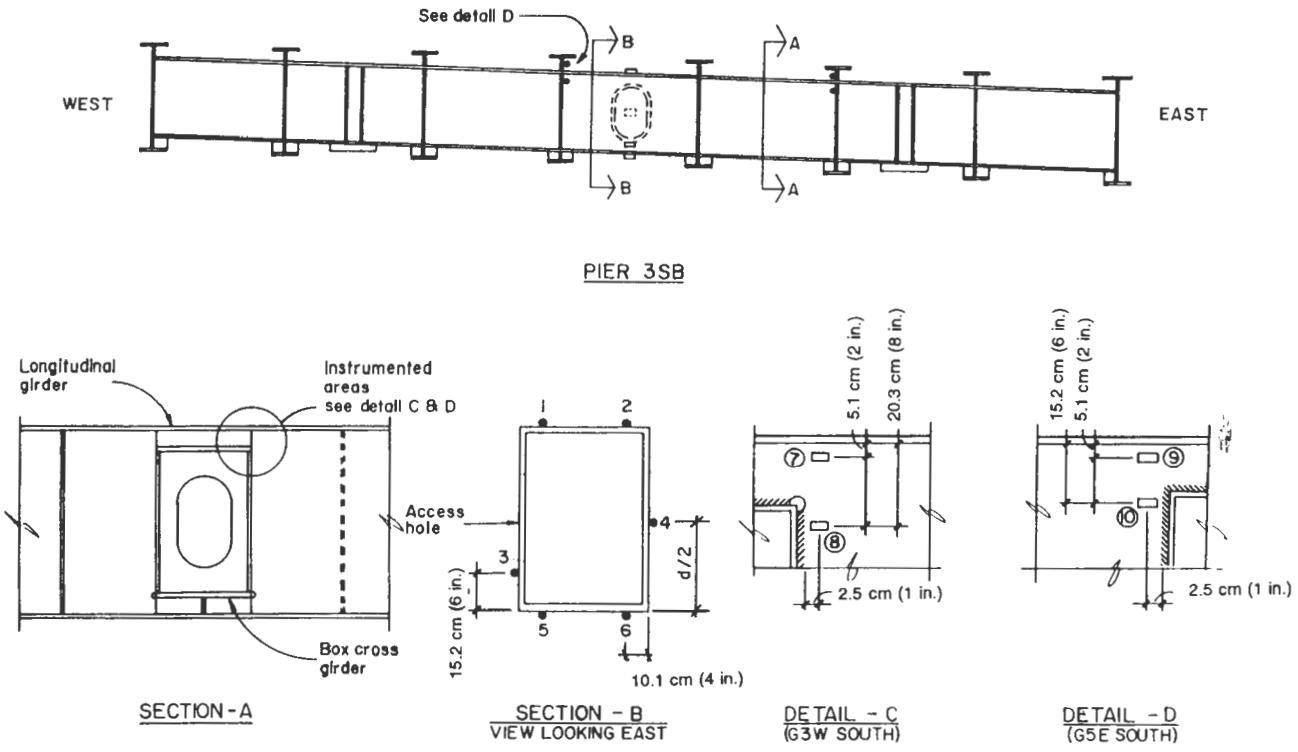

FIGURE 8 Strain gauge layout on cross-girder at southbound Pier 3.

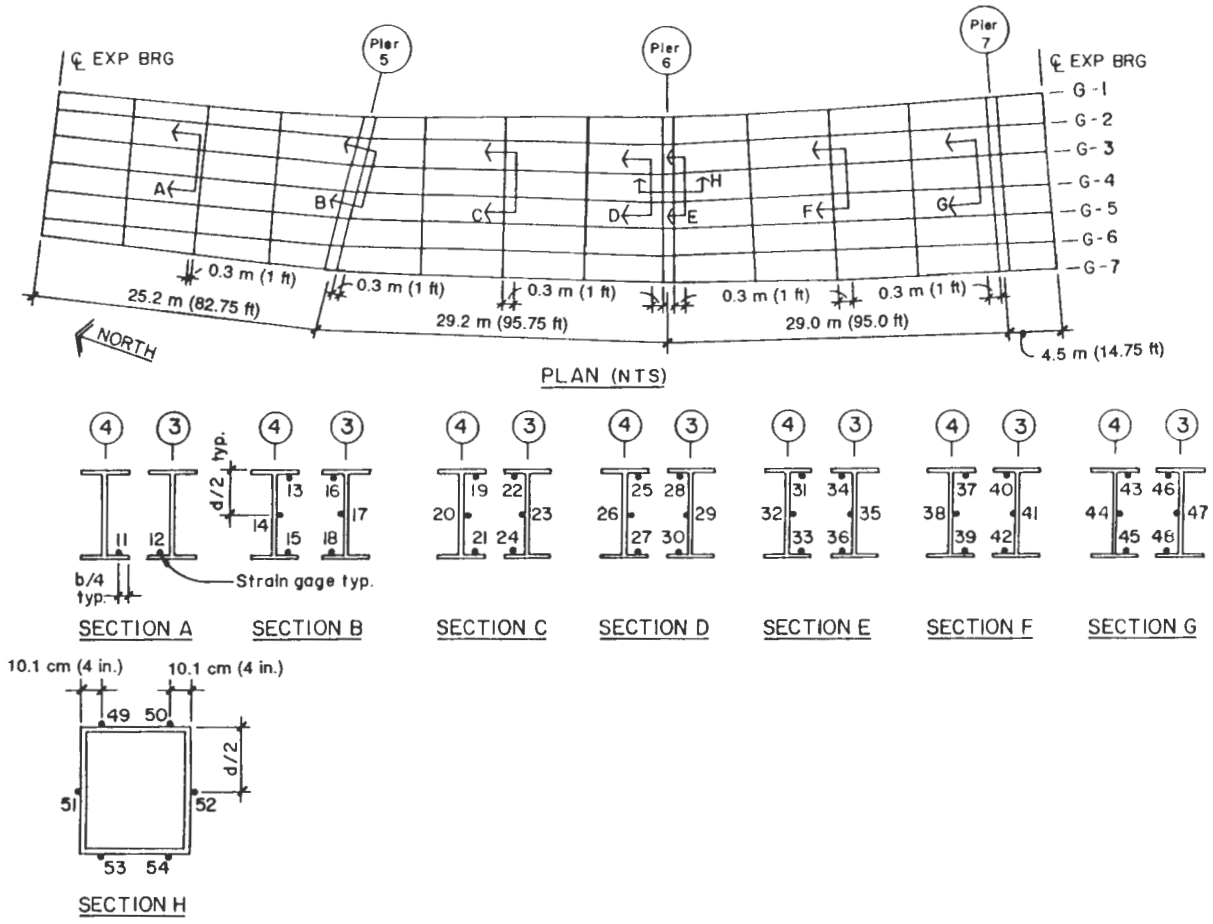

FIGURE 9 Strain gauge layout on longitudinal girders in northbound Spans 4–5 through 6–7.

TABLE 2 Maximum Measured Stress Ranges*

Gage	Stress Range MPa (ksi)	Gage	Stress Range MPa (ksi)
1	-6.9 (-1.0)	28	2.1 (0.3)
2	-6.9 (-1.0)	29	1.4 (<0.2)
3	9.6 (1.4)	39	-8.3 (-1.2)
4	1.4 (<0.2)	31	2.8 (0.4)
5	10.3 (1.5)	32	-4.8 (-0.7)
6	10.3 (1.5)	33	-8.9 (-1.3)
7	3.4 (0.5)	34	1.4 (<0.2)
8	16.5 (2.4)	35	1.4 (<0.2)
9	3.4 (0.5)	36	-6.2 (-0.9)
10	3.4 (0.5)	37	1.4 (<0.2)
11	23.4 (3.4)	38	8.9 (1.3)
12	20.7 (3.0)	39	24.8 (3.6)
13	-6.9 (-1.0)	40	1.4 (<0.2)
14	-8.3 (-1.2)	41	8.3 (1.2)
15	-14.4 (-2.1)	42	18.6 (2.7)
16	-8.3 (-1.2)	43	2.1 (0.3)
17	-10.3 (-1.5)	44	-2.1 (-0.3)
18	-12.4 (-1.8)	45	-10.3 (-1.5)
19	-2.8 (-0.4)	46	1.4 (<0.2)
20	22.0 (3.2)	47	2.1 (0.3)
21	28.9 (4.2)	48	-9.6 (-1.4)
22	1.4 (<0.2)	49	-12.4 (-1.8)
23	8.3 (1.2)	50	-12.4 (-1.8)
24	16.5 (2.4)	51	1.4 (<0.2)
25	2.1 (0.3)	52	1.4 (<0.2)
26	-8.9 (-1.3)	53	12.4 (1.8)
27	12.4 (1.8)	54	12.4 (1.8)

* Negative values represent compression

higher response. However, secondary effects associated with out-of-plane bending or distortion of the girder web most likely account for the increased response measured at Gauge 8.

Measured Stresses in Longitudinal Girders

The maximum tensile stress range was 28.9 MPa (4.2 ksi), measured by Gauge 21, located in the positive moment region of Span 5–6. In general, tensile stress ranges in positive-moment regions averaged 24.1 MPa (3.5 ksi), whereas tensile stress ranges measured in negative-moment regions were less than 3.4 MPa (0.5 ksi). Girder 4 experienced larger stress ranges than did Girder 3. This behavior is due to the traffic lane positions above the girders and the lateral distributions of loads across the bridge. Test data revealed composite action between the concrete deck and girders in the negative-moment region, even though shear studs were not provided.

Discussion of Results

The cross-girders used in the Moline Viaduct would be classified as nonredundant members because their failure may result in collapse of the bridge, whereas the longitudinal girder framing system is a redundant structure providing multiple load paths. The detail used to connect the two members is considered potentially fracture sensitive by an FHWA notice dated April 24, 1978. On the basis of this notice and previous research (*3–5*), the girder to cross-girder connection would be classified as Category E′ detail. Several factors were used to justify this determination: (a) connecting welds were made from both sides of the girder web plate, (b) welds were complete-penetration groove welds, (c) the tension

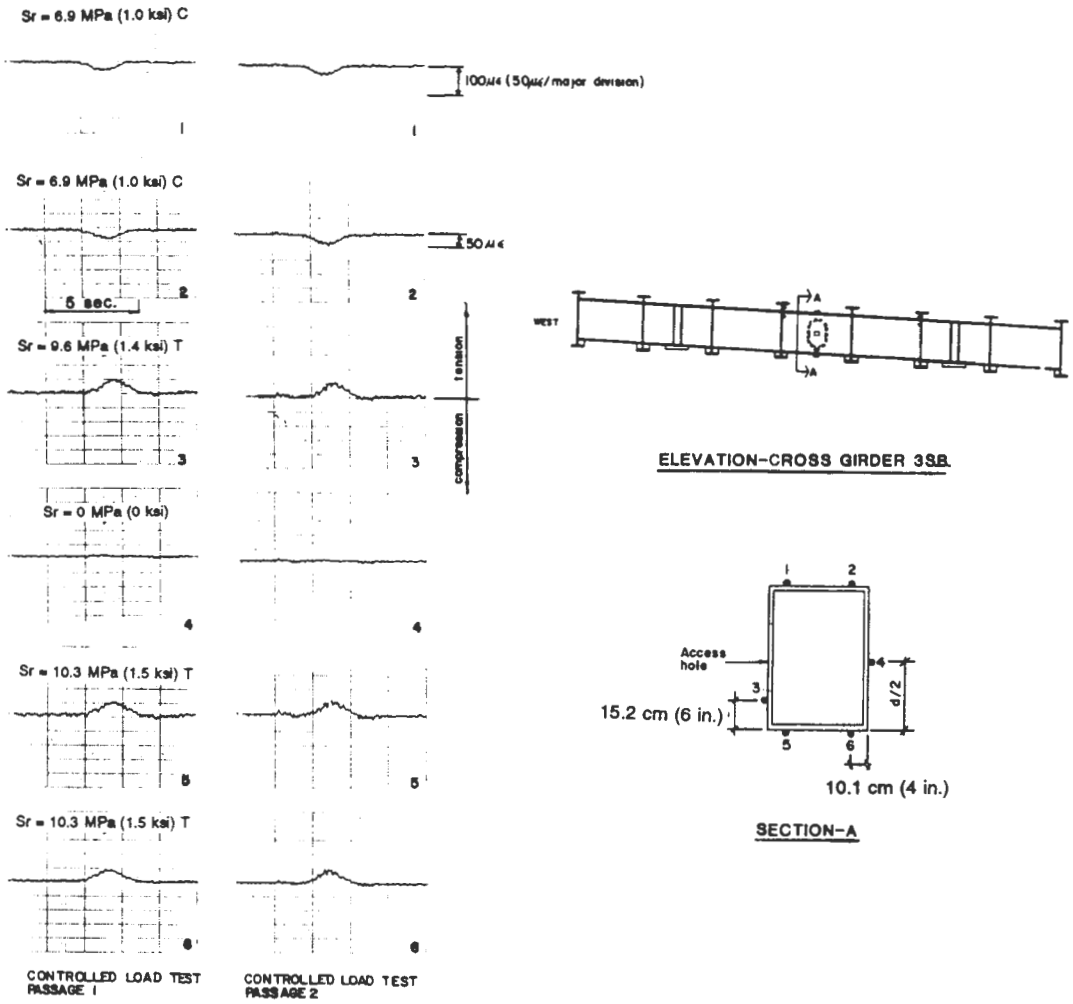

FIGURE 10 Representative strain response for cross-girder at southbound Pier 3.

flange was not welded, (d) slots were not flame cut, and (e) stress relief holes were provided at weld terminations adjacent to the cross-girder tension flange.

Welded details in the cross-girders included Category B′, Category C, and Category E details. Bearing stiffeners and diaphragms would be classified as Category C, whereas groove-welded backer bar details were Category B′ conditions. The discontinuous backer bar detail, however, created a built-in cracklike defect that was probably more severe than Category E. In addition, a number of conditions such as flame-cut gouges and temporary fabrication weldments exhibited poor workmanship and were not in compliance with current AASHTO specifications.

Girder to Cross-Girder Connections

The girder to cross-girder connection detail was exposed to a very complex state of stress resulting from member interaction at the joint, the geometry of the structural framing, welding of residual stresses, and the forces induced during erection. Cracking has occurred in the longitudinal girder web plate adjacent to corners of the cross-girder along the welds used to join the cross-girder to the longitudinal girder. No cracking was found to extend into the nonredundant cross-girder. A total of 82 (3 percent) of the 2,440 corner locations exhibited cracks. A significantly higher incidence of cracking occurred at connection locations in northbound Piers 1 through 4 where stress relief holes had been omitted. Excluding these locations, cracking was observed at 57 (2.3 percent) of the corner locations.

On the basis of inspection findings, review of project welding specifications, and field testing, cracking at the girder to cross-girder connection is believed to have resulted from several conditions that include, but are not limited to, restrained shrinkage of the large welds around the cross-girder perimeter and the forces experienced during erection of the complex curved and su-

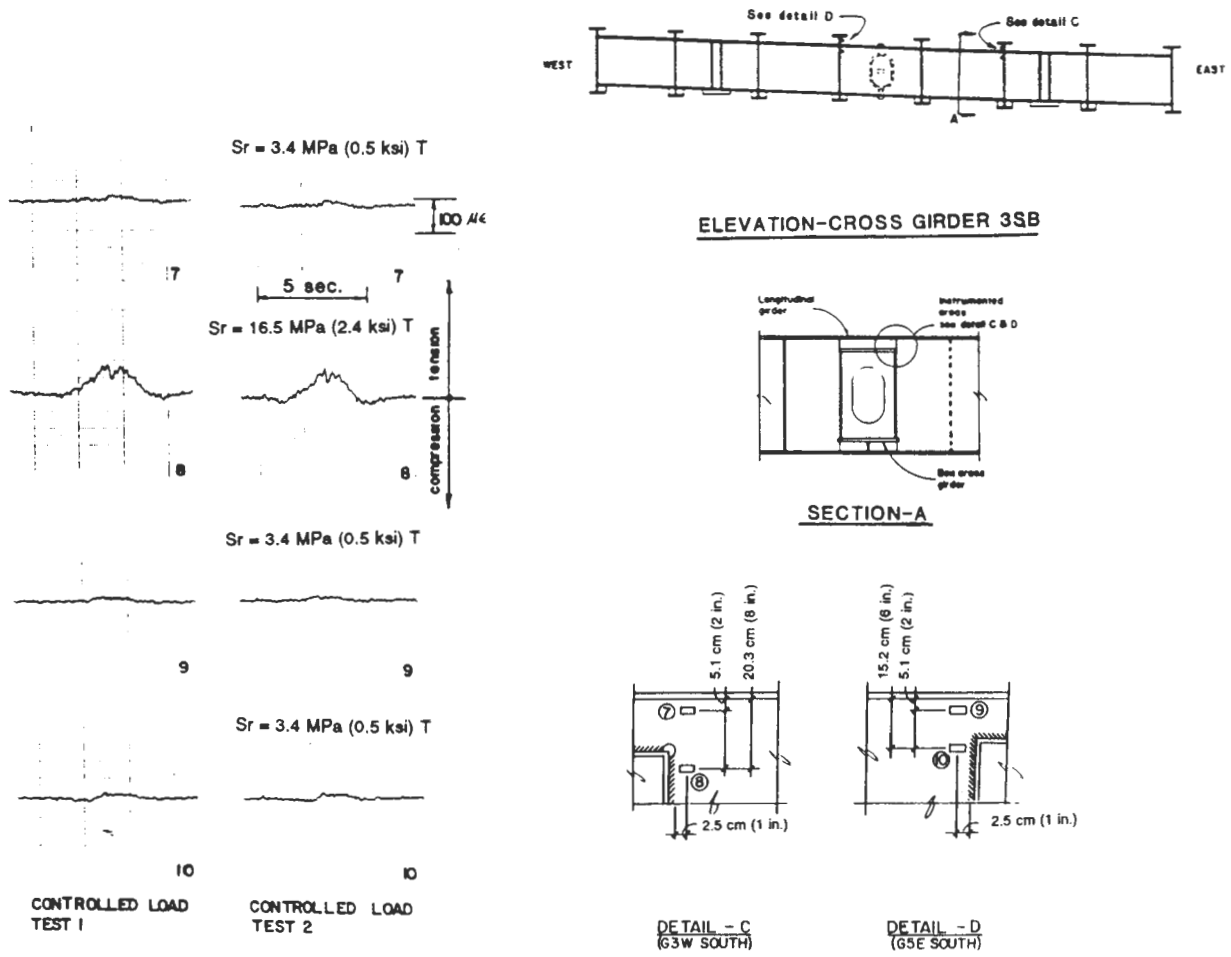

FIGURE 11 Representative strain response adjacent cracked girder to cross-girder connections.

perelevated bridge structure. This conclusion is supported by the following observations: (a) omission of stress relief holes in northbound Piers 1 through 4 resulted in a significantly higher incidence of cracking at these locations, and (b) stress levels in the connection region adjacent to the corners of the cross-girder were measured to be less than 6.9 MPa (1.0 ksi) of tension, which is at a level at which crack growth is not expected.

The fatigue resistance of a Category E′ detail is represented by the following equation:

$$N = A \cdot S_r^{-3.0}$$

where

N = estimated minimum number of cycles to failure,
S_r = allowable stress range [MPa (ksi)], and
A = constant $26.926 \cdot 10^8$ MPa ($3.908 \cdot 10^8$).

This equation is based on a statistical evaluation of available test data (*5*) and represents the lower bound of failures for the tested details. The maximum stress range at which no fatigue crack growth will occur under constant-amplitude load conditions is called the constant-amplitude fatigue limit (CAFL). The CAFL for a Category E′ detail used in a redundant load path structure is given as 17.9 MPa (2.6 ksi). A 20 percent reduction for 100,000, 500,000, and 2,000,000 cycles is generally applied to allowable stress ranges for redundant members to obtain allowable values for nonredundant load path structures. However, for lower fatigue strength details, a more substantial reduction is taken to discourage their use. For example, the CAFL for the nonredundant Category E′ detail has been reduced 50 percent to 8.9 MPa (1.3 ksi). Note that failure of a Category E′ detail used in the fabrication of a nonredundant structure will perform in accordance with the *S-N* curve for that detail without any safety factor applied. In other words, the detail behavior is not influenced by the redundant or nonredundant nature of the structure.

The maximum stress range measured in the longitudinal girder web adjacent to a crack was 16.5 MPa (2.4 ksi) of tension. At other locations the maximum measured tensile stress range was between 2.1 and 3.4 MPa (0.3 and 0.5 ksi). On the basis of a finite-element model the calculated stress ranges were between 4.8 and 6.2 MPa (0.7 and 0.9 ksi) for the control loading (6). A stress histogram was not developed to determine an effective stress range. However, observations of the 6 hr of data obtained during a normal business day and review of the average daily truck traffic suggest that an effective stress range of approximately one-half of the maximum would not be unrealistic. Considering the redundant nature of the longitudinal girder and using the maximum stress range instead of an effective stress range, it can be shown that the measured stress levels are below the Category E′ CAFL. Comparing the Category E′ CAFL with the maximum stress range is conservative and suggests that crack growth would not be expected.

Cross-Girder Fabrication

A number of fatigue-sensitive conditions and instances of poor workmanship including discontinuous backer bar joints and poor-quality connecting tack welds, flame-cut gouges, weld remnants, and welded erection aids were identified in the 49 cross-girders. However, no cracks were found to extend into the cross-girder plates. The most significant condition is represented by the discontinuous backer bar joints, which were oriented perpendicular to the tension stress field and which represented a built-in cracklike defect. No cracking was observed at the discontinuous backer bar detail; however, crack growth would not be visually notable until the crack extended beyond the backer bar.

Field testing of representative cross-girders indicated a maximum stress range of about 12.4 MPa (1.8 ksi) of tension. This stress level, although conservative since it is greater than the effective stress range, is below the crack growth threshold for a Category E detail. The CAFL for a Category E detail used in a nonredundant member is 17.2 MPa (2.5 ksi). Although crack growth is not expected, the severity of the backer bar joint may be such that a fatigue resistance lower than Category E could occur, in which case crack growth may develop.

Recommendations and Conclusions

The study described here confirmed the concerns of IDOT about the fatigue-sensitive nature of the girder to cross-girder connections and cross-girder fabrication details used in the Moline Viaduct. On the basis of findings of the in-depth inspection and field testing program, the following recommendations are provided for retrofitting the girder to cross-girder connections.

1. All existing cracks should be removed by coring. Recommended details were developed for all crack types observed. An example repair detail is shown in Figure 12. The function of the repair is to remove the entire crack and adjacent weld metal. This modification will also provide an excellent surface for future inspection.
2. The sections of material removed during retrofitting should be subjected to fractographic examination to confirm the findings of the present study. The tough-

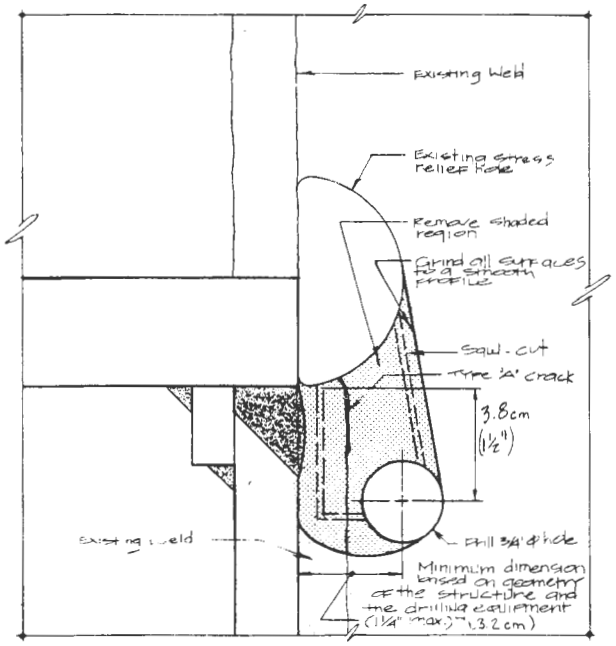

DETAIL-B

PROCEDURE

1. Drill a 1.9 cm (¾ in.) diameter hole through the girder web plate as close as possible to the web plate of the cross-girder, as shown in Detail B.
2. Remove material in shaded area by sawcutting. Grind edges to provide smooth transitions between material removed and existing stress-relief hole.
3. Remove all burrs from cut edge and grind surface to obtain a surface roughness (R_a) of 1000 or less. Grinding operation shall use 1.3 cm (½ in.) diameter or larger carbide burrs.
4. Obtain approval of Engineer before proceeding. All ground and drilled surfaces shall be checked for cracks by magnetic particle or dye penetrant testing.
5. Clean exposed steel surfaces to remove any contaminants or rusting.
6. Paint surfaces with undercoat and final coat.

FIGURE 12 Recommended retrofit for crack Type A.

ness and metallurgical properties of the removed samples should also be determined.

3. New 5.1-cm (2-in.)-diameter half-circle stress relief holes should be provided in northbound Piers 1 through 4 where stress relief holes were omitted during fabrication.

4. An on-going surveillance program should be developed and implemented to identify possible crack growth.

Recommendations for retrofitting the cross-girder are as follows:

1. All discontinuous backer bar joints located within the tension regions of the cross-girder shall be removed by coring. A 3.8-cm (1.5-in.)-diameter core hole shall be cut to encompass the groove weld and discontinuous backer bar detail. The core hole shall be checked for cracklike defects. If no defects are found, a steel plate and gasket shall be placed over the hole and held in place with a high-strength bolt.

2. Several removed cores should be subjected to metallographic examination to ensure that crack growth had not occurred at the detail.

3. Interior surfaces that have experienced corrosion should be cleaned and painted.

4. Removal of a substantial number of fatigue-sensitive details within the cross-girders is not warranted at this time. However, a 5-year surveillance program should be set up to monitor cracked backer bar tack welds, flame-cut gouges, weld remnants, welded erection aids, and so forth for possible crack growth. On the basis of field testing measurements of stress, these details are unlikely to experience crack growth.

The cracking that was observed in the Moline Viaduct appears to have occurred mainly during fabrication and erection, and because stress levels are low, little or no crack growth is expected. Retrofits were developed to eliminate cracking defects at the potentially fracture-sensitive girder to cross-girder connections. No crack extension into the nonredundant cross-girder was observed. Severe cracklike defects associated with the discontinuous backer bar are to be removed. These recommendations along with a surveillance program will ensure many more years of useful service for the Moline Viaduct.

ACKNOWLEDGMENTS

IDOT personnel were very helpful throughout the course of the study. In particular, the support of Donald Pauser, Robert Milano, and the bridge maintenance crew was invaluable. In addition, the help of Todd Ahrens and William Flannigan of the Springfield office was especially appreciated. Besides the authors, the Wiss, Janney, Elstner Associates, Inc., staff included James Donnelly, Gary Klein, Arne Johnson, Victor Monroy, Roger Pelletier, and Don Busse. Consultation with John W. Fisher and John M. Hanson was beneficial in the development of retrofit recommendations.

REFERENCES

1. Fisher, J. W. *Fatigue and Fracture in Steel Bridges, Case Studies*. Wiley-Interscience, New York, 1984, pp. 116–132.
2. *Weld Details*. Federal Highway Administration Notice, N5140.13. FHWA, U.S. Department of Transportation, April 24, 1978, 2 pp.
3. Fisher, J. W., H. Hausammann, M. D. Sullivan, and A. W. Pense. *NCHRP Report 206: Detection and Repair of Fatigue in Welded Highway Bridges*. TRB, National Research Council, Washington, D.C., 1979, 85 pp.
4. Fisher, J. W., B. H. Barthelemy, D. R. Mertz, and J. A. Edinger. *NCHRP Report 227: Fatigue Behavior of Full Scale Welded Bridge Attachments*. TRB, National Research Council, Washington, D.C., 1980, 47 pp.
5. Keating, P. B., and J. W. Fisher. *NCHRP Report 286: Evaluation of Fatigue Tests and Design Criteria on Welded Details*. TRB, National Research Council, Washington, D.C., 1986, 66 pp.
6. Koob, M. J., R. A. Walther, and G. T. Blake. *Evaluation of Girder to Cross-Girder Connections and Bearing Problems of the Moline Viaduct*. Wiss, Janney, Elstner Associates, Inc., 1991, 60 pp.

Improvement of Fatigue Strength of Steel Girders with Tapered Partial-Length Welded Cover Plates

Ahmed F. Hassan and Mark D. Bowman, *Purdue University*

The fatigue strength of beams with tapered cover plate ends, which were repaired with one of three methods, was investigated experimentally. Most of the test specimens were precracked before the cover plate ends were repaired. Three repair methods were investigated: a friction-type bolted splice plate connection; air-hammer peening; and a hybrid combination of the previous two, known as partial bolted splice. Although specimens repaired with the bolted splice plate connection achieved Category B design life after repair, the splice plates did not prevent subsequent crack growth. Also, splice plate thickness was found to have a large influence on crack growth rate. Air-hammer peening was found to be effective in increasing the fatigue life of noncracked cover plate ends and details with small initial cracks. The partial bolted splice repair method was found to significantly improve the fatigue strength of precracked details, although it was not effective in preventing subsequent crack growth.

Cover plates have been widely used to increase the flexural capacity of steel bridge girders at high moment locations. Although cover plates could be riveted, bolted, or welded to the beam member, welding has been widely used in the more recent past because of fabrication simplicity. Welded cover plate ends are known to have a low fatigue resistance and are classified in the AASHTO specifications (*1*) under Categories E and E′.

A particular detail that has been utilized in many of the highway bridges in Indiana, as well as in many other states, involves a partial-length cover plate with a tapered end that is welded to the beam flanges. This paper discusses an experimental evaluation of the fatigue strength of tapered cover plate details repaired using one of three techniques: a friction-type bolted splice plate connection, air-hammer peening, and a combination of the previous two known as a partial bolted splice connection.

Experimental Program

The following sections discuss briefly the design variables, fabrication, experimental procedures, and repair methods used in this study. A more detailed discussion can be found elsewhere (*2*).

Design Variables

Thirty-three W14 × 30 beam specimens were cyclically tested using constant-amplitude load control. A single 245-kN (55-kip) actuator was used in conjunction with

a spreader beam to apply a pair of loads to the top of the beam. The loads were 610 mm (2 ft) apart and were applied in the middle of the 4.88-m (16-ft) span, 457 mm (18 in.) from the cover plate ends.

The beam configuration and specimen dimensions are shown in Figure 1*a*. Tapered cover plates 1.52 m (60 in.) long and 13 mm (0.5 in.) thick were positioned in the center of the beams and welded to both beam flanges. The welded, tapered cover plates investigated had two different widths, as shown in Figure 1*b*: the narrow cover plate (N) was 140 mm (5.5 in.) wide, and the wide cover plate (W) was 203 mm (8 in.) wide. The cover plate width at the tapered end was 51 mm (2 in.) for all cases. Three different cover plate end-weld conditions were used, as shown in Figure 1*c*: no end-weld (N), return end-weld (R), and full end-weld (F). Individual test specimens are identified by using a code that is composed of two letters and a number: the first letter refers to cover plate width (N,W); the second letter refers to end-weld detail (N,R,F); and the number refers to the test number for a given detail.

Three repair methods were investigated: a friction-type bolted splice plate connection, air-hammer peening of the weld toes at the cover plate ends, and a partial bolted splice plate connection. Two splice plate thicknesses were investigated for the bolted splice connection: 8 mm (5/16 in.) and 11 mm (7/16 in.). Only splice plates 11 mm (7/16 in.) thick were used for the partial bolted splice connection.

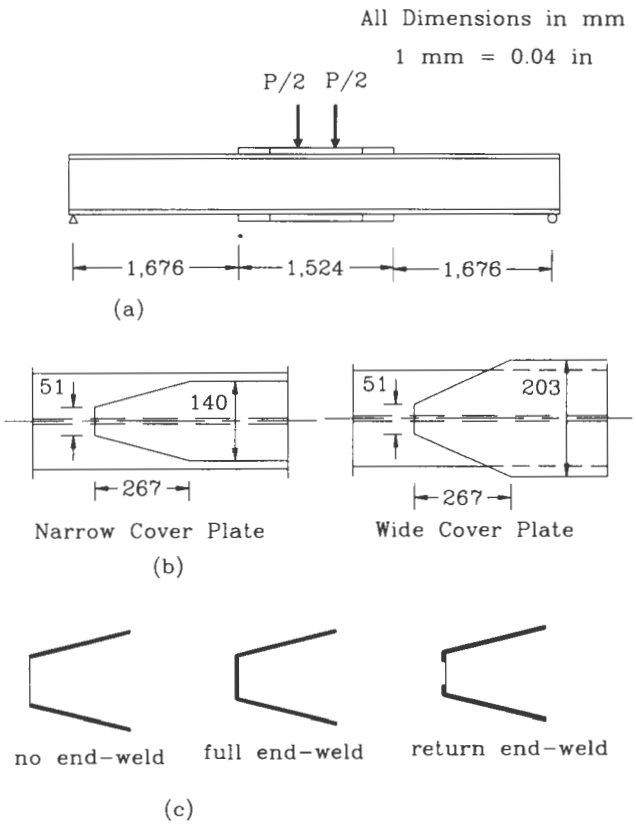

FIGURE 1 Specimen dimensions and cover plate details: (*a*) specimen configuration and dimensions; (*b*) cover plate end details; (*c*) end weld conditions.

Fabrication

All test beams and plates were fabricated from ASTM A36 steel. Eleven W14 × 30 beams 15.55 m (51 ft) long were cut to the required length of 5.03 m (16 ft 6 in.) to obtain the 33 test specimens. Ten of the eleven beams 15.55 m (51 ft) long were obtained from the same heat of steel.

Tack welds were used to hold the cover plates in position on the beam flanges. The cover plates were then manually welded to the beam flanges using the Gas Shielded Flux Cored Arc Welding Process. Flux core wires, E70T-1, 2 mm (5/64 in.) in diameter were used as electrodes to obtain the required 8 mm (5/16 in.) weld size.

Experimental Procedure

The test beams were first cycled until a visible crack was detected through either visual inspection with a 10× magnifying glass or ultrasonic detection. The precracking was achieved by subjecting the test beams to sinusoidal load cycles, with an *R*-ratio of 0.05, that produced a stress range of 138 MPa (20.0 ksi) in the bare beam section immediately adjacent to the cover plate end. When cracks were detected at only one of the two beam ends, a temporary splice plate connection, consisting of one plate 610 × 152 × 25 mm (24 × 6 × 1 in.) and two plates 610 × 51 × 25 mm (24 × 2 × 1 in.), was attached to the cracked end using eight heavy-duty C-clamps to prevent further crack growth. After fatigue cracks developed at both ends of the beam, the two cover plate ends were repaired. The loading was then resumed to evaluate the effectiveness of the repair.

Repair Methods

Bolted Splice Repair

The bolted splice repair connection, shown in Figure 2*a*, was designed to compensate for the cracked flange by assuming that the tension flange was completely severed. Using this assumption, a splice plate thickness of 8 mm (5/16 in.) was selected so that the maximum stress did not exceed 138 MPa (20.0 ksi) in the beam at the cover plate end. Because the splice plates needed to be quite long to extend beyond the taper, it was believed

that the combination of the plate flexibility and the fact that the tension flange was not completely severed (as assumed) meant that significant stresses would still exist at the cover plate end. Consequently, it was postulated that splice plates thicker than those required for the maximum stress limitation would be needed to reduce the stress at the cover plate end. To study this effect, a splice plate connection 11 mm (7/16 in.) thick was also tested.

A total of 19 specimens, with 38 end details, were repaired using the bolted splice plate connection. All of the specimens, with one exception, were precracked before the repair procedure was applied. After repair, 18 specimens were subjected to the same precracking load cycle (138-MPa stress range), while one specimen was subjected to a 103-MPa (15.0-ksi) stress range with an *R*-ratio of 0.05.

Air-Hammer Peening

Air-hammer peening introduces compressive residual stresses by striking the work piece with a hardened tool that is inserted in a pneumatic air hammer. Figure 2*b* shows a sketch of the hardened tool used for the peening procedure. The compressive residual stresses delay the initiation of fatigue cracks or the propagation of existing cracks.

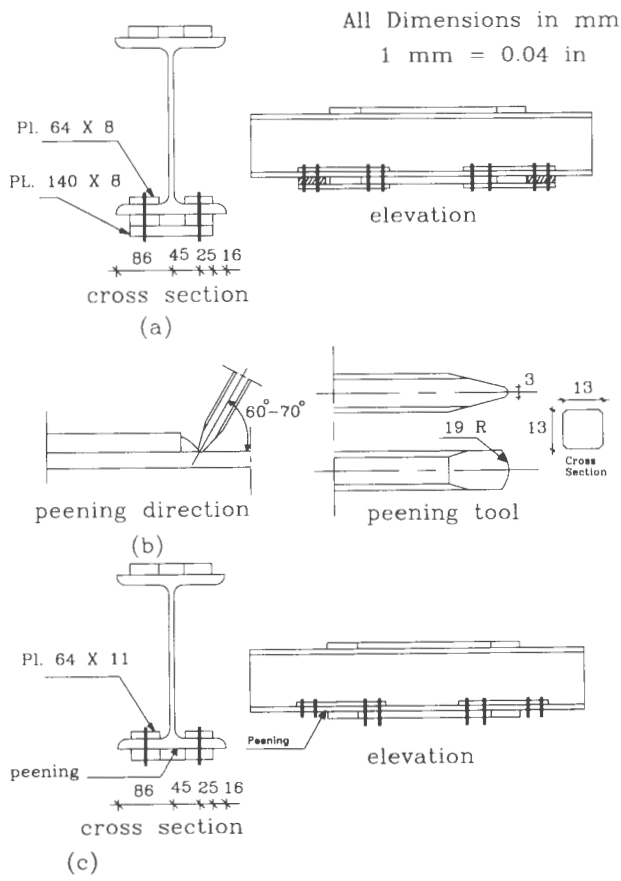

FIGURE 2 Repair methods for cover plate end welds: (*a*) bolted splice connection; (*b*) air-hammer peening; (*c*) partial bolted splice connection.

A total of eight specimens were used to study the effect of peening: five beams were peened after cracking and three were peened before cracking. The three beams peened before cracking were subjected to a 138-MPa (20.0-ksi) stress range for 75,000 cycles and then inspected to confirm that no cracks had developed. The 75,000 cycles of preloading was intended to model damage that may occur in actual bridge girders that have been in service for a number of years, but that have not yet initiated detectable cracks.

Partial Bolted Splice

The partial bolted splice repair method involves the use of both a bolted splice plate connection and air-hammer peening at the weld toe, as shown in Figure 2*c*. Only the top two splice plates, on each side of the web, are used to carry a portion of the flange force. The bottom fibers of the tension flange at the weld toe are peened to introduce compressive residual stresses.

A total of six specimens were repaired using the partial bolted splice repair, all of which were precracked before they were repaired. After repair, five specimens were subjected to the same stress cycle used during the precracking stage (138-MPa stress range), whereas one specimen was subjected to a 103-MPa (15.0-ksi) stress range with an *R*-ratio of 0.05.

Results

Bolted Splice Plate Repair Method

A previous study on the repair of beams with square-ended, welded cover plates using bolted splice plates (*3*) indicated that this detail has a fatigue life described by Category B in the AASHTO specifications (*1*). Sahli et al. (*3*) recommended that the splice plates be designed for the full design moment if the flange were precracked. On the other hand, for noncracked flanges the splice plates need to be designed only for the portion of the moment not carried by the web.

Of the 19 tapered cover plate specimens repaired with the bolted splice method, 23 ends were repaired using the 8-mm (5/16 in.) splice plate detail (all of which were subjected to a 138-MPa stress range), whereas the remaining 15 ends were repaired using the 11-mm (7/16 in.) splice plate detail (13 ends were subjected to 138-MPa stress range, and 2 ends were subjected to 103-MPa stress range). The first specimen tested was repaired with an 8-mm (5/16 in.) splice before any cracks

were initiated; at the end of 1,800,000 loading cycles after repair, both cover plate ends were inspected and no cracks were detected. The remaining 18 specimens were all precycled at 138 MPa (20 ksi) at the cover plate end until small fatigue cracks were detected at both cover plate ends. The beams were then repaired with the splice plate detail. The number of loading cycles applied to the test beam specimens after repair is given in Table 1.

All of the beams, regardless of the crack size before repair or the splice plate thickness, were able to achieve a Category B cyclic life after repair. The 18 specimens, which were subjected to a loading equal to that which caused a 138-MPa (20-ksi) stress range in the bare beam at the cover plate end, all carried 1,800,000 cycles of loading after repair without failing. Although the flanges in a number of beams fractured before reaching 1,800,000 cycles, the splice plates were able to carry the cyclic loading to achieve Category B behavior. In contrast to Sahli, et al. (3), none of the splice plates cracked during the test program. This difference in behavior can be explained by the higher flexibility of the splice plates compared with those used by Sahli et al. (3) because the splice plates needed to be long to extend beyond the cover plate taper.

Out of the 23 ends repaired with the 8-mm (5/16 in.) splice plate detail, 14 beam flanges fractured and the remaining 9 reached at least 1,800,000 cycles without the flange fracturing. For these nonfractured nine ends, four ends developed cracks in the compression flange at the cover plate end. These ends were repaired using a bolted splice plate connection or the temporary repair connection 25 mm (1 in.) thick. In both cases, the stress at the cover plate end was altered. Out of the 15 ends

TABLE 1 Number of Cycles Applied with Bolted Splice Repair

		Number of Loading Cycles		
Specimen	End	Flange Fracture[4]	Total Applied	Comments
DB1[5]	N[1]	1,375,000	1,800,000	Compression flange fractured.
	S[1]	---	1,800,000	Flange did not fracture.
DB2[5]	N[1]	951,000	1,800,000	Compression flange fractured.
	S[1]	951,000	1,800,000	Compression flange fractured.
DB3[5]	N[1]	---	1,800,000	Flange did not fracture.
	S[1]	---	1,800,000	Flange did not fracture.
NR1	N[1]	1,564,000	2,000,000	Hole drilled in web at crack tip.
	S[1]	2,000,000	2,000,000	
NR2	N[2]	2,000,000	2,500,000	Compression flange fractured.
	S[2]	---	2,500,000	Flange did not fracture.
NR3	N[2]	---	3,000,000	Flange did not fracture.
	S[2]	1,883,000	3,000,000	Compression flange fractured.
NR4	N[2]	---	2,000,000	Flange did not fracture.
	S[2]	---	2,000,000	Flange did not fracture.
NR8[3]	N[2]	10,782,000	10,782,000	Compression flange fractured.
	S[2]	7,134,000	10,782,000	Compression flange fractured.
NN1	N[1]	---	1,800,000	Flange did not fracture.
	S[1]	1,333,000	1,800,000	Compression flange fractured.
NN2	N[1]	---	1,800,000	Flange did not fracture.
	S[2]	995,000	1,800,000	Compression flange fractured.
NF1	N[1]	1,049,000	1,800,000	Two holes in web at crack tip.
	S[1]	1,179,000	1,800,000	Two holes in web at crack tip.
NF2	N[1]	1,095,000	1,800,000	Hole drilled in web at crack tip.
	S[2]	1,457,000	1,800,000	Compression flange fractured.
NF3	N[1]	1,680,000	1,800,000	
	S[2]	---	1,800,000	Flange did not fracture.

TABLE 1 Continued

Specimen	End	Number of Loading Cycles: Flange Fracture[4]	Number of Loading Cycles: Total Applied	Comments
WF1	N[2]	1,744,000	1,800,000	Hole drilled in web at crack tip.
	S[1]	900,000	1,800,000	Two holes in web at crack tip.
WF2	N[1]	1,485,000	1,800,000	Hole drilled in web at crack tip.
	S[1]	1,315,000	1,800,000	Hole drilled in web at crack tip.
WF3	N[1]	1,324,000	1,800,000	Hole drilled in web at crack tip.
	S[2]	---	1,800,000	Flange did not fracture.
WR1	N[1]	1,174,000	1,800,000	Hole drilled in web at crack tip.
	S[1]	1,495,000	1,800,000	Hole drilled in web at crack tip.
WR2	N[1]	1,561,000	1,800,000	Hole drilled in web at crack tip.
	S[2]	---	1,800,000	Flange did not fracture.
WR3	N[2]	---	1,800,000	Flange did not fracture.
	S[1]	1,211,000	1,800,000	Hole drilled in web at crack tip.

[1] 8-mm (5/16-in) splice repair connection.

[2] 11-mm (7/16-in) splice repair connection.

[3] Specimen subjected to 103-MPa (15.0-ksi) stress range.

[4] Dash indicates flange did not fracture.

[5] NR type specimen; different heat of steel.

repaired with the 11-mm (7/16 in.) splice plate detail, only one beam flange fractured. Six ends developed fatigue cracks in the compression flange at the cover plate end.

Figure 3 shows the stress range versus the number of loading cycles applied after repair for the bolted splice repair detail. The number of loading cycles corresponds to the end of test, tension flange fracture, or repair of the compression flange using a splice connection, whichever occurred first. The test results are scattered around the number of loading cycles for a Category B design life.

Figure 4 compares the number of loading cycles applied after repair of the precracked flange until fracture of the flange or end of test, whichever occurred first, versus beam end type for 18 of the 19 beams tested (138-MPa stress range tests only are shown). When the compression flange fractured and was repaired with a splice plate, the number of cycles to compression flange repair was used. (After repair of the compression flange, the stress in the tension flange was altered; however, these details still sustained many additional cycles of loading.) It can be seen that all of the NR- and NN-type beams sustained more loading cycles than the Category B design life without the beam tensile flanges fracturing (disregarding specimens with compression flange fractures). The NF, WF, and WR beam results were scattered around the Category B design life value. Although some of the beam flanges fractured before reaching the Category B design life value, the splice plates were able to carry the load, and the tests were continued until the beams reached at least 1,800,000 cycles.

A comparison of splice plate details [8 mm (5/16 in.) versus 11 mm (7/16 in.) thick] is shown in Figure 5 for specimens tested under the 138-MPa (20.0-ksi) stress range. Again, the number of cycles to compression flange repair was used whenever appropriate. It can be seen that all beam flanges repaired with the 11-mm (7/16 in.) splice plate detail surpassed the Category B design life without fracturing (disregarding specimens with compression flange fractures). The beam flanges repaired with the 8-mm (5/16 in.) splice plate detail were not as consistent, with a number of the beam ends fracturing at load repetitions less than the Category B design value.

Figure 6 illustrates the test results reported by Sahli et al. (3) for square-ended cover plates, along with results in the present study. However, in the results reported by Sahli et al. (3), the tests were continued until failure occurred, whereas in the present study the values reported correspond only to flange fracture or compression flange repair—not failure.

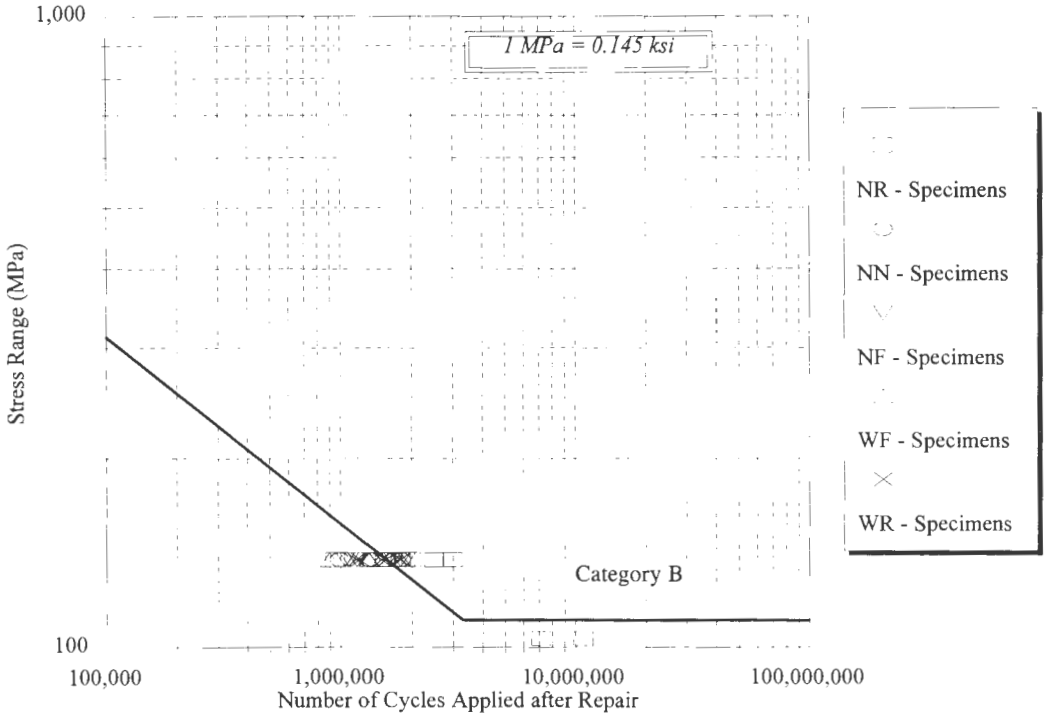

FIGURE 3 Stress range versus number of cycles applied after repair (bolted splice beams).

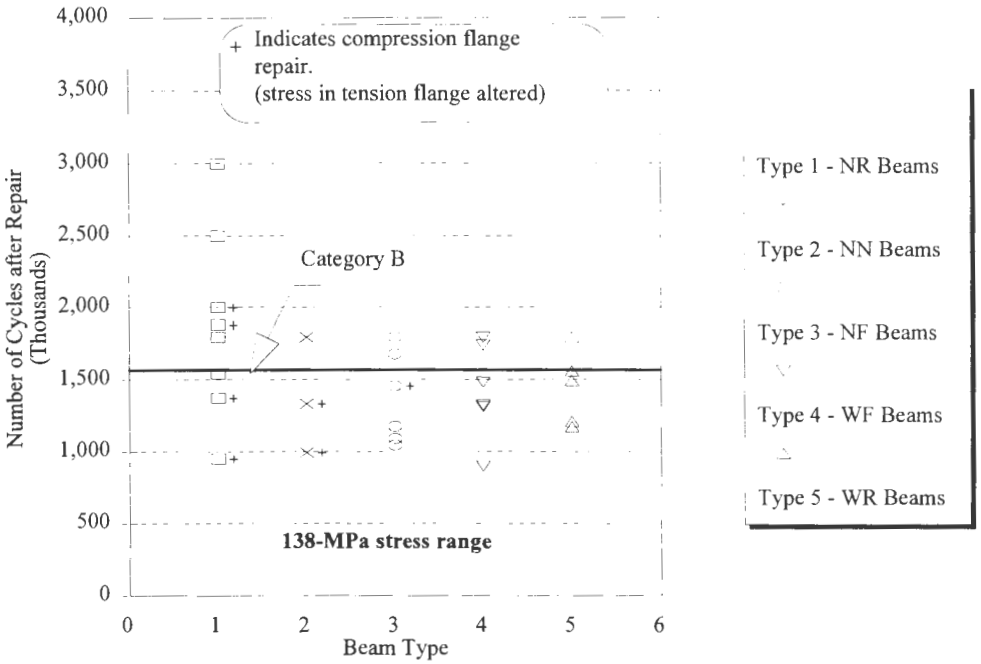

FIGURE 4 Number of loading cycles versus beam type (bolted splice beams).

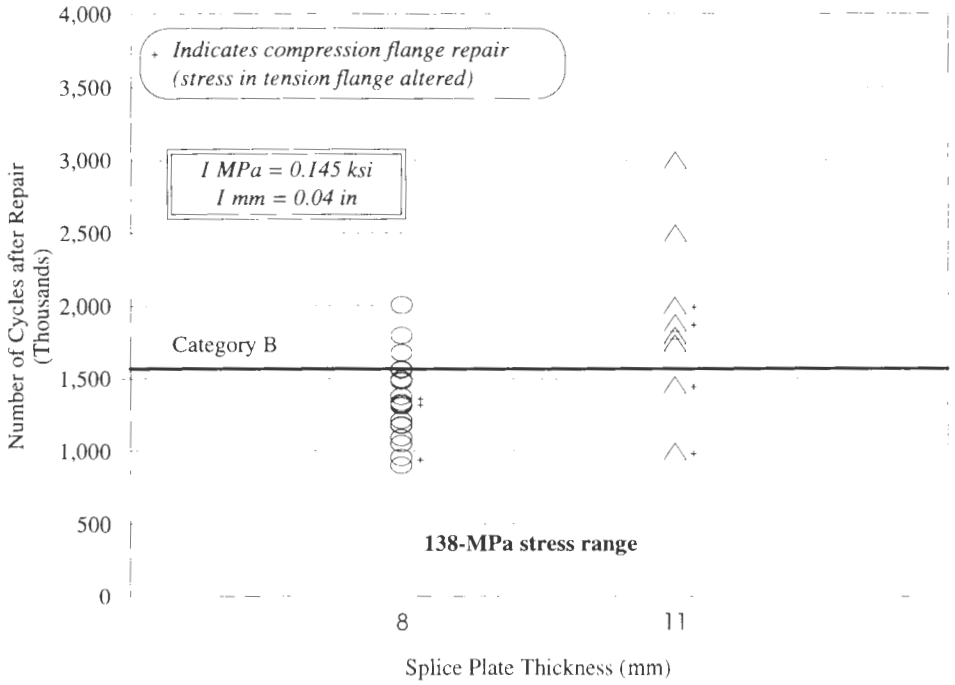

FIGURE 5 Number of cycles versus splice plate thickness.

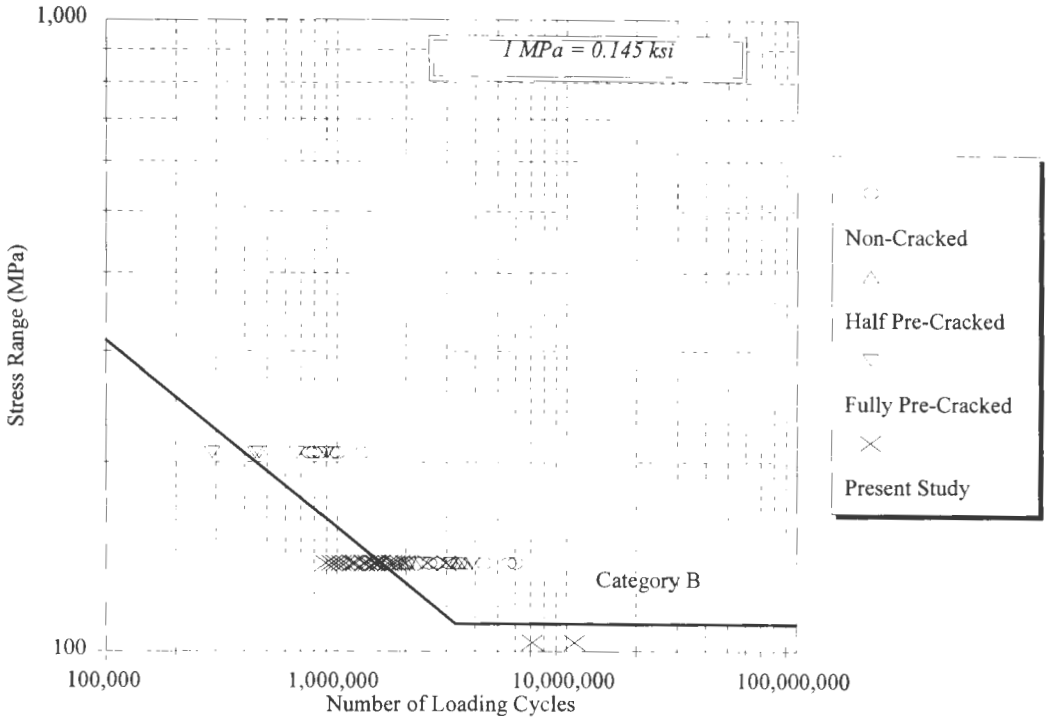

FIGURE 6 Results of comparison of tapered cover plate with square end cover plates (3).

TABLE 2 Number of Cycles Applied after Peening Repair

Specimen	End	Number of Loading Cycles to Flange Fracture	Comments
NR9	N	265,000	1-in thick plates were used.
	S	401,000	
NR10	N	506,000	
	S	436,000	1-in thick plates were used.
NF4	N	590,000	
	S	369,000	1-in thick plates were used.
WR4	N	300,000	
	S	216,000	1-in thick plates were used.
WR5	N	223,000	
	S	160,000	1-in thick plates were used.
NR5[1]	N	1,511,000	
	S	1,186,000	1-in thick plates were used.
NR6[1]	N	1,006,000	1-in thick plates were used.
	S	1,733,000	
NN3[1]	N	308,000	1-in thick plates were used.
	S	413,000	

[1] Specimen Peened after 75,000 of loading cycles, but prior to cracking.

As noted earlier, a distinct difference in the dominant failure mode was observed for the splice plates used to repair the tapered and square-ended cover plates. It is believed that this difference is attributed to the significant flexibility of the splice plate connection used with the tapered cover plate: because of differences in length, the splice plates used by Sahli et al. (*3*) were four times stiffer than those used in the present study. This higher flexibility reduces the force carried by the splice plate and, consequently, increases the stresses in the flange at the weld toe. This would explain why significant crack growth occurred in the present study, whereas little additional crack growth was observed in the tests by Sahli et al. (*3*).

Peening Repair Method

A study on the fatigue strength of beams with square-ended, welded cover plates (*4*) indicated that crack depths less than 1/8 in. could be successfully repaired using air-hammer peening. Three cases were investigated: peening of as-welded specimens (PA), peening of specimens cycled to 75 percent of the lower confidence limit (PL), and peening of specimens after detection of visible cracks (PV). Air-hammer peening increased the fatigue life of the cover plate detail from Category E to Category D for low minimum stress values.

The eight tapered cover plate specimens repaired by peening were all subjected to a 138-MPa (20.0-ksi) stress range. Five specimens were precracked before peening, whereas the remaining three specimens were cycled for 75,000 cycles before peening. The number of loading cycles applied to the test beams until fracture of the tension flange is reported in Table 2.

Figure 7 shows the stress range versus the number of loading cycles applied after repair for the five precracked beams. Considerable scatter in the fatigue life of the peened beams is evident, with the cyclic life extending from Category E (134,000 cycles) to Category C (500,000 cycles). The wide cover plate beams demonstrated the lowest fatigue life. This might be attributed to the fact that the wide cover plate beams initiated longer detectable cracks than the narrow cover plate beams. Figure 7 suggests that by peening existing cracks the fatigue life of the cover plate detail can be improved such that an additional number of loading cycles equivalent to Category D can be applied for the NR and NF beam types. An additional cyclic life equivalent only to Category E was achieved for the WR beam type.

Figure 8 shows the stress range versus the number of cycles applied after repair for the three beams peened before cracking (two NR beams and one NN beam). The test results of the two NR beams suggest that peening of noncracked beams can significantly improve the fatigue life of the detail to reach Category B′. In both

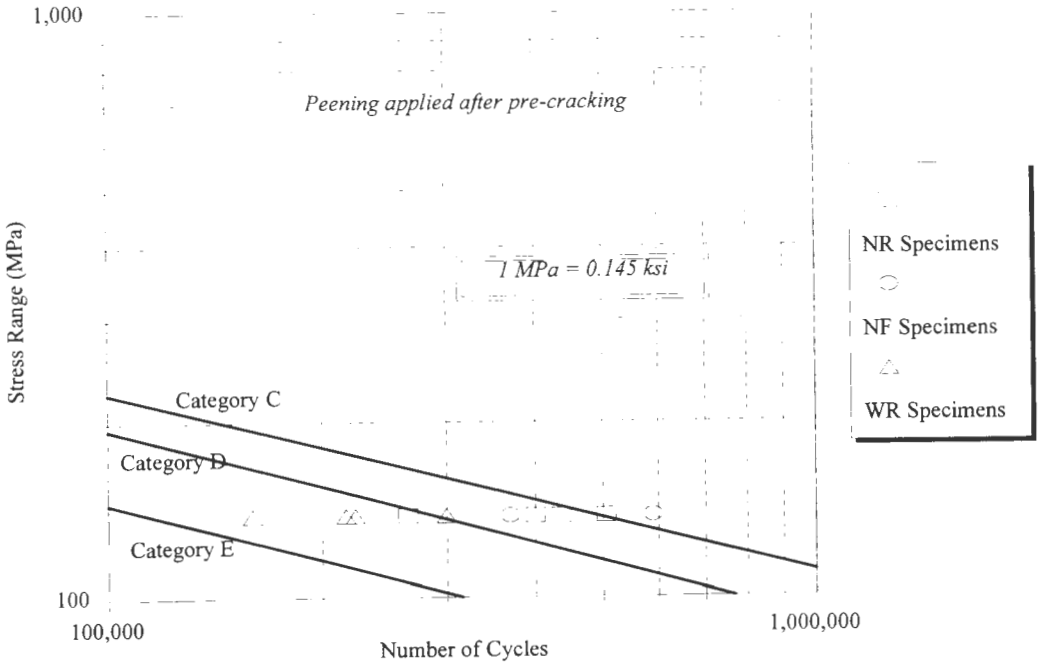

FIGURE 7 Stress range versus number of cycles applied after peening (precracked peening beams).

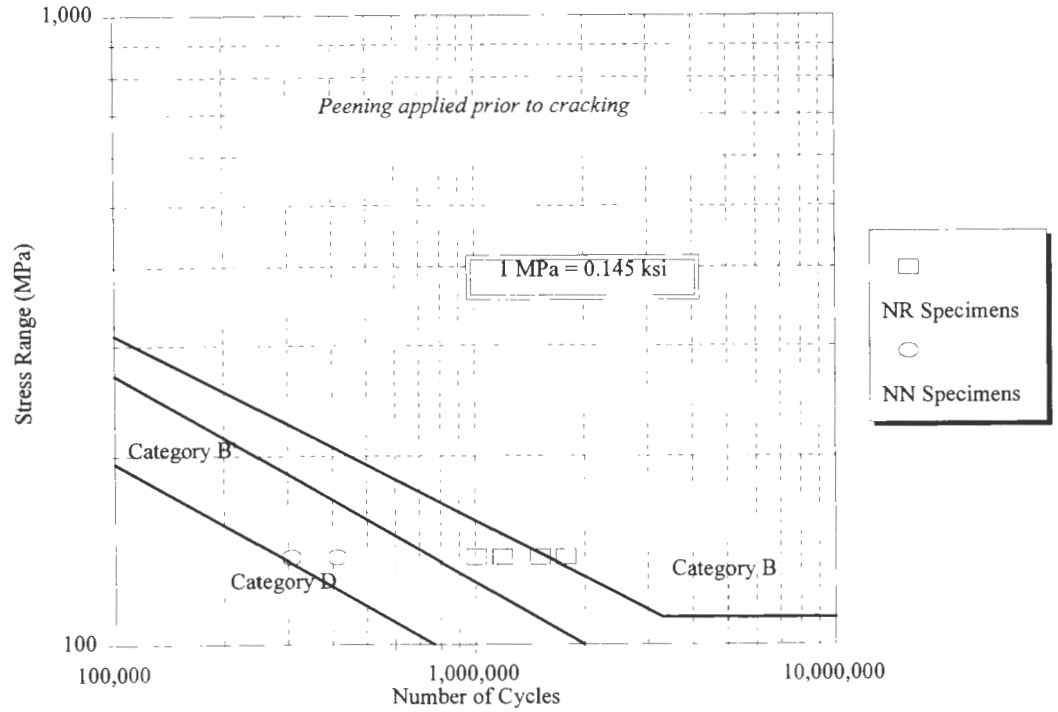

FIGURE 8 Stress range versus number of cycles applied after peening (noncracked peening beams).

beams, the fatigue cracks propagated through the weld, cutting the weld return into two parts. Fatigue cracks in most of the other test specimens initiated at the weld toe, rather than at an interior weld location. The change in crack location demonstrates the effectiveness of the compressive residual stress, induced at the weld toe by peening, in extending the fatigue life.

The NN specimen reached the fatigue design life of Category D only. The no end-weld detail is significantly different from the return and full end-weld details. The welds in the latter details are fully accessible to treatment by peening, whereas the weld end in the no end-weld detail is difficult to peen in those regions adjacent to the tapered cover plate. Also, cracks in the no end-weld details can propagate under the cover plate which is not accessible to peening. Thus, peening is expected to be less effective in the case of the no end-weld detail.

The results of the 24 peened beams tested by Fisher et al. (*4*) are shown in Figure 9, along with the results of the eight peened beams from the present study. Using linear regression analysis of the data by Fisher et al. (*4*), the average fatigue life for the PA, PL, and PV specimens tested at a 138-MPa (20.0-ksi) stress range was found to be about 353,700 cycles, 217,300 cycles, and 211,000 cycles, respectively. The average fatigue life from the present study, however, was about 352,000 cycles for specimens peened after the detection of visible cracks, and 1,369,000 cycles for specimens peened after 75,000 cycles of loading but with no initial cracks that could be detected visually.

Partial Bolted Splice Plate Repair Method

All six beams repaired with the partial bolted splice were precracked before repair. Five beams were subjected to a 138-MPa (20.0-ksi) stress range, whereas the remaining beam was subjected to a 103-MPa (15.0-ksi) stress range. The tension flange in most specimens fractured, although two ends developed fatigue cracks in the compression flange at the cover plate end. The number of loading cycles applied to the test beams after repair is indicated in Table 3.

Figure 10 shows the stress range versus the number of loading cycles applied after repair for the six beams. Considerable scatter in the fatigue life of WR beams repaired with the partial bolted splice technique is evident, with the cyclic life extending from Category C (500,000 cycles) to higher than Category B (1,500,000 cycles). The narrow cover plate beams exhibited a fatigue life greater than Category B′ design life. Although the flange may have fractured, the detail was still capable of sustaining some additional loading cycles; one specimen sustained 874,000 cycles after the flange fractured. The cracks, however, kept growing at a relatively high rate—higher than that for the bolted splice plate

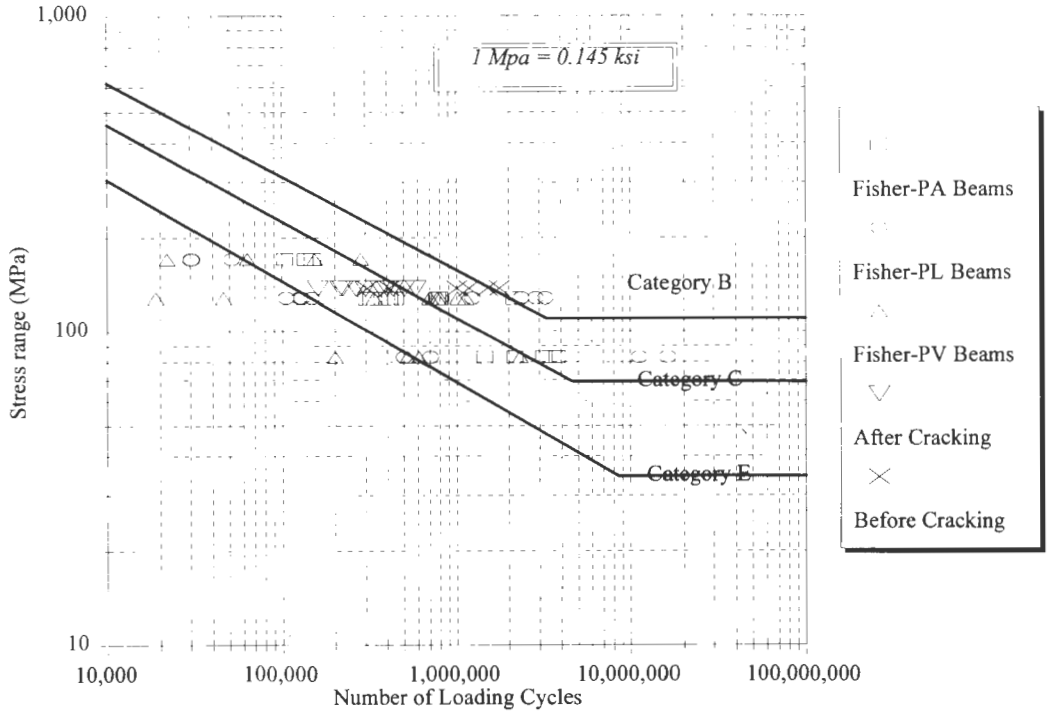

FIGURE 9 Comparison of test results with those of Fisher et al. (*4*).

TABLE 3 Number of Cycles Applied with Partial Bolted Splice Repair

Specimen	End	Number of Cycles: Flange Fracture[2]	Number of Cycles: Total Applied	Comments
NR11	N	---	1,898,000	Flange did not fracture.
	S	1,480,000	1,898,000	Two holes drilled in web at crack tip.
NR12	N	1,347,000	1,800,000	Two holes drilled in web at crack tip.
	S	1,234,000	1,800,000	Two holes drilled in web at crack tip.
WR6	N	1,326,000	2,200,000	Compression flange fractured.
	S	1,326,000	2,200,000	Two holes drilled in web at crack tip.
WR7	N	631,000	1,313,000	Two holes drilled in web at crack tip.
	S	604,000	1,313,000	Two holes drilled in web at crack tip.
NF5	N	1,111,000	1,152,000	Hole drilled in web at crack tip.
	S	800,000	1,152,000	Two holes drilled at web crack tip
NR7[1]	N	8,340,000	8,340,000	
	S	6,540,000	8,340,000	Compression flange fractured.

[1] Specimen subjected to 103.42-MPa (15.0-ksi) stress range.
[2] Dash indicates flange did not fracture.

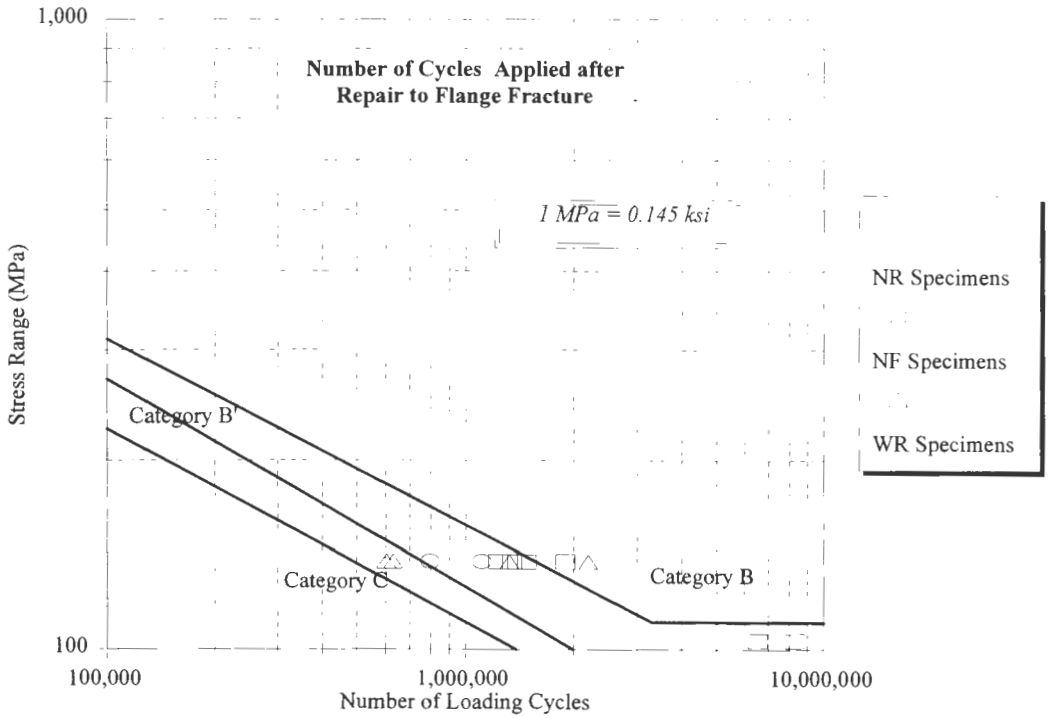

FIGURE 10 Stress range versus number of loading cycles (partial bolted splice beams).

repair method. Also, it should be noted that intentional efforts were made to slow crack growth in the beam web by drilling a hole through the web to eliminate the crack tip. In some cases, an additional hole was required when the crack propagated beyond the first web hole.

Conclusions

Thirty-three W14 × 30 steel sections were tested to examine the fatigue strength of beams with welded partial-length, tapered cover plates that have been repaired. Three repair methods were examined: a friction-type bolted splice plate connection, air-hammer peening, and a combination of the previous two known as partial bolted splice connection. On the basis of the experimental test results and corresponding observations, the following conclusions can be stated:

1. Neither the 8-mm (5/16 in.) nor the 11-mm (7/16 in.) bolted splice plates completely prevented subsequent crack growth, except for the case of repair before crack initiation.
2. Splice plate thickness has a large influence on crack growth rate. Thicker plates decrease the stresses in the beam flange and, consequently, decrease the growth rate.
3. Both the 8-mm (5/16 in.) and the 11-mm (7/16 in.) splice plates significantly improved the fatigue life of the cover plate detail. Even when the flanges fractured, the splice plates were still effective and allowed the detail to achieve a Category B design life after repair.
4. Peening is an effective method for repairing precracked cover plate end details if the crack is small—less than 5 mm long. In that case, peening can extend the fatigue life of the detail an additional number of cycles equivalent to Category D design life.
5. Peening is effective in increasing the fatigue life of noncracked cover plate ends for the return end-weld detail. Tests demonstrated that peening improves the fatigue life of the detail to a Category B′ level.
6. Peening is not recommended for the no end-weld detail. Some portions of the weld cannot be effectively peened, and resultant crack may grow under the cover plate in an unaccessible region.
7. The partial bolted splice plate repair is an effective method of repairing precracked cover plate end details. The method extends the fatigue life of the detail an additional number of cycles equivalent to Category C design life.

ACKNOWLEDGMENT

The authors acknowledge the support of the Joint Highway Research Project of Purdue University, the Indiana Department of Transportation, and FHWA for the research described herein. All tests were performed in the Kettlehut Structural Engineering Laboratory at Purdue University.

REFERENCES

1. *Standard Specifications for Highway Bridges*. AASHTO, Washington, D.C., 1989.
2. Hassan, A. F., and M. D. Bowman. *Fatigue Strength of Steel Beams with Tapered Partial-Length, Welded Cover Plates*. Final Report. Joint Highway Research Project, Indiana HPR-2047-(029). Purdue University, Nov. 1994.
3. Sahli, A. H., P. Albrecht, and D. W. Vannoy. Fatigue Strength of Retrofitted Cover Plates. *Journal of Structural Engineering*, ASCE, Vol. 110, No. 6, June 1984, pp. 1374–1388.
4. Fisher, J. W., M. D. Sullivan, and A. W. Pense. *Improving Fatigue Strength and Repairing Fatigue Damage*. Fritz Engineering Laboratory Report 358.3, Lehigh University, Dec. 1974.

After-Fracture Redundancy of Two-Girder Bridge: Testing I-40 Bridges Over Rio Grande

R. L. Idriss, K. R. White, C. B. Woodward, and D. V. Jauregui,
New Mexico State University

The I-40 bridges over the Rio Grande in Albuquerque, New Mexico, were due to be razed in the fall of 1993 because of geometry and traffic safety considerations, thus providing a unique opportunity for testing them. These medium-span steel bridges represent a common design in the United States and are classified by AASHTO as nonredundant "fracture critical" two-girder steel bridges ("fracture critical" classification means that failure of a primary member would probably cause collapse of the bridge. The subject bridge, built in 1963, is 1,275 ft (390 m) long and consists of three medium-span continuous units with spans of 131, 163, and 131 ft (40, 50, and 40 m) each. The bridge was field tested to determine the impact of a near full-depth girder fracture on the redistribution of loads, the load capacity, and the potential for collapse. Four levels of damage were introduced in the middle span of the north plate girder by making various cuts in the web and the flange of the girder. The final cut resulted in a crack 6 ft (1.8 m) deep in the 10-ft (3.1-m)-deep girder, extending from the bottom flange to the floor beam to girder connection. Data were taken under dead load and under a static live load consisting of an 82,000-lb (365,000-N) truck. The fractured bridge proved to be stable, with minimal deflection and no yielding. The after-fracture response and the load redistribution in the fractured bridge were evaluated. The contribution of the various members to the redundancy of the structure was assessed.

The I-40 bridges over the Rio Grande in Albuquerque were due to be razed in mid-1993 because of geometry and traffic safety considerations. The bridges represent a common design in the United States and are classified as nonredundant "fracture critical" two-girder steel bridges. AASHTO's Standard Specifications for Highway Bridges (*1*) defines nonredundant load path structures as "structure types where failure of a single element could cause collapse." The two-girder bridge design, using welded steel plate girders as the primary structural elements was a popular design in the 1950s and 1960s. A large number of these bridges are currently in service around the United States. These bridges have fatigue-sensitive details and are nearing the limit to their practical fatigue life. In a number of instances, cracks developed in the webs, flanges, secondary members, and connections, resulting in uncertainty about the integrity of these bridges and their safety and creating concern for the practicing bridge engineer.

Experience shows that two-girder highway bridges typically do not collapse when a fracture occurs in a girder. In many instances, they remain serviceable, and damage sometimes is not even suspected until the fracture is discovered incidentally or during inspection (*2,3*). Much still needs to be learned about the after-fracture behavior of these structures and how the load gets redistributed when fracture occurs. The main ob-

jective of the testing was to investigate the behavior of the fractured bridge and the after-fracture redundancy present in the structure. This paper reports on the redundancy present in a fractured two-girder steel bridge.

Bridge Description

The structure, built in 1963, is a 1,275-ft (390-m) long, noncomposite bridge consisting of three-span continuous units with spans of 131, 163, and 131 ft (40, 50, and 40 m) each. The structural unit is a two-girder design welded with bolted splices with a floor system (Figures 1 through 3).

Analytical Model

A preliminary analytical study (*4*) was needed for (*a*) safety consideration and (*b*) gauge placement. A three-dimensional finite element computer model of the bridge was developed (*4*). (Figure 4). A full description of the finite element model appears elsewhere (*4*). The results of this analytical study (*4*) were used to (*a*) evaluate after-fracture behavior and choose defects to implant on the bridge; (*b*) determine the sensor locations and optimize the quality and quantity of the data acquisition devices; and (*c*) calculate the load on the jacks during temporary shoring, the clearance needed at the cut, and the positioning of the truck for static loading.

The preliminary analysis of the structure with a near full-depth crack at midspan of the central span predicted a stable structure, with minimum deflections, and no yielding. The following behavior was observed:

1. Most of the load was observed to be redistributed longitudinally via the north damaged girder to the interior supports, as demonstrated by the large increase in negative moment at the interior supports after fracture (Figure 5), and
2. Some of the load was redistributed in the transverse direction to the intact girder because of the torsional rigidity of the deck, floor beam, and bracing system as shown by the increase in positive moment at midspan of the central span (Figure 6).

Bridge Monitoring: Placement of Strain Gauges

On the basis of the preliminary finite element analysis and load path evaluation, the focus of this study was on monitoring the elements that showed the most significant change in load. The following were mainly monitored:

1. The moment in the north (damaged) girder at the interior girder supports;
2. The moment in the south (intact) girder at midspan and at the interior supports;
3. Forces in the bracing at the vicinity of the crack, because the analytical model predicted a large increase in the bracing load at the crack zone;

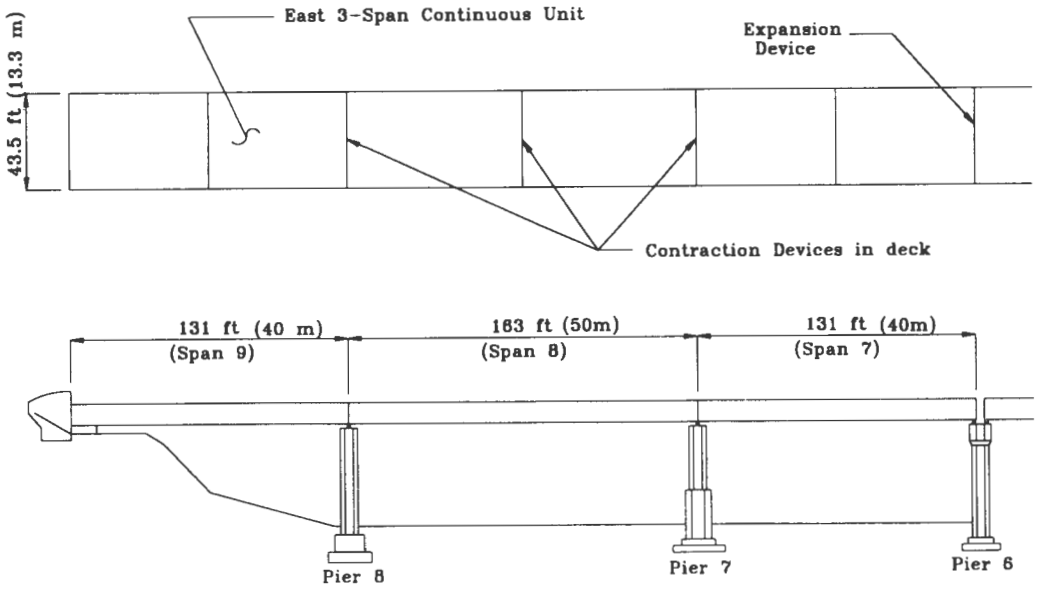

FIGURE 1 Overall plan and elevation of east three-span continuous unit of eastbound I-40 bridge.

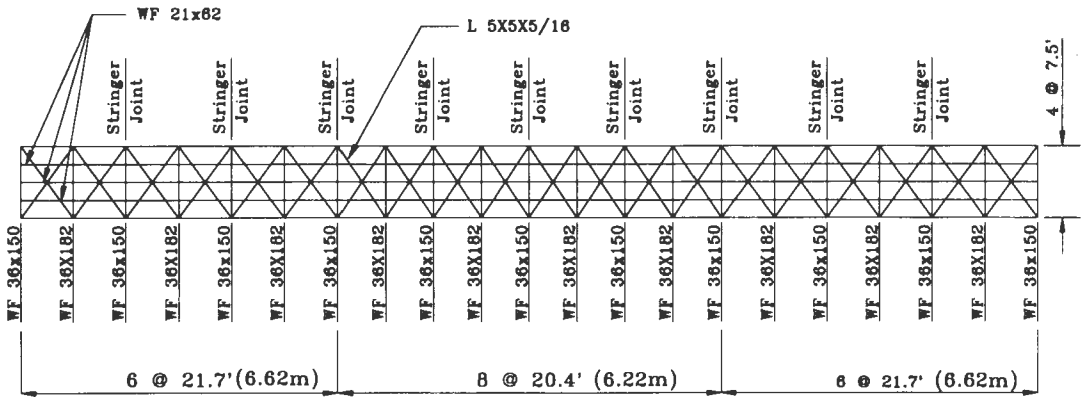

FIGURE 2 Plan view of steel superstructure below bridge deck.

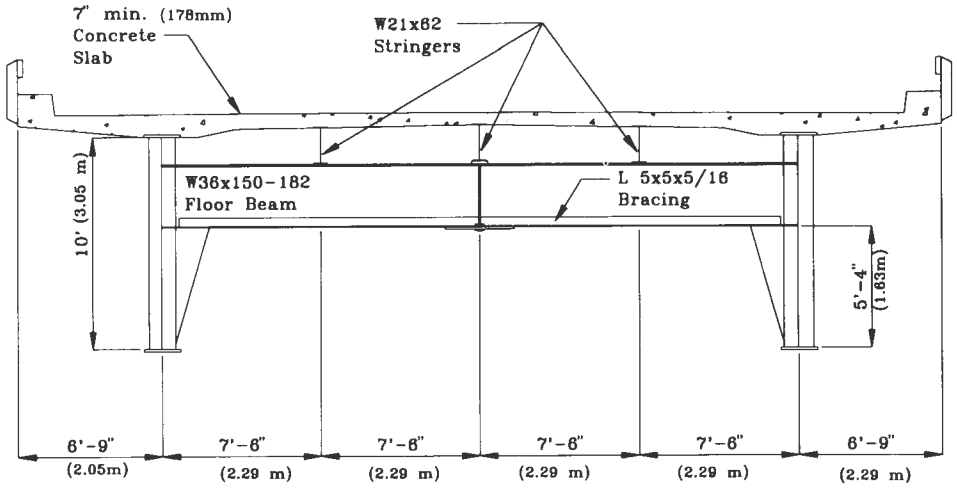

FIGURE 3 Cross section of I-40 bridge at floor beam location.

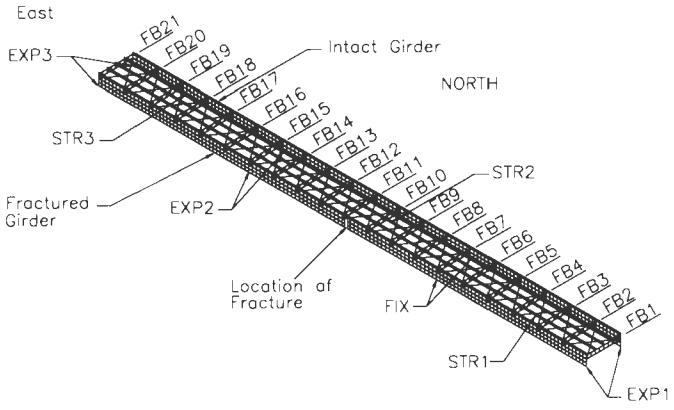

FIGURE 4 Finite element model of I-40 bridge (below reinforced concrete deck).

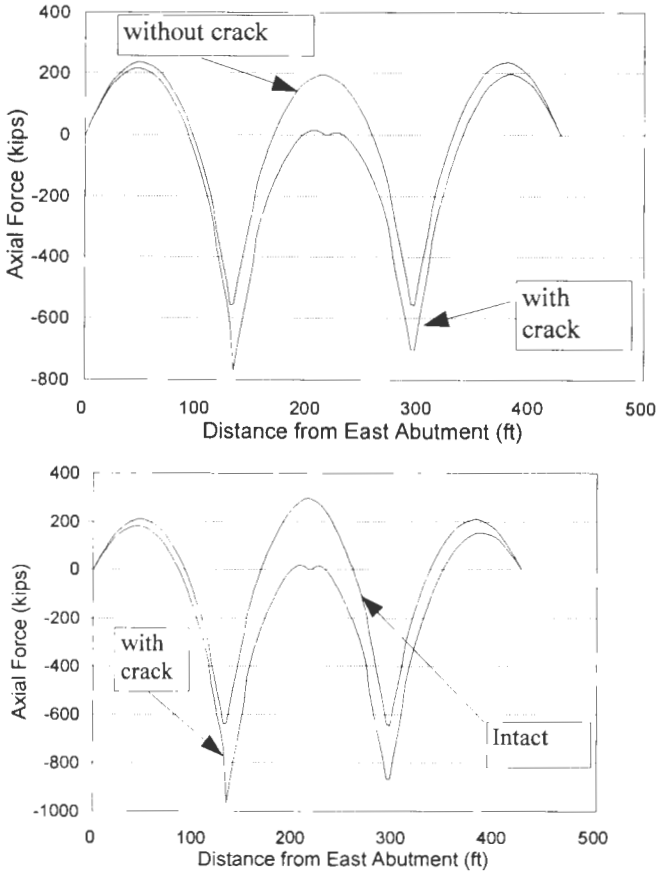

FIGURE 5 *Top*: **North girder bottom flange forces;** ***bottom*****: north girder bottom flange forces under dead load plus two HS-20 truck loadings, no impact (1 kip = 4.45 kN, 1 ft = 0.305 m).**

4. Moments in floor beams at midspan and at the connection to the intact girder. It was anticipated that the floor beams at the vicinity of the crack would transfer load to the intact girder through cantilever action and develop a negative moment at their connection to the intact girder as they cantilever toward the crack; and

5. The load increase in the stringers. For this gauges were placed on the bottom flange of the middle stringer and the stringer closest to the north girder fracture (the stringer at the most remote location to the damage was not monitored).

The strain gauge locations are shown in Figures 7 through 11. Encapsulated, self-compensated, ¼-in. (6.35-mm) metal foil gauges were used (Micro Measurements CEA-06–250UW-305). The deflection was measured at various locations on the north and south girders, particularly at midspan of the west exterior span and at midspan of the central span.

Bridge Testing (*5*)

Static Tests

A general tractor-trailer with a front-to-back axle spacing of 55.18 ft (16.82 m) and weighing 81,620 lb (363 100 N) was furnished by the New Mexico State Highway and Transportation Department for the static tests. The layout and magnitude of the wheel loads are provided in Figure 12. With this configuration, the truck was found to be 95.5 percent of the maximum New Mexico legal load and roughly equivalent to an HS-18.35 in the positive moment region of the test bridge. At this location, it gave maximum positive moment at midspan of the central span and almost maximum negative moment at the interior supports. Influence line studies were used to position the truck.

1. For maximum positive moment at midspan of the central span and almost maximum negative moment at

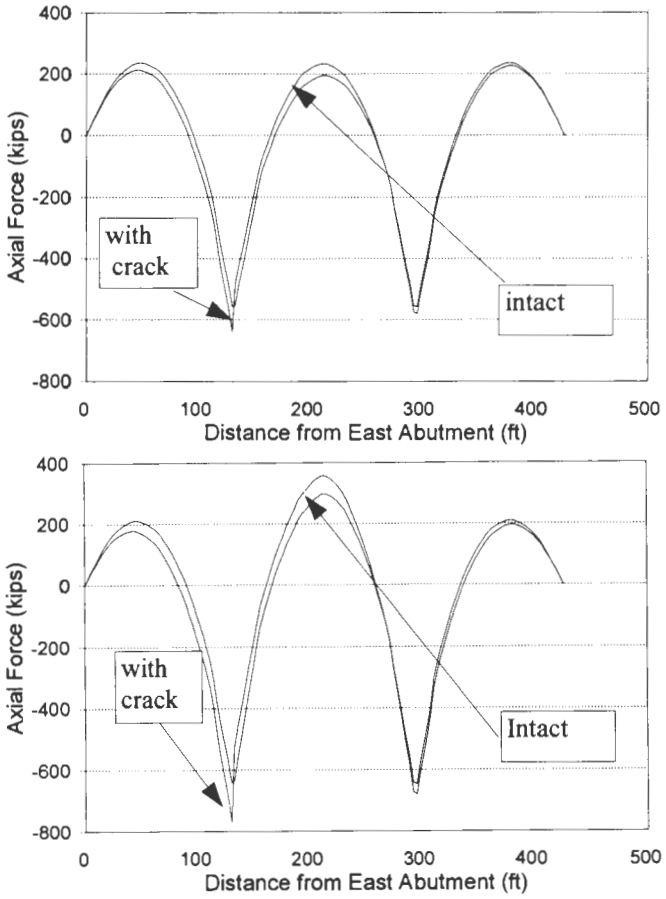

FIGURE 6 *Top*: south girder bottom flange forces under dead load; *bottom*: south girder bottom flange forces under dead load plus two HS-20 truck loadings, no impact (1 kip = 4.45 kN, 1 ft = 0.305 m).

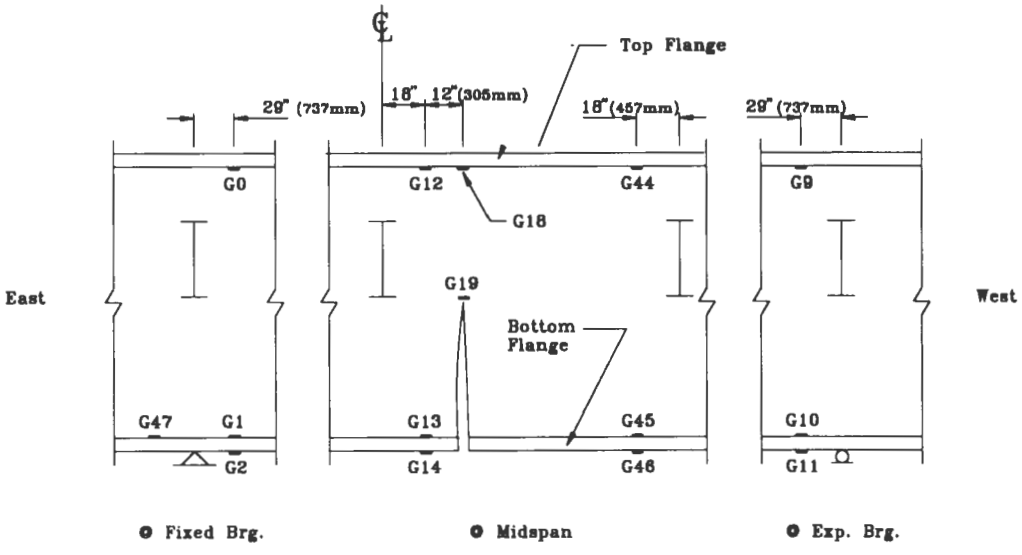

FIGURE 7 Positioning of strain gauges on north (damaged) girder (view from inside looking out).

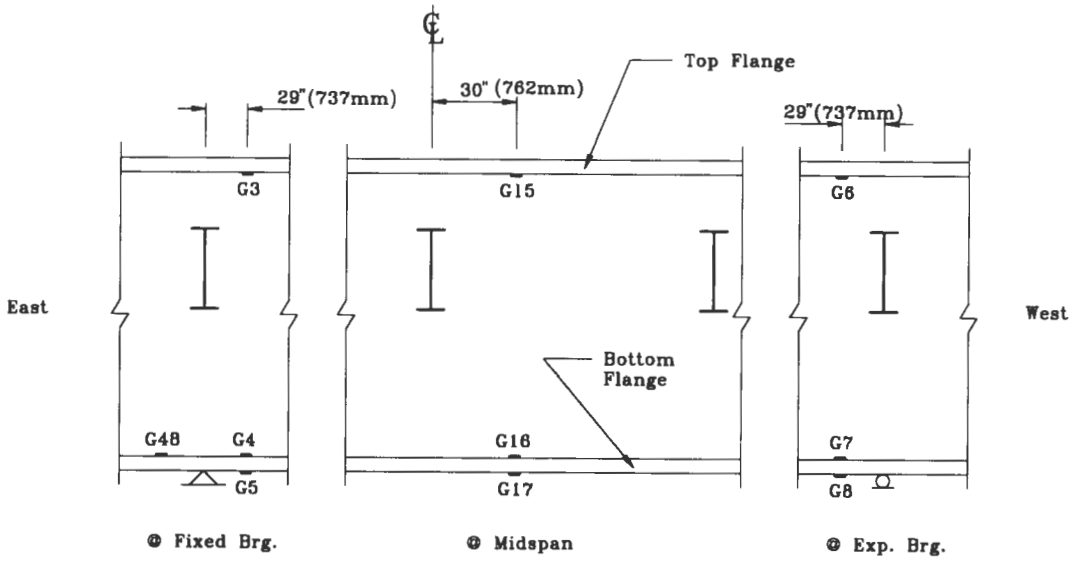

FIGURE 8 Positioning of strain gauges on south (intact) girder (view from inside).

the interior supports, the third axle of the truck was placed at midspan of the central span

2. For minimum moment at midspan of the central span and large moment at the west interior support, the third axle of the truck was placed 75 ft (22.88 m) from the west end of the three-span unit.

Strain gauge zeroing measurements were to be taken with the structure unloaded. Readings were then taken with the third axle of the truck stopped at the above-mentioned locations on the north driving lane. This general procedure was repeated for the pristine structure and for the damaged bridge at each stage of the cuts. In addition, strain readings were taken under dead load before and after the flange cuts. Deflection measurements were scheduled to be taken simultaneously with the strain readings. Temporary shoring was positioned below the cut for safety considerations. The support tower was also used for access, as a platform for jacking up the north girder to relieve stress in the bottom flange before the final flange cut and for splicing the flange cut after the testing.

Damage Description

Four different levels of damage were introduced in the middle span of the north plate girder by making various torch cuts in the web and the flange of the girder. This occurred from September 3–8, 1993. The final cut was to simulate a near full-depth crack in the girder. This type of crack, usually a fatigue crack, develops at

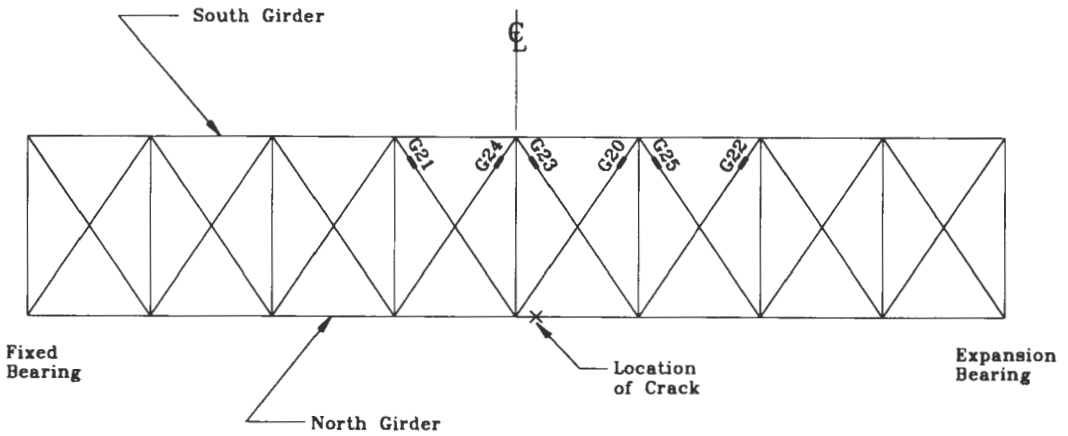

FIGURE 9 Positioning of strain gauges on lateral bracing system (top view).

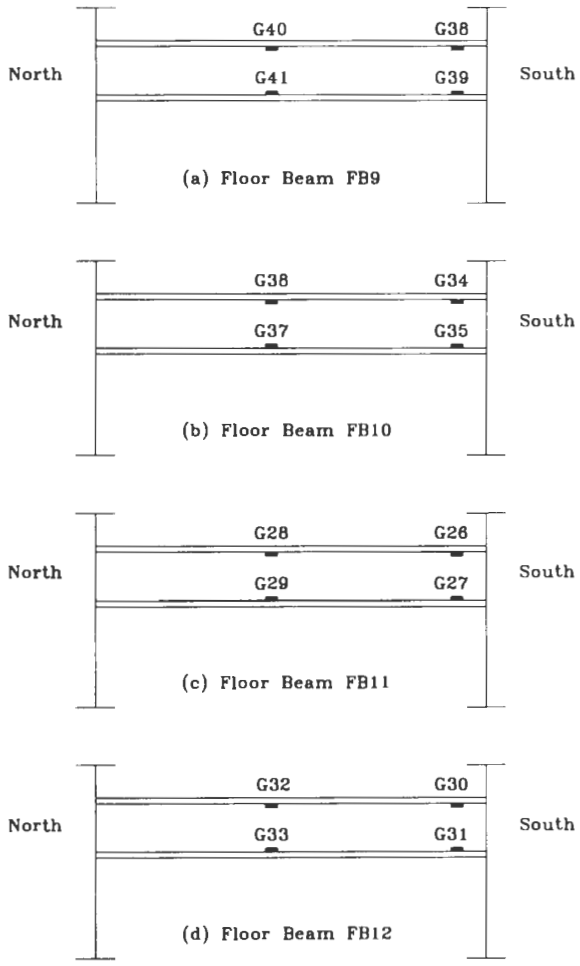

FIGURE 10 Positioning of strain gauges on floor beams.

fatigue-sensitive details in the bridge, often at the girder-to-floor beam connection because of out-of-plane bending of the web. The cut in the girder was done in four stages. Damage was to be inflicted on the bridge by a series of cuts, near midspan of the central span of the north girder 2.5 ft (0.762 m) west of the center of the bridge, midway between two vertical stiffeners. The first-stage cut was a cut in the web 2 ft (0.61 m) deep, originating at the floor beam connection level. Next the cut was continued to the bottom of the web. During this cut of the web, the web bent out of plane approximately 1 in. (25.4 mm). The third stage was to cut the flange halfway in from each side, directly below the web cut. Finally, in the fourth stage, the flange was severed completely, leaving the upper 4 ft of the web and the top flange to carry load at that location.

For the final cut, the north girder was blocked up and jacked upward ½ in. (12.7 mm) to relieve dead load stress in the flange. Computer predictions required the girder to be jacked up ¾ in. (19.1 mm) to relieve the bottom flange stress; however, the wooden blocks beneath the jacks began to crack at about ½ in. (12.7 mm). It was decided that ½ in. (12.7 mm) was enough to alleviate the force in the bottom flange and to allow a safe final cut.

The bottom flange was then severed entirely and the girder was slowly lowered until no contact existed between the jacks and the flange. The final cut resulted in a crack 6 ft (1.83 m) in the 10-ft (3.1-m)-deep girder, extending from the bottom flange to the floor beam to girder connection.

Using the support tower as a reference level, the distance to the bottom flange was measured before and after the final flange cut. The difference of the two measurements represented the added deflection of the

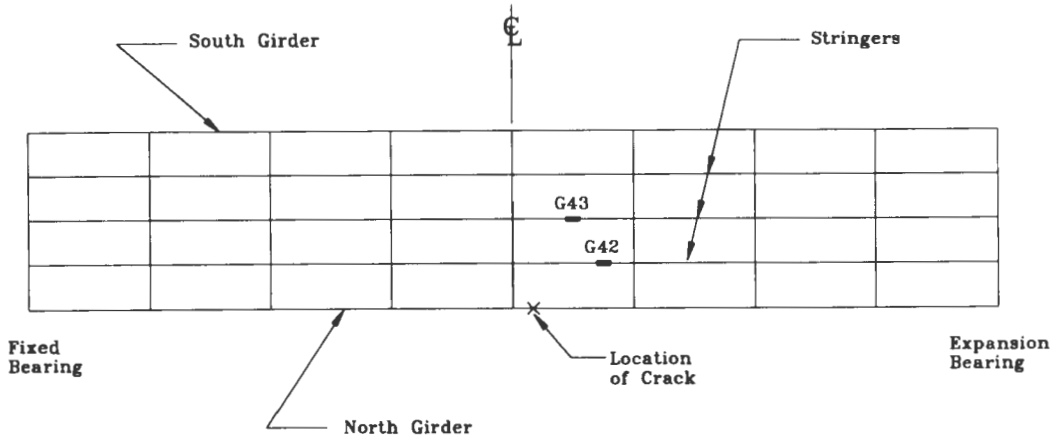

FIGURE 11 Positioning of strain gauges on stringers (top view).

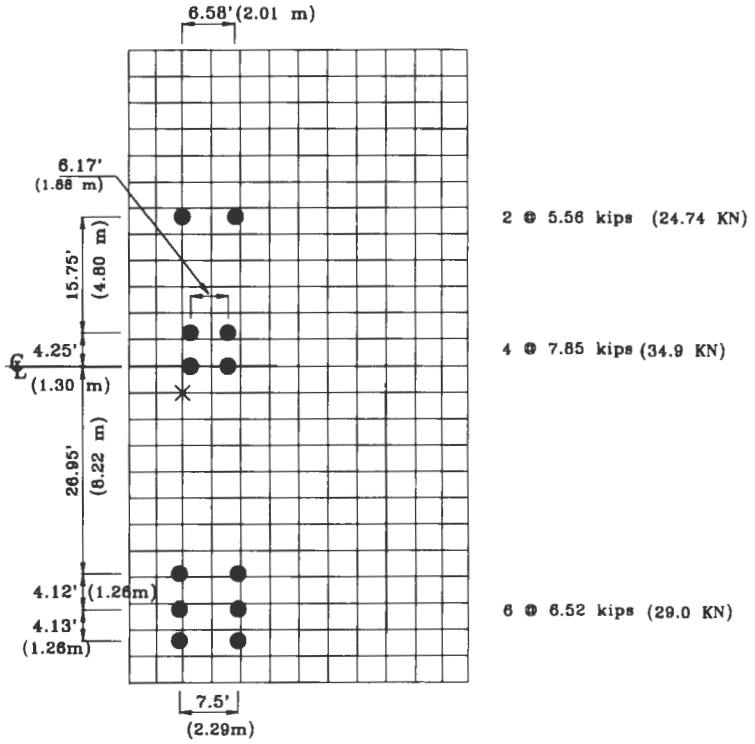

FIGURE 12 Application of HS-18.35 truck to bridge deck.

north girder caused by the mid-depth fracture under dead load. Utilizing this approach, the bottom flange of the girder at the cut deflected by only $^{11}/_{16}$ in. (17.5 mm), and the crack opened $^{3}/_{8}$ in. (9.52 mm).

When the truck was positioned above the cut, the crack opened to $^{3}/_{4}$ in. (19.1 mm) and the girder deflected by an additional $^{1}/_{2}$ in. (12.7 mm), for a total deflection under dead and live load of $1^{3}/_{16}$ in. (30.2 mm). There were no signs of yielding.

On Thursday, Sept. 9, equipment was removed from the bridge site, and the cut flange was spliced for security during the razing of the bridge.

Strain Gauge Data

There was no significant change in strains experienced by the gauged members during the various stages of damage, as shown in Tables 1 through 5 until the bottom flange was completely severed. This shows that load redistribution did not occur until the bottom flange was completely cut. The only noticeable change throughout the various phases was localized and occurred after the second web cut. During this cut, gauges G13 and G14 located on the bottom flange of the damaged girder, closest to the fracture, experienced a surge in tension (Table 1). This shows that the web plus half flange fracture did not alter the bridge stiffness enough to initiate load transfer. It is not until the flange is totally severed that the load redistribution occurs.

Load Redistribution

North (Damaged Girder)

The after-fracture strain readings show that the north girder is the dominant redundant load path. Continuity at the interior supports allowed the girder to redistribute the load longitudinally through cantilever action to the interior supports. This is shown by the significant increase in negative moment at the interior supports as shown by the surge in compression force in the bottom flange of the north girder at the interior supports. This is evident by the large negative changes in strain recorded for the gauges positioned at the fixed support (G2) and at the expansion bearing (G11) as shown in Table 1. The largest strain measured in the structure was measured at the interior supports of the damaged girder. The live load stresses measured at G2 and G11 were 1.32 ksi and 1.50 ksi, respectively. The predicted live load stress at these locations by the finite element model was at 2.0 ksi, which proved to be conservative. The predicted dead load stress (finite element model) was 13 ksi. The total dead and live load stress was 15

TABLE 1 North (Damaged) Girder: Strain Readings Under Truck Loading at Central Span in Microinches per Inch

	No Damage	1st Web Cut	2nd Web Cut	1st Flange Cut	Final Cut
Gage G2 @ Fixed Bearing	-30.9	-30.8	-31.1	-31.5	-46.2
Gage G11 @ Expansion Bearing	-35.4	-35	-35	-35.9	-51.6
Gage G13 @ cut	89.5	89.3	110	122	0
Gage G14 @ cut	87.4	87.8	133	135	0

TABLE 2 Stringers: Strain Readings Under Truck Loading at Central Span in Microinches per Inch

	No Damage	1st Web Cut	2nd Web Cut	1st Flange Cut	Final Cut
STR1 G42	-5.5	-5.0	-5.8	-6.5	2.9
STR2 G43	-0.3	1.8	1.8	1.4	14.9

TABLE 3 South Intact Girder: Strain Readings Under Truck Loading at Central Span in Microinches per Inch

	No Damage	1st Web Cut	2nd Web Cut	1st Flange Cut	Final Cut
G5 (Fixed Bearing)	-3.7	-3	-3.3	-3.2	-2.6
G8 (Expansion Bearing)	-5.5	-4.4	-4.8	-4.9	-5
G17 (Midspan)	19	18.3	17.6	17.4	23.4

TABLE 4 Floor Beams: Strain Readings Under Truck Loading at Central Span in Microinches per Inch

	No Damage	1st Web Cut	2nd Web Cut	1st Flange Cut	Final Cut
FB9 Gage G39	-1.0	-1.1	-1.1	-0.9	1.7
FB10 Gage G35	-3.9	-4	-4.5	-4.5	-6.9
FB11 Gage G27	-7.1	-7.6	-7.9	-7.9	-23.6
FB12 Gage G31	-3.8	-3.9	-3.7	-3.2	-3.3

TABLE 5 Bracing: Strain Readings Under Truck Loading at Central Span in Microinches per Inch

	No Damage	1st Web Cut	2nd Web Cut	1st Flange Cut	Final Cut
Panel East of Crack					
G21	.8	-1.6	-2.0	-2.1	-24.9
G24	28.4	26.2	28.6	30	68.0
Panel @ Crack					
G20	8.5	8.1	9.6	10.5	15.5
G23	20.8	19.2	21.2	21.5	57.0
Panel West of Crack					
G22	-16.5	-19.3	-19.8	-19.7	-58.1
G25	36.2	37.2	37.5	38.3	68.5

ksi, less than the inventory stress level recommended by AASHTO (0.55 times the yield stress) of 20 ksi.

Stringer-Deck System

After fracture, load is shed to the stringer-deck system. The after-fracture strains (Table 2) recorded for gauges G42 and G43 showed the stringers to be carrying more load. In addition, the longitudinal gauge positioned on the bridge deck showed a large surge in compression following the crack.

South Girder

The intact girder has an increase in positive moment at midspan as indicated by the positive change in strain recorded at that location by Gauge G17 (Table 3). A 20 percent increase in tension in the bottom flange at midspan was measured under live load.

Floor Beams

As predicted, the floor beams at the vicinity of the crack redistributed the load to the intact girder. The most drastic change occurred in floor beam FB11 located at the crack. It acted essentially as a cantilever beam because of the lack of support from the damaged girder. This cantilever action is demonstrated by the increase in negative moment at the connection with the intact girder as indicated by the strain measurements at that location (Table 4). Floor beam FB10, located directly west of the crack, also experienced an increase of negative moment at its south end, but not as much as floor beam FB11. The other two floor beams located in the crack zone but further away from the crack, FB9 and FB12, do not show a significant change in behavior.

Lateral Bracing System

Strain readings show a large increase in the load carried by the diagonals (Table 5). There also was a change in load patterns for the lateral bracing. The two diagonals in the bay at the crack were both in tension and experienced a drastic increase in their tensile force (strain measured after fracture was two to three times the strain measured before fracture). Because of twisting in the structure, in the panel east of the crack, one of the diagonals increased in tension while the other went from tension to compression.

Role of the Deck

Longitudinal as well as transverse load redistribution is provided by the deck. After-fracture strains recorded under dead load with the deck rosette are provided in Table 6. The table gives the results gathered during the last two stages of girder cuts. The longitudinal gauge, which was positioned on the bridge deck above the middle stringer, recorded a large surge of compression on completion of the final flange cut. The transverse gauge placed at the same location as the longitudinal gauge indicated an increase in tension in the deck. Before the crack, the deck acts as a continuous beam over the stringers in the transverse direction. When the crack is imposed, the north portion of the bridge near the crack sags downward. Like the floor beams at that location, the deck cantilevers out from the higher supported areas on the south end. This is indicated by an increased tension experienced by the deck in the transverse direction.

Conclusions

When a mid-depth fracture was imposed on the north girder of the three-span unit, it changed the bridge into a new but still stable structure. Deflection at the crack was minimal at $1\frac{3}{16}$ in (30.2 mm) under dead plus live loading, and there was no yielding. The load redistribution was provided in the three-dimensional structure by both primary and secondary members via the deck, stringers, floor beams, and bottom lateral bracing. Most of the load was redistributed longitudinally through the damaged girder and stringer deck system to the interior supports. The main load path proved to be the fractured girder itself as it redistributed the load longitudinally to the interior supports through cantilever action. The floor beams, lateral bracing system, and deck transferred the load to the intact girder, through torsional stiffness of the system. This load transfer in the transverse direction occurred mainly at the vicinity of the crack.

TABLE 6 After-Fracture Strains in Deck Under Dead Load in Microinches per Inch

Gage	First Flange Cut	Final Flange Cut
Longitudinal	-5.5	-138
Transverse	2.6	17.2
@ 45 degrees	-5.4	-47.4

Further Research

The following recommendations are suggested to extend the reported research:

1. Investigate the after-fracture behavior of the bridge with a crack at midspan of an exterior span. This fracture scenario could prove to be more critical than the fracture at midspan of an interior span because the cantilever action provided by the interior supports will not be available at the abutment.
2. Investigate the possible loss of composite action between the girder and the deck with increasing loading.
3. Develop nondestructive monitoring systems for this family of bridges. On the basis of the bridge testing results, this monitoring system can be effective and can focus on the critical zones.

ACKNOWLEDGMENT

This study is part of the overall testing of the I-40 Bridge, in Albuquerque, New Mexico. It was funded by a grant from the National Science Foundation, the New Mexico State Highway and Transportation Department, FHWA, and the New Mexico Alliance for Transportation.

REFERENCES

1. *Standard Specifications for Highway Bridges*, 13th ed. AASHTO, Washington, D.C., 1983.
2. Daniels, J. H., W. Kim, and J. L. Wilson. *NCHRP Report 319: Recommended Guidelines for Redundancy Design and Rating of Two Girder Steel Bridges*. TRB, National Research Council, Washington, D.C., 1989.
3. Schwendeman, L. P., and A. W. Hedgren. Bolted Repair of Fractured I-79 Girder. *Journal of the Structural Division* ASCE, Vol. 104, No. ST10, Oct. 1978, pp. 1567–1669.
4. Idriss, R. L., and D. V. Jauregui. *Load Path Evaluation of the I-40 Bridge*. Report 94-01 to the National Science Foundation. Department of Civil Engineering, New Mexico State University, April 1994.
5. White, K. R., and J. Minor. *Testing of the I-40 Bridge*. Phase 1 Final Report. FHWA, U.S. Department of Transportation, 1994.

Fatigue Assessment of Cable Systems of Long Span Cable-Stayed Bridges

Kazuo Tada, Yuji Fujii, and Harukazu Ohashi, *Honshu-Shikoku Bridge Authority, Japan*
Chitoshi Miki, *Tokyo Institute of Technology, Japan*

Cable systems of a cable-stayed bridge consist of cable and cable anchorage. Cable tension caused by prestress, dead load, and live load acts directly on the cable anchorage. In addition to direct tension, bending deformation caused by live load, temperature changes, and wind load act on the anchored stay cables. Furthermore, wind-induced ocsillations may be considered. Because cable tension and bending deformation occur repeatedly, it is necessary to verify fatigue behavior. The structural details of cable anchorages are complex, making it difficult to evaluate their fatigue resistance. Therefore, fatigue tests were conducted on full-scale specimens that include proposed anchorages and cables to examine their performance. The obtained results show that fatigue cracks initiated at the welded toe of the bearing plate to anchor web plates were caused by plate bending; therefore, some refinements of structural details are necessary. The bending fatigue strength of semi-parallel wire cables socketed by two types of anchorage were both proved to be sufficient for use as stay cables for an 870-m span cable-stayed bridge.

The Tatara Bridge is the world's longest cable-stayed bridge, with a center span of 890 m and a total length of 1,480 m carrying four lanes of traffic (Figure 1). The bridge is located on the Onomichi-Imabari Route, the westernmost of the three routes that are constructed and managed by Honshu-Shikoku Bridge Authority, and will connect Ikuchi Island with Ohmishima Island.

The construction of the substructure was begun in September 1992. The construction of the superstructure started in 1995 with completion scheduled for 1999.

The steel towers of the bridge are 220 m high and are shaped like an inverted Y, with their two legs bent inward beneath the bridge deck. The girders consist of a steel part in the main span and most side spans and prestressed concrete at the end of the side spans. The girders have a single box cross section of 2.7 m in height and 27.4 m in width. Both deck plate and lower flange plate are stiffened by closed trough ribs. The total of 168 cables arranged in 21 rows each suspend the girders. The longest cable is 462 m, made up of 379 galvanized wires and enclosed by polyethylene pipe cover for corrosion protection.

Two types of cable anchorages underwent fatigue test to obtain better structural details: the beam type, in which cable tension is transmitted to the main girder primarily as bending moment; and the column type, in which cable tension is transmitted to the main girder primarily as shearing force. For examining the fatigue performance of cable anchorages, the cyclic axial load was applied.

Cables made of semiparallel wires with HiAm and NS sockets are to be used as the stay cables. The cable fatigue strength under axial loading was proved to be

sufficient; however, the bending fatigue performance was not known. Therefore, the bending fatigue test of cables was conducted.

Cable Anchorage Fatigue Testing

Specimens

Figure 2 shows a specimen of the beam type, and Figure 3 shows that of the column type. Cable tension is supported by an anchor structure fixed to the main girder and is transmitted to the web and flange plates of the main girder as bending moment and shearing force. Comparing the column type with the beam type, the column type has less eccentricity from the main girder web and a longer length of attachment to the main girder web, so the shearing force predominates, whereas in the beam type, bending moment predominates. The cable's inclination angle is set about 20 degrees to the deck plane, which stimulates the uppermost cable of the Tatara Bridge. Welding condition is an important factor for assessing the fatigue strength of such complicated structures as cable anchorages, which are composed of plates welded at narrow and enclosed space. It was necessary to check the welding workability. Therefore the full-sized specimens were fabricated.

Testing Methods

Loading Method

The fatigue testing machine used has a dynamic loading capacity of 4 MN. The specimens were located outside the pedestals and loaded using a loading beam as indicated in Figure 4. Also, the inclined specimens were connected together in the shape of an inverted "V" to reduce the excessive uplift at the base if one specimen was loaded alone without being connected to the other.

Testing Load

As indicated in Table 1, the testing load was much higher than the fatigue design load on the actual bridge. The testing load was about 1.4 times that of the design live load of 1.7 MN, a value determined by the loading capacity of the testing machine and test term available.

Stress Evaluation

The stress conditions of the specimens were analyzed by three-dimensional finite element analysis, and then positions of attachment of strain gauges were determined. Also the difference in stress condition from the actual bridge was investigated for later evaluation of the test results. Before the fatigue testings, a static loading was applied and appropriateness of stress condition was checked by comparing the measurement values with those of the analytical values.

Fatigue Performance of the Beam-Type Anchorage

The test was continued for a total of 2 million repetitions. The fatigue cracks found in the specimen are shown in Table 2. The cracks are numbered in the order in which they were detected. The location of cracks was at the welds of the bearing plate and the welds of the deck plate, as indicated in Figure 5.

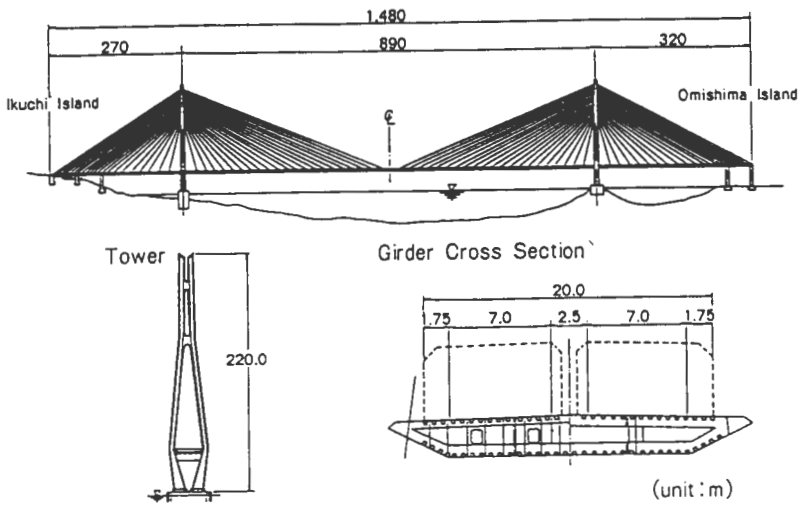

FIGURE 1 General view of Tatara Bridge.

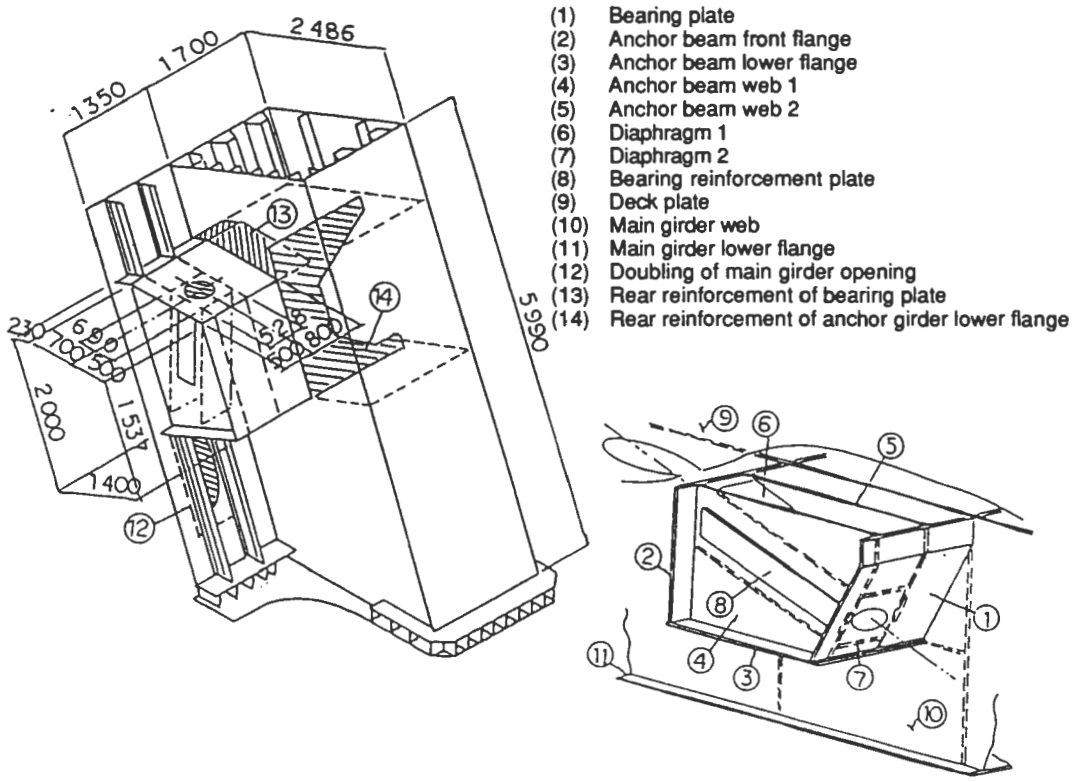

FIGURE 2 Structural details of beam-type anchorage (in millimeters).

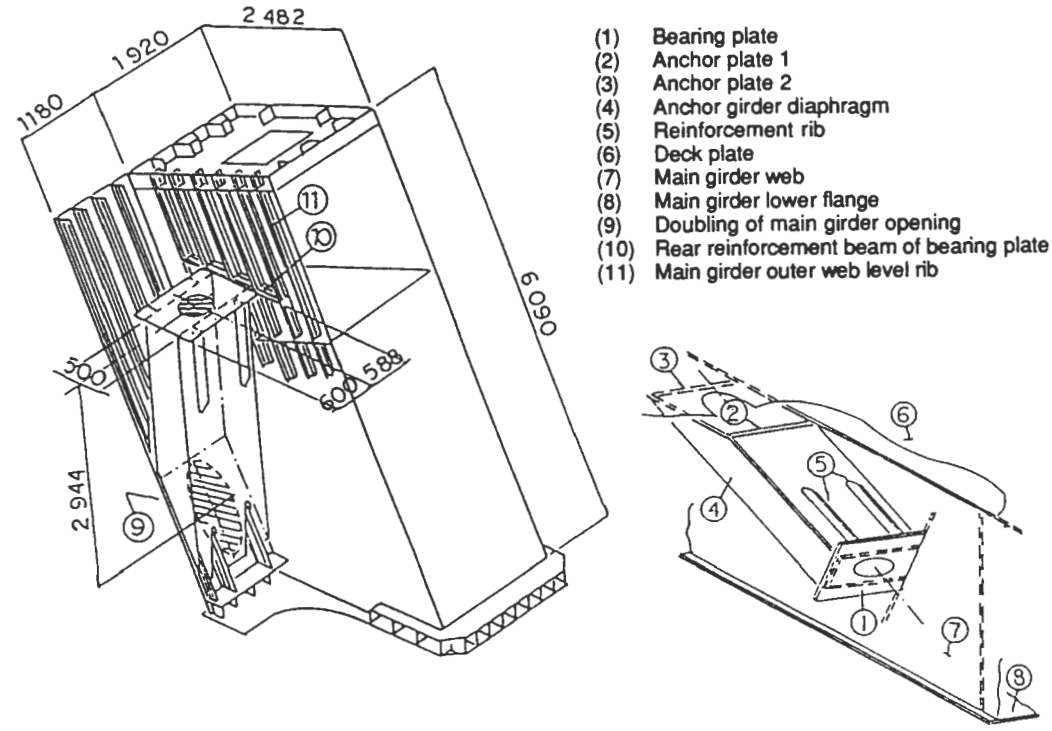

FIGURE 3 Structural details of column-type anchorage (in millimeters).

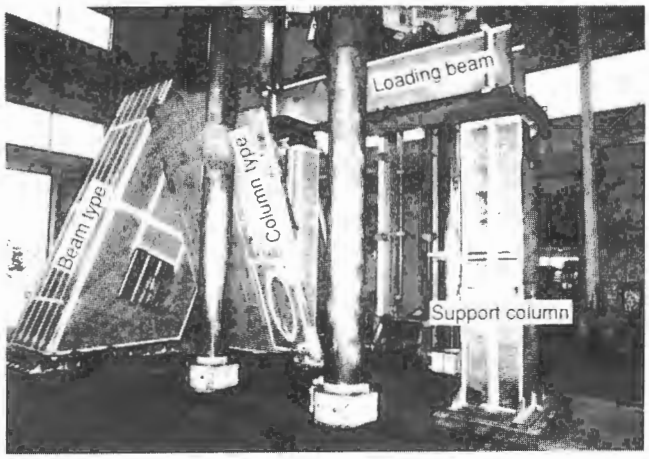

FIGURE 4 Fatigue testing condition for cable anchorages.

Cracks 1 and 2 were discovered at an early stage just below the loading plate. Both cracks originated at the ends of full penetration welds of the anchor beam web, diaphragm, and bearing plate. High tensile stress of over 100 MPa was measured, so it is estimated that even higher stress existed at the welded toe. Because these high tensile stress conditions were caused by plate bending in the bearing plate, testing was temporarily halted after 5 million repetitions, and changes were made as follows:

- The thickness of the loading plate was increased from 100 to 200 mm.
- The area of the loading plate was increased. The support condition of the loading plate to the anchor webs and diaphragms was modified from two-sided support to four-sided support.

After these changes, the testing was resumed. Plate bending was still observed, although the amount became much smaller. Cracks 3 and 8 initiated at the toe of the weld of the bearing plate with the flange plate under the anchor beam. Crack 4 originated on the surface of the bearing plate directly under the loading plate corner. Crack 5 originated at the toe of the full penetration weld of the front flange with the deck plate. Cracks 6 and 7 originated at the toe of the front fillet weld of the doubling plate to deck plate. At these three locations, in-plane stress predominated over out-of-plane bending, and measured stresses were 50 and 80 MPa.

Fatigue Performance of the Column-Type Anchorage

Because the plate thickness of the bearing plate of the column type was 25 mm, same as that of the beam type, it was predicted that cracks caused by plate bending would occur. Therefore, before the testing was started, the bearing plate was strengthened by attaching a 60-mm plate to it with high tensile strength bolts.

The observed fatigue cracks are listed in Table 3, and their schematic drawing is shown in Figure 6.

Crack 1 originated at the full penetration weld of the bearing plate with the main girder web. Stress of over 100 MPa was measured at the vicinity, and it is supposed that the crack was caused by plate bending.

Crack 2 originated at the full penetration weld of the bearing plate and anchorage Plate 2. This crack also seemed to be a result of plate bending.

Cracks 3 and 4 originated at the fillet weld of the reinforcing ribs attached to the bearing plate and the anchorage plate. A stress measurement of the reinforcing ribs revealed almost no out-of-plane bending. Because axial compression force predominated, the cracks are supposed to be a result of the local stress concentration at the tip of the reinforcing ribs.

Evaluation of Fatigue Characteristics of the Anchorage Structures

The following conclusions were drawn from the results of the fatigue testing.

1. The stress range of the actual bridge will be considerably smaller than that of the experiment as mentioned in the section on testing load. It was judged that the cracks other than those around the bearing plate did not constitute a problem in the actual bridge.
2. It is important to consider plate bending in the design of the bearing plates. Possible measures to prevent plate bending include increasing the plate thickness of the bearing plate and modifying the support condition of the bearing plate to a four-sided support structure.

TABLE 1 Testing Loads for Cable Anchorages

Load	Testing loads (MN)	Loading speed (Hz)
Max. load	2.5	
Min. load	0.1	2.0
Amplitude	2.4	

TABLE 2 Cracks Detected in Beam-Type Anchorage

Crack No.	Location of cracks	Number of cycles detected ($\times 10^4$)	Length of crack (mm)	
			When detected	After 2 million cycles
1	Bearing plate to anchor beam web 1 welded toe	34	315	481
2	Bearing plate to diaphragm, and bearing plate to anchor girder web	38	1021	1905
3	Anchor beam lower flange to bearing plate welded toe	655	120	221
4	Bearing plate base plate	82	141	186
5	Deck plate to front flange welded toe	115	38	231
6	Deck plate to cover plate welded toe	132	75	195
7	Deck plate to cover plate welded toe	150	330	334
8	Bearing plate to anchor beam lower flange welded toe	150	120	120

Cable Bending Fatigue Testing

Specimens

The dimensions and structural details of the specimens are shown in Table 4 and Figure 7. Four cables of the nongrout type were prepared by bundling 163 galvanized wire 7 mm in diameter in semiparallel form and fixing both ends in two types of socket, HiAm and NS. In both types, epoxy is poured into the mouth of the socket to relieve stress concentration on the wires caused by bending deformation.

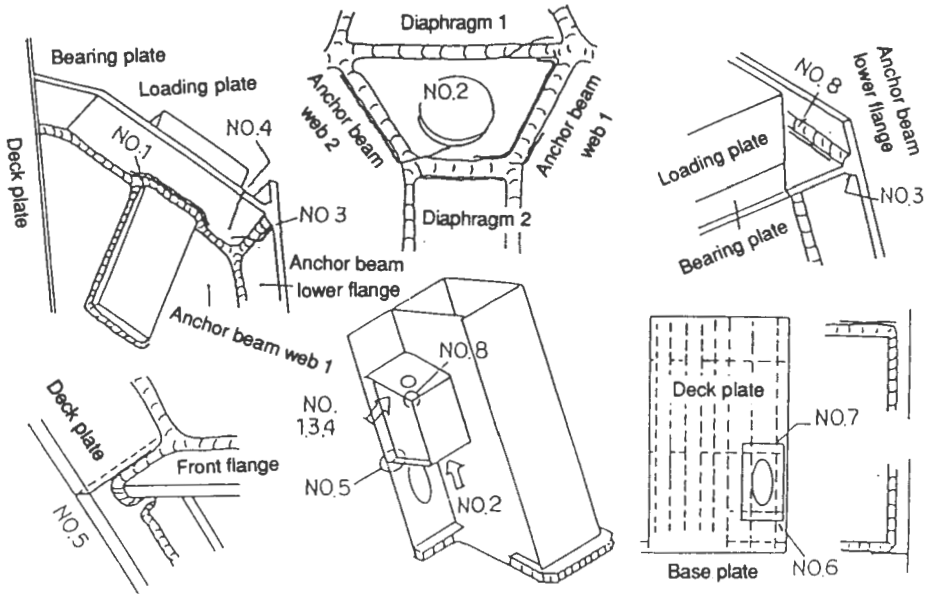

FIGURE 5 Location of cracks in beam-type anchorage.

TABLE 3 Cracks Detected in Column-Type Anchorage

Crack No.	Location of cracks	Number of cycles detected	Length of crack (mm)	
			When detected	After 2 million cycles
1	Bearing plate to main girder outer web welded toe	30	35	115
2	Bearing plate to anchor plate 2 welded toe	126	80	123
3	Bearing plate to anchor plate 2 reinforcement rib welded toe	163	44	50
4	Bearing plate to anchor plate 2 reinforcement rib welded toe	163	12	18

The strain gauges are attached to the wires by removing the polyethylene pipe in Cross Sections A through D as shown in Figure 7. In Cross Sections A, B, and C, the strain gauges were attached to representative wires, and in Cross Section D they were attached to all wires in the outermost layer.

Test Methods

Loading Method

The test apparatus was set up to reproduce the stress conditions of the stay cables, in which cyclic bending with constant axial force was applied (Figure 8). The axial force was applied to the specimen using two 2-MN jacks and then fixed at both ends to the reaction beams. For applying the cyclic bending deformation, a hydraulic actuator (Figure 9) with a dynamic capacity of 250 kN was used for raising and lowering the cables by grasping the center of the cables.

Testing Conditions

The testing conditions are shown in Table 5. The angle of bending indicated as θ in Figure 10 was set higher

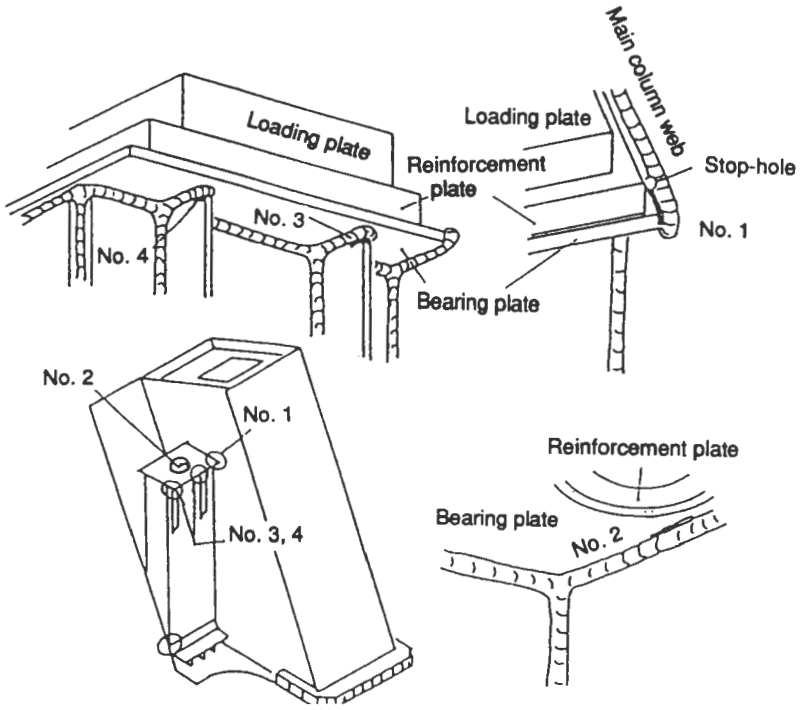

FIGURE 6 Location of cracks in column-type anchorage.

TABLE 4 Dimensions of Anchorage Specimens

Specimen No.	Socket	Cable length (m)	Nominal cross sectional area (mm^2)	Tensile strength of wire (MPa)	Breakage strength of cable (MN)
1	NS	10	6,272	1,570	10
2	NS	8			
3	HiAm	10			
4	HiAm	8			

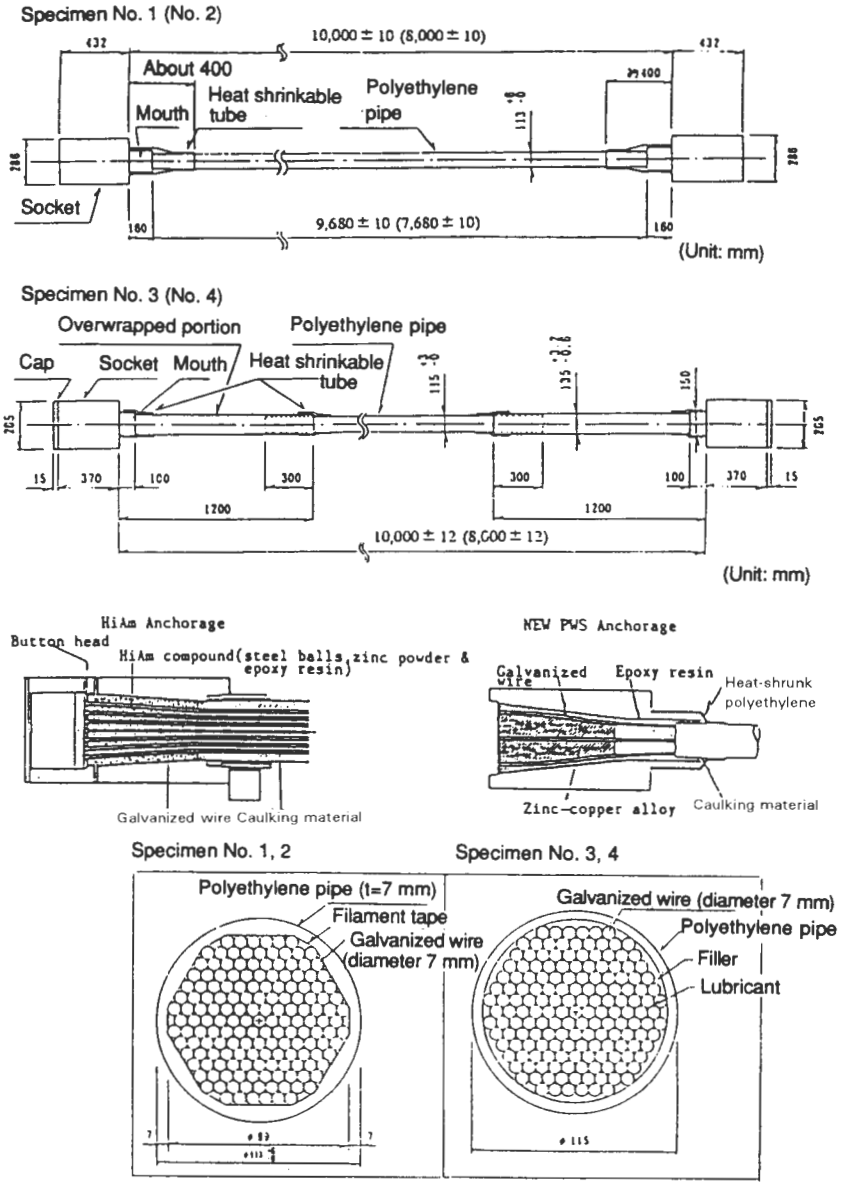

FIGURE 7 Structural details of cables and sockets.

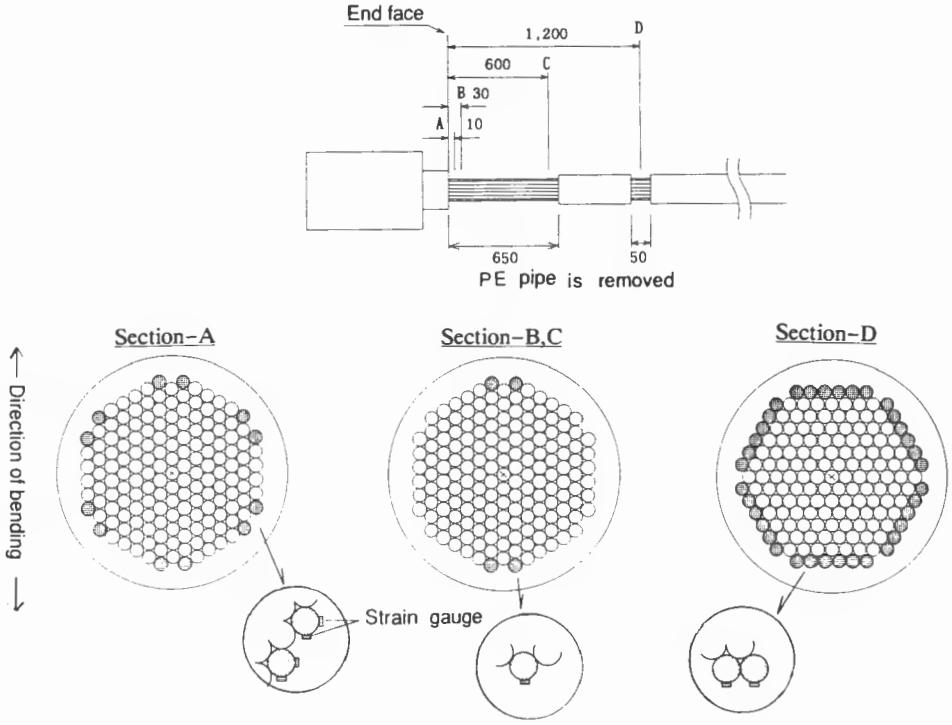

FIGURE 8 Position of strain gauges.

than that predicted for the actual bridge. The bending angle of 1.35 degrees was determined from the capacity of the test apparatus. The applied tensile force was set at 3.5 MN on the basis of the usage range of the actual bridge. Wire breakages were detected by using an acoustic emission sensor throughout the testing.

Test Results

Bending Stress on Cables

The stress behavior of wire at Cross Section A of Specimen 2 when bent at various angles is shown in Figure 11. The other specimens showed similar tendencies. Because of the friction among the wires of a cable, the wire stress did not return to 0 even when the bending angle was returned to 0 and a hysteresis curve resulted.

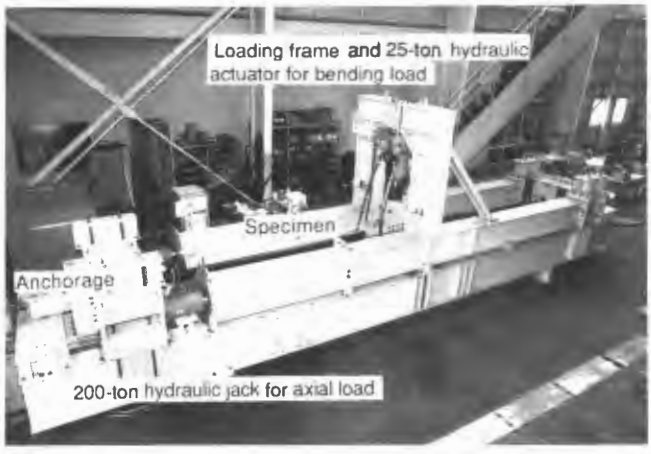

FIGURE 9 Bending fatigue test system for cable.

The measured stress at gauges attached to the surfaces of the wires in the bending direction is the sum of the stresses caused by additional axial stress by the cable's bending deformation, the cable's overall bending stress, and the bending stress of element wires, whereas the gauges attached to the sides of wires measured the stress caused by additional axial stress as a result of bending and cable's overall bending stress. The secondary bending stress defined by the sum of overall bending stress and bending stress of element wires were obtained by eliminating additional axial stress by bending deformation. Table 6 shows components of secondary bending stress at the mouth of the socket at Point A at the bending angle of 1.35 degrees. Large overall bending stress was observed for Specimen 2.

Figure 12 and Table 7 show the bending stress diagram in the axial direction. The bending stress calculated from Wyatt's equation is also plotted in the figure. The calculation of bending stress by Wyatt's equation is conducted for two cases, assuming in one case that the rigidity of the cable is that of a steel rod with the same cross-sectional area as that of the cable used in the experiment, and in the other case that its rigidity is that of one wire 7 mm in diameter, both assuming the

TABLE 5 Testing Conditions for Cables

Specimen No.		Axial force	Bending angle	Loading speed (Hz)
NS	1	3.5 MN	±0.9°	0.35
	2		±1.35°	0.33
HiAm	3		±1.0°	0.35
	4		±1.35°	0.33

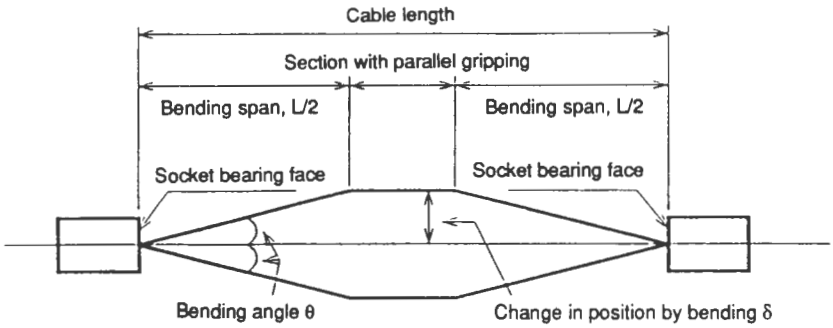

FIGURE 10 Definition of bending angles.

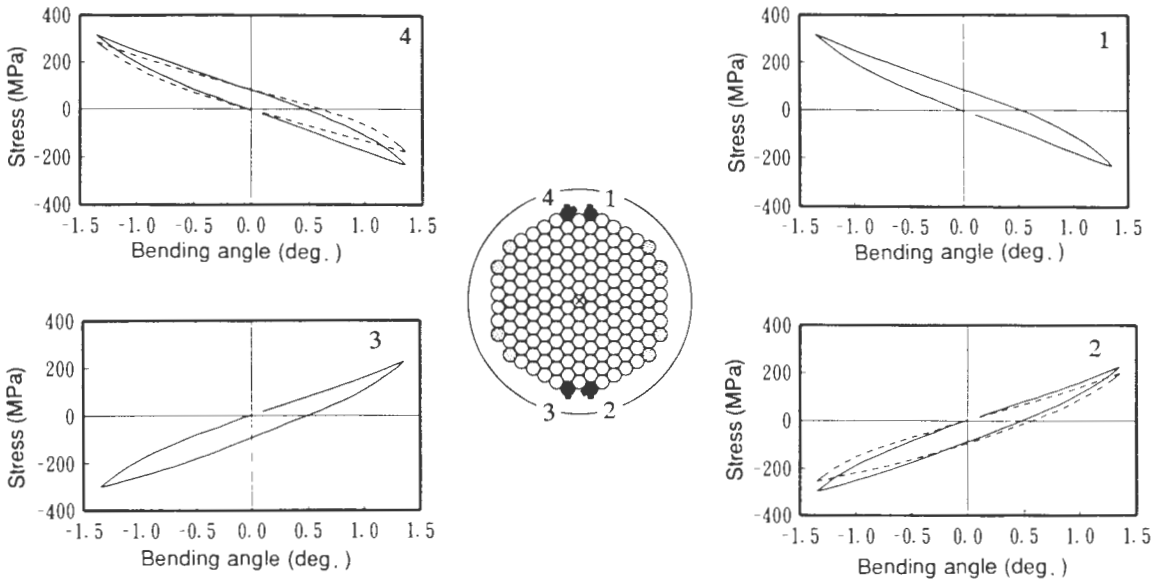

FIGURE 11 Stress behavior of wires (Specimen 2).

TABLE 6 Components of Secondary Bending Stress of Cables in Megapascals (Bending Angle of 1.35 Degrees)

Components	No. 2 (NS)	No. 4 (HiAm)
1. Overall bending stress	220	110
2. Wire Bending stress	50	60
3. (= 1+2) secondary bending stress	270	170

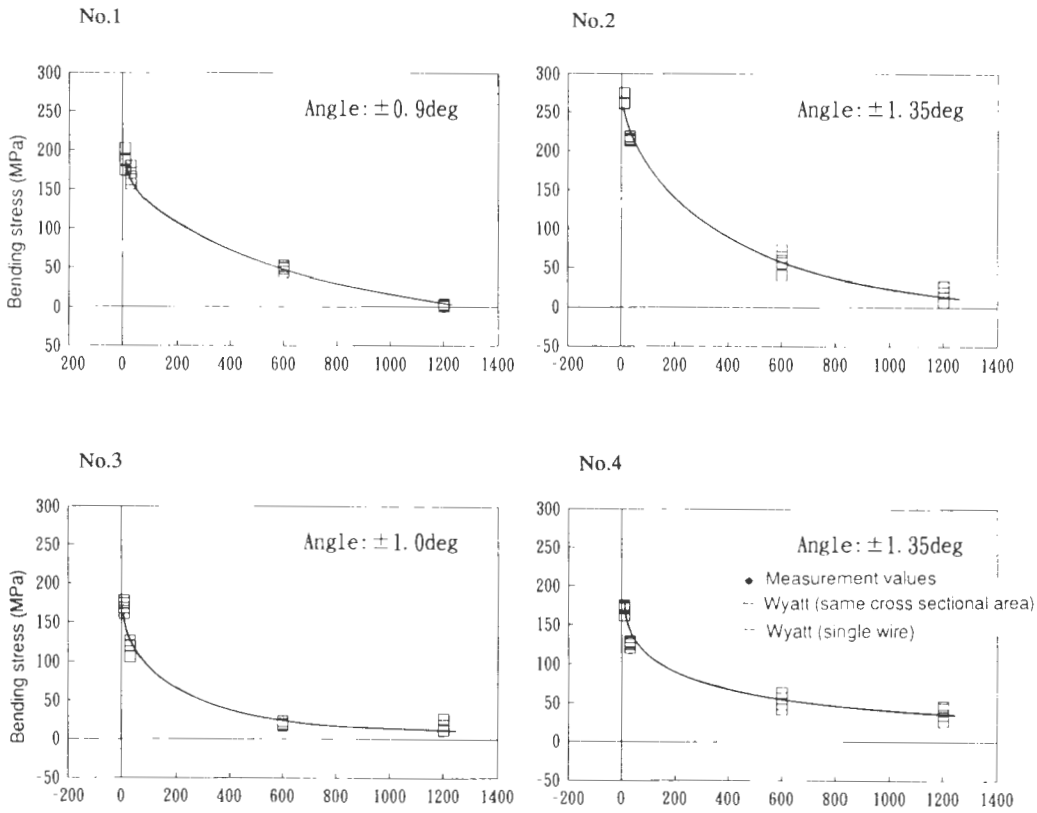

FIGURE 12 Bending stress condition at each cross section.

TABLE 7 Bending Stress of Cables in Megapascals

Cross section	Distance measured from socket mouth (mm)	NS		HiAm	
		No. 1	No. 2	No. 3	No. 4
A	10	190	270	170	170
B	30	170	220	120	130
C	600	50	60	20	50
D	1200	2	20	20	40

TABLE 8 Results of Bending Fatigue Test for Cables

Specimen No.		Total wires broken	Cycles at first wire breakage ($\times 10^4$)	Final No. of cycles ($\times 10^4$)
NS	1	0	-	200
	2	2	36.2	200
HiAm	3	0	-	250
	4	1	26.2	300

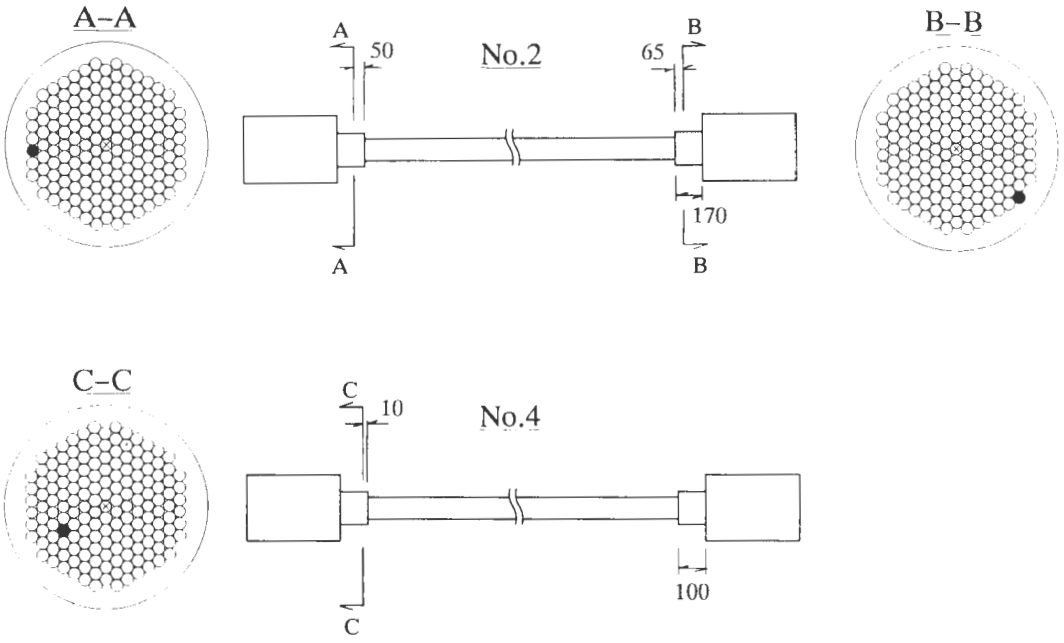

FIGURE 13 Location of wire breakage.

bending fulcrum to be the edge of the socket's mouth, for example:

$$\sigma_b = 2\theta\sqrt{E\sigma_T}\exp(-x \cdot g)$$

$$g = \sqrt{T/EI}$$

where

σ_b = secondary bending stress,
θ = bending angle,
E = Young's modulus,
σ_t = tensile stress,
T = tensile force,
I = moment of inertia, and
x = distance measured from the mouth.

The measured stress at a distance from the mouth is approximately in between the calculated stresses by two cases of assumption. Therefore, it was considered that the actual bending fulcrum is to the rear of the socket mouth.

As indicated in Table 7, there is a difference in bending stress occurring at bending angles of 0.9 and 1.35 degrees in the NS type, whereas in the HiAm type the bending stress occurring at the cross section A is nearly the same. This indicates different conditions of bending stress occurrence, depending on the socket type.

Results of Bending Fatigue Testing

The results of bending fatigue testing are shown in Table 8. The position of wire breakages is shown in Figure 13. The breakages in Specimen 2 occurred 50 mm from the mouth toward the inside of the socket in one wire and at 65 mm in another wire. In Specimen 4, the breakage occurred at 5 mm toward the inside of the socket. Because all the breakages occurred inside the mouth of the socket, the peak bending stress is supposed to occur at the inside of the mouth.

Evaluation of Fatigue Characteristics of Stay-Cables

Only a few wire breakages were found in 2 million repetitions. Because the bending angle was set at 1.35 degrees—larger than that predicted for the actual bridge (1.2 degrees because of design wind load)—it is confirmed that both types of cables have sufficient bending fatigue strength as stay cables.

Conclusions

The fatigue characteristics of cable systems for long span cable-stayed bridges have been investigated through fatigue testing of cable anchorages and cable bending fatigue testing. The original design of structural details for cable anchorage were modified to better details, and bending fatigue strength of socketed cables made of semiparallel wires was proved to be sufficient for stay cables.

Redundancy in Highway Bridge Superstructures

Michel Ghosn, *The City University of New York*
Fred Moses, *University of Pittsburgh*

A framework for considering redundancy in the design and load capacity evaluation of highway bridge superstructures is proposed. Redundancy is defined in terms of the capacity of the bridge system to resist failure at high loads and to resist system serviceability distress compared with its capacity to resist first member failure. The consequences of damage of one member to the overall system capacity is also checked. The proposed framework consists of tables of load modifiers that can be used to assess the redundancy level of typical bridge configurations. The load modifiers are used during the design process to require that members of less redundant configurations be more conservatively designed than is allowed by current standards. On the other hand, highly redundant designs are rewarded by permitting less conservative member designs. For bridges with nontypical configurations that are not covered by the tables, a direct analysis approach is recommended. General guidelines explaining how to perform such an analysis are provided. These include the loads that should be applied, the limit states that should be checked for both intact and damaged conditions, and the target load factors that the bridge should sustain before these limit states are violated. System factors that provide a measure of the system's redundancy can be calculated from the results of the incremental analysis. The load modifiers obtained from the tables and the system factors obtained from the incremental analysis can be used for the design of new bridges or they can be used to calculate rating factors for the evaluation of existing bridges. Thus, bridges with lower levels of redundancy must have their member capacities increased or they will have lower ratings. An example illustrating the proposed procedures is provided.

Bridge redundancy as normally defined consists of the capability of a bridge to continue to carry loads after the damage or the failure of one or more of its members. Member failure can be either ductile or brittle. It could be caused by the application of large live loads or the sudden loss of one element as a result of brittle fracture or an accident such as collision of trucks, ships, or debris.

The framework proposed in this paper for implementing redundancy concepts in the design and evaluation of highway bridges consists of two parts. The first part presents tables of load modifiers that would be used to modify component strengths on the basis of the redundancy of bridge systems with typical geometric configurations. The second part presents guidelines for the redundancy analysis and evaluation of any bridge system using a nonlinear structural anlaysis program. This paper uses a system reliability model to calibrate the proposed load modifiers and provide the analysis guidelines.

Bridge Safety

Although current bridge design and evaluation methods (*1*) have been successfully used for years, these are generally member-oriented procedures that do not provide adequate representations of the safety of the complete bridge system. In many instances, the failure of an individual member does not lead to the failure of the complete bridge system. On the other hand, because of possible large deformations, the bridge may be inadequate for truck traffic at loads that are lower than those that will cause a system failure.

Bridge members are often subjected to fatigue stresses that may lead to fracture and the loss of the load-carrying capacity of a main member. In addition, corrosion, fire, or an accident such as a collision by a truck, ship, or debris could cause the loss of a bridge member or the severing of the prestressing strands. To ensure the safety of the public, bridges should be able to sustain these damages and still operate, albeit at reduced capacity. Therefore, in addition to verifying the safety of the intact structure, the evaluation of a bridge's safety and redundancy should consider the consequences of the failure of critical bridge members.

In summary, a bridge should (*a*) provide a reasonable safety level against first member failure, (*b*) provide an adequate level of safety before it reaches its ultimate system capacity under extreme loading conditions, (*c*) remain functional under regular (or recurrent) traffic loads, and (d) be able to carry some traffic loads after damage or the loss of a component. These four critical limit states are described as follows (for convenient representation, a load model consisting of two AASHTO HS-20 vehicles is assumed to be acting on the structure).

Member Failure

The capacity of the structure to resist first member failure, as defined herein, is expressed in terms of the number of AASHTO HS-20 trucks that it can carry before this first member failure limit state is violated. This HS-20 load multiplier will be referred to as LF_1. For two-lane bridges, LF_1 can be calculated by applying the dead loads and two AASHTO HS-20 vehicles using a linear elastic structural model of the bridge and then incrementing the loads until first member failure occurs.

Ultimate Capacity

The ultimate capacity limit is defined as the maximum possible truck load that can be applied on the bridge before it collapses. The load factor (HS-20 load multiplier) corresponding to the ultimate limit state will be referred to as LF_u. LF_u can be calculated by analyzing the bridge under the effect of the dead loads and two AASHTO HS-20 vehicles using a nonlinear structural model of the bridge and then incrementing the truck loads until the system collapses. Collapse is herein defined as the load level at which a mechanism forms or at which concrete bridge members begin to crush.

System Serviceability Conditions

In a study of system serviceability conditions a maximum live load displacement limit of span length/200 is used as a system serviceability limit state. This displacement limit is based on best engineering judgment and is compatible with displacement limits used by other researchers (*2*). The capacity of a structure to withstand the maximum displacement limit can be expressed in terms of the number of a pair of AASHTO HS-20 trucks that can be placed on the structure before this system serviceability limit state is reached. LF_s is defined as the load multiplier that will cause the violation of the serviceability limit state accounting for the nonlinear behavior of the bridge members. Because redundancy is concerned with the performance of the structure, the displacements are checked in the main members only. The displacements of the slab or secondary members are not checked for this serviceability limit state.

Damaged Conditions

The damaged bridge condition consists of the removal from the structural model of a main load-carrying component that might be subject to brittle fracture or to accidental loss of capacity because of collisions or other causes. The load multiplier corresponding to the ultimate capacity of the damaged structure is defined as LF_d. LF_d can be calculated by analyzing the damaged structure under the effect of the dead loads and two AASHTO HS-20 vehicles on a nonlinear structural model of the bridge and then incrementing the truck loads until the structural system collapses.

Two-lane bridges using the HS-20 load model are used as the basis of the calibration performed in this study. This is based on the observation that maximum lifetime load effects are dominated by the presence of two heavy trucks side-by-side on a bridge and on the observation that two-lane loads produce the most critical loading condition in the linear elastic range for many bridge configurations (*3*). The final results obtained in this study are generalized to be applicable for any number of lanes and any truck load model by requiring that one-lane bridges and bridges with three or

more lanes as well as bridges designed with other than the HS-20 load model must satisfy the same safety criteria derived herein for two-lane bridges.

Redundancy Measures

Redundancy is defined as the capability of a structure to continue to carry loads after the failure of one or more of its members; in particular it should continue to carry load after the failure of a main member. The failure of a main member is thus used herein as the basis of the proposed measures of redundancy. Therefore, a comparison between LF_u, LF_s, LF_d, and LF_1 would provide a measure of the level of bridge redundancy. The system reserve ratios for the ultimate limit state R_u, for the serviceability limit state R_s, and for the damaged condition R_d are defined as follows:

$$R_u = \frac{LF_u}{LF_1}$$

$$R_s = \frac{LF_s}{LF_1}$$

$$R_d = \frac{LF_d}{LF_1} \tag{1}$$

The system reserve ratios R_u, R_s, and R_d are nominal (deterministic) measures of bridge redundancy. For example, when the ratio R_u is equal to 1.0 ($LF_u = LF_1$), the ultimate capacity of the bridge system is equal to the capacity of the bridge to resist failure of its most critical member. Such a bridge is considered nonredundant. As R_u increases, the level of bridge redundancy increases. Similar observations can be made about R_s and F_d. These two ratios, however, may under certain circumstances have values lower than 1.0. A value of R_s less than 1.0 means that the bridge will exhibit a deformation equal to span length/200 at a load level smaller than the load that will cause the first member failure. This situation might occur in certain bridges because LF_1 is calculated using a linear elastic model while LF_s accounts for the nonlinear behavior of the bridge. Similarly, R_d less than 1.0 means that a damaged bridge will be able to carry less live load than the load that will cause the first member failure in the intact structure.

To check whether a bridge system has adequate levels of redundancy it is sufficient to use a structural analysis program to calculate LF_u, LF_s, LF_d, and LF_1 and to verify that R_u, R_s, and R_d are adequate. Minimum acceptable values of R_u, R_s, and R_d should be established by examining the results of bridges that are clearly redundant. In addition, these minimum acceptable values should account for the uncertainties associated with determining the loads and the resistances of bridge superstructures. Minimum acceptable values of R_u, R_s, and R_d are determined in this study using a sysem reliability model similar to that used in development of the AASHTO Load and Resistance Factor Design (LRFD) specifications (*4*).

Reliability Model

The safety index β_{member} for the failure of the first member is expressed herein using the following lognormal format:

$$\beta_{member} = \frac{ln\left(\frac{\overline{LF_1}}{\overline{LL_{75}}}\right)}{\sqrt{V_{LF}^2 + V_{LL}^2}} \tag{2}$$

where $\overline{LF_1}$ is the mean value of the load factor that will cause the first member failure in the bridge assuming elastic analysis. $\overline{LF_1}$, which is the mean value of LF_1, is related to the nominal value by a bias λ_{LF}. LF_1 is a function of the strength capacity of the member represented by the nominal resistance, R, and the nominal dead load, D. $\overline{LL_{75}}$ is the mean value of the maximum expected lifetime live load including impact. The same HS-20 load model is used to express LF_1 and $\overline{LL_{75}}$. A 75-year lifetime is used on the basis of work done elsewhere (*3*). V_{LF} is the coefficient of variation of LF_1, whereas V_{LL} is the coefficient of variation of the maximum expected live load LL_{75}. The denominator in Equation 2 gives an overall measure of the uncertainty in estimating the resistance, the dead load, and the live load including dynamic impact.

The safety index of the system for the ultimate limit state is defined herein with respect to the extreme loading condition as

$$\beta_{ult} = \frac{ln\left(\frac{\overline{LF_u}}{\overline{LL_{75}}}\right)}{\sqrt{V_{LF}^2 + V_{LL}^2}} \tag{3}$$

where $\overline{LF_u}$ is the mean value of the load factor corresponding to the ultimate limit state. LF_u relates to the strength capacity of the system and the dead load. $\overline{LL_{75}}$ and V_{LL} are the same values used to calculate β_{member}. A 75-year exposure period is also used herein for the ultimate limit state. Because of insufficient data, it is assumed that LF_u, LF_s, and LF_d have the same bias value and the same coefficients of variation used for LF_1. The statistical data base used in this study is provided elsewhere (*5*).

For the serviceability limit state, the performance of the complete system can also be measured in terms of a system serviceability safety index, $\beta_{serv.}$, defined as

$$\beta_{serv.} = \frac{ln\left(\frac{\overline{LF_s}}{\overline{LL_2}}\right)}{\sqrt{V_{LF}^2 + V_{LL}^2}} \quad (4)$$

where $\overline{LF_s}$ is the mean load factor to reach the serviceability limit state. $\overline{LF_s}$ relates to the capacity of the bridge system to resist large deformations and the applied dead load. $\overline{LL_2}$ is the mean applied live load for a 2-year exposure period expressed in terms of the HS-20 load model. The 2-year exposure period is used herein to reflect the fact that if a bridge has serviceability problems, these will be noticed during the biennial mandatory bridge inspection period.

Finally, the system's ability to sustain loads after damage can be expressed in terms of a system safety index for damaged conditions, $\beta_{damaged}$, defined as

$$\beta_{damaged} = \frac{ln\left(\frac{\overline{LF_d}}{\overline{LL_2}}\right)}{\sqrt{V_{LF}^2 + V_{LL}^2}} \quad (5)$$

$\overline{LF_d}$ is the mean load factor to reach the ultimate capacity of the damaged system. $\overline{LF_d}$ relates to the residual capacity of the system after one member is damaged and the dead load. A 2-year exposure period is also used for the damaged conditions as with the serviceability conditions.

Redundancy is defined as the capability of a bridge system to continue to carry load after the damage or the failure of one or more of its members. Hence, to study the redundancy of a system, it is useful to examine the difference between the safety indexes of the system expressed in terms of $\beta_{ult.}$, $\beta_{serv.}$ and $\beta_{damaged}$ and the safety index of the most critical member, expressed in terms of β_{member}. The relative safety indexes are defined as follows:

$$\Delta\beta_u = \beta_{ult.} - \beta_{member}$$

$$\Delta\beta_s = \beta_{serv.} - \beta_{member}$$

$$\Delta\beta_d = \beta_{damaged} - \beta_{member} \quad (6)$$

These relative safety indexes give measures of the relative safety provided by the bridge system compared with the nominal safety of first-member failure. The relative safety indexes provide reliability-based measures of redundancy. Thus, a bridge system will provide adequate levels of system redundancy if the relative safety indexes are adequate.

Determination of Target Safety Indexes

The object of this study is to calibrate a set of load modifiers that can be used with the typical design equations to account for the redundancy of typical bridge superstructures. In addition, this study calibrates a step-by-step procedure to check the redundancy of nontypical structures using a nonlinear finite element analysis. To perform the calibration of the load modifiers and the step-by-step procedures, minimum target $\Delta\beta_u$, $\Delta\beta_s$, and $\Delta\beta_d$ values that a bridge should satisfy must be obtained. In this study, these target values are extracted on the basis of a review of the performance of existing redundant designs.

To perform the reliability calibration, a large number of common-type multigirder steel reinforced concrete T-beam and prestressed concrete I-beam bridges were analyzed. Values of the load factors LF_1, LF_u, LF_s, and LF_d, the safety indexes β_{member}, $\beta_{ult.}$, $\beta_{serv.}$, and $\beta_{damaged}$ as well as $\Delta\beta_u$, $\Delta\beta_s$ and $\Delta\beta_d$ were calculated for each bridge configuration. An earlier work (*5*) gives detailed descriptions of the bridges analyzed and the results obtained. The extraction of the target relative safety indexes is performed for the ultimate limit state, serviceability limit state, and the damaged condition on the basis of bridge designs that are known to be redundant. The conclusions obtained for the typical bridge configurations that were studied revealed that a bridge will provide adequate levels of redundancy if all the following conditions are satisfied:

1. It gives a value of $\Delta\beta_u$ greater than or equal to 1.0;
2. It gives a value of $\Delta\beta_s$ greater than or equal to -1.0; and
3. It gives a value of $\Delta\beta_d$ greater than or equal to -0.5.

Load Modifiers for Bridge Design

An earlier work (*4*) defines a load modifier η as a "factor relating to the ductility, redundancy and the operational importance of a bridge." Many formats can be used to apply the load modifier in the LRFD design check equation. Because redundancy as defined in this study relates to the load factors LF, which are a function of the live load margin (R-D), it is proposed to apply the load modifier factor on the live load of the LRFD equation such that the design equation becomes the following:

$$\phi R'_{req.} = \gamma_d D_n + \eta\gamma_l L_n(1 + I) \quad (7)$$

where

η = live load modifier relating to bridge redundancy;
ϕ = resistance factor;
γ_d = dead load factor;
γ_l = live load factor;
$R'_{req.}$ = required member capacity accounting for the bridge system's redundancy;
D_n = nominal or design dead load; and
L_n = $(1 + l)$ is the nominal or design live load including the dynamic impact factor (l).

Equation 7 has a general format that can be used for any AASHTO criteria. For example, for working stress design (WSD) criteria, γ_d and γ_l are given as 1.0 and ϕ is equal to 1/0.55. For the LFD criteria, ϕ will depend on the type of member being analyzed, γ_d is equal to 1.3, and γ_l is 2.17. For the LRFD criteria, ϕ will depend on the type of member being analyzed, γ_d is equal to 1.25 and γ_l is 1.75.

When η is equal to 1.0 Equation 7 becomes the regular design check equation used in current member-oriented practice. A value of η greater than 1.0 indicates that the bridge structure is not adequately redundant, and thus this bridge's members are penalized by requiring higher member capacities than are currently permitted. On the other hand, a value of η less than 1.0 indicates that the bridge is sufficiently redundant and that its members' capacities can be reduced without jeopardizing overall system safety.

Because redundancy is related to maximum system capacity, Equation 7, including the load modifier η, should be applied only when checking the strength limit state of bridge components. The equations for member serviceability limit states should not include η.

The derivation of η values for typical bridge configurations was performed in this study such that typical bridge configurations satisfy the target safety index values determined in the previous section. Values of the load modifier η for typical simply supported prestressed concrete I-beam bridge configurations with identical parallel beams are given in Tables 1 through 3 as a function of the number of beams and the beam spacings. The values in the tables are given for typical simply supported bridges with 120-ft span lengths. Corrections are specified in the tables when the load modifier is influenced by changes in span length. Ghosn and Moses (5) also provide additional tables for multigirder steel bridges and concrete T-beam bridges. They are applicable for any type of specifications (WSD, LFD, or LRFD) with any number of lanes and any load model. The tables are given separately for each system limit state. The final value that should be used is the maximum value obtained from the three limit states. A minimum value of 0.75 is herein recommended as a conservative lower bound on the load modifier.

Bridges that have load modifiers greater than 1.0 do not provide sufficient levels of redundancy. These should be strengthened by increasing their required member capacity using Equation 7. Existing bridges that cannot be strengthened should be assigned lower rating factors.

Equation 7 provides one possible format to include a load modifier (or redundancy) factor in the design equation. The possibility of using other formats will be investigated in future phases of this study.

TABLE 1 Load Modifiers for Prestressed Concrete I-Beam Bridges for Ultimate Limit State

	Load Modifier by Beam Spacing (ft)		
No. of Beams	4	6	8
4	1.20	1.15	1.05
6	1.00	0.80	0.65[a]
8	0.80	0.65[b]	

[a]For bridges less than 120 ft, increase the load modifier shown by 0.05 for every 10 ft. The final load modifier should not be less than 0.75.
[b]For bridges less than 120 ft, increase the load modifier shown by 0.05 for every 10 ft.

TABLE 2 Load Modifiers for Prestressed Concrete I-Beam Bridges for System Serviceability Limit State

	Load Modifier by Beam Spacing (ft)		
No. of Beams	4	6	8
4	0.95[a]	0.95[b]	0.85[a]
6	0.85[a]	0.75	0.75
8	0.75	0.75	

[a]For bridges less than 120 ft, decrease the load modifier shown by 0.05 for every 10 ft.
[b]For bridges less than 120 ft, decrease the load modifier shown by 0.10 for every 10 ft. The final load modifier should not be less than 0.75.

TABLE 3 Load Modifiers for Prestressed Concrete I-Beam Bridges for Damaged Conditions

	Load Modifier by Beam Spacing (ft)		
No. of Beams	4	6	8
4	1.05	0.95	0.90
6	0.90	0.75	0.75[a]
8	0.75	0.75	

[a]For bridges less than 50 ft long, use a load modifier equal to 0.85.

Direct Analysis Approach

Given the target safety indexes determined above and Equations 1 through 6, work by Ghosn and Moses (*5*) illustrates how the values of the system reserve ratios, $R_{u\ \text{req.}}$, $R_{s\ \text{req.}}$, and $R_{d\ \text{req.}}$, that are required to satisfy a minimum level of bridge redundancy are calculated. These required values are summarized in Table 4. A particular bridge system will provide adequate levels of redundancy if the values of R_u, R_s, and R_d calculated for that bridge are higher than the required values given herein.

Therefore, to verify the redundancy level of a bridge with a configuration that is not covered in Tables 1 through 3, a nonlinear finite element analysis should be performed and the values of LF_1, LF_u, LF_s, and LF_d should be calculated. If the values of $R_u = LF_u/LF_1$, $R_s = LF_s/LF_1$ and $R_d = LF_d/LF_1$ obtained are greater than the required values shown in Table 4, then the bridge is sufficiently redundant. If R_u, R_s, or R_d is less than the values shown in Table 4, the bridge has low levels of redundancy and measures should be taken to improve the safety of this bridge. The system reserve ratios are thus defined as

$$r_u = \frac{R_u}{R_{u\ \text{req.}}}$$

$$r_s = \frac{R_s}{R_{s\ \text{req.}}}$$

$$r_d = \frac{R_d}{R_{d\ \text{req.}}} \tag{8}$$

Thus, if r_u, r_s, or r_d are all greater than 1.0, the system is redundant.

The check of R_u, R_s, and R_d is a check on the redundancy of the system. Bridges that are not redundant may still provide high levels of system safety if their members are overdesigned. Therefore, the redundancy check should always be performed in conjunction with a member safety check. This is achieved by comparing the actual capacity of the bridge members to the capacity required by the current member-oriented specifications. In this case, $R_{\text{req.}}$ is defined as the member capacity required to satisfy the current AASHTO specifications. Any acceptable member design criteria can be used. For example, the required member capacity $R_{\text{req.}}$ is calculated for the most critical member using AASHTO's design and evaluation equations:

$$\phi R_{\text{req.}} = \gamma_d D_n + \gamma_l L_n(1 + I) \tag{9}$$

where

ϕ = resistance factor;
γ_d = dead load factor;
γ_l = live load factor;
D_n = nominal or design dead load; and
$L_n(1 + I)$ = nominal or design live load including impact.

The required member load factor, $LF_{1\ \text{req.}}$ is defined as

$$LF_{1\ \text{req.}} = \frac{R_{\text{req.}} - D}{L_{HS\ 20}} \tag{10}$$

where D is the dead load effect on the most critically loaded member and $L_{HS\ 20}$ is the effect of a pair of AASHTO HS-20 vehicles on the most critical member. To provide a measure of the adequacy of the actual member capacity represented by LF_1 to that required by the AASHTO specifications, the member reserve ratio r_1 is defined as the following:

$$r_1 = \frac{LF_1}{LF_{1\ \text{req}}} \tag{11}$$

Bridge members that are designed to exactly match the AASHTO specifications will produce a member reserve ratio of 1.0. Members that are overdesigned will produce r_1 values higher than 1.0.

Using the results of the nonlinear incremental analysis, a system factor ϕ_s is defined as follows:

$$\phi_s = \min(r_1 r_u, r_1 r_s, r_1 r_d) \leq r_1 \times 1.35 \tag{12}$$

The value of 1.35 is used in Equation 12 as a conservative upper limit.

If ϕ_s is less than 1.0, it indicates that the bridge under consideration has an inadequate level of system safety. A system factor greater than 1 indicates that the level of system safety and redundancy is adequate. To improve the redundancy of a bridge system, the geometric configuration of the bridge should be changed by either adding members or providing continuity at the supports. If this cannot be achieved, nonredundant bridges are penalized by requiring their members to provide higher safety levels than those of similar bridges with redundant configurations.

TABLE 4 Required Load Factor Ratios for Direct Analysis

Configuration	System Reserve Ratio	Value
Ultimate limit state	$R_{u\ \text{req.}} = (LF_u/LF_1)_{\text{req.}}$	1.3
Serviceability limit state	$R_{s\ \text{req.}} = (LF_s/LF_1)_{\text{req.}}$	0.7
Damaged condition	$R_{d\ \text{req.}} = (LF_d/LF_1)_{\text{req.}}$	0.8

Note: These values are valid for any number of lanes and for any load model, including HS-20 or HS-25 trucks.

One possible way to increase the capacity of bridges is to increase their member reserve capacities ($R - D$) by a factor of $1/\phi_s$. For example, if a bridge member has a resistance R and a dead load D and a system factor ϕ_s less than 1.0, it should be penalized by requiring a new resistance R', such that

$$R' - D' = \frac{R - D}{\phi_s} \tag{13}$$

where

R' = updated member resistance (after application of the system factor),
D' = updated dead load, and
R and D = original values of the resistance and the dead load.

Values of $(R - D)$ for a bridge that has a system factor greater than 1.0 can be reduced by a factor of $1/\phi_s$, and the bridge will still maintain adequate levels of system safety.

In principle, the same system factor, ϕ_s, could be applied to all the members of the bridge system. In reality, some members may contribute less than other members toward the overall system capacity, and using the same ϕ_s factor for all the members may be inefficient. To be more efficient, the system factor ϕ_s may be applied to the most critical member(s) only and the full analysis may be repeated until the system redundancy requirements are satisfied.

Application of a system factor ϕ_s will improve the bridge members' strengths represented by LF_1 and will also improve system strength expressed in terms of LF_u, LF_s, and LF_d. Thus, the system ratios R_u, R_s, and R_d may remain unchanged and a nonredundant bridge will remain nonredundant. However, by applying the system factor ϕ_s the safety index for one member as well as the system safety indexes will be increased. Thus, nonredundant designs are penalized by requiring higher member safety levels than similar bridges with redundant configurations.

Load Rating of Existing Bridges

As developed earlier, the proposed redundancy framework is used for the design of new bridges or the load capacity evaluation of existing bridges by modifying the strengths of the members using Equations 7 or 12. It is often difficult to change the member capacities of existing bridges because this may require costly rehabilitations. Therefore, instead of changing the member capacities, the evaluating engineer may simply choose to account for bridge redundancy and system safety by changing the load rating.

According to the 1992 AASHTO specifications (*1*), rating an existing bridge is currently performed by calculating a rating factor RF as shown in Equation 14:

$$\phi R_{exist.} = \gamma_d D_n + \gamma_l RF L_n(1 + l) \tag{14}$$

where

RF = rating factor,
ϕ = resistance factor,
γ_d = dead load factor,
γ_l = live load factor,
$R_{exist.}$ = existing member capacity,
D_n = nominal dead load, and
$L_n(1 + l)$ = nominal or design live load including the dynamic impact factor (l).

To account for bridge redundancy during the load rating of existing bridges, the rating factor RF can be expressed as a function of the existing capacity $R_{exist.}$ and the required capacity R', such that

$$RF = 1. + \frac{\phi(R_{exist.} - R')}{\gamma_l L_n(1 + l)} \tag{15}$$

R' in Equation 15 can be calculated using either Equation 7 for typical bridge configurations or Equation 13 for nontypical bridges.

Example

A 100-ft prestressed concrete bridge that satisfies AASHTO's LFD criteria with nominal HS-20 loading is to be checked for redundancy. The cross section of the six-girder simply supported prestressed concrete bridge is shown in Figure 1. The girders are spaced 8 ft center to center, and the deck is 7 in. The longitudinal members are Type IV AASHTO girders with 4.80 in.^{2} of grade 270 prestressing steel at an effective depth of 57 in. from the top of the slab. The same effective depth is assumed for the whole span length. The effective prestressing force is equal to 726 kips. The section's concrete strength is 5,000 psi, whereas the slab's strength is 3,000 psi. According to AASHTO's specifications, the nominal ultimate moment capacity (R) of each girder section was found to be 5,810 kip-ft. Assuming Type IV AASHTO girders, the dead load moment D for every member is equal to 1,970 kip-ft.

Load Modifiers

Equation 7 can be directly used to estimate the required member capacity for this bridge if it were to be designed

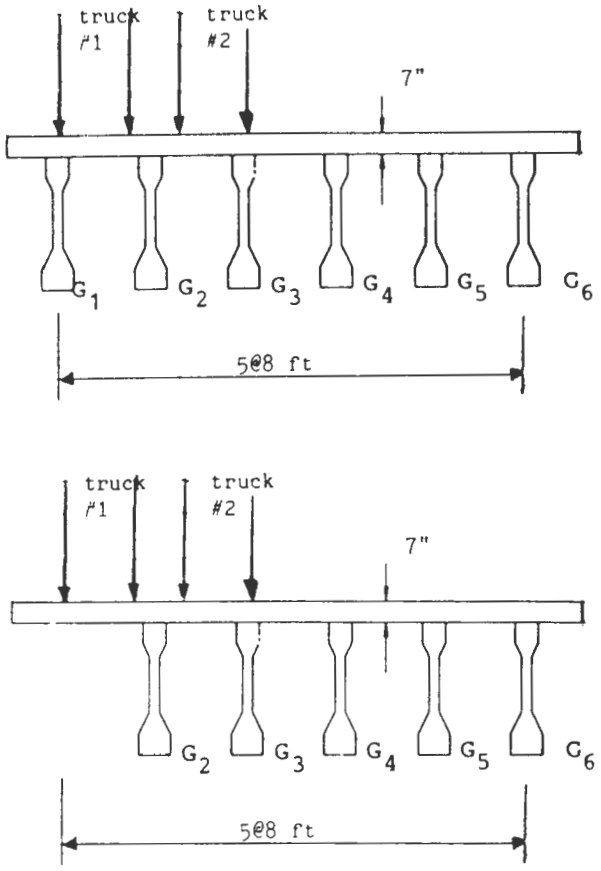

FIGURE 1 Layout of example of prestressed concrete bridge.

taking into consideration its redundancy. Using the LFD criteria, the resistance factor ϕ is 0.95, the dead load factor γ_d is 1.3, and the live load factor γ_l is 2.17. D_n is the dead load moment and for this six-girder prestressed bridge is given as 1,970 kip-ft. L_n is the nominal live load and for this 100-ft bridge is given as 1.45 × 762.5 kip-fit (distribution factor times moment due to one wheel load) or 1,105 kip-ft. The impact factor is given as 0.22. The load modifier η is taken as the highest value from Tables 1 through 3 for six beams at 6-ft spacings for a 100-ft span. The highest value is 0.80. Plugging these figures into Equation 7, the design check equation becomes the following:

$$0.95\ R'_{\text{req.}} = 1.3 \times 1970 + 0.80 \times 2.17 \times 1105 \times 1.22 \quad (16)$$

Equation 16 gives a required updated member capacity of 5,159 kip-ft. This means that because of the high level of redundancy of this bridge configuration, the member capacity can be reduced from 5,810 to 5,159 kip-ft while still providing an acceptable level of system safety.

Direct Analysis

In a first stage, a linear elastic analysis is performed for two AASHTO HS-20 trucks without impact factor applied on the bridge, as indicated in Figure 1. The total moment due to the two HS-20 trucks is 3,050 kip-ft. The most heavily loaded member is the external girder G1. G1 carries a live load $L_{\text{HS-20}}$ = 945 kip-ft constituting 31 percent of the total live load. This value shows that the 1992 AASHTO distribution factor is conservative. The dead load moment (D) was found to be 1,970 kip-ft. Using the results of the elastic analysis, the projected load factor LF_1 that will lead to the failure of the most heavily loaded member can be calculated as follows:

$$LF_1 = \frac{R - D}{L_{HS\ 20}} \quad (17)$$

where

R = actual member capacity given as 5,810 kip-ft,
D = dead load effect equal to 1,970 kip-ft, and
$L_{HS\ 20}$ = 945 kip-ft = effect of the two HS-20 trucks on the most heavily loaded member.

Substituting into Equation 17 leads to a load factor LF_1 of 4.06. This indicates that, by projecting the results of a linear elastic analysis, the first member of the bridge will fail when the pair of HS-20 trucks is incremented by a factor of 4.06.

In a second analysis stage, the AASHTO loads are incremented using a nonlinear model of the bridge structure. The maximum vertical deflections in the longitudinal girders are computed for every load step as the truck load is incremented. Figure 2 gives a plot of load factor versus displacement obtained for this bridge example. A maximum deflection of 6.00 in., corresponding to the span length/200 criterion, is obtained when the load factor is 3.94. This load factor is defined as LF_s. The load was further increased until concrete crushing occurred in external girder G1. This was reached at a value LF_u of 6.42.

The calculation of the capacity of the bridge to sustain load under damaged conditions is also performed. For example, the same incremental analysis is repeated assuming that the external girder G1 was completely removed from the model. Girder G1 was chosen as the damaged girder in this example because it was the most critical member of the intact structure. Figure 1 shows a cross section of the damaged model with the loading pattern used in this analysis. The critical loading pattern in this case was assumed to be the same as that of the intact bridge; this, however, may not necessarily always be true. Different loading patterns should be checked

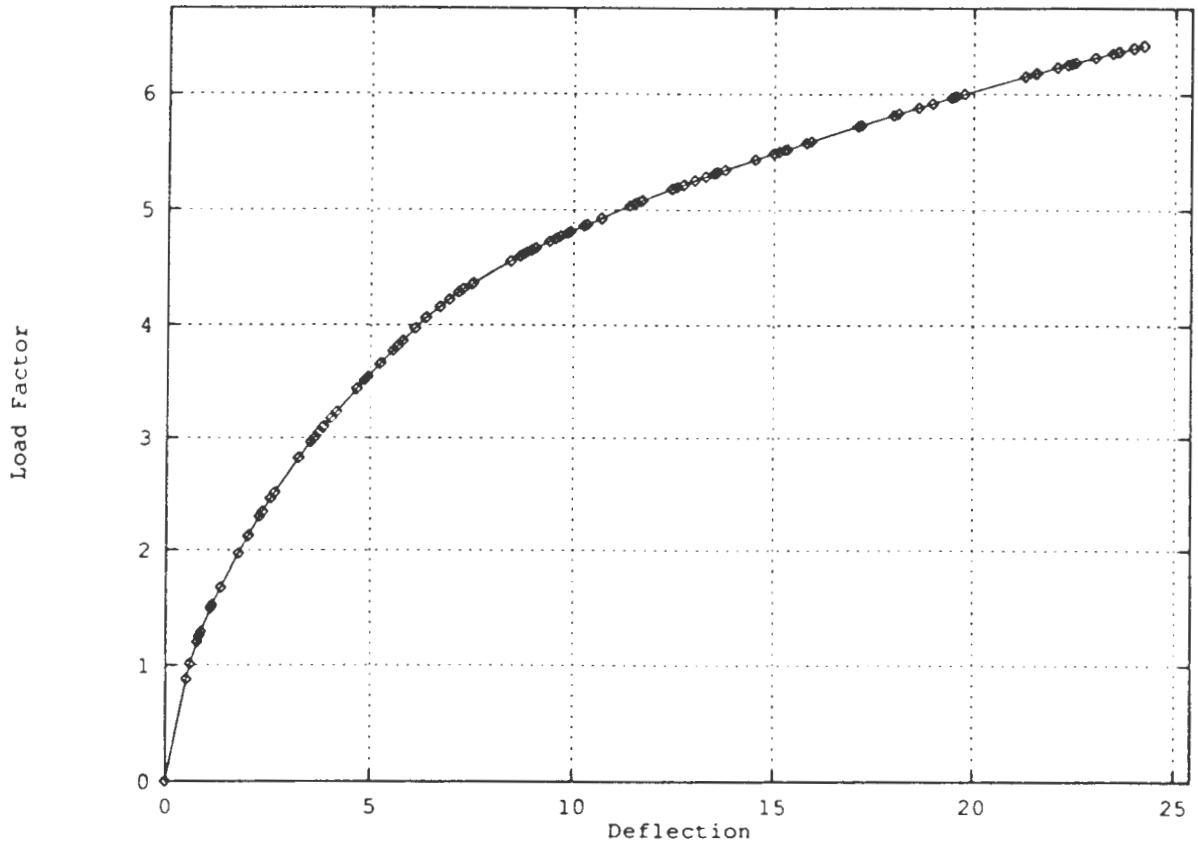

FIGURE 2 Load deflection curve for example of prestressed concrete bridge.

when performing the incremental analysis. The HS-20 loads applied on the damaged bridge are incremented until concrete crushing occurred. This occurred at a load factor LF_d of 5.52. In this case, the member that failed is G2. In this analysis in which the nonlinear behavior of the slab in the transverse direction was considered, the slab is assumed to have high levels of ductility.

The values of LF_u, LF_s, and LF_d obtained from the nonlinear incremental analysis of the prestressed concrete bridge are compared with the member factor $LF_1 = 4.06$. The system reserve ratios obtained are $R_u = LF_u/LF_1 = 1.58$, $R_s = LF_s/LF_1 = 0.97$, and $R_d = LF_d/LF_1 = 1.36$. These system ratios are compared with the required system reserve ratios $R_{u\,\mathrm{req}}$, $R_{s\,\mathrm{req}}$, and $R_{d\,\mathrm{req}}$ given in Table 1. The required values are respectively 1.30, 0.7, and 0.8. The redundancy ratios are obtained as $r_u = R_u/R_{u\,\mathrm{req}} = 1.21$, $r_s = R_s/R_{s\,\mathrm{req}} = 1.38$, and $r_d = R_d/R_{d\,\mathrm{req}} = 1.70$. Because all the redundancy ratios are greater than 1.0, this bridge's geometric configuration is considered to be adequately redundant.

A bridge system that is equally redundant may still be inadequate for truck traffic if its members are inadequately designed. Redundancy recognizes the reserve strength of the bridge system and not individual member strengths. Therefore, the redundancy ratios should be combined with a measure of member safety to verify that the overall system safety is adequate. Checks of member safety can be performed according to any currently acceptable AASHTO criteria, including WSD, LFD, or the proposed LRFD methods. For example, because the bridge was originally designed to satisfy the AASHTO LFD criteria, using Equation 11, the member reserve ratio r_1 for the LFD criteria is 1.0. The system factor ϕ_s is then calculated using Equation 12 as follows:

$$\phi_s = \min\,(r_1 r_u,\ r_1 r_s,\ r_1 r_d)$$

$$\phi_s = \min\,(1.0 \times 1.21,\ 1.0 \times 1.38,\ 1.0 \times 1.70) < 1.0 \times 1.35 \qquad (18)$$

$$\phi_s = \min\,(1.21,\ 1.38,\ 1.70) = 1.21 < 1.35$$

Because ϕ_s is greater than 1.0, this system is redundant and its member capacities can be reduced by a factor of 1.21 without jeopardizing the overall system safety. Using Equation 13 with $D' = D = 1{,}970$ kip-ft and $R = 5{,}810$ kip-ft a value of $R' = 5{,}143$ kip-ft is obtained. This is compared with the value of 5,159 kip-

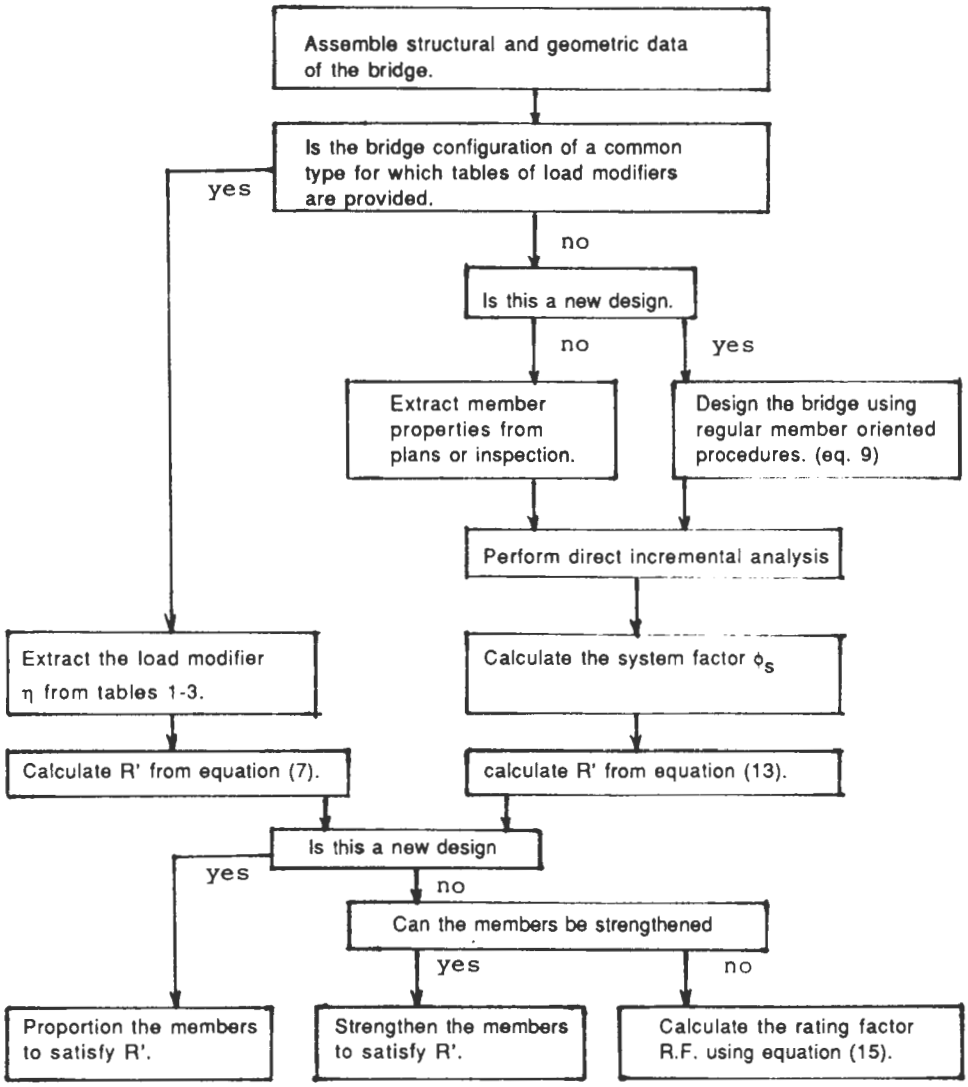

FIGURE 3 Flow chart of proposed framework for redundancy evaluation of bridge systems.

ft obtained using the load modifier tables. The difference between the two methods is less than 1.0 percent.

Other examples illustrating the proposed procedures are provided elsewhere (*5*). The framework proposed in this study to include system redundancy in the bridge design and evaluation of process is summarized in the flow chart of Figure 3.

Conclusions

The objective of this study was to develop a framework for considering redundancy in the design and load capacity evaluation of highway bridge superstructures. This goal was achieved by proposing a method to reward adequately redundant designs by permitting less conservative member designs than is allowed by current standards. On the other hand, designs with insufficient redundancy are penalized by requiring that their members be more conservative. This could be achieved by applying load modifiers during the routine bridge design and evaluation process.

Tables of load modifiers have been developed for typical bridge configurations. For bridges with configurations that are not covered by the tables, a direct analysis approach is recommended. This requires the performance of a nonlinear incremental load analysis to verify whether acceptable behavior, unserviceable conditions, or collapse states occur under maximum expected truck loading. Guidelines necessary to perform such an analysis are provided. The proposed framework could be readily integrated into future editions of the AASHTO standard and LRFD specifications.

The proposed methods are calibrated using reliability techniques. Redundancy is defined in terms of the difference between the reliability index (or safety index) of the bridge system and the reliability index of the members. The load modifier tables and the load factors recommended for the direct analysis approach are calibrated to ensure that highway bridges will provide adequate levels of system safety.

Although reliability techniques are used during the development of the methodology, the reliability model is transparent to the end user. To consider redundancy during the design and evaluation of a bridge structure, the bridge engineer can simply utilize the proposed system factors without referring to reliability theory.

The calibration process investigated the performance of typical simple-span concrete T-beam, prestressed concrete 1-girder bridges, and multigirder steel bridges. A parametric analysis verified that the redundancy of these simple-span bridges is a function of the geometric configuration and is not sensitive to variations in the section properties. The tabulated load modifiers were calculated only for these bridge configurations, assuming that all the members of a bridge are identical. Load modifiers for other configurations can be easily included in the future.

Continuous bridges are not included in the tables pending further investigation. A sensitivity analysis showed that continuous bridges produced higher redundancy levels than did simple span bridges if the sections in negative bending have sufficient levels of ductility. This means that steel sections in negative bending should be compact, and the concrete section should satisfy AASHTO's requirements. On the other hand, if the sections in negative bending are not ductile, continuous bridges may show low levels of redundancy. Future research on bridge redundancy should carefully consider the relationship between member ductility and the redundancy of continuous bridges.

ACKNOWLEDGMENT

This work was sponsored by AASHTO, in cooperation with FHWA and was conducted in the NCHRP, which is administered by TRB of the National Research Council. The opinions and conclusions expressed or implied in this paper are those of the authors and are not necessarily those of TRB, the National Research Council, or FHWA, AASHTO or the individual states participating in NCHRP.

REFERENCES

1. *Standard Specifications for Highway Bridges*, 15th ed., AASHTO, Washington, D.C., 1992.
2. Galambos, T. V., T. R. Leon, and C. W. French. *NCHRP Report 352: Inelastic Rating Procedures for Steel Beam and Girder Bridges*. TRB, National Research Council, Washington, D.C., 1992.
3. Nowak, A. *Calibration Report for NCHRP Project 12-33*. Department of Civil Engineering, University of Michigan, Ann Arbor, May 1992.
4. *LRFD Bridge Design Specifications*, 1st ed., AASHTO, Washington, D.C., 1994.
5. Ghosn, M., and F. Moses. *Redundancy in Highway Bridge Superstructures*. NCHRP Project 12-36, Final Report. March 1994.

WOOD BRIDGES

Load and Resistance Factor Design Code for Wood Bridges

Andrzej S. Nowak, *University of Michigan*
Michael A. Ritter, *Forest Service, U.S. Department of Agriculture*

The development of a load and resistance factor design (LRFD) edition of AASHTO's Standard Specifications for Highway Bridges is complete. A part of this effort involved the development of LRFD provisions for wood bridges. These new specifications include numerous changes and several significant departures from current allowable stress design practices for wood bridges. The live load model is based on the statistical analysis of the actual traffic data. The design load is a superposition of the traditional HS20 truck and lane loading. Dynamic load is applied to wooden components of the superstructure. Strength of material is based on the nominal values derived from in-grade tests, specified for wet-use conditions and 2-month live load duration. The resistance factors are determined consistently for all the limit states considered. The major changes in the approach to summarize the design provisions are presented.

The load and resistance factor design (LRFD) code for bridges was adopted in 1993 (*1*). The document covers all materials, including steel, concrete, and wood. The development of a new specification for wood bridges presented several unique opportunities and challenges. Overall, this project was a rare opportunity to completely revise and update AASHTO wood bridge design requirements (*2*) which traditionally have lagged behind state-of-the-art wood design methodologies. The primary challenge for wood bridges was to develop basic design requirements and procedures for LRFD. Unlike concrete and steel, which have had an LRFD procedure available for several years, LRFD specifications for wood are in the developmental stages (*3,4*).

The state-of-the-art data base for wood bridge design is summarized by Ritter (*5*). There were considerable new developments in the area of structural reliability and code optimization. The parameters of load and resistance are random variables. Therefore, statistical models were derived on the basis of load surveys, material tests, bridge tests, and simulations. New data are available for modeling wood components and structures (*6*). The approach to probability-based analysis of wood bridges was presented by Nowak (*7*).

This paper summarizes selected provisions of the new AASHTO LRFD specifications as they relate to the design of wood bridges. These provisions include topics related to general design features, loads and load distribution, and wood design.

General Design Features

AASHTO's LRFD specifications (*1*) are based on a limit states design approach. As defined in the specification, a limit state represents a condition beyond which the

bridge or component ceases to satisfy the provisions for which it was designed. For general bridge design, four limit states are defined; strength, service, extreme events, and fatigue and fracture. For wood bridge design, the most applicable of these limit states are the strength limit state, which is intended to ensure that the structure will provide the required strength and stability over the design life, and the service limit state, which restricts stress and deformation under regular service conditions. The extreme event limit state, which is intended to ensure structural survival in major earthquakes, floods, and vehicle collisions, will generally not control the design of most wood bridges. The fatigue and fracture limit state, which applies primarily to steel bridges, is not applicable to the design of wood components under current design practices.

In the LRFD specification, each component must satisfy the following equation for each limit state:

$$\eta\Sigma(\gamma_i Q_i) < \phi R_n \quad (1)$$

where

η = load modifier for ductility, redundancy, and operational importance;
γ_i = load factor;
Q_i = load effect;
ϕ = resistance factor; and
R_n = nominal resistance.

Within the general provisions of the LRFD specification, two provisions that affect wood design are noteworthy. In the past, wood structures have not been subject to impact factor adjustments that increase vehicle live load to account for dynamic effects. In the LRFD specification, general requirements for a dynamic load allowance require that the static truck loads be increased 75 percent for the design of deck joints and 33 percent for the design of all other components. For wood design, these values may be reduced by one-half. Another area that has not been addressed for wood bridges in previous allowable stress design (ASD) specifications is live load deflection. The LRFD specification presents a deflection limit for wood bridges equal to the bridge span divided by 425. This deflection limit, which is based on the vehicle live load, including the dynamic allowance, is considered an optional requirement and is left to designer judgment.

Loads and Load Distribution

The major load components for bridges include dead load, live load, dynamic load (impact), environmental loads (wind, earthquake, and temperature), and special (extreme) loads and effects (vessel collision and vehicle collision).

From the statistical point of view, it is convenient to distinguish between weight of structural components and asphalt wearing surface. It has been observed that, on average, self-weight of structural components is 3 to 5 percent larger than the design value. The coefficient of variation is about 0.08 to 0.10. On the other hand, the weight of asphalt varies depending on the actual thickness of the wearing surface. The average thickness is 3.5 in. (90 mm), and the coefficient of variation is 0.25 (*8*). For wood bridges, dead load constitutes a small portion of the total load. The weight of asphalt contributes about 10 percent of the total load.

Live load is often the most important load component for wood bridges. Live load model was derived on the basis of the actual truck survey data (*9,10*). Most of the wood bridges are with short spans. Therefore, the maximum moment is determined by an axle or closely spaced tandem. For example, the histogram of actual axle loads measured in Michigan is shown in Figure 1. The corresponding cumulative distribution function (CDF) is shown in Figure 2 (*11*). The CDF is plotted on the inverse normal probability scale. The average axle load is about 10 kips (45 kN), but the maximum observed values exceed 40 kips (180 kN).

The extreme effect for various periods (up to 75 years) was extrapolated from the available data. The critical load is a result of two side-by-side trucks, each representing the maximum 2-month truck. The design of superstructure components is based on the analysis of moments and shear forces. The maximum expected moments and shears, calculated for various periods, are shown in Figures 3 and 4, respectively. For an easier comparison, the moments and shears are divided by

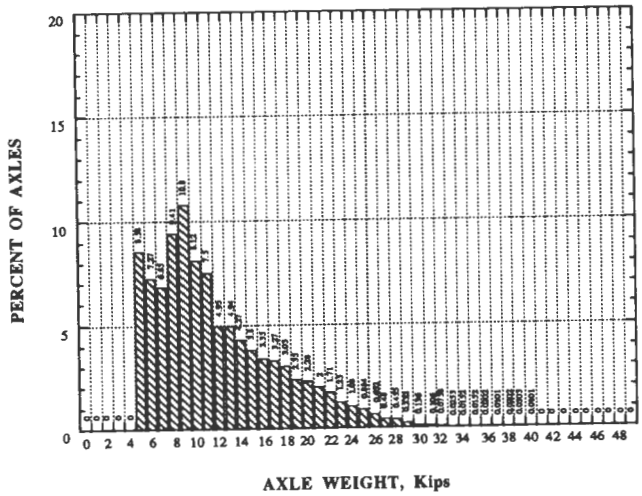

FIGURE 1 Histogram of measured axle loads (1 kip = 4.45 kN).

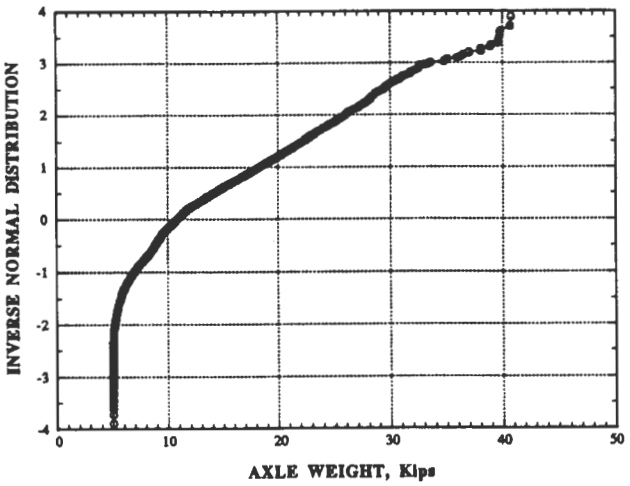

FIGURE 2 CDF of axle loads on normal probability paper (1 kip = 4.45 kN).

corresponding HS20 moments and shears (*2*). The new live load, specified in LRFD AASHTO code, is a superposition of HS20 truck and a uniform lane loading of 640 lb/ft (9.3 kN/m). The ratio of mean to nominal is called a bias factor. The design code is expected to specify design load values so that bias factor is uniform over different spans. The bias factors for AASHTO (1992) and the new LRFD AASHTO (*1*) are shown in Figure 5 for moments and Figure 6 for shears.

The LRFD specification presents load combinations in tabular format with the specified load factors for each type of applied loading (*1*). There are a total of 11 load combinations; 5 for the strength limit state, 2 for the extreme events limit state, 3 for the service limit state, and 1 for the fatigue and fracture limit state. Of these, two strength load combinations and one service load combination will most commonly control design for wood bridges.

Requirements for structural analysis and evaluation in the LRFD specification include guidelines for sophisticated bridge analysis and simplified approximate methods of analysis, which have traditionally been used. In general, the requirements for approximate load distribution for wood bridges are the same as those cur-

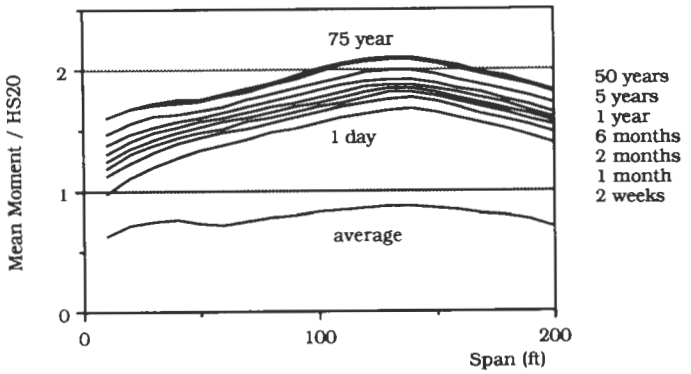

FIGURE 3 Mean maximum moments for various periods (1 ft = 0.305 m).

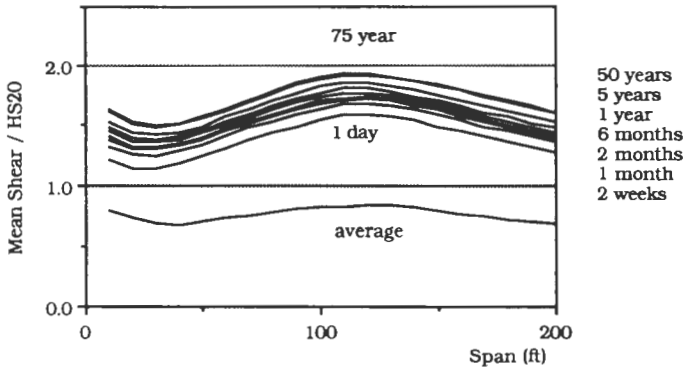

FIGURE 4 Mean maximum shears for various periods (1 ft = 0.305 m).

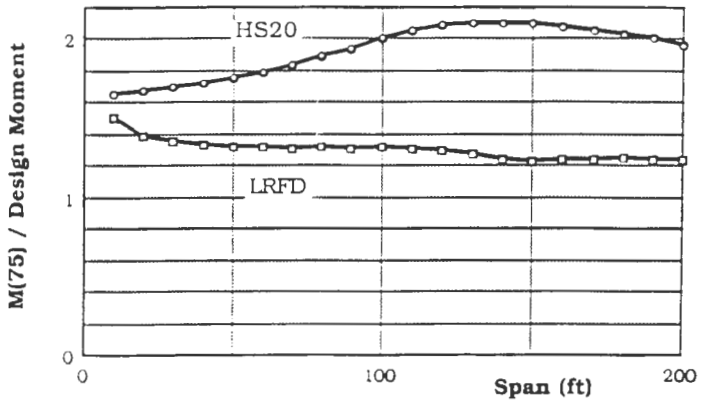

FIGURE 5 Bias factor for moments: for AASHTO (*2*) and LRFD AASHTO (*1*) (1 ft = 0.305 m).

rently presented in the AASHTO allowable stress design (ASD) specification (*2*). An exception is the load distribution criteria for the design of slab-type superstructures. Rather than the traditional criteria based on a longitudinal distribution width as a function of tire width and deck thickness, the following equations are given for an equivalent longitudinal distribution width per lane and are applicable both to wood and concrete superstructures.

With one lane loaded,

$$E = 1.00 + 0.50(L_1 W_1)^{1/2} \quad (2)$$

With more than one lane loaded,

$$E = 7.00 + 0.12(L_1 W_1)^{1/2} < W/N \quad (3)$$

where

E = equivalent distribution width per lane (in feet) (1 ft = 0.305 m);
L_1 = modified span equal to the lesser of the actual span or 60 ft (18 m);
W_1 = modified width equal to the lesser of actual width or 60 ft (18 m),
W = physical edge-to-edge bridge width (ft),
L = physical bridge length (ft), and
N = number of design lanes.

Wood Design

Provisions for the LRFD design of wood components are presented in one chapter of the LRFD AASHTO code (*1*) and include requirements for materials, limit states, component design, bracing, and camber. From a

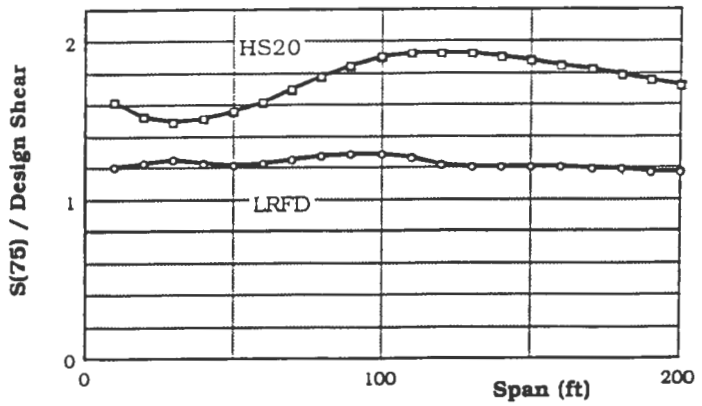

FIGURE 6 Bias factor for shears: for AASHTO (*2*) and LRFD AASHTO (*1*) (1 ft = 0.305 m).

design perspective, the most significant departures from the ASD method involve provisions for base and nominal resistance values for wood materials, resistance factors and the relationship of these factors to limit states and load combinations, and component design requirements.

One key wood design requirement for the AASHTO LRFD specification was the development of a procedure for obtaining base resistance values for various engineered wood products (*1*). Given the large number of wood species, products, and grades used in bridge applications, AASHTO ASD specifications have traditionally included design values for only a limited number of the species and grades of sawn lumber, glued laminated timber, and timber piles (*2*). These values have been obtained directly from national standards, primarily the National Design Specification for Wood (NDS) (*12*) for sawn lumber and timber piles and AITC 117-Design (*13*) for glued laminated timber. This approach has provided consistency between the design values used for bridges and those used for buildings and other structures. In addition, this approach provides the most expedient reference to current design values when industry changes are made. On the basis of these considerations, a procedure for determining base resistance values for wood products was developed that directly incorporates industry standards presented in the NDS and AITC 117-Design (*12,13*).

The properties of material are based on the actual in-grade tests. For example, the CDFs based on the results of bending tests to determine the modulus of rupture (MOR) of Douglas fir are shown in Figure 7 for select structural and Figure 8 for Grades 1 and 2. The CDFs of MOR are plotted on inverse normal probability paper. The results are shown for several sizes. MOR indicates a considerable degree of variation, with coefficient of variation about 0.3. The average MOR is about three to four times larger than the lowest test results. However, new structural types, glulam and stressed wood, allow for a significant reduction of the coefficient of variation. The tests were carried out to determine the MOR for different widths of stressed units, each made of 2 × 8 in. (50 × 200 mm) boards. Three widths were considered: 1, 2, and 3 ft (300, 600, and 900 mm). Examples of CDFs for red pine, white pine, and hem-fir are shown in Figure 9 (*7*). The coefficients of variation are about 0.10 to 0.13, which are considerably lower than those without prestressing.

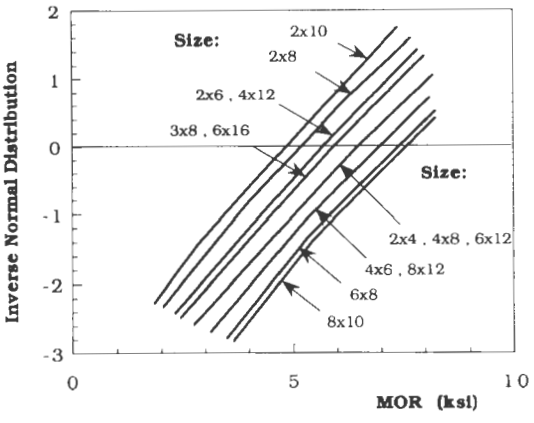

FIGURE 7 MOR for Douglas fir, select structural, on inverse normal probability paper (1 ksi = 6.9 MPa).

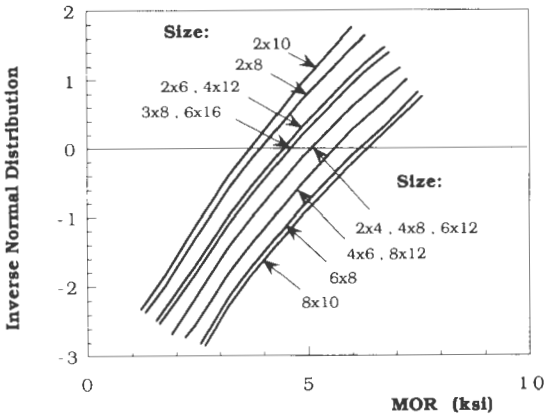

FIGURE 8 MOR for Douglas fir, Grades 1 and 2, on inverse normal probability paper (1 ksi = 6.9 MPa).

The LRFD specification includes tables of base resistance values for selected wood species and grades of sawn lumber, glued laminated timber, and timber piles that are commonly used for wood bridge design (*1*). The base resistance is defined as a value of stress (or modulus of elasticity) that is to be used in the design. The values correspond to wet-use conditions and a 2-month load duration, which corresponds to the most common design conditions. Within these tables, base resistance values are given for flexure (F_{bo}), tension parallel to grain (F_{to}), shear parallel to grain (F_{vo}), compression perpendicular to grain (F_{cpo}), compression parallel to grain (F_{co}), and modulus of elasticity (E_o). To obtain values for species and grades not included in the tables, a direct conversion of ASD values in the NDS or AITC 117-Design (*12,13*) is specified using the following conversion factors given in Table 1.

Base LRFD resistance values obtained from the specification tables or through adjustment of ASD values are based on specific conditions and are intended to serve as a starting point for determining the nominal resistance values used for design. To determine nominal resistance values, base resistance values must be adjusted by factors that compensate for (*a*) differences between

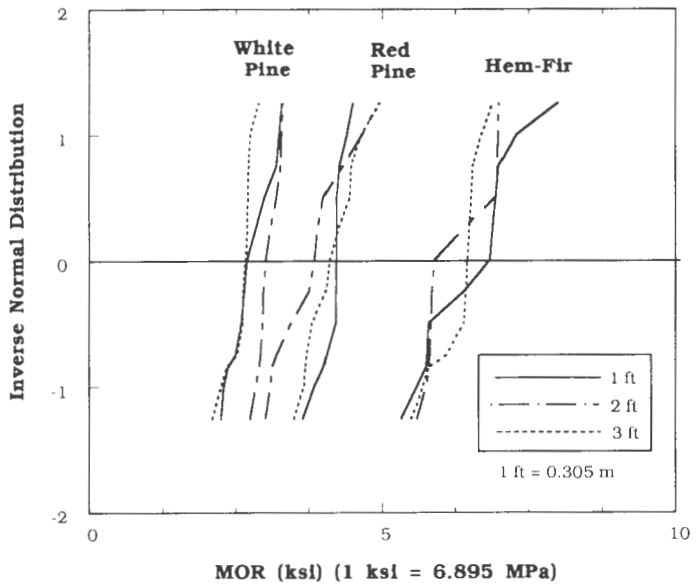

FIGURE 9 MOR for stressed wood units.

the assumptions used to establish the base resistance values and the actual use conditions, (*b*) variations in wood behavior related to the type of stress or member orientation, and (*c*) differences between the physical and mechanical behavior of wood and that of an ideal material assumed in most equations of engineering mechanics. General adjustments that are common to the design of most components are presented in the LRFD specification as follows:

$$F = F_o C_F C_M C_D \tag{4}$$

$$E = E_o C_M \tag{5}$$

where

F = applicable nominal resistance F_b, F_t, F_v, F_{cp}, or F_c,
F_o = applicable base resistance F_{bo}, F_{to}, F_{vo}, F_{cpo}, or F_{co},
C_F = size effect factor based on the member size or volume,
C_M = moisture content factor for adjustment to dry use conditions,
C_D = deck factor applicable to the design of some deck types,
E = nominal modulus of elasticity, and
E_o = base modulus of elasticity.

Additional adjustments that are related only to the design of specific components are included in the component design subsections of the wood design section.

Resistance Factors

As previously presented in the general LRFD design equation, the nominal resistance of a component is multiplied by a resistance factor ϕ. For wood design, the resistance factors for all wood products, species, and grades are as follows:

- Flexture: $\phi = 0.85$,
- Shear: $\phi = 0.75$,
- Compression parallel to grain: $\phi = 0.90$,
- Compression perpendicular to grain: $\phi = 0.90$, and
- Tension parallel to grain: $\phi = 0.80$.

For strength load combination IV, corresponding to the case governed by permanent loads, the resistance

TABLE 1 Conversion Factors for LRFD Base Resistance from NDS ASD Tables

Material	F_{bo}	F_{to}	F_{vo}	F_{cpo}	F_{co}	E_o
Dimension Lumber	2.35	2.95	3.05	1.75	1.90	0.90
Beams and Stringers and Posts and Timbers	2.80	2.95	3.15	1.75	2.40	1.00
Glued laminated timber	2.20	2.35	2.75	1.35	1.90	0.83

factors are multiplied by 0.75 to compensate for the load duration effect on wood properties when components are subjected to the long-term loading.

Component Design Requirements

Within the LRFD wood design section, subsections are provided for component design for members in flexure, shear, compression, tension parallel to grain, combined flexure, and axial loading. These subsections include specific provisions related to design, including additional adjustment factors that are applied to the nominal resistance. An example equation for nominal resistance in flexure follows:

$$M_n = F_b S C_s C_r \tag{6}$$

where

M_n = nominal resistance in flexure,
F_b = specified resistance in flexure from Equation 2,
S = section modulus,
C_s = stability factor, and
C_r = repetitive member factor.

Within the LRFD specifications, values for specific factors such as C_s and C_r are determined from equations or tables presented in the component design subsection.

Conclusions

The new AASHTO LRFD specification (*1*) presents a new approach to bridge design that differs from traditional ASD methodology (*2*). From the perspective of wood bridge design, significant provisions of the LRFD specification include (*a*) the use of load and resistance factors, (*b*) inclusion of a dynamic load allowance for static truck loads, (*c*) a new live load deflection criteria, (*d*) revised load combinations and live load distribution requirements, and (*e*) new values for material strength (base resistance).

References

1. *LRFD Bridge Design Specifications.* AASHTO, Washington, D.C., 1994.
2. *Standard Specification for Highway Bridges.* AASHTO, Washington, D.C., 1992.
3. Murphy, J. F., ed. *Load and Resistance Factor Design for Engineered Wood Construction—A Pre-Standard Report.* American Society of Civil Engineers, New York, 1988.
4. Goodman, J. R. Reliability-Based Design for Engineered Wood Construction: Update and Status of U.S. Progress. In *Proc. 1990 International Timber Engineering Conference* (H. Sugiyama, ed.), Oct. 23–25, 1990, Tokyo, Japan, Vol. 1.
5. Ritter, M. A. *Timber Bridges, Design, Construction, Inspection and Maintenance.* EM7700-B. USDA Forest Service, Washington, D.C., 1990.
6. Nowak, A. S. *Modelling Properties of Timber Stringers.* Report UMEE 83R1. Department of Civil Engineering, University of Michigan, Ann Arbor, May 1983.
7. Nowak, A. S. Reliability Analysis for Wood Bridges. In *Transportation Research Record 1291*, TRB, National Research Council, Washington, D.C., 1991, pp. 315–327.
8. Nowak, A. S. *Calibration of LRFD Bridge Design Code.* NCHRP Project 12-33. TRB, National Research Council, Washington, D.C., 1995.
9. Nowak, A. S., Y-K. Hong, and E-S. Hwang, Modeling Live Load and Dynamic Load for Bridges. In *Transportation Research Record 1289*, TRB, National Research Council, Washington, D.C., 1991, pp. 110–118.
10. Nowak, A. S., and Y-K. Hong. Bridge Live Load Models. *Journal of Structural Engineering*, ASCE, Vol. 117, No. 9, Sept. 1991, pp. 2757–2767.
11. Nowak, A. S., J. Laman, and H. Nassif. *Effect of Truck Loading on Bridges.* Report UMCE 94-22. Department of Civil and Environmental Engineering, University of Michigan, Ann Arbor, Dec. 1994.
12. *National Design Specification for Wood Construction.* National Forest Products Association, Washington, D.C., 1991.
13. *AITC 117-Design; Standard Specifications for Structural Glued Laminated Timber of Softwood Species.* American Institute of Timber Construction, Vancouver, Wash, 1987.

Design, Construction, and Evaluation of Timber Bridge Constructed of Cottonwood Lumber

Michael A. Ritter and James P. Wacker, *Forest Service, U.S. Department of Agriculture*
Everett D. Tice, *Appanoose County Engineering, Iowa*

The Cooper Creek bridge was constructed February 1992 in the city of Centerville, Iowa. The bridge is a two-span continuous stress-laminated deck structure with a length of 12.8 m and a width of approximately 8.1 m. The bridge is unique in that it is one of the first known stress-laminated timber bridge applications to use eastern cottonwood lumber. The performance of the bridge was monitored continuously for 28 months beginning at the time of installation. Performance monitoring involved gathering and evaluating data relative to the moisture content of the wood deck, the force level of stressing bars, the deck vertical creep, and the behavior of the bridge under static load conditions. In addition, comprehensive visual inspections were conducted to assess the overall condition of the structure. On the basis of field evaluations, the bridge is performing well with no structural or serviceability deficiencies.

In 1988, the U.S. Congress passed legislation known as the Timber Bridge Initiative (TBI). The objective of this legislation was to establish a national program to provide effective and efficient utilization of wood as a structural material for highway bridges. Responsibility for the development, implementation, and administration of the timber bridge program was assigned to the U.S. Department of Agriculture (USDA) Forest Service. Within the program, the Forest Service established three primary program areas: demonstration bridges, technology transfer, and research. The demonstration bridge program, which is administered by the Forest Service Timber Bridge Information Resource Center (TBIRC) in Morgantown, West Virginia, provides matching funds on a competitive basis to local governments to demonstrate timber bridge technology through the construction of demonstration bridges (*1*). TBIRC also maintains a technology transfer program to provide assistance and state-of-the-art information about timber bridges. One objective of these program areas is to encourage innovation through the use of new or previously underutilized wood products, bridge designs, and design applications.

As the national wood utilization research laboratory within the USDA Forest Service, the Forest Products Laboratory (FPL) was assigned responsibility for the research portion of the TBI program. As a part of this broad research program, FPL has taken a lead role in assisting local governments in evaluating the field per-

formance of timber bridges, many of which employ design innovations or materials that have not been previously evaluated. Through such assistance, FPL is able to collect, analyze, and distribute information on the field performance of timber bridges to provide a basis for validating or revising design criteria and further improving efficiency and economy in bridge design, fabrication, and construction.

This paper describes the development, design, construction, and field performance of the Cooper Creek bridge located in Appanoose County, Iowa. The bridge is a two-lane, two-span continuous stress-laminated deck with a length of 12.8 m. Built in 1992, the Cooper Creek bridge was constructed entirely with local funds on the basis of technical assistance provided through the Forest Service TBI program. The bridge is unique in that it is one of the first known applications that utilizes Eastern Cottonwood lumber in a stress-laminated deck superstructure.

Objective and Scope

The objective of this project was to design, construct, and evaluate the field performance of the Cooper Creek bridge over a minimum 2-year period beginning at bridge installation. The project scope included data collection and analysis related to the modulus of elasticity (MOE) of bridge laminations, wood moisture content, stressing bar force, vertical deck creep, bridge behavior under static truck loading, and general structure performance. The results of this project will be used to formulate recommendations for the design and construction of similar stress-laminated cottonwood bridges in the future.

Background and Development

The Cooper Creek bridge site is located in Centerville, Iowa, in Appanoose County. The bridge is on West Cottage Street, which serves as the primary access road to a large community park surrounding the Centerville reservoir. The bridge crosses Cooper Creek, which carries daily flow from the backwashing of city water supply filters and occasional overflow from the nearby reservoir dam. The approach roadway is a two-lane gravel road. Traffic is mostly light passenger vehicles with an estimated average daily traffic of 200 vehicles per day.

The Cooper Creek bridge was originally constructed in the 1940s and consisted of steel stringers with a concrete deck supported by concrete abutments. Inspection of the bridge in the mid-1980s indicated that the concrete deck was in poor condition and the steel stringers were badly corroded. Replacement of the bridge, along with another bridge in the reservoir area, was subsequently included within a large waterworks project at the Centerville reservoir. This project was made possible through a grant from the Chariton Valley Resource Conservation and Development (RCD) council to the state of Iowa and was initiated to improve the city water supply system. In the initial stages of the project, both bridges were scheduled to be constructed using reinforced concrete. However, information obtained through the TBIRC prompted the Chariton Valley RCD to change the Cooper Creek bridge to a timber structure using the relatively new stress-laminated deck design concept. A timber bridge was considered the best option by RCD because there was an opportunity to use native Iowa materials and the aesthetics of a timber bridge would blend well into the natural park setting.

As the waterworks project progressed at the Centerville reservoir, difficulties were encountered in the design of the Cooper Creek bridge. Because the concept of stress-laminating timber bridges was new in the United States, little information was available on design criteria and construction specifications. To provide assistance in this area, FPL was contacted for technical advice. Through a series of meetings with state, local, and FPL representatives, options were discussed, and it was determined that a stress-laminated deck bridge constructed of Iowa eastern cottonwood lumber was feasible for the site. Subsequent to these meetings, an agreement was drafted for the design, construction, and field evaluation of the Cooper Creek bridge involving a cooperative effort between the City of Centerville, Chariton Valley RCD, Iowa Department of Transportation, Forestry Division of the Iowa Department of Natural Resources, Iowa Department of Economic Development, TBIRC, and FPL.

Design, Construction, and Economics

The design and construction aspects of the Cooper Creek bridge involved a mutual effort between the City of Centerville, Appanoose County Engineering, which served as the engineering representative for the City of Centerville, and FPL. Construction assistance was also provided by the Centerville Municipal Waterworks. An overview of the design and construction process, as well as cost information for the bridge superstructure, are presented in this section.

Bridge Design

Design of the Cooper Creek bridge superstructure was completed by FPL in collaboration with Appanoose County Engineering. At the time of the design, early

1990, national design specifications for stress-laminated timber bridges did not exist. Those aspects of the design dealing specifically with stress laminating were based primarily on research completed by the University of Wisconsin and FPL (*2,3*). Additionally, FPL experience with stress-laminated decks from an ongoing field evaluation program contributed to the design details. All other aspects of the superstructure design were based on AASHTO's Standard Specifications for Highway Bridges (*4*).

Design requirements for the Cooper Creek bridge called for a crossing of 12.8 m with an out-to-out bridge width of 7.9 m. The bridge was to carry two lanes of AASHTO HS 20–44 loading with a maximum design live-load deflection of 1/360 of the bridge span. In addition to these geometry and loading requirements, several other design requirements were related to the eastern cottonwood lumber laminations. Because of limitations on local supply and fabrication, lamination length was limited to 5.5 m. It was also considered economically advantageous to limit the deck depth to a maximum of 305 mm, although a maximum deck thickness of 356 mm was feasible on the basis of lumber availability.

The first step in the design process was to identify material design values for the Eastern Cottonwood lumber laminations. Because Eastern Cottonwood was not commonly used for structural applications, design values were not included in AASHTO and referenced design values in the National Design Specification for Wood Construction (NDS) (*5*) were limited to material 51 to 102 mm thick and 51 to 102 mm wide. Because the bridge laminations would be greater than 102 mm wide, the NDS values were not entirely applicable to the bridge design. Further examination indicated that the NDS also included design values for Black Cottonwood in widths greater than 102 mm. Subsequent review by FPL of the green, clear wood material properties for the two similar species indicated that modulus of rupture and MOE properties for eastern cottonwood were greater than those for Black cottonwood (ASTM D2555–88). Thus, the decision was made to use the NDS tabulated design values for bending strength and MOE based on black cottonwood, which would result in a slightly conservative design. The design value for compression perpendicular to grain was based on tabulated values for eastern cottonwood, which is independent of member size. The results were tabulated bending design values for visually graded lumber of 5.2 and 4.5 MPa for material graded Numbers 1 and 2, respectively, and MOE values of 8,268 and 7,579 MPa for the same grades. The tabulated value for compression perpendicular to grain was 2.2 MPa for all grades.

Given the required bridge length and limitations on material size, a two-span continuous structure with equal span lengths was selected for the final design (Figure 1). The layout of the bridge laminations was based on available lamination lengths of 1.2 to 5.5 m in 0.6-m increments. To meet span requirements for the continuous deck, a transverse butt joint frequency of one joint every four laminations with a 1.2-m-longitudinal spacing between joints in adjacent laminations was used (*3*). As with most stress-laminated timber bridge decks, it was anticipated that bridge stiffness rather than strength would control the design. After adjusting tabulated design values for wet-use conditions and other applicable modification factors required by AASHTO, it was determined that a full-sawn deck 305 mm thick would meet design requirements if visually graded Number 1 lumber was used. Using this configuration, the calculated design live-load deflection for HS 20–44 loading was 13 mm, or 1/473 of the bridge span. A check of bending stress indicated that the applied stress of 6.4 MPa was less than the allowable of 6.7 MPa.

The stressing system for the Cooper Creek bridge was designed to provide a uniform compressive stress of 0.69 MPa between the lumber laminations. To provide this interlaminar compression, high-strength stressing bars 16 mm in diameter were spaced 610 mm on-center, beginning 305 mm from the bridge ends. The tensile force required in the bars for the 0.69-MPa interlaminar compression was determined to be 128 kN. The bars were specified to comply with the requirements of ASTM A722–86 and provide a minimum ultimate tensile strength of 1 034 MPa. The bar anchorage system was the discrete plate anchorage system consisting of steel bearing plates 254 by 254 by 19 mm with steel anchorage plates 51 by 127 by 25 mm. To provide additional strength in distributing the stressing bar force into the deck without damaging the eastern cottonwood laminations, it was determined that the two outside laminations along the deck edge would be northern red oak sawn lumber.

Following initial deck design, the bridge railing was designed and specifications were summarized. The bridge railing design was a sawn lumber curb and glued laminated timber rail that was based on a crash-tested rail system developed by FHWA (*6*). Specifications for wood members required that all components be pressure treated after fabrication with creosote in accordance with American Wood Preservers' Association Standard C14. To provide protection from deterioration, all steel components including hardware, stressing bars, and anchorage plates were galvanized per AASHTO specifications (*7*).

Construction

Construction of the Cooper Creek bridge was completed by personnel from the city of Centerville, Ap-

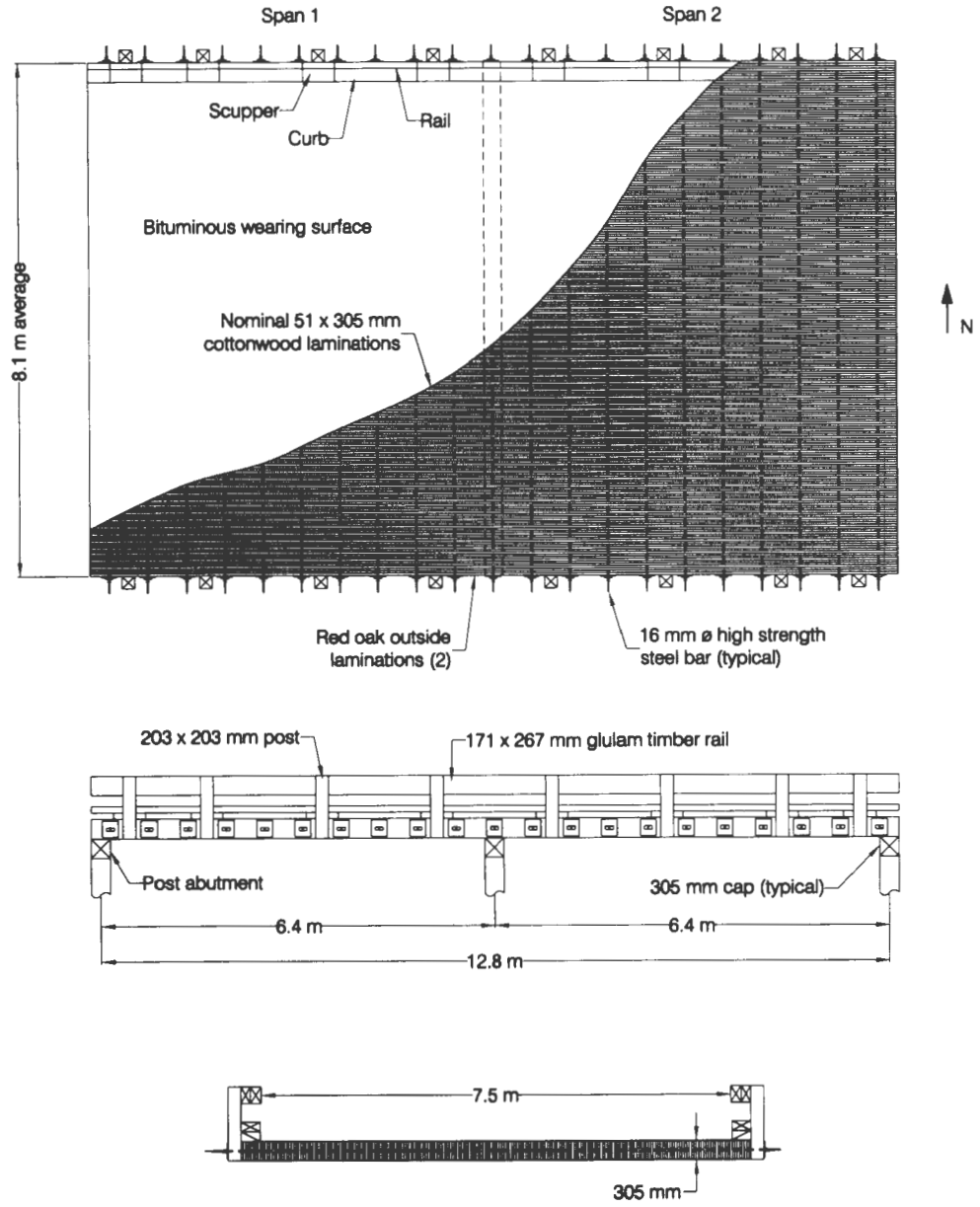

FIGURE 1 Design configuration of Cooper Creek bridge.

panoose County Engineering, the Centerville Municipal Waterworks, and FPL. After the work on the approach roadway, and the design and construction of the sawn lumber post and sill abutments and center bent by Appanoose County Engineering was completed, construction of the bridge superstructure commenced on February 25 and was completed on February 28. The construction process was slowed by rain and cold temperatures, which made work conditions difficult but did not adversely affect the construction process. Construction of the bridge railing and backfill of the approach roadways was completed shortly after the superstructure construction.

Superstructure construction began with delivery of the bridge laminations and other materials to the bridge site. The bridge laminations arrived in banded bundles and were stacked approximately 60 m from the substructure. The laminations had been prefabricated at a local mill in Centerville and were sent to a pressure-treating facility in Nebraska for the creosote treatment. Inspection of the laminations at the site indicated that the material had not been surface planed to a uniform thickness and measurements of lamination ends indicated a range in thickness of 45 to 60 mm. This presented a potential problem for construction at the deck butt joints where uniform contact is required between

laminations for load transfer. To account for this variation, the end thickness of each lamination was measured and written in chalk on the lamination end. The order of lamination placement was then scheduled so that the end thickness of the two laminations at a butt joint was the same. Laminations with odd thicknesses that could not be matched, which were generally 55 mm and thicker, were positioned over the abutments.

The construction of the Cooper Creek bridge involved a unique construction methodology that had not been widely used in the past. Rather than prefabricating the deck in sections, which is common practice for stress-laminated decks with butt joints, scaffolding was erected between the substructures, and laminations were individually placed on the scaffolding supports. This methodology was considered to be the most cost-effective because of the unavailability of a large crane to lift prefabricated bridge sections into place. The scaffolding consisted of a full floor under the deck that was supported by temporary stringers between the bridge abutments and center bent. The elevation of the floor was approximately 1.5 m below the cap elevations of the abutments and bent. Lumber supports were erected on the floor to support the laminations in their final positions as they were placed. Construction access to the scaffolding was provided by plywood ramps that were constructed between the scaffolding floor and the ground.

The deck construction process began by placing approximately 305-mm width of laminations along the south bridge edge (Figure 2*a*). The laminations were nailed together, and wood dowels were inserted into the bar holes to maintain the relative lamination alignment. Stressing bars were then inserted through the bar holes approximately 2.5 m toward the bridge centerline (Figure 2*b*). The bar overhang away from the bridge was supported by a wood frame to prevent excessive bending and damage to the bars (Figure 2*c*). After approximately 2 m of deck width was erected, the bars were pulled through the laminations so that they extended across the bridge width. Bridge construction progressed by sequentially adding laminations. This involved placing the bars through lamination holes and sliding the laminations along the temporary construction supports to the completed deck section (Figure 2*d*). Laminations were sequentially added in this manner until the bridge width was completed and ready for bar tensioning (Figure 2*e* and *f*).

Initial stressing of the bridge occurred immediately after all laminations were in position and steel plates and nuts were placed on stressing bar ends. Bar tensioning was accomplished with a single hydraulic jacking system consisting of a hydraulic pump, a hollow core jack, and a stressing chair (*8*). The stressing operation involved tensioning the first bar at an abutment, then sequentially tensioning all other bars along the bridge length. However, before beginning the stressing, visual inspection of the deck indicated that there were gaps between the laminations at several locations caused by warp in the laminations. To minimize deck distortion across the bridge width during stressing, it was determined that the bar force should be applied gradually over several passes. During the construction process, a total of six passes were completed. The first pass tensioned bars to 25 percent of the design level and was intended to bring all laminations into direct contact. The second pass brought bar force to 50 percent of design. The remaining four passes were at the full design level and were required to bring all bars to a uniform tension. Between the first and final stressing, the deck width narrowed approximately 25 mm as a result of the compression introduced between the laminations.

After the initial stressing, the bridge was restressed several times and the timber railing and asphalt wearing surface were placed. The bridge stressing followed an accelerated procedure, which has not been widely used for other bridges. It is general practice in stress-laminated deck construction to stress the bridge three times: at the time of initial construction, 1 week later, and 6 to 8 weeks after the second stressing (*3*). The Cooper Creek bridge was stressed four times: at construction and at 4, 7, and 14 days after construction. This accelerated procedure was completed because of limitations on equipment availability and provided an opportunity to evaluate bar force loss using an alternative stressing sequence. After the final stressing, the timber curb and rail system were installed. Placement of the asphalt wearing surface occurred approximately 4 months later in early July 1992. The completed bridge is shown in Figure 3.

Cost

Costs for the fabrication and construction of the Cooper Creek bridge superstructure, railing, and asphalt wearing surface totaled $34,200. On the basis of an average deck area of 104 m^2, the cost per square meter was approximately $329.

Evaluation Methodology

Through mutual agreement with the cooperating parties, a bridge monitoring plan for the Cooper Creek bridge was developed and implemented by FPL. The plan included stiffness testing of the lumber bridge laminations before bridge construction and performance monitoring after construction of the deck moisture con-

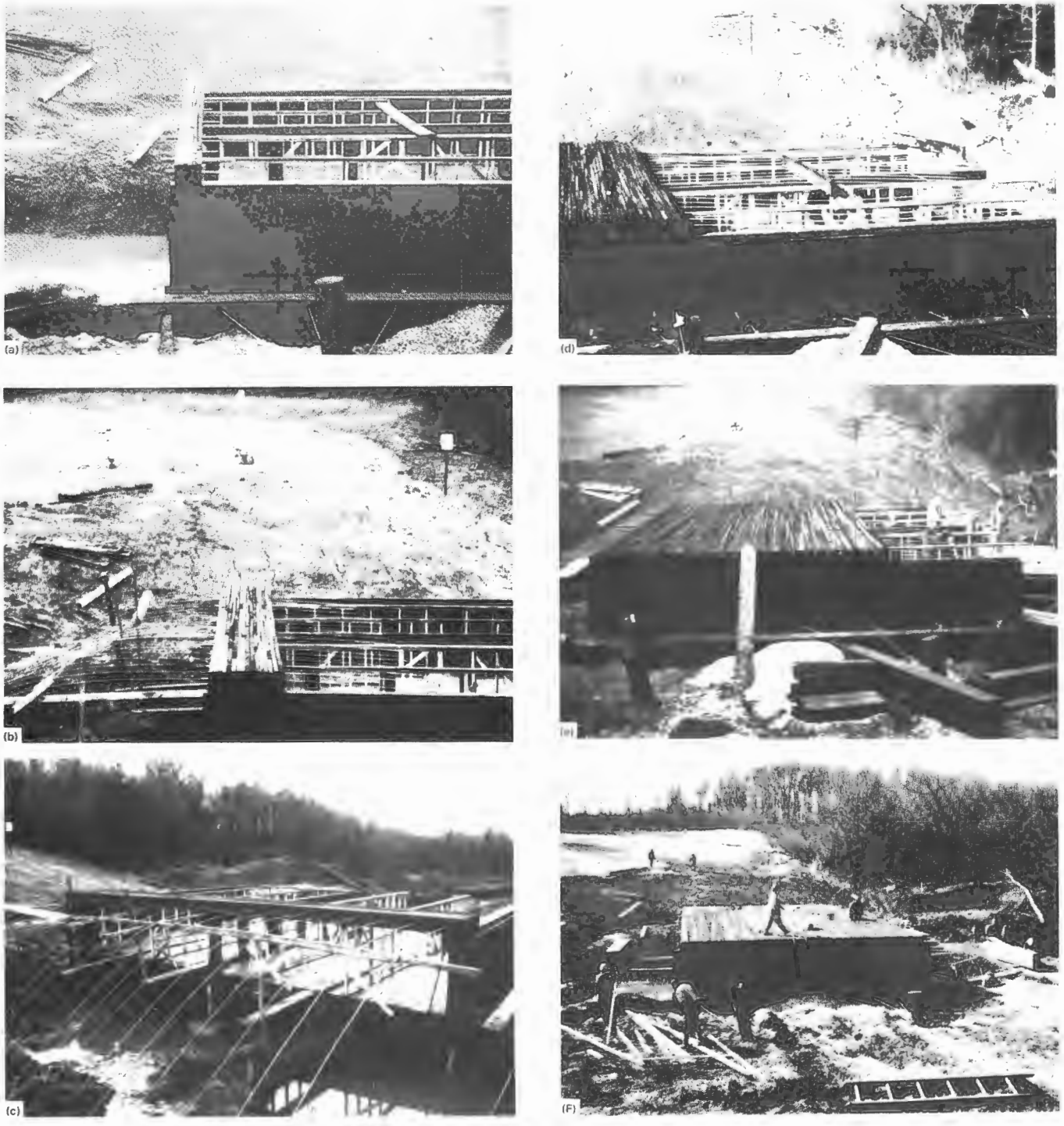

FIGURE 2 Construction sequence for Cooper Creek bridge: (*a*) placement of laminations along south bridge edge; (*b*) insertion of stressing bars; (*c*) support of bar overhang by wood frame; (*d*) sequential addition of laminations; (*e, f*) completed bridge width ready for bar tensioning.

FIGURE 3 Completed Cooper Creek bridge (two views).

tent, stressing bar force, vertical bridge creep, static load test behavior, and general bridge condition. The evaluation methodology used procedures and equipment previously developed and used by FPL on similar structures (*8,9*).

Lamination MOE

At the time of the Cooper Creek bridge design, eastern cottonwood lumber was not widely used for structural applications, and verification of the assumed design MOE was considered necessary. To measure actual lamination MOE values, portable equipment was taken to the bridge site and a group of laminations were tested just before bridge construction using the transverse vibration method (*10*). Using this method, laminations are placed flatwise on instrumented supports and impacted to induce a transverse vibration. On the basis of the vibratory response, the natural frequency of the lamination is measured and converted to MOE. For the Cooper Creek bridge, a total of 50 laminations were tested using this method, 10 each in lengths of 2.4, 3, 3.7, 4.3, and 4.9 m.

Moisture Content

The moisture content of the Cooper Creek bridge was measured using an electrical-resistance moisture meter with 76-mm probe pins in accordance with ASTM D4444–84. Measurements were obtained by driving the pins into the deck underside at depths of 25 to 76 mm, recording the moisture content value from the unit, then adjusting the values for temperature and wood species. Moisture content measurements were taken at the time of bridge installation, approximately 6 months after installation, and at the end of the monitoring period. In addition to the electrical resistance readings, core samples were removed from the bridge deck at the conclusion of the monitoring period to determine moisture content by the oven-dry method in accordance with ASTM D4442–84.

Bar Force

To monitor bar force, four calibrated load cells were installed on the Cooper Creek bridge when the bridge was constructed. Two load cells were placed on each span on the third and seventh stressing bars from each abutment. Load cell measurements were obtained by local personnel by connecting a portable strain indicator to a plug on the load cell. Strain measurements from the indicator were then converted to force levels, on the basis of the laboratory calibration, to determine the tensile force in the bar. Measurements were taken on approximately a bimonthly basis during the monitoring period. At the conclusion of the monitoring period, the load cells were removed, checked for zero balance shift, and recalibrated to determine time-related changes in the initial load cell calibration.

Vertical Creep

Vertical creep of the bridge was measured at the beginning and the end of the monitoring period. Vertical measurements were recorded to the nearest 3 mm by reading the centerspan elevations along deck edges relative to a stringline between supports.

Load Test Behavior

Static load testing of the Cooper Creek bridge was conducted at the end of the monitoring period to determine

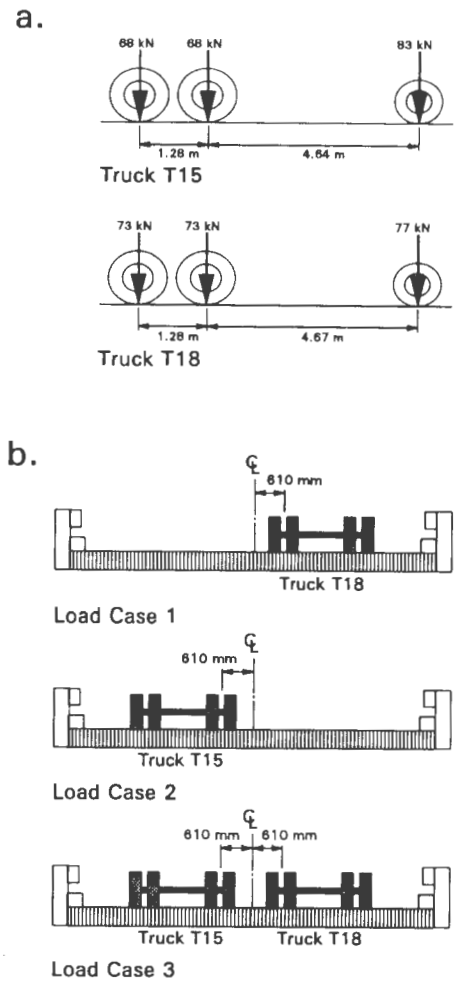

FIGURE 4 (*a*) Load test truck configurations and axle loads (the transverse vehicle track width, measured center to center of the rear tires, was 1.83 m); (*b*) transverse load positions (looking west). For all load cases, the two rear axles were centered over the bridge centerspan with front axles off the span.

the response of the bridge to full truck loading. In addition, an analytical assessment was completed to determine the predicted bridge response using computer modeling and current design recommendations.

Load Testing

Load testing involving positioning fully loaded trucks on the bridge spans and measuring the resulting deflections at a series of locations along the centerspan and abutments. Measurements of each span from an unloaded to loaded condition were obtained by placing calibrated rules at data points on the deck underside and reading values with a surveyor's level to the nearest 0.5 mm. Measurements were taken prior to testing (unloaded), for each load case (loaded), and at the conclusion of testing (unloaded).

Two trucks were used for load testing: Truck T15 with a gross vehicle weight of 219 kN and Truck T18 with a gross vehicle weight of 223 kN (Figure 4*a*). Each of the two spans was tested separately using designated positions in the longitudinal and transverse directions to produce the maximum live-load deflection in accordance with AASHTO recommendations (*4*). Longitudinally, the trucks were positioned with the rear axles at centerspan and the front axles off the span. On Span 1 (west span), the trucks were facing west; on Span 2 (east span), the trucks were facing east. Transversely, the trucks were positioned for three different load cases (Figure 4*b*). For Load Case 1, Truck T18 was positioned in the north lane with the center of the inside wheel line 610 mm from the bridge centerline. For Load Case 2, Truck T15 was positioned in the south lane with the center of the inside wheel line 610 mm from the bridge centerline. Load Case 3 consisted of positioning both trucks on the span in the positions used for Load Cases 1 and 2.

Analytical Assessment

At the conclusion of load testing, the bridge behavior was modeled for load test conditions and AASHTO HS 20–44 loading using an orthotropic plate computer program developed at FPL. In addition, the HS 20–44 predicted deflection was computed using the recommended design method given by the AASHTO Guide Specification for the Design of Stress-Laminated Wood Decks (*11*).

Condition Assessment

The general condition of the Cooper Creek bridge was assessed on five different occasions during the monitoring period. The first assessment occurred at the time of installation. The second through fourth assessments took place during intermediate site visits. The final assessment occurred during the final load test at the conclusion of the monitoring period. These assessments involved visual inspections, measurements, and photo documentation of the bridge condition. Items of specific interest included the bridge geometry and the condition of the timber deck and rail system, asphalt wearing surface, and stressing bar and anchorage system.

Results and Discussion

The performance monitoring of the Cooper Creek bridge extended for 28 months from February 1992

through May 1994. Results and discussion of the performance data follow.

Lamination MOE

Results of individual lamination MOE testing provided a mean flatwise MOE for the eastern cottonwood lumber of 9,299 MPa. The flatwise MOE was converted to an edgewise value by applying a flatwise adjustment factor of 0.965 (*12*). This resulted in an average edgewise MOE of 8,878 MPa. After adjustment for wet-use conditions (moisture content greater than 19 percent), the design-tabulated MOE of 8,268 MPa resulted in an allowable design value of 8,020 MPa. Thus, the actual material MOE exceeded by approximately 11 percent the assumed design value for black cottonwood lumber.

Since completion of the Cooper Creek bridge design, the NDS was revised in 1991 to include tabulated design values for the cottonwood species group, which includes eastern cottonwood (*13*). For visually graded Number 1 material, the revised design MOE for wet-use conditions is 7,441 MPa. The actual material MOE measured for the Cooper Creek bridge exceeds this value by approximately 19 percent.

Moisture Content

Electrical resistance moisture content readings taken at the beginning of the monitoring period indicated an average 25 percent in the outer 25 mm of the deck underside. At the conclusion of the monitoring period, there was a decrease in the average electrical resistance moisture content at the same locations to 22 percent. Moisture content measurements obtained at the end of the monitoring period based on coring and the ovendry method indicated a relatively uniform average moisture content of 26 percent for the inner 51 through 178 mm of the deck underside. It is expected that the outer portions of the laminations will continue to lose moisture toward an equilibrium level but will undergo seasonal fluctuations as a result of climatic variations. The inner portions of the laminations, which remain at a relatively high moisture content, will change more slowly. On the basis of the open exposure of the site and regional climatic conditions, it is estimated that the eventual equilibrium moisture content of the deck will be 16 to 18 percent.

Bar Force

The average trend in bar tension force measured from the load cells indicated that the first three bar stressings ranged from 10 to 15 percent below the design level. The final stressing was approximately 6 percent below the design level at 120 kN (0.65 MPa interlaminar compression). After the final stressing, the bar force decreased rapidly during the first 100 days to 75 kN (0.40 MPa interlaminar compression), which is 58 percent of the design level. During the remainder of the monitoring period, bar force gradually decreased to 60 kN (0.32-MPa interlaminar compression), which is approximately 46 percent of the design level.

The loss in bar force for the Cooper Creek bridge is likely the result of stress relaxation in the wood laminations as a result of the applied compressive force. The slight decrease in average lamination moisture content also contributed to wood shrinkage and a minor loss in bar force. Although the bar force decreased approximately 50 percent during the monitoring period, it did not drop below acceptable levels. However, it was probable that the gradual decrease would continue; therefore, the bridge was restressed at the conclusion of the monitoring period.

The bar force retention for this bridge is similar to or better than that compared with numerous other bridges in the FPL monitoring program (*14*). Thus, it does not appear from the data that the accelerated stressing sequence significantly affected bar force retention. However, a conclusion in this area cannot be justified until additional research is completed on other structures.

Vertical Creep

The laminations of the Cooper Creek bridge were approximately straight between supports after construction. At the conclusion of the monitoring period, the laminations remained in approximately the same position, and there was no measurable sag in the spans.

Load Test Behavior

Results of the static-load test and analytical assessment of the Cooper Creek bridge are presented here. For each load case, transverse deflection measurements are given at the bridge centerspan as viewed from the east end (looking west). No permanent residual deformation was measured at the conclusion of the load testing, and there was no detectable movement at bridge supports. At the time of the tests, the average bridge prestress was approximately 0.32 MPa, which is relatively close to the minimum recommended long-term prestress of 0.28 MPa (*3*).

Load Testing

Transverse deflection plots for Spans 1 and 2 are shown in Figure 5. For Span 1, Load Case 1 resulted in a maximum deflection of 7 mm under the outside wheel line nearest the north deck edge (Figure 5*a*). The maximum deflection of 7 mm for Load Case 2 was measured under the outside wheel line nearest the south deck edge (Figure 5*b*). For Load Case 3, the maximum deflection of 9 mm occurred under the inside wheel line of Truck T18, 610 mm from the span centerline (Figure 5*c*). As could be expected for the same loading on similar spans, the results for Span 2 were similar to those for Span 1. Load Case 1 resulted in a maximum deflection of 7 mm under the outside wheel line nearest the north deck edge (Figure 5*d*). The maximum deflection of 7 mm for Load Case 2 occurred under the outside wheel line nearest the south deck edge (Figure 5*e*). For Load Case 3, the maximum deflection of 9 mm occurred under the inside wheel line of Truck T18, 610 mm from the span centerline (Figure 5*f*).

Analytical Assessment

Results of the actual versus predicted bridge response based on orthotropic plate analysis for Load Case 3 are shown in Figure 6*a*. As seen from the figure, the predicted response is close to the actual response with minor variations at the bridge edges. This was expected because the model included no provisions for edge stiffening, but the actual bridge edges were stiffened with a curb and rail system. Further orthotropic plate analysis assuming two lanes of AASHTO HS 20–44 loading resulted in a maximum predicted live-load deflection of 10 mm at the span centerline (Figure 6*b*). This deflection is equivalent to 1/630 of the span length measured center-to-center of bearings. Deflection computed using AASHTO recommended design procedures was 13 mm or approximately 1/490 of the bridge span.

Condition Assessment

Condition assessments of the Cooper Creek bridge indicated that structural and serviceability performance was good. Inspection results for specific items follow.

Deck Geometry

Measurements of the bridge width at numerous locations indicated that the bridge was approximately 200 mm narrower over the center bent than at the abutments. This is most likely attributable to the lamination layout for consistent thickness at butt joints, which resulted in the placement of the thickest odd-size laminations over the abutments.

Wood Condition

Inspection of the wood components of the bridge showed no signs of deterioration, although minor checking was evident on rail members exposed to wet-dry cycles. In several locations on the curb and railing, bolt heads were slightly crushed into the wood. The crushing did not damage the preservative envelope and was likely caused by bolt overtightening at construction. For all wood components, there was no evidence of wood preservative loss, and preservative or solvent accumulations were not present on the wood surface.

Wearing Surface

The asphalt wearing surface remained in good condition with no cracking or other deterioration. A substantial amount of gravel and other debris was present on the surface from the unpaved road, which could potentially lead to premature deterioration of the surface.

Stressing System

The stressing bar anchorage system performed as designed with no significant signs of distress. There was no indication of crushing of the discrete plate anchorage into the outside oak laminations and no measurable distortion in the bearing plate. The exposed steel stressing bars, hardware, and anchorage plates showed no visible signs of corrosion or other deterioration.

Observations and Recommendations

After 28 months in service, the Cooper Creek bridge is performing well and should provide many years of acceptable service. On the basis of extensive bridge monitoring conducted during that period, the following observations and recommendations were made:

1. It is both feasible and practical to design and construct stress-laminated timber decks with eastern cottonwood lumber.
2. The measured flatwise MOE of the eastern cottonwood laminations resulted in an average edgewise value of 8 878 MPa. This is approximately 19 percent greater than the wet-use value currently specified in the NDS.
3. Stress-laminated decks can be constructed in place using temporary scaffolding for lamination support before bridge stressing. This method of construction is labor intensive but can be a viable option when large equipment required for prefabricated bridge placement is not available.
4. The use of red oak for outside edge laminations enhanced the performance of the discrete plate stressing

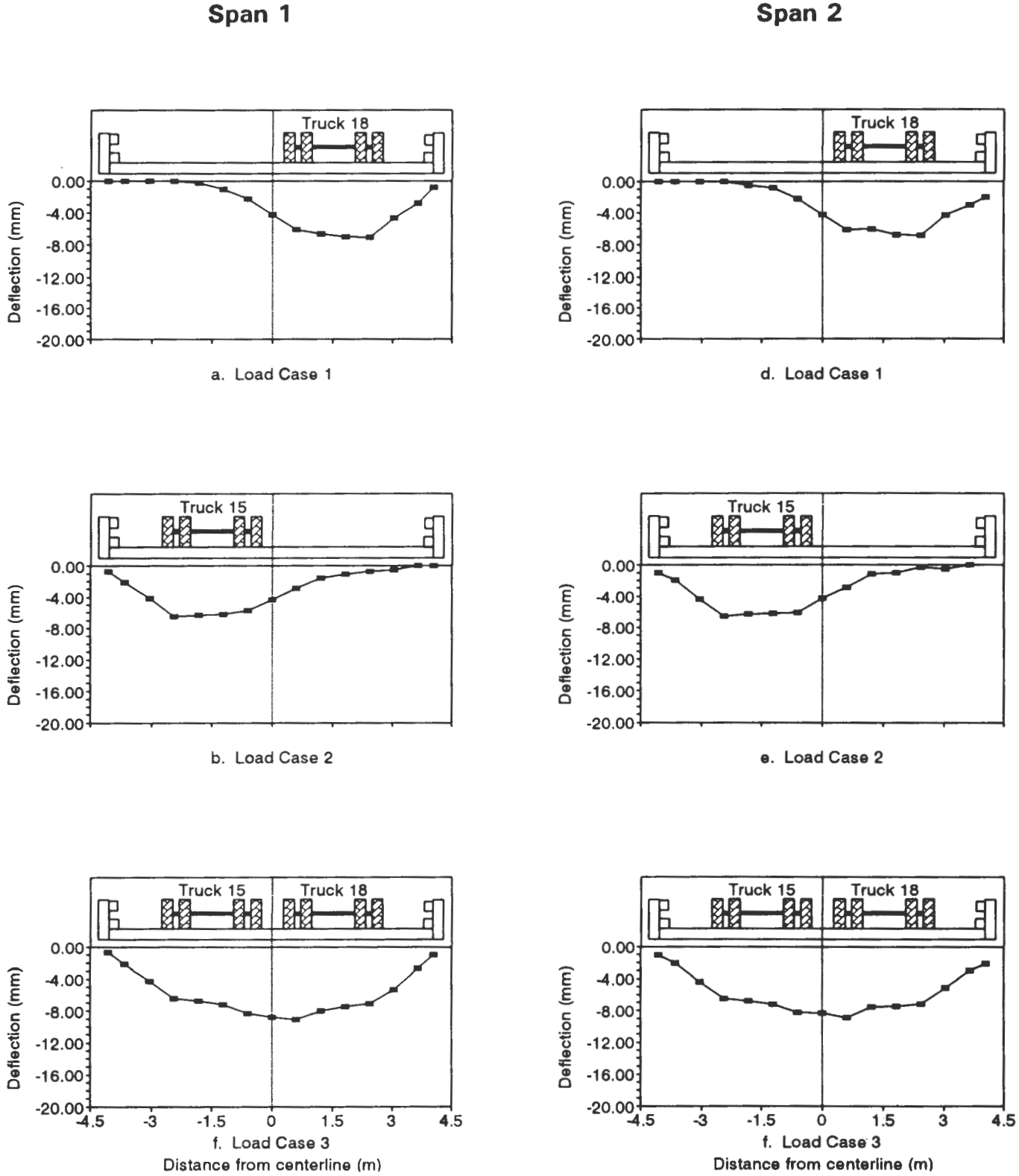

FIGURE 5 Transverse deflection plots for the Cooper Creek load test, measured at the bridge centerspan (looking west). Bridge cross sections and vehicle positions are shown to aid interpretation and are not to scale.

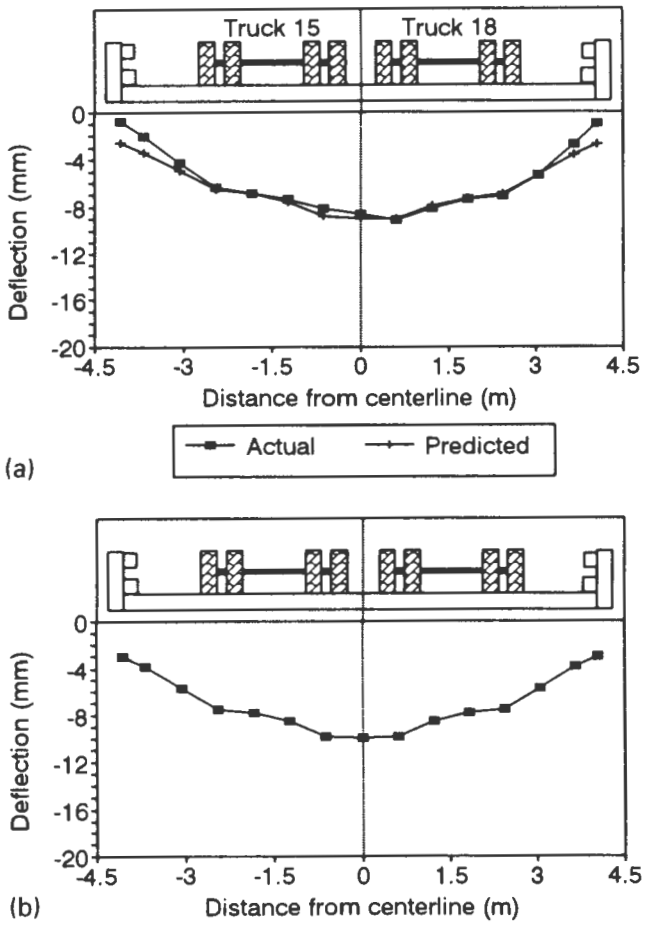

FIGURE 6 (*a*) **Comparison of the actual measured deflections for Load Case 3, Span 1, compared with the predicted deflection using orthotropic plate analysis;** (*b*) **predicted deflection profile at the bridge centerspan for two HS 20–44 trucks, each positioned 610 mm on either side of the bridge longitudinal centerline. Both plots are shown looking west.**

bar anchorage system. The oak provided sufficient strength to adequately distribute the bar force into the deck without wood crushing or anchor plate deformation.

5. The average trend in deck moisture content in the lower 25 mm of the laminations indicates that moisture content changes are occurring slowly, with an average 3 percent decrease during the monitoring period. The average moisture content in the inner 51 to 178 mm of the deck underside is 26 percent, which is expected to slowly decrease as time passes.

6. Stressing bar force decreased approximately 50 percent during the monitoring but remained within acceptable limits. The decrease is primarily attributable to transverse stress relaxation in the wood laminations. The bar force should be checked biannually and restressed as necessary until it reaches a constant level.

7. Creep measurements of the bridge deck indicate that there has been no detectable vertical displacement during the monitoring. The deck remains approximately straight between supports.

8. Load testing and analysis indicates that the Cooper Creek bridge is performing as a linear elastic orthotropic plate when subjected to truck loading. The maximum deflection of two lanes of AASHTO HS 20–44 loading is estimated to be 10 mm, which is approximately 1/630 of the span length measured center-to-center of bearings.

9. Wood checking is evident in the exposed end grain of bridge rail posts and other components. It is likely this would not have occurred if a sealer or cover had been placed over end grain at the time of construction.

10. There are no indications of corrosion on the stressing bars, hardware, or plates.

REFERENCES

1. *The Timber Bridge Initiative.* Fiscal Year 1991 Status Report. USDA Forest Service, State and Private Forestry, Northeastern Area, Radnor, Pa. 1991.
2. Oliva, M. G., A. G. Dimakis, M. A. Ritter, and R. L. Tuomi. *Stress-Laminated Wood Bridge Decks: Experimental and Analytical Evaluations.* Research Paper FPL-RP-495. USDA Forest Service, Forest Products Laboratory, Madison, Wisc., 1990.
3. Ritter, M. A. *Timber Bridges: Design, Construction, Inspection and Maintenance.* EM 7700–8. USDA Forest Service, 1990.
4. *Standard Specifications for Highway Bridges*, 14th ed. AASHTO, Washington, D.C., 1989.
5. *Design Values for Wood Construction.* A Supplement to the 1986 Edition of the National Design Specification. National Forest Products Association, Washington, D.C., 1988.
6. *Memorandum on Crash Tested Bridge Railings.* File Designation HNG-14. FHWA, Washington, D.C.
7. *Standard Specifications for Transportation Materials and Methods of Sampling and Testing*, Vol. 1: *Specifications.* AASHTO, Washington, D.C., 1990.
8. Wacker, J. P., and M. A. Ritter. *Field Performance of Timber Bridges: 1. Teal River Stress-Laminated Deck Bridge.* Research Paper FPL-RP-515. USDA Forest Service, Madison, Wisc., 1992.
9. Ritter, M. A., E. A. Geske, W. J. McCutcheon, R. C. Moody, J. P. Wacker, and L. Mason. Methods for Assessing the Field Performance of Stress-Laminated Timber Bridges. *Proc., 1991 International Timber Engineering Conference.* London, England, Sept. 1991.
10. Ross, R. J., E. A. Geske, G. R. Larson, and J. F. Murphy. Transverse Vibration Nondestructive Testing Using a Per-

sonal Computer. Research Paper FPL-RP-502. USDA Forest Service, Madison, Wisc., 1991.
11. *Guide Specification for the Design of Stress-Laminated Wood Decks*. AASHTO, Washington, D.C., 1991.
12. Williams, G. D., D. R. Bohnhoff, and R. C. Moody. Bending Properties of Four-Layer Nail-Laminated Posts. Research Paper FPL-RP-528. USDA, Forest Service, Madison, Wisc., 1994.
13. NFPA. 1991. *Design Values for Wood Construction. A Supplement to the 1986 Edition of the National Design Specification*. National Forest Products Association, Washington, D.C., 1991.
14. Ritter, M. A., E. A. Geske, L. Mason, W. J. McCutcheon, R. C. Moody, and J. P. Wacker. Performance of Stress-laminated Bridges. *Wood Design Focus*, Vol. 1, No. 3, pp. 12–16, 1990.

Experimental Testing of Composite Wood Beams for Use in Timber Bridges

Michael J. Chajes, Victor N. Kaliakin, and Scott D. Holsinger, *University of Delaware*
Albert J. Meyer, Jr., *Trus Joist MacMillan*

The use of new high-performance materials can play an important role in the search for ways to rebuild and rehabilitate the nation's deteriorating bridges. Innovations in the area of engineered wood products provide new possibilities for the design of timber bridges. Bonding high-strength fiber-reinforced plastic (FRP) composite plates to the tension face of wood beams can improve stiffnesses and strengths. By further incorporating a concrete compression flange, an even more versatile and efficient structural member can be created. The use of concrete-wood-FRP composite beams for timber bridges is investigated. The criteria involved in designing timber beams for bridges are presented. Then, details and results of an experimental study aimed at addressing design-related issues for concrete-wood-FRP composite beams are discussed. In the study, a series of wood, wood-FRP, concrete-wood, and concrete-wood-FRP composite beams were tested. The wood used was a laminated veneer lumber; the reinforcement consisted of carbon FRP plates. Composite action between the concrete flange and the wood web, bond strength between the FRP plates and the wood, and stiffness and ultimate strength properties of the composite beams were evaluated. Results of the tests indicate that composite wood beams show promise for use in timber bridges.

The rebuilding of the infrastructure is a major challenge facing the nation today. The U.S. Department of Transportation's 10th Biennial Report to Congress on *The Status of the Nation's Highways and Bridges: Conditions and Performance*, concluded that approximately 16 percent of Interstate bridges and 42 percent of all bridges are in need of repair (*1*). The cost of replacing all of the nation's deficient bridges is prohibitive. With limited financial resources, the current technology will not solve the problem. "High-tech solutions must be investigated" (*2*) so that innovative new technologies and materials can be used to rebuild the nation's infrastructure.

Both engineered wood and advanced composite materials offer intriguing opportunities in the area of infrastructure rehabilitation. Engineered wood products offer better structural properties than solid sawn lumber, and they are a renewable resource. Furthermore, some of these products can be made using species of trees not usually considered for structural lumber. Engineered wood products are already being used in modern structures. Composite materials, on the other hand, are relatively new to the construction industry. They have many beneficial characteristics, such as a high strength-to-weight ratio and corrosion resistance, but research still needs to be conducted before they can be

safely and reliably used. The work reported herein involves an attempt to improve the performance of engineered wood by using it in combination with both advanced composite materials and concrete.

Background

Recent advances in the production of engineered wood products have caused an increased interest in research on their use. Recent papers by Ritter (*3*) and Wipf et al. (*4*) have cited a growing interest in timber bridges. Wipf et al. state that the use of locally available timber "can stimulate local economies and enhance rural transportation systems." They go on to say that "for this to occur, additional research is needed to further develop timber as a material for transportation structures." Ritter points out that whereas most older bridges were made of timber, only 10 percent of current bridges are. He states that "one of the primary reasons for the decline in timber bridges has been a lack of research and development to advance timber bridge technology to meet modern needs." Most of the structurally deficient bridges are on secondary and rural roads, where spans are short (*5*). In a recent article, Brungraber et al. (*6*) describe how timber can play an important role in the replacement and rehabilitation of bridges in rural America. Similarly, Gutkowski and McCutcheon (*7*) and Behr et al. (*8*) have described how timber can be a cost-effective solution for short-span bridges. New and innovative designs of highway bridges using wood present additional solutions in the repair and replacement of these bridges (*5*). One application being tested is the use of stress-laminated bridge systems, as described by Oliva and Dimakis (*9*) and Moody et al. (*10*). These systems include the use of stress-laminated slab decks, parallel-chord truss systems, and T- and box sections. In addition to novel design concepts, newly created engineered wood products offer even more possibilities (*11*). The new types of engineered wood include laminated veneer lumber (LVL), parallel-strand lumber, and laminated-strand lumber. These products are manufactured by bonding together wood veneers or strands of Douglas fir, southern pine, and other species under heat and pressure using thermal-setting resins such as phenol-formaldehyde. The process produces a piece of wood typically 38 mm thick, 0.6 or 1.2 m wide, and up to 25 m long (*11*). The use of engineered wood to date has been limited in bridge applications, but continued research, along with the recently written timber bridge manual (*12*), will help to change this trend.

The use of fiber-reinforced plastic (FRP) composite materials in new structures, and in the rehabilitation of deteriorating ones, also shows great promise. Composite materials have the beneficial characteristics of being noncorrosive and generally resistant to chemicals, having a high strength-to-weight ratio, and being nonmagnetic and nonconductive. Several researchers have recently discussed possible applications of composite materials for civil structures (*13–24*).

Of particular relevance to this paper is past work on the bonding of composite plates to the tension face of wood beams (*25–28*). Triantafillou et al. (*25,26*) have shown experimentally that both nonprestressed and prestressed composite plates bonded to the tension face of plain wood beams significantly increases their stiffness and strength. A carbon fiber–reinforced plastic (CFRP) plate having an area of 1 percent of the wood member led to a 60 percent increase in stiffness. Triantafillou et al. also presented an analytical method for computing the maximum safe prestress that can be used. In the work by Davalos et al. (*27,28*), glass fiber–reinforced plastic plates were bonded to glulam beams and tested. The reinforced beams displayed higher strengths along with a 30 percent increase in stiffness compared with unreinforced beams. In fact, composite reinforced glulam beams were used in the recently constructed Taylor Lake pedestrian bridge in The Dalles, Oregon (*29*). Comparison of the design to one involving standard materials showed the composite glulams to be an economical solution.

In addition to the work on FRP-wood beams, a few studies have involved nonengineered wood-concrete beams. Richart and Williams (*30*) and McCullough (*31*) concluded that the concrete would provide an excellent wearing surface (road deck) and that smaller-dimensioned lumber beams could be used. In the tests performed, the composite beams exhibited satisfactory behavior, with some slippage occurring along the wood-concrete interface. A variety of shear connectors were studied, and triangular plate units were found to work best. Neither shrinkage nor repeated loads proved to be a problem. Later work by Pincus (*32,33*) involved the study of T-beams made of concrete flanges and wood webs. The effectiveness of both mechanical shear connectors and epoxy adhesives was studied and found to be sufficient to provide full composite action. Finally, recent work by Ahmadi and Saka (*34*) has investigated the behavior of timber-concrete floors. This work, like that of Pincus, indicates that it is possible to use full composite action to get stiffer and stronger beams. Ahmadi and Saka suggest that the increase in strength and stiffness can result in a 50 percent savings in timber joist costs.

The research on both wood-FRP and wood-concrete composite beams shows promising results, but no work appears to have been done involving the combination of all three materials. The rest of this paper addresses the potential use of concrete-engineered wood-FRP beams for timber bridges.

Design of Timber Bridge Beams

A complete manual treating the design, construction, inspection, and maintenance of timber bridges was written recently (*12*). When AASHTO *LRFD Specification for Highway Bridge Design* (*35*) was written, the timber bridge manual was used as a guideline. The remainder of this paper will refer to guidelines detailed in the timber bridge manual (*12*). For design, the allowable stress methodology is followed. Beams are designed for bending, deflection, shear, and bearing. As a result, values for allowable bending stress, F_b; shear stress, F_v; bearing stress, $F_{c\perp}$ (compression perpendicular to the grain); and modulus of elasticity, E (flexural modulus) are needed. Typical values of F_b, F_v, $F_{c\perp}$, and E for southern pine are 10.7 MPa, 0.62 MPa, 1.4 MPa, and 11.0 GPa, respectively; for LVL they are 20.2 MPa, 2.0 MPa, 5.2 MPa, and 13.8 GPa, respectively.

With regard to bending, the applied bending stress (f_b) must be lower than the adjusted allowable bending stress, $F_{b'}$. In determining $F_{b'}$, the allowable bending stress for the wood (F_b) is modified by several factors to account for load duration, moisture content, fire retardance, temperature, and size effects. In addition, the adjusted allowable stress also takes into account lateral stability and beam slenderness.

In designing wood beams for deflection, both short- and long-term deformations are considered. For both cases, deflections are computed using standard beam equations derived for linear-elastic, isotropic materials (e.g., $\Delta = 5wL^4/384E'I$ for a simply supported beam with a uniformly distributed load w and length L). In computing an adjusted modulus for the wood (E'), modifications are made for moisture content, fire retardance, and temperature. Although the standard equations are relatively accurate for short-term elastic deflections, they cannot account for the long-term effects of creep. To do so, it is common to increase the dead-load deflection by anywhere from 50 percent for engineered wood to 100 percent for unseasoned lumber. Ritter (*12*) recommends limiting short-term deflections to $L/360$ and long-term deflections to $L/240$.

Beams must be designed not only for normal bending stresses f_b, but also for shear stresses, f_v. For timber beams, horizontal as opposed to vertical shear will always govern (*12*). As with bending, design for shear requires that the maximum applied shear stress f_v be less than the adjusted allowable value, $F_{v'}$. In modifying the allowable shear stress, F_v, effects of moisture content, fire retardance, and temperature are accounted for.

The final design criterion for timber beams is bearing. The designer must ensure that a beam's bearing area is large enough to prevent excessive deformation. The procedure is similar to design for shear in that the applied bearing stress $f_{c\perp}$ must be less than the adjusted allowable bearing stress, $F_{c\perp'}$, which is modified for effects of moisture content, fire retardance, and temperature.

All of these criteria are intended for use in designing wood beams (engineered and nonengineered). The idea of designing concrete-wood-FRP composite beams raises the following questions:

1. Can FRP plates be bonded effectively to the tension face of the wood?
2. Can concrete flanges be made to act compositely with a wood web, and what is the maximum effective flange width?
3. What effect will the concrete and FRP have on the flexural stiffness of the beams, and how can accurate deflections be computed?
4. What effect will the concrete and FRP have on the ultimate load-carrying capacity and failure mode of the beams?
5. Which material will govern design for bending and shear, and how can stresses in these materials be computed?
6. How will varying the stiffness and strength of the FRP plates and concrete affect beam behavior?
7. Will concrete flanges, being part of a continuous deck, eliminate lateral stability problems once the concrete has cured, and what amount of bracing is necessary before curing?
8. How will the composite beams behave under sustained loads?
9. What will be the long-term durability of the composite beams?
10. Do the factors used for adjusting allowable wood stresses need to be reevaluated for use with composite beam design?

To gather information about concrete-wood-FRP beam behavior needed to help answer some of these questions, an experimental study was conducted.

Experimental Study Involving Composite Wood Beams

The experimental study included testing thirteen 1.83-m-long beams to failure. The beams, consisting of different combinations of engineered wood, CFRP plates, and concrete, included three plain wood beams (W1–W3), three wood beams with a CFRP plate attached to the tension face (WF1–WF3), four wood beams with a concrete compression flange attached (CW1–CW4), and three concrete-wood-CFRP beams (CWF1–CWF3). Dimensions for a typical CWF beam are shown in Figure 1. The cross-sectional dimensions of the other

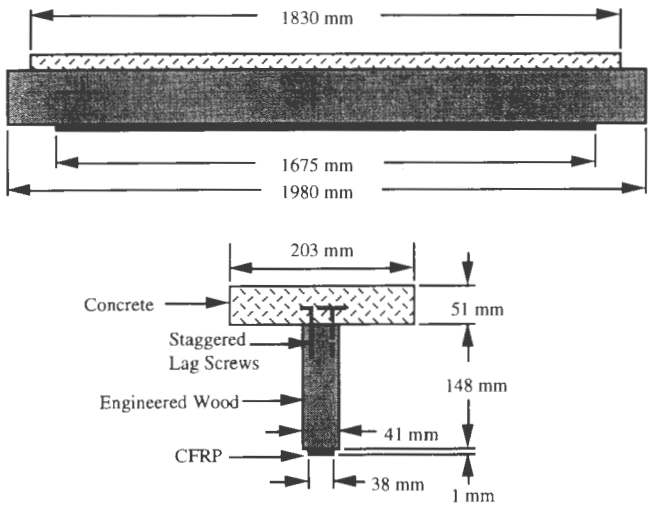

FIGURE 1 Typical CWF beam.

beams were identical to the CWF beams, with the concrete flange or the CFRP plate absent.

Beam Fabrication

To create composite beams, concrete flanges needed to be added to the CW and CWF beams and CFRP plates needed to be attached to the WF and CWF beams. To form the 51-mm-deep compression flanges, concrete having a water-to-cement ratio of approximately 0.40 by weight was cast directly onto the wood beams. A 100-mm^2 welded wire fabric was used as nominal reinforcement. Three batches of concrete were used to fabricate the CW and CWF beams, and standard 6-in.-diameter concrete test cylinders were poured with each batch. The concrete beams and cylinders were allowed to cure for 28 days before being tested. Results of the compression tests performed on the cylinders are presented in a subsequent section.

In attempts to achieve composite action, mechanical shear connectors were used. The connectors consisted of Grade 2 lag screws having a yield strength of 262 MPa. For three of the CW beams (CW1–CW3), 6.35-mm-diameter screws, staggered and longitudinally spaced at 76.2 mm, were used. For one CW beam (CW4) and all three CWF beams, 9.53-mm-diameter screws, staggered and longitudinally spaced at 50.4 mm, were used. The second arrangement was adopted after tests of beams CW1–CW3 indicated that composite action was lost before beam failure.

The CFRP plates were attached to the wood using a resorcinol-phenolformaldehyde adhesive in combination with a paraformaldehyde hardener. The bonding technique involved cleaning the wood and CFRP surfaces with acetone, applying a thin layer of adhesive to the wood, positioning the CFRP strip on the wood, and applying a uniform clamping pressure. The adhesive was then allowed to cure at room temperature for 24 hr before the pressure was removed.

Bond tests were performed to determine the resulting ultimate bond strength of the wood-CFRP connection. The tests consisted of loading three double-lap butt joints in tension to failure. From the tests, the average ultimate shear stress of the bond was found to be 3.95 MPa.

Material Properties

The CFRP plates used were made from unidirectional laminates. Each plate had a cured thickness of 1.0 mm, a width of 38 mm, and a length of 1675 mm. Carbon fiber–reinforced plates were chosen instead of glass or aramid fiber–reinforced plates because of the higher stiffness of the CFRP material.

To find the tensile properties of the CFRP plates, three tension samples were prepared and tested in accordance with ASTM D3039/3039M-93. The CFRP plates behaved linearly to failure with an average tensile modulus of 124 GPa and an ultimate strength of 1500 MPa.

The LVL used was made of southern pine. Because of the orthotropic nature of wood, its properties are different in the three mutually perpendicular directions; for wood, these directions are parallel to the grain, normal to the growth rings, and tangential to the growth rings. The second two directions are considered perpendicular to the grain. To determine values for the elastic moduli, ultimate shear stress, and ultimate bearing stress of the LVL, four types of wood samples were tested in accordance with ASTM D143–83. Test results indicated a uniaxial tensile modulus of 17.8 GPa (ultimate tensile strains ranged from 0.0025 to 0.0035 mm/mm), a uniaxial compression modulus of 8.3 GPa, an ultimate shear stress of 8.4 MPa, and an ultimate bearing stress of 28.2 MPa. Bending characteristics of the wood (flexural modulus, E, and flexural stiffness, EI) were assessed on the basis of the behavior of beams (W1–W3). The results (presented later) indicate a flexural modulus for the wood of 14.6 GPa. Finally, it should be noted that the approximate moisture content of the wood was 8 percent.

As mentioned previously, standard concrete test cylinders were cast when the CW and CWF beams were constructed. Results of compression tests on the cylinders indicate ultimate compressive strengths (f'_c) of 42.7 MPa for CW1–CW3, 42.0 MPa for CW4, and 29.6 MPa for the three CWF beams. The lower concrete

strength associated with the CWF beams was a result of a slightly higher water-cement ratio.

Beam Test Procedure

All 13 beams were tested in four-point bending with the loads applied at the one-third points. The beams were loaded monotonically to failure using an 890-kN Universal testing machine. During the test, deflections were measured at midspan and beneath the loads. Gauges were used to record longitudinal strains through the beam's depth at both midspan and in the shear span. For the beams with CFRP plates, care was taken to ensure that the plates were not clamped beneath the end supports. The test setup and instrumentation plan is shown schematically in Figure 2.

Although slip between the CFRP and the wood, or between the wood and concrete, was not measured directly, the distribution of strains measured in the shear span allowed slip to be identified. Furthermore, glass slides were bonded to the side of the wood web and the underside of the concrete flange. By doing this, relative slip caused the glass slide to break.

Test Results

Results of the 13 beam tests are presented in Table 1. A detailed discussion of the test results is presented in the sections that follow.

Load-Displacement Behavior and Failure Mode of Test Beams

All three wood beams (W1–W3) displayed virtually identical linear load-deflection behavior to failure (Figure 3*a*). Furthermore, linear strain distributions through the depth of the members at midspan were recorded at the load, causing $\Delta = L/360 = 5.1$ mm (serviceability limit), and at 95 percent of the failure load (Figure 4). All wood beams failed in flexure due to splitting or snapping of wood fibers in the tension zone. At failure, outer-fiber tensile strains averaged 0.0033 mm/mm.

Like the wood beams, the three WF beams displayed both linear load-deflection behavior to failure (Figure 3*b*) and linear strain distribution at midspan (Figure 4). Flexural failure of these beams was caused by the tensile failure of the wood. For all three beams, the CFRP plates remained bonded to the wood up to failure. The primary difference between the W and WF beams was that the CFRP plate enabled the WF beams to reach an average outer-fiber tensile strain at failure of 0.0048 mm/mm (compared with 0.0033 mm/mm for the W beams).

Initially, both the CW and CWF beams behaved in a similar manner. They exhibited linear response, in terms of displacements and strain profiles at midspan, beyond the serviceability limit of $\Delta = 5.1$ mm (Figures 3*c*, 3*d*, and 4*a*). With regard to the strain profile, it can be seen that the concrete flange caused a significant upward shift of the neutral axis as compared with the W and WF beams. Upon further loading, the beams eventually began to lose composite action (at this point in the loadings, breakage of the glass slides was observed). Loss of

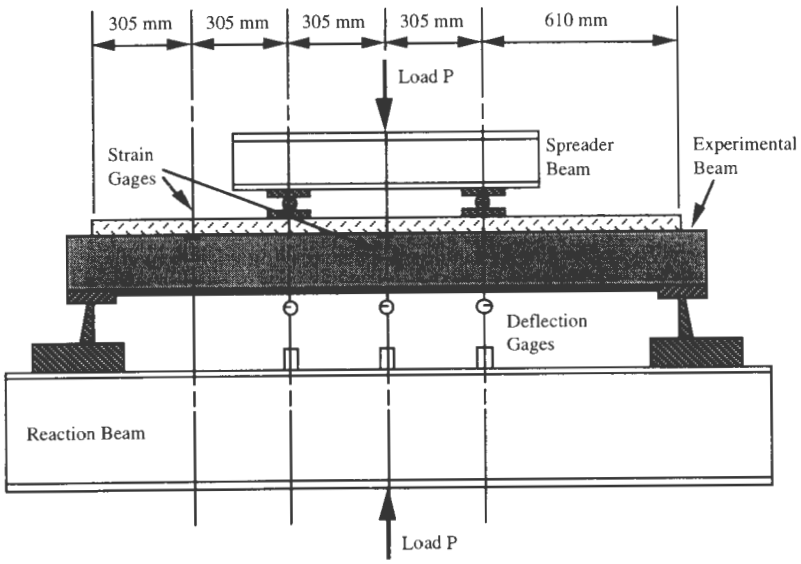

FIGURE 2 Typical beam test setup.

TABLE 1 Test Results for Each Beam

Beam	Concrete Strength, MPa	Mode of Failure	Load to Cause Δ=L/360, N	Ultimate Beam Strength, N
W1	NA[a]	Flexural Failure of Wood	6,715	27,812
W2	NA[a]	Flexural Failure of Wood	6,420	27,812
W3	NA[a]	Flexural Failure of Wood	6,882	28,925
WF1	NA[a]	Flexural Failure of Wood	7,679	43,387
WF2	NA[a]	Flexural Failure of Wood	8,287	37,825
WF3	NA[a]	Flexural Failure of Wood	8,147	37,825
CW1[b]	42.7	Flexural Failure of Wood	26,216	57,850
CW2[b]	42.7	Flexural Failure of Wood	28,814	56,737
CW3[b]	42.7	Flexural Failure of Wood	28,925	62,300
CW4[c]	42.0	Shear Failure of Wood	27,145	75,650
CWF1[c]	29.6	Shear Failure of Wood	27,456	73,425
CWF2[c]	29.6	Shear Failure of Wood	28,419	84,550
CWF3[c]	29.6	Shear Failure of Wood	28,244	80,100

[a] Not applicable.

[b] 6.35 mm diameter lag screws spaced at 76.2 mm.

[c] 9.53 mm diameter lag screws spaced at 50.4 mm.

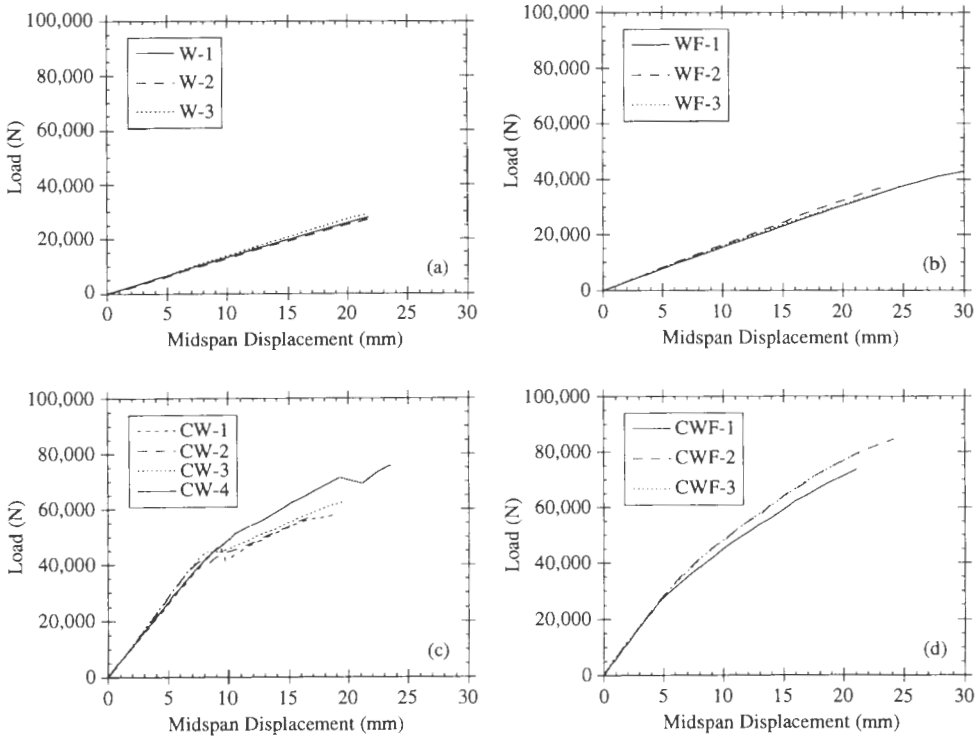

FIGURE 3 Load versus midspan deflection behavior: (*a*) W beams, (*b*) WF beams, (*c*) CW beams, (*d*) CWF beams.

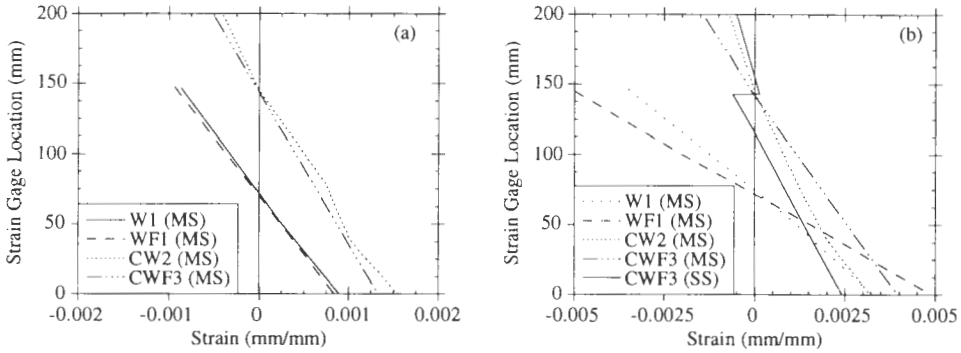

FIGURE 4 Strain profiles at midspan (MS) and in shear span (SS): (*a*) service load region ($\Delta = L/360$) and (*b*) at 95 percent of ultimate load.

composite action results in the reduced stiffness exhibited in the load-deflection response (Figures 3*c* and 3*d*) and in a disjointed shear-span strain distribution (typical) of Beam CWF3 (Figure 4*b*). Although the increased size and decreased spacing of lag screws used in Beams CW4 and CWF1–CWF3 appeared to eliminate the abrupt loss of composite action seen in beams CW1–CW3, some loss of composite action still occurred before failure.

The initial displacement of the CW and CWF beams was similar, but the presence of the composite plate caused the failure modes to differ. All of the CWF beams experienced longitudinal shearing of the wood web. As can be seen in Figure 4*b*, when Beam CWF3 failed, the midspan tensile strain at the outer fiber had not reached the level achieved by the WF beams (0.0048 mm/mm). In fact, the average tensile strain at the outer fiber at midspan was 0.0042 for the CWF beams. Unlike the CWF beams, failure of Beams CW1–CW3 was caused by tensile failure of the wood. Without the presence of the CFRP plate, these beams failed when the wood at midspan reached tensile strains at the outer fiber averaging 0.0032 mm/mm. Of the CW beams, only CW4 experienced a shear failure of the wood. For this beam, tensile failure of the wood did not occur even though an outer-fiber tensile strain of 0.0040 mm/mm was reached.

Changes in Stiffness and Strength of Test Beams

Using deflections recorded along the constant moment region, moment-curvature plots for the various beams were computed. By comparing both moment-curvature and load-deflection plots in the service load region (Figure 5), it is seen that both the CFRP plate and the concrete flange led to increases in stiffness as compared with the wood beams. A comparison of average slopes (*EI*) of the moment-curvature response of the WF, CW, and CWF beams with the slope of the W (control) beams reveals increases in flexural stiffness of 21, 487, and 533 percent, respectively (Table 2). By dividing the flexural stiffness of the beams by their moments of inertia, one can find values for the flexural modulus. Doing so for the W beams results in a modulus of 14.6 GPa, which is within 6 percent of the design value of

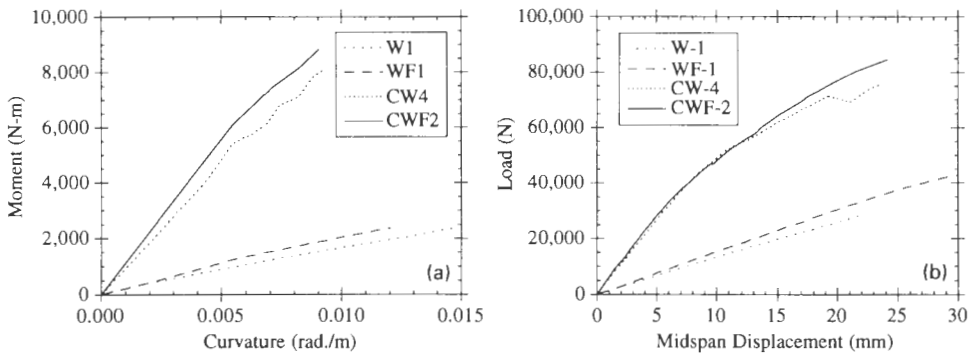

FIGURE 5 Comparison of typical (*a*) moment-curvature behavior in service load region ($\Delta \leq L/360$) and (*b*) load versus midspan deflection behavior to failure.

TABLE 2 Stiffness Increase for Beams in Service Load Region ($\Delta \leq L/360$)

Beams	Flexural Stiffness (EI)[a], N-m^2	Flexural Stiffness of Wood Beams (EI)[a], N-m^2	Percentage Increase
WF1, WF2, WF3	195,282	161,492	+21
CW1, CW2, CW3, CW4	947,460	161,492	+487
CWF1, CWF2, CWF3	1,021,529	161,492	+533

[a]All values are averages of like beams.

13.8 GPa. Converting the CFRP plate and concrete flange into equivalent amounts of wood produces flexural moduli of 15.2, 14.9, and 15.0 GPa for the WF, CW, and CWF beams, respectively. These values are all within 7 percent of the measured flexural moduli of the W beams, which indicates that accurate short-term service-load deflections can be computed by first converting the composite cross section to equivalent amounts of wood, and then using the wood's flexural modulus.

As for ultimate strengths, the WF, CW, and CWF beams show increases over the W beams of 40, 168, and 181 percent, respectively (Table 3). In addition, all three beam types exhibited larger deflections at failure than did the wood beams (Figure 5*b*). The larger deflections translated are consistent with the observed 44.7 percent increase in ultimate tensile strain of the wood at failure between the W and WF beams (0.0033 to 0.0048 mm/mm). Finally, it is interesting that the increases in stiffness (21 percent) and strength (40 percent) of the WF beams compared with the W beams were produced by adding a CFRP plate that has a cross-sectional area that is only 0.6 percent of the wood member.

Conclusions and Design Implications

Thirteen beams were tested to assess the use of composite beams made of various combinations of concrete, engineered wood, and CFRP materials in timber bridge design. Although additional research will be needed to answer fully all of the important questions surrounding the design of such beams, the research results presented herein provide the following insights:

- CFRP plates can be bonded effectively to the tensile face of engineered wood beams.
- Although concrete compression flanges were made to act compositely with wood webs beyond the serviceability limit, some loss of composite action was experienced before failure. Improved methods for developing full composite action should be sought.
- The incorporation of CRFP plates and concrete flanges led to significant increases in flexural stiffness and ultimate strength over plain engineered wood beams.
- CFRP plates adhered to the tension face of engineered wood beams led to increases in the tensile strain capacity of the wood.
- For all beams tested, failure of the wood (either in flexure or shear) initiated the overall failure. For the W and WF beams, flexural failure of the wood occurred. However, the large increase in flexural capacity associated with the CW and CWF beams changed the mode of failure from flexure to shear for some beams.
- Accurate service-load deflections can be computed by converting the concrete and CFRP plate into equivalent amounts of wood.

In summary, the test results indicate that adding concrete and CFRP to engineered wood beams can improve significantly their overall flexural behavior. However, before final design criteria are developed, several issues still

TABLE 3 Ultimate Strength Increase for Beams

Beams	Ultimate Beam Strength[a], N	Wood Beam Strength[a], N	Percentage Increase
WF1, WF2, WF3	39,679	28,183	+40
CW1, CW2, CW3, CW4	75,650	28,183	+168
CWF1, CWF2, CWF3	79,358	28,183	+181

[a]All values are averages of like beams.

must be addressed, including the behavior of composite beams under sustained and repeated loads, the long-term durability of the bonded composite plates, the behavior of full-scale beams, and the identification of appropriate methods of analysis needed to predict ultimate beam strength as well as behavior at service loads.

ACKNOWLEDGMENTS

The first author is grateful for support received from the National Science Foundation, J. B. Scalzi, Program Director. The authors would also like to extend thanks to Trus Joist MacMillan and the University of Delaware's Center for Composite Materials for their support of this research. Finally, the authors would like to thank graduate students William Finch, Jr., Ted Januskza, and Ted Thomson, Jr., along with undergraduate students Caryn Bohn, Natalie Czaplicki, Charlene Eliasson, and Cory Farschman for their help during the preparation and testing of beams and small-scale specimens.

REFERENCES

1. Cooper, J. D. A New Era in Bridge Engineering Research. *Proc., 2nd Workshop on Bridge Engineering Research in Progress*, National Science Foundation, Reno, Nev., 1990, pp. 5–10.
2. Scalzi, J. B. Looking Ahead to the 21st Century. *Proc., 2nd Workshop on Bridge Engineering Research in Progress*, National Science Foundation, Reno, Nev., 1990, pp. 1a–1b.
3. Ritter, M. A. *Current Timber Research and Development in the United States*. Forest Products Laboratory, U.S. Department of Agriculture, Madison, Wisc., 1993.
4. Wipf, T. J., M. A. Ritter, S. R. Duwadi, and R. C. Moody. *Development of a 6-Year Research Needs Assessment for Timber Transportation Structures*. Report FPL-GTR-74. Forest Products Laboratory, U.S. Department of Agriculture, Madison, Wisc., 1993.
5. Oliva, M. G., R. L. Tuomi, and A. G. Dimakis. New Ideas for Timber Bridges. In *Transportation Research Record 1053*, TRB, National Research Council, Washington, D.C., 1986, pp. 59–64.
6. Brungraber, R., R. Gutkowski, W. Kindya, and R. McWilliams. Timber Bridges: Part of the Solution for Rural America. In *Transportation Research Record 1106*, TRB, National Research Council, Washington, D.C., 1987, pp. 131–139.
7. Gutkowski, R. A., and W. J. McCutcheon. Comparative Performance of Timber Bridges. *Journal of Structural Engineering*, ASCE, Vol. 113, No. 7, July 1987, pp. 1468–1485.
8. Behr, R. A., E. J. Cundy, and C. H. Goodspeed. Cost Comparison of Timber, Steel, and Prestressed Concrete Bridges. *Journal of Structural Engineering*, ASCE, Vol. 116, No. 12, Dec. 1990, pp. 3448–3456.
9. Oliva, M. G. and A. G. Dimakis. Behavior of Stress-Laminated Timber Highway Bridge. *Journal of Structural Engineering*, ASCE, Vol. 114, No. 8, Aug. 1988, pp. 1850–1869.
10. Moody, R. C., M. A. Ritter, and H. GangaRao. Applications of Wood Materials for Innovative Bridge Systems. *Proc., 1st Materials Engineering Congress*, Denver, Colo., 1990, pp. 423–432.
11. Coger, T., ed. Engineered Wood Products Manufactured by Trus Joist MacMillan. *Crossings*, USDA Forest Service, Morgantown, W.Va., 1993, pp. 1–2.
12. Ritter, M. A. *Timber Bridges: Design, Construction, Inspection, and Maintenance*. Report EM 7700-8. U.S. Department of Agriculture, 1992.
13. Ballinger, C. A. Development of Composites for Civil Engineering. *Advanced Composite Materials in Civil Engineering Structures*, ASCE, Las Vegas, Nev., 1991, pp. 288–301.
14. Ballinger, C. A. Development of Fibre-Reinforced Plastic Products for the Construction Market—How Has and Can It Be Done. *Advanced Composite Materials in Bridges and Structures*, Canadian Society for Civil Engineering, Sherbrooke, 1992, pp. 3–13.
15. Bank, L. C. Questioning Composites. *Civil Engineering*, ASCE, Vol. 63, No. 1, Jan. 1992, pp. 64–65.
16. Chajes, M. J., T. A. Thomson, T. F. Januszka, and W. W. Finch. Flexural Strengthening of Concrete Beams Using Externally Applied Composite Materials. *Construction and Building Materials*, Vol. 8, No. 3, Sept. 1994, pp. 191–201.
17. Chajes, M. J., T. F. Januszka, T. A. Thomson, W. W. Finch, and D. R. Mertz. Shear Strengthening of Reinforced Concrete Beams Using Externally Applied Composite Fabrics. *ACI Structural Journal* (in press).
18. Head, P. R. Design Methods and Bridge Forms for the Cost-Effective Use of Advanced Composites in Bridges. *Advanced Composite Materials in Bridges and Structures*, Canadian Society for Civil Engineering, Sherbrooke, 1992, pp. 15–30.
19. Hoa, S. V. Design of a Composite Box Beam for Building Applications. *Advanced Composite Materials in Bridges and Structures*, Canadian Society for Civil Engineering, Sherbrooke, 1992, pp. 501–512.
20. McCormick, F. C. Advancing Structural Plastics into the Future. *Journal of Structural Engineering*, ASCE, Vol. 114, No. 3, March 1988, pp. 235–243.
21. Measures, R. M. Smart Structures—A Revolution in Civil Engineering. *Advanced Composite Materials in Bridges and Structures*, Canadian Society for Civil Engineering, Sherbrooke, 1992, pp. 31–59.
22. Meier, U., and H. Kaiser. Strengthening of Structures with CFRP Laminates. *Advanced Composite Materials in Civil Engineering Structures*, ASCE, Las Vegas, Nev., 1991, pp. 224–232.
23. Saadatmanesh, H., and M. R. Ehsani. Fiber Composite Plates Can Strengthen Beams. *Concrete International*, Vol. 12, No. 3, March 1990, pp. 65–71.
24. Sotiropoulos, S. N., and H. GangaRao. Bridges Systems Made of FRP Components. *Proc., 2nd Workshop on*

Bridge Engineering Research in Progress, National Science Foundation, Reno, Nev., 1990, pp. 295–298.
25. Triantafillou, T. C., N. Plevris, and N. Deskovic. Nonprestressed and Prestressed FRP Sheets as External Reinforcement of Wood Members. *Proc., Materials Engineering Congress*, ASCE, Atlanta, GA., 1992, pp. 710–717.
26. Triantafillou, T. C., and N. Deskovic. Prestressed FRP Sheets as External Reinforcement of Wood Members. *Journal of Structural Engineering*, ASCE, Vol. 118, No. 5, May 1992, pp. 1270–1284.
27. Davalos, J. F., H. A. Salim, and U. Munipalle. Glulam-GFRP Composite Beams for Stress-Laminated T-System Bridges. *Advanced Composite Materials in Bridges and Structures*, Canadian Society for Civil Engineering, Sherbrooke, 1992, pp. 455–464.
28. Davalos, J. F., E. Barbero, and U. Munipalle. Glued-Laminated Timber Beams Reinforced with E-Glass/Polyester Pultruded Composites. *Proc., 10th Structures Congress*, ASCE, San Antonio, Tex., 1992, pp. 47–50.
29. Leichti, R. J., P. C. Gilham, and D. A. Tingley. The Taylor Lake Bridge: A Reinforced-Glulam Structure. *Wood Design Focus*, Vol. 4, No. 2, 1993.
30. Richart, F. E., and C. B. Williams, Jr. *Tests of Composite Timber and Concrete Beams*. Bulletin Series 343. University of Illinois Engineering Experiment Station, 1943, pp. 1–62.
31. McCullough, C. B. Oregon Tests on Composite (Timber-Concrete) Beams. *Proceedings*, ACI, Vol. 39, No. 4, 1943.
32. Pincus, G. Bonded Wood-Concrete T-Beams. *Journal of the Structural Division*, ASCE, Vol. 95, No. 10, Oct. 1969, pp. 2265–2279.
33. Pincus, G. Behavior of Wood-Concrete Composite Beams. *Journal of the Structural Division*, ASCE, Vol. 96, No. 10, Oct. 1970, pp. 2009–2019.
34. Ahmadi, B. H., and M. P. Saka. Behavior of Composite Timber-Concrete Floors. *Journal of Structural Engineering*, ASCE, Vol. 119, No. 10, Oct. 1993, pp. 3111–3130.
35. *LRFD Specification for Highway Bridge Design*. AASHTO, Washington, D.C., 1994.

Dynamic Response of Stress-Laminated-Deck Bridges

M. A. Ritter, *Forest Service, U.S. Department of Agriculture*
D. L. Wood, T. J. Wipf, and Chintaka Wijesooriya, *Iowa State University*
S. R. Duwadi, *Federal Highway Administration*

The dynamic response of three stress-laminated wood bridges was determined from field test results using a heavily loaded truck. Deflections at the bridge midspan were measured at various vehicle speeds using a high-speed data acquisition system, and a dynamic amplification factor (DAF) was computed. These tests represent only a portion of the field testing, which is part of a larger research study that also includes analytical research. Experimental data described will be used to validate analytical models. The objective of the larger study is to determine the dynamic behavior of stress-laminated wood bridges so that reliable design specifications can be developed. The three bridges represent contrasting approach conditions at the bridge entrance, asphalt and gravel roadways and bridge surfaces, and different natural frequencies. Results show that for smooth in situ conditions at the bridge entrance and an asphalt roadway surface, maximum DAF is 1.08 for a bridge with a relatively high calculated natural frequency (10.6 Hz). For rough conditions at the bridge entrance approach and an asphalt roadway surface, maximum DAF is 1.34 for a bridge with a high calculated natural frequency (10.6 Hz) and 1.20 for a bridge with a low calculated natural frequency (3.2 Hz). The DAF was found to be very high (1.50) at high vehicle speeds for the bridge with gravel surface approach conditions and a calculated frequency of 7.8 Hz.

Wood has been used as a bridge material in the United States for hundreds of years. Despite the exclusive use of wood bridges during much of the 19th century, the 20th century brought a significant decline in the percentage of wood bridges relative to those of other materials. Currently, approximately 10 percent of the bridges listed in the National Bridge Inventory are wood (*1*). There has been a renewed interest in wood as a bridge material recently, and several national programs have been implemented to further develop wood bridge systems. The Timber Bridge Initiative and the Intermodal Surface Transportation Efficiency Act, passed by Congress in 1988 and 1991, respectively, made available funding for timber bridge research (*2*). Part of this research is aimed at refining and developing design criteria for wood bridge systems. This project to investigate the dynamic characteristics of wood bridges is part of that program and involves a cooperative research study among Iowa State University, the USDA Forest Service, Forest Products Laboratory; and FHWA. The first phase of the project is to assess the dynamic characteristics of stress-laminated deck bridges.

Stress-laminated timber bridge decks consist of a series of wood laminations that are placed edgewise between supports and stressed together with high-strength

steel bars (*3*). The bar force, which typially ranges from 111.2 to 355.9 kN (25,000 to 80,000 lb), squeezes the laminations together so that the stressed deck acts as a solid wood plate. The concept of stress laminating was developed in Ontario, Canada, in 1976 as a means of rehabilitating nail-laminated lumber decks that delaminated as a result of cyclic loading and variations in wood moisture content (*4,5*). In the 1980s, the concept was adapted for the construction of new bridges, and many structures were successfully built or rehabilitated in Ontario using the stress-laminating concept. The first stress-laminated bridges in the United States were built in the late 1980s. Since then, several hundred stress-laminated timber bridges have been constructed, primarily on low-volume roads.

Background

Highway bridges must be designed for the dynamic loads imposed by passing vehicles. Traditionally, bridges have been designed for static loads and a factor is applied to increase loads to compensate for the dynamic effects. In AASHTO's *Standard Specifications for Highway Bridges*, the dynamic allowance is applied as an impact factor (*6*). The impact factor is computed on the basis of span length and is limited to a maximum of 1.3. Historically, AASHTO has not required that the impact factor be applied for wood bridges because of the ability of wood to absorb shock and carry greater loads for short durations. However, new AASHTO load and resistance factor design (LRFD) specifications require that wood bridges be designed for 50 percent of the dynamic allowance required for steel and concrete bridges.

Recently, the exclusion or reduction of dynamic loading design requirements for wood bridges has been questioned. Many in the design community believe that some adjustment for dynamic effect is appropriate for wood bridges. Unfortunately, little information is available to support changes to current design standards. Since the 1950s, a significant amount of research on the related topic of bridge dynamics, mostly of an analytical nature, and a moderate amount of experimental research have been performed. However, none of the research has dealt specifically with wood bridges, nor has it considered relatively short spans that are typical of wood bridges.

Over the past decade many articles have been published on bridge dynamic behavior. In the interest of brevity, only one article, which is a summary of most of the pertinent experimental dynamics research performed before its publication, is summarized here to discuss the important issues related to experimental evaluation of bridge dynamics. The article by Bakht and Pinjarkar (*7*) presents a testing procedure for determining a single dynamic amplification factor (DAF) for a bridge. Using a single vehicle is not representative of the loads that a bridge will encounter in its life; therefore, a single vehicle can only provide insight into dynamic loading behavior and should not be used to determine a single value of DAF. The only way that a representative value can be determined is to collect data under normal traffic over long periods. From data collected, a statistical procedure using the mean and variance of the measured DAF values with a safety index for highway bridges can be used to obtain a single value.

From previous research, Bakht and Pinjarkar (*7*) found that the DAF decreases with an increase in vehicle weight. Therefore light vehicles, whose loading is insignificant compared with design loads, cause dynamic amplifications that are misleading and excessive. To avoid this, data from light vehicles should not be used to calculate DAF. And DAFs at points away from the load can be greater than those directly under the load. Deflections at points away from the load, which are typically smaller and less important than those under the loading, should not be used in determining DAF; data should be taken only from locations where large deflections occur. Bakht and Pinjarkar suggest using only data from the point at which the maximum static deflection occurs at the monitored cross section.

The use of an artificial bump placed on the road surface to account for riding surface irregularities is common. Bakht and Pinjarkar note that this practice may produce overly conservative results on bridges where the road is well-maintained. A bump should be placed only if the bridge is not expected to be paved for a long time, or if unevenness at the bridge entrance or expansion joints is expected. The authors also point out that there is little uniformity in how the DAF is calculated. Bakht and Pinjarkar (*7*) list eight equations, all giving a slightly different value for a given situation.

Objective

The objective of the research presented here was to determine the dynamic performance characteristics of three stress-laminated timber bridges. The results for these bridges will be combined with results from additional tests still to be performed and complementary analytical research to prepare design criteria to be submitted to AASHTO for inclusion in the *Standard Specification for Highway Bridges* (*6*).

Research Methods

Static and dynamic tests were performed on the three bridges: Trout Road, Little Salmon, and Lampeter. Ver-

tical deflections were measured for several vehicle velocities for two road approach roughnesses. Dynamic deflection data were compared with static deflections to quantify a DAF for each test. The field tests were designed to observe bridge deflections and vertical accelerations of the test vehicle axles. Only the bridge deflection data are presented in this paper.

Bridge Description

The three bridges—Trout Road, Little Salmon, and Lampeter—are located in the commonwealth of Pennsylvania. The bridges are conventional stress-laminated wood decks constructed of sawn lumber (Figure 1). A summary of the characteristics for each bridge is presented in Table 1.

Note that the Little Salmon Bridge was unpaved and the roadway was surfaced with gravel and contained potholes. The region approximately 1.53 m (5 ft) before the bridge entrance was smoothed by filling the potholes with gravel. There was a zero grade in the region approximately 4.58 m (15 ft) before the entrance and a downward grade of approximately 3 percent before this immediate region where no attempt was made to eliminate the potholes. For these reasons, the approach conditions were characterized as irregular.

Both Trout Road and Lampeter bridges were paved asphalt and contained zero grade approach profiles. Immediate approach conditions at the abutment for the Lampeter Bridge could be characterized as excellent (smooth). However, the Trout Road Bridge had a rut at the abutment joint at the entrance that created an irregular surface. The rut was approximately 38.1 mm (1½ in.) deep. Thus, the approach condition was defined as irregular.

Test Vehicles

The vehicles used for bridge testing were three-axle dump trucks provided by the bridge owner. Each vehicle had multileaf spring suspension on the rear axles. Specific vehicle configurations and loads for each bridge are presented in Figure 2. The track width of each test vehicle was 1.83 m (6 ft).

FIGURE 1 Field test bridges: *top*, Trout Road; *middle*, Little Salmon; *bottom*, Lampeter.

Instrumentation

The dynamic response of the bridge at midspan was recorded during the passage of three-axle trucks traveling at constant velocity. The instrumentation system was designed for portability and allowed several tests to be performed in a day. Deflections were measured at approximately 0.61-m (2-ft) intervals across the entire bridge width using a Celesco string-type direct current potentiometer. Such transducers have been used successfully for dynamic application in the laboratory for responses with similar frequency ranges found in these field tests. A frame consisting of

TABLE 1 Characteristics of Tested Bridges

Item	Trout Road	Little Salmon	Lampeter
Year Built	1987	1988	1992
Wood Species	Douglas Fir	Red Oak	Red Oak
Bridge Width (out-out)	7.84 m	4.73 m	9.03 m
Bridge Length (out-out)	14.64 m	7.93 m	7.11 m
Bridge Span (c-c bearings)	14.00 m	7.62 m	6.76 m
Deck Thickness	406.4 mm	304.8 mm	406.4 mm
Approach Roadway Type	Smooth asphalt pavement	Irregular gravel	Smooth asphalt pavement
Approach Grade	0%	0%*	0%
Bridge Entrance Conditions	Irregular	Irregular	Smooth
Fundamental Experimental Frequency	3.9 Hz	8.6 Hz	N/A
Fundamental Calculated Frequency	3.2 Hz	7.8 Hz	10.6 Hz
Damping Ratio	4.0%	3.0%	N/A

*This grade applies to the region approximately 4.58 m (3.0 ft) in front of the bridge entrance. In the region prior to this, the grade was approximately 3% downward.
1 m = 3.28 ft

surveying tripods supporting a board 50.8 × 304.8 mm (2 × 12 in.) was used to support the displacement transducers (Figure 3). Data were collected using a Hewlett-Packard (HP) 3852A data acquisition/control system (DAS) equipped with two HP 44711 24-channel FET multiplexers and an HP 44702 14-bit high-speed voltmeter. The DAS was controlled and the data were processed and stored in a portable 486DX-33 PC running IBASIC for Windows. Figure 4 (*top*) is a schematic of the test components, and Figure 4 (*bottom*) is a photograph of the DAS setup in the field. The entire system was powered by a portable generator and triggered when the vehicle crossed the tap switch at the bridge entrance.

Acceleration data were also collected on the vehicle simultaneously with the bridge displacement transducer data. The setup consisted of a Gould digital storage oscilloscope (DSO) and two PCB accelerometers. The accelerometers were high-sensitivity integrated-circuit piezoelectrics with a quartz trishear design. The accelerometers were mounted on the vehicle frame over the front and rear axles (Figure 5). They were wired into conditioner modules and from there into the DSO. The DSO was connected to a laptop computer via IEEE-488 interface. Transition software from Gould controlled the DSO so that it waited for a trigger to collect the signals from both channels. Data were then transferred to the laptop, and the DSO was reset for the next trigger. Power to the laptop and oscilloscope was provided by either batteries or the electrical system of the vehicle through the fuse box or cigarette lighter.

A tape switch that was mounted to the front bumper of the vehicle was used to trigger the DSO. A board 50.8 × 304.8 mm (2 × 4 in.) was attached parallel to the bumper to extend the tape switch approximately 0.61 m (2 ft) to the side of the truck to hit a vertical rod placed on the roadway that would trigger the DSO. The rod was positioned so that the DSO was triggered simultaneously with the DAS. This allowed data from both files to be combined to analyze the interaction responses between the vehicle and bridge. A schematic of the vehicle DAS layout, which was located in the passenger cab of the vehicle, is shown in Figure 5 (*bottom*).

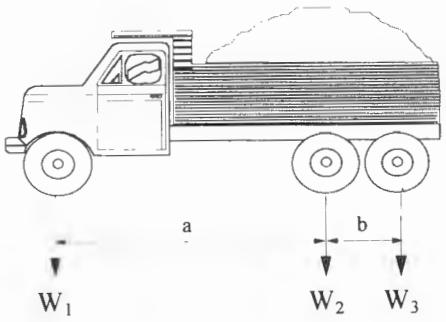

Item	Trout Road	Little Salmon	Lampeter
W1	68.9 kN	44.9 kN	60.9 kN
W2	92.3 kN	81.6 kN	79.2 kN
W3	91.6 kN	80.1 kN	76.5 kN
Total Weight	252.8 kN	206.6 kN	216.6 kN
a	3.52 m	3.68 m	4.09 m
b	1.37 m	1.30 m	1.40 m
Rear Suspension Type	Multi-leaf springs	Multi-leaf springs	Multi-leaf springs

1 m = 3.28 ft
1 kN = 0.2248 kips

FIGURE 2 Test vehicle properties.

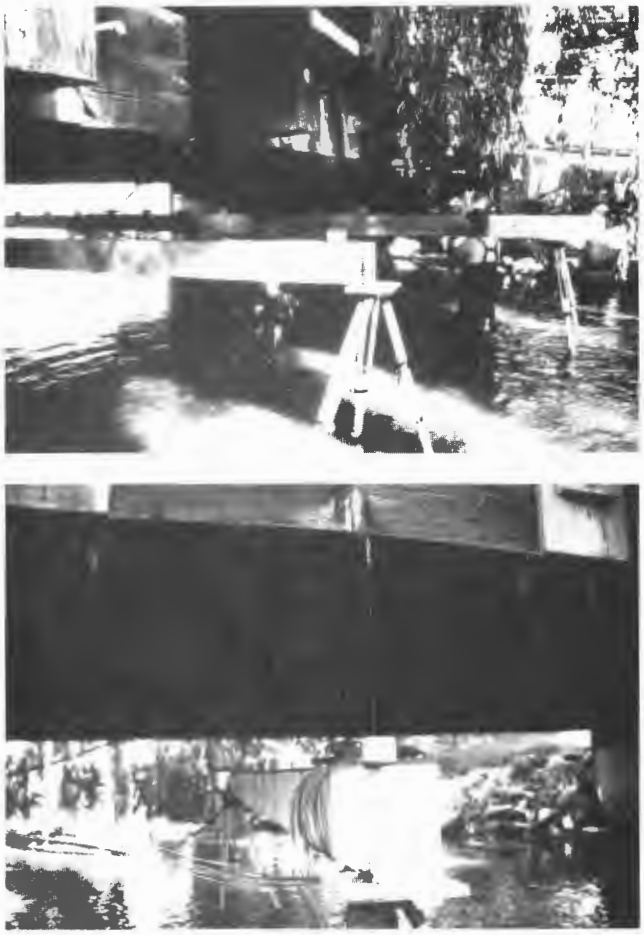

FIGURE 3 Layout of instrumentation for displacement transducer data.

Test Procedure

The dynamic load behavior of the bridge was evaluated for several vehicle velocities for in situ and artificial rough approach conditions at the bridge entrance. Two transverse vehicle positions were used for two-lane bridges: (a) eccentric, with the left wheel line (driver side) 2 ft to the right of centerline, and (b) concentric, with the axle of the truck centered on the bridge (i.e., straddling the centerline). For the single-lane bridge (Little Salmon), only the concentric vehicle position was used. String lines were used to provide a guide for the driver. Visual records were obtained on each run, indicating vehicle deviation from the string line position. Generally, the truck was very close to the required position.

To obtain a basis by which the dynamic load effects could be compared, crawl tests were performed for each loading position. During these crawl tests, the vehicle velocity was approximately 8.05 km/hr (5 mph). Deflections at higher velocities were then obtained; velocities ranged from 16.1 to 64.4 km/hr (10 to 40 mph), depending on the geometry and condition of the approach and available stopping distance beyond the bridge. The artificial rough approach condition was simulated using a board 50.8 × 304.8 mm (2 × 4 in.) placed at the bridge entrance (Figure 6).

The vehicle speedometer was used to control the desired vehicle speed during the tests. However, tape switches were installed at the entrance and at the end of the bridge to verify vehicle velocity.

Data Processing

A plot of bridge deflection and vehicle position along the bridge (using the vehicle front axle as a reference) was made for each displacement transducer location at the bridge midspan. Initially, crawl tests were performed on each bridge to establish a basis for calculating the bridge dynamic response. Figure 7 (*top*) shows a typical response for such a test. Note the small amount of dynamic activity even at crawl speeds, but this was smoothed by fitting a curve to the response. The maximum deflection obtained in this way is referred to by

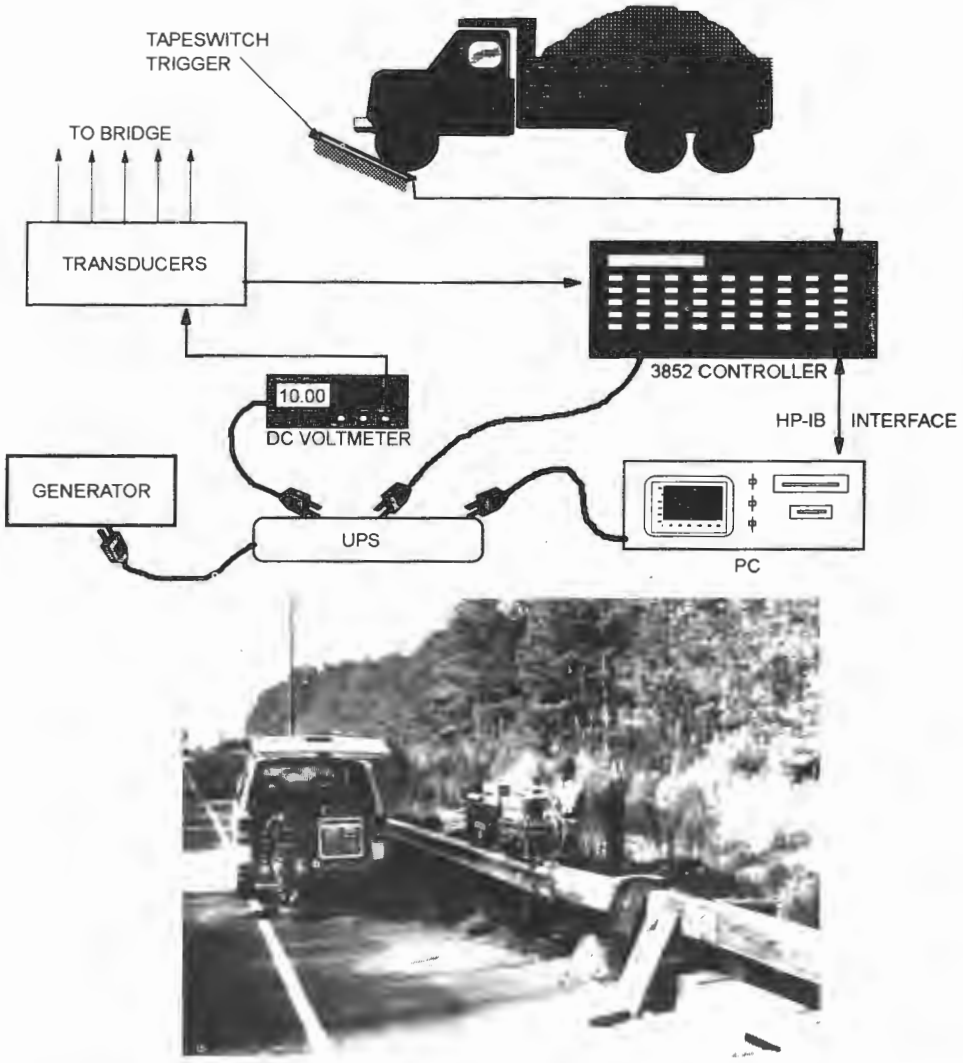

FIGURE 4 Bridge data acquisition system: *top*, layout of test components; *bottom*, data acquisition system in the field.

δ_{stat}. Figure 7 (*bottom*) shows a typical dynamic response relative to the static crawl response just described. The maximum dynamic deflection is referred to by δ_{dyn}.

The DAF was computed for each bridge. Each displacement transducer location was scanned to find the maximum absolute crawl deflection, and this data point was then used as the reference point for the calculation of DAF. As per recommendations by Bakht and Pinjarkar (7), this approach yields the most useful design information. Note that, typically, the data point that had the highest crawl deflection also had the highest dynamic response. Referring to Figure 7, the DAF was computed using the following:

$$DAF = 1 + \left(\frac{\delta_{dyn} - \delta_{stat}}{\delta_{stat}}\right) \quad (1)$$

Deflection data were also used to calculate the fundamental frequency of each bridge (Table 1), using the free vibrations of the bridge after the vehicle left the span. This free vibration was also used to determine the amount of damping in the bridge (Table 1). The free vibrations for the Lampeter Bridge were too small to allow a frequency domain analysis to be performed.

The calculated analytical fundamental frequency for each bridge shown in the table was based on finite element analysis. As noted, the experimental values are greater than the analytical values. This is typical, because analytical bridge models do not account for the rotational restraint at the abutments that is inherent in most bridges.

The deck was modeled using rectangular shell elements with four nodes, each with 6 degrees of freedom. However, during the analysis, the in-plane displace-

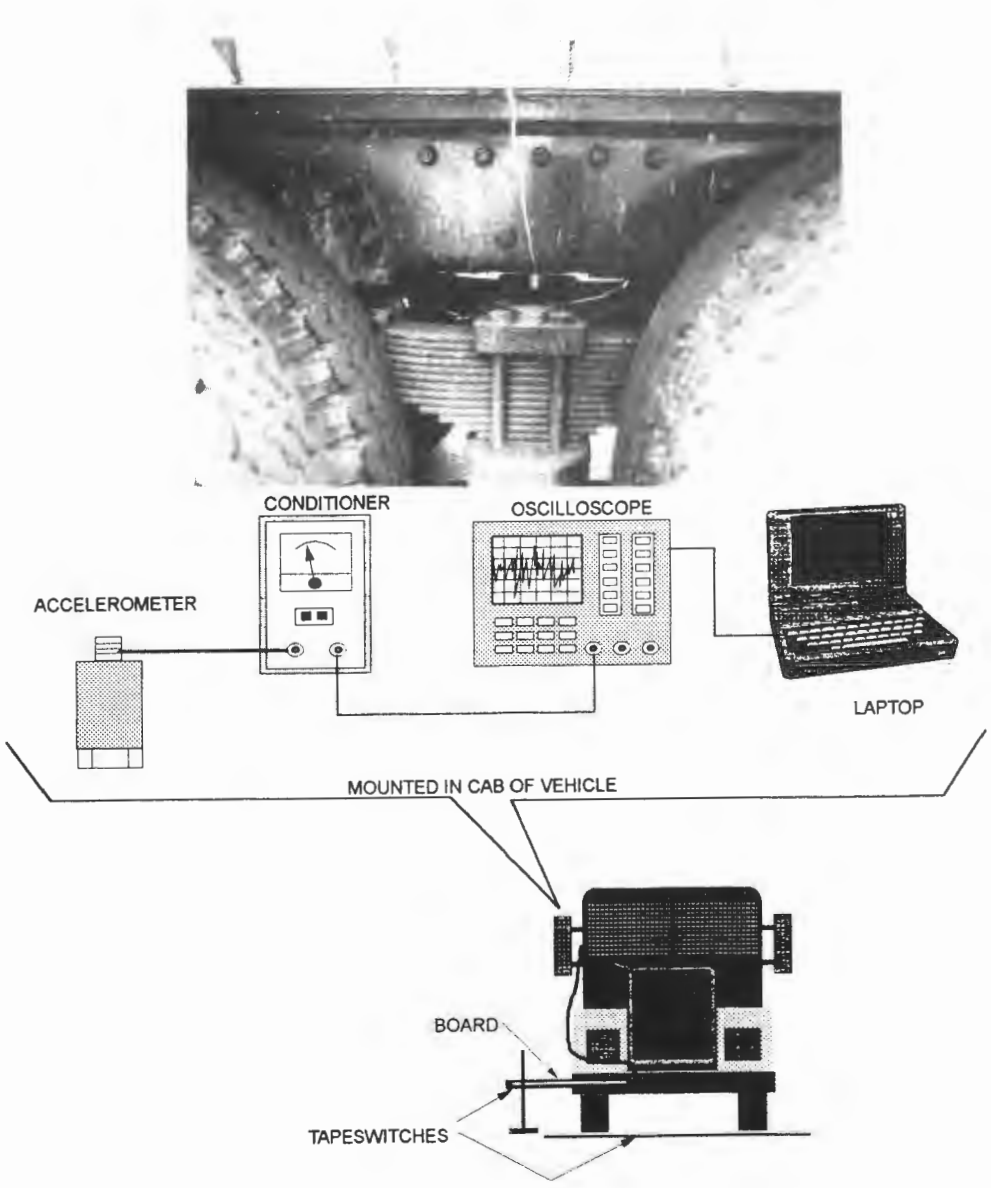

FIGURE 5 Vehicle data acquisition system: *top*, accelerometer mounted on frame; *bottom*, schematic of layout.

ments and rotation were restrained to reduce the total number of degrees of freedom of the bridge model. This had no effect on the analysis, because deck elements behave as plate elements and do not develop in-plane forces or moments.

Test Results

Plots of bridge deflection and vehicle position (using the front axle as the reference point) for various speeds and both in situ and artificial rough approaches are shown in Figures 8 through 10 for each bridge. The legends indicate transverse axle positions (eccentric or concentric), location of the displacement transducer data used for the plot, vehicle velocity, and in situ or artificial rough approach, denoted by (b) for bump along with the vehicle velocity. The Trout Road bridge, as previously mentioned, had an inherently rough approach as a result of ruts in the asphalt surface immediately in front of the bridge approach; therefore, these data should be assumed to be similar to a rough approach condition even though the data are presented as in situ.

A general observation for each bridge is that the dynamic response was significantly greater for the rough approach than for the in situ approach for the Lampeter

FIGURE 6 Artificial bump at bridge entrance.

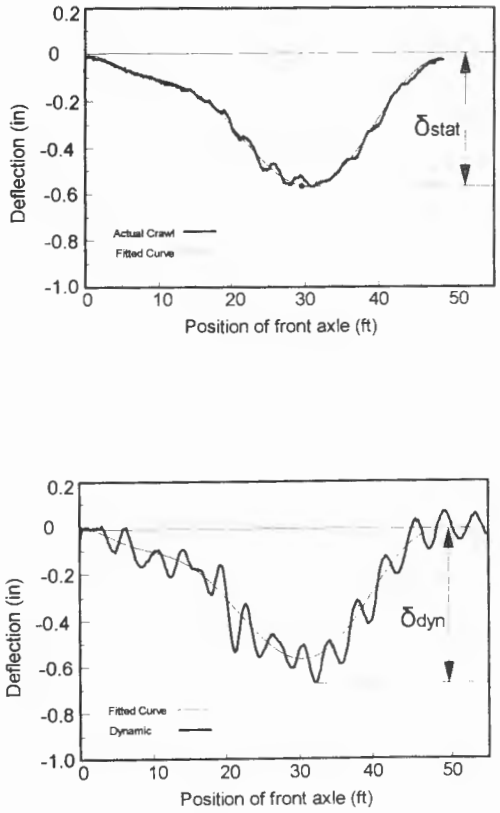

FIGURE 7 Typical displacement transducer data for bridge test: *top*, determination of δ_{stat}; *bottom*, determination of δ_{dyn} (1 in. = 25.4 mm; 1 ft = 0.3048 m).

Bridge. Also, for most velocities on the Little Salmon Bridge, the rough approach dynamic response was greater than the in situ response. Primarily because of the irregular approach condition, these comparisons were not as consistent for the Lampeter Bridge. Another general observation for both the Little Salmon and Lampeter bridges is that the dynamic response for the rough approach exhibited more oscillations than for the in situ approach for similar velocities. Also note for both the Trout Road and Lampeter bridges that the dynamic response was generally greater for the eccentric load position than for the concentric load position. There was excellent repeatability of the results for Lampeter at 53.0 and 52.0 km/hr (32.9 and 32.3 mph) for rough approach conditions.

To clearly quantify the dynamic behavior shown in the plots, the DAFs were calculated for each test for the three bridges and are shown in Figure 11. The maximum DAF for the Trout Road Bridge was 1.20 and occurred for an eccentric load position. As shown, the trend in DAF was similar for both concentric and eccentric positions, with the maximum values occurring at the lower velocities. Bridge roadway horizontal geometry did not allow tests to be performed at speeds in excess of 40.3 km/hr (25 mph).

The trend in DAF values for the Lampeter Bridge was similar for both the in situ and the rough (bump) approach conditions throughout the range of velocities. As shown, the DAF generally increased with increasing velocity, and the maximum DAFs occurred at the higher speeds. The values of DAF for eccentric loading were generally greater than for concentric loading. The maximum DAF was 1.08 for the in situ approach and 1.34 for the rough approach.

Trends in the Little Salmon responses of DAF and vehicle velocity were not as regular as for the other two bridges, primarily because of the irregularity of the approach conditions. For the concentric rough approach, the DAF generally decreased as velocity increased. The maximum DAF was 1.20 and occurred at the lower velocity. However, at lower speeds for the in situ conditions, the trend of decreasing DAF with increasing velocity was also observed; at high velocities, the DAF

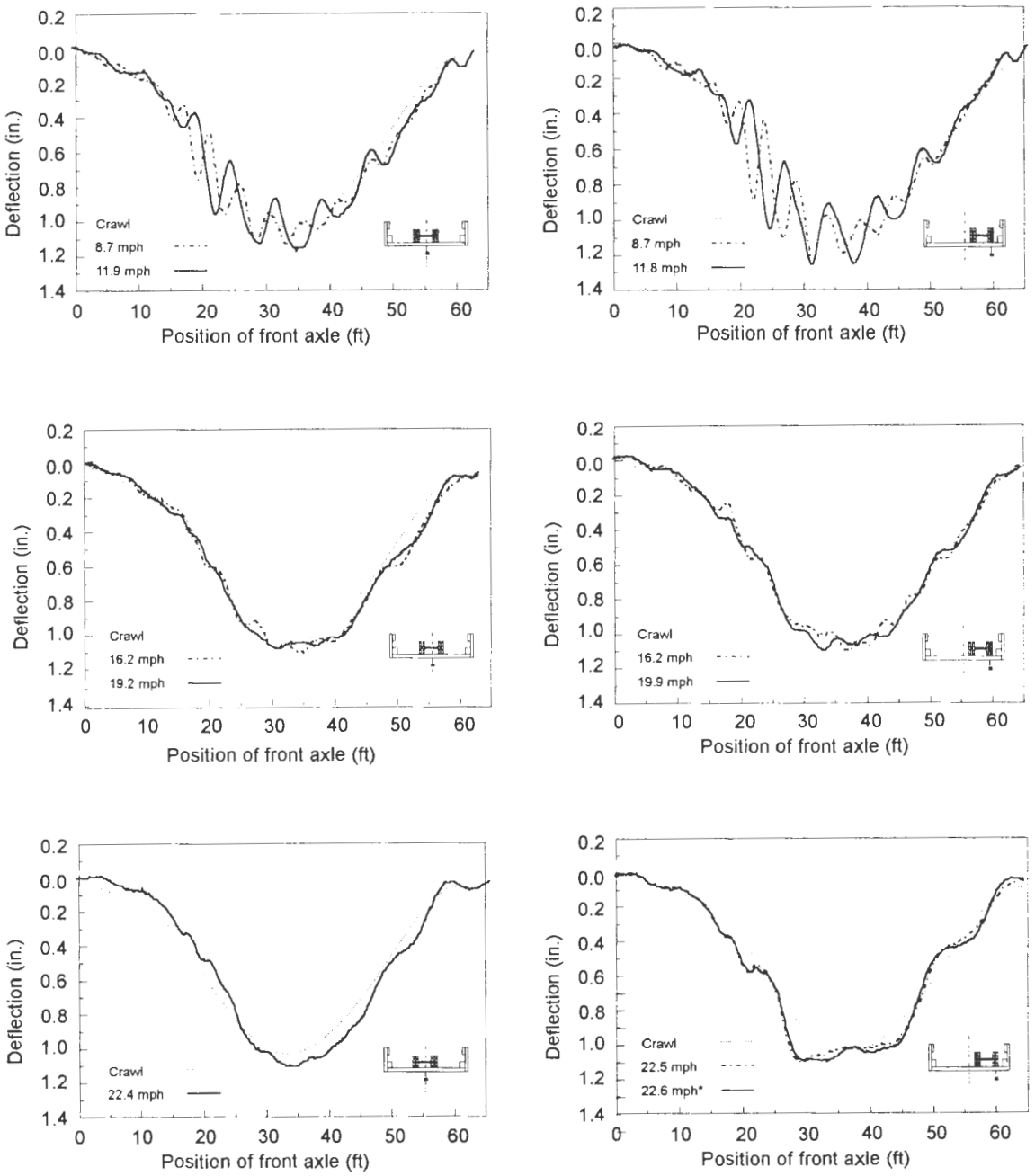

FIGURE 8 Dynamic response for Trout Road Bridge (1 in. = 25.4 mm; 1 ft = 0.3048 m).

increased. In fact, the maximum DAF occurred at the highest velocity and was extremely high (1.50). A possible explanation for this extreme value is that because of the highly irregular approach conditions, the high velocity accentuated the initial conditions of the vehicle (longitudinal pitch and vertical bounce).

Another observation involving the rear axle spacing parameter relative to vehicle velocity is worthy of mention. When the time for the two rear axles to pass a common point is equivalent to the natural period of the bridge, a pseudoresonance condition has been observed experimentally in research by Foster and Oehler (*8*). This condition may affect whether the components of the dynamic response due to each rear axle add or cancel. From the fundamental frequencies for each bridge (Table 1), the natural periods are 0.238, 0.12, and 0.10 sec. for the Trout Road, Little Salmon, and Lampeter bridges, respectively. The velocities at which the rear axle spacing for the test vehicle satisfied pseudoresonance conditions were 20.8, 38.8, and 50.6 km/hr

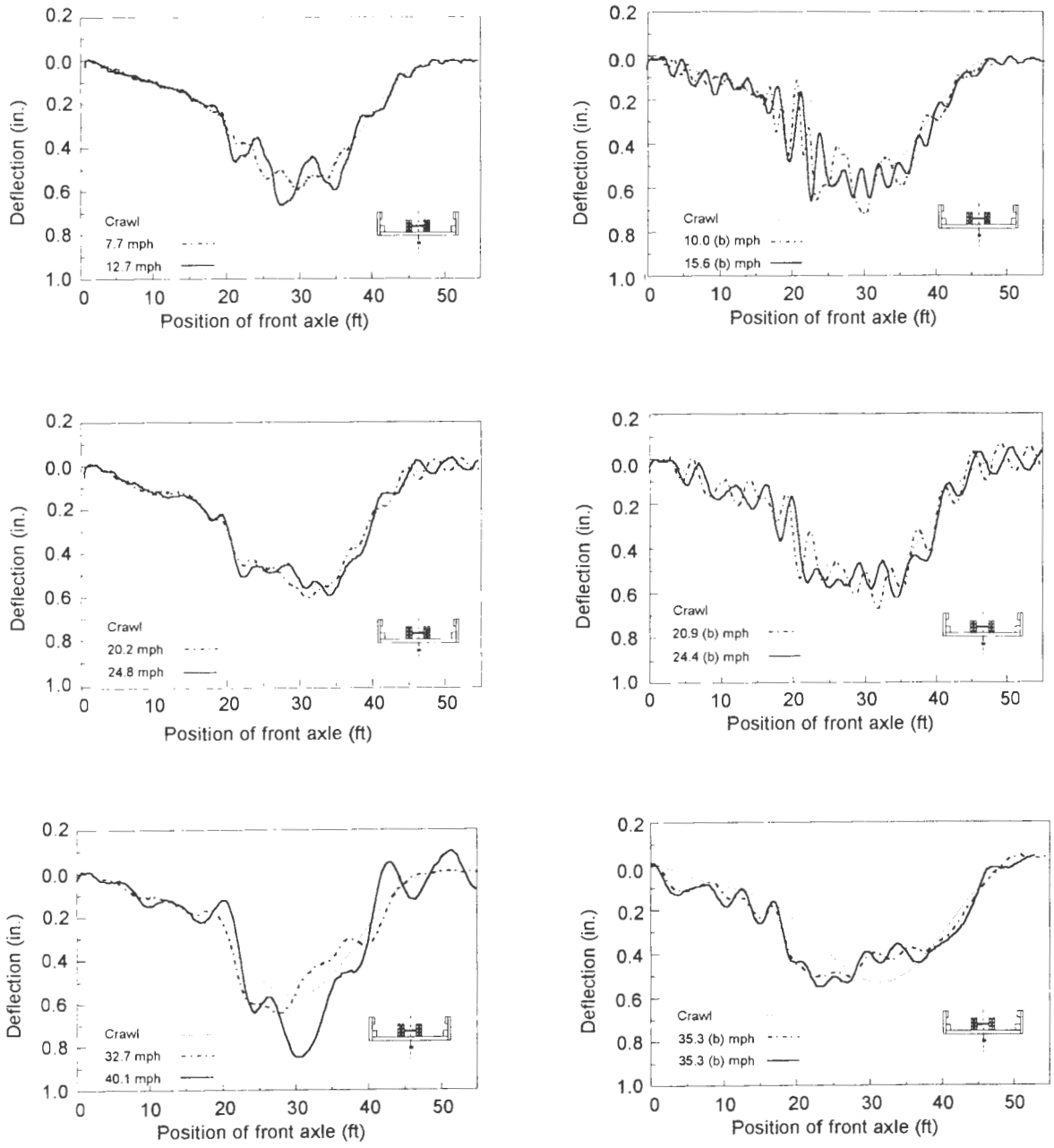

FIGURE 9 Dynamic response for Little Salmon Bridge (1 in. = 25.4 mm; 1 ft = 0.3048 m).

(12.9, 24.1, and 31.4 mph) for the Trout Road, Little Salmon, and Lampeter bridges, respectively. These velocities correspond reasonably well with the velocities at which the maximum DAF occurred for the Trout Road and Lampeter bridges.

Concluding Remarks

In this study, a field testing program was developed to measure the dynamic behavior of stress-laminated bridges. Three bridges with three distinct geometric, material, and roadway approach conditions were tested as part of a larger research program. The dynamic behavior of each bridge was described on the basis of deflections measured at midspan for a heavily loaded three-axle truck at different velocities. The monitoring system used for the field testing proved to be reliable, portable, and easy to set up.

DAFs were determined for each bridge, and the dynamic behavior was discussed. The trends in DAF and vehicle velocity were fairly consistent for the Lampeter

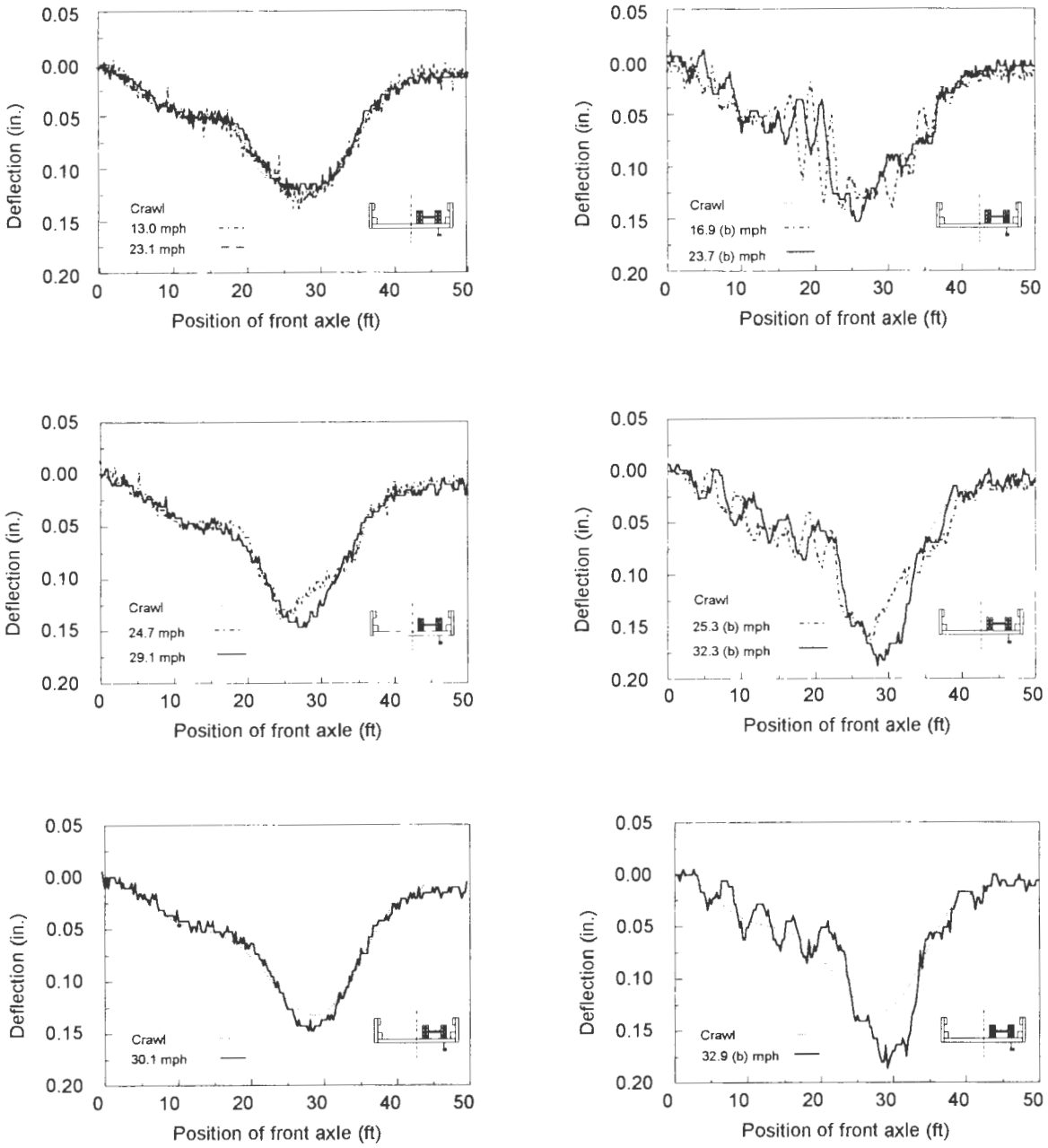

FIGURE 10 Dynamic response for Lampeter Bridge (1 in. = 25.4 mm; 1 ft = 0.3048 m) *(continued on next page)*.

and Trout Road bridges, which had asphalt-paved roadways. In contrast, the DAF trends were not as consistent for the Little Salmon Bridge, which was on a gravel roadway. Generally, eccentric load positions resulted in higher DAFs than did concentric load positions. The DAFs for rough approach conditions (bump) were significantly greater than for in situ conditions for the Lampeter Bridge, which has a relatively high calculated fundamental frequency (10.6 Hz).

Results of the field tests clearly show that dynamic effects may be significant in short-span timber bridges. Further, the extremely high DAF measured for the Little Salmon Bridge at 64.4 km/hr (40 mph) verifies the significant effect of the initial conditions of a vehicle entering a bridge. These initial conditions can be random, depending on vehicle characteristics and approach conditions. Therefore, relying only on limited field data to describe overall dynamic behavior is not appropriate. A rational approach is needed that uses either significant statistical experimental data taken over a long period or analytical data based on validation from experimental tests. With regard to the latter, data presented

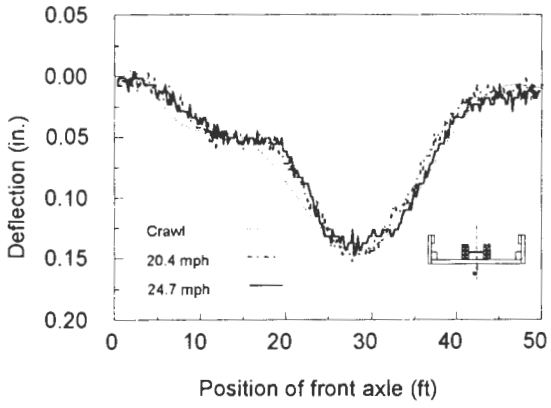

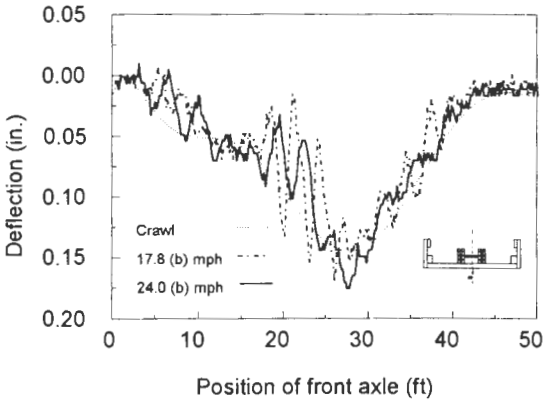

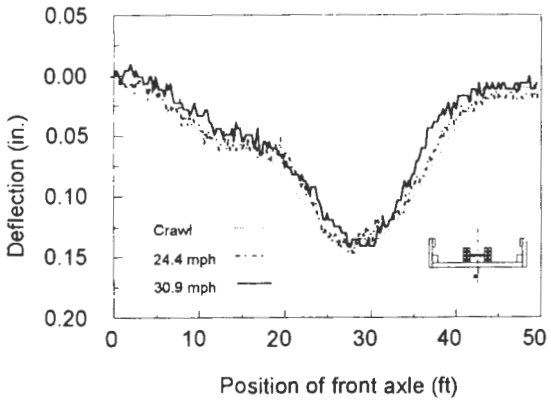

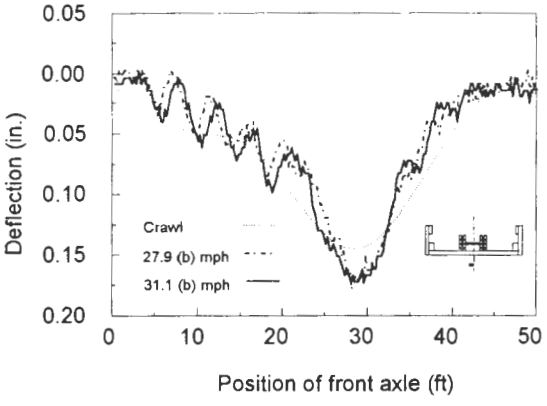

FIGURE 10 *(continued)*

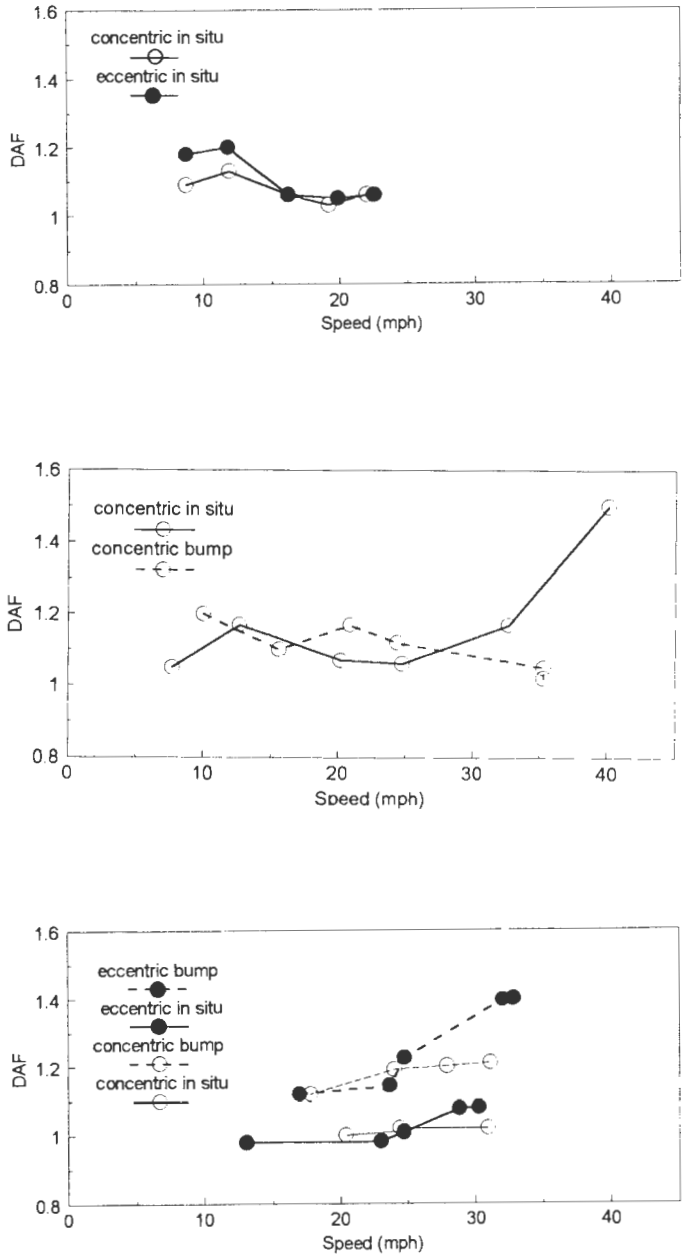

FIGURE 11 DAFs for field-tested bridges: *top*, Trout Road; *middle*, Little Salmon; *bottom*, Lampeter (1 mph = 1.61 km/hr).

in this paper should represent a significant contribution toward that end.

ACKNOWLEDGMENTS

The authors thank all of the state, county, city, and Forest Service personnel who provided assistance during the field testing. Special thanks to James P. Wacker of the Forest Products Laboratory for his help during the testing of both the Trout Road and Lampeter bridges. We also thank Padmini Narasingham for her help with data reduction and plotting.

REFERENCES

1. *National Bridge Inventory*. FHWA, U.S. Department of Transportation, 1992.

2. Duwadi, S. R., and M. A. Ritter. *Status of Research on Timber Bridges and Related Topics.* Research Update. Structures Division, Turner-Fairbank Research Center, FHWA, McLean, Va., 1994.
3. Ritter, M. A. *Timber Bridges: Design, Construction, Inspection and Maintenance.* Report EM 7700-8. USDA Forest Service, 1990.
4. Taylor, R. J., and P. F. Csagoly. *Transverse Post-Tensioning of Longitudinally Laminated Timber Bridge Decks.* Ministry of Transportation and Communications, Downsview, Ontario, Canada, 1979.
5. Taylor, T. J., B. Batchelor, and K. Van Dalen. *Prestressed Wood Bridges.* Structural Research Report. SRR-83-01. Ministry of Transportation and Communications, Downsview, Ontario, Canada, 1983.
6. *Standard Specifications for Highway Bridges.* AASHTO, Washington, D.C., 1992.
7. Bahkt, B., and S. G. Pinjarkar. *Review of Dynamic Testing of Highway Bridges.* Structural Research Report SRR-89-01. Ministry of Transportation of Ontario, Downsview, Canada, 1989.
8. Foster, G. M., and L. T. Oehler. Vibration and Deflection of Rolled Beam and Plate-Girder Bridges. In *Highway Research Record 124*, HRB, National Research Council, Washington, D.C., 1956.

Crash-Tested Bridge Railings for Timber Bridges

Michael A. Ritter, *Forest Service, U.S. Department of Agriculture*
Ronald K. Faller, *University of Nebraska–Lincoln*
Sheila R. Duwadi, *Federal Highway Administration*

Bridge railing systems in the United States historically have been designed on the basis of static load criteria given in the AASHTO *Standard Specifications for Highway Bridges*. In the past decade, full-scale vehicle crash testing has been recognized as a more appropriate and reliable method of evaluating bridge railing acceptability. In 1989 AASHTO published *Guide Specifications for Bridge Railings*, which gives the recommendations and procedures to evaluate bridge railings by full-scale vehicle crash testing. In 1993 NCHRP published *Report 350: Recommended Procedures for the Safety Performance Evaluation of Highway Features*, which provides criteria for evaluating longitudinal barriers. From these specifications, a cooperative research program was initiated to develop and crash test several bridge railings for longitudinal wood decks. The research resulted in the successful development and testing of five bridge railing systems for longitudinally laminated wood bridge decks in accordance with the AASHTO Performance Level 1 and Performance Level 2 requirements and the Test Level 4 requirements of *NCHRP Report 350*.

The primary purpose of a bridge railing is to safely contain vehicles that cross the bridge. To meet this objective, railings must be designed to withstand the force of vehicle impact.

In designing railing systems for highway bridges, engineers traditionally have assumed that vehicle impact forces can be approximated by equivalent static loads that are applied to railing elements. Although railing loads are actually dynamic, the equivalent-static-load method has been used for many years as a simplified approach to standardized railing design. Currently, the AASHTO *Standard Specifications for Highway Bridges* (*1*) requires that rail posts be designed to resist an outward transverse static load of 44.5 kN (10,000 lb). A portion of this load is also applied to posts in the inward transverse, longitudinal, and vertical directions and to the rail elements. These requirements are identical for all bridges regardless of bridge geometry or traffic conditions. Thus, a railing for a single-lane bridge on a low-volume road must meet the same loading requirements as a railing for a bridge on a major highway.

Despite the widespread use of design requirements based primarily on static load criteria, the need for more appropriate criteria for full-scale vehicle crash tests has long been recognized. The first U.S. guidelines for full-scale vehicle crash testing were published in 1962 (*2*) in a one-page document that provided basic guidelines for the test vehicle mass, approach speed, and impact angle and provided a degree of uniformity to the traffic barrier research in progress at the time.

Through subsequent use of this document, the need for additional comprehensive guidelines became apparent, and several reports were published during the 1970s through NCHRP. In 1981 NCHRP released *NCHRP Report 230: Recommended Procedures for the Safety Performance Evaluation of Highway Appurtenances* (3). This comprehensive report has been the primary source of crash testing criteria for more than a decade and continues to serve as the basis for current bridge railing testing requirements.

Although crash test criteria have been available for many years, the requirement to implement crash testing as a means of evaluating bridge railings in the United States depended on the jurisdiction. Some states implemented extensive bridge railing crash testing programs, whereas others continued to use static load design exclusively. The first recognition of full-scale crash testing in a national bridge specification came in 1989, when AASHTO published the *Guide Specifications for Bridge Railings* (or AASHTO Guide Specifications) (4). This work presents recommendations for the development, testing, and use of crash-tested bridge railings and refers extensively to NCHRP 230 for crash testing procedures and requirements.

A primary concept of the AASHTO Guide Specifications is that bridge railing performance needs differ greatly from site to site and that railing designs and costs should match site needs. Thus, recommended requirements for railing testing are based on three performance levels: Performance Level 1 (PL-1), PL-2, and PL-3. The PL-1 requirements represent the weakest system, and the PL-3 the strongest system. The relationship between the railing performance level and requirements for a specific bridge depend on a number of factors, such as the type of roadway, design speed, average daily traffic, and percentage of trucks in the traffic mix. The recently published *NCHRP Report 350: Recommended Procedures for the Safety Performance Evaluation of Highway Features* (5) provides for six test levels to evaluate longitudinal barriers: Test Level 1 (TL-1) through TL-6. Although this document does not include objective criteria for relating a test level to a specific roadway type, the lower test levels generally are intended for use on roadways with lower service levels and certain types of work zones, whereas the higher test levels are intended for use on higher-service-level roadways. Most highways on which wood bridges are installed will require railings that meet either the AASHTO PL-1 or PL-2 requirements or the NCHRP 350 TL-1 through TL-4 requirements. A railing that meets either PL-3, TL-5, or TL-6 requirements currently has a very limited application for wood bridges because of the high traffic volume and speeds associated with these levels.

The AASHTO Guide Specifications are optional, and the use of static load design criteria is permitted. However, emphasis on the use of crash-tested railings for new federally funded projects has increased significantly the role of full-scale crash testing as a means of evaluating railing performance. It is anticipated that AASHTO will adopt the guide specifications in the future, making crash-tested railings mandatory for most bridges. FHWA has officially adopted *NCHRP Report 350* as a replacement for *NCHRP Report 230*. At this time, it is unclear if AASHTO will adopt the Report 350 criteria into its guide specifications or retain the current criteria based on Report 230.

As of August 1990, 25 bridge railings had been successfully crash tested in accordance with the requirements of the AASHTO Guide Specifications and approved for use on federal-aid projects by FHWA (6). Of these railings, 24 are for concrete bridge decks and 1 is for a wood deck. For wood bridges to compete with other bridges in the future, a range of crash-tested bridge railings for different wood bridge types will be required. Because of this need, national emphasis was placed on developing a limited number of crash-tested railings for wood bridges.

Objective and Scope

To meet the need for crashworthy railings for wood bridges, the Forest Products Laboratory, USDA Forest Service, in cooperation with the Midwest Roadside Safety Facility of the University of Nebraska at Lincoln, FHWA, and the wood products industry, initiated a program to develop crash-tested bridge railings for longitudinal wood decks. The program objectives were to develop five crashworthy railings: three to meet AASHTO PL-1, one to meet AASHTO PL-2, and one to meet *NCHRP Report 350* TL-4. The scope of the project was limited to railings for longitudinal wood decks, 252 mm (10 in.) or greater in thickness, and constructed of glued-laminated (glulam) timber, spike-laminated lumber, or stress-laminated lumber. In each system, the lumber laminations are placed edgewise and oriented with the lumber length parallel to the direction of traffic. A brief description of each longitudinal deck bridge type is provided in *Timber Bridges: Design, Construction, Inspection, and Maintenance* (7).

Longitudinal glulam timber decks are constructed of panels that consist of individual lumber laminations glued together with waterproof structural adhesives. The panels are 1.07 to 1.38 m (3.5 to 4.5 ft) wide and effectively function as a large, solid block of wood. To form the bridge deck, panels are placed side by side and interconnected by transverse distributor beams bolted to the deck underside at intervals of 2.4 m (8 ft) or less. These distributor beams are designed to transfer vertical

loads between adjacent panels. They are not designed to resist lateral loads.

Spike-laminated decks are constructed of sawn lumber laminations 102 mm (4 in.) in nominal thickness. The individual laminations are interconnected with spikes that are typically 8 or 9.5 mm (5/16 or 3/8 in.) in diameter and 356 to 406 mm (14 to 16 in.) long. The decks are commonly manufactured in panels that are 1.5 to 2.1 m (5 to 7 ft) wide and interconnected with transverse distributor beams in a manner similar to longitudinal glulam timber decks.

Stress-laminated decks are constructed of sawn lumber laminations that are typically 51 to 102 mm (2 to 4 in.) in nominal thickness. The laminations are stressed together with high-strength steel bars that are placed in holes drilled through the center of the wide faces of the laminations. When tensioned, the bars create compression between the laminations, and the entire deck effectively acts as a solid, orthotropic wood plate.

Test Requirements and Evaluation Criteria

Test requirements and evaluation criteria for this project followed procedures defined in the AASHTO Guide Specifications (including applicable references to *NCHRP Report 230*) and the *NCHRP Report 350* criteria. These procedures establish a uniform methodology for testing and evaluating railings so that the safety performance of different railing designs, tested and evaluated by different agencies, can be compared. It is impractical and impossible to test all railings for all possible vehicle and impact conditions. Therefore, the procedures specify a limited number of tests using severe vehicle impact conditions and a set of criteria against which test results may be evaluated.

Test Requirements

Vehicle impact requirements for railing crash testing depend on the railing performance or test level and are specified as requirements for vehicle type and weight, impact speed, and impact angle relative to the longitudinal railing axis. Testing for PL-1 requires two vehicle impact tests, and testing for PL-2 and TL-4 requires three vehicle impact tests. A summary of the requirements for PL-1, PL-2, and TL-4 is given in Table 1. In some cases, all tests for a given level may not be required if a railing with similar geometry and strength was tested previously and found to be satisfactory.

In addition to vehicle impact requirements, the AASHTO Guide Specifications and the *NCHRP Report 350* criteria also specify requirements for data acquisition and construction of the bridge railings. Requirements for data acquisition are referenced to Reports 230 and 350 and include specific data collection parameters and techniques that must be completed before, during, and after the crash test. Construction requirements specify that the bridge railing be designed, constructed, erected, and tested in a manner representative of actual installations. To assess properly the performance of most bridge railings, they must also be evaluated as a system in combination with the bridge superstructure for which it is intended. This is very important for railings for wood bridges, because the attachment of the railing to the bridge deck and the ability of the wood superstructure to resist applied railing loads may often be the controlling parameters.

Evaluation Criteria

Evaluation criteria for full-scale crash testing are based on three appraisal areas: structural adequacy, occupant risk, and vehicle trajectory after the collision. Criteria for structural adequacy are intended to evaluate the ability of the railing to contain, redirect, or permit controlled vehicle penetration in a predictable manner. Occupant risk evaluates the degree of hazard to occupants of the impacting vehicle. Vehicle trajectory after the collision is concerned with the path and final position of the impacting vehicle and the probable involvement of the impacting vehicle with other traffic. Note that these criteria address only the safety and dynamic performance of the railing and do not include service criteria such as aesthetics, economics, bridge damage, or post-impact maintenance requirements. The following evaluation criteria are summarized from the AASHTO Guide Specifications for PL-1 and PL-2 testing (similar evaluation criteria are provided in *NCHRP Report 350*):

1. The railing shall contain the vehicle; neither the vehicle nor its cargo shall penetrate or go over the installation. Controlled lateral deflection of the railing is acceptable.
2. Detached elements, fragments, or other debris from the railing shall not penetrate or show potential for penetrating the passenger compartment or present undue hazard to other traffic.
3. Integrity of the passenger compartment must be maintained with no intrusion and essentially no deformation.
4. The vehicle shall remain upright during and after collision.
5. The railing shall smoothly redirect the vehicle. A redirection is deemed smooth if the rear of the vehicle does not yaw more than 5 degrees away from the railing

from time of impact until the vehicle separates from the railing.

6. The smoothness of the vehicle-railing interaction is further assessed by the effective coefficient of friction μ, where $\mu = 0.0-0.25$ is good, $\mu = 0.26-0.35$ is fair, and $\mu \geq 0.36$ is marginal. Requirements for computing μ are given in the AASHTO Guide Specifications.

7. The impact velocity of a hypothetical front-seat passenger against the vehicle interior, calculated from vehicle accelerations and 610-mm (2-ft) longitudinal and 305-mm (1-ft) lateral displacements, shall be less than 9.15 m/sec (30 ft/sec) in the longitudinal direction and 7.63 m/sec (25 ft/sec) in the lateral direction. In addition, the highest 10-msec average vehicle accelerations subsequent to the instant of hypothetical passenger impact should be less than 147 m/sec^2 (483 ft/sec^2) in the longitudinal and lateral directions.

8. Vehicle exit angle from the barrier shall not be more than 12 degrees. Within 30.5 m (100 ft) plus the length of the test vehicle from the point of initial impact with the railing, the railing side of the vehicle shall move no more than 6.1 m (20 ft) from the line of the traffic face of the railing.

Development Phase

Using a fundamental understanding of the performance characteristics of each deck type, development work was initiated to formulate a methodology for the railing tests. Because of economics and time, it was considered impractical to develop and test different railing systems for each longitudinal deck type. Instead, a more feasible approach was undertaken to develop several railing systems that could be adapted to each of the three longitudinal deck types, without modifications that would result in reduced performance. To accomplish this, it was determined that railing development and testing should use the weakest deck type. This decision was based on the premise that if successful tests could be completed on the weakest deck, the railing could be adapted to stronger decks without hurting performance.

In assessing the potential resistance of each deck type to transverse railing impact forces, the strength of the wood and mechanical reinforcement was considered. Of primary concern was loading that could introduce tension perpendicular to grain stress in the wood deck.

Of the three deck types, the stress-laminated deck was considered the strongest for transverse railing loads, because the high-strength steel bars are continuous across the deck width. Loads developed at vehicle impact can be effectively distributed across the deck by the bars, making the entire deck width effective in resisting the applied loads.

The spike-laminated deck was considered to be of intermediate strength. If railing loads are applied transverse to the panel length, the loads are resisted by the spikes in withdrawal. Because of this, tension perpendicular to grain in the lumber laminations is not a concern; however, the spikes could be pulled from the deck, resulting in longitudinal separations between the laminations, and additional reinforcement would be required.

The glulam timber deck was considered to be the weakest in resisting railing loads, because the glulam timber panels act as solid pieces of wood, and loads applied transverse to the panel length are most likely to introduce tension perpendicular to grain and failure in the upper panel section. Mechanical reinforcement was considered necessary for longitudinal glulam timber

TABLE 1 Vehicle Impact Requirements for PL-1, PL-2, and TL-4 Bridge Railings

AASHTO Performance Level (4)	Impact Conditions		
	Small Car (816 kg)	Pickup Truck (2,449 kg)	Medium Single-Unit Truck (8,165 kg)
1	80.5 km/h 20 deg	72.4 km/h 20 deg	
2	96.6 km/h 20 deg	96.6 km/h 20 deg	80.5 km/h 15 deg
NCHRP 350 Test Level (5)	**Impact Conditions**		
	Small Car (820 kg)	Pickup Truck (2,000 kg)	Single-Unit Van Truck (8,000 kg)
4	100 km/h 20 deg	100 km/h 25 deg	80 km/h 15 deg

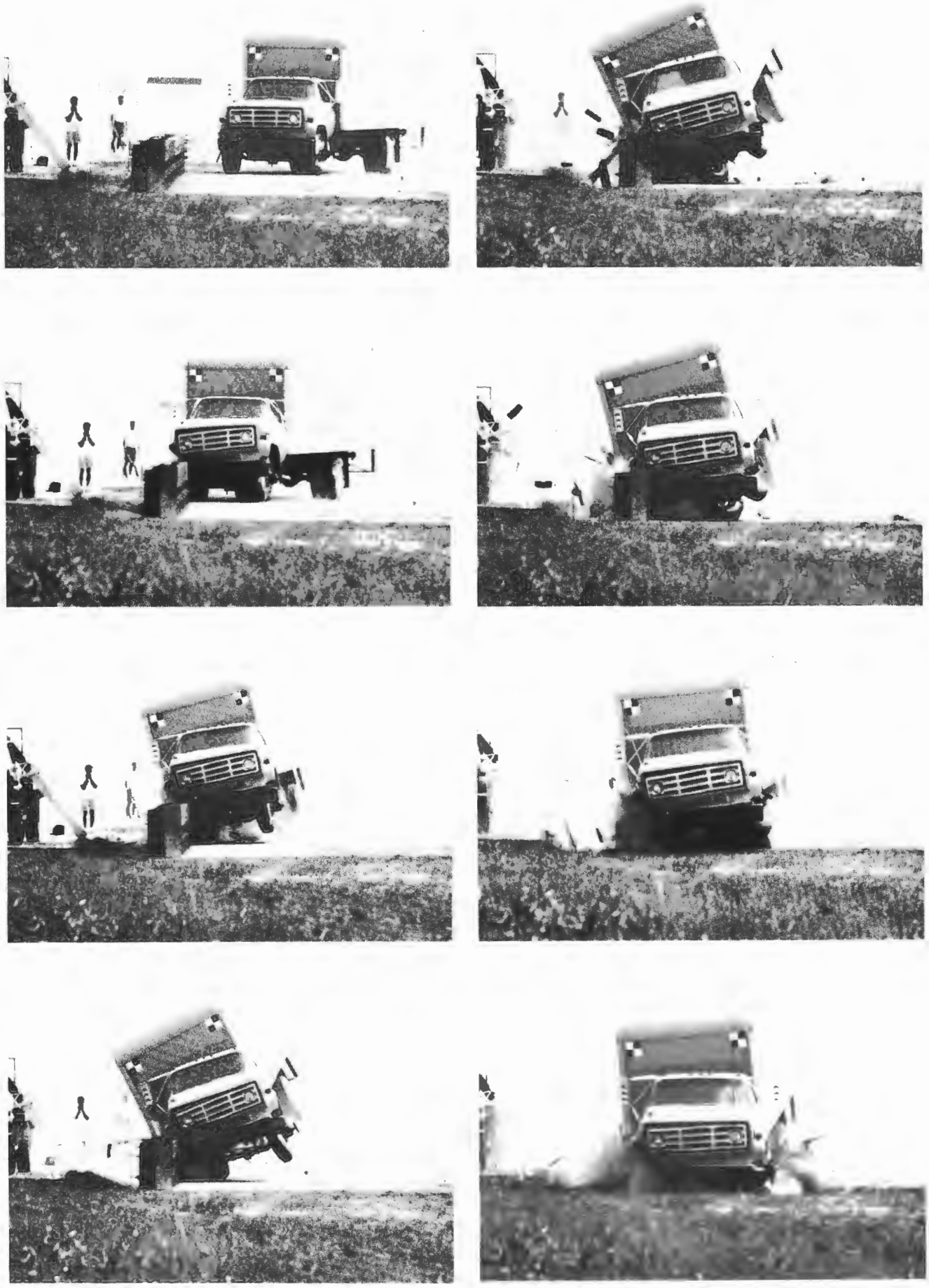

FIGURE 1 Crash-test sequence for 8172-kg (18,000-lb) truck traveling at 80.5 km/hr (50 mph), hitting railing at 15-degree angle to longitudinal railing axis.

decks to resist railing loads without damage. Thus, the glulam timber deck was considered the weakest deck for transverse railing loads and was selected for full-scale crash testing. If bridge railings performed acceptably on the glulam timber system, it was rationalized that the railings could be adapted to the other longitudinal wood bridge decks with no reduction in railing performance.

The primary emphasis of the railing design process was to develop railings that would meet the requirements for the AASHTO Guide Specifications and *NCHRP Report 350*. In addition, it was determined that consideration be given to (a) the extent of probable damage to the structure after vehicle impact and the difficulty and cost of required repairs; (b) adaptability of the railing to different wood deck types; (c) cost of the railing system to the user, including material, fabrication, and construction; (d) ease of railing construction and maintenance; and (e) aesthetics.

The conclusion of the development phase involved the design of several railing systems and preparation of plans and specifications for testing. The selection and design of these final systems were based on a review of other railings that had been crash tested successfully, as well as those that are used on wood bridges but had not been crash tested. To the extent possible, feasible designs were evaluated using computer simulation models. Although several proven computer models were used, it was difficult to adapt the programs for wood components because the behavior and properties of the wood systems at ultimate loading were unknown. Data collected during the crash testing were used to refine input parameters and more accurately predict railing performance in subsequent tests.

Test Methodology

Testing of all bridge railings was completed at the Midwest Roadside Safety Facility in Lincoln, Nebraska. The site is located at an airport and was formerly a taxiway and parking area for military aircraft. It includes approximately 11 ha (27 acres) of concrete pavement and 1.6 ha (4 acres) of soil surface. To complete railing testing, a test bridge was constructed that measured approximately 2.4 m (8 ft) wide and 28.6 m (93.75 ft) long, in five simply supported spans measuring 5.72 m (18.75 ft) each. The deck was constructed of glulam timber panels 273 mm (10.75 in.) thick and 1.2 m (4 ft) wide. The glulam timber for the deck was Combination 2 Douglas fir given in the AASHTO *Standard Specifications for Highway Bridges* (*1*) and was treated with pentachlorophenol in heavy oil in accordance with American Wood Preservers' Association (AWPA) Standard C14 (*8*). Two glulam timber panels were placed side by side to achieve the 2.4-m (8-ft) width, and transverse distributor beams were attached to the deck underside per AASHTO requirements (*1*). The test bridge was supported by concrete footings that were placed in excavations so that the top of the test bridge was level with the concrete surface at the site.

FIGURE 2 Bridge railings successfully crash tested to AASHTO PL-1 (photographs taken before testing).

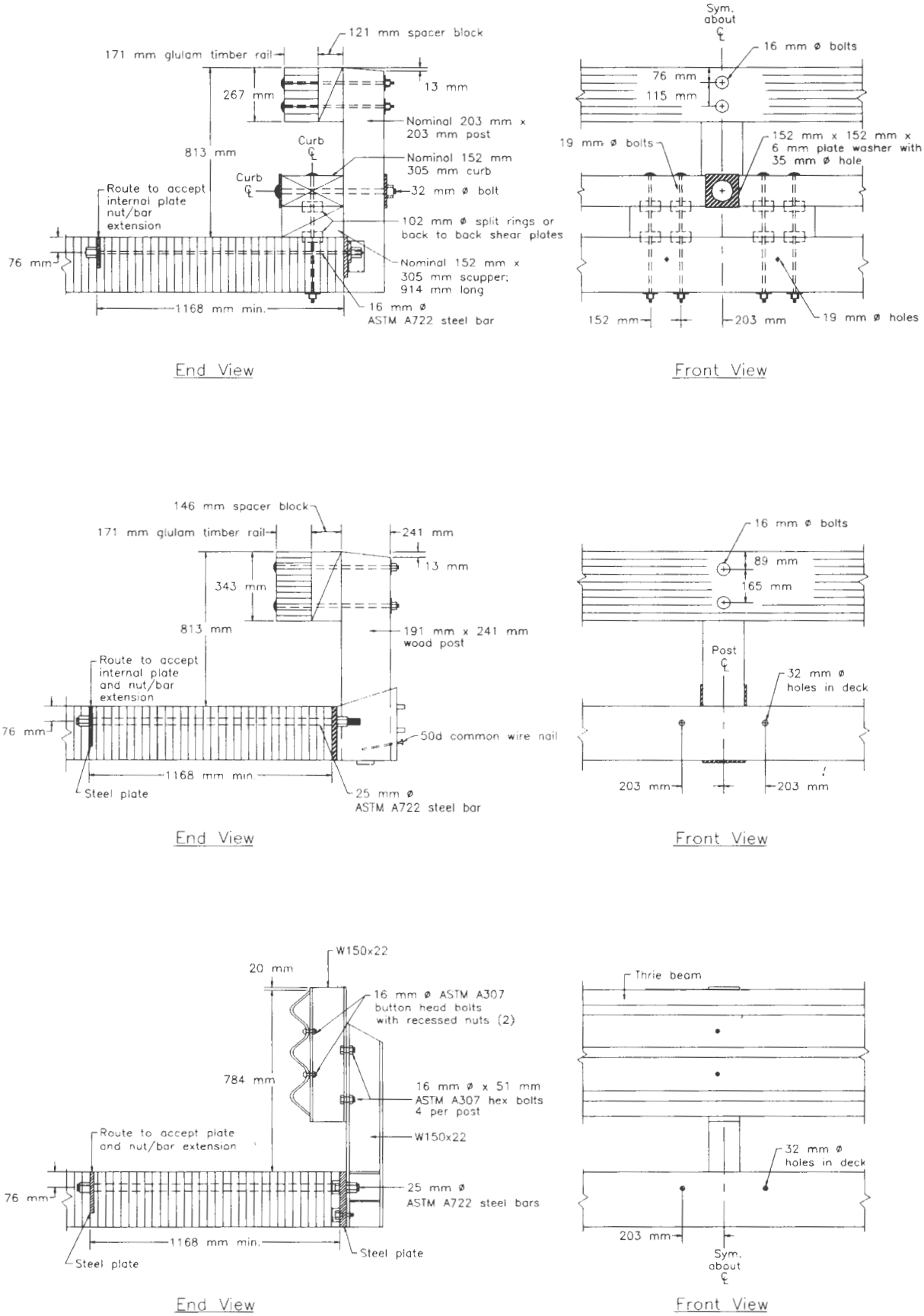

FIGURE 3 Drawings of bridge railings successfully crash tested to AASHTO PL-1: *top*, glulam timber rail with curb; *middle*, glulam timber rail without curb; *bottom*, steel rail.

Vehicle propulsion and guidance were provided by steel cable configurations. For propulsion, a reverse cable tow with a 1:2 mechanical advantage was used. A cable was attached to the front of the vehicle, routed through a series of pulleys, and connected to a tow vehicle that traveled in a direction opposite to the test vehicle. The unoccupied test vehicle was then pulled by the tow vehicle and released from the tow cable approximately 9.2 m (30 ft) before impact. A vehicle guidance system developed by Hinch was used to steer the test vehicle (*9*). Using this system, the left front wheel hub is attached to a tensioned steel cable that maintains the vehicle's direction along a designated straight path. Approximately 9.2 m (30 ft) from impact, the guidance connection is sheared off and the vehicle separates from the guidance cable. A crash-test sequence for an 8172-kg (18,000-lb) vehicle is shown in Figure 1.

Data acquisition parameters and techniques for the crash testing program were based on requirements of the AASHTO Guide Specifications and *NCHRP Report 350* and followed three testing phases: pretest, test, and posttest. In the pretest phase, the as-built bridge railing and vehicle were documented using photography and drawings that indicated the applicable configuration, dimensions, and vehicle weight. During the test phase, data on the vehicle impact speed, impact angle, trajectory, and accelerations were collected primarily through the use of high-speed motion picture photography and accelerometers mounted on the vehicle. In the posttest phase, the condition of the railing, bridge superstructure, and vehicle were documented using photography and standardized damage assessment methods, including the traffic accident data scale (*10*) and vehicle damage index (*11*). Additional instrumentation was placed

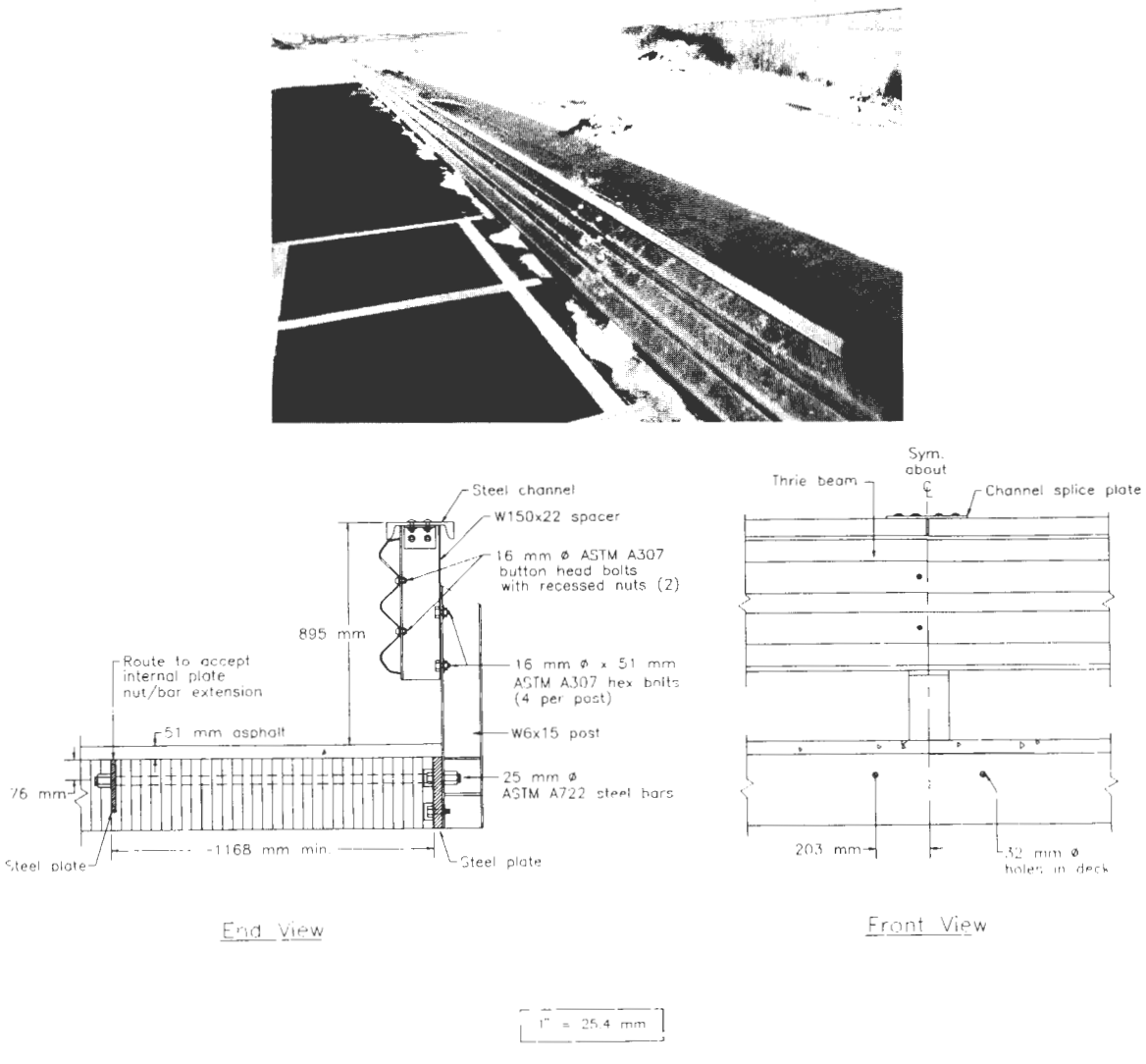

FIGURE 4 Steel thrie beam bridge railing successfully crash tested to AASHTO PL-2 (photograph taken before testing).

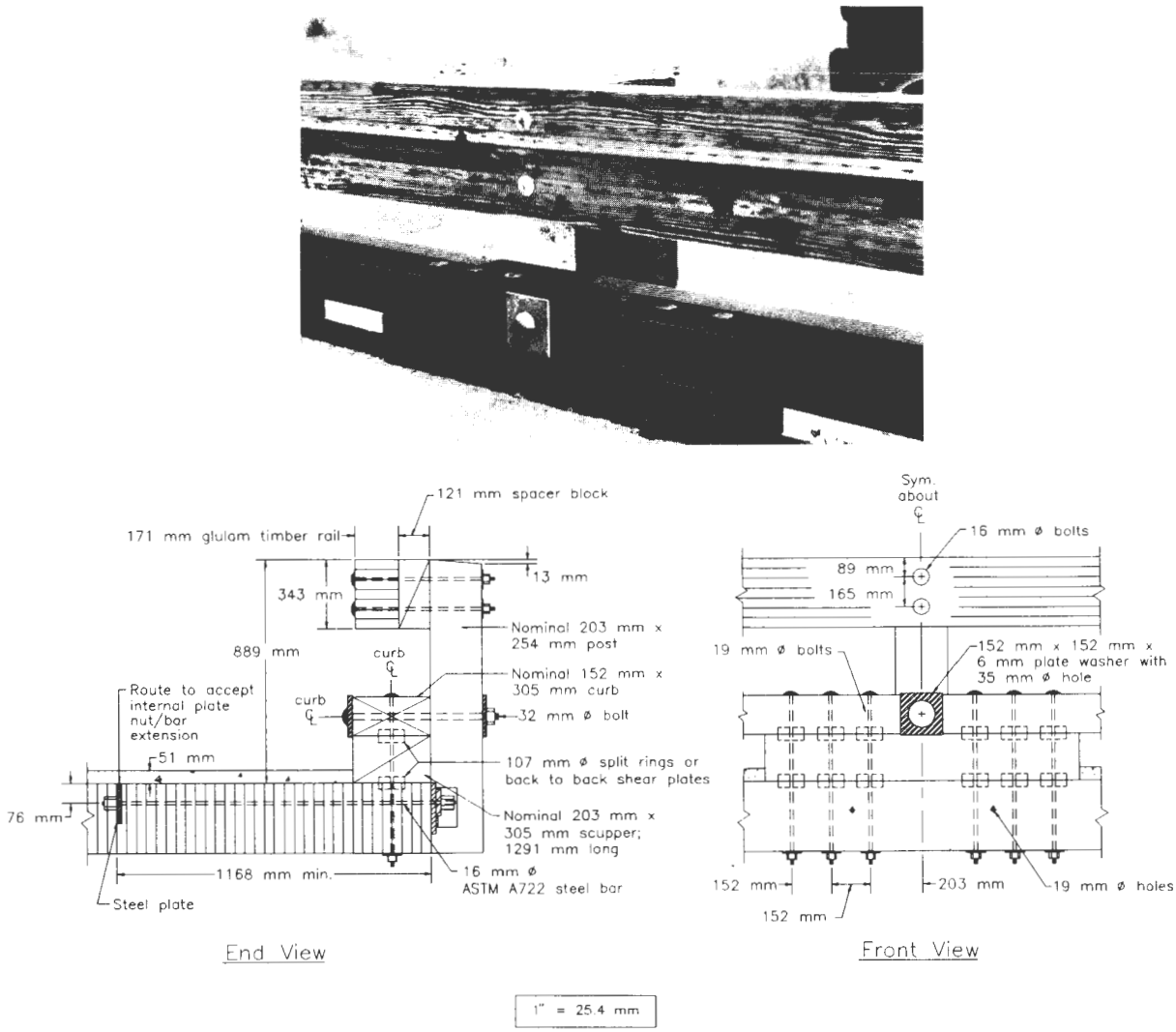

FIGURE 5 Glulam timber bridge railing successfully crash tested to *NCHRP Report 350* TL-4 (photograph taken before testing).

on some railings to assess vehicle impact forces transmitted to the bridge railing and superstructure.

Results and Discussion

As a result of the development and testing program, five bridge railings were successfully developed and tested for longitudinal wood decks. Three of these railings were tested at PL-1, one was tested at PL-2, and one was tested at TL-4. Each railing was tested on the glulam timber deck and is adaptable to the spike-laminated and stress-laminated decks. All designs used posts spaced 1.9 m (6.25 ft) on center and high-strength steel bars through a portion of the bridge deck to act as reinforcement in distributing railing loads without damage to the bridge. Glulam timber for the rail members was Combination 2 Douglas fir as given in the AASHTO *Standard Specifications for Highway Bridges* (*1*), treated with pentachlorophenol in heavy oil to AWPA C14 requirements (*8*). Sawn lumber for posts, curbs, scuppers, and spacer blocks was No. 1 Douglas fir (*1*), treated with creosote to AWPA C14 requirements (*8*).

A detailed discussion of the testing and results for each railing system is beyond the scope of this paper but is presented in detail in previous publications (*12*,*13*). Overall, no damage to the test bridge was evident from any of the vehicle impact tests. For the railing systems with glulam timber rails, damage to the railing was primarily gouging and scraping resulting from the vehicle impact. All glulam timber railing remained

intact and serviceable after the tests, and replacement of the railing was not considered necessary. For the steel thrie beam railings, there was permanent deformation in the rail and post in the vicinity of the impact location. This would necessitate replacement of specific railing and post members, but damage was relatively minor considering the severity of the impact. A brief description of each railing design follows.

PL-1 Railings

The three tested PL-1 railings included a glulam timber railing with curb, a glulam timber railing without curb, and a steel thrie beam railing. Photographs and drawings of the PL-1 railings are shown in Figures 2 and 3, respectively.

The glulam timber railing with curb consisted of a single glulam timber railing mounted on a sawn lumber post. The post was connected with a single bolt to a lumber curb that was supported by scupper blocks. The curb and scupper blocks were connected to the bridge deck with bolts and timber connectors.

The glulam timber railing without curb consisted of a single glulam timber railing mounted on a sawn lumber post. The lower portion of the post was placed in a steel box that was attached to the bridge deck with high strength steel bars.

The steel railing consisted of a 10-gauge steel thrie beam railing mounted to a steel, wide flange post. The lower end of the post was bolted to a steel plate that was connected to the bridge deck with high-strength steel bars.

PL-2 Railing

The one PL-2 railing included a steel thrie beam railing, as shown in Figure 4. The steel railing was a modified version of that tested at PL-1. Minor changes in the railing geometry and the addition of a steel channel section above the rail element were necessary to resist the increased loads at PL-2.

TL-4 Railing

The one TL-4 railing included a glulam timber railing with curb, as shown in Figure 5. The railing consisted of a single glulam timber railing mounted on a sawn lumber post and was a modification of the curb system tested at PL-1. Because of the greater loads at TL-4, railing and post sizes were increased, as were bolts and timber connectors attaching the curb and scupper to the bridge deck.

Concluding Remarks

This program clearly demonstrates that crashworthy railing systems are feasible for longitudinal wood decks. Even at high-impact conditions required by AASHTO PL-2 and *NCHRP Report 350* TL-4, the railing systems performed well with no significant damage to the bridge superstructure. The development of crashworthy railing systems has overcome a significant barrier to the use of longitudinal deck wood bridges.

References

1. *Standard Specifications for Highway Bridges.* AASHTO, Washington, D.C., 1989.
2. *Full-Scale Testing Procedures for Guardrails and Guide Posts.* Highway Research Circular 482. HRB, National Research Council, Washington, D.C., 1962.
3. *NCHRP Report 230: Recommended Procedures for the Safety Performance Evaluation of Highway Appurtenances.* TRB, National Research Council, Washington, D.C., 1981.
4. *Guide Specifications for Bridge Railings.* AASHTO, Washington, D.C., 1989.
5. Ross, H. E., Jr., D. L. Sicking, R. A. Zimmer, and J. D. Michie. *NCHRP Report 350: Recommended Procedures for the Safety Performance Evaluation of Highway Features.* TRB, National Research Council, Washington, D.C., 1993.
6. *Memorandum on Crash Tested Bridge Railings.* File Designation HNG-14. FHWA, U.S. Department of Transportation, Aug. 13, 1990.
7. Ritter, M. A. *Timber Bridges: Design, Construction, Inspection, and Maintenance.* Report EM-7700-8. USDA Forest Service, DC, 1990.
8. *Book of Standards.* American Wood Preservers' Association, Woodstock, Md., 1992.
9. Hinch, J., T. L. Yang, and R. Owings. *Guidance Systems for Vehicle Testings.* ENSCO, Inc., Springfield, Va., 1986.
10. *Vehicle Damage Scale for Traffic Accident Investigators.* Traffic Accident Data Project Technical Bulletin 1. National Safety Council, Chicago, Il., 1971.
11. Collision Deformation Classification; Recommended Practice J224. In *SAE Handbook*, Vol. 4, Society of Automotive Engineers, Warrendale, Pa., 1985.
12. Faller, R. K., M. A. Ritter, J. C. Holloway, B. G. Pfeifer, and B. T. Rossen. Performance Level 1 Bridge Railings for Timber Decks. In *Transportation Research Record 1419*, TRB, National Research Council, Washington, D.C., 1993.
13. Rosson, B. T., R. K. Faller, and M. A. Ritter. *Performance Level 2 and Test Level 4 Bridge Railings for Timber Decks.* In *Transportation Research Record*, TRB, National Research Council, Washington, D.C., to be published.

Steering Committee Biographical Information

David B. Beal, *Chairman,* received bachelor's and master's degrees from the University of Connecticut. He is currently supervisor of the Construction Services Section in the Structures Design and Construction Division of the New York State Department of Transportation. In this position he is responsible for all issues relating to the fabrication and construction of bridges. Before this assignment he was head of the Structural Research Group for the Department, which has the responsibility for performance of laboratory and field tests on steel and concrete bridges, concrete bridge decks, and corrugated metal culverts. He has authored and coauthored numerous reports and other publications on these subjects. Mr. Beal was Adjunct Assistant Professor of Civil Engineering at Union College in Schenectady, N.Y., from 1979 to 1987. He was chairman of the project panels for the NCHRP research on thermal effects in concrete bridges and nondestructive load testing for bridge evaluation and testing and has been a panel member on several other studies. Mr. Beal was Chairman of the TRB Committee on Dynamics and Field Testing of Bridges and is currently Chairman of the Structures Section.

Craig A. Ballinger is a professional consulting engineer specializing in structural engineering and research; bridge inspection, maintenance, strength evaluation, repair and strengthening, and management; and the structural behavior of epoxy-coated reinforcing and prestressing, adhesives, and other new materials. He holds a B.S. from the University of Michigan and an M.S. from the University of Washington. After working with Wilbur Smith Associates and the Federal Highway Administration, he established Craig Ballinger & Associates. He is a member of the American Concrete Institute, American Society of Civil Engineers, and International (FIP) Committee on Prestressed Concrete. He is currently Chairman of the TRB Committee on Structural Fiber Reinforced Plastics.

Protasio Ferreira e Castro is currently Professor of Construction Technology at Fluminense Federal University in Rio de Janeiro, Brazil. He received a degree in civil engineering from the Rio de Janeiro Federal University, an M.Sc. from Fluminense Federal University, and a Ph.D. from the University of London. Dr. Castro has served as Member Counselor of the Conselho Regional de Engenharia e Arquitetura (Engineers and Architects Regional Council), Member Counselor of the Instituto Brasileiro do Concreto, and President of the COPMAT (Building Materials Professors Committee). His expertise is in structural design of bridges and road pavements. He has carried out load tests and developed quality control programs for concrete structures. As a former member of the Brazilian Federal Highway Department, he was in charge of the Road Research Center of the Road Research Institute, and he also headed CONSULTOP (Consulting Engineers for Constructions and Designs). In 1988 Dr. Castro received the Gilberto Molinari Award of IBRACON (Brazilian Concrete Institute) and the Pontes Correa Award of ABPv (Brazilian Paving Association).

Thomas J. Collins is the President of Collins Engineers, Inc. He received a bachelor's degree in civil engineering from Marquette University and a Master of Business Administration from the University of Connecticut. He is a licensed professional engineer and structural engineer in a number of states, a certified inshore hydrographer, and a diver with more than 20 years' experience in the inspection, evaluation, and design of highway and railroad bridges and waterfront structures. He coauthored the Federal Highway Administration manual *Underwater Inspection of Bridges* and is currently principal investigator for FHWA Demonstration Project 97, Bridge Integrity. He is a member of the American Society of Civil Engineers' task committee on underwater inspection of structures and the American Railway Engineering Association's Committee 15—Steel Structures and Chairman of the TRB Subcommittee on Inspection and Maintenance of Underwater Components of Structures.

Bruce M. Douglas is Professor and Director at the Center for Civil Engineering Earthquake Research of the University of Nevada at Reno. Since obtaining his B.S. from the University of Santa Clara and his M.S. and Ph.D. from the University of Arizona, he has been lecturer, Assistant Professor, Research Associate and then Associate Director of the Seismological Laboratory, and Chairman of the Department of Civil Engineering at the University of Nevada. He has held positions with several structural engineering firms and with the State of California Bridge Department. Dr. Douglas is a member

of the American Society of Civil Engineers, Seismological Society of America, American Society for Engineering Education, Earthquake Engineering Research Institute, New Zealand Society for Earthquake Engineering, International Association for Bridge and Structural Engineering, and the TRB Committees on Concrete Bridges and Construction of Bridges and Structures. He chairs the TRB Task Force on Seismic Design of Bridges.

Donald J. Flemming, State Bridge Engineer for the Minnesota Department of Transportation (Mn/DOT), graduated from the University of Minnesota. During his 34 years in bridge design and construction with Mn/DOT, Mr. Flemming has held numerous positions, including Assistant District Engineer, State Bridge Construction and Maintenance Engineer, and Bridge Standards Engineer. Memberships held by Mr. Flemming include the American Society of Civil Engineers, the Minnesota Society of Professional Engineers, and the Surveyors and Engineers Society. Mr. Flemming serves as Chairman for the AASHTO Timber Bridge Committee, the AASHTO Culvert Committee, and the TRB Committee on General Structures. He is a member of the AASHTO Loads and Load Distribution Committee, the AASHTO Welding Committee, and the TRB Committee on Steel Structures.

Robert J. Heywood is a Principal Researcher in the Physical Infrastructure Centre, School of Civil Engineering, Queensland University of Technology, Australia. His research interests center around improving the efficiency of Australian transport by considering bridges and vehicles as interrelated elements in the transport system. He graduated from the University of Queensland in 1974 and undertook his master's and Ph.D. study part-time at the same university. He joined Queensland University of Technology in 1985 after a decade of consulting experience in Australia and overseas. He has held a visiting appointment at the University of Michigan and is a member of the Dynamic Interaction between Vehicles and Infrastructure Experiment (DIVINE) of the Organization for Economic Cooperation and Development and the TRB Committee on Dynamics and Field Testing of Bridges.

Robert N. Kamp is a part-time consulting engineer in Albany, New York. He received his bachelor's degree from Syracuse University, where he is now a member of the College of Engineering Advisory Board. Mr. Kamp worked for the New York State Department of Transportation and its predecessor, the Department of Public Works, in the Syracuse and Rochester areas and in the main office at Albany. His work included the field-office design and construction of highways and the main-office direction of the operation and maintenance of the New York State Barge Canal System. He completed his departmental career with 13 years as Assistant Director of Structures Design and Construction. After retiring he managed the Albany office of Wilbur Smith Associates for three years and worked four more years for the firm in marketing and special projects. Since that time he has marketed bridge-related specialty products and been involved in the development and teaching of a training course for bridge engineers. Mr. Kamp has chaired the TRB Committees on Fabrication and Inspection of Metal Structures and Structures Maintenance and Management and has been a member of several other committees during the past 25 years. He has been a member of the Steering Committee for each of the previous three Bridge Engineering Conferences and has served on a number of NCHRP panels. He is a Fellow of the American Society of Civil Engineers and a member of the American Concrete Institute, the Consulting Engineers Council of New York State, the Society of Military Engineers, the Association for Bridge Design and Construction, the Eastern New York Technical Council, the Albany Society of Engineers, the Precast Concrete Association of New York, the Technology Club of Syracuse, and the Highway Users Federation, and currently serves as president of the New York State Society of Professional Engineers.

Ramankutty Kannankutty is Director of Engineering Design of the Minneapolis Department of Public Works. After obtaining his B.S. from Madras University and an M.S. in concrete technology from the Indian Institute of Science, he left India and obtained an M.S. in structural engineering from South Dakota School of Mines and Technology and a graduate certificate in public administration from the University of Southern California. His professional engineering and project management experience has been in the areas of street and bridge design, bridge inspection and construction, transportation planning and programming, citizen participation, and financial management of state and Federal Highway Administration funded projects. Mr. Kannankutty has received several awards for public works and bridge projects in Minneapolis. He has published papers on structural engineering, public policy, and automation. He is a member of the American Public Works Administration; City Engineers' Association of Minnesota; Minnesota State Aid Screening Committee; and Financial Advisory Board, City of New Brighton; former member of the TRB Committee on Dynamics and Field Testing of Bridges; and chairs the TRB Committee on Construction of Bridges and Structures.

Chitoshi Miki is Professor of Civil Engineering at the Tokyo Institute of Technology, Japan. He received his bachelor's and master's degrees and Ph.D. from the In-

stitute and except for 1979 to 1982, when he was Associate Professor at the University of Tokyo, and 1984, when he was Visiting Researcher at Lehigh University, he has been associated with the Institute since 1972. His research fields are fatigue and fracture control of steel structures, application of fracture mechanics, maintenance technology of bridges, and bridge design. Dr. Miki's international activities include member of the International Institute of Welding Commission 13 (fatigue) and Chairman of the Joint Intelligence Collecting Agency Chile Bridge Rehabilitation. He is a member of the Japan Society of Civil Engineering; Welding, Material Science, Steel Construction, Testing and Materials; and the International Association for Bridge and Structural Engineering.

A. P. Moser is Acting Dean of Engineering at Utah State University. He received a B.S. and M.S. from Utah State University and a Ph.D. from the University of Colorado. Dr. Moser has had extensive experience in both industry and academia. He received two patents and was given special recognition for his work with national standards organizations. In addition to major contributions to the field of research on buried structures and composite materials, he organized and directed a short course at Utah State University titled Piping Systems Institute and received a special award from the University Extension for his pioneering work with industry in developing this course. He is a world authority on the structural response and properties of pipes made from composite and plastic materials. He serves on the TRB Committees on Culverts and Hydraulic Structures and on Corrosion. He has published widely, including a book, *Buried Pipe Design*, published by McGraw-Hill.

Andrzej S. Nowak has been a Professor in the Department of Civil and Environmental Engineering at the University of Michigan since 1979. He received his M.S. and Ph.D. from Warsaw University of Technology in Poland. His major research interests include structural reliability and bridge structures. He was actively involved in the development of the Load and Resistance Factor Design (LRFD) code for bridges developed by AASHTO (NCHRP Project 12–33). Professor Nowak has received research grants from federal and state agencies including the National Science Foundation, Federal Highway Administration, U.S. Department of Transportation, National Academy of Sciences, Michigan Department of Transportation, and the Scientific Affairs Division of the North Atlantic Treaty Organization. He has chaired 15 doctoral committees and published more than 180 papers in journals and conference proceedings. An active member of several national and international professional organizations, he chairs the TRB Committee on Dynamics and Field Testing of Bridges, ACI Committee 348 (Safety of Structures), and ASCE Committee on Safety of Buildings.

Wojciech Radomski is Director of the Institute of Roads and Bridges at Warsaw University of Technology and bridge consultant in the Warsaw Management of Public Roads. His academic degrees are from Warsaw University of Technology, where he also served as assistant, lecturer, Associate Professor, and Professor. Professor Radomski has been on the faculty at Kanazawa University, Japan, and has been a bridge consultant in several design offices in Warsaw. He is a member of the Association of Polish Engineers and Technicians of Transport; the Polish Academy of Sciences and Polish Society of Bridge Engineers; and the Editorial Board of *Cement and Concrete Composites*, and is Editor-in-Chief of *Archives of Civil Engineering* of the Polish Academy of Sciences. His Ph.D. thesis won a prize given by the Polish Ministry of Science; he has also been awarded a prize for a book entitled *Fundamentals of Bridge Structures*, by the Warsaw University of Technology for science activity, and by the Association of Polish Engineers and Technicians of Transport. He has authored or coauthored numerous papers published in Polish and in English in Poland and abroad.

James E. Roberts is Director, Engineering Service Center, and Chief Structural Engineer (State Bridge Engineer) with the California Department of Transportation (Caltrans). He received a B.S. in civil engineering from the University of California at Berkeley and an M.S. in structural engineering from the University of Southern California. He has been with Caltrans for 42 years and has had a wide range of experience in many areas of both engineering and administration with a major emphasis in structures. A Fellow of the American Society of Civil Engineers, Structural Engineers Association of Central California, Professional Engineers in California Government, Sacramento Engineers Club, American Concrete Institute, American Welding Society, National Society of Professional Engineers, Society of American Military Engineers, Modern Transit Society, Engineering Council of Sacramento Valley, American Association of State Highway and Transportation Officials, American Segmental Bridge Institute, and Rotary International, he has been the recipient of 10 professional awards.

Charles W. Roeder is Professor of Civil Engineering at the University of Washington at Seattle, having served in various posts at the University since 1977. He received a B.S. from the University of Colorado at Boulder, an M.S. from the University of Illinois at Urbana, and a Ph.D. from the University of California at Berkeley. His research areas include seismic behavior of

mixed steel and reinforced concrete structures, lateral stability of partially restrained beams, temperature effects on structures, and the behavior of composite connections. Dr. Roeder has received awards and honors from the University of Colorado, the University of Illinois, the 1977 James F. Lincoln Design Competition Award, the J. James R. Croes Medal and the Raymond C. Reese Research Prize from ASCE, and the 1986 Special Commendation Award from ACI. He is a member of the American Society of Civil Engineers, the American Institute of Steel Construction, the Earthquake Engineering Research Institute, the American Welding Society, and the ASCE Committee on Composite Construction and Technical Administrative Committee on Metals. He is Chairman of the TRB Committee on Steel Bridges and a member of the National Research Council Steering Committee for the Second World Congress on Joint Sealing and Bearing Systems.

Arunprakash M. Shirole is Director of the Structures Design and Construction Division and Deputy Chief Engineer for the New York State Department of Transportation. He received a Bachelor of Technology with honors in civil engineering from the Indian Institute of Technology, Bombay, India; Master of Science in civil engineering from South Dakota School of Mines and Technology; and Master of Business Administration from the University of Minnesota. Mr. Shirole was also a Transportation Fellow at Harvard University. He has published some 30 papers and other publications in national and international journals and is internationally recognized as an authority on bridge management systems. He is a member of the Subcommittee on Bridges and Structures and Chairman of Committee T-11 on Research of the American Association of State Highway and Transportation Officials and Chairman of TRB Committees on Construction Management and Bridge Management. He was an advisor to the Strategic Highway Research Program (SHRP) from its inception and Chairman of its Expert Panel on Structures Research. In 1995 the 26,000-member American Public Works Association selected Mr. Shirole for its prestigious Top Ten Public Works Leader in North America award. Mr. Shirole is an elected Fellow of the Institution of Engineers.

Robert A. P. Sweeney is System Officer for Canadian National Railways' bridges, buildings, culverts, tunnels, and miscellaneous other structures. He holds a doctorate in engineering from Li Institution of Science and Technology, and his areas of expertise include theoretical and practical carrying capacity, design, maintenance, testing, and asset preservation of railway and highway bridges. Before joining Canadian National Railways, he was Design Engineer with the Quebec Department of Highways. In addition to having published many reports, he has lectured extensively. Dr. Sweeney is a member of domestic and international engineering associations, commissions, and NCHRP panels, Chairman of the NSF-American Railway Association Committee on Railroad Bridge Research, and the current chairman of the TRB Committee on Concrete Bridges.

Paul Zia is Distinguished University Professor and Alumni Distinguished Graduate Professor at North Carolina State University. He received a bachelor's degree from the National Chiao Tung University (China), master's degree from the University of Washington, and Ph.D. from the University of Florida. He served as head of the Department of Civil Engineering at NCSU from 1979 to 1988. In addition to teaching and research in precast, prestressed, and reinforced concrete structures as well as high-performance concrete, he has served as a consultant to the design and construction industry. He has been involved in investigations of many complex structural problems, including the Montreal Olympic Stadium, Miami rapid transit system, several nuclear containment structures, and large sports arenas. An active member of the American Concrete Institute (ACI), American Society of Civil Engineers (ASCE), Prestressed Concrete Institute (PCI), American Society for Engineering Education, National Society of Professional Engineers, and TRB, he has served as chairman or member of many technical and administrative committees of these organizations. He is a former member of the Executive Committee of TRB and served as president of ACI from 1989 to 1990. A member of the National Academy of Engineering, Dr. Zia has received many awards, including the Lamme Medal and Western Electric Fund Award from ASEE; T. Y. Lin Award, Raymond C. Reese Award, and A. J. Boase Award from ASCE; Joe W. Kelly Award from ACI; and Martin P. Korn Award from PCI. He was elected an Honorary Member of ASCE in 1988. In recognition of his distinguished accomplishments, in 1993 the NCSU Board of Trustees awarded him the University's highest honor, the Alexander Quarles Holladay Medal of Excellence.

The **Transportation Research Board** is a unit of the National Research Council, which serves the National Academy of Sciences and the National Academy of Engineering. The Board's purpose is to stimulate research concerning the nature and performance of transportation systems, to disseminate the information produced by the research, and to encourage the application of appropriate research findings. The Board's program is carried out by more than 330 committees, task forces, and panels composed of more than 3,900 administrators, engineers, social scientists, attorneys, educators, and others concerned with transportation; they serve without compensation. The program is supported by state transportation and highway departments, the modal administrations of the U.S. Department of Transportation, and other organizations and individuals interested in the development of transportation.

The National Academy of Sciences is a private, nonprofit, self-perpetuating society of distinguished scholars engaged in scientific and engineering research, dedicated to the furtherance of science and technology and to their use for the general welfare. Upon the authority of the charter granted to it by the Congress in 1863, the Academy has a mandate that requires it to advise the federal government on scientific and technical matters. Dr. Bruce M. Alberts is president of the National Academy of Sciences.

The National Academy of Engineering was established in 1964, under the charter of the National Academy of Sciences, as a parallel organization of outstanding engineers. It is autonomous in its administration and in the selection of its members, sharing with the National Academy of Sciences the responsibility for advising the federal government. The National Academy of Engineering also sponsors engineering programs aimed at meeting national needs, encourages education and research, and recognizes the superior achievements of engineers. Dr. Harold Liebowitz is president of the National Academy of Engineering.

The Institute of Medicine was established in 1970 by the National Academy of Sciences to secure the services of eminent members of appropriate professions in the examination of policy matters pertaining to the health of the public. The Institute acts under the responsibility given to the National Academy of Sciences by its congressional charter to be an adviser to the federal government and, upon its own initiative, to identify issues of medical care, research, and education. Dr. Kenneth I. Shine is president of the Institute of Medicine.

The National Research Council was organized by the National Academy of Sciences in 1916 to associate the broad community of science and technology with the Academy's purpose of furthering knowledge and advising the federal government. Functioning in accordance with general policies determined by the Academy, the Council has become the principal operating agency of both the National Academy of Sciences and the National Academy of Engineering in providing services to the government, the public, and the scientific and engineering communities. The Council is administered jointly by both the Academies and the Institute of Medicine. Dr. Bruce M. Alberts and Dr. Harold Liebowitz are chairman and vice chairman, respectively, of the National Research Council.

Abbreviations used without definitions in TRB publications:

AASHO	American Association of State Highway Officials
AASHTO	American Association of State Highway and Transportation Officials
ASCE	American Society of Civil Engineers
ASME	American Society of Mechanical Engineers
ASTM	American Society for Testing and Materials
FAA	Federal Aviation Administration
FHWA	Federal Highway Administration
FRA	Federal Railroad Administration
FTA	Federal Transit Administration
IEEE	Institute of Electrical and Electronics Engineers
ITE	Institute of Transportation Engineers
NCHRP	National Cooperative Highway Research Program
NCTRP	National Cooperative Transit Research and Development Program
NHTSA	National Highway Traffic Safety Administration
SAE	Society of Automotive Engineers
TRB	Transportation Research Board

NATIONAL ACADEMY PRESS
ISBN 0-309-06109-